Bitlis Eren Üniversitesi
Fen Bilimleri Dergisi

Bitlis Eren University
Journal of Science

ISSN : 2147-3129
e-ISSN : 2147-3188

Cilt / *Volume*: 11 Sayı / *Number*: 3 Yıl / *Year*: 2022

Yazışma Adresi

Bitlis Eren Üniversitesi
Lisansüstü Eğitim Enstitüsü
13000, Merkez, Bitlis/TÜRKİYE
Tel: 0 (434) 2220071

https://dergipark.org.tr/tr/pub/bitlisfen

BEU FBD

Bitlis Eren Üniversitesi Fen Bilimler Dergisi

Bitlis Eren University Journal of Science

Yıl/*Year:* 2022 - Cilt/*Volume:* 11 - Sayı/*Number:* 3

Editör (Yayın) Kurulu / *Editorial Board*

Danışma Kurulu / *Advisory Board*

Dergi Hakkında / *About Journal*

Bitlis Eren Üniversitesi Fen Bilimleri Dergisi, mühendislik ve temel bilimler alanlarındaki gelişmeleri ve yenilikleri takip etmek, meslek kuruluşlarının, araştırmacıların ve bireylerin ulusal ve uluslararası gelişimlerine katkıda bulunmak ve bu alanlarda elektronik bir kaynak oluşturmak amacıyla yayımlanmaktadır. Derginin yazım dili Türkçe veya İngilizcedir. Fen Bilimleri Dergisi, Bitlis Eren Üniversitesi Lisansüstü Eğitim Enstitüsü yayını olup, 2012 yılından bu yana ücretsiz ve açık erişimli olarak yayın hayatına devam etmektedir. Mühendislik ve temel bilimlerin bilgi tabanına ve teknolojik gelişmelere ışık tutması amacıyla bu alanlarda yapılmış deneysel ve teorik ilerlemeleri konu alan özgün araştırma makalelerine yer verilmektedir. Dergiye gönderilen çalışmaların benzerlik oranı %15'i geçmemelidir. Yazım kurallarına uymayan makaleler, hakemlere gönderilmeden önce düzeltilmek üzere yazara geri gönderilir. Bu nedenle, derginin yazım kuralları dikkate alınmalıdır. Ayrıca, editörlerden yazarlara iletilen düzeltmelere veya taleplere 30 gün içerisinde cevap verilmediği takdirde ilgili makaleler reddedilir. Makaleler şekiller ve tablolar dâhil 20 sayfayı geçmemelidir. Dergiye yayın için gönderilen makaleler en az iki hakem tarafından değerlendirilir. Yazarlardan hakem önerisi talep edilmemektedir. Makalelerin dergide yayımlanabilmesi için hakemler tarafından olumlu görüş bildirilmesi gerekmektedir. Dergi Editör Kurulu, hakem raporlarını (*en aziki hakemin değerlendirmeleri geldikten sonra*) dikkate alarak makalelerin yayımlanmak üzere kabul edilip edilmemesine karar verir. Fen Bilimleri Dergisi, yılda dört defa (*Mart, Haziran, Eylül, Aralık*) yayımlanmaktadır. **Dergimiz Tübitak-Ulakbim Mühendislik ve Temel Bilimler Veri Tabanı Dergi Listesinde taranmaktadır.**

B.E.Ü. Fen Bilimleri Dergisi 11(3), 2022 / *B.E.U. Journal of Science 11(3), 2022*
İÇİNDEKİLER / *CONTENTS*

Bitlis Eren Üniversitesi Fen Bilimleri Dergisi
BİTLİS EREN UNIVERSITY JOURNAL OF SCIENCE
ISSN: 2147-3129/e-ISSN: 2147-3188
VOLUME: 11 NO: 3 PAGE: 733-743 YEAR: 2022
DOI: 10.17798/bitlisfen.997662

Pr1.4-xLaxSr1.6Mn2O7 (x: 0; 0,4; 0,7; 1,0) Çift Perovskit Manganit Bileşiklerin Yapısal ve Elektriksel Özelliklerinin İncelenmesi

Atilla COŞKUN[1*], Büşra ZOR[1]

[1]*Muğla Sıtkı Koçman Üniversitesi Fen Fakültesi Fizik Bölümü 48000 Muğla Türkiye*
(ORCID: 0000-0002-6695-0696) (ORCID: 0000-0002-8838-0102)

Anahtar Kelimeler: Sol-jel, XRD, AFM, Metakl-yalıtkan,

Öz:
Bu çalışmada sol-jel yöntemi kullanılarak hazırlanan ve 1000 ºC'de hava ortamında 24 saat sinterlenen $Pr_{1.4-x}La_xSr_{1.6}Mn_2O_7$ (x:0; 0.4; 0.7; 1.0) bileşiklerinin yapısal, morfolojik ve elektriksel özellikleri incelenmiştir. X-ışınları kırınım desenleri (XRD) analizleri sonucunda, bileşiklerin farklı oranlarda I4/mmm uzay grubuna sahip (tetragonal) çift perovskit ve $R\bar{3}c$ uzay gurubuna sahip (trigonal) tek perovskit bileşiklerinden meydana geldiğini ortaya koymuştur. Tüm bileşikler içerisinde baskın olan perovskit fazın, tek perovskit faz olduğu ve artan La katkılamasına bağlı olarak bu fazın ağırlık yüzdesinin arttığı yapılan XRD arıtımları sonucunda bulunmuştur. Bileşiklerin atomik kuvvet mikroskobu (AFM) ve enerji dağılımlı x-ışını spektroskopi (EDS) ataçmanına sahip taramalı elektron mikroskobu (SEM) analizlerinden, La iyonlarının Pr iyonları ile yer değiştirmesine bağlı olarak, yüzeydeki tanelerin büyüdüğü ve boşlukların azaldığı bulunmuştur. EDS analizleri sonucunda hedeflenen bileşiklerin stokiyometrilerine uygun bir şekilde başarılı olarak üretildiklerini ortaya koymuştur. Sıcaklığa bağlı olarak değişen elektriksel direnç ölçümlerinden (R-T), yarıiletken davranış gösteren ve La iyonu içermeyen $Pr_{1.4}Sr_{1.6}Mn_2O_7$ bileşiğinin direnç davranışının La iyonlarının yapıya girmesi ile değiştiği ve en çok La içeren bileşiğin yaklaşık 165,4 K'de metal-yalıtkan (T_{IM}) faz geçişi gösterdiği bulunmuştur.

Investigation of Structural and Electrical Properties of Pr1.4-xLaxSr1.6Mn2O7 (x: 0; 0.4; 0.7; 1.0) Double Perovskite Manganite Compounds

Anahtar Kelimeler: Sol-gel, XRD, AFM, Metakl-insulator,

Abstract:
In this study, the structural, morphological and electrical properties of Pr1.4-xLaxSr1.6Mn2O7 (x:0; 0.4; 0.7; 1.0) compounds prepared using the sol-gel method and sintered for 24 hours in air at 1000 ºC were investigated. As a result of X-ray diffraction patterns (XRD) analysis, it was revealed that the compounds were composed of double perovskites with I4/mmm space group (tetragonal) and single perovskite compounds with R3̄c space group (trigonal) in different ratios. It was found as a result of XRD refinements that the dominant perovskite phase among all compounds was the only perovskite phase and the weight percentage of this phase increased due to the increasing La doping. From the scanning electron microscopy (SEM) analyzes of the compounds with atomic force microscopy (AFM) and energy dispersive x-ray spectroscopy (EDS) attachment, it was found that the grains on the surface grew and the voids decreased due to the displacement of La ions with Pr ions. As a result of EDS analysis, it was revealed that the targeted compounds were successfully produced in accordance with their stoichiometry. From the electrical resistance measurements (R-T) that change depending on the temperature, it is seen that the resistive behavior of the Pr1.4Sr1.6Mn2O7 compound, which shows

*Sorumlu yazar: acoskun@mu.edu.tr
Geliş Tarihi: 20.09.2021, Kabul Tarihi: 02.07.2022

semiconductor behavior and does not contain La ions, changes with the introduction of La ions into the structure, and that the compound containing the most La is a metal-insulator (TIM) at approximately 165.4 K.) was found to show a phase transition.

1. Giriş

Manyetokalorik etkiye (MKE) dayanan manyetik soğutma (MS) sistemlerinin, günümüzde kullanılan gazlı soğutma teknolojilerine alternatif olabileceğinin ortaya çıkması, bu sistemler üzerinde oldukça yoğun çalışmalar yapılmasına neden olmuştur [1-3]. Özellikle bu konudaki çalışmalara öncülük eden Gd ve Gd bazlı alaşımların oda sıcaklığı civarında yüksek MKE değerlerine sahip olduklarının keşfinden sonra [4-6], farklı alaşımlar üzerine yapılan çalışmalar da ivme kazanmıştır. Ancak bu alaşımların nadir toprak elementi içeriyor olmalarından dolayı, herhangi bir soğutma sisteminde kullanılmaları söz konusu olduğunda, oldukça yüksek maliyetlerin ortaya çıkacağı anlaşılmıştır. Dolayısıyla çalışmalar, daha ucuza mal edilebilecek ve nadir toprak elementleri içermeyen oksitli bileşiklerin bulunması üzerine yoğunlaşmıştır. Araştırmaların sonucunda, genel formülü ABO_3 olan bazı perovskit bileşiklerin oda sıcaklığı civarında yüksek MKE sergiledikleri bulunmuştur [7-9]. Bu bileşiklerden biri olan $LaMnO_3$ antiferromanyetik ve yalıtkan özellik göstermektedir. Ancak, bir miktar lantanın +1 veya +2 değerlikli elementlerle değiştirilmesi sonucunda, bu bileşiğin manyetik ve elektriksel özelliklerinde büyük değişiklikler meydana gelmektedir. A bölgesini genellikle lantan ve lantan yerine belirli oranlarda katılan +2 değerlikli Ca, Sr. Ba, Pb gibi veya +1 değerlikli Ag, Na, K gibi iyonların, B bölgesini ise mangan iyonlarının temsil ettiği ve literatürde manganitler ($(La_{1-x}A_x)MnO_3$) olarak adlandırılan bileşikler oldukça popüler olarak günümüzde de çalışılmaktadır [10-13]. Bu bileşiklerin üretim aşamalarının kolay ve hızlı olması, ilk üretimden sonra elde edilen tanelerin nano boyuttan başlayarak sinterleme sıcaklığındaki ayarlamalara bağlı olarak istenilen büyüklüklere ayarlanabilmesi, üretim aşamasında genellikle nitratlı tuzların seçilmesinden dolayı oldukça ucuza mal edilmeleri ve yapılan çok küçük katkılamalarda bile paramanyetik-ferromanyetik faz geçiş sıcaklığında (Curie sıcaklığı, T_C) oldukça büyük oynamaların olması bu bileşiklerin Gd ve Gd bazlı alaşımlara karşı üstünlüklerinden bazıları olarak sayılabilir.

Manganit bileşiklerinde A-bölgesinin yanı sıra Mn iyonlarının yer aldığı B-bölgesine de farklı element katkılamalarının yapıldığı çalışmalara rastlanılmaktadır [14-16]. Bunlardan başka, A ve B-bölgelerine eş zamanlı yapılan katkılamaların olduğu çalışmalara da literatürde rastlanılmaktadır [17,18]. Hem A-bölgesi hem de B-bölgesine yapılan element katkılamalarının amacı, oda sıcaklığı civarında, düşük manyetik alan uygulamalarında yüksek MKE değerine sahip bileşiklerin elde edilmesidir. Özellikle yapılan farklı miktarlardaki katkılamalar sonucunda elde edilen bileşikler, yapısal olarak da faz dönüşümü sergilediklerinde oldukça ilginç fiziksel özelliklere sahip oldukları bulunmuştur.

Yukarıda sözü edilen manganit ailelerinden başka, çift perovskit manganit bileşikleri olarak da adlandırılan ve kimyasal formları $A_{2-2x}B_{1+2x}Mn_2O_7$ (A, La, Nd veya Pr gibi üç değerlikli bir nadir toprak elementi ve B, iki değerlikli Sr, Ca veya Ba gibi bir element) olan bileşikler üzerinde de çalışmalar yapılmaktadır [19-21]. Bu çift perovskit manganit aileleri, tabakalı kristal yapıları ve anizotropik değişim etkileşimleri ile yaygın $La_{1-x}A_xMnO_3$ tipi perovskit manganit bileşiklerinden farklılıklar gösterir. Ayrıca uygulanan dış manyetik alana karşı göstermiş oldukları devasa manyeto direnç özelliği ile de manyetik sensor elemanı olarak kullanılma potansiyelleri oldukça yüksektir. Bu bileşiklerin T_C civarında gösterdikleri manyetik entropi değişimlerinin oldukça geniş olması, teknolojik olarak bu bileşiklerin önemini arttırmaktadır [22].

Bu çalışmada, sol-jel yöntemi kullanılarak, A bölgesinde farklı miktarlarda, iki farklı nadir toprak elementi içeren $Pr_{1.4-x}La_xSr_{1.6}Mn_2O_7$ (x:0; 0.4; 0.7; 1.0) çift perovskit manganit bileşikleri nano boyutta üretilmiş, yapısal ve elektriksel özelliklerinin değişimleri incelenmiştir.

2. Materyal ve Metot

$Pr_{1.4-x}La_xSr_{1.6}Mn_2O_7$ (x:0; 0.4; 0.7; 1.0) çift perovskit manganit bileşikleri sol-jel yöntemi kullanılarak nano boyutta üretilmişlerdir. Bu bileşikleri üretmek için, yüksek saflıkta $Pr(NO_3)_3{*}6H_2O$, $La(NO_3)_3{*}6H_2O$, $Mn(NO_3)_2{*}4H_2O$, $Sr(NO_3)_2$ tuzları kullanılmıştır. Bileşikleri uygun stokiyometrik oranlarda elde etmek için, hassas terazi kullanılarak tartma işlemleri gerçekleştirilmiştir. Saf su nitrat tuzlarını çözdürmek için kullanılmıştır. Sıvı hale getirilen başlangıç tuzlarının tamamı 600 ml'lik beher içerisine alınarak ısıtıcılı manyetik karıştırıcı üzerine konulmuştur. Bu işlem her bir bileşik için ayrı ayrı yapılmıştır. Manyetik karıştırıcı üzerinde kademeli olarak, 100 ^oC'den 350 ^oC'ye kadar olacak şekilde ısıtma işlemi kontrollü olarak yapılmıştır. Bileşiklerin polimer yapı

oluşturup jel haline gelmesi için sitrik asit ve etilen glikol karıştırma işleminin hemen başında sıvı karışıma eklenmiştir. Karışım içerisindeki etilen glikol ve sitrik asit için, 1 mol metal bileşik için 10 mol sitrik asit ve 10 mol etilen glikol katsayısı baz alınmıştır. Jelleşme sonucunda elde edilen çökelti kendi beheri içerisinde, yüksek sıcaklık fırınında 600 ^{o}C'de 10 saat yakılmıştır. Böylece toz çökelti içerisindeki organik kirlilik ve kalıntıların yanarak bileşik içerisinden uzaklaşması sağlanmıştır. Bu işlemin sonunda, homojen, nano boyutta, dört farklı kimyasal forma sahip başlangıç toz bileşikleri elde edilmiştir. Daha sonra toz bileşiklere şekil vermek amacıyla, her birinden 1 gram alınarak presleme aparatı yardımıyla yaklaşık 4 ton basınç uygulanarak (30-40 sn arası) 1,3 cm çapında dairesel tabletler elde edilmiştir. Tabletler, yüksek sıcaklıklara dayanıklı alimüna kayıklar üzerine yerleştirilmiş ve aynı anda 1000 ^{o}C'de hava ortamında 24 saat sinterlenmişlerdir.

Bileşiklerin kristal yapı özelliklerinin (örgü parametreleri, simetri grupları) belirlenmesi için Bruker D8 Advance X-ışını difraktometresi kullanılmıştır. Ölçümler, 0.01^{o} adımlarla 20^{o}<2θ<90^{o} arasında gerçekleştirilmiştir. Bileşiklerin yüzey morfolojileri ve tane büyüklükleri değişimleri, JEOL, JSM 5800 marka, enerji dağılımlı x-ışını spektroskopisine (EDS) sahip, alan emisyonlu taramalı elektron mikroskobu (FE-SEM) ve NT-MTD marka atomik kuvvet mikroskobu (AFM) kullanılarak incelenmiştir. Metal-yalıtkan faz geçiş sıcaklıklarının (T_{IM}) bulunması için 10-320 K sıcaklık aralığında çalışan Janis marka düşük sıcaklık kapalı devre kriyostat sistemi kullanılmıştır.

3. Bulgular ve Tartışma

3.1 XRD Analizleri

Şekil 1'de XRD desenlerini kullanarak malzeme analizi (arıtım) yapan programı MAUD kullanılarak elde edilen XRD grafikleri (teorik ve deneysel) verilmiştir. Arıtım aşamasında bileşiklerin hem tek hem de çift perovskit yapıyı aynı anda içerdiği bulunmuştur. Bu nedenle dört bileşiğin arıtımı yapılırken hem I4/mmm tetragonal simetriye sahip çift perovskit, hem de $R\bar{3}c$ trigonal simetriye sahip tek perovskit faz, eş zamanlı olarak arıtıma eklenmiştir. Arıtımlar sonucunda elde edilen, kristal yapı içerisindeki tek ve çift perovskit fazların hacimsel yüzdeleri ve kristal örgü parametreleri Tablo 1'de verilmiştir. Tablo 1'deki verilerden de görüleceği üzere dört bileşik içerisindeki baskın olan perovskit fazın, tek perovskit faz olduğu görülmektedir. Bu çalışmada sistematik olarak A bölgesindeki Pr yerine üç farklı miktarda La katkılaması yapılmıştır. La içermeyen $Pr_{1.4}Sr_{1.6}Mn_2O_7$ bileşiği, en fazla çift perovskit fazın içermektedir. Bileşikler içerisindeki La katkı miktarı arttıkça tek perovskit fazın hacimsel yüzdesinin arttığı, çift perovskit fazın hacimsel yüzdesinin ise azaldığı bulunmuştur. Tek perovskit fazın **a** örgü parametresi La katkı miktarı arttıkça artarken, aksine, çift perovskit fazın **a** örgü parametresi La katkı miktarı arttıkça azalmıştır. Çift perovskit fazın **c** örgü parametresi La katkı miktarı arttıkça artarken, tek perovskit fazın **c** örgü parametresinde sistematik bir değişiklik gözlenmemiştir.

Tablo 1. Bileşiklerin kristal örgü parametreleri ve fazların hacimsel yüzdeleri

	$Pr_{1.4}Sr_{1.6}Mn_2O_7$		**$Pr_{1.0}La_{0.4}Sr_{1.6}Mn_2O_7$**		**$Pr_{0.7}La_{0.7}Sr_{1.6}Mn_2O_7$**		**$Pr_{0.4}La_{1.0}Sr_{1.6}Mn_2O_7$**	
	I4/mmm	**$R\bar{3}c$**	**I4/mmm**	**$R\bar{3}c$**	**I4/mmm**	**$R\bar{3}c$**	**I4/mmm**	**$R\bar{3}c$**
a=b (Å)	**3,8848**	5,4592	**3,8791**	5,4667	**3,8734**	5,4752	**3,8693**	5,4845
c (Å)	19,2476	13,3385	19,1818	13,3535	19,1788	13,3553	19,1261	13,3557
Faz yüzdeleri	**31,98**	68,02	**27,39**	72,61	**25,61**	74,39	**21,88**	78,12

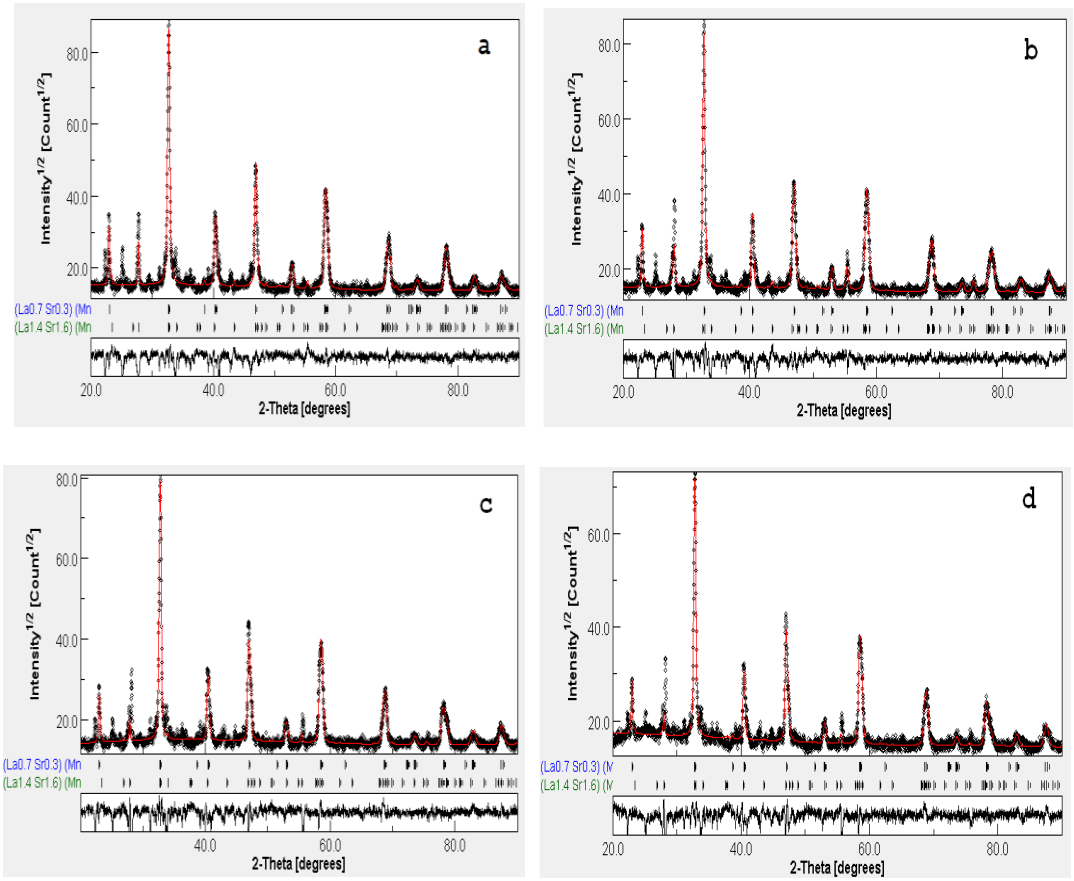

Şekil 1. Bileşiklerin arıtımları yapılmış XRD desenleri, sırasıyla a) $Pr_{1.4}Sr_{1.6}Mn_2O_7$ b) $Pr_{1.0}La_{0.4}Sr_{1.6}Mn_2O_7$ c) $Pr_{0.7}La_{0.7}Sr_{1.6}Mn_2O_7$ d) $Pr_{0.4}La_{1.0}Sr_{1.6}Mn_2O_7$

3.2. AFM Analizleri

Bileşiklerin AFM görüntüleri kontak mod kullanılarak, cihazın maksimum alan tarama sınırı olan 50 µm x 50 µm ebatlarında alınmıştır. Daha sonra ise isteğe bağlı alan sınırları seçilerek farklı bölgelerin yüzey taraması iki boyutlu olarak yapılmıştır. İki boyutlu görüntü üzerinden, program yardımıyla aynı yüzeylerin üç boyutlu görüntüsü eş zamanlı olarak taranmıştır. Şekil 2'de bileşiklerin 5 µm x 5 µm ebatlarında alınan iki ve üç boyutlu görüntüleri verilmektedir. La iyonlarının Pr iyonları ile yer değiştirmesi sonucunda elde edilen bileşiklerde, La iyon katkısının artmasına bağlı olarak bileşiklerin yüzey morfolojilerinin değiştiği, tanelerin birleşerek daha büyük tane oluşumlarını meydana getirdiği görülmektedir. Sistematik olarak, La katkı miktarının artması taneler arasındaki boşlukların da azalmasına neden olmuş ve yüzeyde daha sıkı paketli ve katmanlı bir şekilde tane oluşumu, özellikle, bileşiklerin üç boyutlu görüntülerinden açıkça gözlenmiştir.

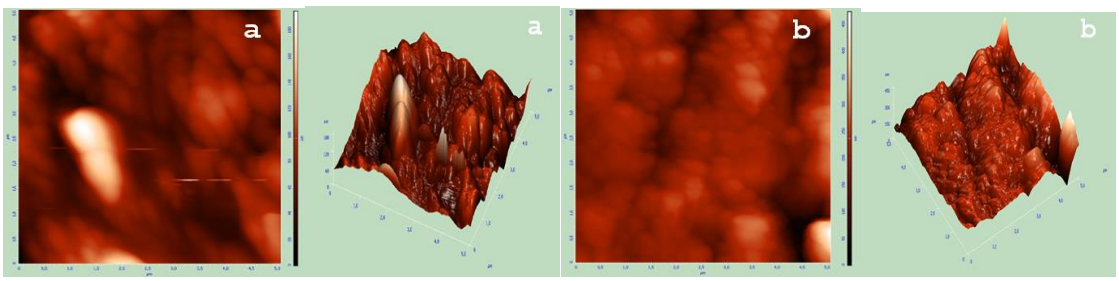

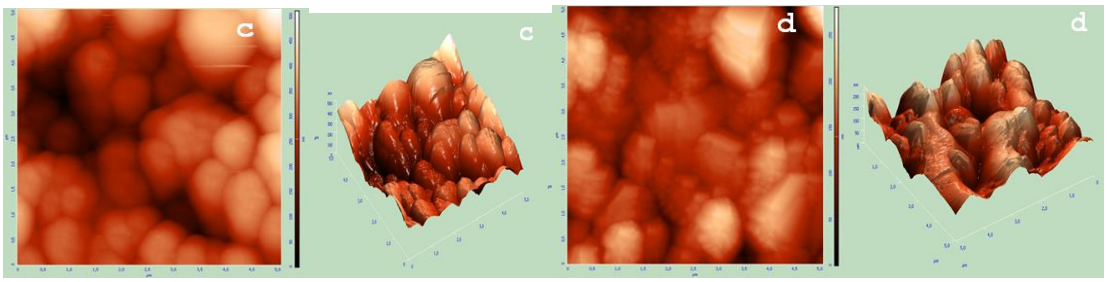

Şekil 2. Bileşiklerin (2-D, üstte) ve (3-D, altta) AFM görüntüleri, sırasıyla a) $Pr_{1.4}Sr_{1.6}Mn_2O_7$ b) $Pr_{1.0}La_{0.4}Sr_{1.6}Mn_2O_7$ c) $Pr_{0.7}La_{0.7}Sr_{1.6}Mn_2O_7$ d) $Pr_{0.4}La_{1.0}Sr_{1.6}Mn_2O_7$

3.3 SEM Analizleri

Bileşiklerin büyütülen yüzeylerinin SEM görüntüleri Şekil 3'de gösterilmiştir. Bu büyütmede alınan görüntülerin yüzeyindeki tanelerin büyüklüğü hakkında çok net bir bilgi vermek mümkün değildir. Çünkü yüzeydeki tane oluşumlarının sınırları belirgin değildir. Ancak görüntülerdeki ilk göze batan özellik, La katkısının artışına bağlı olarak tanelerin bir araya gelerek kümeli bir yapı oluşumuna neden olmalarıdır. Özellikle bu oluşum, La katkı miktarı bileşik içerisinde arttığında artmış ve bir araya gelen tanelerin yüzeyin üstünde farklı şekil ve yönlerde birikmeleri ile kendini göstermiştir. Bileşiklerin yüzeyinde artan La katkısına bağlı olarak boşlukların azaldığı görülmektedir.

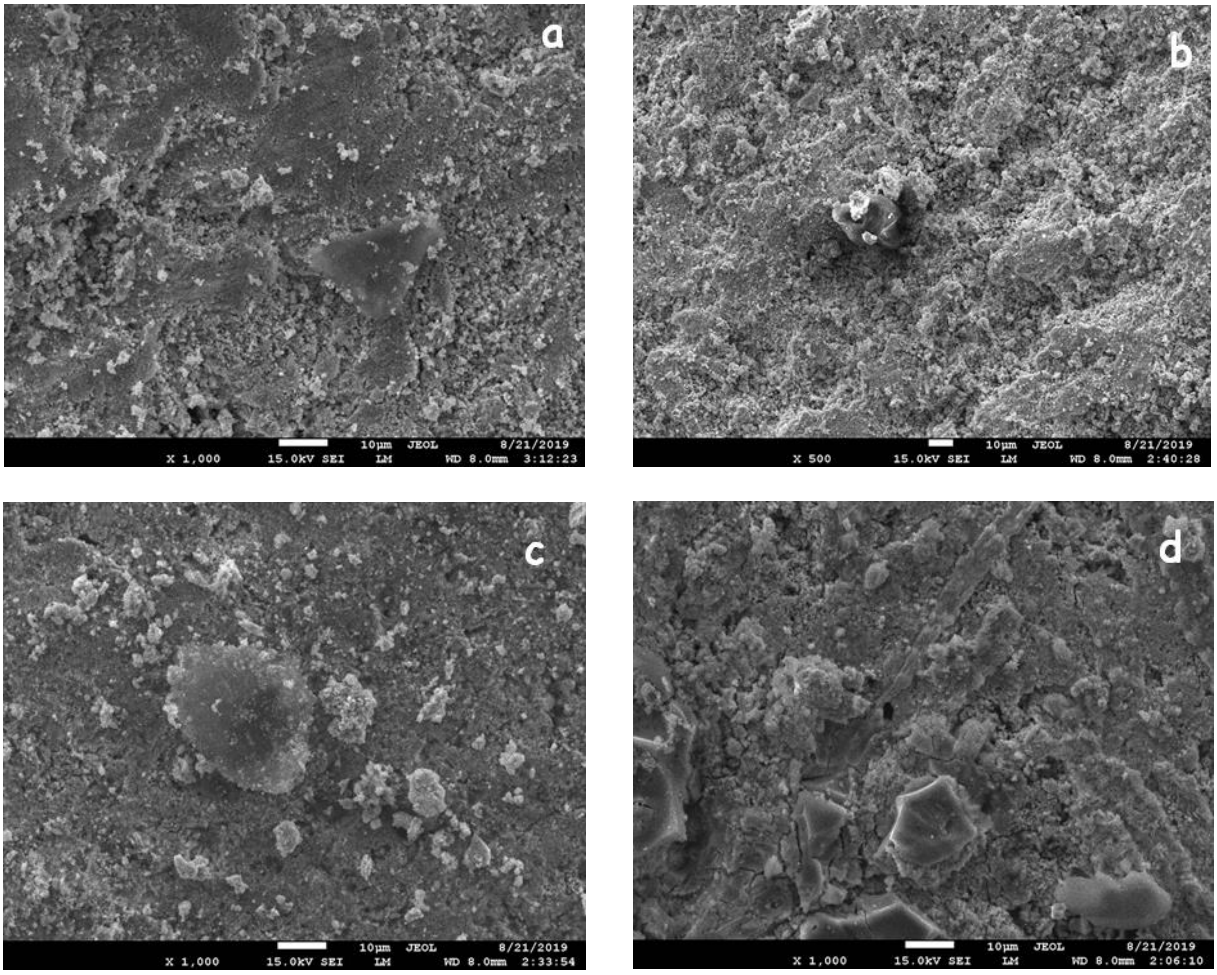

Şekil 3. Bileşiklerin SEM görüntüleri, sırasıyla a) $Pr_{1.4}Sr_{1.6}Mn_2O_7$ b) $Pr_{1.0}La_{0.4}Sr_{1.6}Mn_2O_7$ c) $Pr_{0.7}La_{0.7}Sr_{1.6}Mn_2O_7$ d) $Pr_{0.4}La_{1.0}Sr_{1.6}Mn_2O_7$

3.4. EDS Analizleri

Bileşiklerin EDS analizleri, 250 büyütmede elde edilen SEM görüntülerinin dört farklı bölgesinden alınarak yapılmıştır. Şekil 4'de, La katkısı içermeyen $Pr_{1.4}Sr_{1.6}Mn_2O_7$ bileşiğinin EDS yapılan dört farklı bölgesinin işaretlendiği SEM fotoğrafı, bu bölgelerin EDS spektrumları, ağırlık yüzdeleri tablosu ve bunların kullanılması ile bileşiğin hesaplanan yaklaşık kimyasal formülünü gösteren grafikler verilmiştir. Bu bileşiğe ait elementlerin ağırlık yüzdelerini gösteren Tablo' da, B4-2 olarak işaretlenen bölgedeki elementlere ait ağırlık yüzdelerinin diğer bölgelerden oldukça farklı olduğu görülmektedir. Bileşiğin kimyasal formülü hesaplanırken bu bölge ayrı tutularak ve diğer üç bölgenin ortalaması alınarak hesaplamalar yapılmıştır. Hesaplamalar yapılırken hem çift hem de tek perovskit olma ihtimali göz önüne alınmış, iki ihtimalde hesaplanmıştır. B4-2 bölgesinin kimyasal formülü $Pr_{0.7}Sr_{0.3}MnO_{3-x}$ olarak (tek perovskit), diğer üç bölgenin ortalamasının kimyasal formülü ise $Pr_{1.4}Sr_{1.55}Mn_{2.5}O_{7+x}$ olarak (çift perovskit) bulunmuştur. Bu iki farklı perovskit ailesinin varlığı, bu bileşiğe ait XRD analizlerinde de ortaya çıkarılmıştı. $Pr_{1.4}Sr_{1.6}Mn_2O_7$ bileşiğinin EDS analizi sonucunda elde edilen sonuçlarının, XRD arıtımı sonucunda elde edilen bulguları desteklediği görülmektedir.

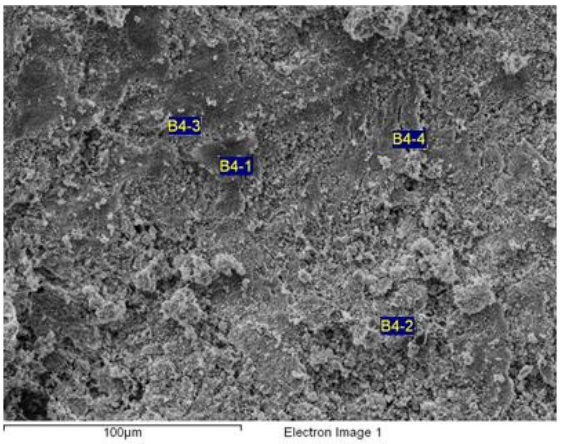

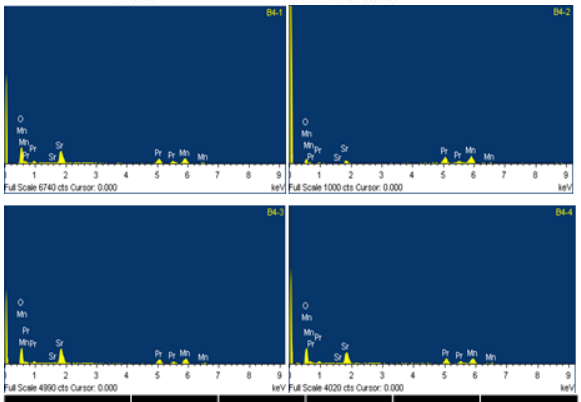

Bölge	B4-1	B4-2	B4-3	B4-4	Ortalama
O K	26.21	11.15	25.15	25.03	25.46
Mn K	22.96	28.62	22.79	23.58	23.11
Pr L	29.78	51.01	29.18	32.92	30.62
Sr L	21.06	9.11	22.79	18.74	20.86
Hesaplanan Kimyasal Formül	$Pr_{1.4}Sr_{1.55}Mn_{2.5}O_{7+x}$				

Şekil 4. $Pr_{1.4}Sr_{1.6}Mn_2O_7$ bileşiğinin EDS yapılan dört farklı bölgesinin işaretlendiği SEM fotoğrafı, bu bölgelerin EDS spektrumları, ağırlık yüzdeleri tablosu ve bunların kullanılması ile hesaplanan bileşiğin kimyasal formülü

$Pr_{1.0}La_{0.4}Sr_{1.6}Mn_2O_7$, $Pr_{0.7}La_{0.7}Sr_{1.6}Mn_2O_7$ ve $Pr_{0.4}La_{1.0}Sr_{1.6}Mn_2O_7$ bileşiklerinin EDS yapılan dört farklı bölgesinin işaretlendiği SEM fotoğrafları, bu bölgelerin EDS spektrumları, elementlerin ağırlık yüzdeleri tabloları ve hesaplamalar sonucunda elde edilen, bileşiklere ait kimyasal formüller sırasıyla Şekil 5, Şekil 6 ve Şekil 7'de verilmiştir. La katkılı bileşiklerin tamamının spektrumlarında La iyonlarının varlığının olması, bu elementin başarılı bir şekilde A-bölgesindeki Pr iyonlarının yerine girdiğinin bir göstergesidir. Bu bileşiklerin dört farklı bölgesinden elde edilen elementlerin ağırlık

yüzdelerinin, ortalamaları alınmış ve bu ortalamadaki değerler hem tek hem de çift perovskit olma ihtimaline göre kimyasal formüllerin hesaplanmasında kullanılmıştır. Hesaplamaların sonucu, La katkılı bileşiklerin tamamının kimyasal formüllerinin çift perovskit fazla uyumlu olduğu ve neredeyse hedeflenen kompozisyonun aynısının elde edildiğini göstermiştir.

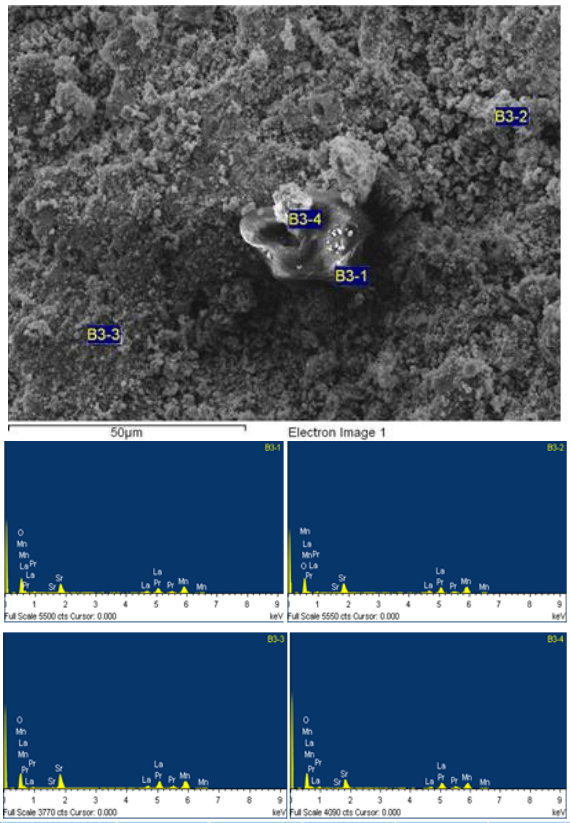

Bölge	B3-1	B3-2	B3-3	B3-4	Ortalama
O K	21.52	21.01	18.64	22.17	20.83
Mn K	25.69	24.81	24.30	19.98	23.70
La L	12.09	11.30	10.59	10.13	11.02
Pr L	25.55	26.29	28.82	31.40	28.01
Sr L	15.15	16.07	17.65	16.33	16.3
Hesaplanan Kimyasal Formül					$PrLa_{0.4}Sr_{1.1}Mn_{2.1}O_{7-x}$

Şekil 5. $Pr_{1.0}La_{0.4}Sr_{1.6}Mn_2O_7$ bileşiğinin EDS yapılan dört farklı bölgesinin işaretlendiği SEM fotoğrafı, bu bölgelerin EDS spektrumları, ağırlık yüzdeleri tablosu ve bunların kullanılması ile hesaplanan bileşiğin kimyasal formülü

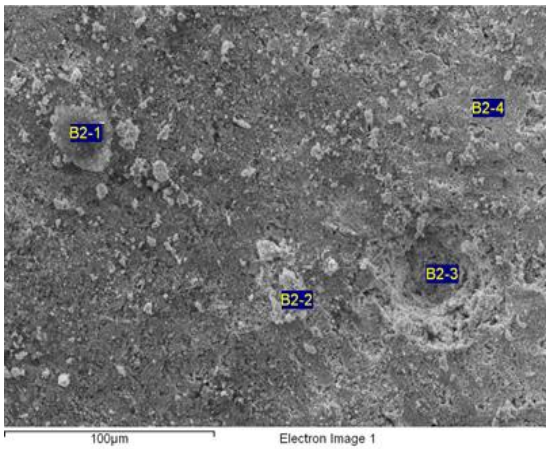

Bölge	B2-1	B2-2	B2-3	B2-4	Ortalama
O K	24.29	20.39	22.53	23.73	22.73
Mn K	22.72	23.40	24.06	23.22	23.35
La L	16.18	19.37	14.75	16.08	16.59
Pr L	17.90	18.53	13.11	15.59	16.28
Sr L	19.35	18.31	25.54	21.37	21.14
Hesaplanan Kimyasal Formül					$Pr_{0.7}La_{0.72}Sr_{1.5}Mn_{2.3}O_{7+x}$

Şekil 6. $Pr_{0.7}La_{0.7}Sr_{1.6}Mn_2O_7$ bileşiğinin EDS yapılan dört farklı bölgesinin işaretlendiği SEM fotoğrafı, bu bölgelerin EDS spektrumları, ağırlık yüzdeleri tablosu ve bunların kullanılması ile hesaplanan bileşiğin kimyasal formülü

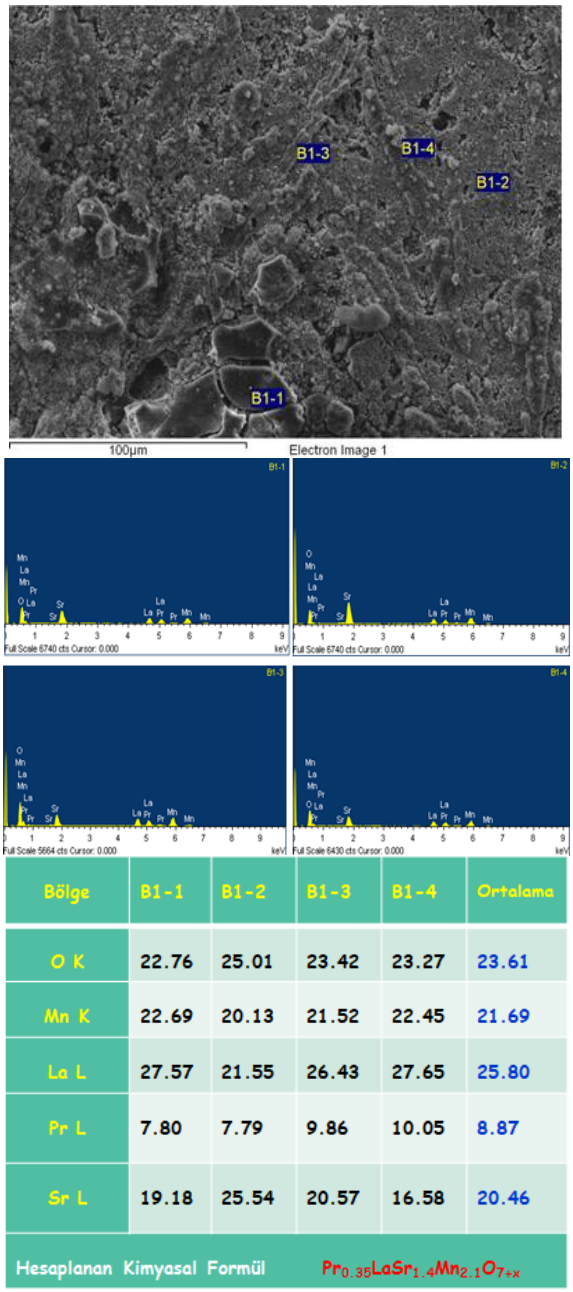

Bölge	B1-1	B1-2	B1-3	B1-4	Ortalama
O K	22.76	25.01	23.42	23.27	23.61
Mn K	22.69	20.13	21.52	22.45	21.69
La L	27.57	21.55	26.43	27.65	25.80
Pr L	7.80	7.79	9.86	10.05	8.87
Sr L	19.18	25.54	20.57	16.58	20.46
Hesaplanan Kimyasal Formül			$Pr_{0.35}LaSr_{1.4}Mn_{2.1}O_{7+x}$		

Şekil 7. $Pr_{0.4}La_{1.0}Sr_{1.6}Mn_2O_7$ bileşiğinin EDS yapılan dört farklı bölgesinin işaretlendiği SEM fotoğrafı, bu bölgelerin EDS spektrumları, ağırlık yüzdeleri tablosu ve bunların kullanılması ile hesaplanan bileşiğin kimyasal formülü

3.5 Sıcaklıkla Değişen Direnç Ölçümü (R-T) Analizleri

Şekil 8'de bileşiklere ait sıcaklıkla değişen direnç değerlerini gösteren grafikler bulunmaktadır. $Pr_{1.4}Sr_{1.6}Mn_2O_7$ bileşiğin direnç değişiminin, oda sıcaklığından 150 K'e kadar olan kısımda neredeyse aynı kaldığı, ancak 150 K'in altındaki sıcaklıklarda aniden arttığı görülmektedir. Bu tür bir direnç değişimi klasik yarıiletken davranıştan kaynaklanmaktadır. Dolayısıyla, iki farklı perovskit fazı içeren (tüm bileşikler içerisinde en fazla çift perovskit faz içerdiği XRD analizleri sonucunda bulunmuştu) bu bileşiğin yarıiletken özellik gösterdiğini söylemek mümkündür. La iyonlarının yer aldığı bileşiklerin direnç eğrilerinde oldukça dikkat çekici değişiklikler vardır. Öncelikle yapısında daha fazla La iyonu içeren bileşiklerin direnç değerlerinde kayda değer düşüşler olduğu söylenebilir. Bu durumu, La iyonlarının yapıya girmesi sonucunda, bileşiklerin tanelerinin büyümesine ve yüzeydeki boşlukların azalmasına bağlamak mümkündür. Çünkü tanelerin büyümesine bağlı olarak tane sınırları azalmış ve iletim mekanizması için direnç merkezleri olan tane sınırlarının azalmasına bağlı olarak, serbest elektronların hareketi kolaylaşmış; dolayısıyla bileşiklerin direnç değerlerinde azalma meydana gelmiştir. $Pr_{1.0}La_{0.4}Sr_{1.6}Mn_2O_7$ bileşiği T_{IM} faz geçişi göstermemekle birlikte, sıcaklığın azalması ile direnç değerlerinde dalgalı bir düşüş söz konusudur. Bu dalgalanmaların, azalan sıcaklıkla birlikte birbirlerine üstünlük sağlamaya çalışan, birbirinden farklı elektriksel özellik gösteren tek ve çift perovskit fazlardan kaynaklandığı düşünülmektedir. $Pr_{0.7}La_{0.7}Sr_{1.6}Mn_2O_7$ bileşiğinin direnç eğrisinde de benzer davranış gözlenmekle birlikte, yaklaşık 150 K sıcaklığı civarında (2-3 K aralığında) bir tepe oluşumu meydana gelmiştir. Bu tepe oluşumunun, bu bileşik içerisinde artan tek perovskit fazın baskınlığından kaynaklandığı ile ilişkilendirebiliriz. La katkısının en fazla olduğu $Pr_{0.4}La_{1.0}Sr_{1.6}Mn_2O_7$ bileşiğinin direnç davranışı, sahip olduğu T_{IM} faz geçişi nedeniyle diğer bileşiklerden ayrılmaktadır. Öncelikle, $Pr_{0.7}La_{0.7}Sr_{1.6}Mn_2O_7$ bileşiğinde 150 K civarında gözlenen tepenin bu bileşikte daha yüksek sıcaklıklara kayarak, yaklaşık 200 K civarında meydana geldiği bulunmuştur. Ayrıca bu bileşiğin, 165,4 K değerinde T_{IM} faz geçişine sahip olduğu görülmektedir.

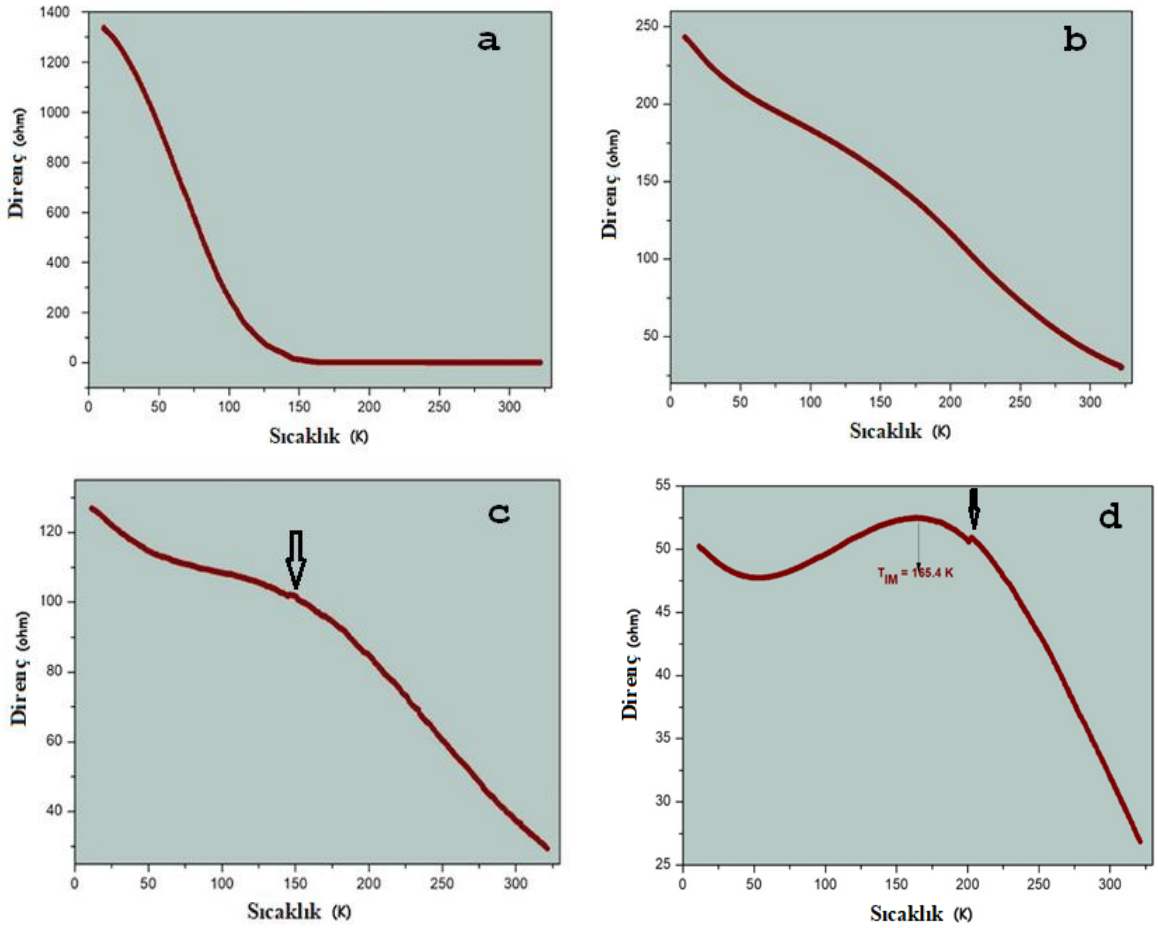

Şekil 8. Bileşiklerin sıcaklıkla değişen direnç eğrileri a) $Pr_{1.4}Sr_{1.6}Mn_2O_7$ b) $Pr_{1.0}La_{0.4}Sr_{1.6}Mn_2O_7$ c) $Pr_{0.7}La_{0.7}Sr_{1.6}Mn_2O_7$ d) $Pr_{0.4}La_{1.0}Sr_{1.6}Mn_2O_7$

4. Sonuç ve Öneriler

Bu çalışmada sol-jel yöntemi kullanılarak üretilmiş olan $Pr_{1.4-x}La_xSr_{1.6}Mn_2O_7$ (x:0; 0.4; 0.7; 1.0) bileşiklerinin yapısal, morfolojik ve elektriksel özellikleri incelenmiştir. XRD analizlerinden bileşiklerin tek ve çift perovskit fazı aynı anda kristal yapılarında içerdiği bulunmuştur. Kristal yapı içerisinde La iyonlarının Pr iyonları ile yer değiştirmesi sonucunda, artan La miktarına bağlı olarak bileşiklerdeki çift perovskit fazın hacimsel oranının azaldığı, tek perovskit fazınkininse arttığı bulunmuştur. Benzer şekilde, çift perovskit fazın **a** ve **c** örgü parametresi La katkılamasındaki artışa bağlı olarak azalırken, tek perovskit fazın **a** ve **c** örgü parametresi ise artmıştır. Tek perovskit fazın artan kristal örgü parametrelerini, La ve Pr iyonlarının iyonik yarıçapı ile ilişkilendirebiliriz. Dokuz koordinasyona sahip La iyonunun iyonik yarıçapı 1,216 Å iken aynı koordinasyona sahip Pr iyonununki ise 1,179 Å'dur. Dolayısıyla daha büyük atomların kristal yapıya girmesi sonucunda kristal örgü parametrelerinde bir artış meydana gelmiştir. Arıtım sonucunda elde edilen bulgular ve La ve Pr iyonlarının iyonik yarıçapları göz önüne alındığında, La iyonlarının tek perovskit fazın A-bölgesine, Pr iyonlarının ise çift perovskit fazın A-bölgesine yerleştiğini söylemek mümkündür. Artan La katkısına bağlı olarak, bileşiklerin yüzey morfolojileri değiştiği, yüzeydeki tanelerin büyüdüğü AFM ve SEM analizlerinden bulunmuştur. EDS analizlerinden hedeflenen stokiyometrilere uygun bileşiklerin başarılı bir şekilde üretildikleri görülmektedir. Başlangıçta yarıiletken özellik gösteren $Pr_{1.4}Sr_{1.6}Mn_2O_7$ çift perovskit manganit bileşiğinde, yapı içerisine La iyonları girmesindeki artışa bağlı olarak aşama aşama iletkenlik özellik kazandığı bulunmuştur. La iyonlarının yapıya girmesi sonucunda tanelerin büyümesi, buna bağlı olarak kristal örgü parametrelerindeki artışlar, serbest elektronların kristal yapı içerisinde daha az engelle karşılaşarak, daha rahat hareket etmelerine sebep olduğu düşünülmektedir. Bunun sonucunda La katkılı bileşiklerin direnç değerlerinde düşüş meydana gelirken, $Pr_{1.4}Sr_{1.6}Mn_2O_7$ bileşiği yarıiletken davranıştan artan La katkısına bağlı olarak, iletken davranışa doğru bir elektriksel faz geçişi sergilediği ortaya çıkarılmıştır.

Teşekkür

Yazarlar Muğla Sıtkı Koçman Üniversitesi Araştırma Laboratuvarları Araştırma ve Uygulama Merkezi Müdürlüğüne, XRD ve SEM-EDS analizlerindeki katkıları için teşekkür etmektedirler.

Yazarların Katkısı

Atilla Coşkun: Makale yazımı, karakterizasyon ölçümleri
Büşra Zor: Örnek üretimi, AFM ölçümleri

Çıkar Çatışması Beyanı

Yazarlar arasında herhangi bir çıkar çatışması bulunmamaktadır.

Araştırma ve Yayın Etiği Beyanı

Yapılan çalışmada araştırma ve yayın etiği kurallarına uyulmuştur.

Kaynaklar

[1] A. C. Hudgins and A. S. Pavlovic Jr., "Magnetocaloric Effect in Dysprosium," *J. Appl. Phys*, vol. 36, pp. 3628-3630, 1965.

[2] G. V. Brown, "Magnetic Heat Pumping Near Room Temperature," *J. Appl. Phys*, vol. 47, pp. 3673-3680, 1976.

[3] T. Hashimoto, T. Numasawa, M. Shino and T. Okada, "Magnetic Refrigeration in the Temperature Range from 10 K to Room Temperature: The Ferromagnetic Refrigerants," *Cryogenics* vol. 21, pp. 647-653, 1981.

[4] V. K. Pecharsky and K. A. Gschneidner Jr, "Giant Magnetocaloric Effect in $Gd_5(Si_2Ge_2)$," *Phys. Rev. Lett*, vol. 78, pp. 4494-4497, 1997.

[5] V. K. Pecharsky and K. A. Gschneidner Jr, "Phase Relationships and Crystallography in the Pseudobinary System Gd_5Si_4-Gd_5Ge_4," *J.Alloys and Compounds*, vol. 260, pp. 98-106, 1997.

[6] K. A. Gschneidner Jr. and V. K. Pecharsky, "Magnetocaloric Materials," *Annual Review of Materials Science*, vol. 30, pp. 387-429, 2000.

[7] N. T. Hien and N. P. Thuy, "Preparation and Magnetocaloric Effect of $La_{1-x}Ag_xMnO_3$ (x= 0.10-0.30) Perovskite Compounds," *Physica B*, vol. 319, pp. 168-173, 2002.

[8] D. T. Morelli, A. M. Mance, J. V. Mantese and A. L. Micheli, "Magnetocaloric Properties of Doped Lanthanum Manganite Films," *J. Appl. Phys*, vol. 79, pp. 373-375, 1996.

[9] Z. B. Guo, Y. W. Du, J. S. Zhu, H. Huang, W. P. Ding and D. Feng, "Large Magnetic Entropy Change in Perovskite-Type Manganese Oxides," *Phys. Rev. Lett*, vol. 78, pp. 1142-1145, 1997.

[10] A. O. Ayas, M. Akyol and A. Ekicibil, "Structural and Magnetic Properties with Large Reversible Magnetocaloric Effect in in $(La_{1-x}Pr_x)_{(0.85)}Ag_{0.15}MnO_3$ $(0.0 < x < 0.5)$ Compounds," *Philosophical Magazine*, vol. 96, no. 10, pp. 922-937, 2016.

[11] E. Taşarkuyu, A. E. Irmak, A. Coşkun and S. Aktürk, "Structural, Magnetic and Transport Properties of $La_{0.70}Sr_{0.21}K_{0.09}MnO_3$," *Journal of Alloys and Compounds*, vol. 588 pp. 422–427, 2014.

[12] S. Das and T. K. Dey, "Magnetocaloric Effect in Potassium Doped Lanthanum Manganite Perovskites Prepared by a Pyrophoric Method," *J. Phys.: Condens. Matter*, vol. 18, pp. 7629-7641, 2006.

[13] A. Gaur and G. D. Varma, "Sintering Temperature Effect on Electrical Transport and Magnetoresistance of Nanophasic $La_{0.7}Sr_{0.3}MnO_3$," *J. Phys.: Condens. Matter*, vol. 18, pp. 8837-8846, 2006.

[14] I. Dhiman, A. Das, A. K. Nigam and R. K. Kremer, "Effect of B-Site Doping in $(La_{0.3}Pr_{0.7})_{0.65}$ $Ca_{0.35}Mn_{1-x}B_xO_3$ (B= Fe, Cr, Ru and Al) Manganites," *Journal of Magnetism and Magnetic Materials*, vol. 334, pp. 21-30, 2013.

[15] A. Maignan, F. Damay, A. Barnabé, C. Martin, M. Hervieu, and B. Raveau, "The Effect of Mn-site Doping on the Magnetotransport Properties of CMR Manganites," *Philosophical Transactions of the Royal Society A*, vol. 356, no. 1742, pp. 1635-1659, 1998.

[16] A. Coşkun, E. Taşarkuyu, A. E. Irmak, M. Acet, Y. Samancıoğlu and S. Aktürk, "Magnetic Properties of $La_{0.65}Ca_{0.30}Pb_{0.05}Mn_{0.9}B_{0.1}O_3$ (B= Co, Ni, Cu and Zn)," *Journal of Alloys and Compounds*, vol. 622, pp. 796-804, 2015.

[17] A. Mishra and S. Bhattacharjee, "Effect of A- or B-site Doping of Perovskite Calcium Manganite on Structure, Resistivity, and Thermoelectric Properties," *Journal of the American Ceramic Society*, vol. 100, no. 10, pp. 4945-4953, 2017.

[18] M. H. Ghozza, I. S. Yahia and S. I. El-Dek, "Role of B-site Cation on the Structure, Magnetic and Dielectric Properties of Nanosized $La_{0.7}Sr_{0.3}Fe_{1-x}M_xO_3$ (M = Mn; Co and x = 0, 0.5)," *Perovskites. Mater. Res. Express*, vol. 7, pp. 056104-056128, 2020.

[19] R. Dudric, F. Goga, M. Neumann, S. Mican and R. Tetean, "Magnetic Properties and Magnetocaloric Effect in $La_{1.4-x}Ce_xCa_{1.6}Mn_2O_7$ Perovskites Synthesized by Sol–Gel Method," *Journal of Materials Science*, vol. 47, pp. 3125-3130, 2012.

[20] G. Yu, B. Xu, J. Xiong, X. Liu, L. Liu and S. Yuan, "Effect of Cr Doping in the Bilayer manganite $La_{1.4}Sr_{1.6}Mn_2O_7$," *Journal of Magnetism and Magnetic Materials*, vol. 323, no. 15, pp. 1925-1928, 2011.

[21] D. Louca, G. H. Kwei and J. F. Mitchell, "Local Lattice Effects in the Layered Manganite $La_{1.4}Sr_{1.6}Mn_2O_7$.," *Phys. Rev. Lett*, vol. 80, pp. 3811-3814, 1998.

[22] A. H. Wang, G. H. Cao, Y. Liu et al., "Magnetic entropy change of the layered perovskites $La_{2-2x}Sr_{1+2x}Mn_2O_7$," *Journal of Applied Physics*, vol. 97, pp. 103906-103909, 2005.

Bitlis Eren Üniversitesi Fen Bilimleri Dergisi
BİTLİS EREN UNIVERSITY JOURNAL OF SCIENCE
ISSN: 2147-3129/e-ISSN: 2147-3188
VOLUME: 11 NO: 3 PAGE: 744-750 YEAR: 2022
DOI: 10.17798/bitlisfen.1049002

An Investigation of Anticholinesterase and Anticancer Effects of *Verbascum insulare Boiss. Et Heldr.* Extracts Growing in Muş Region

Yusuf ALAN[1], Züleyha ALMAZ[1*]

[1]*Department of Molecular Biology and Genetics, Faculty of Arts and Sciences, Mus Alparslan University, Mus, 49250, Turkey*
(ORCID: 0000-0003-0007-0212) (ORCID: 0000-0002-4532-4311)

Keywords: *Verbascum insulare* Boiss. Et Heldr., Anticancer, Anticholinesterase.

Abstract

Since the existence of humanity, plants have been used in many treatment methods. Members of the genus *Verbascum*, a member of the Scrophulariaceae family, also known as mullein, have recently received great attention due to their remarkable biological activities and have been evaluated in traditional therapeutic uses against various ailments. In this study, the anticholinesterase and anticancer activities of *Verbascum* member *Verbascum insulare* Boiss. Et Heldr. collected from Muş region were investigated. *V.insulare* leaf ethanol (L-EtOH), leaf purified water (L-PW), root ethanol (R-EtOH), and root purified water (R-PW) extracts were obtained. The anticancer activity of the extracts against HT-29, MCF-7, and L-929 cell lines was examined using the 3-(4,5-dimethyl-thiazol-2-yl)-2,5-diphenyltetrazolium bromide (MTT) test, and the anticholinesterase activity of the extracts was determined. It was found that the ethanol extract showed higher anticancer activity against cancer cell lines than the pure water extract and had more effective anticholinergic influences. It is aimed to shed light on the biological effects of *Verbascum insulare* Boiss. Et Heldr, which is thought to be a natural source of bioactive compounds for the development of phytopharmaceuticals targeting oxidative stress-related diseases such as cancer and neurological diseases. No study has been found in the literature on the anticancer and anticholinesterase activity of this plant yet. Therefore, the results obtained from this study will contribute significantly to the development of herbal medicine in the future.

1. Introduction

Nowadays, plants are of great interest all over the world as an effective therapeutic agent for the treatment and prevention of diseases. In addition, plants, which form an important component of foodstuffs, have formed the basis of traditional medicine throughout history. It has been determined that there are approximately 420,000 plant species on earth, and more than 35,000 of these plants are used for medicinal purposes [1]. *Verbascum* genus, a member of the Scrophulariaceae family, also known as "king's candle or mullein" in the flora of Turkey, has 233 species, 185 of which are endemic, and more than 100 hybrids [2]. In traditional Turkish medicine, all aerial parts of *Verbascum* L. (Scrophulariaceae) species are used as a drying agent for wounds such as inflammatory skin disorders. In addition, some species of the plant are reported to have expectorant, mucolytic and sedative properties used in the treatment of respiratory ailments such as bronchitis, tuberculosis, and asthma [3]. *Verbascum nubicum* Murb species showed significant hepatoprotective, anti-inflammatory, and antioxidant effects[4]. *Verbascum bombyciferum* Boiss inhibited several enzymes, including acetylcholinesterase and butyrylcholinesterase[5]. In a study investigating the

*Corresponding author: z.turkoglu@alparslan.edu.tr
Received: 27.12.2021, Accepted: 29.04.2022

antiproliferative effect of different extracts of *Verbascum sinaiticum* against Hep-2, MCF-7, and Vero cell lines, it was determined that the ethanol extract of the plant exhibited high antiproliferative potential against the tested cell lines [6]. In a study of the phytochemical examination of *Verbascum thapsus*, it was determined that luteolin and 3-O-fucopyranosylsaikogenin F compounds induced apoptosis of A549 lung cancer cells and showed promising antiproliferative activities as a result [7]. Phenolic content of *Verbascum insulare* Boiss. Et Heldr., antimicrobial, antioxidant, and DNA protective activities of different extracts were determined. It was found that ethanolic extract indicated higher antioxidant and antifungal activity and increased DNA stability than pure aqueous extract [2].

Due to the increase in the number of older adults, the prevalence of diseases such as cancer and neurodegenerative disorders has increased greatly in the world in recent years. Alzheimer's disease (AD) is the most common neurodegenerative disease that progresses over time and is very difficult to diagnose, seen in middle-aged and elderly individuals. This disease is characterized by early progressive loss of neuronal cells [8]. Cancer is characterized by inappropriate cell proliferation and resistance to cell death. The common causative factor of AD and cancer is thought to be aging. It is possible to associate cancer and Alzheimer's disease with various mechanisms, and one of these mechanisms is that both diseases increase oxidative stress and thus tumor or neuronal cells become vulnerable [9]. It is known that oxidative stress increases colon and breast cancer types [10]. Consequently, new, safe and effective therapeutic approaches are needed to control these diseases. Considering the above, many *Verbascum* species can be considered promising raw materials for the design of new pharmaceutical products. While many *Verbascum* species have been studied, more research is needed to provide scientifically validated information, particularly on poorly studied species. Our aim with this research article is to investigate the anticholinesterase and anticancer activities of the medicinally important plant *V.insulare* and determine whether it can be used in the pharmaceutical industry.

2. Material and Method

2.1. The Extraction and Collection of Plant Samples

V.insulare plant was collected during the vegetation period in 2018 from Guzeltepe village of Mus province. The identification of the collected plant samples according to the Flora of Turkey was done by Murat Kurşat (Bitlis, Turkey). The plant samples were turned into herbarium material (Y. Alan: 4913) and stored in Muş Alparslan University, Central Research Laboratories Application and Research Center. The leaves and roots of the plant were removed and left to dry in the shade. *V.insulare* leaf ethanol (L-EtOH), leaf purified water (L-PW), root ethanol (R-EtOH), and root purified water (R-PW) extracts were prepared according to our previous study [2].

2.2. Cholinesterase Inhibition Assay

Acetylcholinesterase (AChE) from Electric eel (*Electrophorus electricus*) and butyrylcholinesterase (BChE) from equine serum were obtained from Sigma- Aldrich (St. Louise, MO). The inhibitory effects of *V. insulare* extracts against AChE and BChE were measured using a slight modification of Ellman's spectrophotometric method [11] as described previously [12] and using commercially available galantamine as the reference compound. Acetylthiocholine iodide (AChI), butyrylthiocholine iodide (BChI) were used as the substrate in the reaction, 5′dithiobis-2 -nitrobenzoic acid (DTNB) was used as Ellman's reagent were purchased from Sigma - Aldrich. The absorbance of the reaction mixture was measured at 412 nm three times within 5 min of the start of the reaction on a Thermo Fisher Scientific Multiskan Go Finland, and the results are reported as mean ± standard deviation. Activity (%) was plotted to determine the inhibitory effects of *V. insulare* extracts on AChE and BChE. IC_{50} values were obtained by activity (%) versus compound plots.

2.3. The Application of Extracts to Cell Lines

Human colon cancer cell line (HT-29), human breast cancer cell line (MCF-7), and healthy mouse fibroblast cell line (L-929) were used. Dulbecco's Modified Eagle Medium (DMEM) was used as the medium for these cell lines. *V. insulare* extracts were prepared in the DMEM at concentrations of 0.1, 0.2 and 0.5 mg/mL, and the 3-(4,5-dimethyl-thiazol-2-yl)-2,5-diphenyltetrazolium bromide (MTT) test was applied to determine their cytotoxicity [13]. For the

MTT test, $5x10^3$ cells were seeded in 100 µL of the medium in each well of 96 well plates. The inoculated cells were incubated in a 5% CO_2 incubator for 24-48 hours. 100 µl of the diluted extracts in the medium was added to the cell lines. Only 100 µl of the medium was added to the cells in the control wells. Samples were incubated for 24 hours. After incubation, the medium in the wells was removed with the help of a vacuum pump. 10 µl of MTT solution and 90 µl of medium were added to each well and placed in a CO_2 incubator at 37℃ for 4 hours. After 4 hours, the medium containing MTT was removed from the 96 well plate. 100 µl of Dimethylsulfoxide (DMSO) was added to each well, and their optical density (OD) was measured with a microplate reader (Thermo Fisher Scientific Multiskan Go, Finland) at 540 nm wavelength. A cell line medium without a sample was used as the control group. The average absorbance values obtained by reading the control wells was taken, and this value was accepted as 100% viable cells. The % inhibition rates of the cells were calculated with the help of the following formula.

$$\% \text{ inhibition} = 1 - \left(\frac{\text{OD}_{\text{Sample}}}{\text{OD}_{\text{Control}}}\right) \text{x}100$$

2.4. Statistical Analysis

The % inhibition results of the cell culture and the cholinesterase inhibitory activity were compared among themselves using the t-test following One Way ANOVA. Those with $p<0.05$ were statistically significant, and the statistical significance level was indicated with the symbol "*". In this respect, $P<0.05$ (significant); *, $P<0.01$ (very significant); **, $P<0.001$ and $P<0.0001$ (extremely significant); ***-**** and $P>0.05$ (not significant), ns.

3. Results and Discussion

3.1. Anticholinergic Activity

Today, the inhibition of cholinesterases has emerged as an encouraging approach to alleviate the symptoms of Alzheimer's disease. Therefore, inhibition of AChE and BChE enzymes is one of the main goals of researchers. Various cholinesterase inhibitors such as galantamine, tacrine, and rivastigmine are produced synthetically. However, these drugs have side effects such as nausea, diarrhea, dizziness, and vomiting [14]. For these reasons, the discovery of natural and safe enzyme inhibitors has become inevitable. Therefore, the enzyme inhibition properties of *V. insulare* extracts tested against AChE and BChE enzymes were examined by comparing them with galantamine(Table 1 and Figure 1).

Table 1. AChE/BChE inhibition assays for LEtOH (ethanolic leaf), LPW (aqueous leaf pure), REtOH (ethanolic root) and RPW (aqueous root pure) extracts of *V.insulare*

Extracts	AChE inhibition IC_{50}	BChE inhibition IC_{50}
LEtOH	0.013±0.001	0.042±0.002
LPW	0.014±0.002	0.049±0.003
REtOH	0.038±0.002	0.046±0.002
RPW	0.044±0.005	0.052±0.003
*Galantamine	0.078±0.006	0.117±0.010

*Galantamine was used as a positive control for Cholinesterase enzymes and determined as µM levels. Cholinesterase inhibitory activity of the extracts was tested against AChE and BChE at 500 µg/mL concentration.

All extracts of *V. insulare* exhibited potent AChE and BChE inhibitory activity at 500 µg/mL. In addition, these extracts showed a better AChE and BChE inhibitory effect than galantamine, a cholinesterase inhibitor used as a therapeutic agent in the treatment of Alzheimer Demands. Galantamine which is used as standard cholinesterase inhibitor was found to have IC_{50} values of 0.078±0.006 µmol/L and 0.117±0.010 µmol/L, respectively, against AChE and BChE enzymes. LEtOH extract of *V. insulare* showed a stronger inhibitory effect for both enzymes than galantamine and other extracts. When the extracts and galantamine activities were compared, it was determined that the extracts showed a highly significant difference from galantamine in general ($P<0.0001$). It has also been reported that many *Verbascum* species inhibit cholinesterase enzymes. For example, in the study of Angeloni et al., aqueous and methanolic extracts of *Verbascum bombyciferum* were obtained using different techniques such as HAE (homogenizer assisted), MAC (maceration), and infusion was found to exhibit anticholinesterase effects. They found that especially water extracts (maceration: 0.30 ± 0.08 mg GALAE/g and homogenizer assisted extraction: 0.28 ± 0.02 mg GALAE/g) were more weaker inhibitors of AChE when compared to methanolic extracts (homogenizer assisted extraction: 1.89 ± 0.15 mg GALAE/g and maceration: 2.02 ± 0.20 mg GALAE/g) [5]. It was found that aqueous and methanolic extracts of *V. oocarpum* showed an anticholinesterase effect, and the inhibition range varied between 66.7 ± 1.2 and 28.8± 0.5 at 200 µg/mL. As a result, it was determined

that the plant extracts had moderate AChE and BChE inhibitory activities [15]. Verbascoside isolated from the aqueous extract of *V. mucronatum* Lam was found to inhibit cholinesterase enzymes. According to their data, verbascoside exhibited moderate inhibition of AChE compared to galantamine but was ineffective against BChE [16].

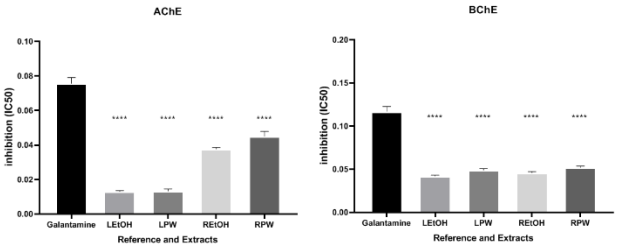

In a study to determine the anticholinesterase activity of extracts of two endemic *Verbascum* species using five different solvents, the hexane extract of (*V. oocarpum)* one species (AChE = 2.35 and BChE = 4.68 mg GALAE/g) and the ethyl acetate extract of (*V. euphraticum)* the other species of (AChE = 1.96 and BChE = 3.29mg GALAE/g) were reported to show high anticholinesterase activities. In this context, cholinesterase inhibition assays can offer the potential therapeutic value of many *Verbascum* species to control neurodegenerative complications [17].

3.2. The Cytotoxicity of Extracts against Cancer and Healthy Cell Lines

V.*insulare* extracts at different concentrations (0.1, 0.2, and 0.5 mg/mL) were treated with HT-29, L-929, and MCF-7 cells for 24 hours, and the % inhibition values of the cell lines were calculated with the measured absorbance spectrophotometrically. The MTT test determined the inhibition of cell proliferation. The % inhibition graphs of cell lines are given in Figure 2.

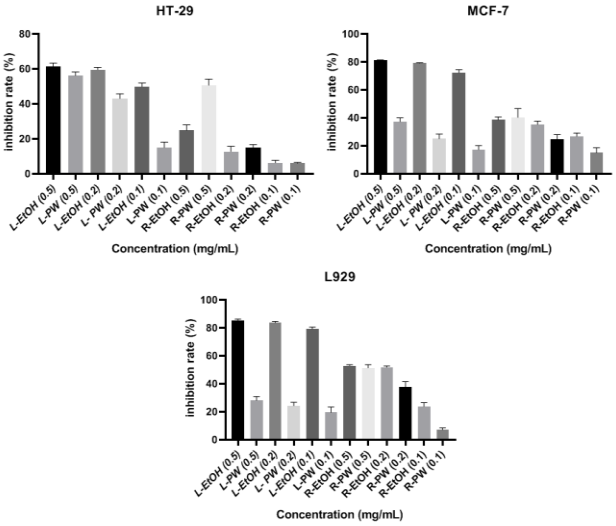

L-EtOH extract at 0.2 and 0.1 mg/mL concentrations against the HT-29 cell line displayed a highly significant difference compared to L-PW. In addition, it was determined that the R-PW extract displayed a highly significant difference from the R-EtOH extract. L-EtOH extract at all concentrations displayed a highly significant difference compared to L-PW against MCF-7 and L-929 cell lines. At the same time, it was determined that the 0.2 and 0.1 mg/mL concentrations of R-EtOH extract against MCF-7 and L-929 cell lines showed a highly significant difference compared to R-PW. When evaluated in general, it was determined that the antiproliferative properties of ethanol extracts were higher than those of pure water extracts in all cell lines. It is known that plants have been used in cancer treatment since ancient times. The compounds found in the extracts obtained from the plants used for this purpose show significant anticancer activity[18]. In previous studies, it has been reported that these compounds found in extracts obtained from plants have anticancer effects [19].

Although there are studies on species belonging to different *Verbascum* genus in the literature, no anticancer study has been found on the *V.insulare* species used. A study reported that the methanolic extract obtained from the *Verbascum* genus had a cytotoxic effect against the melanoma cell line but was ineffective against the ovarian cell line [20].

IIiescu et al. determined that the methanolic extract from the aerial parts of *Verbascum nigrum* did not affect the cytotoxicity of HaCaT cells but showed a significant effect on A431 cells [21]. The effects of extracts obtained from plants vary according to cell lines. The data obtained in this study also vary according to cell lines, as in previous studies. Tatlı and Akdemir compared the cytotoxic effect of methanol and ethyl acetate extracts of some *Verbascum* species in Turkey and reported that ethyl

acetate extract showed a stronger cytotoxic effect against cancerous cell lines [20]. In a different study, the cytotoxicity of *V. sinaiticum* Benth flower extracts prepared with different solvents against mammary adenocarcinoma MCF-7 was examined, and it was seen that ethanol extract showed the best cytotoxicity [6]. It was also reported that the hydroethanolic leaf extract of the same plant showed the best cytotoxic effect against HepG2 and MRC-5 cell lines [22]. The cytotoxic effect of methanol and hydromethanol extracts obtained from *V. calvum* were compared, and it was reported that the methanol extract displayed important antiproliferative effects against A-549 lung cancer cell line [23]. The plant extracts obtained using different solvents consist of different compounds.
For this reason, it has been determined that the extracts exhibit different anticancer activities in studies. According to the results of this study, it was determined that ethanol extract showed a better antiproliferative effect than pure water extract. This study supports the view that the cytotoxic effect may be due to the compounds contained in the extract, as in previous studies.

4. Conclusion and Suggestions

It is known that the damage caused by oxidative stress in cells and tissues may play a role in the development of many diseases such as Alzheimer's and cancer in the organism. In the key enzyme inhibition theory, which is effective for the management of neurological diseases such as Alzheimer's, inhibition of these enzymes can alleviate existing symptoms. For this purpose, the presence of natural inhibitors for cholinesterase inhibition is very important. In this study, anticancer activity of *V.insul*are, a species belonging to the genus *Verbascum*, against human colon cancer cell line (HT-29), human breast cancer cell line (MCF-7), and healthy mouse fibroblast cell line (L-929), and enzyme (AChE, BChE) inhibitory effects were investigated for the first time. It was determined that the ethanol extract from the extracts obtained by using different plant parts and solvents showed better anticholinesterase activity and antiproliferative properties than the pure water extract. In addition, leaf ethanol extract showed the best activity for both biological activity tests. This is thought to be due to the fact that the extracts prepared in different parts of the plant and in different solvents contain different compounds. It is anticipated that future studies will isolate and purify the active compounds and investigate their effects on a wider variety of cancer cells and enzymes. However, *in vivo* tests, namely more studies, are needed to explore the full mode of action of the active compounds in herbal medicine development and to test the safety of the extracts used here.

Contributions of the authors

Corresponding author: Data curation, writing (original draft, review & editing), investigation, visualization methodology, *in vitro* studies and interpretation of experimental results.
Coauthor: Methodology, investigation, visualization, literature review, *in vitro* studies, and interpretation of experimental results.

Conflict of Interest Statement

There is no conflict of interest between the authors.

Statement of Research and Publication Ethics

Research and publication ethics compiled within the study.

References

[1] S.-Y. Pan *et al.*, "New perspectives on how to discover drugs from herbal medicines: CAM's outstanding contribution to modern therapeutics," *Evidence-Based Complementary and Alternative Medicine,* vol. 2013, 2013.

[2] Y. Alan and N. Yilmaz, "Phenolic substance contents and biological activities of verbascum insulare boiss. and heldr. Extracts," *J steroids,* vol. 33, p. 35, 2019.

[3] I. Süntar, I. I. Tatlı, E. K. Akkol, H. Keleş, Ç. Kahraman, and Z. Akdemir, "An ethnopharmacological study on Verbascum species: from conventional wound healing use to scientific verification," *Journal of ethnopharmacology,* vol. 132, no. 2, pp. 408-413, 2010.

[4] H. A. E. H. El Gizawy, M. A. Hussein, and E. Abdel-Sattar, "Biological activities, isolated compounds and HPLC profile of Verbascum nubicum," *Pharmaceutical biology,* vol. 57, no. 1, pp. 485-497, 2019.

[5] S. Angeloni *et al.*, "An insight into Verbascum bombyciferum extracts: Different extraction methodologies, biological abilities and chemical profiles," *Industrial Crops and Products,* vol. 161, p. 113201, 2021.

[6] W. H. Talib and A. M. Mahasneh, "Antiproliferative activity of plant extracts used against cancer in traditional medicine," *Scientia pharmaceutica,* vol. 78, no. 1, pp. 33-46, 2010.

[7] Y.-L. Zhao *et al.*, "Isolation of chemical constituents from the aerial parts of Verbascum thapsus and their antiangiogenic and antiproliferative activities," *Archives of pharmacal research,* vol. 34, no. 5, pp. 703-707, 2011.

[8] J. A. Dumas and P. A. Newhouse, "The cholinergic hypothesis of cognitive aging revisited again: cholinergic functional compensation," *Pharmacology Biochemistry and Behavior,* vol. 99, no. 2, pp. 254-261, 2011.

[9] J. E. Lee, D. Kim, and J. H. Lee, "Association between alzheimer's disease and cancer risk in South Korea: an 11-year nationwide population-based study," *Dementia and neurocognitive disorders,* vol. 17, no. 4, pp. 137-147, 2018.

[10] A. F. Yücel, Ö. Kemik, A. S. Kemik, S. Purisa, and İ. S. Tüzün, "Relationship between the levels of oxidative stress in mesenteric and peripheral serum and clinicopathological variables in colorectal cancer," *Balkan Medical Journal,* vol. 2012, no. 2, pp. 144-147, 2012.

[11] G. L. Ellman, K. D. Courtney, V. Andres Jr, and R. M. Featherstone, "A new and rapid colorimetric determination of acetylcholinesterase activity," *Biochemical pharmacology,* vol. 7, no. 2, pp. 88-95, 1961.

[12] Z. Almaz, A. Oztekin, A. Tan, and H. Ozdemir, "Biological evaluation and molecular docking studies of 4-aminobenzohydrazide derivatives as cholinesterase inhibitors," *Journal of Molecular Structure,* p. 130918, 2021.

[13] M. E. Alkış, Ü. Keleştemür, Y. Alan, N. Turan, and K. Buldurun, "Cobalt and ruthenium complexes with pyrimidine based schiff base: Synthesis, characterization, anticancer activities and electrochemotherapy efficiency," *Journal of Molecular Structure,* vol. 1226, p. 129402, 2021.

[14] N. Martins and I. C. Ferreira, "Neurocognitive improvement through plant food bioactives: A particular approach to Alzheimer's disease," in *Food Bioactives*: Springer, 2017, pp. 267-298.

[15] S. Kanbolat *et al.*, "Antioxidant, antimicrobial, cytotoxic, anticholinesterase, antityrosinase activities and characterisation of volatile compounds of Verbascum oocarpum by SPME and GC-FID/MS," *Journal of Pharmaceutical Research International,* pp. 1-12, 2018.

[16] C. Kahraman, I. I. Tatlı, I. E. Orhan, and Z. S. Akdemir, "Cholinesterase inhibitory and antioxidant properties of Verbascum mucronatum Lam. and its secondary metabolites," *Zeitschrift für Naturforschung C,* vol. 65, no. 11-12, pp. 667-674, 2010.

[17] G. Zengin *et al.*, "Evaluation of chemical constituents and biological properties of two endemic Verbascum species," *Process Biochemistry,* vol. 108, pp. 110-120, 2021.

[18] J. Iqbal *et al.*, "Plant-derived anticancer agents: A green anticancer approach," *Asian Pacific Journal of Tropical Biomedicine,* vol. 7, no. 12, pp. 1129-1150, 2017.

[19] G. M. Cragg and D. J. Newman, "Plants as a source of anti-cancer agents," *Journal of ethnopharmacology,* vol. 100, no. 1-2, pp. 72-79, 2005.

[20] İ. İ. TATLI and Z. S. Akdemir, "Cytotoxic activity on some Verbascum species growing in Turkey," *Hacettepe University Journal of the Faculty of Pharmacy,* no. 2, pp. 77-86, 2006.

[21] I. A. Iliescu *et al.*, "Verbascum nigrum: cytotoxicity evaluation in A431 epidermoid carcinoma cells and untargeted LC-HR-MS/MS metabolite profiling," *Chemistry & Biodiversity*, vol. 17, no. 12, p. e2000644, 2020.

[22] J. Tauchen *et al.*, "In vitro antioxidant and anti-proliferative activity of Ethiopian medicinal plant extracts," *Industrial Crops and Products*, vol. 74, pp. 671-679, 2015.

[23] H. I. M Amin, F. H. Hussain, G. Gilardoni, Z. M. Thu, M. Clericuzio, and G. Vidari, "Phytochemistry of Verbascum Species Growing in Iraqi Kurdistan and Bioactive Iridoids from the Flowers of Verbascum calvum," *Plants*, vol. 9, no. 9, p. 1066, 2020.

Bitlis Eren Üniversitesi Fen Bilimleri Dergisi
BİTLİS EREN UNIVERSITY JOURNAL OF SCIENCE
ISSN: 2147-3129/e-ISSN: 2147-3188
VOLUME: 11 NO: 3 PAGE: 751-758 YEAR: 2022
DOI: 10.17798/bitlisfen.1076888

Effect of Silane-Coated SiO_2 Nanoparticles on the Hardness Values of Glass FRP Composites

Çağrı UZAY[1*], M. Safa KAMER[1]

[1]*Kahramanmaraş Sütçü İmam University, Dept. of Mechanical Engineering, Kahramanmaraş, Turkey (ORCID: 0000-0002-7713-8951) (ORCID: 0000-0003-3852-1031)*

Keywords: Nanoparticle, Silane-coated SiO_2, Fiber-reinforced polymer composite, Microhardness, Microstructure.

Abstract

In this study, silane-coated SiO_2 nanoparticles (as-received) were used as secondary reinforcement for glass fiber-reinforced polymer (FRP) composites, and the microhardness values of the developed composites were investigated. The nanoparticles were dispersed within the polymer epoxy at 1.5 and 3 wt.% ratios, respectively. Two different types of silane coating were used that were KH550 and KH570. The mixture of the epoxy resin and nanoparticles were subjected to ultrasonic homogenization to achieve a fine dispersibility of the SiO_2 nanoparticles. Then the matrix was prepared with a suitable hardener at a weight ratio of 100:25. The strengthened polymer matrix was reinforced by woven glass fiber fabrics (primary reinforcing element). The vacuum bag method was applied to produce silane-coated nano SiO_2 filled glass FRP composites. A digital microhardness testing device was used to determine the Vickers hardness values. While the pure glass/epoxy composite has resulted in a hardness of 20.69 HV, the maximum hardness value was recorded as 36.56 HV and it was obtained with 3 wt.% KH550-SiO_2 filled glass/epoxy. The incorporation of silane-coated SiO_2 nanoparticles has provided dramatic enhancements in terms of microhardness, approximately from 28 to 77%. The microscopic examination was also conducted via an optical microscope and the images were found helpful to explain the test results. Therefore, the findings of this study have shown that silane-coated nano SiO_2 filler can be used as secondary reinforcement where high hardness and better wear resistance are desired for glass/epoxy composite applications.

1. Introduction

Although the fiber-reinforced polymer (FRP) composites offer lightness, high strength, and stiffness, particularly for the weight-critical applications in automotive and aerospace, they still have some drawbacks such as delamination, sudden and brittle fracture [1]. The main reason could be the poor interfacial adhesion of the fiber and the matrix. Therefore, nano and microparticles, in very low contents, have been used as the reinforcing elements within the polymer matrix to overcome the FRPC's limitations and leading to obtaining better interfacial strength and so the high mechanical properties [2-5]. Reinforcing polymers with nano or microparticles is called the matrix toughening method [6, 7]. The mechanical, tribological, thermal, and dielectric properties could be improved with that method. The most commonly used particles that acted as filler material are titanium dioxide (TiO_2), silicon carbide (SiC), silica (SiO_2), boron carbide (B_4C), carbon nanotube (CNT), graphene oxide (GO), boron nitride (BN) [8-11].

The particle effects on the mechanical properties in terms of tensile, flexural and impact have highly been studied by many researchers [12-17]. However, the research on hardness instrumentation, wear resistance and tribology has been limited. Radhwan et al. [1] investigated the Vickers hardness values of the aluminum (Al) filled

*Corresponding author: cagriuzay@ksu.edu.tr
Received: 21.02.2022, Accepted: 07.07.2022

epoxy composites depending upon the particle content, and they found that 10% addition of filler yielded 14.5 gf/μm^2 hardness, whereas 40% addition of filler yielded 32.7 gf/μm^2 hardness value. The improvement was slowed down after 20% Al addition. Atiqah et al. [18] investigated the effects of honeycomb natural fiber addition into the epoxy polymer composite based on the Brinell hardness instrumentation. Except for 9 wt.% addition of fiber elements, the hardness values were reported in a decreasing trend for the additions of 3.wt%, 6 wt.%, and 12 wt.%, respectively. Reddy et al. [19] used tungsten carbide (WC) nanoparticles at weight ratios of 1, 2, 3, and 4% to reinforce the epoxy matrix. From 1 to 2 wt.% addition of WC nanoparticles increased the Vickers hardness value, but after 2 wt.%, the hardness values decreased. The reduction was attributed to the poor adhesion and agglomeration of the particles at relatively higher filler contents

The nano SiO_2 particles are inorganic and have a widespread usage area due to their low cost, availability, high surface area, heat resistance and insulative features [5, 14, 20, 21]. However, the use of pure nano SiO_2 particles may cause agglomeration easily, even at very low contents. Because the particles highly tend to react with water [17]. Therefore, silane coupling agents are generally used for surface treatments of the SiO_2 nanoparticles to avoid agglomeration. The synergistic effect of silanization and nano SiO_2 reinforcement has led to obtaining better mechanical and thermal properties [17, 22]. On the other hand, silanization is performed as an additional process for treating SiO_2 surfaces.

When the literature studies were examined, it can be inferred that the filler type, size, and content affect the polymer composites' hardness. In this study, silane-coated nano SiO_2 particles were supplied as received, and then they were used as a secondary reinforcement to modify the epoxy. The modified epoxy was reinforced by glass fibers. The developed nanofiller added glass FRP composites with different silane types (KH550 and KH570), and filler contents (1.5 and 3 wt.%) were subjected to microhardness instrumentation to reveal the effects of filler type and content on the hardness values. The microscopic examinations also confirmed that the composite parameters have significantly affected the results.

2. Material and Method

2.1. Materials

This study used glass fiber fabrics and epoxy resin set to manufacture glass fiber-reinforced polymer (FRP) composites. In addition, silane-coated SiO_2 nanoparticles (as received) were used as secondary reinforcement for the FRP composites. The glass fiber fabrics and epoxy resin set were supplied from Dost Kimya Inc. (Turkey), whereas the nanoparticles were supplied from Nano Grafi Inc. (Turkey). The materials' properties based on the manufacturers' technical data sheet are given in Tables 1 - 3. As seen in Table 3, two different types of silane coating were used that are KH550 (γ -aminopropyl-triethoxy silane) and KH570 (γ -methacryloxy propyl trimethoxy silane).

Table 1. Physical and mechanical properties of glass fibers

Property	Value
Fiber description	Plain woven fabric, 3K, 200 g/m^2
Density (kg/m^3)	2560
Tensile strength (MPa)	3400
Tensile modulus (GPa)	73
Tensile strain (%)	2.75

Table 2. Physical and mechanical properties of polymer matrix

Property	Value
Constituents	Epoxy resin (L160) + hardener (H160) (mixed at a weight ratio of 100:25)
Density (kg/m^3)	1180-1200
Tensile strength (MPa)	70-80
Tensile modulus (GPa)	3.2-3.5
Tensile strain (%)	5-6.5
Impact strength (kJ/m^2)	40-50
Compression strength (MPa)	80-100

Table 3. Physical properties of silane-coated SiO_2 nanoparticles

SiO_2 nanoparticles	
Type	Nanoparticle
Particle size (nm)	18-35
Specific surface area (m^2/gr)	150-550
Amount of silane coating (%)	3-4
Purity of KH550-coated SiO_2 nanoparticles (%)	> 96.3
Purity of KH570-coated SiO_2 nanoparticles (%)	> 95.9

2.2. Silane-Coated Nano SiO_2 Filled Glass FRP Composite Manufacturing

The manufacturing of silane-coated nano SiO_2 filled glass FRP composites was carried out in two stages. Firstly, the polymer matrix was modified as follows;

- The nanoparticles were weighed according to the predetermined percent ratios (1.5 and 3 wt.%) of the matrix (Figure 1a),
- The nanoparticles were dispersed into the epoxy resin, and the mixture was subjected to homogenization by using an ultrasonic homogenizer (Figure 1b),
- A suitable hardener at a predetermined ratio was poured into the mixture (Figure 1c), and it was stirred manually.

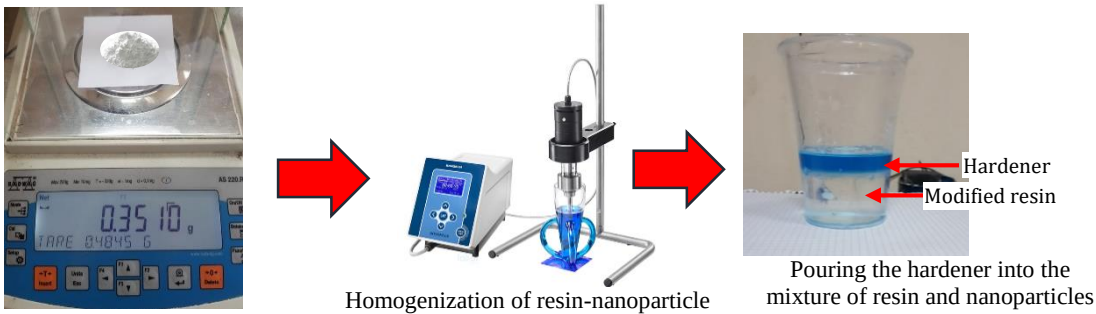

Determination of the weight fraction silane-coated SiO_2 nanoparticles (a)

Homogenization of resin-nanoparticle mixture using ultrasonic homogenizer (b)

Pouring the hardener into the mixture of resin and nanoparticles (c)

Figure 1. Polymer matrix modification process

Four different modified matrix materials were prepared according to the types of silane coating and nanoparticle percent ratios. Then, the modified matrix materials were used to make glass fiber-reinforced laminates. The manufacturing process was based on the vacuum bagging method, as schematically presented in Figure 2. The lamination was conducted on an open mold, a tempered glass. The matrix impregnation of the glass fiber fabrics was performed by hand lay-up. A total of 21 glass fiber fabrics were stacked to achieve approximately 4 mm thickness of the composite structure. Then, a release film, a vacuum breather, and a vacuum bag were placed, respectively. Lastly, the composite system was sealed with sealant tape, and it was left for curing. The curing process was carried out at ambient temperature under a vacuum for 24 hours.

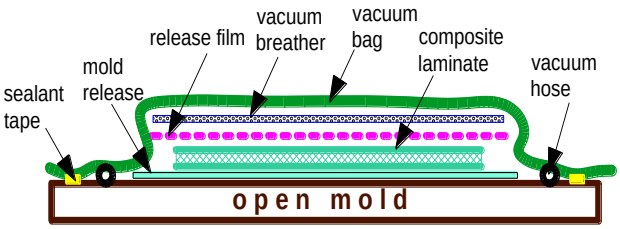

Figure 2. Vacuum bagging method for the lamination process

2.3. Hardness Test

Microhardness values of the produced composite materials were measured by applying the Vickers test method. In this method, the force is applied for 15 seconds by a diamond indenter, which inserts a pyramid form after the penetration of the indenter. Figure 3 shows the digital microhardness testing device used in the present study. Before the hardness measurements, the surface of the specimens was grounded with a 1200 grit size emery paper.

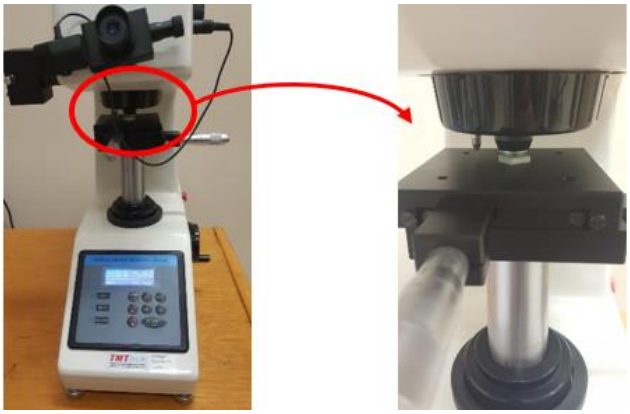

Figure 3. Digital microhardness testing device used in the present study

The Vickers hardness value (HV) can be calculated according to Equation (1) [23]. In the equation, F (N) is the applied force, and d (mm) is the arithmetic average of two diagonals of the pyramid. Both the F values of 1.962 and 2.942 N were used during the instrumentation.

$$HV \cong \frac{1.854 \times F}{d^2} \qquad (1)$$

Figure 4 shows an example of how the HV hardness value is determined. The microstructure of the composite specimen was examined with a microscope after the penetration of the indenter. Then

the diagonals of the pyramid form were measured. The recorded lengths of the diagonals were in μm. The digital microhardness testing device then determined the HV hardness value based on Equation (1).

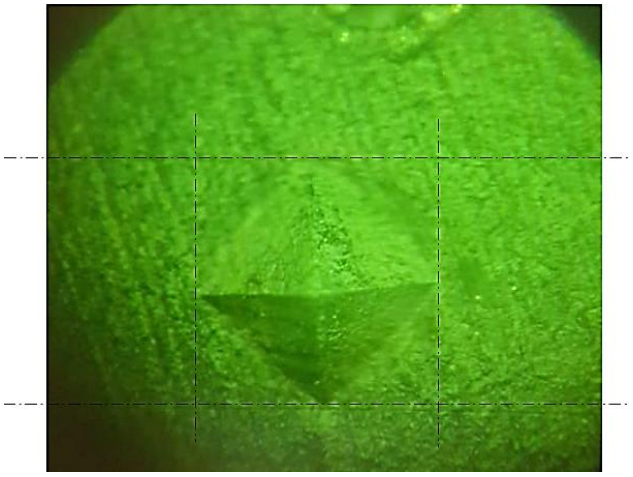

Figure 4. The examination of the pyramid's diagonals

3. Results and Discussion

3.1. Hardness Measurements

Pure glass FRP composite was firstly subjected to hardness measurement under two different loads that were 1.962 and 2.942 N. The reason to apply two different loads was to see the consistency of the results under different loads. Table 4 shows the hardness values of pure glass FRP composite. As seen in Table 4, the measurements yielded a hardness value of 20.997 and 21.177 HV, respectively. The difference between the two values is below 1%, and the standard deviations were found to be low and similar. Also, Singh et al. [24] found the glass FRP composite's HV hardness value as approximately 21.5, which is very close to the findings in the present study. Therefore, the microhardness measurements of the silane-coated nano SiO_2 filled glass FRP composites were carried out by applying 2.942 N. The results are given in Table 5.

Table 4. HV hardness values of the pure glass FRP composite

Applied load	Measurements			Arithmetic Average	Standard deviation
	1	2	3		
1.962 N	22.6	20.02	20.37	20.997	1.142
2.942 N	19.63	22.38	21.52	21.177	1.149

Table 5. HV hardness values of the silane-coated nano SiO_2 filled glass FRP composites

Composites	Measurements			Arithmetic Average	Standard deviation
	1	2	3		
1.5 wt.% KH550/SiO_2 - G/E	28.06	29.03	30.08	29.057	0.825
3 wt.% KH550/SiO_2 - G/E	37.00	35.08	37.61	36.563	1.078
1.5 wt.% KH570/SiO_2 - G/E	26.49	25.64	27.47	26.533	0.747
3 wt.% KH570/SiO_2 - G/E	30.39	30.53	31.69	30.870	0.582

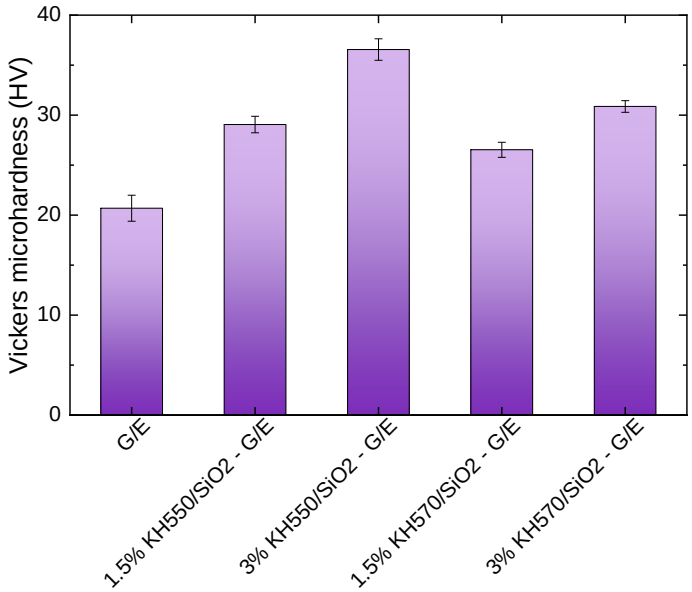

Figure 5. Comparison of Vickers microhardness values of pure and silane-coated SiO_2 filled glass FRP composites

As seen in Table 5, HV hardness values of the silane-coated nano SiO2 filled glass FRP composites were determined higher than that of pure glass FRP composite. This is because the presence of the nanoparticles did not allow the indenter to penetrate deeper [25]. However, the increments vary depending on both silane coating and filler percent within the polymer matrix. The KH550 silane coating has provided 37.21 (at 1.5 wt.% addition of SiO_2) and 72.66% (at 3 wt.% addition of SiO_2) higher HV hardness value, respectively, when compared to the results of pure glass FRP composite. On the other hand, KH570 silane coating has provided 25.30 (at 1.5 wt.% addition of SiO_2) and 45.77% (at 3 wt.% addition of SiO_2) higher HV hardness value, respectively. Therefore, it can be inferred that the silane type of KH550 has contributed more significant HV values than the KH570 silane coating of SiO_2 nanoparticles. The lower values might be attributed to the relatively poor adhesion bonding between the KH570 coated nanoparticles and the matrix [18]. The comparison of the pure and silane-coated SiO_2 filled glass FRP composites were presented in Figure 5.

3.2. Microstructural Examinations

The microstructural examinations of the pure and silane-coated SiO_2 filled glass FRP composites were carried out by utilizing an optical microscope. Figure 6 shows the microscope images that were magnified by 40X. When the pure glass FRP was examined (Figure 6a), it can be inferred that the surface of the specimen was observed smoother than the others. Also, the wear tracks of the emery paper can easily be seen. In Figure 6b, there is almost no wear track, and relatively fewer wear tracks were observed in Figure 6d, which could explain the higher wear resistance of the composite structures due to the presence of silanized SiO_2 nanoparticles. The surface of the specimens in Figures 6c and 6e were highly wavier due to the higher amount of nanoparticle contents. This is why 3 wt.% addition of nanoparticles has resulted in higher hardness values than that of 1.5 wt.% addition. However, KH550-coated SiO_2 filled glass FRP composite's wavy surface was observed more homogeneous than that of the KH570 coated SiO_2 filled glass FRP composite. The best wear resistance obtained by 3 wt.% KH550/ SiO_2-G/E composite could be due to homogeneous dispersibility and improved integration of the filler and the polymer matrix.

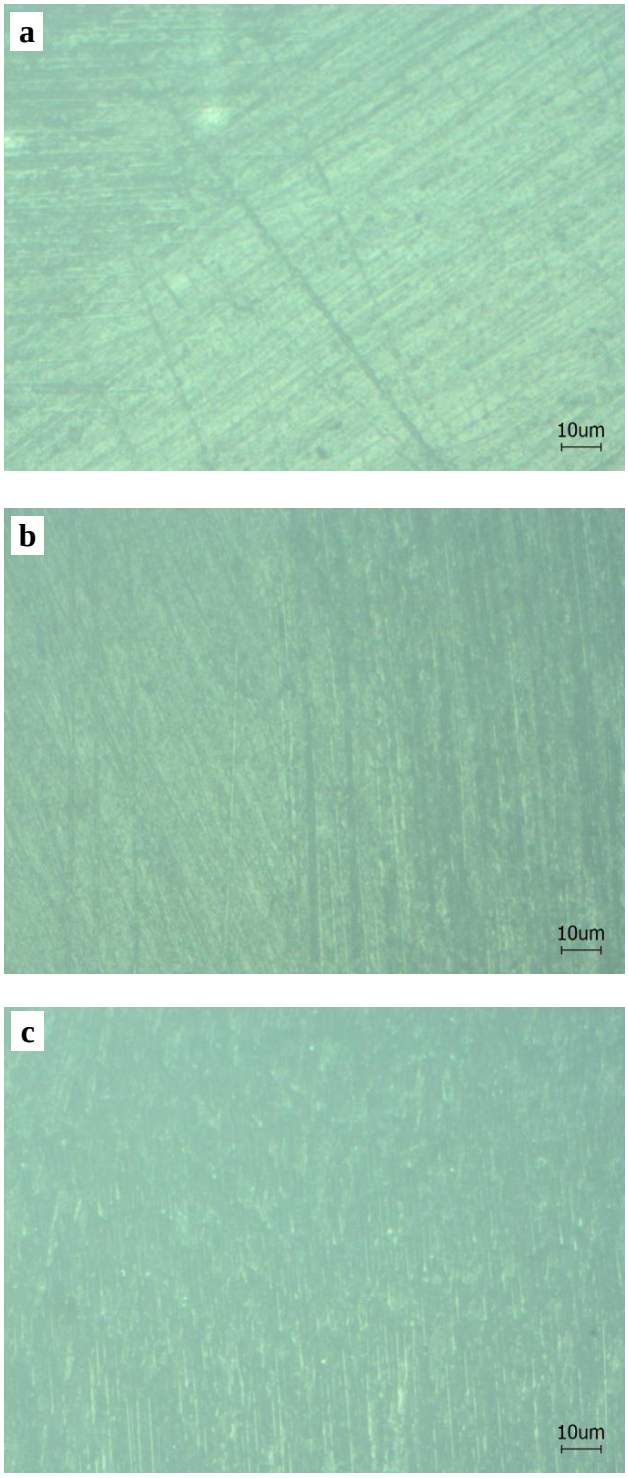

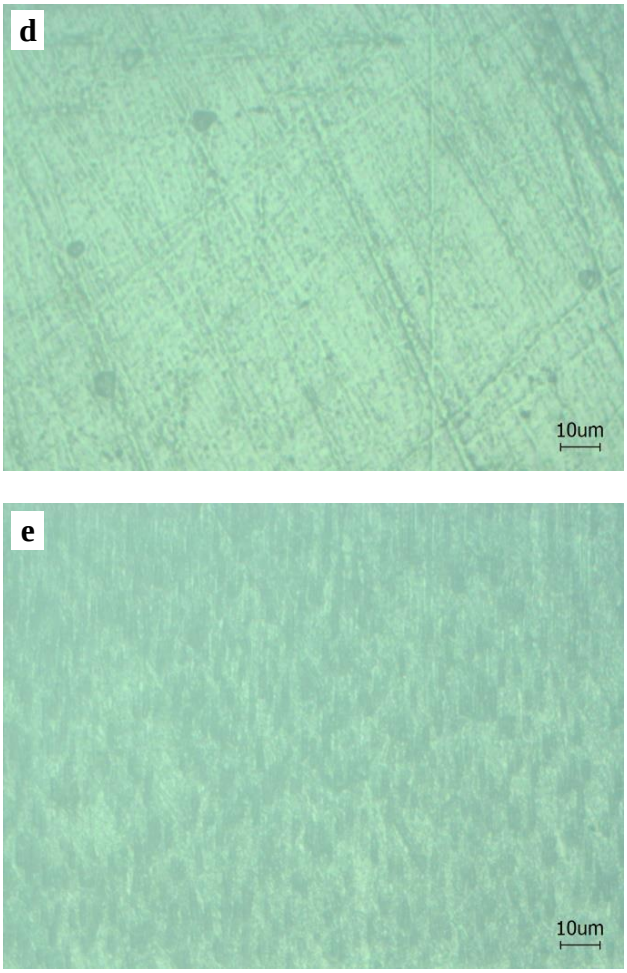

Figure 6. Optical microscope images (40X) of the glass FRP composites; a) pure, b) 1.5 wt.% KH550-SiO_2 filled, c) 3 wt.% KH550-SiO_2 filled, d) 1.5 wt.% KH570-SiO_2 filled, e) 3 wt.% KH570-SiO_2 filled

4. Conclusion

In this study, glass/epoxy composites were successfully strengthened with two different silane-coated SiO_2 nanoparticles that were KH550-coated SiO_2 and KH570-coated SiO_2. The Vickers microhardness measurements have shown that pure glass FRP composite resulted in the lowest hardness value (21.177 HV under 2.942 N). The addition of silane-coated SiO_2 nanoparticles into the polymer matrix considerably improved the hardness of the developed composite structures. The increments have varied according to both silane coatings and nanoparticle percent within the epoxy. Increasing the nanoparticle percent has dramatically enhanced the HV hardness values up to the 72.66%. However, KH550-coated nano SiO_2 filled glass FRP composites have contributed higher hardness values than KH570 coating. This could be attributed to the better integration of SiO_2 nanoparticles and the polymer matrix thanks to the KH550 silane coating. The optical microscope images also confirmed the findings.

The glass fibers offer cost-effective solutions and have widespread application areas such as automotive body parts, ship and boat building, wind turbine blades, and repair and maintenance. Therefore, dispersion of silane-coated SiO_2 nanoparticles at very low ratios into the epoxy improves the wear resistance of the glass/epoxy composites by increasing the structural hardness and can be cost-effectively used for the aforementioned industrial fields.

Acknowledgment

This study was supported by Kahramanmaraş Sütçü İmam University, Scientific Research Projects Coordination Unit under a grant number of 2020/9-32 M.

Authors' Contributions

Ç. Uzay contributed to the planning of the study, literature review, writing, evaluation of the results, and editing. M.S. Kamer carried out the experiments, evaluation of the results, and editing.

Statement of Conflicts of Interest

There is no conflict of interest between the authors.

Statement of Research and Publication Ethics

The authors declare that this study complies with Research and Publication Ethics.

References

[1] H. Radhwan, S. Sharif, Z. Shayfull, M. A. Suhaimi, M. T. M. Khushairi, and K. Fathullah, "Experimental study mechanical behaviour of epoxy resin composites filled with aluminium particles," *AIP Conference Proceedings*, vol. 2129, no. 1, p. 020157, 2019.

[2] A. Elmarakbi, R. Ciardiello, A. Tridello, F. Innocente, B. Martorana, F. Bertocchi, F. Cristiano, M. Elmarakbi, and G. Belingardi, "Effect of graphene nanoplatelets on the impact response of a carbon fibre reinforced composite", *Mater Today Commun*, vol.25, 2020.

[3] C. Kostagiannakopoulou, X. Tsilimigkra, G. Sotiriadis, and V. Kostopoulos, "Synergy effect of carbon nano-fillers on the fracture toughness of structural composites," (in English), *Compos Part B-Eng*, vol. 129, pp. 18-25, 2017.

[4] S. K. Singh, A. Kumar, and A. Jain, "Mechanical and viscoelastic properties of SiO2/epoxy nanocomposites post-cured at different temperatures," *Plastics, Rubber and Composites*, vol. 50, no. 3, pp. 116-126, 2021.

[5] Z. J. Wu, M. Wang, and Z. Wang, "The gas phase SiO2/epoxy nanocomposites with enhanced mechanical and thermal properties," (in English), *High Perform Polym*, vol. 27, no. 4, pp. 469-475, 2015.

[6] M. Quaresimin, K. Schulte, M. Zappalorto, and S. Chandrasekaran, "Toughening mechanisms in polymer nanocomposites: From experiments to modelling," *Compos Sci Technol*, vol. 123, pp. 187-204, 2016.

[7] S. S. Vinay, M. R. Sanjay, S. Siengchin, and C. V. Venkatesh, "Effect of Al2O3 nanofillers in basalt/epoxy composites: Mechanical and tribological properties," (in English), *Polym Composite*, vol. 42, no. 4, pp. 1727-1740, 2021.

[8] İ. Aktitiz, K. Aydın, and A. Topcu, "Characterization of TiO2 Nanoparticle–Reinforced Polymer Nanocomposite Materials Printed by Stereolithography Method," *Journal of Materials Engineering and Performance*, vol. 30, no. 7, pp. 4975-4980, 2021.

[9] N. Geren, D. C. Acer, C. Uzay, and M. Bayramoglu, "The effect of boron carbide additive on the low-velocity impact properties of low-density foam core composite sandwich structures," *Polym Composite*, vol. 42, no. 4, pp. 2037-2049, 2021.

[10] P. S. Shuttleworth, A. M. Diez-Pascual, C. Marco, and G. Ellis, "Flexible Bionanocomposites from Epoxidized Hemp Seed Oil Thermosetting Resin Reinforced with Halloysite Nanotubes," *J Phys Chem B*, vol. 121, no. 11, pp. 2454-2467, 2017.

[11] J. Y. Zheng *et al.*, "Behavior of epoxy resin filled with nano-SiO2 treated with a Eugenol epoxy silane," *J Appl Polym Sci*, vol. 138, no. 14, 2021.

[12] J. Abenojar, J. Tutor, Y. Ballesteros, J. C. del Real, and M. A. Martinez, "Erosion-wear, mechanical and thermal properties of silica filled epoxy nanocomposites," *Compos Part B-Eng*, vol. 120, pp. 42-53, 2017.

[13] M. Landowski, M. Budzik, and K. Imielinska, "Water absorption and blistering of glass fibre-reinforced polymer marine laminates with nanoparticle-modified coatings," *J Compos Mater*, vol. 48, no. 23, pp. 2805-2813, Sep 2014.

[14] M. Megahed, A. A. Megahed, and M. A. Agwa, "The influence of incorporation of silica and carbon nanoparticles on the mechanical properties of hybrid glass fiber reinforced epoxy," *J Ind Text*, vol. 49, no. 2, pp. 181-199, 2019.

[15] J. C. Santos, L. M. G. Vieira, T. H. Panzera, M. A. Schiavon, A. L. Christoforo, and F. Scarpa, "Hybrid glass fibre reinforced composites with micro and poly-diallyldimethylammonium chloride (PDDA) functionalized nano silica inclusions," *Materials & Design (1980-2015)*, vol. 65, pp. 543-549, 2015.

[16] C. Su, X. Wang, L. N. Ding, and Z. S. Wu, "Enhancement of mechanical behavior of FRP composites modified by silica nanoparticles," *Constr Build Mater*, vol. 262, 2020.

[17] L. H. Wang, C. Tang, X. B. Wang, and W. Zheng, "Molecular dynamics simulation on the thermodynamic properties of insulating paper cellulose modified by silane coupling agent grafted nano-SiO2," *Aip Adv*, vol. 9, no. 12, 2019.

[18] A. Atiqah, M. N. M. Ansari, and L. Premkumar, "Impact and hardness properties of honeycomb natural fibre reinforced epoxy composites," *Materials Today: Proceedings*, vol. 29, pp. 138-142, 2020.

[19] M. Reddy, S. Valasingam, and K. Srinadh, "Micro Hardness and Erosive Wear Behavior of Tungsten Carbide Filled Epoxy Polymer Nano Composites," *International Journal of Mathematical, Engineering and Management Sciences*, vol. 5, pp. 405-415, 2020.

[20] Bagci, H. Imrek, and O. M. Khalfan, "Optimization of Test Parameters That Influence Erosive Wear Behaviors of Glass Fiber-Reinforced Epoxy Composites by Using the Taguchi Method," *J Tribol-T Asme*, vol. 137, no. 1, 2015.

[21] A. K. Pun, Siddhartha, and A. K. Singh, "Thermo-mechanical and Erosion Wear Peculiarity of Hybrid Composites Filled with Micro and Nano Silicon Dioxide Fillers - A Comparative Study," *Silicon-Neth*, vol. 11, no. 4, pp. 1885-1901, 2019.

[22] S. Safi, A. Zadhoush, and M. Ahmadi, "Flexural and Charpy impact behaviour of epoxy/glass fabric treated by nano-SiO2 and silane blend," *Plastics, Rubber and Composites*, vol. 46, no. 7, pp. 314-321, 2017.

[23] G. Vander Voort and G. Lucas, "Microindentation hardness testing," *Metal Progress*, vol. 154, pp. 21-25, 1998.

[24] V. Singh, P. Kumar, and V. K. Srivastava, "Influence of cement particles on the mechanical and buckling behavior of laminated GFRP composites with variation of end conditions of buckling," *Mater Res Express*, vol. 5, no. 6, 2018.

[25] T. Ahmad, R. Ahmad, M. Kamran, B. Wahjoedi, I. Shakoor, F. Hussain, F. Riaz, Z. Jamil, S. Isaac, and Q. Ashraf, "Effect of Thal silica sand nanoparticles and glass fiber reinforcements on epoxy-based hybrid composite," *Iran Polym J*, vol. 24, no. 1, pp. 21-27, 2015.

Bitlis Eren Üniversitesi Fen Bilimleri Dergisi
BİTLİS EREN UNIVERSITY JOURNAL OF SCIENCE
ISSN: 2147-3129/e-ISSN: 2147-3188
VOLUME: 11 NO: 3 PAGE: 759-769 YEAR: 2022
DOI: 10.17798/bitlisfen.1077393

Recurrent Neural Network Based Model Development for Energy Consumption Forecasting

Halit ÇETİNER[1*]

[1]*Isparta University of Applied Sciences, Vocational School of Technical Sciences, Isparta, Turkey (ORCID: 0000-0001-7794-2555)*

Keywords: GRU, LSTM, Forecasting of energy consumption, RNN.

Abstract

The world population is increasing day by day. As a result, limited resources are decreasing day by day. On the other hand, the amount of energy needed is constantly increasing. In this sense, decision makers must accurately estimate the amount of energy that society will require in the coming years and make plans accordingly. These plans are of critical importance for the peace and welfare of society. Based on the energy consumption values of Germany, it is aimed at estimating the energy consumption values with the GRU, LSTM, and proposed hybrid LSTM-GRU methods, which are among the popular RNN algorithms in the literature. The estimation performances of LSTM and GRU algorithms were obtained for MSE, RMSE, MAPE, MAE, and R^2 values as 0.0014, 0.0369, 6.35, 0.0292, 0.9703 and 0.0017, 0.0375, 6.60, 0.0298, 0.9650, respectively. The performance of the proposed hybrid LSTM-GRU method, which is another RNN-based algorithm used in the study, was obtained as 0.0013, 0.0358, 5.89, 0.0275, and 0.9720 for MSE, RMSE, MAPE, MAE and R^2 values, respectively. Although all three methods gave similar results, the training times of the proposed hybrid LSTM-GRU and LSTM algorithms took 7.50 and 6.58 minutes, respectively, but it took 4.87 minutes for the GRU algorithm. As can be understood from this value, it has been determined that it is possible to obtain similar values by sacrificing a very small amount of prediction performance in cases with time limitations.

1. Introduction

The operation of electrical networks has been costly and difficult to maintain for years. The main purpose of those who operate electricity networks is to maintain the balance between production and consumption in any emergency or weather condition. There is a trend towards renewable energy sources to reduce the damage to the environment while providing sustainable energy needs. One of the main reasons for this trend is that, depending on the energy consumption in the building sector, CO2 emissions occur at rates of 38% and 36% in the USA [1] and Europe [2], respectively. It is reported that the energy obtained by using fossil fuels causes an increase in the CO2 emission rate. Harmful emissions, such as CO2 from fossil fuels used to obtain energy, also cause global warming [3]. For the stated reasons, there is a tendency towards renewable energy sources both to provide energy efficiency and to not cause global warming.

The production of scientifically based structures instead of classical structures will enable the creation of structures that consume less energy. It is seen that new plans and projects are put into action by using high investments around the world in order to create structures that consume less energy. [4] conducted studies on the extent to which renewable energy sources reduce the harmful emissions of fossil fuels to the environment in the Latin American region for sixteen years. There are studies trying to find the points to which building

*Corresponding author: halitcetiner@isparta.edu.tr
Received: 22/02/2022, Accepted: 24/06/2022

designers should pay attention in the construction of new types of buildings with low energy consumption [5]. While they talk about the importance of parameters that building designers should implement for energy savings, they report that human life is affected by energy consumption.

The production of scientific-based structures instead of classical structures will enable the creation of structures that consume less energy. It is seen that new plans and projects are put into action by using high investments around the world in order to create structures that consume less energy. Koengkan et al. [4] conducted studies on the extent to which renewable energy sources reduce the harmful emissions of fossil fuels to the environment in the Latin American region for sixteen years. There are studies trying to find the points to which building designers should pay attention in the construction of new types of buildings with low energy consumption [5]. While they talk about the importance of parameters that building designers should implement for energy saving, they report that human life is affected by energy consumption.

With the development and spread of renewable energy sources, production has become more intermittent. In order to maintain distribution in case of interruption, it is necessary to estimate how much the consumption of the generated energy will be during the year. Furthermore, there is a serious increase in consumption as a result of the rapidly increasing population growth in the world. As a result of increasing population growth, there is an increase in the energy demand consumed. There are studies that state that energy demand is not only a population-dependent situation [6]. With the growth of the population and economy, a significant increase in energy consumption is observed [3], [7], [8]. It is estimated that a large part of the world's population will migrate from rural areas to urban areas in the coming years [9]. To support this information, an increase in the population of one quarter of the city with the largest population of a country like China is observed in the world. Energy consumption in the country of China is reported to grow at an annual rate of 5.6%, approximately three times the world average [10]. In this situation, it is stated that it is necessary to save energy by reducing harmful emissions in all countries with an increasing urbanization rate, especially China [7]. When this information is evaluated, it is an undeniable fact that there is a great increase in the world population.

Plans are proposed every year by different countries in order to control energy consumption around the world [11]. The main purpose of these plans is to prevent energy waste by controlling unnecessary energy consumption. Energy should be consumed, managed, and planned in an efficient and waste-free manner in all areas, especially in the building. Accurate consumption management and planning require effective energy consumption forecasting models. For this purpose, deep learning-based energy consumption estimation models are proposed using data from the ENTSO-E Transparency Platform, which distributes electricity to the European market.

The main contributions of this study to the literature for estimating energy consumption are listed below.

- Data normalization has been applied so that energy consumption data consisting of large data collections can be evaluated accurately and quickly.
- Two different models based on LSTM and GRU have been developed to accurately analyze the energy consumption estimation on the normalized data.
- To measure the performance of three different deep learning models based on the proposed LSTM, GRU, and LSTM-GRU, the traditional measurement metrics R^2 score, MAPE, RMSE, MSE, and MAE values are presented comparatively.
- When the results obtained from the R^2 score, MAPE, RMSE, MSE, and MAE values are examined, it is seen that a 0.98 accuracy rate is obtained from the proposed LSTM-GRU based model.

The next sections of the article are planned as follows. In the second part, the energy consumption dataset and the deep learning models run on this dataset are introduced. In the third section, the results of the R^2 score, MAPE, RMSE, MSE, and MAE performance obtained from the proposed deep learning models are presented comparatively. In the last section, the results of the study are evaluated. At the same time, suggestions for further work are presented.

2. Material and Methods

This part of the study is given under two subtitles: Material and Method. First of all, the information about the data set used in the study is discussed in detail in the material section.

2.1. Material

The data set used in this article was shared by the ENTSO-E Transparency Platform, which distributes electricity to the European market [12]. The dataset contains energy consumption data in megawatts (MW) for European countries from January 2015 to August 2020 at 15, 30 minute, and 1-hour time intervals. The dataset used in the study is a publicly available dataset that contains energy consumption data of fifteen countries, from Austria to Spain, and from France to Germany. In this dataset, Germany dataset was used for performance measurements.

The data was initially normalized in the 0-1 range. The quarter, hour, month, year, day of the year, day of the week, day of the month, week of year values presented in Table 1 are used as input features in the study. The energy in MW produced was used as the output value. The detailed information about the used features is presented in Table 1. In the study, 44,565 of the 44,568 energy consumption data, the details of which are presented in Table 1, were used. As seen in studies in the literature [13], dividing the data into two as training and testing according to the K-fold 5 value positively affected the performance of the study. For this reason, the energy consumption data in the study are divided into two separate parts as training and testing according to the K-fold 5 value, as it is in the studies [13]. The methods presented here in Section 2.2 Methods section performed training and testing operations on the K-fold 5 value on the data in Table 1.

Table 1. Features used in energy consumption estimation

Raw inputs date	Inputs								Outputs
Datetime	Quarter	Hour	Month	Year	Day of year	Day of week	Day of month	Week of year	MW
2015-01-01 00:00:00	1	0	1	2015	1	3	1	1	41342.5
2015-01-01 01:00:00	1	1	1	2015	1	3	1	1	40135
….	….	…	…	…	….	…	….	…	…
2017-05-15 15:00:00	2	15	5	2017	135	0	15	20	60972.5
….	….	…	…	…	….	…	….	…	…
2019-07-11 08:00:00	3	11	7	2019	192	3	11	28	66236
….	….	…	…	…	….	…	….	…	…
2020-01-31 23:00:00	1	23	1	2020	31	4	31	5	49399.5

2.2. Methods

In the study, algorithms in the RNN structure were used, which are frequently used in time series data in the literature. Firstly, the GRU structure was used for this purpose. After this structure, the LSTM structure, which is an RNN algorithm and was suggested later in the literature, was used.

2.2.1. GRU

The GRU algorithm does not use a memory unit to control the information flow in the RNN structure. If desired, it can be used directly in all confidential situations without any information control. GRU-based models have fewer parameters than advanced RNN models. For this reason, there is less processing load, and as a

result, it can be trained quickly. At the same time, less data is needed to generalize. The biggest disadvantage of the GRU method is that its success may be low when processing too much backward data in the backlink algorithm [14]. On the other hand, it is preferred because the training period mentioned above is short and there are situations where it can still give good results.

The GRU structure generally has two gates [15]. These gates are reset and updated gates. The reset gate determines how the new entry into the GRU unit is combined with the memory one step ahead. Another gate in the GRU, the update gate, determines how much of the previous state is retained. The equations used for these gates are detailed below.

$$Update\ gate\ (u_t) = \sigma\left(W^u x_t + U^{(u)} h_{t-1}\right) \quad (1)$$

$$Reset\ gate\ (s_t) = \sigma\left(W^s x_t + U^{(s)} h_{t-1}\right) \quad (2)$$

$\boldsymbol{W}$ used in Eqs. (1) and (2) represents at time t. $\boldsymbol{h_{t-1}}$ shows hidden layer values at time t-1 in Eqs. (1) and (2). $\boldsymbol{U}$ represents the GRU cell units in Eqs. (1) and (2). $\boldsymbol{\sigma}$ represents the sigmoid activation function.

2.2.2. LSTM

In general, there are problems with vanishing and exploding gradients in RNN structures [16], [17]. The main reason for this problem is that the weight matrices (W(k)) in the structure of the network are updated by multiplying one after the other. As a result, the gradient is encountered as being lost in the backpropagation stage of the RNN algorithms or exploding unstable to large values. As mentioned above, the main cause of this instability is sequential collisions. Despite all these disadvantages, RNN structures naturally give good results in short-term backpropagation between the previous step and the current step [18]. However, it gives lower results in long-term backpropagation processes. This problem is aimed at being solved using the LSTM method with the use of long-term memory [19]. Since the data is evaluated in short sequences in the LSTM method, the problems of back propagation operations in RNN algorithms are solved [20]. At the base of the LSTM algorithm, there are three gates and one layer shown in Figure 1 [17].

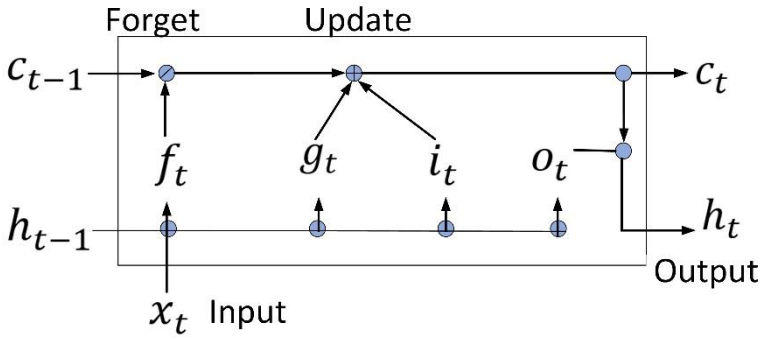

Figure 1. LSTM cell structure

The terms f_t, i_t, and o_t respectively presented in Figure 1 refer to forgetting entry and exit gates at time t. g_t represents the state layer. The contents of these variables are presented in Eqs. (3)-(6).

$$f_t = \sigma\left(W_f X_t + U_f h_{t-1} + b_f\right) \quad (3)$$

$$i_t = \sigma(W_i X_t + U_i h_{t-1} + b_t) \quad (4)$$

$$o_t = \sigma(W_o X_t + U_o h_{t-1} + b_o) \quad (5)$$

$$g_t = tanh\left(W_g x_t + R_g h_{t-1} + b_g\right) \quad (6)$$

W, R, and b are used in Eqs. (3)-(6) represent the weights, repetition weights, and biases between gates, respectively.

3. Results and Discussion

As stated in Section 2.1, in the experimental study, the data were first subjected to the normalization process. -The training and test data for K-fold 5 value are then divided into two groups. Finally, the system is trained with the training data according to the GRU algorithm

described in Section 2.2.1. The parameters used in the GRU algorithm during the training phase are presented in Table 2 in detail.

Table 2. GRU setting parameters

Parameter	Value
Layers	7
Loss	Mean absolute error
Optimizer	Adam
Epochs	50
Batch size	32
Activation	tanh

The layers in Table 2 represent the layers in the GRU algorithm, and the function in Eq. (7) is used in the optimizer GRU algorithm. Although SGD and RMSprop optimization methods were used other than Adam, the best results were obtained with the Adam optimization method. The parameters used in Table 2 and the normalized state of the training and test data of the energy consumption obtained as a result of the GRU algorithm are presented in Figure 2.

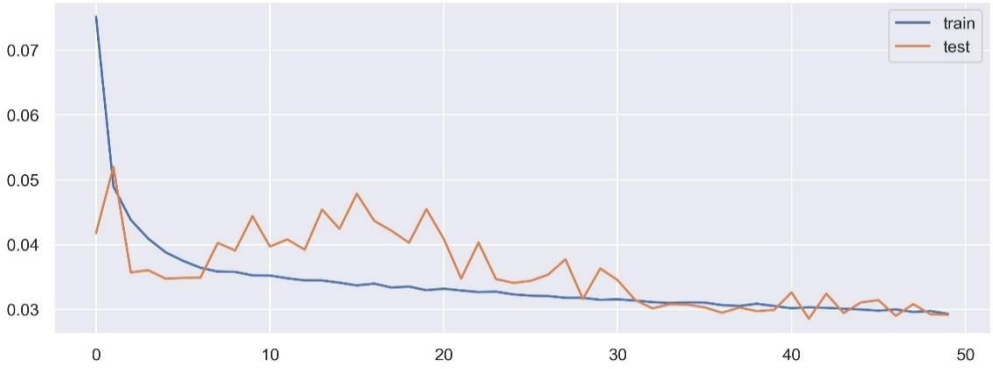

Figure 2. GRU model training and test loss graph

Figure 3 depicts the data converted to real values. As can be seen in Figure 3, the difference between the actual values and the predicted values is very close. At this stage, R^2 score, MSE, RMSE, and MAPE values were used in error evaluation processes. The values obtained by the GRU algorithm are presented in detail in Section 4.

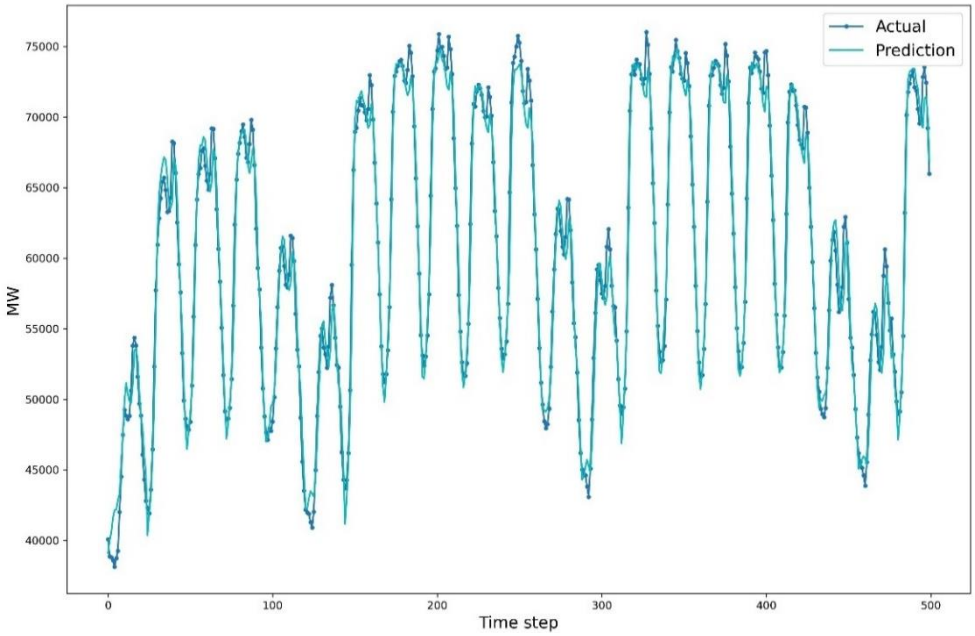

Figure 3. Predictions made by GRU model

In the second stage of the study, training and testing of the system were carried out using the LSTM algorithm described in Section 2.2.2 and the parameters presented in Table 3. At this stage, unlike in Table 2, the number of layers was increased by using ReLU for the activation function.

Table 3. LSTM setting parameters

Parameter	Value
Layers	10
Loss	Mean absolute error
Optimizer	Adam
Epochs	50
Batch size	32
Activation	ReLU

The results of the training and test values obtained with the LSTM algorithm are presented in Figures 4 and 5. While the normalized version of the obtained values is presented in Figure 4, the actual values are shown in Figure 5.

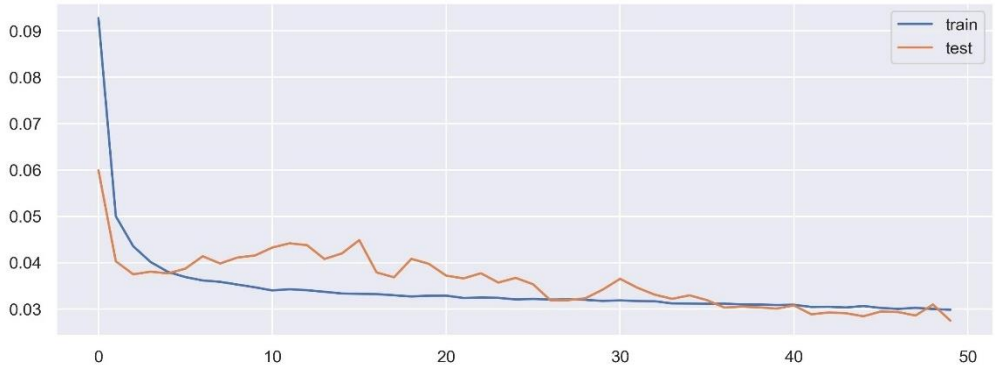

Figure 4. LSTM model training and test loss graph

When Figures 4 and 5 are examined, the difference between the actual values and the predicted values is very close. At this stage, as in the GRU algorithm, R^2 score, MSE, RMSE, and MAPE functions were used to measure the error values.

The results of the training and test values obtained with the LSTM algorithm are presented in Figures 4 and 5. While the normalized version of the obtained values is presented in Figure 4, the actual values are shown in Figure 5.

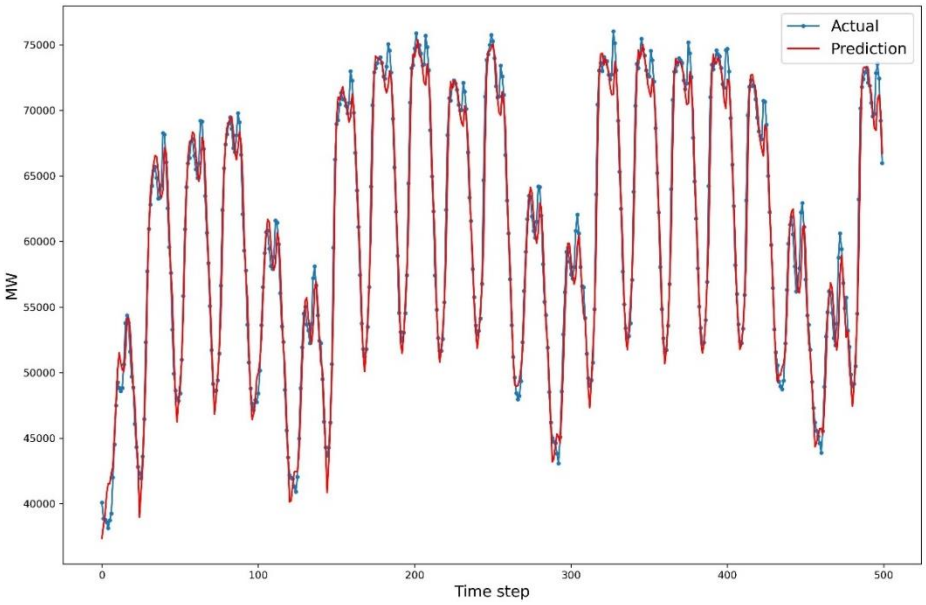

Figure 5. Predictions made by LSTM model

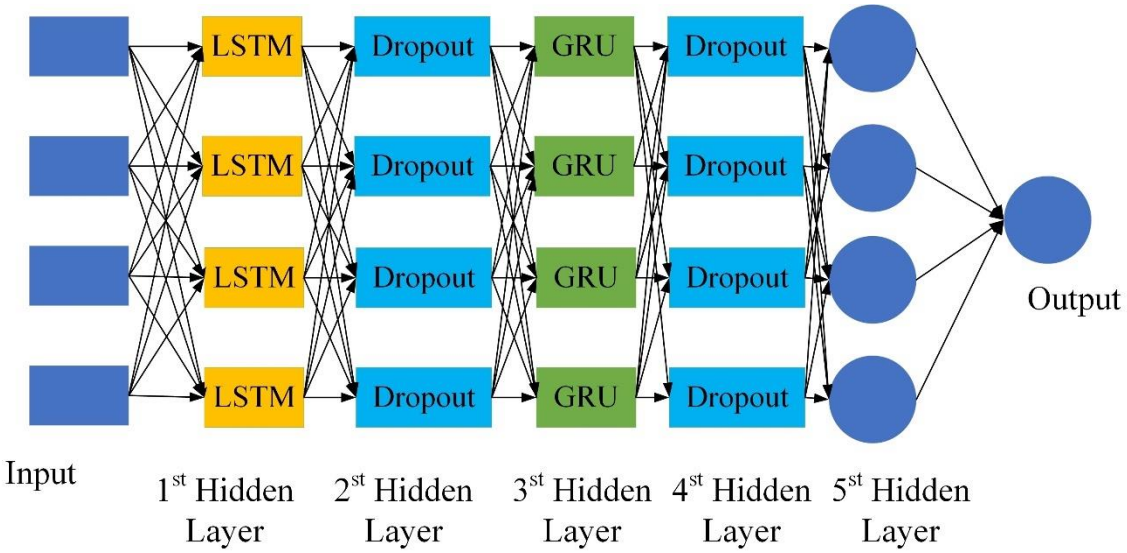

Figure 6. Proposed LSTM-GRU hybrid model

LSTM and GRU based LSTM-GRU hybrid model, the first layer is LSTM with 100 hidden neurons tanh activation function, the second layer is a forgetting layer with a rate of 20 percent. The third layer consists of a GRU layer with 20 hidden neurons. In the fourth layer, the forgetting layer, with a rate of 20 percent, has been added. In the fifth and sixth layers, there are 64 and 1 hidden neuron fully connected layers.

All features are first given to the model as input to the LSTM layer. Each LSTM neuron creates weights by performing operations on the data. The output obtained from the LSTM layer is left at 20% to prevent overfitting and is transmitted to the third layer, the GRU layer. In this layer, the weighing process continues. The resulting weighted values were transferred to the fully connected layer, leaving it for the second time for overfitting. The fully connected layer acts as a normal neural network layer. The weight values obtained from this layer are transmitted to the output neuron and the weight is produced. Error values were obtained by comparing the obtained output value with the real energy data. The update process continued until the minimum error value was obtained, as much as the number of iterations in other models. In the specified update processes, the loss, optimizer, epochs, and batch size values specified in Table 2 and Table 3 were treated as the same as the values used in other GRU and LSTM models.

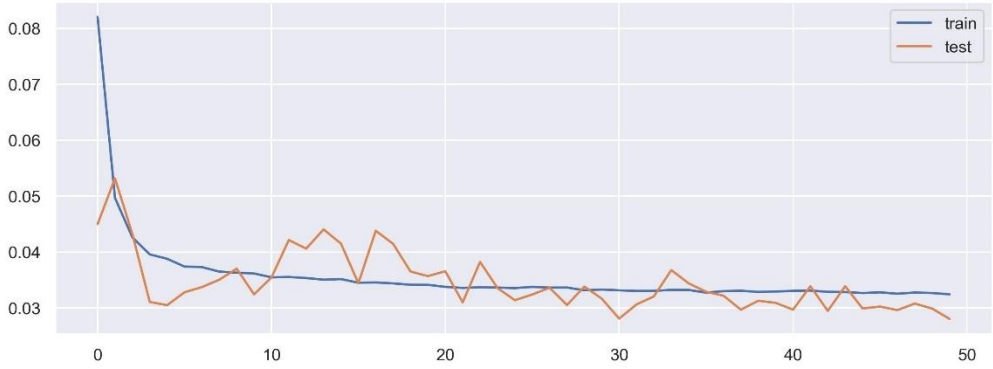

Figure 7. Proposed LSTM-GRU model training and test loss graph

When Figures 7 and 8 are examined, the difference between the actual values and the predicted values is very close. At this stage, as in the LSTM and GRU algorithms, R^2 score, MSE,

RMSE, and MAPE functions were used to measure the error values.

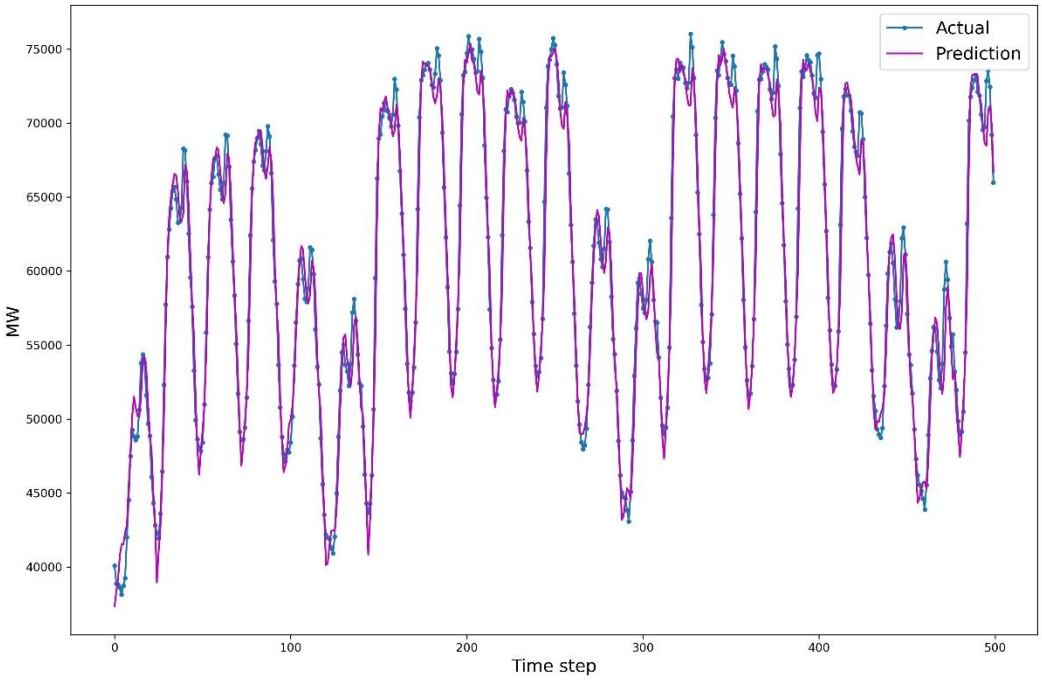

Figure 8. Predictions made by the LSTM-GRU model

Recent studies in the field of energy consumption [21]–[23] show that the problem of estimating energy consumption is still a unsolved area. In the first of these studies [21], it is stated that energy costs increase as industrialization and population increase. For this reason, it is reported that it is important to model energy use effectively with different models. When Table 4 and Table 5 are examined, it is seen that the fine-tuned structure of the proposed hybrid model gives more successful results than the GRU and LSTM models with the same settings. This success rate has been measured based on the best performance criteria in the literature. In addition, LSTM, and GRU [24] give better results in time series predictions than classical machine learning methods. At the same time, unlike [21]–[23] studies, the GRU method has been shown to consume less memory and be faster.

None of the LSTM, GRU, and hybrid models proposed in the article have been published in any study in the literature. For the first time in this study, the characteristics were run according to the details given in Table 2, Table 3, and Figure 6. In terms of the specified features, it differs from the studies published in recent years [21]–[23]. With the technical progress and development of machine learning algorithms such as ANN, the deep integration of LSTM and ANN structures instead of fully connected ANN gave a better result than the ANN method alone [25].

With the support of the mentioned international article, in this study, the ensemble hybrid model and the GRU model, which is a faster architecture close to LSTM and LSTM, are combined. In the results obtained by combining, the results of the proposed models in terms of MAPE, MAE, MSE, RMSE, and R^2 performance criteria are given, while in the study [21], only R^2 and MSE results are given in detail. At the same time, while this study was evaluated only in terms of ANN, LSTM was evaluated in terms of GRU and hybrid models. The difference between the LSTM model, which has different hidden layers, and the classical ANFIS-based models is compared in the estimation of energy consumption [22]. The model we propose is different from the study [22], both in terms of the GRU model and the hybrid model. The models used in the study of Bilgili et al [22] were evaluated according to the MAPE measurement metric. In our proposed study, MSE, RMSE, MAE and R^2 measurement metrics were used in addition to the MAPE measurement metric. Finally, the effect of short-term and long-term

variables on energy consumption estimation was examined with a machine learning algorithm called Random Forest [23]. In this study, deep learning models with better results have been developed by making connections between layers in the proposed models, instead of connecting layers with all their attributes to each other with a small structure.

4. Conclusion and Suggestions

It is stated that there is a tendency towards renewable energy sources instead of fossil fuels, which can cause high CO2 emissions. Renewable energy sources, on the other hand, are interrupted from time to time as there is no continuous access. In this case, energy consumption should be managed by providing accurate estimates. Data normalization was performed on the recommendations of [26] in the study on the fuel consumption imperative. In order to perform an accurate consumption analysis in line with the recommendations of [27], time series data consisting of 15, 30 minute, and 1-hour time intervals were used in this article. With the study we carried out, it was aimed to estimate the energy consumption values in Germany. For this purpose, 44,565 data were used in the [12] data set. The data used were separated as training and test data according to the K-fold 5 value but were normalized.

In the next step, training and testing processes were carried out according to the parameters determined in both models using the GRU, LSTM, and LSTM-GRU models, which are popular RNN [28]–[31] models in the literature. The MSE, RMSE, MAPE, MAE, and R^2 score values are presented in Eqs. (7)-(11) were used to measure the prediction success of both designed systems, respectively [32].

$$MSE = \frac{1}{m}\sum_{i=1}^{m}\left(Y_i - \hat{Y}_i\right)^2 \quad (7)$$

$$RMSE = \sqrt{\frac{1}{m}\sum_{i=1}^{m}\left(Y_i - \hat{Y}_i\right)^2} \quad (8)$$

$$MAPE = \frac{100}{m}\sum_{i=1}^{m}\left[\frac{Y_i - \hat{Y}_i}{Y_i}\right] \quad (9)$$

$$MAE = \frac{100}{m}\sum_{i=1}^{m}\left[\frac{Y_i - \hat{Y}_i}{Y_i}\right] \quad (10)$$

$$R^2 = 1 - \frac{\sum(Y_i - \hat{Y}_i)^2}{\sum(Y_i - \bar{Y})^2} \quad (11)$$

The results of the performance measurement used for both methods are presented in Table 4. As can be seen from the results presented in Table 4, the performance results obtained from the LSTM, GRU, and proposed hybrid LSTM-GRU algorithms are close to each other. The proposed hybrid LSTM-GRU algorithm performed one level better than the other proposed models. It can be used to create energy consumption forecasting models in a similar way in both models.

Table 4. Results obtained on the normalized Germany energy consumption data set

Algorithm	R^2 Score	MSE	RMSE	MAE	MAPE
Hybrid Model	0.9720	0.0013	0.0358	0.0275	5.89
LSTM Model	0.9703	0.0014	0.0369	0.0292	6.35
GRU Model	0.9650	0.0017	0.0375	0.0298	6.60

On the other hand, when the training time of both methods is compared, it has been determined that the system is trained in a shorter time with the GRU method. The training times obtained for both models proposed in the article are presented in Table 5. At this stage, which algorithm should be chosen for similar topics may be preferred depending on the hardware and time of the users.

Table 5. Training times

Training Algorithm	Time (Min)
LSTM Model	6.58
GRU Model	4.87
Hybrid Model	7.50

Contributions of the authors

The contributions of each author to the article should be indicated.

Conflict of Interest Statement

There is no conflict of interest between the authors.

Statement of Research and Publication Ethics

The study is complied with research and publication ethics.

References

[1] B. Becerik-Gerber, M. Siddiqui, L. Birilakis, O. E-Anwar, N. El-Gohary, T. Mahfouz, G. Jog, S. Li, and A. Kandil, "Civil engineering grand challenges: Opportunities for data sensing, information analysis, and knowledge discovery" *J. Comput. Civ. Eng.*, vol. 28, no. 4, 2014.

[2] A. S. Ahmad, M.Y. Hassan, H. A. Rahman, F. Hussin, H. Abdullah, and R. Saidur, "A review on applications of ANN and SVM for building electrical energy consumption forecasting" *Renew. Sustain. Energy Rev.*, vol. 33, pp. 102–109, 2014, doi: https://doi.org/10.1016/j.rser.2014.01.069.

[3] K. Amasyali and N. M. El-Gohary, "A review of data-driven building energy consumption prediction studies" *Renew. Sustain. Energy Rev.*, vol. 81, pp. 1192–1205, 2018, doi: https://doi.org/10.1016/j.rser.2017.04.095.

[4] M. Koengkan, J. A. Fuinhas, and N. Silva, "Exploring the capacity of renewable energy consumption to reduce outdoor air pollution death rate in Latin America and the Caribbean region" *Environ. Sci. Pollut. Res.*, vol. 28, no. 2, pp. 1656–1674, 2021.

[5] M. Moreno, B. Úbeda, A. Skarmeta, and M. Zamora, "How can We Tackle Energy Efficiency in IoT BasedSmart Buildings?" *Sensors*, vol. 14, no. 6, pp. 9582–9614, May 2014, doi: 10.3390/s140609582.

[6] M. E. Günay, "Forecasting annual gross electricity demand by artificial neural networks using predicted values of socio-economic indicators and climatic conditions: Case of Turkey" *Energy Policy*, vol. 90, pp. 92–101, 2016.

[7] H. Zhong, J. Wang, H. Jia, Y. Mu, and S. Lv, "Vector field-based support vector regression for building energy consumption prediction" *Appl. Energy*, vol. 242, pp. 403–414, 2019, doi: https://doi.org/10.1016/j.apenergy.2019.03.078.

[8] J.-S. Chou, D.-N. Truong, and C.-C. Kuo, "Imaging time-series with features to enable visual recognition of regional energy consumption by bio-inspired optimization of deep learning" *Energy*, vol. 224, 2021, doi: https://doi.org/10.1016/j.energy.2021.120100.

[9] N. H. A. Bahar, L. Michaela, S. Made, and V. V. Josh, "Meeting the food security challenge for nine billion people in 2050: What impact on forests?" *Glob. Environ. Chang.*, vol. 62, May 2020, doi: 10.1016/j.gloenvcha.2020.102056.

[10] T. Huo, H. Ren, X. Zhang, W. Cai, W. Feng, N. Zhou, and X. Wang, "China's energy consumption in the building sector: A Statistical Yearbook-Energy Balance Sheet based splitting method" *J. Clean. Prod.*, vol. 185, pp. 665–679, 2018, doi: https://doi.org/10.1016/j.jclepro.2018.02.283.

[11] Y. Zhang, C.-Q. He, B.-J. Tang, and Y.-M. Wei, "China's energy consumption in the building sector: A life cycle approach" *Energy Build.*, vol. 94, pp. 240–251, 2015, doi: https://doi.org/10.1016/j.enbuild.2015.03.011.

[12] F. Raucent, "Western Europe Power Consumption" *Entsoe Transparency Platform*, 2022. [Online]. Available: https://transparency.entsoe.eu/. [Accessed: May. 12, 2022].

[13] H. Çetiner and B. Kara, "Recurrent Neural Network Based Model Development for Wheat Yield Forecasting" *J. Eng. Sci. Adiyaman Univ.*, vol. 9, no. 16, pp. 204–218, 2022, doi: 10.54365/adyumbd.1075265.

[14] J. Wang, Y. Zhang, L.-C. Yu, and X. Zhang, "Contextual sentiment embeddings via bi-directional GRU language model" *Knowledge-Based Syst.*, vol. 235, 2022, doi: 10.1016/j.knosys.2021.107663.

[15] L. Hu, C. Wang, Z. Ye, and S. Wang, "Estimating gaseous pollutants from bus emissions: A hybrid model based on GRU and XGBoost" *Sci. Total Environ.*, vol. 783, 2021.

[16] F. Informatik, Y. Bengio, P. Frasconi, and J. Schmidhuber, "Gradient Flow in Recurrent Nets: the Difficulty of Learning Long-Term Dependencies" *A F. Guid. to Dyn. Recurr. Neural Networks*, Mar.

2003.
[17] H. Çetiner and İ. Çetiner, "Analysis of Different Regression Algorithms for the Estimate of Energy Consumption" *Eur. J. Sci. Technol.*, no. 31, pp. 23–33, Dec. 2021, doi: 10.31590/ejosat.969539.
[18] Z. Pang, F. Niu, and Z. O'Neill, "Solar radiation prediction using recurrent neural network and artificial neural network: A case study with comparisons" *Renew. Energy*, vol. 156, pp. 279–289, 2020, doi: https://doi.org/10.1016/j.renene.2020.04.042.
[19] D. T. Çetin and S. Metlek, "Forecasting of Turkish sovereign sukuk prices using artificial neural network model" *Acta Infologica*, vol. 5, no. 2, pp. 241–254, 2021.
[20] J. Q. Wang, Y. Du, and J. Wang, "LSTM based long-term energy consumption prediction with periodicity," *Energy*, vol. 197, 2020.
[21] M. Demircioğlu and S. Eşiyok, "Energy consumption forecast of Turkey using artificial neural networks from a sustainability perspective" *Int. J. Sustain. Energy*, pp. 1–15, Jan. 2022, doi: 10.1080/14786451.2022.2026357.
[22] M. Bilgili, N. Arslan, A. Şekertekin, and A. Yaşar, "Application of long short-term memory (LSTM) neural network based on deep learning for electricity energy consumption forecasting" *Turkish J. Electr. Eng. Comput. Sci.*, vol. 30, no. 1, pp. 140–157, 2022.
[23] P. C. Albuquerque, D. O. Cajueiro, and M. D. C. Rossi, "Machine learning models for forecasting power electricity consumption using a high dimensional dataset" *Expert Syst. Appl.*, vol. 187, 2022, doi: https://doi.org/10.1016/j.eswa.2021.115917.
[24] S. Ranjit, S. Shrestha, S. Subedi, and S. Shakya, "Comparison of algorithms in foreign exchange rate prediction" in *2018 IEEE 3rd International Conference on Computing, Communication and Security (ICCCS)*, pp. 9–13, 2018.
[25] M. Kowsher, A. Tahabilder, Md. Z. I. Sanjid, N. J. Prottasha, Md. S. Uddin, Md. A. Hossain, Mc. A. K. Jilani, "LSTM-ANN & BiLSTM-ANN: Hybrid deep learning models for enhanced classification accuracy" *Procedia Comput. Sci.*, vol. 193, pp. 131–140, 2021, doi: https://doi.org/10.1016/j.procs.2021.10.013.
[26] Y. Wei, X. Zhang, Y. Shi, L. Xia, S. Pan, J. Wu, M. Han, and X. Zhao, "A review of data-driven approaches for prediction and classification of building energy consumption" *Renew. Sustain. Energy Rev.*, vol. 82, pp. 1027–1047, 2018.
[27] S. García, A. Parejo, E. Personal, J. I. Guerrero, F. Biscarri, and C. León, "A retrospective analysis of the impact of the COVID-19 restrictions on energy consumption at a disaggregated level" *Appl. Energy*, vol. 287, 2021.
[28] K. E. ArunKumar, D. V Kalaga, C. M. S. Kumar, M. Kawaji, and T. M. Brenza, "Comparative analysis of Gated Recurrent Units (GRU), Long Short-Term Memory (LSTM) cells, Autoregressive Integrated Moving Average (ARIMA), Seasonal Autoregressive Integrated Moving Average (SARIMA) for forecasting COVID-19 trends" *Alexandria Eng. J.*, 2022.
[29] E. Ahmadzadeh, H. Kim, O. Jeong, N. Kim, and I. Moon, "A Deep Bidirectional LSTM-GRU Network Model for Automated Ciphertext Classification" *IEEE Access*, 2022.
[30] S. S. Bhadouria and S. Gupta, "Combined LSTM GRU Model for Prediction of Congestion State in QUIC Protocol" in *Proceedings of International Conference on Computational Intelligence and Emerging Power System*, pp. 123–131, 2022.
[31] W. Li, H. Wu, N. Zhu, Y. Jiang, J. Tan, and Y. Guo, "Prediction of dissolved oxygen in a fishery pond based on gated recurrent unit (GRU)" *Inf. Process. Agric.*, vol. 8, no. 1, pp. 185–193, 2021.
[32] H. Çetiner, "Yaprak Hastalıklarının Sınıflandırılabilmesi İçin Önceden Eğitilmiş Ağ Tabanlı Sinir Ağı Geliştirimi" *Adıyaman Üniversitesi Mühendislik Bilim. Derg.*, vol. 15, pp. 442–456, Sep. 2021, doi: 10.54365/adyumbd.988049.

Bitlis Eren Üniversitesi Fen Bilimleri Dergisi
BİTLİS EREN UNIVERSITY JOURNAL OF SCIENCE
ISSN: 2147-3129/e-ISSN: 2147-3188
VOLUME: 11 NO: 3 PAGE: 770-778 YEAR: 2022
DOI: 10.17798/bitlisfen.1079499

An Emotion Recognition Model Using Facial Expressions in Distance Learning

Beyza Esin ÖZSEVEN[1*], Naim ÇAĞMAN[2]

[1]*Tokat Gaziosmanpaşa University, Institute of Graduate Studies, Department of Mathematics, Tokat*
[2]*Tokat Gaziosmanpaşa University, Faculty of Science and Letters, Department of Mathematics, Tokat*
(ORCID: 0000-0003-4888-8259) (ORCID: 0000-0003-3037-1868)

Keywords: Distance Learning, Emotion Recognition, Facial Expression, Emotion Classification, Emotional Analysis.

Abstract

The most important factor on the success of the student is the student's readiness for the lesson, motivation, cognitive and emotional state. In face-to-face education, the educator can follow the student visually throughout the lesson and can observe his emotional state. One of the most important disadvantages of distance learning is that the emotional state of the student cannot be followed instantly. In addition, the processing time of emotion detection, in which real-time emotion detection will be performed, should be short. In this study, a method for emotion recognition is proposed by using distance and slope information between facial landmarks. In addition, the feature size was reduced by detecting only those that are effective for emotion recognition among the distance and slope information with statistical analysis. According to the results obtained, the proposed method and feature set achieved 86.11% success. In addition, the processing time is at a level that can be used in distance learning and can detect real-time emotion.

1. Introduction

Student motivation, cognitive and emotional state are important factors on learning performance [1]. In the physical learning environment, the educator and the student are in a face-to-face relationship, and appropriate educational conditions can be provided by responding appropriately according to the emotional state of the student [2]. However, in distance learning, the structure of the learning space and content is often presented in a static manner, without consideration of students' feelings, without interaction and without feedback from the educator. Therefore, determining the student's emotional states and reactions to a given situation is one of the most important elements for any distance learning environment [3]. Information received from the student, speech, facial expression, and vital signals (heart rate, etc.) are used for emotion recognition.

Getting information from the student is the simplest method [4]. The student is asked about his feeling and action is taken according to the answer received from the student. This method will give negative results on students who try to hide their emotions. In addition, students may react negatively when faced with such questions outside of the classroom [2]. Another important point is that emotions are not constant and change in a negative situation. For example, a student who starts the lesson happily may be upset when he cannot answer the question. Therefore, the emotional state should be constantly monitored throughout the learning process. Troung et al. tested the emotional state determined by the participant with the observer. According to the results obtained, the emotional state obtained in the two situations is different [5]. Students' descriptions of their emotions were examined in various papers [5, 6]. According to the results obtained, there are differences between self-assessment and observer evaluation.

It is a known fact that people reflect their emotions in their speech [7, 8]. Verbal communication includes some acoustic cues that aid in emotion recognition [9]. Acoustic feature-based

*Corresponding author: beyza_esin@hotmail.com
Received: 26.02.2022, Accepted: 23.08.2022

mostly used features are pitch, speech rate, formant frequencies, energy and phonetic features. [10]. In recent years, mel-frequency cepstral coefficients (MFCCs) have been used successfully in speech emotion recognition (SER) studies [11]–[21]. SER consists of two main parts. These are acoustic feature detection and classification. For acoustic feature detection, tools such as Praat [22], OpenSmile [23], OpenEar [24], SPAC [25]can be used, as well as coding with the help of software such as MATLAB. Classifiers such as SVM, HMM, GMM, AFDBN, ANN, k-NN, RBF are used for classification [2]. Although there are many studies on SER, there are various factors that negatively affect the success of the system. Acoustic features are affected by factors such as the speaker, sentence, and language of the speaker. Also, some emotion pairs contain similar acoustic attributes. For example, boredom and sadness have similar sound characteristics [26]. Another disadvantage of using SER in distance learning is that the SER system cannot be used actively since the student is mostly in the listening position.

Another method used for emotion recognition is facial expressions [27]. Sometimes a facial expression is more effective than speaking too many words. Emotional reactions affect the muscles under the skin of the face and facial expressions are formed. For example, in disgust, the mouth and nose muscles act in such a way as to produce facial disfigurement [28]. Facial expressions can be recognized from still images or camera images with image processing methods. These facial expressions can be used for person recognition or emotional recognition. Facial deformation, facial expression of emotional state is similar for all people, despite differences in gender, ethnicity, and age [29], [30]. Facial features fall into two categories: appearance and geometric features. In geometric-based methods, various points on the face are followed [31]. Accurate finding and tracking of facial features are imperative in geometric-based techniques. In many real applications, finding and detecting facial features is a time-consuming, complex, and error-prone process. Therefore, appearance-based techniques have also been proposed. These techniques model appearance changes such as wrinkles and furrows [2]. Compared to other emotion recognition methods, the use of facial expressions gives more successful results. The weakness for distance learning is that the student's face is mostly static during the learning process.

Physiological sensors can be used to emotion recognition with the help of various vital signals (heart rate, blood pressure, respiration, electro-dermal activity, electroencephalograms, electro-cardiograms, and electromyograms etc.) [32]. Thus, changes in physiological signals can be associated with emotion [33]. Emotion recognition based on vital signals is not usable for distance learning as it requires special hardware. When wearable technologies become widespread, their usability for distance learning will increase. A comparison of emotion detection methods in distance education is given in Table 1.

Table 1. Advantages and disadvantages of emotion recognition methods in distance education [2].

Method	Advantages	Disadvantages
Getting information from the student	- Easy to apply - No need for additional equipment	- It is boring for the student - Student's emotional changes cannot be detected during the lesson. - The student may not be honest
SER	- Suitability for language learning - Distinguish between high arousal and low arousal feelings	- Not available for all learning content - Inability to distinguish emotions with the same arousal
Facial Expression	- Identifying 7 basic emotional states - Availability of webcams	- Processes are time consuming - There may not be enough change in the faces of the students.
Vital Signals	- Distinguish between high arousal and low arousal feelings - High precision if using many parameters	- Needs some special tools and sensors not available for all students - Connecting sensors may disturb the student

Vital signals from the methods used for emotion recognition as described above are not available for distance learning. According to the information received from the student, emotion recognition will not give accurate results for distance learning as it will be both misleading and stable. Although emotion recognition through speech has achieved high success in various studies, its usability in distance learning is low as the student will mostly be in the listening position in the course. Emotion recognition through facial expressions has been

determined as the most suitable method that can provide efficient results for distance learning systems. In this study, a model based on facial points for emotion recognition was created using image processing, analytical geometry, statistics and SVM classifier, and the success of the model was analyzed. In the next part of the study, the relevant studies in the literature, the materials and methods used in the third part, the analysis of the proposed model in the fourth part, and the results and discussion are given.

2. Related Works

Emotion recognition from facial expressions consists of image acquisition, preprocessing, feature detection, classification and postprocessing processes. Most systems based on facial expressions classify them into categories of joy, sadness, surprise, fear, anger, disgust, and nervousness [34]. Feature extraction is the process of obtaining features that will be used to distinguish emotions from images. For this process, the features obtained by filtering methods over the model or face image that refer to the change of various points on the face are used. Gabor filters [35], principal component analysis [36], linear discriminant analysis [37] and facial action coding (a system for classifying human facial movements according to their facial appearance) [38] are used to obtain the features [39]. After the features are obtained, a classifier is needed for emotion recognition. The most widely used classifier at this stage are SVM [39].

Gabor wavelet [39], SVM [40, 41], k-NN [41], deep learning [42–46] methods were used in studies using image processing for emotion recognition using facial expressions in distance learning. According to the results of the study, in which gabor wavelet, principal component analysis and linear discriminant analysis were used for filtering and feature extraction, the highest success was obtained with gabor wavelet [39]. In addition, it has been found that deep learning methods increase the success rate between 1% and 5% compared to traditional methods [42]. Image processing-based methods operate on the image of the entire face. Another method used to detect facial expressions is the use of images of the eye and mouth region [47].

The relationships between facial expressions and learning styles in distance learning were also analyzed by image processing methods. In the study using deep learning, a database was created showing which emotion is associated with which learning style [43]. Facial expressions are also used to determine the current education level of the student. To determine the education level of the student, besides facial expressions, exam results, current level and time spent in the test were used [48]. In the study, in which the distance education environment was modeled using facial expressions and fuzzy logic, the answers given by the students to the questions and their emotional states were used. According to the facial expressions obtained here and the answers given by the student, the next learning level of the student was determined [44]. In another deep learning-based study, facial expressions were used to suggest suitable materials to students [46].

There are studies that refer to specific points on the face, facial muscle movements and moving points on the face for emotion recognition. Ayvaz et al. (2017), the coordinates of the points determined on the percentage were determined as features, and the highest success in classification was obtained with SVM and k-NN [41]. The Facial Action Coding System (FACS) [49], which references facial muscle movements, and the facereader [50], which detects moving points on the face, were used in the study aiming to evaluate the emotional state of students during the course in distance learning [51].

According to the results of studies on emotion detection in distance learning, machine learning methods and image processing have been used in many studies. Depending on the feature size, these methods require both a lot of workload and hardware. In addition, emotion recognition for distance learning systems is a process that requires continuity and needs to be done in real time. Therefore, emotion recognition system with low processing complexity and high success rate will increase the performance of distance learning systems.

3. Materials and Methods

A subset of the FACES [52] dataset, which is available for use and consists of 72 images, was used to test the proposed emotion recognition model. This dataset contains 6 emotional expressions (Anger, Disgust, Fear, Happiness, Neutral, Sadness). For each image in this data set, 70 points on the face were used. These points were obtained with faceSDK [53].

FaceSDK can be used in many programming languages (Microsoft Visual C++, C#, Objective C, Swift, Java, VB, Delphi, and Python) is a plugin. An example of face points obtained with FaceSDK is given in Figure 1.

Figure 1. Face dots obtained with the faceSDK for an example image in the FACES dataset.

Before the details of the proposed emotion recognition model, definitions of some basic concepts are given below.

Definition 1 (Emotional State)**.** $E = \{e_1, e_2, \dots, e_n\}$ be the set containing *n* different facial expressions. Emotional state $\sigma = (\epsilon_1, \epsilon_2, \dots, \epsilon_n)$ is defined as a probability distribution over *E* with [44]

$$\epsilon_1 = P(E = e_i), 0 \le \epsilon_i \le 1 \; for \; 1 \le i \le n \; and \sum_i \epsilon_i = 1 \qquad (1)$$

According to Definition 1, σ contains *n* facial expressions, and in the proposed approach, the emotional state includes probability degrees of six facial expression classes: anger (ϵ_1), disgust (ϵ_2), fear (ϵ_3), happiness (ϵ_4), sadness (ϵ_5) and neutral (ϵ_6).

Definition 2 (Facial Landmarks)**.** Facial landmarks (*fp)*, contain specific points on the face to be derived from each facial expression. These points are obtained with faceSDK [53] and defined as

$$fp = \{p_1, p_2, \dots, p_k\}, 1 \le k \le 70, for \; \forall E \qquad (2)$$

Definition 3 (Distance between landmarks). The distance between landmarks (*dist*) expresses the distance between each landmark obtained on the percentage and the other point. Analytical geometry is used to calculate these distances and is defined as

$$\text{Distance: } |AB| = \sqrt{(x_2 - x_1)^2 + (y_2 - y_1)^2} \; for \; A = (x_1, y_1) \; and \; B = (x_2, y_2) \qquad (3)$$

$$\text{Distance between landmarks: } dist = \{|p_1p_2|, |p_1p_3|, \dots, |p_ip_j|\}, 1 \le i \le 69, 1 \le j \le 70 \; for \; \forall fp \; and \; i \ne j \qquad (4)$$

Definition 4 (Slope between landmarks). The slope between landmarks (*slp*) expresses the slope between each landmark obtained in the percentage and the other point. These slopes are defined as

$$\text{Slope: } m = \frac{y_2 - y_1}{x_2 - x_1} \; for \; A = (x_1, y_1) \; and \; B = (x_2, y_2) \qquad (5)$$

$$\text{Slope between landmarks: } slp = \left\{\frac{p_{y_2} - p_{y_1}}{p_{x_2} - p_{x_1}}, \frac{p_{y_3} - p_{y_1}}{p_{x_3} - p_{x_1}}, \dots, \frac{p_{y_j} - p_{y_i}}{p_{x_j} - p_{x_i}}\right\}, 1 \le i \le 69, 1 \le j \le 70, for \; \forall fp \; and \; i \ne j \qquad (6)$$

Definition 5 (Detection of emotion-based landmarks). Detection of emotion-based landmarks is the detection of emotion with the help of features obtained using the information obtained from Definitions 3 and 4. However, the distance and slope data between points over 70 points in each face image increase the feature size. Therefore, those features that do not vary according to emotion can be statistically detected and removed from the feature set. Since the distance and slope data do not show normal distribution, the Kruskal-Wallis test can be used for this purpose.

The Kruskal-Wallis test (KW) is defined as

$$KW = \left[\frac{12}{N(N+1)} \sum t\bar{R}^2\right] - 3(N+1) \qquad (7)$$

where N is the total number of people/observations in the groups, g is the number of groups, $\bar{R}$ is the group mean rank, t is the number of people in each group.

Detection of emotion-based landmarks: Detection of emotion-based landmarks are defined as

$$DEL = \{KW(dist, slp)\}, p \le 0.05 \qquad (8)$$

The information given from Definition 1 has been created for the system to learn in the emotion recognition process. In the learning process, emotion-based facial points are obtained in line with the definitions given above by using the face points obtained with the faceSDK in the ready-made facial expression dataset. The resulting face points are used

for training the SVM. The block diagram of the emotion recognition model is given in Figure 2.

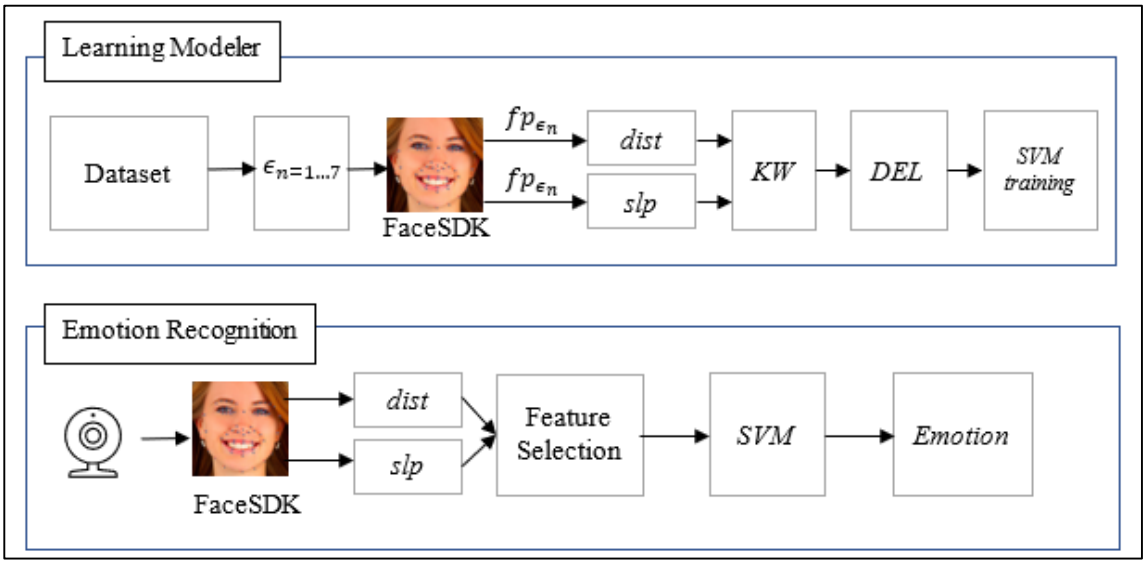

Figure 2. Emotion recognition model

The model given in Figure 2 has two stages: learning modeling and emotion recognition. The learning modeler must be activated once the system is first used and is used to detect DELs on ready datasets and train the classifier. The parameters to be used for SVM should be determined at the learning modeler stage. The emotion recognition stage should be used for real-time emotion detection when using the distance learning system. Here, emotion recognition is done by reducing the feature set and classifying it with the trained SVM.

4. Experimental Results

The slope and distance information of 70 facial landmarks obtained from each image were calculated and 4830 (*slp: slope, dist: distance*) features were obtained for each image. While calculating the slope value at the overlapping landmarks, infinite values depending on the 0 value were obtained. The features containing these values were removed from the data set and the number of features was reduced to 4618.

The Kruskal-Wallis test was applied to determine the remaining features related to emotional expression. Since the significance level is generally 95% in statistical analysis, the significance level was determined as 95% for Kruskal-Wallis. As a result of the analysis, 3328 of 4618 features were found to be related to emotional expressions.

SVM classifier was used to test the emotion recognition success of the dataset containing all features and reduced features, and the tests were carried out with WEKA [54]. The LibSVM library in WEKA was used and linear kernel was used. In addition, the normalization results are compared to eliminate measurement differences and reduce the classifier processing time. In the normalization process, the values of the features are normalized between 0-1. The results obtained are given in Table 2.

Table 2. Success rates of the proposed emotion detection model

Features	Normalization	Success Rate	Processing Time
4618	No	80.55%	0.27 seconds
3328	No	80.54%	0.08 seconds
4618	Yes	86.11%	0.18 seconds
3328	Yes	8472%	0.05 seconds

According to the results given in Table 2, distance and slope information can be used for emotion recognition. Reducing the feature set with Kruskal-wallis reduces the processing time by approximately 70%. Since emotion recognition will be performed in real time in the distance learning system, the processing time is as important as the success rate. Facial landmarks detection has a processing time of 0.00027 seconds and emotion recognition has a processing time of 0.05 seconds. In other words, facial emotion recognition takes a total of 0.05027 seconds. However, 0.05 seconds here is the time for both the learning modeler and emotion recognition. The processing time here will vary depending on the hardware used. Analyzes were made with a laptop computer with standard hardware (i5 processor, 8 GB RAM).

5. Conclusion and Discussion

The most important disadvantage of distance learning systems is the low interaction between the educator and the student. Although this disadvantage is tried to be eliminated with live lessons, the educator cannot fully follow the cognitive and emotional state of the student. For this reason, the emotional states of students in distance learning systems are also tried to be followed by the educator. For emotion recognition, information from the student, voice analysis, facial analysis and vital signals are used. Among these methods, the most suitable method for the student in distance learning is the use of facial expressions. Emotion recognition speed is as important as emotion recognition success in detecting emotion from facial expressions. Because instant emotion detection is necessary in live lessons. Therefore, the methods and models used for emotion recognition are important.

The aim of this study is to perform real-time and high-speed emotion recognition from facial expressions in distance learning systems. For this purpose, distance and slope information between facial landmarks were used. Effective ones from these landmarks were obtained by statistical analysis and the feature size was reduced. In addition, the processing time was shortened by normalization.

In the literature in recent years, deep learning-based methods have come to the fore. However, the computational complexity of these methods is higher than traditional methods such as SVM, k-NN. For this reason, the SVM classifier was used in the proposed model and the emotion recognition success was 86.11% with 0.18 seconds processing time and 84.72% with 0.05 seconds processing time. These times include the sum of both training and testing time of the model. Since the distance learning system will be carried out on server computers with special hardware, this period will be shortened even more. The learning modeler will be used only once after the distance learning system is activated, and emotion recognition will be performed with the training data there. Therefore, the processing time for emotion recognition will be approximately 0.00327 (0.00027 facial landmarks, 0.003 emotion recognition) seconds while the system is running. Since the Kruskal-Wallis test is used only for the learning modeler, the processing time is not considered. In addition, the normalization process also has very low processing time, which can be ignored.

Standard cameras have 30 fps and capture 30 frames per second. In other words, each frame is obtained in 0.033 seconds. Considering the image formation time and the time spent for emotion recognition, emotion recognition can be performed on real-time images simultaneously and without delay with the methods used.

The proposed model can be used for continuous monitoring of students' emotional states in live lessons, as well as exams in distance education, determination of readiness level and identification of students with the help of face landmarks.

Authors' Contributions

The authors' contributions to the paper are equal.

Statement of Conflicts of Interest

There is no conflict of interest between the authors.

Statement of Research and Publication Ethics

The authors declare that this study complies with Research and Publication Ethics

References

[1] N. Saberi and G. A. Montazer, 'A new approach for learners' modeling in e-learning environment using LMS logs analysis', in *6th National and 3rd International conference of e-Learning and e-Teaching*, 2012, pp. 25–33.

[2] M. Imani and G. A. Montazer, 'A survey of emotion recognition methods with emphasis on E-Learning environments', *Journal of Network and Computer Applications*, vol. 147, p. 102423, 2019.

[3] C. Villiger *et al.*, 'Effectiveness of an extracurricular program for struggling readers: A comparative study with parent tutors and volunteer tutors', *Learning and Instruction*, vol. 60, pp. 54–65, 2019.

[4] A. A. Kardan and Y. Einavypour, 'Multi-Criteria Learners Classification for Selecting an Appropriate Teaching Method', in *Proceedings of the World Congress on Engineering and Computer Science*, 2008, pp. 22–24.

[5] K. P. Truong, D. A. Van Leeuwen, and F. M. De Jong, 'Speech-based recognition of self-reported and observed emotion in a dimensional space', *Speech communication*, vol. 54, no. 9, pp. 1049–1063, 2012.

[6] C. Busso and S. S. Narayanan, 'The expression and perception of emotions: Comparing assessments of self versus others', presented at the Ninth annual conference of the international speech communication association, 2008.

[7] D. Morrison and L. C. De Silva, 'Voting ensembles for spoken affect classification', *Journal of Network and Computer Applications*, vol. 30, no. 4, pp. 1356–1365, 2007.

[8] N. Sadoughi and C. Busso, 'Speech-driven animation with meaningful behaviors', *Speech Communication*, vol. 110, pp. 90–100, 2019.

[9] E. Mendoza and G. Carballo, 'Vocal tremor and psychological stress', *Journal of Voice*, vol. 13, no. 1, pp. 105–112, 1999.

[10] M. Pantic and L. J. Rothkrantz, 'Toward an affect-sensitive multimodal human-computer interaction', *Proceedings of the IEEE*, vol. 91, no. 9, pp. 1370–1390, 2003.

[11] H. Cao, R. Verma, and A. Nenkova, 'Speaker-sensitive emotion recognition via ranking: Studies on acted and spontaneous speech', *Computer speech & language*, vol. 29, no. 1, pp. 186–202, 2015.

[12] F. Chenchah and Z. Lachiri, 'A bio-inspired emotion recognition system under real-life conditions', *Applied Acoustics*, vol. 115, pp. 6–14, 2017.

[13] W. Dai, D. Han, Y. Dai, and D. Xu, 'Emotion recognition and affective computing on vocal social media', *Information & Management*, vol. 52, no. 7, pp. 777–788, 2015.

[14] C.-C. Lee, E. Mower, C. Busso, S. Lee, and S. Narayanan, 'Emotion recognition using a hierarchical binary decision tree approach', *Speech Communication*, vol. 53, no. 9–10, pp. 1162–1171, 2011.

[15] K. Mannepalli, P. N. Sastry, and M. Suman, 'A novel adaptive fractional deep belief networks for speaker emotion recognition', *Alexandria Engineering Journal*, vol. 56, no. 4, pp. 485–497, 2017.

[16] S. Mariooryad and C. Busso, 'Compensating for speaker or lexical variabilities in speech for emotion recognition', *Speech Communication*, vol. 57, pp. 1–12, 2014.

[17] V. V. Nanavare and S. K. Jagtap, 'Recognition of human emotions from speech processing', *Procedia Computer Science*, vol. 49, pp. 24–32, 2015.

[18] C. S. Ooi, K. P. Seng, L.-M. Ang, and L. W. Chew, 'A new approach of audio emotion recognition', *Expert systems with applications*, vol. 41, no. 13, pp. 5858–5869, 2014.

[19] T. Özseven, 'A novel feature selection method for speech emotion recognition', *Applied Acoustics*, vol. 146, pp. 320–326, 2019.

[20] T. M. Rajisha, A. P. Sunija, and K. S. Riyas, 'Performance analysis of Malayalam language speech emotion recognition system using ANN/SVM', *Procedia Technology*, vol. 24, pp. 1097–1104, 2016.

[21] P. Vasuki and C. Aravindan, 'Improving emotion recognition from speech using sensor fusion techniques', in *TENCON 2012 IEEE Region 10 Conference*, 2012, pp. 1–6.

[22] P. Boersma, 'Praat, a system for doing phonetics by computer', *Glot. Int.*, vol. 5, no. 9, pp. 341–345, 2001.

[23] F. Eyben, M. Wöllmer, and B. Schuller, 'Opensmile: the munich versatile and fast open-source audio feature extractor', in *Proceedings of the 18th ACM international conference on Multimedia*, 2010, pp. 1459–1462.

[24] F. Eyben, M. Wöllmer, and B. Schuller, 'OpenEAR—introducing the Munich open-source emotion and affect recognition toolkit', in *2009 3rd international conference on affective computing and intelligent interaction and workshops*, 2009, pp. 1–6.
[25] T. Özseven and M. Düğenci, 'SPeech ACoustic (SPAC): A novel tool for speech feature extraction and classification', *Applied Acoustics*, vol. 136, pp. 1–8, 2018.
[26] A. Jaimes and N. Sebe, 'Multimodal human–computer interaction: A survey', *Computer vision and image understanding*, vol. 108, no. 1–2, pp. 116–134, 2007.
[27] M. IqbalQuraishi, J. Pal Choudhury, M. De, and P. Chakraborty, 'A framework for the recognition of human emotion using soft computing models', *International Journal of Computer Applications*, vol. 40, no. 17, pp. 50–55, 2012.
[28] K. Shanmugarajah, S. Gaind, A. Clarke, and P. E. Butler, 'The role of disgust emotions in the observer response to facial disfigurement', *Body Image*, vol. 9, no. 4, pp. 455–461, 2012.
[29] C. Darwin, 'The expression of the emotions in man and animals (1872)', *The Portable Darwin*, pp. 364–393, 1993.
[30] P. Ekman and W. V. Friesen, 'Constants across cultures in the face and emotion.', *Journal of personality and social psychology*, vol. 17, no. 2, p. 124, 1971.
[31] D. Ghimire and J. Lee, 'Geometric feature-based facial expression recognition in image sequences using multi-class adaboost and support vector machines', *Sensors*, vol. 13, no. 6, pp. 7714–7734, 2013.
[32] F. Nasoz, C. L. Lisetti, K. Alvarez, and N. Finkelstein, 'Emotion recognition from physiological signals for user modeling of affect', presented at the Proceedings of the 3rd Workshop on Affective and Attitude User Modelling (Pittsburgh, PA, USA, 2003.
[33] S. Koelstra *et al.*, 'Deap: A database for emotion analysis; using physiological signals', *IEEE transactions on affective computing*, vol. 3, no. 1, pp. 18–31, 2011.
[34] L. Li, L. Cheng, and K. Qian, 'An e-learning system model based on affective computing', in *2008 international conference on cyberworlds*, 2008, pp. 45–50.
[35] J. G. Daugman, 'Complete discrete 2-D Gabor transforms by neural networks for image analysis and compression', *IEEE Transactions on acoustics, speech, and signal processing*, vol. 36, no. 7, pp. 1169–1179, 1988.
[36] M. Turk and A. Pentland, 'Eigenfaces for recognition', *Journal of cognitive neuroscience*, vol. 3, no. 1, pp. 71–86, 1991.
[37] K. Delac, M. Grgic, and S. Grgic, 'Independent comparative study of PCA, ICA, and LDA on the FERET data set', *International Journal of Imaging Systems and Technology*, vol. 15, no. 5, pp. 252–260, 2005.
[38] S. D'Mello, R. W. Picard, and A. Graesser, 'Toward an affect-sensitive AutoTutor', *IEEE Intelligent Systems*, vol. 22, no. 4, pp. 53–61, 2007.
[39] A. K. Oryina and A. O. Adedolapo, 'Emotion recognition for user centred e-learning', in *2016 IEEE 40th Annual Computer Software and Applications Conference (COMPSAC)*, 2016, vol. 2, pp. 509–514.
[40] K. Bahreini, R. Nadolski, and W. Westera, 'Data fusion for real-time multimodal emotion recognition through webcams and microphones in e-learning', *International Journal of Human–Computer Interaction*, vol. 32, no. 5, pp. 415–430, 2016.
[41] U. Ayvaz, H. Gürüler, and M. O. Devrim, 'Use of facial emotion recognition in e-learning systems', *Information technologies and teaching aids*, no. 60, вип. 4, pp. 95–104, 2017.
[42] Y. Guo, D. Tao, J. Yu, H. Xiong, Y. Li, and D. Tao, 'Deep neural networks with relativity learning for facial expression recognition', in *2016 IEEE International Conference on Multimedia & Expo Workshops (ICMEW)*, 2016, pp. 1–6.
[43] F. L. Gambo, G. M. Wajiga, and E. J. Garba, 'A Conceptual Framework for Detection of Learning Style from Facial Expressions using Convolutional Neural Network', in *2019 2nd International Conference of the IEEE Nigeria Computer Chapter (NigeriaComputConf)*, 2019, pp. 1–5.
[44] M. Megahed and A. Mohammed, 'Modeling adaptive E-Learning environment using facial expressions and fuzzy logic', *Expert Systems with Applications*, vol. 157, p. 113460, Nov. 2020, doi: 10.1016/j.eswa.2020.113460.
[45] A. Pise, H. Vadapalli, and I. Sanders, 'Facial emotion recognition using temporal relational network: an application to E-learning', *Multimedia Tools and Applications*, pp. 1–21, 2020.

[46] S.-Y. Lin, C.-M. Wu, S.-L. Chen, T.-L. Lin, and Y.-W. Tseng, 'Continuous Facial Emotion Recognition Method Based on Deep Learning of Academic Emotions', *Sensors and Materials*, vol. 32, no. 10, pp. 3243–3259, 2020.

[47] D. Yang, A. Alsadoon, P. C. Prasad, A. K. Singh, and A. Elchouemi, 'An emotion recognition model based on facial recognition in virtual learning environment', *Procedia Computer Science*, vol. 125, pp. 2–10, 2018.

[48] H. Hesham, M. Nabawy, O. Safwat, Y. Khalifa, H. Metawie, and A. Mohammed, 'Detecting Education level using Facial Expressions in E-learning Systems', in *2020 International Conference on Electrical, Communication, and Computer Engineering (ICECCE)*, 2020, pp. 1–6.

[49] P. Ekman and W. V. Friesen, *Facial action coding system: Investigator's guide*. Consulting Psychologists Press, 1978.

[50] M. J. Den Uyl and H. Van Kuilenburg, 'The FaceReader: Online facial expression recognition', in *Proceedings of measuring behavior*, 2005, vol. 30, no. 2, pp. 589–590.

[51] M. Soltani, H. Zarzour, M. C. Babahenini, M. Hammad, A.-S. Mohammad, and Y. Jararweh, 'An emotional feedback based on facial action coding system for MOOCs with computer-based assessment', in *2019 Sixth International Conference on Social Networks Analysis, Management and Security (SNAMS)*, 2019, pp. 286–290.

[52] N. C. Ebner, M. Riediger, and U. Lindenberger, 'FACES—A database of facial expressions in young, middle-aged, and older women and men: Development and validation', *Behavior research methods*, vol. 42, no. 1, pp. 351–362, 2010.

[53] 'Luxand - Detect and Recognize Faces and Facial Features with Luxand FaceSDK'. https://www.luxand.com/facesdk/ (accessed Jun. 16, 2021).

[54] I. H. Witten, E. Frank, L. E. Trigg, M. A. Hall, G. Holmes, and S. J. Cunningham, 'Weka: Practical machine learning tools and techniques with Java implementations', *(Working paper 99/11). Hamilton, New Zealand: University of Waikato, Department of Computer Science.*, 1999.

Bitlis Eren Üniversitesi Fen Bilimleri Dergisi
BİTLİS EREN UNIVERSITY JOURNAL OF SCIENCE
ISSN: 2147-3129/e-ISSN: 2147-3188
VOLUME: 11 NO: 3 PAGE: 779-783 YEAR: 2022
DOI: 10.17798/bitlisfen.1086972

Normal Surfaces Associated with Adjoint Curves in E3

Ahmet SAZAK[1*], Talat KÖRPINAR[2]

[1]*Mus Alparslan University, Varto Vocational School, Mus, TURKEY*
[2]*Mus Alparslan University, Faculty of Science And Literature, Mus, TURKEY*

(ORCID: 0000-0002-5620-6441) (ORCID: 0000-0003-4000-0892)

Keywords: Weingarten Surface, Normal surface, Serret-Frenet frame, Adjoint curve.

Abstract
In this study, we work on the surfaces determined in relation to associated curves. We study normal surfaces defined with the help of adjoint curves, a special type of associated curve. For this, we first remember the basic equations of the 3-dimensional Euclidean space, which is the space we work with, and the adjoint curve issue. Then, by computing the first and second fundamental forms, principal curvatures, and mean and Gaussian curvatures of the normal surface of an adjoint curve, we obtain the characterizations of this surface and related some results.

1. Introduction

Surfaces and curves in differential geometry is a valuable topic that paves the way for studies in applied sciences by providing geometric expressions to fields such as physics, engineering and geophysics that serve technology. The subject of surfaces associated with curves, which we will discuss in this study, is one of the special examples of this. These surfaces, which are formed as a result of the motion of a curve or line depending on another curve, provide important conveniences in terms of giving geometric expressions to the subject [1-13].

Tangent, normal, and binormal surfaces, which are formed as a result of the motion of a curve in the direction of tangent, unit normal and binormal vector field due to the change of the time parameter, can be given as examples of surfaces associated with curves. Associated curves have an important place in determining the behavior and characterization of surfaces. The surfaces established with the help of adjoint curves, which is a type of associated curve, form the framework of our study [14-17].

In this study, we define the normal surfaces of adjoint curves and obtain the characterizations of these surfaces and some related results. First, we define the normal surface determining by the movement of the adjoint curve in the direction of the normal vector field. Then we obtain some results with the help of first and second fundamental forms, principal curvatures, Gaussian curvature, and mean curvature of this surface.

2. Preliminaries

In this part, we review the basic definitions and formulas related to the frame elements and the concept of adjoint curves that we have studied in the 3D Euclidean space. Next, we will discuss some fundamentals that have an important place in determining the behavior and characterization of a surface.

The Serret Frenet(SF) formulas in 3D Euclidean are given as

$$\begin{bmatrix} \nabla_s \boldsymbol{T} \\ \nabla_s \boldsymbol{N} \\ \nabla_s \boldsymbol{B} \end{bmatrix} = \begin{bmatrix} 0 & \mu & 0 \\ -\mu & 0 & \rho \\ 0 & -\rho & 0 \end{bmatrix} \begin{bmatrix} \boldsymbol{T} \\ \boldsymbol{N} \\ \boldsymbol{B} \end{bmatrix},$$

where μ, ρ are curvature and torsion of λ, respectively. Let s be the length of the arc [1]. Then, the SF frame formulas are given as

$$\boldsymbol{T} = \lambda'(s), \quad \boldsymbol{N} = \frac{\lambda''(s)}{\|\lambda''(s)\|}, \quad \boldsymbol{B} = \boldsymbol{T} \times \boldsymbol{N}.$$

Definition 1. Let $\{\boldsymbol{T}_\lambda, \boldsymbol{N}_\lambda, \boldsymbol{B}_\lambda\}$ be the SF frame of λ curve with s parameter. Then, the adjoint curve of λ according to the SF frame is defined as [2]

*Corresponding author: a.sazak@alparslan.edu.tr
Received 13.03.2022, Accepted: 26.09.2022

$$\delta(s) = \int_{s_0}^{s} \boldsymbol{B}_\lambda(s)ds.$$

A surface that passes a straight line through each point is called a ruled surface. Surfaces such as cone, cylinder, helicoid, conical surface can be given as examples of ruled surfaces. A ruled surface is expressed as

$$\varphi(s,t) = \lambda + t\boldsymbol{X},$$

where the vector field X is the direction of the surface and the curve λ is the base curve of the surface [5].

Then we can construct a ruled surface whose base curve is curve λ and whose direction is the normal(unit) vector field of λ. This surface is called the normal surface defined by the curve λ. Hence, we give the definition:

Definition 2. The normal surface of a regular curve λ is defined by $\varphi(s,t) = \lambda + t\boldsymbol{N}$ [5].

Theorem 3. Let $\{\boldsymbol{T}_\lambda, \boldsymbol{N}_\lambda, \boldsymbol{B}_\lambda\}$ be the SF frame of λ curve with s parameter, δ be adjoint curve of λ according to the SF frame and μ_λ and ρ_λ be curvature and torsion of λ. Denote by $\{\boldsymbol{T}_\delta, \boldsymbol{N}_\delta, \boldsymbol{B}_\delta\}$ the SF frame elements for δ and denote by ρ_δ and μ_δ be torsion and curvature of δ. Then, the relationship between δ and λ can be given by the following equations [2]:

$$\boldsymbol{T}_\lambda = \boldsymbol{B}_\delta, \quad \boldsymbol{N}_\lambda = -\boldsymbol{N}_\delta, \quad \boldsymbol{B}_\lambda = \boldsymbol{T}_\delta,$$
$$\mu_\delta = \rho_\lambda \quad \rho_\delta = \mu_\lambda.$$

The normal(unit) vector field for any surface $\varphi(s,t)$ is defined by the equation

$$n = \frac{\varphi_s \wedge \varphi_t}{\|\varphi_s \wedge \varphi_t\|},$$

where $\varphi_t = \partial\varphi/\partial t$, $\varphi_s = \partial\varphi/\partial s$ and, t is parameter representing time. Then, the first and the second fundamental forms of φ are given by following equations:

$$\boldsymbol{I} = Eds^2 + 2Fdsdt + Gdt^2,$$
$$\boldsymbol{II} = eds^2 + 2fdsdt + gdt^2,$$

where

$$E = \langle\varphi_s, \varphi_s\rangle,\ F = \langle\varphi_s, \varphi_t\rangle,\ G = \langle\varphi_t, \varphi_t\rangle,$$
$$e = \langle\varphi_{ss}, n\rangle,\ f = \langle\varphi_{st}, n\rangle,\ g = \langle\varphi_{tt}, n\rangle. \quad (1)$$

Also, Gaussian and mean curvatures K and H are given as

$$H = \frac{Eg-2Ff+Ge}{2(EG-F^2)},\ K = \frac{eg-f^2}{EG-F^2} \quad (2)$$

and principal curvatures are defined by [3-7]

$$k_1 = \sqrt{H^2-K} + H,\ k_2 = H - \sqrt{H^2-K}. \quad (3)$$

Theorem 4. A surface is minimal surface if and only if it has vanished mean curvature of this surface [1].

Theorem 5. A surface is a flat (developable) surface if and only if it has vanished Gaussian curvature of this surface [1].

Definition 6. If the relationship between the mean and Gaussian curvatures of a surface can be given by equation $H_sK_t - H_tK_s = 0$, then this surface is a Weingarten surface [12].

3. Normal Surfaces of Adjoint Curves

In this section, we discuss certain characterizations and results for the normal surface of an adjoint curve with the help of information given in the previous section.

Theorem 7. Let δ be adjoint curve of λ curve with arc length parameter. Then, first and second fundamental forms of normal surface of δ are given by the following equations:

$$\boldsymbol{I}_\delta = (t^2\mu_\lambda^2 + (1-t\rho_\lambda)^2)ds^2 + dt^2,$$
$$\boldsymbol{II}_\delta = \frac{t\mu_\lambda'(1-t\rho_\lambda)+t\mu_\lambda\rho_\lambda'}{\sqrt{t^2\mu_\lambda^2+(1-t\rho_\lambda)^2}}ds^2 + \frac{2\mu_\lambda}{\sqrt{t^2\mu_\lambda^2+(1-t\rho_\lambda)^2}}dsdt.$$

Proof. From the definition of normal surface, the normal surface of δ is written as

$$\varphi^\delta(s,t) = \delta + t\boldsymbol{N}_\delta.$$

As a result, the following equalities are obtained:

$$\varphi_s^\delta = t\mu_\lambda\boldsymbol{T}_\lambda + (1-t\rho_\lambda)\boldsymbol{B}_\lambda,$$
$$\varphi_{ss}^\delta = t\mu_\lambda'\boldsymbol{T}_\lambda + (t\mu_\lambda^2 + t\rho_\lambda^2 - \rho_\lambda)\boldsymbol{N}_\lambda - t\rho_\lambda'\boldsymbol{B}_\lambda,$$
$$\varphi_t^\delta = -\boldsymbol{N}_\lambda, \quad \varphi_{tt}^\delta = 0, \quad \varphi_{st}^\delta = \mu_\lambda\boldsymbol{T}_\lambda - \rho_\lambda\boldsymbol{B}_\lambda.$$

and, from the equalities, unit standart normal vector field of φ^δ surface is found as

$$n_\delta = \frac{\varphi_s^\delta \times \varphi_t^\delta}{\|\varphi_s^\delta \times \varphi_t^\delta\|} = \frac{(1-t\rho_\lambda)\boldsymbol{T}_\lambda - t\mu_\lambda\boldsymbol{B}_\lambda}{\sqrt{t^2\mu_\lambda^2+(1-t\rho_\lambda)^2}}.$$

These equalities are obtained similarly for the normal surface of λ curve. Then, with the help of Theorem 3 and of the equations given at the beginning of this section, we obtain

$$E = t^2\mu_\lambda^2 + (1-t\rho_\lambda)^2, \quad F = 0, \quad G = 1,$$
$$e = \frac{t\mu_\lambda'(1-t\rho_\lambda)+t\mu_\lambda\rho_\lambda'}{\sqrt{t^2\mu_\lambda^2+(1-t\rho_\lambda)^2}},\ f = \frac{\mu_\lambda}{\sqrt{t^2\mu_\lambda^2+(1-t\rho_\lambda)^2}},\ g = 0. \quad (4)$$

Hence, the first and the second fundamental forms of normal surfaces of δ are obtained as

$$\boldsymbol{I}_\delta = (t^2\mu_\lambda^2 + (1-t\rho_\lambda)^2)ds^2 + dt^2,$$
$$\boldsymbol{II}_\delta = \frac{t\mu_\lambda'(1-t\rho_\lambda)+t\mu_\lambda\rho_\lambda'}{\sqrt{t^2\mu_\lambda^2+(1-t\rho_\lambda)^2}}ds^2 + \frac{2\mu_\lambda}{\sqrt{t^2\mu_\lambda^2+(1-t\rho_\lambda)^2}}dsdt.$$

Corollary 8. Let δ be adjoint curve of λ curve with arc length parameter. Then, mean (H_δ) and Gaussian

(K_δ) curvatures of the normal surfaces of δ are given by the following equations:

$$K_\delta = \frac{-\mu_\lambda^2}{(t^2\mu_\lambda^2+(1-t\rho_\lambda)^2)^2}, \quad H_\delta = \frac{t\mu_\lambda'(1-t\rho_\lambda)+t\mu_\lambda\rho_\lambda'}{2\sqrt{(t^2\mu_\lambda^2+(1-t\rho_\lambda)^2)^3}}. \tag{5}$$

Proof. Using equations (4), we obtain

$$K_\delta = \frac{e_\delta g_\delta - f_\delta^2}{E_\delta G_\delta - F_\delta^2} = \frac{-\mu_\lambda^2}{(t^2\mu_\lambda^2+(1-t\rho_\lambda)^2)^2},$$
$$H_\delta = \frac{E_\delta g_\delta - 2F_\delta f_\delta + G_\delta e_\delta}{2(E_\delta G_\delta - F_\delta^2)} = \frac{t\mu_\lambda'(1-t\rho_\lambda)+t\mu_\lambda\rho_\lambda'}{2\sqrt{(t^2\mu_\lambda^2+(1-t\rho_\lambda)^2)^3}}.$$

Theorem 9. Let δ be adjoint curve of λ curve with arc length parameter. Then, the normal surface of δ is minimal if and only if

$$\frac{\mu_\delta'}{\mu_\lambda'} = \frac{t\mu_\delta - 1}{\mu_\lambda}.$$

Proof. From Theorem 3, $H_\delta = 0$. Therefore, we obtain $t\mu_\lambda'(1-t\rho_\lambda) + t\mu_\lambda\rho_\lambda' = 0$ with the help of (5). Using $\rho_\lambda = \mu_\delta$, the following result is obtained:

$$\frac{\mu_\delta'}{\mu_\lambda'} = \frac{t\mu_\delta - 1}{\mu_\lambda}.$$

We can easily obtain the following results with the help of Corollary 8:

Corollary 10. Let δ be adjoint curve of λ curve with arc length parameter. Then, principal curvatures of normal surface of δ are given by

$$k_{\delta_1} = [\sqrt{(\mu_\lambda'(1-t\rho_\lambda)+t\mu_\lambda\rho_\lambda')^2 + 4\mu_\lambda^2\rho_\lambda^2(\mu_\lambda^2+(1-t\rho_\lambda)^2)} + 2\mu_\lambda'(1-t\rho_\lambda) + 2t\mu_\lambda\rho_\lambda']/\sqrt{4(\mu_\lambda^2+(1-t\rho_\lambda)^2)^3},$$

$$k_{\delta_2} = [-\sqrt{(\mu_\lambda'(1-t\rho_\lambda)+t\mu_\lambda\rho_\lambda')^2 + 4\mu_\lambda^2\rho_\lambda^2(\mu_\lambda^2+(1-t\rho_\lambda)^2)} + 2\mu_\lambda'(1-t\rho_\lambda) + 2t\mu_\lambda\rho_\lambda']/\sqrt{4(\mu_\lambda^2+(1-t\rho_\lambda)^2)^3}.$$

Corollary 11. Let δ be adjoint curve of λ curve with arc length parameter. If the curvature and the torsion of δ is constant, then principal curvatures of normal surface of δ are given by

$$k_{\delta_1} = \frac{\mu_\lambda}{t^2\mu_\lambda^2 + (1-t\rho_\lambda)^2}, \quad k_{\delta_2} = \frac{-\mu_\lambda}{t^2\mu_\lambda^2 + (1-t\rho_\lambda)^2}.$$

Theorem 12. Let δ be adjoint curve of curve λ with arc length parameter. Then, the normal surface of δ is a flat surface if and only if it has vanished the curvature of the curve λ.

Proof. From Theorem 5 and equations (5), the proof is easily obtained.

Corollary 13. Let δ be adjoint curve of arc length parametrised curve λ. In this case, the following conditions are provided:

i) Let the curvature of λ be a nonzero constant. Then, the normal surface of δ is minimal if and only if the torsion of curve λ is a constant,

ii) Let be the curvature of λ isn't constant and the torsion of λ be constant. Then, the normal surface of δ is minimal if and only if the torsion of δ satisfies

$$\rho_\lambda = \frac{1}{t},$$

iii) If the normal surface of δ is a flat surface, then this surface is minimal.

Proof. From Theorem 4, Theorem 5, equations (5), all 3 cases claimed are plainly achieved.

Theorem 14. Let δ be adjoint curve of curve λ with arc length parameter. Then, the normal surface of δ is a Weingarten surface if and only if

$$3\mu_\lambda\rho_\lambda^2(t\rho_\lambda-1)[(\mu_\lambda'(t\rho_\lambda-1)-t\mu_\lambda\rho_\lambda')(\mu_\lambda\mu_\lambda'-t\rho_\lambda' + t^2\rho_\lambda\rho_\lambda') + (\mu_\lambda^2+(1-t\rho_\lambda)^2)(\mu_\lambda''+t\mu_\lambda\rho_\lambda''+t\rho_\lambda\mu_\lambda'')] = (\mu_\lambda^2+(1-t\rho_\lambda)^2)^4[(\mu_\lambda\rho_\lambda'-\mu_\lambda'\rho_\lambda)(\mu_\lambda^2+(1-t\rho_\lambda)^2) - 3(\rho_\lambda-t\rho_\lambda^2)(\mu_\lambda'(1-t\rho_\lambda)-t\mu_\lambda\rho_\lambda')](\mu_\lambda^2\mu_\lambda'\rho_\lambda-\mu_\lambda'\rho_\lambda - \mu_\lambda^3\rho_\lambda' - \mu_\lambda\rho_\lambda' - t^2\rho_\lambda^3\mu_\lambda' + t^2\rho_\lambda^2\mu_\lambda\rho_\lambda' + 2t\rho_\lambda^2\mu_\lambda')).$$

Proof. From Definition 2, if the normal surface of δ is a Weingarten surface, then

$$(H_\delta)_s(K_\delta)_t - (H_\delta)_t(K_\delta)_s = 0. \tag{6}$$

The partial derivatives of the Gaussian and mean curvatures of the normal surface of δ according to the s and t parameters are obtained as

$$(H_\delta)_t = [2(\mu_\lambda\rho_\lambda'-\mu_\lambda'\rho_\lambda)(\mu_\lambda^2+(1-t\rho_\lambda)^2)^3 - 6(\rho_\lambda-t\rho_\lambda^2)(\mu_\lambda^2+(1-t\rho_\lambda)^2)^2(\mu_\lambda'(1-t\rho_\lambda)-t\mu_\lambda\rho_\lambda')]/[4(\mu_\lambda^2+(1-t\rho_\lambda)^2)^{\frac{9}{2}}],$$
$$(H_\delta)_s = [3(\mu_\lambda'(t\rho_\lambda-1)-t\mu_\lambda\rho_\lambda')(t^2\rho_\lambda\rho_\lambda' - t\rho_\lambda' + \mu_\lambda\mu_\lambda') + 3(\mu_\lambda^2+(1-t\rho_\lambda)^2)(\mu_\lambda'' + t\rho_\lambda\mu_\lambda'' + t\mu_\lambda\rho_\lambda'')]/[2(\mu_\lambda^2+(1-t\rho_\lambda)^2)^{\frac{5}{2}}],$$
$$(K_\delta)_t = \frac{4\mu_\lambda^2\rho_\lambda^3(t\rho_\lambda-1)}{(\mu_\lambda^2+(1-t\rho_\lambda)^2)^3},$$
$$(K_\delta)_s = [2\mu_\lambda\rho_\lambda(\mu_\lambda^2\mu_\lambda'\rho_\lambda + t\rho_\lambda^2(t\mu_\lambda\rho_\lambda' + 2\mu_\lambda') - \mu_\lambda'\rho_\lambda - t^2\rho_\lambda^3\mu_\lambda' - \mu_\lambda^3\rho_\lambda' - \mu_\lambda\rho_\lambda')]/[(\mu_\lambda^2+(1-t\rho_\lambda)^2)^3].$$

From equation (6), the following result is obtained

$$3\mu_\lambda\rho_\lambda^2(t\rho_\lambda-1)[(\mu_\lambda'(t\rho_\lambda-1)-t\mu_\lambda\rho_\lambda')(\mu_\lambda\mu_\lambda'-t\rho_\lambda' + t^2\rho_\lambda\rho_\lambda') + (\mu_\lambda^2+(1-t\rho_\lambda)^2)(\mu_\lambda''+t\mu_\lambda\rho_\lambda''+t\rho_\lambda\mu_\lambda'')] = (\mu_\lambda^2+(1-t\rho_\lambda)^2)^4[(\mu_\lambda\rho_\lambda'-\mu_\lambda'\rho_\lambda)(\mu_\lambda^2+(1-t\rho_\lambda)^2) - 3(\rho_\lambda-t\rho_\lambda^2)(\mu_\lambda'(1-t\rho_\lambda)-t\mu_\lambda\rho_\lambda')](\mu_\lambda^2\mu_\lambda'\rho_\lambda-\mu_\lambda'\rho_\lambda - \mu_\lambda^3\rho_\lambda' - \mu_\lambda\rho_\lambda' - t^2\rho_\lambda^3\mu_\lambda' + t^2\rho_\lambda^2\mu_\lambda\rho_\lambda' + 2t\rho_\lambda^2\mu_\lambda')).$$

Example. Let a unit speed curve λ be given as

$$\lambda(s) = (\frac{1}{\sqrt{2}}cos(s), \frac{1}{\sqrt{2}}sin(s), \frac{s}{\sqrt{2}}).$$

Then, Serret-Frenet frame and curvatures of γ are obtained as

$$\boldsymbol{T}_\lambda = \lambda^{'} = (-\frac{1}{\sqrt{2}}sin(s), \frac{1}{\sqrt{2}}cos(s), \frac{1}{\sqrt{2}}),$$

$$\boldsymbol{N}_\lambda = \frac{\lambda^{''}}{\|\lambda^{''}\|} = (-cos(s), -sin(s), 0),$$

$$\boldsymbol{B}_\lambda = \boldsymbol{T}_\lambda \times \boldsymbol{N}_\lambda = (\frac{1}{\sqrt{2}}sin(s), \frac{-1}{\sqrt{2}}cos(s), \frac{1}{\sqrt{2}}),$$

and

$$\mu_\lambda = <\boldsymbol{T}_\lambda', \boldsymbol{N}_\lambda> = \frac{1}{\sqrt{2}},$$

$$\rho_\lambda = <\boldsymbol{N}_\lambda', \boldsymbol{B}_\lambda> = \frac{1}{\sqrt{2}}.$$

Let δ be adjoint curve of λ. Then, we have

$$\delta(s) = \int \boldsymbol{B}_\lambda(s)ds$$

$$\delta(s) = (-\tfrac{1}{\sqrt{2}}cos(s), \tfrac{-1}{\sqrt{2}}sin(s), \tfrac{s}{\sqrt{2}}) + c,$$

$$\boldsymbol{T}_\delta = (\frac{1}{\sqrt{2}}sin(s), \frac{-1}{\sqrt{2}}cos(s), \frac{1}{\sqrt{2}}),$$

$$\boldsymbol{N}_\delta = (cos(s), sin(s), 0),$$

$$\boldsymbol{B}_\delta = (-\frac{1}{\sqrt{2}}sin(s), \frac{1}{\sqrt{2}}cos(s), \frac{1}{\sqrt{2}}),$$

$$\mu_\delta = \frac{1}{\sqrt{2}}, \quad \rho_\delta = \frac{1}{\sqrt{2}}.$$

Also, the normal surface of δ is expressed as

$$\varphi^\delta(s,t) = \delta + t\boldsymbol{N}_\delta.$$

Then, we obtain

$$\varphi_s^\delta = (1 - \frac{t}{\sqrt{2}})\boldsymbol{T}_\delta + \frac{t}{\sqrt{2}}\boldsymbol{B}_\delta,$$

$$\varphi_{ss}^\delta = (\frac{1}{\sqrt{2}} - t)\boldsymbol{N}_\delta,\ \varphi_{st}^\delta = \frac{\boldsymbol{B}_\delta - \boldsymbol{T}_\delta}{\sqrt{2}},$$

$$\varphi_t^\delta = \boldsymbol{N}_\delta, \quad \varphi_{tt}^\delta = 0.$$

and, from the equalities, it's obtained

$$n_\delta = \frac{(\sqrt{2}-t)\boldsymbol{T}_\delta + t\boldsymbol{B}_\delta}{\sqrt{2+2t^2-2\sqrt{2}t}}.$$

Then, we obtain

$$E = t^2 - \sqrt{2}t + 1,\ F = 0, \quad G = 1,$$

$$e = 0, \quad f = \sqrt{\frac{1}{2t^2-2\sqrt{2}t+2}}, \quad g = 0.$$

Therefore, the first and the second fundamental forms, the mean and the Gaussian curvature and the principal curvatures of the normal surface are obtained as

$$\boldsymbol{I}_\delta = (t^2 - \sqrt{2}t + 1)ds^2 + dt^2,$$

$$\boldsymbol{II}_\delta = \sqrt{\frac{2}{t^2 - \sqrt{2}t + 1}}dsdt,$$

$$K_\delta = \frac{-1}{2(t^2 - \sqrt{2}t + 1)^2}, \qquad H_\delta = 0,$$

$$k_{\delta_1} = \frac{1}{(\sqrt{2}t^2 - 2t + \sqrt{2})}, \quad k_{\delta_2} = \frac{-1}{(\sqrt{2}t^2 - 2t + \sqrt{2})}.$$

Hence, this normal surface example, where we try to exemplify the normal surface of the adjoint curve of a regular curve with constant curvature and torsion, provides the claims of Theorem 7, Corollary 11, Theorem 12 and Corollary 13-(i).

5. Conclusion

Our general aim in this study was to present a specific study on curves and surfaces, which are important topics in differential geometry. We have given the characterizations of the normal surfaces of the adjoint curves we have studied in 3D Euclidean space by obtaining the time-dependent equations of motion. Here, we obtained mean curvature, which gives results about the minimality of the surface, and Gaussian curvature and principal curvatures, which give results about the geometric shapes of the surface under certain conditions. In addition, by examining the cases where such surfaces are minimal and flat, we revealed the relationship between these two cases.

We hope that this study, under the general title of curves and differential geometry of surfaces, will make a specific contribution to studies in the fields of mathematics and applied sciences. Our next study will be about some special surfaces of adjoint curves.

Contributions of the authors

The authors contributed equally to the article.

Conflict of Interest Statement

There is no conflict of interest between the authors.

Statement of Research and Publication Ethics

The study is complied with research and publication ethics.

References

[1] M. Do Carmo, Differential Geometry of Curves and Surfaces, Prentice-Hall, Englewood Cliffs, 1976.

[2] S. K. Nurkan, I. A. Güven and M. K. Karacan, "Characterizations of adjoint curves in Euclidean 3-space", Proc Natl Acad Sci. India Sect A Phys Sci., vol. 89, pp. 155-161, 2019.

[3] G. U. Kaymanli, S. Okur and C. Ekici, "The Ruled Surfaces Generated By Quasi Vectors", IV. International Scientific and Vocational Studies Congress - Science and Health, Ankara, Turkey, November, 2019.

[4] R. Lopez, "Differential geometry of curves and surfaces in Lorentz-Minkowski space", MiniCourse taught at IME-USP, Sao Paulo, Brasil, October, 2008.

[5] F. Sakai, "Weil divisors on normal surfaces", Duke Mathematical Journal, vol. 51, no. 4, pp. 877-887, 1984.

[6] R. Lopez, Z. M. Sipus, L.P. Gajcic and I. Protrka, "Harmonic evolutes of B-scrolls with constant mean curvature in Lorentz-Minkowski space" , International Journal of Geometric Methods in Modern Physics, vol. 16, no. 5, 2019.

[7] I. Aydemir and K. Orbay, " The Ruled Surfaces Generated By Frenet Vectors of Timelike Ruled Surface in the Minkowski Space R_1^3", World Applied Science Journal, vol. 6, no. 5, pp. 692-696, 2009.

[8] I. Protrka, "Harmonic Evolutes of Timelike Ruled Surfaces in Minkowski Space", 18th Scientific-Professional Colloquium on Geometry and Graphics, Beli Manastir, Croatia, September 6-10, 2015.

[9] I. Protrka, "The harmonic evolute of a helicoidal surfaces in Minkowski 3-space", Proceedings of the Young Researcher Workshop on Differential Geometry in Minkowski Space, Granada, Spain, pp. 133-142, 2017.

[10] A. Sarıoglugil and A. Tutar, "On Ruled Surface in Euclidean Space E3", Int. J. Contemp. Math. Sci., vol. 2, no. 1, pp. 1-11, 2007.

[11] G. Y. Senturk and S. Yuce, "Characteristic properties of the ruled surface with Darboux frame in E3", Kuwait J. Sci., vol. 42, no. 2, pp. 14-33, 2015.

[12] W. Kühnel, “Ruled W-surfaces”, Arch. Math. (Basel), vol. 62, pp. 475-480, 1994.

[13] Y. Ünlütürk and C. Ekici, "Parallel Surfaces of Spacelike Ruled Weingarten Surfaces in Minkowski 3-space", New Trends in Mathematical Sciences, vol.1, no. 1, pp. 85-92, 2013.

[14] J. H. Choi and Y. H. Kim, "Associated curves of a Frenet curve and their applications", Appl. Math. Comput., vol. 218, no. 18, pp. 9116-9124, 2012.

[15] T. Körpınar, M. T. Sarıaydın, and E. Turhan, "Associated curves according to Bishop frame in Euclidean 3-space" , Adv. Model. Optim., vol. 15, no. 3, pp. 713-717, 2013.

[16] N. Macit and M. Düldül, "Some new associated curves of a Frenet curve in E3 and E4", Turkish J. Math., vol. 38, pp. 1023-1037, 2014.

[17] S. Yılmaz, "Characterizations of some associated and special curves to type-2 Bishop frame in E3", Kırklareli University J. Eng. Sci., vol. 1, pp. 66-77, 2015.

Bitlis Eren Üniversitesi Fen Bilimleri Dergisi
BİTLİS EREN UNIVERSITY JOURNAL OF SCIENCE
ISSN: 2147-3129/e-ISSN: 2147-3188
VOLUME: 11 NO: 3 PAGE: 784-790 YEAR: 2022
DOI: 10.17798/bitlisfen.1097813

The Effect of Foaming on Mechanical and Morphological Properties of Polypropylene

Yeşim ASLAN[1], Yeliz ALBRECHTSEN[2], Münir TAŞDEMİR[3*]

[1]*Marmara University, Institute of Pure and Applied Science, Istanbul, Türkiye*
[2]*Tekkan Plastik Sanayi ve Ticaret A.Ş., Kocaeli / Türkiye*
[3]*Marmara University, Technology Faculty, Met. and Mat. Eng. Dep., Istanbul, Türkiye*
(ORCID: 0000-0002-1649-1639) (ORCID: 0000-0002-6596-9440) (ORCID: 0000-0001-8635-7251)

Keywords: Polypropylene, Composites, Chemical Foaming, Plastic Injection, Mechanical Properties.

Abstract

The automotive industry is among the priority technology areas of our country, and the reduction of vehicle weight and fuel consumption and thus CO_2 emissions without compromising safety criteria are among the priority research areas. For this reason, R&D studies on increasing the use of polymer-based materials in the automotive industry are of great importance. In order to produce "high strength and weight reduction parts" in plastic moulding technologies, advanced technologies that focus on cost reduction and efficiency are being implemented rapidly. The chemical foaming process, which provides many advantages such as reducing the consumption of plastic material used, reducing the total moulding cycle time, using fewer tonnage injection moulding machines, and thus reducing the energy costs, is one of the innovative technologies that have been implemented since a very recent time. In this study, chemical foaming agents were used at a rate of 1-2-3 wt% in natural fiber-reinforced recycled composite polypropylene raw material. Polypropylene samples were obtained by injection moulding in the sizes and shapes in accordance with the standards. Tensile, hardness, impact and three- point bending tests would be done. With increasing the amount of foaming agent, mechanical properties decreased.

1. Introduction

Manufacturing science has opened up new frontiers, effectively moving component design down to materials design. Natural lignocellulosic fibers are renewable, completely or partially recyclable, and biodegradable because their raw materials consisted of flax, cotton, hemp, and wood materials. Today, natural fiber-reinforced polymer composites are growing rapidly in many studies and industrial applications because they are eco-friendly, sustainable, light, high performance, perfectly versatile, and easy to process at favorable costs [1]-[4].

The plastic injection molding method produces multidimensional and complex geometries in high numbers, and low cycle times. Besides, the injection molding method reduces the consumption of raw materials and improves the lightness of the materials by using chemical admixtures. Microcellular polymers may be the new trend to substitute compact plastics. The contribution of chemical foaming agents in polymer compounds provides their unique properties such as low density, outstanding strength/weight ratio, excellent insulating ability, energy absorptive performance, and splendid impact resistance. It is possible to foam many commercially important polymers using physical or chemical foaming agents. Three methods of producing polymer foams take place in the literature: chemical foaming, physical foaming - MuCell® , and microspheres [5], [6]. In this research we are dealing only with the injection molding proces. The chemical foaming process is similar to the standard injection process. However, when chemical blowing agents are added to create polymer foams, the fluidity and solidification behaviors of the plastic completely change [7], [10]. The injection molding processing

*Corresponding Author: munir@marmara.edu.tr
Received: 03.04.2022, Accepted: 05.09.2022

technology uses a conventional injection molding machine allowing different chemical foaming agents, shaped parts with a compact outer skin, and foamed cores with different mechanical characteristics [11]-[14].

This study will explore the effects of chemical foaming agent content on the mechanical and morphological properties of microcellular natural fibre-reinforced polypropylene composites.

2. Material and Methods

A commercial 20wt% hemp fibre-reinforced polypropylene compound (NAFIlean-PF2 555, Karel Kalıp SAN.A.Ş., Turkey) was used in this work. ITP825-818, HYDROCEROL, Clariant A.Ş. were used not only as a nucleating agent but also as a chemical foaming agent. ITP 825 includes 40% active material and good distribution in the melt. However, ITP 818 has 65% active material and it shows very high gas efficiency.

Table 1. Samples ratios of 20wt % hemp fibre reinforced PP with different ITP loading

Groups	PP+20% Hemp fibre (wt%)	ITP 825 (wt%)	ITP 818 (wt%)
1	100	-	-
2	99	1	-
3	98	2	-
4	97	3	-
5	99	-	1
6	98	-	2
7	97	-	3

The commercial natural fibre-reinforced recycled polypropylene matrix composite which is given in Figure 1(a), was dried in an oven at 105 ℃ for 24 hours. Figure 1(b) shows Hydrocerol. Afterwards, 20wt% hemp fibre-reinforced polypropylene matrix composite was mixed with each chemical foaming agent due to the ratio of 1-2-3 wt%, which is given in Table 1. Each mixture was prepared at 2 kg and was charged as to the plastic injection moulding machine which was given in Figure 1(f), Table 2 showed the process conditions. Figure 1(c) shows the tensile strength test's mould and the obtained sample. Figure 1(d) was illustrated plate moulds which were used to produce hardness and three-point bending test samples. In figure 1(e), are shown the moulds for obtaining the Izod impact test samples.

Elasticity modulus, yield strength, tensile strength at break, and hardness properties of each sample were examined by the mechanical tests at room temperature. The tension tests were applied according to ASTM D638 standards (Zwick Z010, Germany). The hardness test was performed by ASTM D2240 (Zwick, Germany). In order to investigate fracture behaviour, the Izod impact test was carried out at room temperature and unnotched according to the ASTM D256 method via the Zwick B5113 impact tester (Zwick, Germany). The bending strength, elasticity modulus, and % bending strain analyses were performed by using the three-point bending method to ASTMD 790.

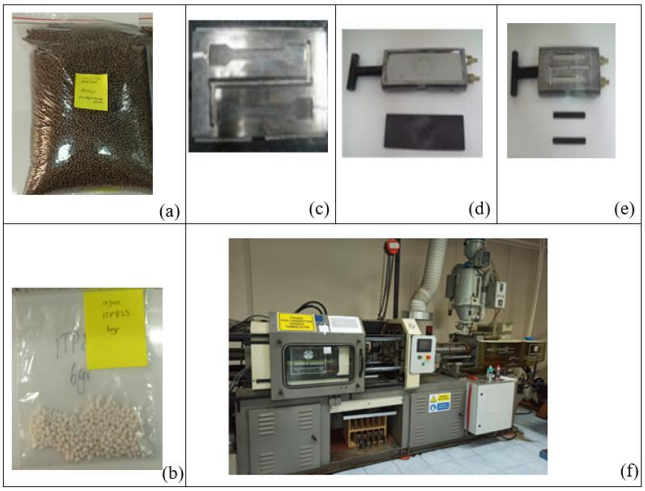

Figure 1. Sample Preparation: (a): The commercial 20 wt% hemp fibre reinforced polypropylene, (b): Hydrocerol, c): Tensile strength test mould, (d): Plate mould, (e): Izod impact test mould and sample, (f): Plastic injection moulding machine

Table 2. Process condition of 20wt% hemp fibre reinforced PP with different ITP loading

Process Condition	Injection
Temperature (°C)	190-220
Hold pressure (bar)	75
Hold time in mould (s)	8.6
Screw speed (rpm)	75
Mould temperature (°C)	45-50
Filling speed cm^3/s	23

3. Results and Discussion

Figure 2 shows tensile strength properties 20wt% hemp fibre reinforced PP and ITP loading. The tensile strength of the composite decreased with increasing Hydrocerol content. The tensile strength of 20%wt. hemp fibre PP decreased from 28 MPa and 20.5 MPa to 21.8 MPa and 24.1 MPa, respectively with ITP 825. The tensile strength of 20wt% hemp fibre PP

decreased from 28.0 MPa and 25.6 MPa to 24.0 MPa and 26.2 MPa respectively, loaded with ITP 818. The tensile strength is sharply decreased for the samples loaded with ITP 825. The obvious decrease in the tensile strength for the samples loaded with not only ITP 825 but also ITP 818 may be the result of formed bubble size and or bubble distribution. Bledzki et al. have studied microcellular injection moulded PP/wood fibre composites on cell morphology and the effect of physical properties and mechanical properties, and was shown to decrease the tensile strength of PP by wood fibre and microcellular structure [15].

After foaming, the tensile modulus of all of 20wt% hemp fibre reinforced PP foams was lower than that of neat 20%wt. hemp fibre reinforced PP. However the trends were change, Zeng et.al. reported that tensile strength tends to be increased with decreasing cell size [17]. Chen et.al. have studied microcellular polylactic acid (PLA) foams with various cell size and cell morphologies and figured out different trends of tensile strength might be ascribed to the heterogeneities of macrostructural changes resulting from the changes in cell microstructure [18].

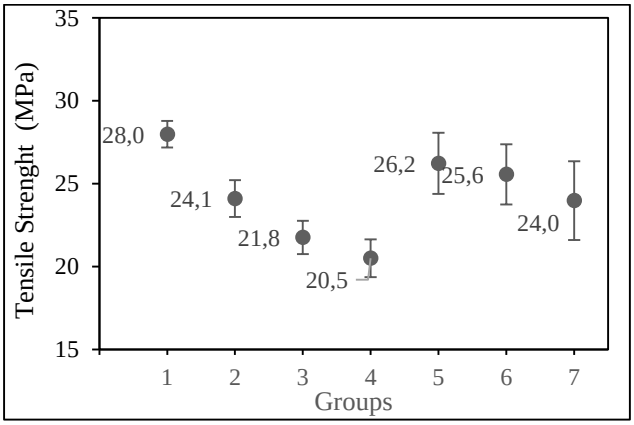

Figure 2. Tensile strength of 20wt% hemp fibre reinforced PP with different ITP loading

The effects of ITP on the elasticity modulus hemp fibre-PP is given in Figure 3. The elasticity modulus of hemp fibre-PP decreases from 1152 MPa and 623.4 MPa to 780.2 MPa to 756.8 MPa loaded with ITP 825, corresponding to 1152 MPa, and 739 MPa to 807.4 MPa, and 831.4 MPa loaded with ITP 818. It can be observed that the addition of Hydrocerol decreased elasticity modulus significantly. For both types of Hydrocerol 1wt% and 2wt% doping ITP samples, elasticity modulus decreased as the same however, 3wt% ITP 825 reinforced samples are greater than 3wt% ITP 818 elasticity modulus decreased. The elastic modulus of sample 1 was the highest because includes no chemical foaming agent. However, the chemical foaming agent action causes dissolved CO_2 to get between the polymer chains, such as plasticization, polymer chain mobility leads to decreased crystallinity and imperfect crystals with more close-packed lammeals. [18].

Because of the fact, include chemical foaming agent in 20wt% hemp fibre reinforced PP, decrease the elastic modulus.

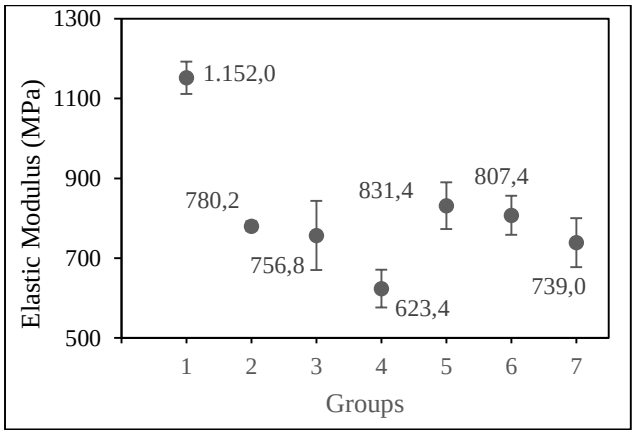

Figure 3. Elasticity modulus of 20wt% hemp fibre reinforced PP with different ITP loading

Figure 4 shows the hardness (Shore D) behavior of 20wt% hemp fibre reinforced PP with different Hydrocerol loading. The hardness of the hemp fibre-PP mixed with (1,2,3 wt%) ITP 825 decreased from 62.4 shore D and 61.0 Shore D to 60.8 Shore D and 59.5 Shore D, respectively. On the other hand, the hardness of the hemp fibre-PP (1,2,3 wt%) ITP 818 samples are measured as 59.5 Shore D, 59.0 Shore D, and 58.9 Shore D. In comparison between ITP 825 and ITP 818 samples hardness is increased greater than ITP 818. Cakir et.al have been explained the decrease in shell layer thickness as a result of an increase in the amount of foam agent so, increasing the softer cellular region with decreasing shell layer thickness is effective in reducing hardness [16].

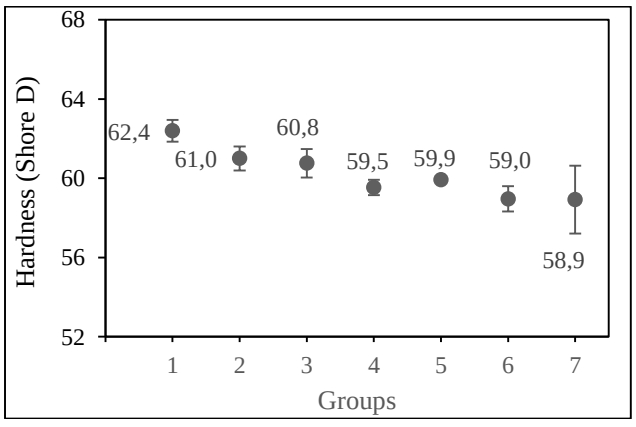

Figure 4. Hardness properties of 20wt% hemp fibre reinforced PP with different ITP loading

The relationship between the unnotched Izod impact strength and the hemp fibre-PP with different Hydrocerol (ITP 818 and ITP 825) contributions are shown in Figure 5. Generally, the inclusion of ITP in the hemp fibre - PP Izod impact strength of the composite is found to be decreasing. For example, the Izod impact strength of the samples with (1,2,3 wt%) ITP 825 is measured as 17.6 kJ/m^2, 14,3 kJ/m^2, and 12.6 kJ/m^2 respectively. On the other hand, Maruf Billah et. al. have studied polypropylene matrix natural fibre-reinforced composited V-notch specimens sample for impact test. Polypropylene was reported 10-14 times more brittle with the notch [19].

The Izod impact strength of 20%wt. hemp fibre reinforced PP is 19.1 kJ/m^2. On the other hand, the Izod impact strength of the three samples with (1,2,3 wt%) of ITP 818 is measured as 18.4 kJ/m^2, 16,3 kJ/m^2, and 12,5 kJ/m^2 respectively. In comparison with the Izod impact strength of 2 % wt. ITP 825 and ITP 818 samples decreased greater at ITP 825. Maruf Billah et. al. have studied effect of PET fibre content on the impact resistance of hybrid PP composites with the coupling agent. They showed good adhesion with coupling agent MAPP increasing the impact resistance of the composites [20]. However, the chemical foaming agent increased the free volume in the structure, according to free volume increase, impact resistance decreased.

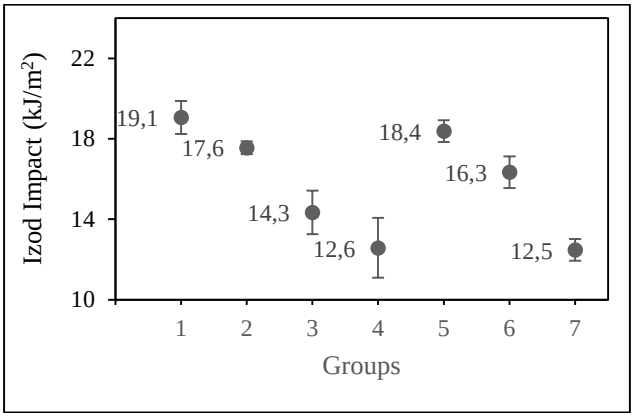

Figure 5. Izod Impact test of 20wt% hemp fibre reinforced PP with different ITP loading

Figure 6, 7 and 8 are shown the three-point bending test measurements on the samples. The bending strength properties are shown in Figure 6. According to the three points bending tests hemp fibre-PP at 1 wt% Hydrocerol increased the bending elasticity modulus which is shown in Figure 7. However, the addition of 2wt% and 3wt% ITP 818 are decreased the bending elasticity modulus. The effect of ITP types and contribution on the the % bending strain illustrates in Figure 8. Also, the % bending strain is developed of ITP 818 (1,2,3wt%) addition samples. However, ITP 825 (1,2,3wt%) is decreased the % bending strain.

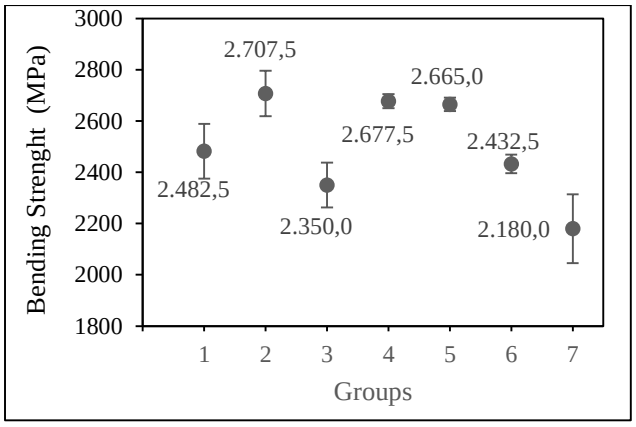

Figure 6. Three-point bending test of 20wt% hemp fibre reinforced PP with different ITP loading: bending strength

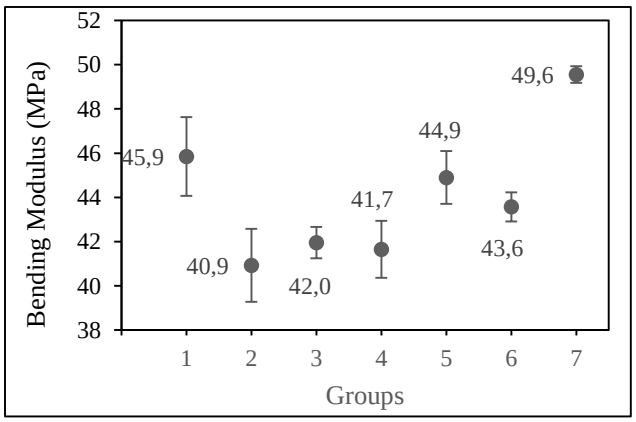

Figure 7. Three-point bending test of 20wt% hemp fibre reinforced PP with different ITP loading: bending modulus

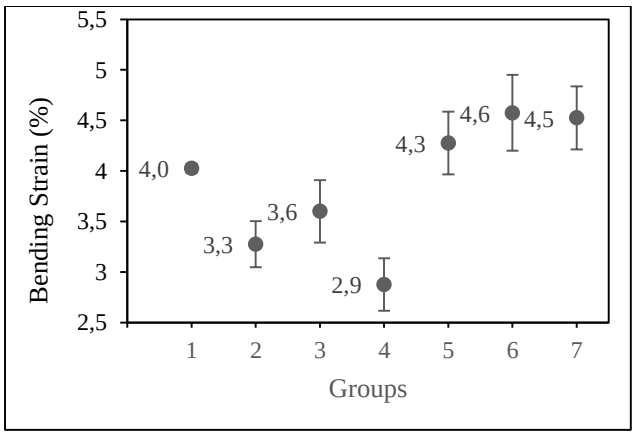

Figure 8. Three-point bending test of 20wt% hemp fibre reinforced PP with different ITP loading: bending strain (%)

The micrograph of 20wt% hemp fibre reinforced PP with different ITP loading is presented in Figure 9. The influence of ITP types and contribution on the structure and size of the microcells on a surface was observed by SEM micrographs. Figure 9(a) illustrates 20wt% hemp fibre reinforced PP composite structure, there is no microcellular structure. Figure 9(b) is given hemp fibre reinforced PP with 2wt% ITP 825 which is the cell size of about 60 μm. On the other hand, Figure 9(c) is shown 3 wt% ITP 825 addition which is cell size of about 60-140 μm. It seems that when the ratio of ITP 825 foaming agent's increases, the bubble's size increases. Figure 9(d) and Figure 9(e) are shown 2 wt% and 3wt% ITP 818 addition, respectively. When the foaming agent addition increases in the wt% ratio, bubble size decreases and bubbles dispersion is nonhomogeneous and also opened-cell and closed-cell distribution is nonhomogenous in the structure. This cell structure distribution influences trend of mechanical properties of the composites.

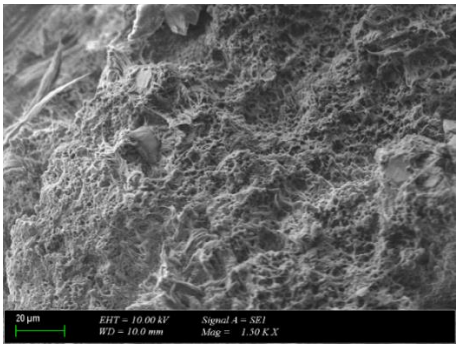

(a) PP+20wt% Hemp fibre (without ITP)

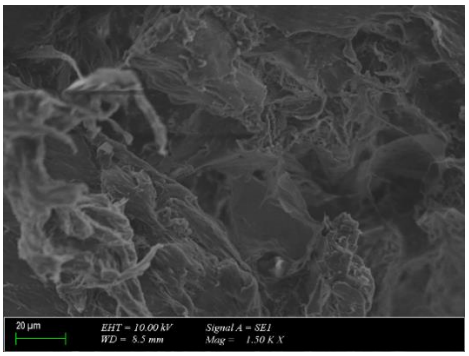

(b) ITP 825 (2wt%)

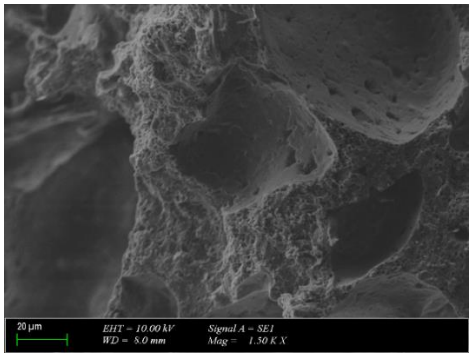

(c)ITP 825 (3wt%)

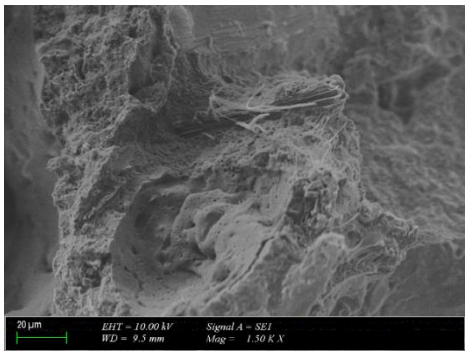

(d) ITP 818 (2wt%)

Figure 9. Micrograph photo of 20wt% hemp fibre reinforced PP with different ITP loading

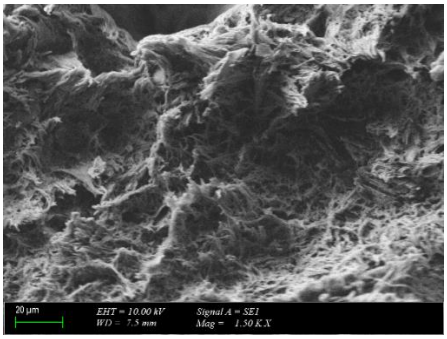

(e) ITP 818 (3wt%)

Figure 9. (continue)

4. Conclusion and Suggestions

This study aimed to investigate the mechanical behaviour of the chemical foaming agent in polypropylene matrix composites. Hydrocerol (ITP 818 and ITP 825) was used as a potential foaming agent in natural fibre-reinforced polypropylene matrix composites at the range of 1, 2, and, 3wt% The samples were obtained by injection moulding. The effect of Hydrocerol on the mechanical properties such as; the tensile elastic modulus, tensile strengths, hardness, Izod impact strength, and the bending test of 20wt% hemp fibre reinforced polypropylene was investigated. The following results were the elasticity

modulus, the tensile strength, the hardness, Izod impact strength 20wt% hemp fibre reinforced PP decreased, as the Hydrocerol concentration increased. Microcellular structure, increase polymer chain distance, decrease the crystallinity. On the other hand, the presence of bubbles containing gas and whose mechanical characteristics become very weaker. The bending strain of 20wt% hemp fibre reinforced PP increased as the ITP concentration increases. The bending elasticity modulus improved by 1wt% Hydrocerol addition until 2 wt% dropped the bending elasticity modulus. The bending strength ITP 825 (1,2,3wt%) greater decreased than ITP 818 (1,2,3 wt%). In the studies, the chemical foaming effect on the mechanical properties was expected. According to morphological analysis, the foaming agents were shown to created bubbles on the microstructure. On the other hand, the advantages of chemical foaming at weight reduction will be examined, and the effect of chemical foaming on physical properties will be studied.

Contributions of the Authors

Authors did the work together and co-authored the publication

Conflict of Interest Statement

There is no conflict of interest between the authors.

Statement of Research and Publication Ethics

The study is complied with research and publication ethics

References

[1] E. Bodros, C. Baley, "Study of the tensile properties of stinging nettle fibres", *Materials Letters,* vol. 62(14), pp.2143-2145, 2008.

[2] M.M. Alam, T. Ahmed, M.M. Haaque, M.A. Gafur, A.H. Kabir, "Mechanical properties of natural fiber containing polymer composites", *Polymer-Plastics Technology and Engineering,* vol. 48(1), pp.110-113, 2009.

[3] G. Sui, M.A. Fuqua, C.A. Ulven, W.H. Zhong, "A plant fiber reinforced polymer composite prepared by a twin-screw extruder", *Bioresource Technology,* vol. 100(3), pp.1246-1251, 2009.

[4] S.V. Joshi, L.T. Drzal, A.K. Mohanty, S. Arora, "Are natural fiber composites environmentally superior to glass fiber reinforced composites?", *Composites Part A: Applied science and manufacturing,* vol.35(3), pp.371-376, 2004.

[5] S. Ries, A. Spörrer, V. Altstädt, "Foam injection molding of thermoplastic elastomers: Blowing agents, foaming process and characterization of structural foams", *In AIP Conference Proceedings, American Institute of Physics,* vol. 1593(1), pp. 401-410, 2014.

[6] M.C. Guo, M.C. Heuzey, P.J. Carreau, "Cell structure and dynamic properties of injection molded polypropylene foams", *Polymer Engineering & Science,* vol.47(7), pp. 1070-1081, 2007.

[7] H. Wu, G. Zhao, G. Wang, W. Zhang, Y. Li, "A new core-back foam injection molding method with chemical blowing agents", *Materials & Design,* vol. 144, pp. 331-342, 2018.

[8] J.R. Ruiz, M. Vincent, J.F. Agassant, "Numerical modeling of bubble growth in microcellular polypropylene produced in a core-back injection process using chemical blowing agents", *International Polymer Processing,* vol.31(1), pp. 26-36, 2016.

[9] J.A. Reglero Ruiz, M. Vincent, J.F. Agassant, A. Claverie, S. Huck, "Morphological analysis of microcellular PP produced in a core-back injection process using chemical blowing agents and gas counter pressure", *Polymer Engineering & Science,* vol.55(11), pp. 2465-2473, 2015.

[10] H. Wu, G. Zhao, J. Wang, G. Wang, W. Zhang, "Effects of process parameters on core-back foam injection molding process", *Express Polymer Letters,* vol.13(4), pp. 390-405, 2019.

[11] A.K. Bledzki, W. Zhang, O. Faruk, "Microfoaming of flax and wood fibre reinforced polypropylene composites", *Holz als Roh-und werkstoff*, vol. 63(1), pp. 30-37, 2005.
[12] A.K. Bledzki, O. Faruk, "Microcellular Wood–PP Composites in Extrusion, Injection and Compression Moulding Process", *Blowing Agents and Foaming Processes*, vol. 20, pp. 1-10, 2005.
[13] A.K. Bledzki, O. Faruk, "Microcellular wood fiber reinforced PP composites: Cell morphology, surface roughness, impact, and odor properties", *Journal of cellular plastics,* vol. 41(6), pp. 539-550, 2005.
[14] A.K. Bledzki, O. Faruk, "Microcellular wood fiber reinforced polypropylene composites: A comparative study between injection molding and extrusion process", *In ANTEC Society of Plastics Engineers Conference,*vol. 2, pp. 2665-2669, 2004.
[15] A.K. Bledzki, O. Faruk, "Microcellular Injection Molded Wood Fiber-PP Composites: Part II - Effect of Wood Fiber Length and Content on Cell Morphology and Physico-mechanical Properties", *Journal of Cellular Plastics*, vol. 42(1), pp. 77–88, 2006.
[16] S. Cakir, M. Aycicek, E. Altun, A. Akinci, "The effect of foaming agent on mechanical and physical properties of polypropylene", *Mater Sci: Adv Compos Mater*, vol. 2, pp.1-7, 2018.
[17] C. Zeng, N. Hossieny, C. Zhang, B. Wang, and S. M. Walsh, "Morphology and tensile properties of PMMA carbon nanotubes nanocomposites and nanocomposites foams," *Compos. Sci. Technol.*, vol. 82, pp. 29–37, doi: 10.1016/j.compscitech.2013.03.024, 2013.
[18] J. Chen *et al.*, "Cell structure and mechanical properties of microcellular PLA foams prepared via autoclave constrained foaming," *Cell. Polym.*, vol. 40, no. 3, pp. 101–118, doi: 10.1177/0262489320930328, 2021.
[19] M. M. Billah, M. S. Rabbi, and A. Hasan, "Injection molded discontinuous and continuous rattan fiber reinforced polypropylene composite: Development, experimental and analytical investigations," *Results Mater.*, vol. 13, p. 100261, doi: 10.1016/j.rinma.2022.100261, 2022.
[20] R. Várdai *et al.*, "Improvement of the impact resistance of natural fiber–reinforced polypropylene composites through hybridization," *Polym. Adv. Technol.*, vol. 32, no. 6, pp. 2499–2507, doi: 10.1002/pat.5280, 2021.

Bitlis Eren Üniversitesi Fen Bilimleri Dergisi
BİTLİS EREN UNIVERSITY JOURNAL OF SCIENCE
ISSN: 2147-3129/e-ISSN: 2147-3188
VOLUME: 11 NO: 3 PAGE: 791-797 YEAR: 2022
DOI: 10.17798/bitlisfen.1102823

A Determination of the Corrosion and Microstructure Properties of AlSi10Mg Material Produced by Different Direct Metal Laser Sintering (DMLS) Process Parameters

Mustafa Safa YILMAZ[1*]

[1]*Fatih Sultan Mehmet Vakıf University, ALUTEAM*
(ORCID: 0000-0003-2614-9121)

Keywords: Additive Manufacturing, Direct Metal Laser Sintering (DMLS), Parameter optimization, Corrosion, AlSi10Mg.

Abstract
Additive Manufacturing (AM) has been developing with increasing interest recently. The development of this technology will accelerate with the increase in material, process, and product quality. It is therefore essential to investigate these shortcomings of additive manufacturing products. In this study, the microstructure and corrosion properties of the material (AlSi10Mg) were investigated by changing the production parameters in the Direct Metal Laser Sintering (DMLS) process. Energy density was considered in parameter selection. Depending on the process parameters, the corrosion, topography, and mechanical properties of the DMLS-AlSi10Mg material were investigated in detail. It has been determined that the corrosion resistance and hardness of the material are directly related to porosity.

1. Introduction

The advantages of Additive Manufacturing (AM) are that it can construct complex-shaped parts without the need for other processes [1][2][3][4]. Powder bed fusion (PBF) technologies are the most popular processes for metal AM technologies that are called selective laser melting (SLM), direct metal laser sintering (DMLS), and electron beam melting (EBM) [5][6][7]. DMLS uses the layer-by-layer production of metallic parts and semifinished products directly from the metal powders [8] [9] [10]. The DMLS system has many advantages: the production of complex parts (according to casting or rolling), no need for expensive tools required in production, a low amount of sawdust and waste, a cost advantage in low-numbered production, and accessibility to the final product within hours [11] [12]. AlSi10Mg alloy is generally used in pressure casting. Since this alloy has a ratio close to its eutectic composition, it has high fluidity and low shrinkage [13]. Due to these advantages, the most widely used alloy in Additive Manufacturing is AlSi10Mg alloy. AlSi10Mg alloy produced with AM is widely used in automotive, marine, medical, and aerospace [14] [15] [16].

Many parameters must be controlled in additive manufacturing technologies. The slightest change in parameters can cause severe deterioration or improvement in the material. As a result of the parametric changes, changes in the energy values are loaded into the DMLS system. This energy value creates significant differences in the materials, and many studies are ongoing on this subject [5] [17] [18] [19].

As a result of production parameters, kinetic effects such as segregations, dislocations, and residual stresses in the material cause changes in the material's mechanical and corrosion properties. In addition, if the production parameters are not well optimized, more serious defects such as porosity and cracks may occur in the material. This study examines the difference in the power and scan speed values (effect the energy density) used by the system and the change in the microstructure, surface properties, and corrosion properties.

*Corresponding Author: m.safayilmaz@gmail.com
Received: 13.04.2022, Accepted: 25.09.2022

2. Material and Method

The productions were made with AlSi10Mg alloy powders, and its chemical analysis (Table 1) and SEM picture (Figure 1) were given.

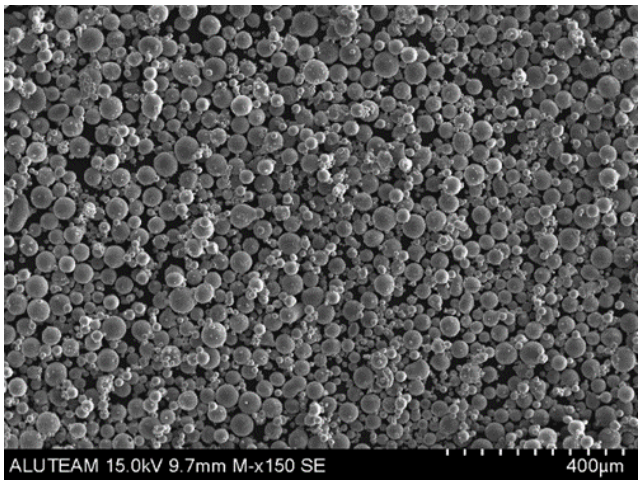

Figure 1. AlSi10Mg metal powder SEM image.

The details of parameter design, which is the focus of the study, are given in Table 2 and show the changes in energy density with different laser power and speed. Increasing the scanning speed and scanning distance increases the production speed, while low values of these two parameters cause an increase in energy density. In this study, the effect of scanning speed was investigated by keeping the scanning distance constant. In addition, different values of laser power were tried to change the energy density. While manufacturing, some parameters were kept constant (0.19 mm hatch distance (h),30 µm Layer thickness (t)), and the scan lines of every layer within the core region were rotated by 67° concerning the previous layer's scan lines. In addition, the formula used to calculate the energy density is given in Table 2. How different parameters affect the energy can be seen here.

Table 1. AlSi10Mg powder's chemical analysis (wt.%), d50 = 35±5 µm

Si	Fe	Mn	Cu	Ni	Zn	Mg	Sn	Al
9-11	≤0.55	≤0.45	≤0.05	≤0.05	≤0.10	0.2-0.45	≤0.05	Other

Table 2. AlSi10Mg powder's chemical analysis (wt.%), d50 = 35±5 µm

Sample	Laser power (P, Watt)	Scan Speed (v, mm/s)	Energy input (E*, joule)
E1	150	1000	26.31
E2	370	1600	40.57
E3	250	1000	43.85
E4	370	1000	64.91
E5	370	600	108.18
E6**	370	1300	49.93
**DMLS AlSi10Mg manufacturing standard parameters.			
E=P/(v.h.t)			

The specimens were manufactured with 40x15x5 mm (x-y-z) size via the EOS M290 DMLS machine. X-ray diffraction (XRD)-(Bruker D8), Scanning electron microscopy (SEM) - (Hitachi SU3500), optical microscopy (OM), Hardness test (Shimadzu Vickers hardness device (HV 0.05)), corrosion analysis (IVIUM/Vertex-CompactStat), surface roughness measurement (Mitutoyo SJ210) and porosity measurement methods (ImageJ) were used for characterization analysis.

Before corrosion investigation, specimens were physically polished with SiC pare and diamond suspension (1 micron), washed with acetone and dried. Potentiodynamic polarization experiments were applied at 0.5 mV/s and 25 ℃ in an aerated 3.5 wt% NaCl solution. The surface area was 1 cm2, and open-circuit potential (OCP) was stabilized for 1800 s before potentiodynamic tests.

3. Results and Discussion

The phases of the produced samples were examined (Figure 2). As can be seen from the spectral results, no elements other than aluminium and silicon were detected in the internal structure, and an amorphous phase was not formed.

The relation between the energy input level and the roughness is given in Figure 3. Surface roughness measurements (10 measurements were

made) were made from the laser trace surfaces of each sample. It is seen that the surface roughness values are directly influenced by the energy input [5] [20] [21] [22] [23]. Surface roughness is also high with a high energy input parameter (E5). With the same scanning speed but increasing in laser power experiments (the increase in laser power increases the energy), the roughness value increased (E1, E3, E4).

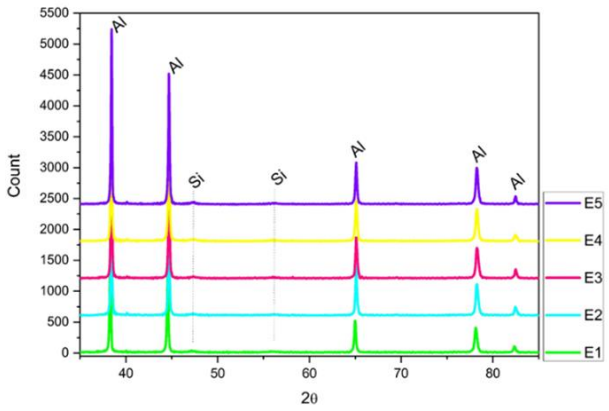

Figure 2. XRD results of additively manufactured samples.

The results of the inner porosity (15 measurements were made from the optical images with the ImageJ software program) are given in Figure 4. Many parameters in additive manufacturing systems affect the amount of porosity in the material's internal structure [23]. This study investigated the effect of the change in the amount of energy. Pore formation in additive manufacturing changes with many parameters. Although the energy levels are close (E2, E3, E6), there are differences in the amount of porosity in different parameters from the standard parameter (E6). This situation shows the importance of optimum power and laser speed in production. When the total energy amount is low (E1), the powder material does not melt and remains a void in the structure. In cases where energy is high (E5), gas gaps are trapped in the melt pool due to the evaporation effect [17][21][24][25].

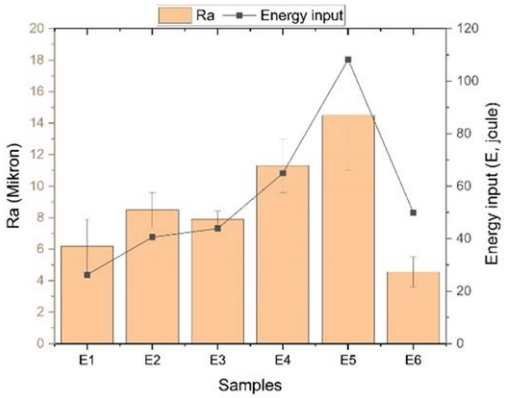

Figure 3. Energy input and surface roughness results of samples

Although they have different laser power and scanning speeds, minimum porosity levels were obtained in samples with values close to optimum energy levels (E3 and E2).

The hardness values of the samples produced with different parameters and without any heat treatment are shared in Figure 4. The mechanical properties of the material are directly related to the porosity in the structure [14] [21] [26]. It is seen that the hardness values are proportional to the internal porosity ratio of the samples.

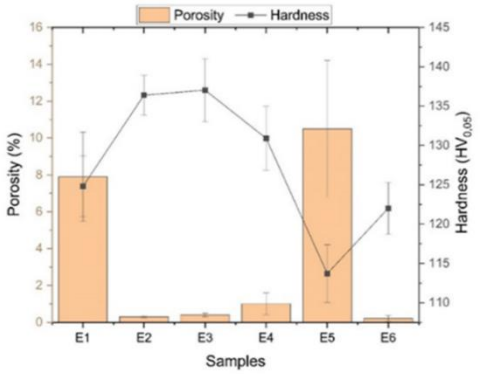

Figure 4. Hardness and porosity results of samples

It is known that there are microstructure changes in additive manufacturing products with changing process parameters [27] [28] [29]. As shown in Figure 5, an optical microscope study was carried out, and gas evaporation and lack of fusion errors are visible. Gas evaporation formation (E5) occurs due to the high energy input. On the other hand, a lack of fusion errors occurs due to insufficient energy (E1) or slow scanning speeds [27] [28] [30].

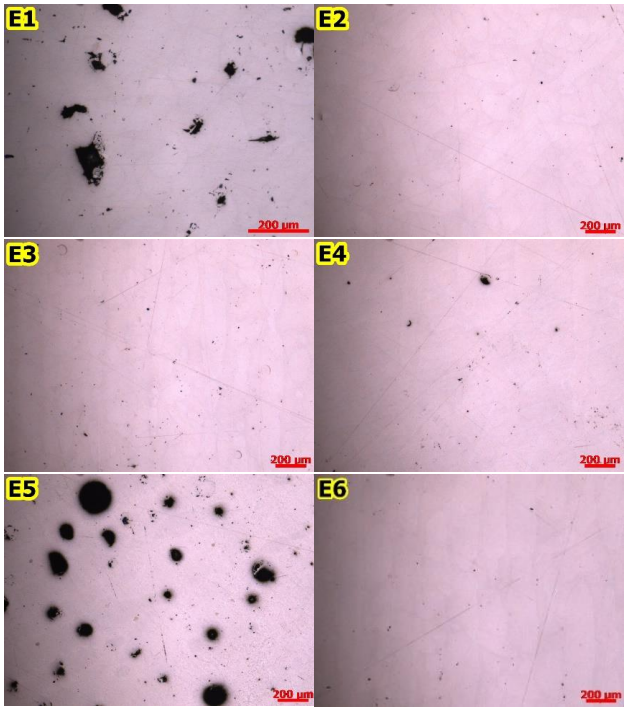

Figure 5. Optical images of samples

Table.3 and Figure 6 were given to examine the corrosion properties of the material. It is E_{cor} (corrosion potential), which shows the thermodynamic resistance of the material against oxidation [31] [32]. A high E core value indicates that the material starts to corrode later. The I_{cor} value represents the progression rate of corrosion. The relationship was determined between the porosity values of the material and the corrosion resistance (Table.3 and Figure 6).

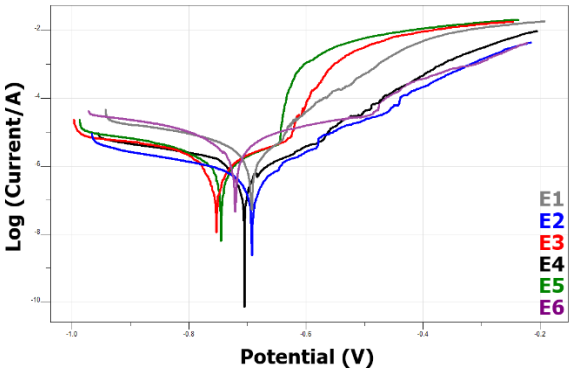

Figure 6. Corrosion (Tafel polarization) graphs of the samples

Table 3. Corrosion results of samples

Sample	E_{cor} (V)	I_{cor} (µA/cm2)	Corrosion rate (mm/year)	Polarization resistance (kΩ)
E1	-0.6936	1.84	0.0006035	1.31
E2	-0.6925	0.40	0.0003696	8.23
E3	-0.7535	1.12	0.0003664	4.24
E4	-0.7053	1.21	0.0003984	4.94
E5	-0.7457	2.82	0.0009231	2.76
E6	-0.7213	0.47	0.0005389	9.98

Surface SEM images share corrosion formation details (Figure 7). The corrosion rate was higher in the samples with a high porosity value, which is expected. It contains the electrochemical solution of the cavities in the material and creates regional differences in concentration and pH [33]. As a result of this difference, the material erosion is higher than the surfaces without porosity [34]. The surface SEM images show that corrosion is more active around the voids in the material.

Further corrosion of E1, E4 and E5 samples is explained in this way. It is expected that less corrosion is observed in the E6 sample (the standard production parameter for the DMLS system), and the E2 and E3 parameters showed similar corrosion properties. The corrosion intensity on the surfaces of E1, E4 and E5 samples, which contain more porosity, is visible.

Corrosion properties can vary according to the material's internal structure features. One of these properties is the amount of internal stress. It is known that the corrosion rate increases as the internal stress in the material increases. It is thought that the high amount of energy in production and the high internal stress are also effective in accelerating corrosion in E5 and E4 samples.

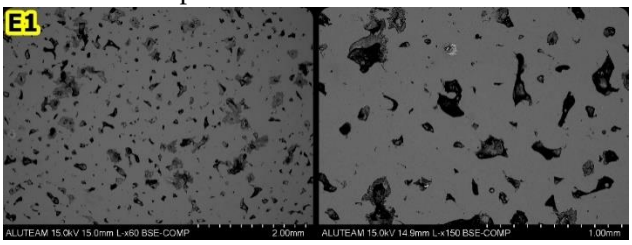

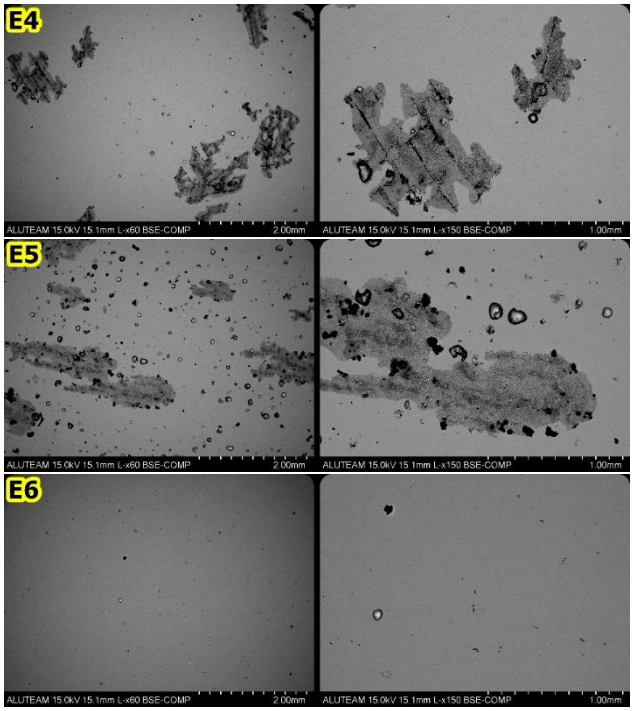

Figure 7. Corrosion (Tafel polarization) surfaces SEM images of the samples

I_{cor} values of the materials were determined by calculating from the graphics in Figure.6. A low I_{cor} value indicates that the material is more resistant to corrosion. It is seen that the surface corrosion images in Figure.7 and I_{cor} values support each other.

4. Conclusion and Suggestions

The results obtained from the investigation can be listed as follows;

- With the process parameter change, different phases did not occur in the material, and even peak shift and expansion behaviours were not observed in the results.
- A direct relationship was determined between the energy used in the system and the surface roughness.
- The porosity values in the material increased with the energy density being too high or too low. It has been determined that different kinetics occur in these changes.
- Although there is no direct effect of the process parameter on the hardness values, it has been observed that it is seriously related due to the porosity in the structure.
- It has been determined that the material's corrosion resistance is directly related to the porosity level in the structure.

Acknowledgement

Fatih Sultan Mehmet Vakif University Aluminum Test Training and Research Center is supported by Istanbul Development Agency (ISTKA) and T.R. Ministry of Development.

References

[1] Maamoun, A.H., Elbestawi, M., Dosbaeva, G.K., Veldhuis, S.C., "Thermal post-processing of AlSi10Mg parts produced by Selective Laser Melting using recycled powder". *Addit. Manuf.* 21, 234–247 (2018). https://doi.org/10.1016/j.addma.2018.03.014

[2] Domröse, R., Grünberger, T., "Identification of process phenomena in DMLS by optical in-process monitoring". (2015)

[3] Pantělejev, L., Štěpánek, R., Koutný, D., Paloušek, D., "Mechanical properties of AlSi10Mg alloy processed by SLM". *Mater. Eng. - Mater. inžinierstvo*. 24, 108–114 (2018)

[4] Yusuf, S.M., Gao, N., "Influence of energy density on metallurgy and properties in metal additive manufacturing". *Mater. Sci. Technol.* (United Kingdom). 33, 1269–1289 (2017). https://doi.org/10.1080/02670836.2017.1289444

[5] Thijs, L., Montero Sistiaga, M.L., Wauthle, R., Xie, Q., Kruth, J.P., Van Humbeeck, J., "Strong morphological and crystallographic texture and resulting yield strength anisotropy in selective laser melted tantalum". *Acta Mater*. (2013). https://doi.org/10.1016/j.actamat.2013.04.036

[6] Buchbinder, D., Meiners, W., Wissenbach, K., Poprawe, R., "Selective laser melting of aluminum die-cast alloy—Correlations between process parameters, solidification conditions, and resulting mechanical properties". *J. Laser Appl*. 27, S29205 (2015). https://doi.org/10.2351/1.4906389

[7] Zakay, A., Aghion, E., "Effect of Post-heat Treatment on the Corrosion Behavior of AlSi10Mg Alloy Produced by Additive Manufacturing". *Jom*. 71, 1150–1157 (2019). https://doi.org/10.1007/s11837-018-3298-x

[8] Palumbo, B., Del Re, F., Martorelli, M., Lanzotti, A., Corrado, P., "Tensile properties characterization of AlSi10Mg parts produced by direct metal laser sintering via nested effects modeling". *Materials* (Basel). 10, (2017). https://doi.org/10.3390/ma10020144

[9] Krishnan, M., Atzeni, E., Canali, R., Calignano, F., Manfredi, D., Ambrosio, E.P., Iuliano, L., "On the effect of process parameters on properties of AlSi10Mg parts produced by DMLS". *Rapid Prototyp. J.* 20, 449–458 (2014). https://doi.org/10.1108/RPJ-03-2013-0028

[10] Trevisan, F., Calignano, F., Lorusso, M., Pakkanen, J., Aversa, A., Ambrosio, E.P., Lombardi, M., Fino, P., Manfredi, D., "On the selective laser melting (SLM) of the AlSi10Mg alloy: Process, microstructure, and mechanical properties". *Materials* (Basel). 10, (2017). https://doi.org/10.3390/ma10010076

[11] Oter, Z.C., Coskun, M., Akca, Y., Surmen, O., Yilmaz, M.S., Ozer, G., Tarakci, G., Khan, H.M., Koc, E., "Support optimization for overhanging parts in direct metal laser sintering". *Optik* (Stuttg). 181, 575–581 (2019). https://doi.org/10.1016/j.ijleo.2018.12.072

[12] Herzog, D., Seyda, V., Wycisk, E., Emmelmann, C., "Additive manufacturing of metals". *Acta Mater*. 117, 371–392 (2016). https://doi.org/10.1016/j.actamat.2016.07.019

[13] Girelli, L., Tocci, M., Gelfi, M., Pola, A., "Study of heat treatment parameters for additively manufactured AlSi10Mg in comparison with corresponding cast alloy". *Mater. Sci. Eng. A.* 739, 317–328 (2019). https://doi.org/10.1016/j.msea.2018.10.026

[14] Brandl, E., Heckenberger, U., Holzinger, V., Buchbinder, D., "Additive manufactured AlSi10Mg samples using Selective Laser Melting (SLM): Microstructure, high cycle fatigue, and fracture behavior". *Mater. Des*. (2012). https://doi.org/10.1016/j.matdes.2011.07.067

[15] Ghasri-Khouzani, M., Peng, H., Attardo, R., Ostiguy, P., Neidig, J., Billo, R., Hoelzle, D., Shankar, M.R., "Comparing microstructure and hardness of direct metal laser sintered AlSi10Mg alloy between different planes". *J. Manuf. Process*. 37, 274–280 (2019). https://doi.org/10.1016/j.jmapro.2018.12.005

[16] Girelli, L., Tocci, M., Montesano, L., Gelfi, M., Pola, A., "Optimization of heat treatment parameters for additive manufacturing and gravity casting AlSi10Mg alloy". *IOP Conf. Ser. Mater. Sci. Eng*. 264, 0–8 (2017). https://doi.org/10.1088/1757-899X/264/1/012016

[17] Manfredi, D., Calignano, F., Krishnan, M., Canali, R., Ambrosio, E.P., Atzeni, E., "From powders to dense metal parts: Characterization of a commercial alsimg alloy processed through direct metal laser sintering". *Materials* (Basel). (2013). https://doi.org/10.3390/ma6030856

[18] Kruth, J.P., Mercelis, P., Van Vaerenbergh, J., Froyen, L., Rombouts, M., "Binding mechanisms in selective laser sintering and selective laser melting". *Rapid Prototyp. J.* 11, 26–36 (2005). https://doi.org/10.1108/13552540510573365

[19] Simchi, A., Direct laser sintering of metal powders: "Mechanism, kinetics and microstructural features". *Mater. Sci. Eng. A.* (2006). https://doi.org/10.1016/j.msea.2006.04.117

[20] Fox, J.C., Moylan, S.P., Lane, B.M., "Effect of Process Parameters on the Surface Roughness of Overhanging Structures in Laser Powder Bed Fusion Additive Manufacturing". *In: Procedia CIRP* (2016)

[21] Greco, S., Gutzeit, K., Hotz, H., Kirsch, B., Aurich, J.C., "Selective laser melting (SLM) of AISI 316L—impact of laser power, layer thickness, and hatch spacing on roughness, density, and microhardness at constant input energy density". *Int. J. Adv. Manuf. Technol.* (2020). https://doi.org/10.1007/s00170-020-05510-8

[22] Girelli, L., Giovagnoli, M., Tocci, M., Pola, A., Fortini, A., Merlin, M., La Vecchia, G.M., "Evaluation of the impact behaviour of AlSi10Mg alloy produced using laser additive manufacturing". *Mater. Sci. Eng. A.* 748, 38–51 (2019). https://doi.org/10.1016/j.msea.2019.01.078

[23] Rashid, R., Masood, S.H., Ruan, D., Palanisamy, S., Rahman Rashid, R.A., Elambasseril, J., Brandt, M., "Effect of energy per layer on the anisotropy of selective laser melted AlSi12 aluminium alloy". *Addit. Manuf.* 22, 426–439 (2018). https://doi.org/10.1016/j.addma.2018.05.040

[24] Wang, D., Yang, Y., Su, X., Chen, Y., "Study on energy input and its influences on single-track,multi-track, and multi-layer in SLM". *Int. J. Adv. Manuf. Technol.* 58, 1189–1199 (2012). https://doi.org/10.1007/s00170-011-3443-y

[25] Karimi, P., Sadeghi, E., Ålgårdh, J., Andersson, J., "EBM-manufactured single tracks of Alloy 718: Influence of energy input and focus offset on geometrical and microstructural characteristics". *Mater. Charact.* 148, 88–99 (2019). https://doi.org/10.1016/j.matchar.2018.11.033

[26] Hrabe, N., Quinn, T., "Effects of processing on microstructure and mechanical properties of a titanium alloy (Ti-6Al-4V) fabricated using electron beam melting (EBM), Part 2: Energy input, orientation, and location". *Mater. Sci. Eng. A.* (2013). https://doi.org/10.1016/j.msea.2013.02.065

[27] Shamsaei, N., Yadollahi, A., Bian, L., Thompson, S.M., "An overview of Direct Laser Deposition for additive manufacturing; Part II: Mechanical behavior, process parameter optimization and control". *Addit. Manuf.* 8, 12–35 (2015). https://doi.org/10.1016/j.addma.2015.07.002

[28] Aboulkhair, N.T., Everitt, N.M., Ashcroft, I., Tuck, C., "Reducing porosity in AlSi10Mg parts processed by selective laser melting". *Addit. Manuf.* 1, 77–86 (2014). https://doi.org/10.1016/j.addma.2014.08.001

[29] Kempen, K., Thijs, L., Yasa, E., Badrossamay, M., Verheecke, W., Kruth, J.P., "Process optimization and microstructural analysis for selective laser melting of AlSi10Mg". *22nd Annu. Int. Solid Free. Fabr. Symp. - An Addit. Manuf. Conf. SFF 2011*. 484–495 (2011)

[30] Mukherjee, T., Wei, H.L., De, A., DebRoy, T., "Heat and fluid flow in additive manufacturing – Part II: Powder bed fusion of stainless steel, and titanium, nickel and aluminum base alloys". *Comput. Mater. Sci.* 150, 369–380 (2018). https://doi.org/10.1016/j.commatsci.2018.04.027

[31] Prashanth, K.G., Debalina, B., Wang, Z., Gostin, P.F., Gebert, A., Calin, M., Kühn, U., Kamaraj, M., Scudino, S., Eckert, J., "Tribological and corrosion properties of Al-12Si produced by selective laser melting". *J. Mater. Res.* (2014). https://doi.org/10.1557/jmr.2014.133

[32] Shahriari, A., Khaksar, L., Nasiri, A., Hadadzadeh, A., Amirkhiz, B.S., Mohammadi, M., "Microstructure and corrosion behavior of a novel additively manufactured maraging stainless steel". *Electrochim. Acta.* 339, 135925 (2020). https://doi.org/10.1016/j.electacta.2020.135925

[33] Özer, G., Tarakçi, G., Yilmaz, M.S., Öter, Z.Ç., Sürmen, Ö., Akça, Y., Coşkun, M., Koç, E., "Investigation of the effects of different heat treatment parameters on the corrosion and mechanical properties of the AlSi10Mg alloy produced with direct metal laser sintering". *Mater. Corros.* (2019). https://doi.org/10.1002/maco.201911171

[34] Yılmaz, M.S., Özer, G., Öter, Z.Ç., Ertuğrul, O., "Effects of hot isostatic pressing and heat treatments on structural and corrosion properties of direct metal laser sintered parts". *Rapid Prototyp.* J. 27, 1059–1067 (2021). https://doi.org/10.1108/RPJ-10-2020-0245

Bitlis Eren Üniversitesi Fen Bilimleri Dergisi
BİTLİS EREN UNIVERSITY JOURNAL OF SCIENCE
ISSN: 2147-3129/e-ISSN: 2147-3188
VOLUME: 11 NO: 3 PAGE: 798-811 YEAR: 2022
DOI: 10.17798/bitlisfen.1102752

A Convolutional Neural Networks Model for Breast Tissue Classification

Mustafa Berkan BİÇER[1*], Hüseyin YANIK[2]

[1]*Electrical and Electronics Engineering, Engineering Faculty, Tarsus University, Tarsus, Mersin, Turkiye.*
[2]*Electrical and Electronics Engineering, Engineering Faculty, Mersin University, Mersin, Turkiye*
(ORCID: 0000-0003-3278-6071) (ORCID: 0000-0002-4386-5536)

Keywords: Breast tissue, classification, convolutional neural networks, machine learning, self-organizing fuzzy.

Abstract
The diagnosis of breast cancer and the determination of the cancer types are essential pieces of information for cancer research in monitoring and managing the disease. In recent years, artificial intelligence techniques have led to many developments in medicine, as any information about the patient has become more valuable. In particular, artificial intelligence methods used in the detection and classification of cancer tissues directly assist physicians and contribute to the management of the treatment process. This study aims to classify breast tissues with ten different tissue characteristics by utilizing the breast tissue data set, which has 106 electrical impedance spectroscopies taken from 64 patients in the UCI Machine Learning Repository database. Various machine learning algorithms including k-nearest neighbors, support vector machine, decision tree, self-organizing fuzzy logic, and convolutional neural networks are used to classify these tissues with an accuracy of 81%, 78%, 82%, 92%, and 96%, respectively. This study demonstrated the benefit of the usage of convolutional neural networks in cancer detection and tissue classification. Compared to traditional methods, convolutional neural networks provided better and more reliable results.

1. Introduction

Machine learning algorithms aim to analyze large data sets and intend to use the obtained information in a valuable way. Advances in machine learning and data processing techniques have directly affected many areas, especially the fields of the automotive [1], entertainment sector, digital markets [2], texture [3], fashion, defense [4] industries, and health [5]. Development of these algorithms leads to a variety of studies being done in these areas, especially in medicine.

The development of artificial intelligence techniques in parallel with technology has brought many developments in the field of health. These developments have made data on patients more valuable. Among these disease data sets, especially the analysis of data sets related to the diagnosis and classification of cancer diseases with artificial intelligence algorithms, produces direct results to help physicians and brings out results that will contribute to managing the treatment process.

Breast cancer is a type of cancer that grows slowly but can cause death rapidly when metastasizing and is the first leading cause of death after lung cancer among women with cancer in the world [6]. Research shows that the most important risk factor for the spread of breast cancer is the density of the breast tissue [7]. As with other types of cancer, the diagnosis of breast cancer at an early stage and the determination of cancerous tissue are of great importance in terms of monitoring the disease and implementing treatment.

It is known that the electrical impedance of breast tissue is compatible with the electrical properties of human tissue, which includes both resistance and capacitance, and that the electrical properties of biological tissues show significant

*Corresponding author: mberkanbicer@tarsus.edu.tr
Received: 13.04.2022, Accepted: 12.08.2022

differences depending on the structure and frequency [8]. Therefore, it is a complex and difficult process to define tissue characteristics using traditional methods. Advanced technical approaches provided by the developments in technology have become very useful in this context.

Electrical impedance techniques have emerged for use in obtaining and imaging tissue characteristics, have been used for a long time [9], and allow impedance mapping [10]. In a study presented by Jossinet in 1998 [10], significant differences were observed in the impedance and phase angle values in the examination between 6 different breast tissues in the range of 488 Hz to 1 MHz. These results suggest that electrical impedance spectroscopy (EIS) is a primary modality for classifying breast tissues and especially for the detection of breast cancer. Da Silva et al. proposed a breast tissue classification study using EIS [11]. Using the data obtained from 106 patients in an interventional way with EIS, the breast tissues were characterized and classified into 6 different types. Furthermore, a new data set was obtained in this study, which is called the UCI breast tissue data set [11]. Kerner et al. presented a classification study of breast tissue using EIS in 26 patients [12]. Images obtained from a multi-frequency EIS system are reconstructed using nonlinear differential equations, and an 83% performance rate is achieved on these images based on a special visual criterion.

Enachescu et al. presented a method based on the UCI breast tissue data set to detect and predict the presence of cancerous tissue in the breast [13]. In their study, the learning vector quantization (LVQ) method was used and an accuracy of 77% was obtained in the detection of breast tissue. Wu and Ng studied tissue classification on the UCI breast tissue data set using the radial-based function with different classifiers; naive bayes (NB), simple average (SA), and majority vote (MV). They achieved accuracies of 64%, 67%, 67%, and 80%, respectively [14].

In their study, Prasad et al. classified the UCI breast tissue data set by creating a fuzzy logic classification model, and an accuracy of 72% was achieved in the overall classification [15].

There are studies in the literature using hybrid algorithms. Alonso et al. tried to classify the UCI breast tissue data set using the logistic regression, NB, and the k-nearest neighbor (kNN) algorithms, and they achieved a success rate of 77% [16]. Also, the performance rate increased to 96% with a hybrid algorithm using a Bayesian approach. Daliri developed a hybrid algorithm by using the extreme learning machine (ELM) and support vector machines (SVM) methods and applied the hybrid algorithm to the UCI breast tissue data set [17]. In [17], an average value of 88% accuracy was obtained in classifying six different breast tissues in the data set. Eroğlu et al. classified the UCI breast tissue data set using ensemble learning algorithms such as random forest, SVM, and traditional artificial neural networks [18]. Using these methods, authors have achieved accuracies ranging from 76% to 83%. Liu et al. used the SVM algorithm for the classification of the UCI breast tissue data set and an average accuracy of 80% was obtained [19]. In the study of Ayyappan, breast tissue classification was carried out with different machine learning classifiers [20]. Since different results were obtained with different classifiers, the highest performance rate was obtained using bagging classification with 96%. Rahman et al. applied ensemble learning-based machine learning algorithms to the UCI breast tissue data set and classified different breast tissues [21]. The random forest (RF), decision trees (DT), AdaBoost, and gradient boosted regression trees have achieved 78%, 86%, 60%, and 75% success, respectively. Sadad et al. proposed a fuzzy c-means and region-growing based algorithm for segmentation and classification of tumours in mammograms [22]. Local binary pattern gray-level co-occurrence matrix and local phase quantization techniques were used to extract features [22]. A precision of 98.2% was achieved for the MIAS data set with DT and 95.8% was obtained for the DDSM data set using the kNN classifier [22]. Zhang et al. presented a convolutional neural network (CNN) based study to identify abnormal breast tissues taken from the MIAS data set [23]. An improved nine-layer CNN was proposed and a comparison of three activation functions; rectified linear unit (ReLU), leaky ReLU, and parametric ReLU, was made. In addition, six different pooling techniques were compared, and an accuracy of 94% was obtained with the combination of parametric ReLU and rank-based stochastic pooling.

In this study, different algorithms were utilized for the classification of breast tissues in the UCI breast tissue data set, and it was aimed to distinguish EIS measurements most efficiently. For this purpose, the classification accuracies of traditional algorithms such as SVM, kNN, and DT and advanced algorithms such as SOFLC and CNN were compared using the features of the breast tissue. Despite the fact that tissue classification and cancer detection studies have accelerated with the development of artificial neural network technology in recent years, one of the most important issues in CNN-based studies is that efficiency and cost are directly proportional. Therefore, attention is paid to keeping the efficiency high and maintaining the speed

of the algorithm while creating the CNN model. The question of whether the accuracy can be increased by using CNN for the UCI breast tissue data set has been the main motivation for this study. In addition to that, a new classifier called self-organizing fuzzy logic (SOFL) is applied to the same data set in order to evaluate the performance of it in such a highly used and cited data set.

2. Material and Method

In this study, it is aimed to classify six different breast tissues using UCI breast tissue data set [11] containing 106 different EIS measurements. Details concerning the data collection procedure are given in [10] and the properties of the data set can be seen in Table 1.

Table 1. Data set features

Parameter	Properties
Data set characteristic	Multivariate
Feature characteristic	Real number
Number of data	106
Number of features	10
Number of classes	6

The names and abbreviations of the six classes and the number of samples in each are given in Table 2. These samples were obtained from 64 different patients. In addition to that, the definitions of the features in the data set are given in Table 3. Using these features, the classification of six different breast tissues and detection of cancerous tissue can be done. Descriptive statistics for the data set are calculated for each feature and class in the data set, and given in the Table 4. As seen in Table 4, the range of values taken by each feature is at different levels. While the values of PA500 and HFS parameters are much less than 1, the values of Area, P, and I0 parameters are quite large.

Table 2. Breast tissue types and data population

Class	Abbreviation	Number of samples
Carcinoma	car	21
Fibroadenoma	fad	15
Mastopathy	mas	18
Glandular	gla	16
Connective	con	14
Adipose	adi	22

Table 3. Feature information of data set

Parameter	Details
I0	Impedivity (ohm) at zero frequency
PA500	Phase angle at 500 kHz
HFS	High-frequency slope of phase angle
DA	Impedance distance between spectral ends
Area	Area under spectrum
A/DA	Area normalized by impedance distance between spectral ends
Max IP	Maximum of the spectrum
DP	Distance between impedivity (ohm) at zero frequency and real part of the maximum frequency point
P	Length of the spectral curve
Class	6 different classes

The calculated correlation values between features are given in Table 5. When the correlation matrix given in Table 5 is examined, the features of P, DR, Area, and HFS features show high correlations with the I0 and Max IP, DA, A/DA, and PA500 features, respectively. The machine learning algorithms used in this study will be discussed in turn by considering the accuracy values obtained for test data. Statistics and confusion matrix plots regarding the results obtained with the presented classifiers are given in the Results and Discussion Section.

Table 4. Descriptive statistics for the data set

	Case	I0	PA500	HFS	DA	Area	A/DA	Max IP	DR	P	Class
Count	106.000	106.000	106.000	106.000	106.000	106.000	106.000	106.000	106.000	106.000	106.000
Mean	53.500	784.252	0.120	0.115	190.569	7335.155	23.474	75.381	166.711	810.638	3.500
Standard Deviation	30.744	753.950	0.069	0.101	190.801	18580.314	23.355	81.346	181.310	763.019	1.806
Minimum Value	1.000	103.000	0.012	-0.066	19.648	70.426	1.596	7.969	-9.258	124.979	1.000
1st Quartile	27.250	250.000	0.067	0.044	53.846	409.647	8.180	26.894	41.781	270.215	2.000
2nd Quartile	53.500	384.937	0.105	0.087	120.777	2219.581	16.134	44.216	97.833	454.108	3.000
3rd Quartile	79.750	1487.990	0.170	0.167	255.335	7615.205	30.953	83.672	232.990	1301.559	5.000
Maximum Value	106.000	2800.000	0.358	0.468	1063.441	174480.476	164.072	436.100	977.552	2896.583	6.000

Table 5. Correlation of the features in the data set

	I0	PA500	HFS	DA	Area	A/DA	Max IP	DR	P
I0	1.000	-0.394	0.029	0.820	0.560	0.612	0.824	0.733	0.989
PA500	-0.394	1.000	0.509	-0.090	0.084	0.230	-0.050	-0.077	-0.346
HFS	0.029	0.509	1.000	0.107	0.206	0.356	0.371	0.012	0.102
DA	0.820	-0.090	0.107	1.000	0.731	0.648	0.753	0.974	0.774
Area	0.560	0.084	0.206	0.731	1.000	0.830	0.735	0.676	0.574
A/DA	0.612	0.230	0.356	0.648	0.830	1.000	0.813	0.541	0.679
Max IP	0.824	-0.050	0.371	0.753	0.735	0.813	1.000	0.600	0.862
DR	0.733	-0.077	0.012	0.974	0.676	0.541	0.600	1.000	0.666
P	0.989	-0.349	0.102	0.774	0.574	0.679	0.862	0.666	1.000

2.1. Support Vector Machine

Support vector machine (SVM) is a vector space-based supervised artificial learning technique, adopted to solve the classification of single or multi-label data and regression problems, depending on the distance between two points in the data sets [24]. Although linear and nonlinear SVMs kernels can be applied according to the structure of the data, the linear SVM kernel is preferred in this study. While 76.42% of the data was used in the training of the presented SVM model, the remaining part of the data was used to test.

2.2. k-Nearest Neighbors (kNN)

Cover and Hart proposed the k-nearest neighbors (kNN) algorithm, which is one of the most widely used supervised machine-learning algorithms [25]. This algorithm is generally used in solving classification problems. It is generally used when all the features in a data set are continuous.

In kNN classification, firstly, the *k* value is determined in the algorithm. The *k* value corresponds to the number of elements to be examined. The distance between samples whose classes are known and new samples whose classes are tried to be found in the data set is calculated. Distances are computed using distance functions and sorted by their values. The nearest neighbors of the new sample are obtained, and the nearest class is selected based on distance functions. In this study, the Euclidean distance function (EDF) is used to perform the calculation as it is the most commonly used one in the literature. The mathematical expression of EDF is given in Eq. (1).

$$d(x,y) = \sqrt{\sum_{i=1}^{N} (x_i - y_i)^2} \quad (1)$$

d represents the distance between two points, and *x* and *y* denote the predicted and true values, respectively. There are many approaches to choosing the *k* value as it may vary depending on the data set. There are some important criteria when choosing the precise *k* value. Choosing a small *k* value causes noise to have bigger deflections on the result, while choosing a large *k* value increases the computational cost of the study. Generally, when trying different *k* values, the square root of the number of data points is taken as the upper limit value, and searching should start with a small value. The values between 1 and 10 as the *k* value were tried iteratively, and the value of 5 that gives the best accuracy for the classification problem was selected.

2.3. Decision Trees

Decision trees (DT) are relational probability maps in the form of a kind of tree. Quinlan inducts this algorithm and it helps to visualize and create feature thresholds based on decisions. In addition, DT demonstrates the best separation of a decision mathematically according to the characteristics of a data set [26].

Generally, a DT starts with a single node, and each node gives another opportunity to the next two possibilities, and the tree grows to the best separation. Nodes can vary between probability, decision, or end nodes based on their location.

DT classifiers classify as rule-based machine learning algorithms in multi and continuous feature data sets. Each decision tree branch is branched with feature-based threshold rules and causes new decisions that provide the opportunity to determine the correct class within the framework of these decisions.

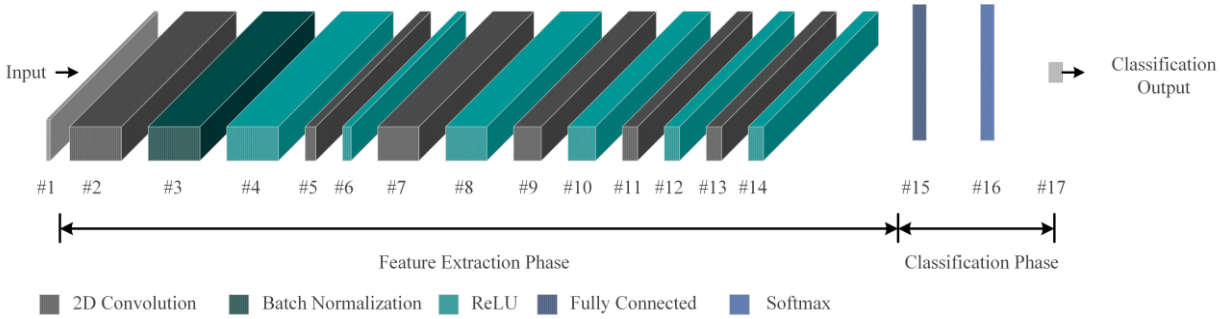

Figure 1. Proposed CNN classifier structure

2.4. Self-Organizing Fuzzy Logic Classifier (SOFLC)

The self-organizing fuzzy logic classifier (SOFLC) defines prototypes using input data via the offline training process [27]. In order to classify the data, it creates a 0-degree AnYa fuzzy rule-based system. After the first classification is done offline, the SOFLC model can update itself to fit the template of the new data by changing the system structure and meta-parameters as new data is generated. The values of the distance/dissimilarity parameter and granularity level were chosen as Euclidean and 34, respectively.

2.5. Convolutional Neural Networks

A convolutional neural network (CNN) is a multi-layered neural network structure that is often used in the feature extraction and classification of two-dimensional visual data and is an important part of the deep learning concept [28]. The differences between CNN and conventional neural networks (NN) are that CNN contains more layers than NNs and data features are extracted from the network structure. Hereby, the raw data to be classified can be given directly as an entry to the network. A CNN model can be easily applied to two-dimensional data such as images and videos. There are large CNN models developed and trained for various purposes in the literature. Despite some models are successful in classifying the training data, the accuracy of the model may be lower in different data sets or test data [28]–[30]. Therefore, it is important to design a CNN model suitable for the data, and learning parameters should be selected very carefully to prevent overfitting and underfitting as well. Since the breast tissue data set contains six different tissues, the output layer of the proposed CNN model has been selected to be a six-element classifier and the input layer is selected to be a nine-element. The constructed CNN model is shown in Figure 1. Details of the proposed CNN classifier and layers shown in Figure 1 are given in Table 6.

Table 6. Layer information about the proposed CNN model

#	Layer	Sizes	Learnable Parameter Sizes
1	Input	9×1×1	-
2	2D Convolution	9×1×93	Weights: 3×3×1×93 Biases: 1×1×93
3	Batch Normalization	9×1×93	Offset: 1×1×93 Scale: 1×1×93
4	ReLU	9×1×93	-
5	2D Convolution	9×1×48	Weights: 3×3×93×48 Biases: 1×1×48
6	ReLU	9×1×48	-
7	2D Convolution	9×1×89	Weights: 3×3×48×89 Biases: 1×1×89
8	ReLU	9×1×89	-
9	2D Convolution	9×1×68	Weights: 3×3×89×68 Biases: 1×1×68
10	ReLU	9×1×68	-
11	2D Convolution	9×1×55	Weights: 3×3×68×55 Biases: 1×1×55
12	ReLU	9×1×55	-
13	2D Convolution	9×1×55	Weights: 3×3×55×55 Biases: 1×1×55
14	ReLU	9×1×55	-
15	Fully Connected	1×1×6	Weights: 6×495 Biases: 6×1
16	Softmax	1×1×6	-
17	Classification Output	-	-

The initial weights for each layer of the CNN model are assigned using the *Xavier* weight initializer. The model was trained using 81 (76.42%) data points, and the remaining 25 (23.58%) data was used to test the model. In the training phase of the model, the number of data was kept the same, but after each training, the data was chosen randomly.

3. Results and Discussion

In this study, the UCI breast tissue data set was used, and by using this data set, the breast tissues were classified with the use of machine learning methods. In Table 7, methods used in classification, training

and test data distribution and performance rates are given.

Table 7. Classification performances

Classifiers	Accuracies (%)		
	Training	Test	All
SVM	83	88	84
kNN	81	92	84
DT	83	92	85
SOFLC	**83**	**92**	**85**
CNN	**100**	**96**	**99**

The DT structure and the chain of rules obtained in this study are illustrated in Figure 2. In this way, the relationship between properties and tissue characteristics can be observed. Also, evaluation metrics of the classifiers are computed using Eq. (2) – (9),

$$Accuracy = \frac{tp + tn}{tp + tn + fp + fn} \quad (2)$$

$$Sensitivity = \frac{tp}{tp + fn} \quad (3)$$

$$Specificity = \frac{tn}{tn + fp} \quad (4)$$

$$Precision = \frac{tp}{tp + fp} \quad (5)$$

$$False\ Positive\ Rate = \frac{fp}{fp + tn} \quad (6)$$

$$F_1\ score = \frac{2 \times tp}{2 \times tp + fp + fn} \quad (7)$$

$$MCC = \frac{tp \times tn - fp \times fn}{\sqrt{(tp + fp) \times (tp + fn) \times (tn + fp) \times (tn + fn)}} \quad (8)$$

$$Kappa = \frac{2 \times (tp \times tn - fn \times fp)}{(tp + fp) \times (fp + tn) \times (tp + fn) \times (fn + tn)} \quad (9)$$

where *tp*, *tn*, *fp* and *fn* represent *true positive (TP)*, *true negative (TN)*, *false positive (FP)* and *false negative (FN)*, respectively. While performing numerical calculations, the 5-fold cross-validation method was used. The training and test data, which are separated equally, were randomly chosen in each cycle, and the overall accuracy was calculated by averaging each accuracy value obtained in each fold. Accuracy, sensitivity, specificity, precision, false positive rate (FPR), F_1 score, Matthews correlation coefficient (MCC), and Cohen's Kappa values are calculated for each class separately and for all classes with the equations given with Eq (2) – (9) are tabulated in Table 8–12. As seen in Table 8, the accuracies of the SVM classifier were obtained as 82.7% and 88.0%, respectively, for training and testing. The MCC values range from 0.824 to 0.849 for training, test, and all data. These values show that there is an acceptable correlation between the predicted and the target classes.

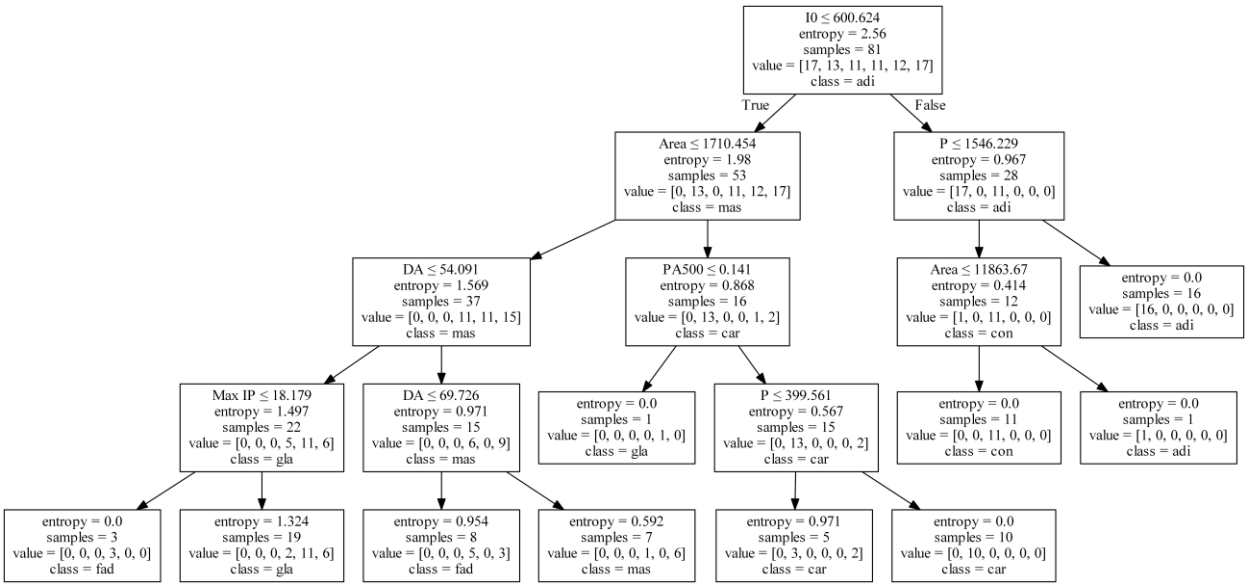

Figure 2. Decision tree and the rules identifying the relationship between features and tissues

Table 8. Detailed statistical results on SVM classification

	Class	Accuracy	Sensitivity	Specificity	Precision	FPR	F_1 score	MCC	Kappa	TP	FP	FN	TN
Train	Carcinoma	1.000	1.000	1.000	1.000	0.000	1.000	1.000	0.605	16	0	0	65
	Fibro-adenoma	0.938	0.938	0.938	0.789	0.062	0.857	0.823	0.583	15	4	1	61
	Mastopathy	1.000	1.000	1.000	1.000	0.000	1.000	1.000	0.753	10	0	0	71
	Glandular	0.667	0.667	0.971	0.800	0.029	0.727	0.689	0.739	8	2	4	67
	Connective	0.667	0.667	0.957	0.727	0.043	0.696	0.646	0.730	8	3	4	66
	Adipose	0.667	0.667	0.924	0.667	0.076	0.667	0.591	0.656	10	5	5	61
	All	0.827	0.823	0.965	0.831	0.035	0.824	0.791	0.378	-	-	-	-
Test	Carcinoma	1.000	1.000	1.000	1.000	0.000	1.000	1.000	0.520	6	0	0	19
	Fibro-adenoma	1.000	1.000	1.000	1.000	0.000	1.000	1.000	0.600	5	0	0	20
	Mastopathy	1.000	1.000	1.000	1.000	0.000	1.000	1.000	0.680	4	0	0	21
	Glandular	0.667	0.667	0.909	0.500	0.091	0.571	0.510	0.737	2	2	1	20
	Connective	0.750	0.750	1.000	1.000	0.000	0.857	0.846	0.725	3	0	1	21
	Adipose	0.667	0.667	0.955	0.667	0.045	0.667	0.621	0.770	2	1	1	21
	All	0.880	0.847	0.977	0.861	0.023	0.849	0.830	0.568	-	-	-	-
All	Carcinoma	1.000	1.000	1.000	1.000	0.000	1.000	1.000	0.585	22	0	0	84
	Fibro-adenoma	0.952	0.952	0.953	0.833	0.047	0.889	0.862	0.587	20	4	1	81
	Mastopathy	1.000	1.000	1.000	1.000	0.000	1.000	1.000	0.736	14	0	0	92
	Glandular	0.667	0.667	0.956	0.714	0.044	0.690	0.641	0.739	10	4	5	87
	Connective	0.688	0.688	0.967	0.786	0.033	0.733	0.692	0.729	11	3	5	87
	Adipose	0.667	0.667	0.932	0.667	0.068	0.667	0.598	0.682	12	6	6	82
	All	0.840	0.829	0.968	0.833	0.032	0.830	0.799	0.423	-	-	-	-

- Not Applicable.

When the Kappa values are examined, it shows that there is a moderate level of agreement, and there is also the possibility of chance during classification.

According to Table 9 regarding the kNN classifier, the accuracy for the training data was 81.5%, while the accuracy for the test data was 92%. In fact, since the kNN classifier does not contain a training phase, the most important factor determining the performance is the appropriate selection of training and test data. While the FPR parameter for this classifier had very low values, MCC results were obtained as 0.780 and 0.898 for training and test, respectively. These results show that the predicted classes had an acceptable correlation with the target classes. Also, it is seen that the kNN and SVM classifiers exhibit similar Kappa performance.

Table 9. Detailed statistical results on kNN classification

	Class	Accuracy	Sensitivity	Specificity	Precision	FPR	F_1 score	MCC	Kappa	TP	FP	FN	TN
Train	Carcinoma	0.857	0.857	0.985	0.923	0.015	0.889	0.868	0.674	12	1	2	66
	Fibro-adenoma	0.875	0.875	0.969	0.875	0.031	0.875	0.844	0.617	14	2	2	63
	Mastopathy	0.833	0.833	0.971	0.833	0.029	0.833	0.804	0.712	10	2	2	67
	Glandular	0.917	0.917	0.942	0.733	0.058	0.815	0.785	0.678	11	4	1	65
	Connective	1.000	1.000	0.942	0.750	0.058	0.857	0.841	0.663	12	4	0	65
	Adipose	0.467	0.467	0.970	0.778	0.030	0.583	0.539	0.721	7	2	8	64
	All	0.815	0.825	0.963	0.815	0.037	0.809	0.780	0.333	-	-	-	-
Test	Carcinoma	1.000	1.000	1.000	1.000	0.000	1.000	1.000	0.360	8	0	0	17
	Fibro-adenoma	1.000	1.000	0.950	0.833	0.050	0.909	0.890	0.570	5	1	0	19
	Mastopathy	1.000	1.000	1.000	1.000	0.000	1.000	1.000	0.840	2	0	0	23
	Glandular	1.000	1.000	1.000	1.000	0.000	1.000	1.000	0.760	3	0	0	22
	Connective	0.750	0.750	0.952	0.750	0.048	0.750	0.702	0.695	3	1	1	20
	Adipose	0.667	0.667	1.000	1.000	0.000	0.800	0.799	0.803	2	0	1	22
	All	0.920	0.903	0.984	0.931	0.016	0.910	0.898	0.712	-	-	-	-
All	Carcinoma	0.909	0.909	0.988	0.952	0.012	0.930	0.913	0.601	20	1	2	83
	Fibro-adenoma	0.905	0.905	0.965	0.864	0.035	0.884	0.855	0.606	19	3	2	82
	Mastopathy	0.857	0.857	0.978	0.857	0.022	0.857	0.835	0.741	12	2	2	90
	Glandular	0.933	0.933	0.956	0.778	0.044	0.848	0.826	0.697	14	4	1	87
	Connective	0.938	0.938	0.944	0.750	0.056	0.833	0.807	0.671	15	5	1	85
	Adipose	0.500	0.500	0.977	0.818	0.023	0.621	0.588	0.740	9	2	9	86
	All	0.840	0.840	0.968	0.837	0.032	0.829	0.804	0.423	-	-	-	-

- Not Applicable.

Table 10 contains detailed statistical classification results for the DT classifier. The accuracy values for the DT classifier were greater than 82.7%. The MCC values of the DT classifier, which exhibits similar Kappa performance to SVM and kNN, were also similar to the aforementioned models. When Table 11, which contains the results of the classification made using SOFLC, is examined, the accuracy values were in a similar range to those of SVM, kNN, and DT classifiers. On the other hand, the MCC and Kappa parameters had similarities with the mentioned models, although they have minor differences. In the SOFLC model, the MCC value for the test phase was higher than for the other models. The statistical values obtained by the proposed CNN model are shown in Table 12. When the values are examined, the model, which performs much better than previous models in terms of accuracy, sensitivity, and specificity, had the lowest FPR rates.

Table 10. Detailed statistical results on DT classification

	Class	Accuracy	Sensitivity	Specificity	Precision	FPR	F_1 score	MCC	Kappa	TP	FP	FN	TN
rain	Carcinoma	1.000	1.000	1.000	1.000	0.000	1.000	1.000	0.630	15	0	0	66
	Fibro-adenoma	1.000	1.000	1.000	1.000	0.000	1.000	1.000	0.654	14	0	0	67
	Mastopathy	1.000	1.000	1.000	1.000	0.000	1.000	1.000	0.753	10	0	0	71
	Glandular	0.857	0.857	0.910	0.667	0.090	0.750	0.698	0.626	12	6	2	61
	Connective	1.000	1.000	0.886	0.579	0.114	0.733	0.716	0.645	11	8	0	62
	Adipose	0.294	0.294	1.000	1.000	0.000	0.455	0.498	0.738	5	0	12	64
	All	0.827	0.859	0.966	0.874	0.034	0.823	0.819	0.378	-	-	-	-
Test	Carcinoma	1.000	1.000	1.000	1.000	0.000	1.000	1.000	0.440	7	0	0	18
	Fibro-adenoma	0.857	0.857	1.000	1.000	0.000	0.923	0.901	0.493	6	0	1	18
	Mastopathy	1.000	1.000	1.000	1.000	0.000	1.000	1.000	0.680	4	0	0	21
	Glandular	1.000	1.000	0.958	0.500	0.042	0.667	0.692	0.882	1	1	0	23
	Connective	0.800	0.800	1.000	1.000	0.000	0.889	0.873	0.648	4	0	1	20
	Adipose	1.000	1.000	0.958	0.500	0.042	0.667	0.692	0.882	1	1	0	23
	All	0.920	0.943	0.986	0.833	0.014	0.858	0.860	0.712	-	-	-	-
All	Carcinoma	1.000	1.000	1.000	1.000	0.000	1.000	1.000	0.585	22	0	0	84
	Fibro-adenoma	0.952	0.952	1.000	1.000	0.000	0.976	0.970	0.615	20	0	1	85
	Mastopathy	1.000	1.000	1.000	1.000	0.000	1.000	1.000	0.736	14	0	0	92
	Glandular	0.867	0.867	0.923	0.650	0.077	0.743	0.704	0.685	13	7	2	84
	Connective	0.938	0.938	0.911	0.652	0.089	0.769	0.737	0.648	15	8	1	82
	Adipose	0.333	0.333	0.989	0.857	0.011	0.480	0.487	0.774	6	1	12	87
	All	0.849	0.848	0.970	0.860	0.030	0.828	0.816	0.457	-	-	-	-

- Not Applicable.

Table 11. Detailed statistical results on SOFLC classification

	Class	Accuracy	Sensitivity	Specificity	Precision	FPR	F_1 score	MCC	Kappa	TP	FP	FN	TN
Train	Carcinoma	1.000	1.000	0.954	0.842	0.046	0.914	0.896	0.577	16	3	0	62
	Fibro-adenoma	0.727	0.727	0.957	0.727	0.043	0.727	0.684	0.740	8	3	3	67
	Mastopathy	0.286	0.286	0.970	0.667	0.030	0.400	0.369	0.767	4	2	10	65
	Glandular	1.000	1.000	0.928	0.706	0.072	0.828	0.809	0.653	12	5	0	64
	Connective	1.000	1.000	0.986	0.917	0.014	0.957	0.951	0.718	11	1	0	69
	Adipose	0.941	0.941	1.000	1.000	0.000	0.970	0.963	0.596	16	0	1	64
	All	0.827	0.826	0.966	0.810	0.034	0.799	0.779	0.378	-	-	-	-
Test	Carcinoma	1.000	1.000	1.000	1.000	0.000	1.000	1.000	0.600	5	0	0	20
	Fibro-adenoma	0.750	0.750	0.952	0.750	0.048	0.750	0.702	0.695	3	1	1	20
	Mastopathy	0.750	0.750	1.000	1.000	0.000	0.857	0.846	0.725	3	0	1	21
	Glandular	1.000	1.000	0.952	0.800	0.048	0.889	0.873	0.648	4	1	0	20
	Connective	1.000	1.000	1.000	1.000	0.000	1.000	1.000	0.760	3	0	0	22
	Adipose	1.000	1.000	1.000	1.000	0.000	1.000	1.000	0.600	5	0	0	20
	All	0.920	0.917	0.984	0.925	0.016	0.916	0.904	0.712	-	-	-	-
All	Carcinoma	1.000	1.000	0.965	0.875	0.035	0.933	0.919	0.582	21	3	0	82
	Fibro-adenoma	0.733	0.733	0.956	0.733	0.044	0.733	0.689	0.729	11	4	4	87
	Mastopathy	0.389	0.389	0.977	0.778	0.023	0.519	0.493	0.758	7	2	11	86
	Glandular	1.000	1.000	0.933	0.727	0.067	0.842	0.824	0.652	16	6	0	84
	Connective	1.000	1.000	0.989	0.933	0.011	0.966	0.961	0.728	14	1	0	91
	Adipose	0.955	0.955	1.000	1.000	0.000	0.977	0.971	0.597	21	0	1	84
	All	0.849	0.846	0.970	0.841	0.030	0.828	0.810	0.457	-	-	-	-

- Not Applicable.

The CNN model, which had the highest MCC values compared to the models examined within the scope of the study, also performed well according to the Kappa parameter, which is an indicator of compatibility. As it can be seen from the tables, the classifier with the lowest accuracy for test data was SVM, while the highest classifier performance was achieved by the proposed CNN model. While the lowest accuracy value was obtained with kNN in the classification of training and all data, the proposed CNN model reached the highest accuracy value. As it can be seen from the tables, the proposed CNN model shows great success in breast tissue classification.

Table 12. Detailed statistical results on CNN classification

	Class	Accuracy	Sensitivity	Specificity	Precision	FPR	F_1 score	MCC	Kappa	TP	FP	FN	TN
Train	Carcinoma	1.000	1.000	1.000	1.000	0.000	1.000	1.000	0.605	16	0	0	65
	Fibro-adenoma	1.000	1.000	1.000	1.000	0.000	1.000	1.000	0.728	11	0	0	70
	Mastopathy	1.000	1.000	1.000	1.000	0.000	1.000	1.000	0.654	14	0	0	67
	Glandular	1.000	1.000	1.000	1.000	0.000	1.000	1.000	0.704	12	0	0	69
	Connective	1.000	1.000	1.000	1.000	0.000	1.000	1.000	0.728	11	0	0	70
	Adipose	1.000	1.000	1.000	1.000	0.000	1.000	1.000	0.580	17	0	0	64
	All	1.000	1.000	1.000	1.000	0.000	1.000	1.000	1.000	-	-	-	-
Test	Carcinoma	0.800	0.800	1.000	1.000	0.000	0.889	0.873	0.648	4	0	1	20
	Fibro-adenoma	1.000	1.000	1.000	1.000	0.000	1.000	1.000	0.680	4	0	0	21
	Mastopathy	1.000	1.000	1.000	1.000	0.000	1.000	1.000	0.680	4	0	0	21
	Glandular	1.000	1.000	0.952	0.800	0.048	0.889	0.873	0.648	4	1	0	20
	Connective	1.000	1.000	1.000	1.000	0.000	1.000	1.000	0.760	3	0	0	22
	Adipose	1.000	1.000	1.000	1.000	0.000	1.000	1.000	0.600	5	0	0	20
	All	0.960	0.967	0.992	0.967	0.008	0.963	0.958	0.856	-	-	-	-
All	Carcinoma	0.952	0.952	1.000	1.000	0.000	0.976	0.970	0.615	20	0	1	85
	Fibro-adenoma	1.000	1.000	1.000	1.000	0.000	1.000	1.000	0.717	15	0	0	91
	Mastopathy	1.000	1.000	1.000	1.000	0.000	1.000	1.000	0.660	18	0	0	88
	Glandular	1.000	1.000	0.989	0.941	0.011	0.970	0.965	0.690	16	1	0	89
	Connective	1.000	1.000	1.000	1.000	0.000	1.000	1.000	0.736	14	0	0	92
	Adipose	1.000	1.000	1.000	1.000	0.000	1.000	1.000	0.585	22	0	0	84
	All	0.991	0.992	0.999	0.990	0.002	0.991	0.989	0.966	-	-	-	-

- Not Applicable.

Confusion matrix plots obtained utilizing the SVM, kNN, DT, SOFLC, and CNN classifiers are illustrated in Figure 3 (a) – (e).

(a)

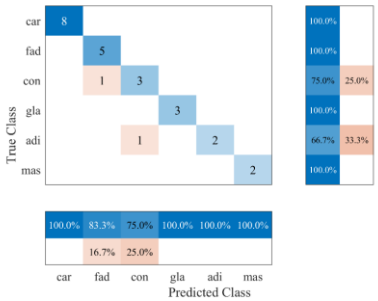

(b)

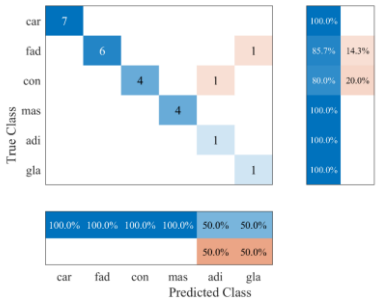

(c)

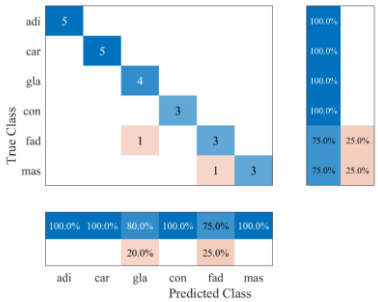

(d)

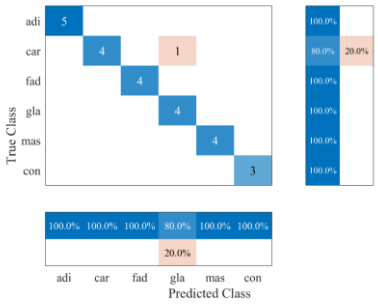

(e)

Figure 3. Confusion matrixes related to the classification result obtained from (a) SVM, (b) kNN, (c) DT, (d) SOFLC and (e) CNN classifiers

Table 13 shows the comparison of machine learning methods applied in this study with successful algorithms in the literature. Table 13 shows that the proposed CNN model gave the highest accuracy rate for training, test and entire data. In the classification of all tissues, it was observed that the SOFLC stands out in terms of overall speed and performance. In the classification between tumour tissue and normal tissue, CNN has achieved a success rate of 100% in training and 96% in test, showing the most successful result in determining tumour tissue. As a result, it is thought that increasing the number of samples in the data set will further stabilize the accuracy and increase the performance of CNN, especially in classification. The increase in the features in the data set along with the increase in the amount of data will also contribute to achieving better results in future studies.

Table 13. Test accuracy comparison of classification results with different approaches

	S1	S2	S3	S4	S5
(Wu and Ng 2007)	RBF	RBF+SA	RBF+MV	RBF+NB	-
	64.83%	66.81%	66.46%	80.27%	-
(Daliri 2015)	ELM	-	-	-	-
	88.95%	-	-	-	-
(Eroğlu et al. 2014)	SVM	RF	ANN	-	-
	81.13%	83.96%	76.41%	-	-
(Liu et al. 2015)	SVM	-	-	-	-
	80.62%	-	-	-	-
(Rahman et al. 2019)	RF	ERT	DT	GBT	ADB
	85.19%	81.48%	78.10%	74.08%	62.96%
This Study	SVM	kNN	DT	SOFLC	CNN
	88.00%	92.00%	92.00%	**92.00**%	**96.00**%

4. Conclusion and Suggestions

In this study, a convolutional neural network model having six convolution layers for breast tissue classification is proposed. The model was trained and tested using the breast tissue data set from UCI. To compare the performance of the proposed model, SVM, DT, kNN, and SOFLC models are also trained for classification using the same data set. The accuracy percentages for the classifier models SVM, kNN, DT, SOFLC, and the proposed CNN for the test data were obtained as 88%, 92%, 92%, and 96%, respectively. As compared to state-of-the-art methods used on this data set, the results demonstrated that the proposed model had a higher accuracy. The inclusion of six convolution layers with pooling layers in between, as well as the quantity of convolution filters, are the most significant factors that contribute to the proposed model's increased performance. A recently proposed technique called SOFLC was also utilized, and its performance was compared to that of conventional and convolutional neural networks. On the basis of accuracy and computational cost, SOFLC appears to be a promising method, although CNN outperforms in terms of total performance.

Contributions of the authors

The authors are equally contributed to the article.

Conflict of Interest Statement

There is no conflict of interest between the authors.

Statement of Research and Publication Ethics

The study is complied with research and publication ethics.

References

[1] T. Holleczek, C. Zysset, B. Arnrich, D. Roggen, and G. T. G, "Towards an interactive snowboarding assistance system," in International Symposium on Wearable Computers, September 4-7, 2009, pp. 147–148.

[2] T. T. Nguyen and G. Armitage, "A survey of techniques for internet traffic classification using machine learning," IEEE Commun. Surv. Tutor, vol. 10, no. 4, pp. 56-76.

[3] G. Cohen, S. Afshar, J. Tapson, and A. Schaik, "EMNIST: Extending MNIST to handwritten letters," in 2017 International Joint Conference on Neural Networks (IJCNN), May 14-19, 2017, pp. 2921–2926.

[4] A. L. Buczak and E. Guven, "A survey of data mining and machine learning methods for cyber security intrusion detection," IEEE Commun. Surv. Tutor, vol. 18, no. 2, pp. 1153-1176, 2016.

[5] A. Rajkomar, J. Dean, and I. Kohane, "Machine learning in medicine," N. Engl. J. Med, vol. 380, no. 14, pp. 1347-1358, 2019.

[6] C. E. DeSantis, S. A. Fedewa, A. G. Sauer, J. L. Kramer, R. A. Smith, and A. Jemal, "Breast cancer statistics, 2015: Convergence of incidence rates between black and white women," CA. Cancer J. Clin, vol. 66, no. 1, pp. 31-42, 2016.

[7] J. Jossinet and M. Schmitt, "A review of parameters for the bioelectrical characterization of breast tissue," Ann. NY. Acad. Sci, vol. 873, no. 1, pp. 30-41, 2006.

[8] S. Gabriel, R. W. Lau, and C. Gabriel, "The dielectric properties of biological tissues: III. Parametric models for the dielectric spectrum of tissues," Physics in Medicine and Biology, vol. 41, no. 11, pp. 2271-2293, 1996.

[9] W. K. Wg, "Impedance cardiography as a noninvasive means to monitor cardiac function," JAAMI J. Ass. Advan. Med. Instrum, vol. 4, no. 2, pp. 79-84, 1970.

[10] J. Jossinet, "The impedivity of freshly excised human breast tissue," Physiol. Meas, vol. 19, no. 1, pp. 61-75, 1998.

[11] J. E. Silva, J. P. M. Sá, and J. Jossinet, "Classification of breast tissue by electrical impedance spectroscopy," Med. Biol. Eng. Comput, vol. 38, no. 1, pp. 26-30, 2000.

[12] T. E. Kerner, K. D. Paulsen, A. Hartov, S. K. Soho, and S. P. Poplack, "Electrical impedance spectroscopy of the breast: clinical imaging results in 26 subjects," IEEE Trans. Med. Imaging, vol. 21, no. 6, pp. 638-645, 2002.

[13] D. Enachescu and C. Enachescu, "Learning vector quantization for breast cancer prediction," Portuguese conference on artificial intelligence, December 5-8, 2005, pp. 177–180.

[14] Y. Wu and S. C. Ng, "Combining neural learners with the naive bayes fusion rule for breast tissue classification," in 2nd IEEE Conference on Industrial Electronics and Applications, May 23-25, 2007, pp. 709–713.

[15] D. K. Prasad, C. Quek, and M. K. H. Leung, "A hybrid approach for breast tissue data classification," in TENCON 2009 – 2009 IEEE Region 10 Conference, Jan 23-27 2009, pp. 1–4.

[16] F. Calle-Alonso, C. J. Pérez, J. P. Arias-Nicolás, and J. Martín, "Computer-aided diagnosis system: A Bayesian hybrid classification method," Comput. Meth. Prog. Bio, vol. 112, no. 1, pp. 104-113, 2013.

[17] M. R. Daliri, "Combining extreme learning machines using support vector machines for breast tissue classification," Comput. Methods Biomech. Biomed. Eng, vol. 18, no. 2, pp. 185-191, 2015.

[18] K. Eroğlu, E. Mehmetoglu, and N. Kılıç, "Success of ensemble algorithms in classification of electrical impedance spectroscopy breast tissue records," in 22nd Signal Processing and Communications Applications Conference (SIU), April 23-25, 2014, pp. 1419–1422.

[19] C. Liu, T. Chang, and C. Li, "Breast tissue classification based on electrical impedance spectroscopy," in Proceedings of the 2015 International Conference on Industrial Technology and Management Science, 2015, pp. 237–240.

[20] G. A. Ayyappan and K. S. Kumar, "Novel classification approach-1 on breast tissue dataset," Indian Journal of Computer Science and Engineering, vol. 9, no. 4, pp. 115-118, 2018.

[21] S. M. Rahman, M. A. Ali, O. Altwijri, M. Alqahtani, N. Ahmed, and N. U. Ahamed, "Ensemble-based machine learning algorithms for classifying breast tissue based on electrical impedance spectroscopy," in Advances in Artificial Intelligence, Software and Systems Engineering, Cham, 2020, pp. 260–266.

[22] T. Sadad, A. Munir, T. Saba, and A. Hussain, "Fuzzy C-means and region growing based classification of tumor from mammograms using hybrid texture feature," J. Comput. Sci, vol. 29, pp. 34-45, 2018.

[23] Y.-D. Zhang, C. Pan, X. Chen, and F. Wang, "Abnormal breast identification by nine-layer convolutional neural network with parametric rectified linear unit and rank-based stochastic pooling," J. Comput. Sci, vol. 27, pp. 57-68, 2018.
[24] J. A. K. Suykens and J. Vandewalle, "Least squares support vector machine classifiers," Neural Process. Lett, vol. 9, no. 3, pp. 293-300, 1999.
[25] T. Cover and P. Hart, "Nearest neighbor pattern classification," IEEE Trans. Inf. Theory, vol. 13, no. 1, pp. 21-27, 1967.
[26] J. R. Quinlan, "Induction of decision trees," Mach. Learn, vol. 1, no. 1, pp. 81-106, 1986.
[27] X. Gu and P. P. Angelov, "Self-organising fuzzy logic classifier," Inform. Sciences, vol. 447, pp. 36-51, 2018.
[28] A. Krizhevsky, I. Sutskever, and G. E. Hinton, "ImageNet classification with deep convolutional neural networks," in Advances in Neural Information Processing Systems, vol. 25, 2012.
[29] C. Szegedy, "Going deeper with convolutions," 2015 IEEE Conference on Computer Vision and Pattern Recognition (CVPR), June 07-12, 2015.
[30] K. Simonyan and A. Zisserman, "Very deep convolutional networks for large-scale image recognition," 2014. [Online]. Available: arXiv:1409.1556.

Bitlis Eren Üniversitesi Fen Bilimleri Dergisi
BİTLİS EREN UNIVERSITY JOURNAL OF SCIENCE
ISSN: 2147-3129/e-ISSN: 2147-3188
VOLUME: 11 NO: 3 PAGE: 812-819 YEAR: 2022
DOI: 10.17798/bitlisfen.1106917

The Development of Broadband Microstrip Patch Antenna for Wireless Applications

Cem GÜLER[1*], Sena Esen BAYER KESKİN[2], Rukiye B.AYMAZ[3]

[1]*Department of Airframe and Powerplant Maintenance, Kırklareli Unıversity, Turkey*
[2]*Dept. of Elec. and Elec. Engineering, Faculty of Engineering, Kırklareli Unıversity, Turkey*
[3]*Department of Electrical Engineering, Faculty of Engineering, Kocaeli University, Turkey*
(ORCID: 0000-0002-6631-7559) (ORCID: 0000-0001-8309-3393) (ORCID: 0000-0002-1683-6190)

Keywords: Microstrip patch antenna, Wireless Applications, Bandwidth, CST Microwave Studio, ISM 2.4 GHz band, Return Loss.

Abstract

In recent years, the use of unlicensed wireless communication bands has been widely used in different applications such as biomedical, military, and textile/wearable systems. This paper presents the design of the broadband microstrip patch antenna operating in the ISM 2.4 GHz band (2400-2485 MHz). The study includes a three-dimensional antenna model, a simulation phase, and a fabrication/measurement phase. The small volume of microstrip antennas has low fabrication costs and easy fabrication, which has accelerated the work in this area. For the low cost of the antenna, FR-4 with a relative dielectric constant of 4.3 and a loss tangent tan 0.02 is preferred as the substrate material. The dielectric material thickness is determined as 1.6mm. The length of the feed line and the dimensions of the rectangular patch were found by mathematical calculations with the transmission line model. In the ISM band, antennas with low return loss and high bandwidth are required. The most important disadvantage of the patch antennas is their narrow bandwidth, which should be increased optimally. There are slots on the antenna, which is an especially simple method in order to improve the bandwidth parameters of the antenna. In the paper, four different designs are presented, the results are compared, and the proposed antenna has a rational bandwidth of 42.2% (979 MHz bandwidth), 24.529 dB return loss, and 2.68 dBi directivity gain at -10 dB at the resonance frequency of 2.316 GHz. The changes made in the antenna design have improved the resultant bandwidth compared to the conventional microstrip patch antenna. The proposed antenna is suitable for use in ISM band applications.

1. Introduction

The ISM Band (Industrial, Scientific, and Medicine) is the frequency spectrum without the use of many countries 'licenses. The 2.45 GHz ISM band is a band accepted worldwide by the ITU (International Telecommunication Union) [1]. The ISM frequency band is frequently used for wireless communication in biomedical applications [2], military applications [3], and textile applications [4]. Communication can be defined as the transfer of information from one point to another. The information transfer can be done by modulating the information into the electromagnetic wave. When this wave reaches its destination, it is demodulated to obtain the actual information signal. Nowadays, antennas are the most important components of communication connections. In many areas, such as high-performance vehicles, aircraft, spacecraft, radar systems, satellites, and missile applications; microstrip antennas have become a popular antenna type among microwave antennas due to their advantages, such as low cost, performance, easy installation, and production with modern printed circuit technology [5]. The concept of a microstrip antenna was first introduced by GA Deschamps in

*Corresponding author: cemguler@klu.edu.tr
Received: 21.04.2022, Accepted: 05.08.2022

1953 [6] but has not been implemented for many years. In 1955, Gutton and Baissinot patented the first microstrip structure [7]. The first microstrip antenna communication experiments were conducted by Munson on the missile data system in the 1970s. Howell in 1972 and Munson in 1974 introduced the first easily applicable microstrip antenna structure [8]. The development of the microstrip antenna has accelerated with printed circuit technology. In 2003, S. Weigand performed frequency analysis according to patch and cleft dimensions [9]. Besides, it is an up-to-date issue since it allows different designs. In addition, the most important disadvantage is the narrow bandwidth. Narrow bandwidth is wanted in security applications but refused for broadband applications. Several methods have been used to increase bandwidth. In 2005, Deshmukh and Kumar examined the flow paths formed by the U-shaped slot cut on the patch and observed that the pattern increased the bandwidth by spreading to two frequencies [10]. A.Khidre et al. presented a broadband U-slot patch probe-fed antenna on a 67 mm x 74 mm Rogers RT/duroid substrate [11]. Another widely used method to increase the bandwidth in the literature is to open slots on the patch in various ways [12-14]. Lee et al. achieved a 20%-30% impedance bandwidth by loading a U-shaped slot onto a rectangular patch fed by a coaxial probe. The antenna has a width of 35.5 mm and a length of 26 mm. The gain at 4.1 GHz is 7.30 dB. The bandwidth at 3 dB is 28.50% at 3.79-5.05 GHz [15]. In another study, an antenna design with a circular patch fed by a microstrip line operates at a frequency of 2.49 GHz. It has achieved a bandwidth of 80 MHz and a directivity gain of 2.611 dBi [16]. Several methods have been introduced, such as using slits [17], slots [18], DGS (Defected Ground Structure) [19], partial ground plane [20-21], split-ring resonator [22], substrate integrated waveguide (SIW) [23], dielectric rezonator (DRA) [24], using air gap [25], shorting pin [26] and using EBG (Electromagnetic Band Gap) structures [27]. Although there are many studies in the literature to increase the bandwidth, the easiest way to increase the bandwidth is to use slots in the patch plane and make changes in the ground plane [10-27].

This paper presents the design of a slotted microstrip patch antenna operating in the ISM 2.4 GHz band (2400-2485 MHz). Four types of antennas are presented to observe the effect of slots on resonance frequency, bandwidth, return loss, and gain. The design and simulation of the antennas are carried out in the CST Microwave Studio program. The dimensions of the first antenna were taken as reference and the length of the feed line and patch dimensions of the antennas were kept constant, the slots were opened, various parameters were optimized, and the proposed antenna was reached. In the first stage, the antenna, the dimensions of which are calculated by the transmission line model, is drawn, and the slot is not used in this antenna, the results should be improved. Slots are opened in the patch on the second antenna. On the third antenna, the ground is cut off. Finally, the proposed antenna is achieved by opening slots on both the patch and the ground, which optimizes the parameters. The other proposed antennas compared to the other three antennas have the widest bandwidth and resonance frequency of 2.316 GHz, -10 dB with a bandwidth of 979 MHz and a directional gain of 2.68 dBi.

2. Material and Method

FR-4 has a relative dielectric constant and is preferred as the substrate material for the designed antennas. Dielectric material thickness is determined as 1.6 mm. The transmission line model is used for the design of a microstrip patch antenna. The dimensions of the rectangular patch on the antenna, the length of the feed line, and other parameters are calculated by the transmission line model and mathematical calculations. The results are optimized, and the antenna is simulated. The slots are then used to improve the results. Figure 1 shows the front and rear views of the antennas.

Moreover, to better understand the design of the antenna proposed in Figure 2, parameters are assigned to the lengths and the values of these parameters are given in Table 1.

Table 1. Proposed antenna dimensions

Parameter	Dimension	Parameter	Dimension
W	50	c	4.5
L	55	d	5
W_P	24.5	f	18
L_P	22.5	p	2
W_F	3	r	5
a	11	z	1
b	23	h	1.6

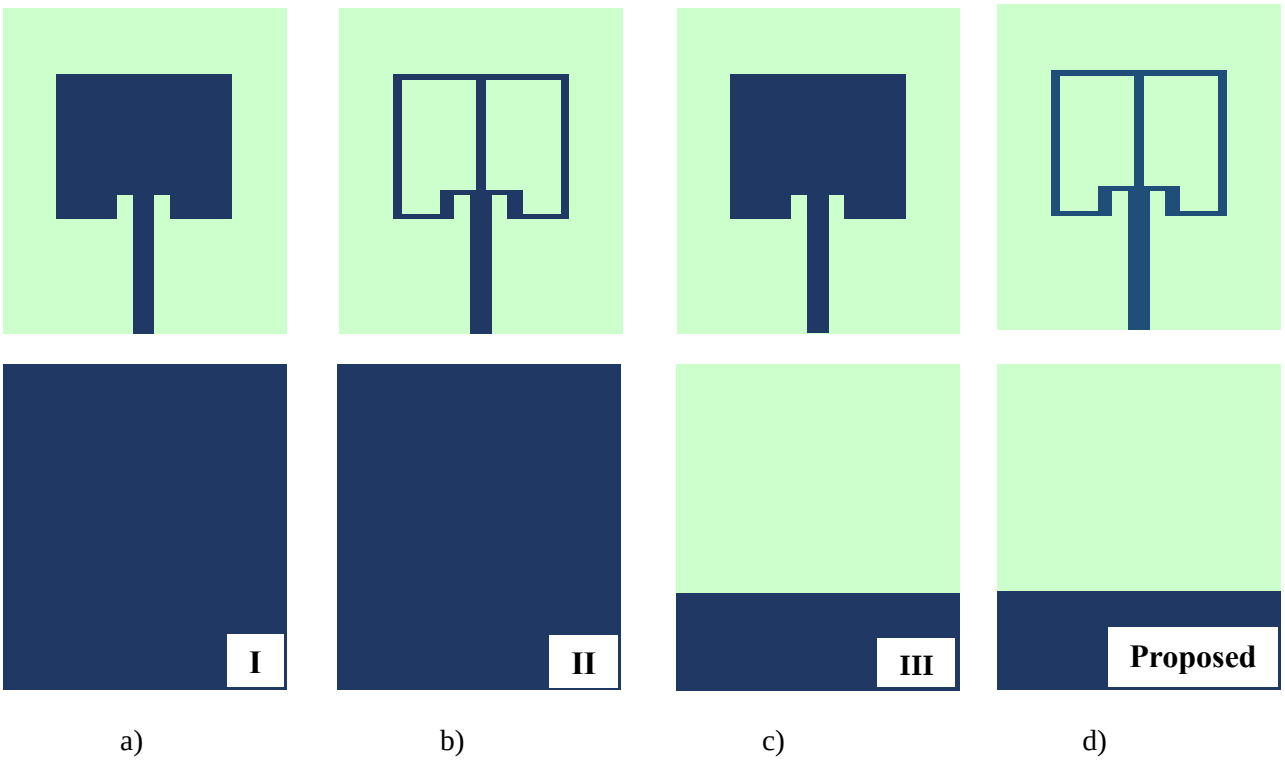

Figure 1. (a) Conventional patch antenna – Antenna I, (b) Slotted patch antenna – Antenna II, (c) Partial ground structure antenna – Antenna III, (d) Partial ground structure with slotted patch antenna – Proposed antenna

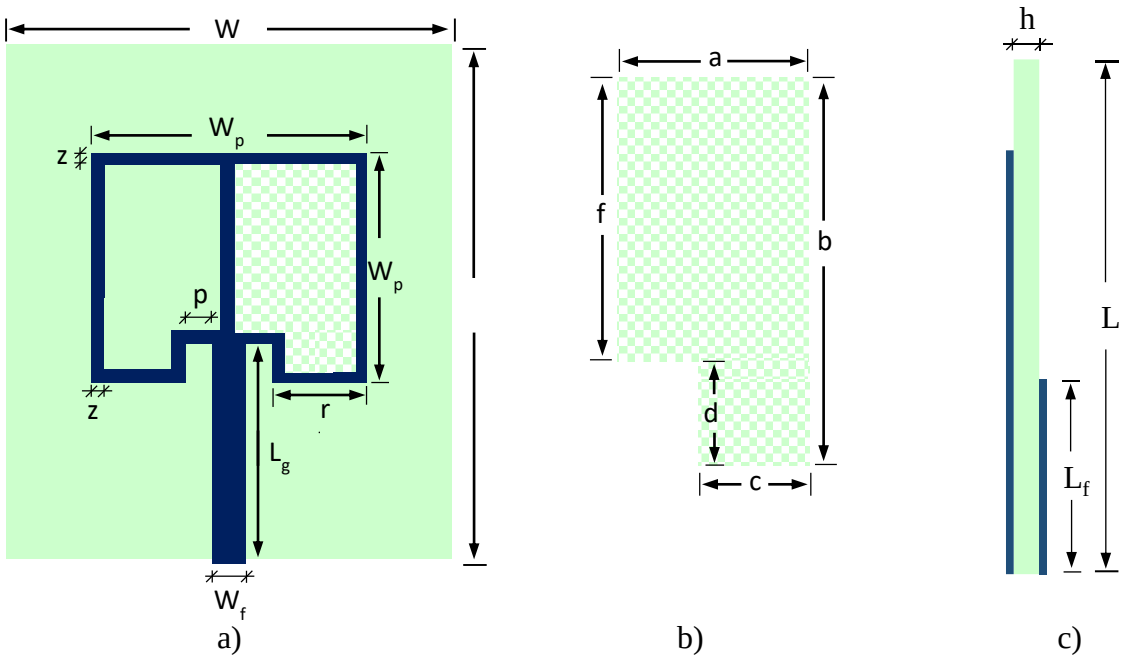

Figure 2. (a) Front view of the proposed antenna, (b) Detailed view of the slot, (c) (c) Detailed view of the feed patch and partial ground plane

Antenna dimensions are obtained using mathematical equations [5]. Width of the rectangular patch,

$$W = \frac{1}{2 f_r \sqrt{\mu_0 \varepsilon_0}} \sqrt{\frac{2}{\varepsilon_r + 1}} = \frac{c}{2 f_r} \sqrt{\frac{2}{\varepsilon_r + 1}} \quad (1)$$

The equation is given by (1). Here, c the speed of light, f_r the resonance frequency, ε_0 the dielectric constant of the cavity, μ_0 the magnetic permeability of the cavity. The actual length of the rectangular patch;

$$L = \frac{c}{2 f_r \sqrt{\varepsilon_{eff}}} - 2\Delta L \quad (2)$$

Here is the ε_{eff} effective dielectric constant. Equation (3) from ε_{eff} and equation (4) from ΔL are provided.

$$W/h > 1$$

$$\varepsilon_{eff} = \frac{\varepsilon_r + 1}{2} + \frac{\varepsilon_r - 1}{2} \left[1 + 12 \frac{h}{W} \right]^{-1/2} \quad (3)$$

$$\Delta L = 0.412 h \frac{\left(\varepsilon_{eff} + 0.3\right)\left(\frac{W}{h} + 0.264\right)}{\left(\varepsilon_{eff} - 0.258\right)\left(\frac{W}{h} + 0.8\right)} \quad (4)$$

The dimensions of dielectric material are given in Equation (5) and equation (6)

$$W_m = 6h + W \quad (5)$$

$$L_m = 6h + L \quad (6)$$

The antenna is excited using the microstrip line supply. To match the input impedance between the feeder line and the antenna, the feed inset is used as shown in Figure 2 (a). The physical slots next to the input feed form the input capacitance, which can affect the resonance frequency by about 1%. The length of the recess can be calculated from the equation (7).

$$R_{in}(y = y_0) = \frac{1}{2(G_1 \pm G_{12})} \cos^2\left(\frac{\pi}{L} y_0\right) \quad (7)$$

3. Results and Discussion

The antenna is designed in the CST Microwave Studio program, and the LKPF S63 is used as a printed circuit board scraping machine. FR-4 dielectric substrate is selected as the dielectric material. The thickness of the dielectric layer is used in h=1.6mm and the thickness of the copper is used 0.035mm. The completed antenna is shown in Figure 3.

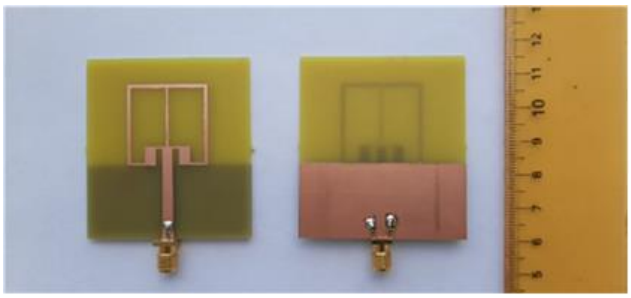

Figure 3. Front and back side view of the proposed antenna

The simulated and measured reflection coefficient S_{11} is given in figure 4. Antenna I does not shine below -10 dB, thus, it cannot be said that it works efficiently. Antenna II has a bandwidth value of 60 MHz and has a -16.37 dB return loss at a resonant frequency of 2.405 GHz. Antenna III has a bandwidth value of 300 MHz and a -27.39 dB return loss at a center frequency of 2.64 GHz. The proposed antenna reflection coefficient is shown in figure 5 and has a 979 MHz bandwidth and -24.529 dB return loss at -10 dB between 2.0767 - 3.0558 GHz.

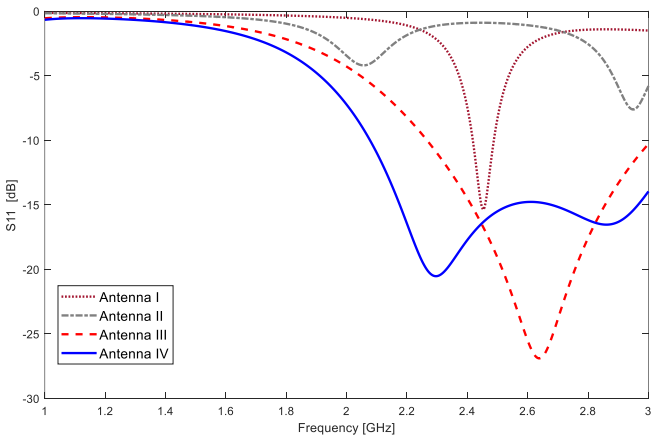

Figure 4. S_{11} simulation comparison results of antennas

A comparison between measurement results and the simulation results provided by the CST Microwave Studio software is presented in Figure 5. The slight difference between the simulation and the measurement results may have occurred due to the fabrication tolerances, SMA connector and coaxial cable losses.

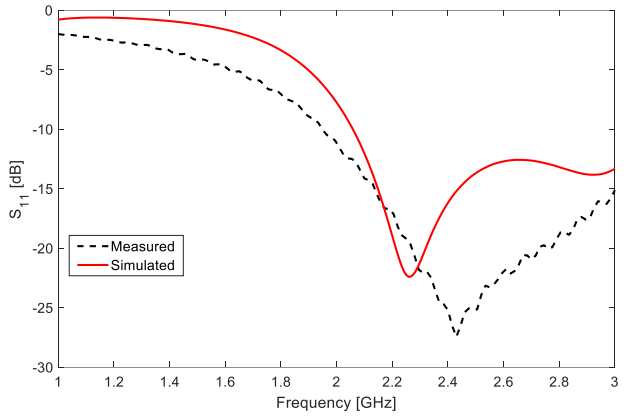

Figure 5. S_{11} simulation and measurement results of the proposed antenna

The 2-D radiation pattern of the proposed antenna is plotted together in plane E and plane H in figure 6 at a frequency of 2.316 GHz.

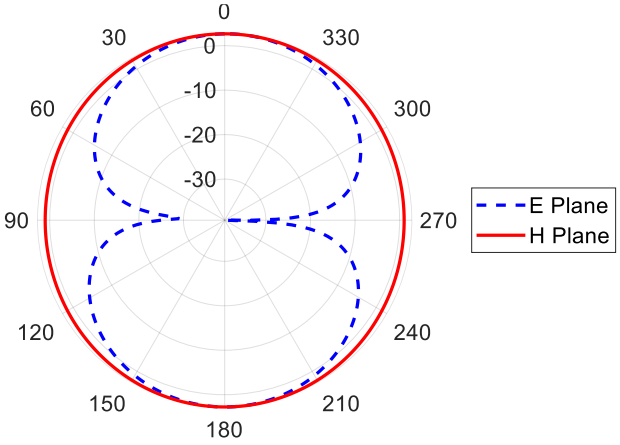

Figure 6. 2-D Radiation pattern of patch antenna at 2.316 GHz frequency

Figure 7 shows a comparison of the frequency-gain graph for the antenna I, antenna II, antenna III, and proposed antenna. The directivity gain variation of antenna I varies between 2.56 dBi and 6.8 dBi. Antenna II directivity gain varies between 2.49dBi and 5.75 dBi. The antenna III directivity gain with the change in the ground plane is obtained as 1.83 dBi to 3.309 dBi. The directivity gain value of the slot and partial ground plane proposed antenna opened in the latest patch plane ranges from 1.85 dBi to 3.3 dBi, and at the center resonant frequency it is obtained as 2.68 dBi. The application of a partial ground plane reduces the antenna gain, but the bandwidth obtained with antenna I is 2.91%, while the bandwidth value of the proposed antenna is 42.2%.

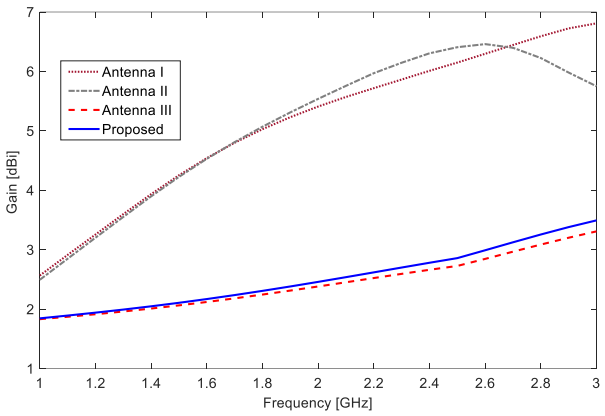

Figure 7. Frequency - Directivity Gain graph of the proposed antenna

Figure 8 shows the rectangular microstrip patch antenna gain diagram at 2.316 GHz frequency. The antenna has a gain of 2.68 dBi at a resonance frequency of 2.316 GHz.

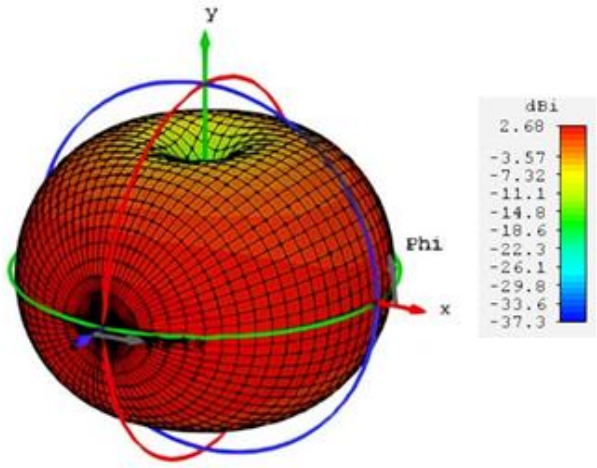

Figure 8. 3-D gain diagram of patch antenna at 2.316 GHz frequency

Figure 9 shows the proposed antenna of the surface current graph. The maximum surface current amplitude is found to be 150 dBμA/m at 2.316 GHz resonance frequency.

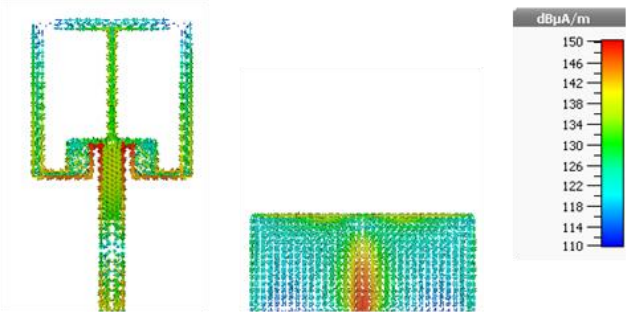

Figure 9. Graph of surface currents of the proposed antenna

Figure 10 shows the frequency-standing wave ratio (VSWR) of the proposed antenna, which is caused by reflections resulting from the impedance difference between the transmission line and the load. Regarding the amplitudes of the transmission signal and the reflected signal; a standing wave occurs when the maximum and minimum points overlap. VSWR is found by proportioning the maximum and minimum voltage levels of this standing wave.

It is desirable that the VSWR is less than 2. Antenna II does not radiate. The VSWR value is 1.37 at a frequency of 2.405 GHz for antenna II, and the VSWR value is greater than 2. The VSWR value is 1.16 at a frequency of 2.64GHz for antenna III. The VSWR value of the proposed antenna at 2.31 GHz resonance frequency is found to be 1.17.

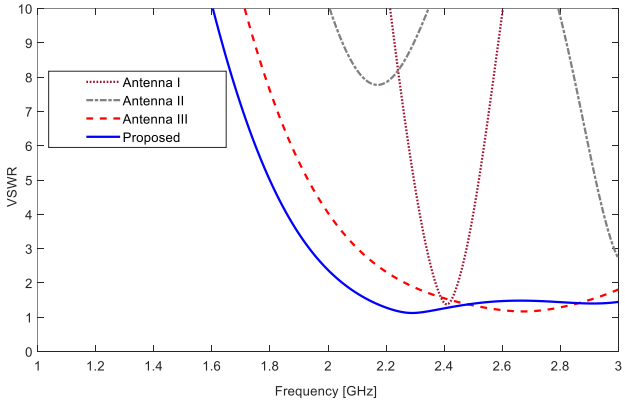

Figure 10. Graph of standing wave ratio (VSWR) of the proposed antenna

The bandwidth, return loss, directivity gain, and VSWR of the antennas compared in this paper are given in Table 2. It is seen from the table that the proposed antenna reaches the maximum bandwidth.

Table 2. Comparison of antennas

Parameter	Antenna I	Antenna II	Antenna III	Antenna IV
Center Frequency	2.405 GHz	-	2.64 GHz	2.31 GHz
Bandwidth	60 MHz	-	300 MHz	979 MHz
Return Loss	-16.37 dB	-	-27.39 dB	-24.529 dB
Directivity Gain	6.3 dBi	-	2.87 dBi	2.68 dBi
VSWR	1.37	-	1.16	1.17

4. Conclusion and Suggestions

Microstrip antennas are preferred in communication systems because of their easy manufacturability, low-cost effect, and small volume antennas. This paper introduces the slotted antenna operating in the ISM 2.4 GHz band (2400-2485 MHz) for usage in wireless and mobile communications. When the measurement results are compared with the results obtained from the CST Microwave Studio program, the results are found as consistent with each other. The proposed antenna has a bandwidth of 979 MHz at -10 dB at a resonance frequency of 2.316 GHz, and a directivity gain of 2.68 dBi, which gives the best results compared with the Antenna I-II and III designs. As can be seen from the results, opening slots on the antenna increased the bandwidth and had a positive effect on the gain value. The antenna is suitable for usage in the ISM band, which is widely used in wireless communication systems.

Contributions of the authors

All authors contributed equally to the study.

Conflict of Interest Statement

There is no conflict of interest between the authors.

Statement of Research and Publication Ethics

The study is complied with research and publication ethics.

References

[1] International Telecommunications Union-Radio Communications, (ITUR), Radio Regulations, SA.1346, ITU, Geneva (Switzerland).

[2] S. Kiani, P. Rezaei, and M. Fakhr, "A CPW-fed wearable antenna at ISM band for biomedical and WBAN applications," Wireless Netw., vol. 27, no. 1, pp. 735–745, 2021.

[3] A. Utsav, A. Abhishek, P. Suraj and R. K. Badhai, "An IoT Based UAV Network for Military Applications," 2021 Sixth International Conference on Wireless Communications, Signal Processing and Networking (WiSPNET), 2021, pp. 122-125, doi: 10.1109/WiSPNET51692.2021.9419470.

[4] B. A. Babu, P. S. Pokkunuri, M. Boddapati, S. S. Srigakolapu, M. Chintha and T. S. C. Donepudi, "Design and Analysis of a Compact Textile MIMO Antenna for ISM Band Wearable Applications," 2022 IEEE Delhi Section Conference (DELCON), 2022, pp. 1-5, doi: 10.1109/DELCON54057.2022.9752912.

[5] C. A. Balanis, Antenna theory: Analysis and design, 4th ed. Hoboken, NJ: Wiley-Blackwell, 2016.

[6] J. Sosa-Pedroza, F. Martinez-zuñiga, and M. Enciso-Aguilar, "Planar Antennas for Satellite Communications", in Satellite Communications. London, United Kingdom: IntechOpen, 2010 [Online]. Available: https://www.intechopen.com/chapters/11711 doi: 10.5772/intechopen.83939.

[7] H. Gutton and G. Baissinot, "Flat Aerial for Ultra High Frequencies," French Patent No. 703113, 1995.

[8] R. Munson, "Conformal microstrip antennas and microstrip phased arrays," IRE trans. antennas propag., vol. 22, no. 1, pp. 74–78, 1974.

[9] S. Weigand, G. H. Huff, K. H. Pan, and J. T. Bernhard, "Analysis and design of broad-band single-layer rectangular u-slot microstrip patch antennas," IEEE Trans. Antennas Propag., vol. 51, no. 3, pp. 457–468, 2003.

[10] A. A. Deshmukh and G. Kumar, "Compact broadband U-slot-loaded rectangular microstrip antennas," Microw. Opt. Technol. Lett., vol. 46, no. 6, pp. 556–559, 2005.

[11] A. Khidre, K.-F. Lee, A. Z. Elsherbeni, and F. Yang, "Wide band dual-beam U-slot microstrip antenna," IEEE Trans. Antennas Propag., vol. 61, no. 3, pp. 1415–1418, 2013.

[12] P. N. Shinde and J. P. Shinde, "Design of compact pentagonal slot antenna with bandwidth enhancement for multiband wireless applications," Int. J. Electron. Commun., vol. 69, no. 10, pp. 1489–1494, 2015.

[13] N. Ojaroudi and M. Ojaroudi, "Bandwidth enhancement of an ultra-wideband printed slot antenna with WLAN band-notched function," Microw. Opt. Technol. Lett., vol. 55, no. 7, pp. 1448–1451, 2013.

[14] Y. Sung, "Bandwidth enhancement of a microstrip line-fed printed wide-slot antenna with a parasitic center patch," IEEE Trans. Antennas Propag., vol. 60, no. 4, pp. 1712–1716, 2012.

[15] K. F. Lee, K. M. Luk, K. F. Tong, S. M. Shum, T. Huynh, and R. Q. Lee, "Experimental and simulation studies of the coaxially fed U-slot rectangular patch antenna," IEE Proc. - Microw. Antennas Propag., vol. 144, no. 5, p. 354, 1997.

[16] R. Islam, F. Mahbub, S. B. Akash, I. A. Prince, F. Tasnim, and N. T. Navia, "Design of a compact circular patch antenna operating at ISM-band for the WiMAX communication systems," in 2021 IEEE International Conference on Communication, Networks and Satellite (COMNETSAT), 2021.

[17] S. E. Bayer Keskin and B. Aymaz, "Design and Analysis of a New Wideband Microstrip Patch Antenna for ISM Applications"," International Conference on Life and Engineering Sciences, 2019.

[18] A. A. Eldek, A. Z. Elsherbeni, and C. E. Smith, "Rectangular slot antenna with patch stub for ultra-wideband applications and phased array systems," Electromagn. Waves (Camb.), vol. 53, pp. 227–237, 2005.

[19] A. K. Arya, M. V. Kartikeyan, and A. Patnaik, "Defected ground structure in the perspective of microstrip antennas: A review," Frequenz, vol. 64, no. 5–6, 2010.

[20] N. Sharma and S. S. Bhatia, "Stubs and slits loaded partial ground plane inspired hexagonal ring-shaped fractal antenna for multiband wireless applications: design and measurement," Prog Electromag Res C, vol. 112, pp. 99–111, 2021.

[21] R. Kumar, R. Sinha, A. Choubey, and S. K. Mahto, "A compact microstrip feedline printed antenna with perturbed partial ground plane for UWB applications," Int. J. RF Microw. Comput-Aid. Eng., vol. 31, no. 9, 2021.

[22] M. Ameen and R. K. Chaudhary, "Compact radiator antenna: A new approach to enhance the bandwidth using ENG-TL and C-CSRR mushroom meta-resonator," Int. J. Electron. Commun., vol. 134, no. 153697, p. 153697, 2021.

[23] Mekaladevi, N. Devi, and Jayakumar, "Design and performance analysis of SIW cavity-backed sectored slot antenna for ISM band applications," in 2021 Sixth International Conference on Wireless Communications, Signal Processing and Networking (WiSPNET), 2021.

[24] P. R. Meher, B. R. Behera, and S. K. Mishra, "A compact circularly polarized cubic DRA with unit-step feed for Bluetooth/ISM/Wi-Fi/Wi-MAX applications," Int. J. Electron. Commun., vol. 128, no. 153521, p. 153521, 2021.

[25] A. G. Ambekar and A. A. Deshmukh, "Wideband dual polarized compact design of pi-shape microstrip antenna for gsm, ism, and satellite applications," Prog. Electromagn. Res. C Pier C., vol. 111, pp. 241–256, 2021.

[26] A. Shah and P. Patel, "Suspended embroidered triangular e-textile broadband antenna loaded with shorting pins," Int. J. Electron. Commun., vol. 130, no. 153573, p. 153573, 2021.

[27] W.-L. Chen, G.-M. Wang, and C.-X. Zhang, "Bandwidth enhancement of a microstrip-line-fed printed wide-slot antenna with a fractal-shaped slot," IEEE Trans. Antennas Propag., vol. 57, no. 7, pp. 2176–2179, 2009.

Bitlis Eren Üniversitesi Fen Bilimleri Dergisi
BİTLİS EREN UNIVERSITY JOURNAL OF SCIENCE
ISSN: 2147-3129/e-ISSN: 2147-3188
VOLUME: 11 NO: 3 PAGE: 820-827 YEAR: 2022
DOI: 10.17798/bitlisfen.1108112

Removal of detergents in car wash wastewater by sub-surface flow constructed wetland

Tuğba NACAR[1], Deniz UÇAR[2*], Zehra ŞAPÇI AYAS[3]

[1]*Deptartment of Environmental Engineering, Harran University, Sanliurfa, Turkey*
[2]*Department of Environmental Engineering, Bursa Technical University, Bursa, Turkey*
[3]*Department of Environmental Engineering, Van Yuzuncu Yil University, Van, Turkey*
(ORCID: 0000-0002-5217-0947) (ORCID: 0000-0002-0536-6250) (ORCID: 0000-0002-7811-2235)

Keywords: Constructed Wetland, Water Reuse, Sodium Lauryl Sulfate, Water Treatment, Detergent.

Abstract
Suspended substances in car washes can often be easily removed by physicochemical processes. The main problem is removing dissolved substances such as detergents from the water. In this study, the biodegradable substance Sodium Lauryl Sulfate (SLS) was removed from the car wash wastewater by the use of *Phragmites australis* in the subsurface constructed wetland. For this study, 4 plexiglass reactors having an effective volume of 10.8 L with the dimensions of 15 cm × 45 cm × 20 cm were used. The experiments were conducted with vegetation, which was called SCW, and without vegetation, which was named the control group (CG), as two groups. A serial connection of two reactors was performed for each group. Up to 90%, detergent removal was observed with the vegetation in the SCW with a loading rate of 75 L/(m^2.d) The effluent quality showed that the treated water can be reused car washing or irrigation for landscaping.

1. Introduction

The car wash industry uses a huge amount of freshwater such as 200 L-900 L depending on the car wash type. The chemical composition of car wash wastewater contains greases, detergents, waxes, salts, dust, metals, and organic matter [1]. Sand, dust, and detergent are reported as common contaminants in wastewater [2].

Detergents, which may consist of surfactants, adjuvants, bleaches, and several additives functionality, counteract the external tension of the aquatic to form micelles and eradicate grime. Surfactants are in control of the cleaner influence in washing products, and they can be categorized into four groups: anionic, cationic, non-ionic, and amphoteric [3]. For many years, Sodium Lauryl Sulfate (SLS), an anionic detergent, has been utilized as an antibacterial surfactant [4], [5]. It accumulates in seawater and sediments because of untreated wastewater discharges. In 2001, a study by Della Croce et al. reported that an average of 60,000 tons of cleansers are discharged into the Mediterranean annually [6].

Some car wash wastewater is discharged directly into municipal wastewater systems [7], while others are treated using a variety of technologies, including primary sedimentation or filtration techniques for the removal of suspended solids and oil. These are followed by the application of detergent removal processes such as membrane bioreactors or coagulation processes. Finally, the treated water is reused or discharged into sewer systems. The detergent in the wastewater can be filtered by hydrophobic interaction chromatography, size exclusion chromatography, ion-exchange chromatography, dialysis, and ethyl acetate extraction [8]. However, these promising technologies are generally expensive and require a skilled workforce. Car wash services are usually small in size, and it is difficult to employ qualified operators for the above-mentioned high-tech treatment units. Therefore, a system that does not produce sludge and does not require chemicals

*Corresponding author: deniz.ucar@btu.edu.tr
Received:23.04.2022, Accepted:05.08.2022

should be established with a low initial investment and operating costs for sustainable operation.

As stated in recent works, the wetland process has shown promising applications for treating grey wastewater with a high detergent concentration. For example, in linear alkylbenzene sulfonate (LAS), which is another common anionic surfactant, the removal efficiency was measured at 77% after 15 days of HRT and the treated water was used for gardening [3]. Another research was focused on horizontal flow wetlands cultivated with helophytes, graminoids, tropical, and subtropical plants. The removal efficiency of chemical oxygen demand (COD), biochemical oxygen demand (BOD), and total suspended solids (TSS) were reported more than 85% [9].

As a result of contracted wetlands (CWs) being considered as an economical and sustainable alternative for wastewater treatment [10], reusing technology is being investigated and improved in most districts due to serious water shortages in several countries. Some research on CW effluents indicates that these effluents can be used for irrigation, flushing toilets, and industrial purposes [11]. With this technique, if approved for the car wash industry, water problems of scarcity and contamination might be solved. So, the results of the experimental study were also evaluated based on reusability.

In the study, the objectives were; (1) to evaluate the performance of the subsurface constructed wetland for removal of SLS based on COD, turbidity, alkalinity, and conductivity parameters, (2) to assess the subsurface constructed wetland operation condition base on vegetated or non-vegetated, (3) to evaluate the effect of hydraulic retention time on the removal efficiency, and (4) to evaluate the reusability of the effluents regarding feasible option or not.

2. Materials and Method

2.1. Synthetic Wastewater Preparation

Synthetic wastewater was prepared by adding 1 ml of detergent taken from Shell Petrol A.Ş. to 1 L of tap water. It is a biodegradable detergent based on SLS. The chemical structure of SLS and its properties are given in detail in the literature [12]. The characterization of synthetic wastewater is given in Table 1.

Table 1. The characterization of t synthetic wastewater

Parameter	Value
pH	8.55 ± 0.3
Turbidity (NTU)	0.64±0.4
Alkalinity (mg $CaCO_3$/L)	129±7
Conductivity (µS/cm)	402.3±48.6
COD (mg/L)	142.2±19
Loading Rate (L/(m^2.d))	75

2.2. Experimental Set-Up and Procedure

Subsurface constructed wetland experiments were conducted in batch mode using 4 Plexiglas reactors having an effective volume of 10.8 L with the dimensions of 15 cm × 45 cm × 20 cm (Figure 1). Two reactors were used as main experimental groups (SCW), and the others were used as control groups (CG). The two reactors in the group were connected by pipeline so that they could be connectedin series. Those pipelines were mounting influences and effluents of the reactors which opened a diameter of 1 cm spherical geometry nozzle. The first reactor of each group was fed synthetic wastewater by a peristaltic pump (Perimax, SPETEC, Germany).

A media (pebble stone and soil) was put in all reactors. Because its size affects the system's ability to function, this particle size distribution was designed following numerous recommendations for tolerable hydraulic conductivity; the declining magnitude along the stream route decreased the risk of clogging [13]–[15], which is crucial for the long-term stabilization of SCWs. The depth of media was set at 7 cm of pebble stone (sizes ranging between 15-80 mm) and 9 cm of red soil in whole reactors. Reed plants (*Phragmites australis*) were planted only in two reactors, called the experimental SCW reactors. The reed plants were collected from the natural area side of the creek, flowing around the Harran University Campus, Turkey. Their roots were carefully put inside the pebble stone in the SCW.

At the beginning of the research, the whole reactors in each group were tested by feeding 5 L of tap water daily to observe the stability of the reactors. To understand the stabilization condition of the reactors, turbidity values of the influent wastewater and the effluent

water were observed daily until they had stabilized.

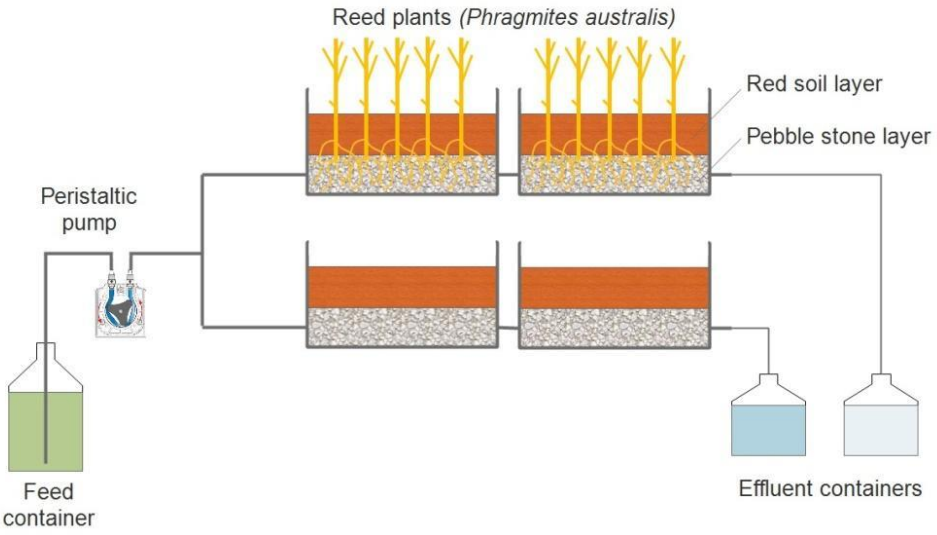

Figure 1. The configuration of the lab-scale subsurface constructed wetland with vegetation (SCW) and without vegetation (control group (CG))

1

2.3. Analytical methots

Samples were centrifuged at 3000 RPM (3024 RFC) for 10 minutes prior to analysis. The conductivity and the temperature in the aqua were measured by WTW equipment (Multi (3620 IDS) probe, Weilheim, Germany), and the pH was determined using a pH-meter (pH 211 Microprocessor, Hanna Instruments, Woonsocket, RI, USA). The alkalinity and COD analyses were carried out according to 2320-B, and 5220-A (closed reflux method), respectively [16].

Concentrations of detergents in aqueous solutions can be determined by different measurement methods according to their types. It can be measured as total phosphate by measuring the phosphate in their structure, as well as mass spectrophotometry or chromatographic methods. A study by Lau *et al.* mentions that detergents can also be measured as COD equivalents [17]. In the study, detergent was assessed by COD analysis.

The removal efficiencies of COD and alkalinity were determined as a percentage and calculated as:

$$R\ (\%) = (1- (Ce/Ci))*100 \quad (1)$$

initial days of operation, only tap water was fed to the reactors to clean initial impurities based on reactor media and red soil. After 13 days of operation, it was observed that each reactor stabilized (influent and

where Ci and Ce represent the concentration of a particular component in the influent and in the effluent flow of the reactor, respectively.

2.4. Evaluation of reusability

Overall, reclaimed wastewater transportation and dissemination denotes a higher charge in an application project and subsequently limits its economic sustainability [18]. SCW applications are more appropriate for the countryside where self-serve car washes have generally. It is important to understand that its effluents are applicable to the car wash again or irrigation for landscaping. Therefore, the reclaimed wastewater quality was evaluated in Cyprus (KDP 379/2015), Italy (Ministry Decree (DM) 185/2003), and USEPA (2012) guidelines, as done before by Arden and Ma, (2018) and Otter et al., (2020).

3. Results and Discussion

3.1. Treatment Performance

The stability of the reactors was monitored by influent and effluent turbidity measurements. During the effluent turbidity were equalized). After this stabilization period, the experiments were performed at a wastewater loading rate of 75 L/(m^2.day) by feeding with synthetic wastewater.

The electrical conductivity (EC) indicates the total amount of ions (nitrogen, phosphorus, etc.). In our study, synthetic water made with dissolved detergent in tap water was used. Therefore, the influent wastewater included mainly phosphate coming from detergent and other ions in tap water. To observe detergent changes in the study, the EC value was preferred mainly because its analysis simply and rapidly uses inexpensive sensors. Hence, to find a correlation between the detergent concentration (DC) in the solution and the EC, correlation experiments were carried out. The result of the correlation experiments indicated as

EC= 17.164 x DC (2)

The correlation coefficient of 0.98 indicates a strong positive correlation (Eq (2)). Although the correlation between them in the synthetic wastewater was found well, a similar correlation between the DC in the effluent and the EC value in the effluent water was not observed**.** Moreover, the EC value was observed to be more affluent than the influent at the same reactors (Figure 2). Besides, the EC value change of each reactor was also observed to be dissimilar. While the average EC value in the influent wastewater was measured as 402.3±48.6 µS/cm (Table 1), the values from both the SCW effluent and the CG effluent were measured as 464.2±31.8 µS/cm and 454.6±34.1 µS/cm, respectively. This situation might be caused by the presence of some impurities in the effluent water. The impurities may originate from biochemical or chemical products such as bacterial and/or fungal products, organic substances, some ions getting from the stone surfaces, and organic leakages of photosynthetic activity production from the root in the reactors [20].

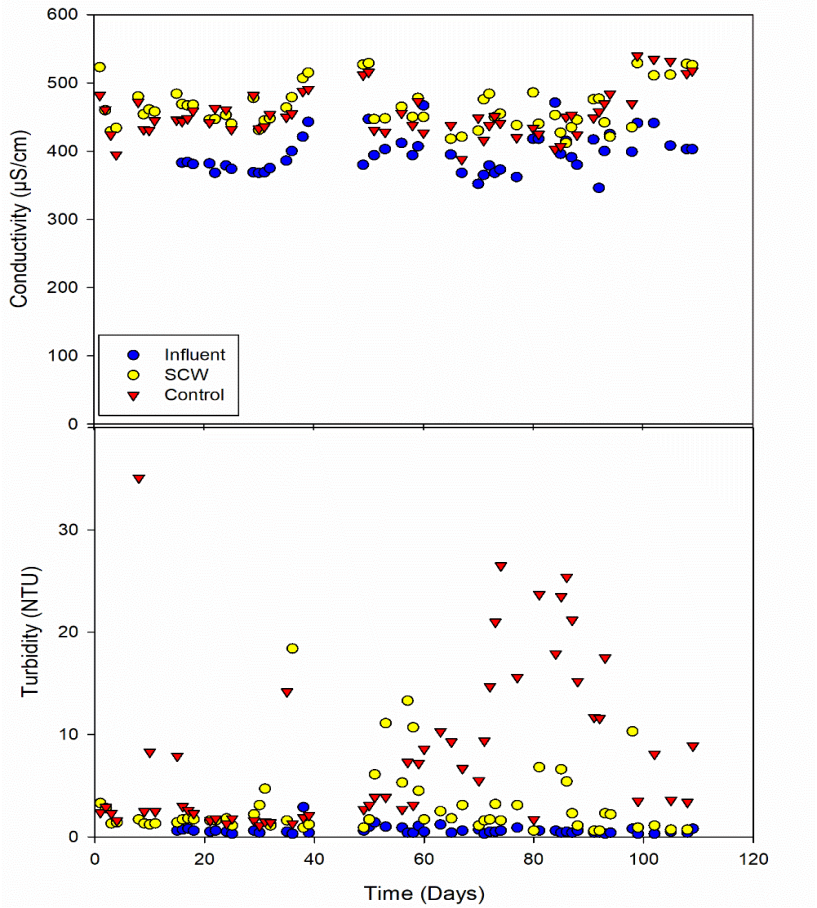

Figure 2. Conductivity and turbidity variations.

In the first 40-day start-up period, the effluent turbidity values of the SCW and the CS were determined at the levels of 2.50±3.5 and 4.3±7.2 NTU, respectively (Figure 2). However, between 40 and 108 days, the turbidity values in the effluent waters of the SCW and the effluents of the control reactors were measured averagely as 3.55±3.46 and 10.8±7.56 NTU, respectively. An almost

similar trend was observed for the COD removal efficiencies in each group, as shown in Figure 3.

Pebbles used as reactor filter material are adsorption surfaces in the system. Therefore, some of the particles, such as microorganisms, their products, and other impurities, can be adsorbed onto pebbles. These microorganisms make microbial biofilms, communities of microorganisms attached to a living or inert surface in an aqueous environment and surrounded by a matrix of extracellular polymeric substances [21]. When these attachments on the surface of the pebbles reach a certain size, such as in trickling filters (regeneration of the filter material), microbial flocks can be observed in the effluent water [15]. Therefore, if these microorganisms in SCW grow without control, the SCW process may block and create short circuits. In the study, as mentioned above, the turbidity value between 40 and 108 days was determined to be higher than that in the feed. The reason for the increase may be microorganisms detached from the sorbent. On the other hand, Figure 2 indicated that the turbidity value of the SCW became stable more quickly than the CG. The probable reason for the difference between the two systems could be thatthe SCW system has a natural filtration mechanism due to the presence of plant roots.

The concentrations of detergents in aqueous solutions can also be determined by different measurement methods according to their types. It can be measured as total phosphate by measuring the phosphate in its structure as well as mass spectrophotometry or chromatographic methods. A study by Lau *et al.* reported that detergents can also be measured as COD equivalents [17]. Correlation experiments were performed to find a correlation between the detergent concentration (DC) in the solution and the COD value. The result of the experiments is indicated as

$$COD = 161.93 \times DC \quad (3)$$

The correlation coefficient of 0.99 indicates a strong positive correlation (Eq (3)). As mentioned above, a similar correlation was observed between DC and EC. However, the correlation between the DC in the effluent and the EC value in the effluent water was not determined as suitable. Hence, to observe the change of the DC in systems, the COD parameter was preferred in the study. The COD analyses were started after the 13th day since the systems were fed only with tap water for the first 13 days. Figure 3 shows that the treatment mechanisms reached a steady state in the first 40 days and their components adapted to the ambient conditions. In this period, the average COD removal efficiencies in the SCW effluent and the CG effluent were calculated as 52% and 47%, respectively. Figure 3 indicates that the variance between the effluent COD concentrations of the SCW and the CG was growing after the 40^{th} day. This situation can be interpreted with the adaptation of the reeds placed in the SCW to the environment and the increase of biochemical reactions in these reactors. Between the 40^{th} and 108^{th} days of the experiments, the effluent COD concentrations of the SCW and the CG were measured as 36.9±12.9 mg/L and 80.9±17 mg/L, respectively, and the calculated removal efficiencies, 74%, and 44%, respectively.

Throughout the study, the average effluent COD value of the SCW and the CG was determined as 45.8±22.1 mg/L, and 77.5±19.8 mg/L, respectively. The possible reasons for the removal of the CG are (1) the use of detergent in oxidation/reduction reactions by the microorganisms in the environment, or (2) adsorption on stone surfaces. Dhouib et al., (2003) reported that *Citrobacter braakii* species can reduce sodium lauryl ether sulfate-based surfactants at a rate of 0.065 g/(L.h) under 20-hour HRT conditions. Other studies reveal that microorganisms can reduce anionic surfactants at various rates [23]–[25]. Another removal of surfactants from the water environment may also be adsorbed by the adsorption process. Some of the adsorbent materials, such as peach kernels, olive seeds, natural asphaltite, and coal tar pitch, have been reported in the literature for this purpose [26].

The COD removal efficiency was observed more in the SCW than in the CG. It can be interpreted as the reed roots in this reactor helping the biodegradation process or directly taking the SLS into the plants. Various CW applications in the treatment of greywater and industrial wastewater (paper industry, petrochemical, textile, metal processing, alcohol production, fish and seafood processing, dairy wastewater, and food industries, etc.) in the literature were reported similarly [10], [27]. Moreover, the existence of vegetation upturns water retention time, so the contact time between substrate materials and contaminants is extended. It could cause the adsorption of impurities onto sorbent resources in the CWs to be enhanced. According to P-sorption capacity investigation in the literature, the vegetated batch reactor demonstrated better performance than the non-vegetated ones [28]. This study shows that the detergents in car washing wastewater can be removed with SCW (including vegetation) and non-vegetated ones. On the other hand, if the SCW (including

vegetation) system is preferred, its removal efficiency can provide more than a non-vegetated system.

No significant difference was observed in pH between the SCW and the control group. The pH values of influents and effluents from both the SCW and the CG were measured as 8.55 ± 0.3, 8.18 ± 0.48, and 8.18 ± 0.47, respectively (Figure 4).

During the first 40 days in the experiments, start-up period, the alkalinity value of the effluent from the SCW and the CG was observed to be almost the same value, 174.7±23.9, and 158.6±16.3 mg $CaCO_3$/L, respectively (Figure 4). After the start-up

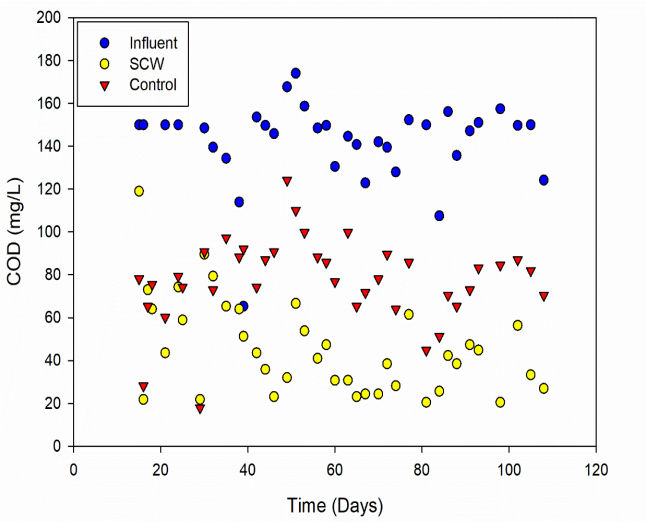

Figure 3. Chemical oxygen demand variations throughout the study

period, the alkalinity value of each group was shown to be uptrend. The alkalinity value between the 40th days to 108th days both in the SCW and in the CG increased from 174.7±23.9 to 220.7±21.2 mg $CaCO_3$/L (the increasing ratio is 71%), from 158.6±16.3 to 189.4±22.1 mg $CaCO_3$/L (the increasing ratio is 46%), respectively. The reason for these uptrends might be an influence of biochemical reactions in the reactors. There are several possible predictions for biochemical growth within the reactor. One of them may be the reduction of both approximately 35 mg/L sulphate in the tap water and sulphate in the detergent structure via the oxidation process due to having organic substances in the soil. Another possible reaction might be the transformation of existing microorganisms into organisms in particulate form and then into dissolved and biodegradable forms of organic matter according to the Dead Regeneration Model [29]. The conversion of these organics to volatile fatty acids in an oxygen-free environment may be another factor that affects alkalinity concentrations.

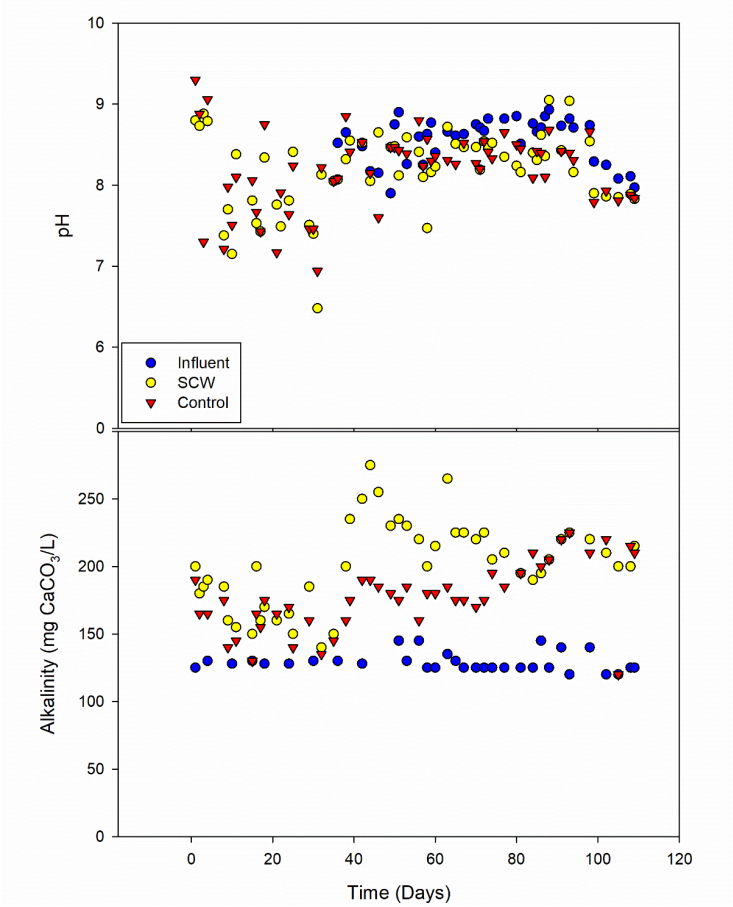

Figure 4. pH and alkalinity variations throughout the study.

3.2. Treatment Performance

A few studies reported car wash wastewater treatment for reuse in the literature. In the study, regarding the United States Environmental Protection Agency guidelines and European Country Standards, the water quality of end-uses of recycled water was evaluated as done by previous researchers [10], [19].

During the study, no significant difference was observed in the pH between influent and effluent for each group. The pH levels were found limit within the unrestricted and also restricted levels of the USEPA guidelines (2012). Besides, in terms of turbidity, although feeding water was prepared with tap water, therefore the turbidity in influent water was very low, and turbidity levels of both effluents are measured <10 NTU. The values are not suitable because the turbidity guideline for unrestricted reuse is 2 NTU [30].

While the load of the influent COD value was 142.2±19 mg/L, the average COD effluent values in the SCW effluent and the CG were measured as 63.5±26.3 mg/L and 70.8±23.9 mg/L, respectively.

The study of Otter et al., (2020) reviewed wastewater reuse quality requirements. Regarding their study, the effluents based on COD value were archives of Cyprus (KDP 379/2015) and Italy (Ministry Decree (DM) 185/2003) standards. Before using the treated water for irrigation of the landscape or reuse for the car wash industry, the treated water should be investigated in detail and diminish environmental risks.

4. Conclusion and Suggestions

Using a high amount of wastewater with a low pollution load produced in the car wash industry is important to save water, and money and to protect environmental health. Dissolved detergent is the most important component in the car wash water. Since oil and suspended solids do not dissolve, they can be easily removed from the water by a simple precipitation/filtration and flotation process. SCW has a high potential for the treatment of car wash water due to its advantages such as low installation cost, low maintenance requirement, and not needing a qualified person. During the study, the average COD removal efficiency was determined to be around 68%, and the maximum observed COD removal was calculated to be 87%. The operation of the SCW with vegetation (*Phragmites australis*) showed a higher removal ratio than without the vegetation group. Even though the effluent qualities were achieved by some European Standards for reuse, we did not focus on bacterial conditions, and therefore, a disinfection process should be installed in the system before the application of the system.

Funding

The present study did not receive any official funding

Acknowledgment

The authors extend their sincere appreciation to the Shell /Turkey

Contributions of the Authors

The authors confirm that the contribution is equally
for this paper.

Conflict of Interest Statement

There is no conflict of interest between the authors.

Statement of Research and Publication Ethics

The study is complied with research and publication ethics

References

[1] Z. B. Gönder, G. Balcıoğlu, I. Vergili, and Y. Kaya, "An integrated electrocoagulation–nanofiltration process for carwash wastewater reuse," *Chemosphere*, vol. 253, p. 126713, 2020.

[2] A. Lobo, Á. Cambiella, J. M. Benito, C. Pazos, and J. Coca, "Effect of a previous coagulation stage on the ultrafiltration of a metalworking emulsion using ceramic membranes," *Desalination*, vol. 200, no. 1–3, pp. 330–332, 2006.

[3] M. E. Pérez-López, A. E. Arreola-Ortiz, and P. M. Zamora, "Evaluation of detergent removal in artificial wetlands (biofilters)," *Ecol. Eng.*, vol. 122, pp. 135–142, 2018.

[4] S. Tasneem, A. Nabi, N. Hasan, M. A. Malik, and K. M. Khedher, "Thermodynamic insights into molecular interactions of sodium lauryl sulfate (SLS) with caffeine and theophylline in aqueous media at different temperatures," *J. Mol. Liq.*, vol. 305, p. 112776, 2020.

[5] H. K. Ozden and A. A. Selcuk, "Is there a role of toothpastes in the development of recurrent aphthous stomatitis? A prospective controlled clinical trial with skin patch testing," *Oral Surg. Oral Med. Oral Pathol. Oral Radiol.*, vol. 131, no. 1, pp. 43–48, 2021.

[6] E. Brunelli, E. Talarico, B. Corapi, I. Perrotta, and S. Tripepi, "Effects of a sublethal concentration of sodium lauryl sulphate on the morphology and Na+/K+ ATPase activity in the gill of the ornate wrasse (Thalassoma pavo)," *Ecotoxicol. Environ. Saf.*, vol. 71, no. 2, pp. 436–445, 2008.

[7] I. A. R. Boluarte *et al.*, "Reuse of car wash wastewater by chemical coagulation and membrane bioreactor treatment processes," *Int. Biodeterior. Biodegrad.*, vol. 113, pp. 44–48, 2016, doi: 10.1016/j.ibiod.2016.01.017.

[8] B. S. Antharavally *et al.*, "Efficient removal of detergents from proteins and peptides in a spin column

format," *Anal. Biochem.*, vol. 416, no. 1, pp. 39–44, 2011.
[9] A. Zraunig *et al.*, "Long term decentralized greywater treatment for water reuse purposes in a tourist facility by vertical ecosystem," *Ecol. Eng.*, vol. 138, pp. 138–147, 2019.
[10] S. Arden and X. Ma, "Constructed wetlands for greywater recycle and reuse: a review," *Sci. Total Environ.*, vol. 630, pp. 587–599, 2018.
[11] X. Nan, S. Lavrnić, and A. Toscano, "Potential of constructed wetland treatment systems for agricultural wastewater reuse under the EU framework," *J. Environ. Manage.*, vol. 275, p. 111219, 2020.
[12] N. Pandya *et al.*, "SLES/CMEA mixed surfactant system: Effect of electrolyte on interfacial behavior and microstructures in aqueous media," *J. Mol. Liq.*, vol. 325, p. 115096, 2021.
[13] J. Vymazal, "The use of sub-surface constructed wetlands for wastewater treatment in the Czech Republic: 10 years experience," *Ecol. Eng.*, vol. 18, no. 5, pp. 633–646, 2002.
[14] Y. Q. Zhao, G. Sun, and S. J. Allen, "Anti-sized reed bed system for animal wastewater treatment: a comparative study," *Water Res.*, vol. 38, no. 12, pp. 2907–2917, 2004.
[15] J. Zhao, Y. Zhao, Z. Xu, L. Doherty, and R. Liu, "Highway runoff treatment by hybrid adsorptive media-baffled subsurface flow constructed wetland," *Ecol. Eng.*, vol. 91, pp. 231–239, 2016.
[16] APHA, *Standard Methods for the Examination of Water and Wastewater*. Washington DC, USA, 2005.
[17] W. J. Lau, a. F. Ismail, and S. Firdaus, "Car wash industry in Malaysia: Treatment of car wash effluent using ultrafiltration and nanofiltration membranes," *Sep. Purif. Technol.*, vol. 104, no. August, pp. 26–31, 2013, doi: 10.1016/j.seppur.2012.11.012.
[18] L. Segui, O. Alfranca, and J. Garcia, "Techno-economical evaluation of water reuse for wetland restoration: a case study in a natural park in Catalonia, Northeastern Spain," *Desalination*, vol. 246, no. 1–3, pp. 179–189, 2009.
[19] P. Otter *et al.*, "Disinfection for decentralized wastewater reuse in rural areas through wetlands and solar driven onsite chlorination," *Sci. Total Environ.*, vol. 721, p. 137595, 2020.
[20] Z. Sapci and E. B. Ustun, "Heavy metal uptakes by Myriophyllum verticillatum from two environmental matrices: the water and the sediment," *Int. J. Phytoremediation*, vol. 17, no. 3, pp. 290–297, 2015.
[21] D. B. Barbosa *et al.*, "Silver and phosphate nanoparticles: Antimicrobial approach and caries prevention application," in *Nanobiomaterials in Clinical Dentistry*, Elsevier, 2019, pp. 225–242.
[22] A. Dhouib, N. Hamad, I. Hassaïri, and S. Sayadi, "Degradation of anionic surfactants by Citrobacter braakii," *Process Biochem.*, vol. 38, no. 8, pp. 1245–1250, 2003.
[23] O. O. Amengialue, I. N. Ibeh, A. P. Egharevba, M. N. O. Omoigberale, and O. Edobor, "Studies on the bacterial flora of synthetic-detergent effluent and their biodegradation potentials," *Glob. J. Biol. Agric. Heal. Serv.*, vol. 2, no. 4, pp. 14–19, 2013.
[24] R. Margesin and F. Schinner, "Low-temperature bioremediation of a waste water contaminated with anionic surfactants and fuel oil," *Appl. Microbiol. Biotechnol.*, vol. 49, no. 4, pp. 482–486, 1998.
[25] H. Feitkenhauer and U. Meyer, "Anaerobic digestion of alcohol sulfate (anionic surfactant) rich wastewater–batch experiments. Part I: influence of the surfactant concentration," *Bioresour. Technol.*, vol. 82, no. 2, pp. 115–121, 2002.
[26] B. Tsyntsarski *et al.*, "Removal of detergents from water by adsorption on activated carbons obtained from various precursors," *Desalin. Water Treat.*, vol. 52, no. 16–18, pp. 3445–3452, 2014.
[27] K. Skrzypiecbcef and M. H. Gajewskaad, "The use of constructed wetlands for the treatment of industrial wastewater," *J. Water L. Dev.*, vol. 34, no. 1, pp. 233–240, 2017.
[28] Y. Wang, Z. Cai, S. Sheng, F. Pan, F. Chen, and J. Fu, "Comprehensive evaluation of substrate materials for contaminants removal in constructed wetlands," *Sci. Total Environ.*, vol. 701, p. 134736, 2020.
[29] D. Orhon, *Modeling of Activated Sludge Systems*. Pennsylvania: CRC press, 1997.
[30] US EPA, "Guidelines for water reuse," Washington DC, USA, 2012. doi: EPA/600/R-12/618.

Bitlis Eren Üniversitesi Fen Bilimleri Dergisi
BİTLİS EREN UNIVERSITY JOURNAL OF SCIENCE
ISSN: 2147-3129/e-ISSN: 2147-3188
VOLUME: 11 NO: 3 PAGE: 828-835 YEAR: 2022
DOI: 10.17798/bitlisfen.1122251

Reducing Inventory Levels in a Supermarket through the Six Sigma Method

Saadet AİŞEOĞLU[1], İzzettin Hakan KARAÇİZMELİ[1*]

[1]*Industrial Engineering Department, Harran University, Şanlıurfa, Türkiye*
(ORCID: 0000-0003-2467-0933) (ORCID: 0000-0002-8540-8050)

Keywords: Supermarkets, Six Sigma, Inventory, Process Improvement, Retail.

Abstract
Being one of the most active industries in an increasingly globalized world, the retail sector has become a rapidly developing sector in Türkiye. Businesses in this sector must follow inventory policies that enable them to minimize costs and maximize profits to be able to survive on the market. For this reason, effective management of inventory is crucially important in this industry, as well as in others. The Six Sigma method, a management tool that emphasizes continuous improvement and increases the efficiency of processes, was used in the present study to reduce the inventory levels in a large supermarket offering both wholesale and retail products in Türkiye. In this study, the causes of high inventory levels were investigated by following the steps of the Six Sigma method. After the collected data were analyzed, some improvement actions were taken to reduce the inventory levels, and a monitoring system was established to ensure sustainability. It was found that there were deficiencies in the inventory tracking and demand forecasting processes. The main reason for this was found to be the purchasing organization. The results also revealed that unnecessary purchases were made. The Six Sigma studies on supermarkets in Türkiye are limited, so this study sets an example of Six Sigma, which is a systematic process improvement method for the retail industry.

1. Introduction

Türkiye has recently attracted substantial domestic and foreign investments, and the retail sector has become a rapidly growing sector in Türkiye. In this sector, competition is getting more and more intense in parallel with the growth rate, so companies need to follow an inventory policy that minimizes cost and maximizes profit to survive. In addition, they must use their existing resources in the most appropriate way. An inventory is the whole set of items that are held before they reach the end user. Inventory should be kept at the optimum level with the principle of minimum inventory and maximum availability, without raising costs or reducing sales.

The development of Six Sigma dates back to the 1980s. The American company Motorola sold its Quasar TV manufacturing company to the Japanese company Matsushita in the 1970s due to its inefficiency. The idea of developing a new method in Motorola was triggered when Matsushita made sharp changes in the operation of the processes and significantly reduced the defect rate of the enterprise, and this led to the development of the Six Sigma method [1].

Six Sigma is an improvement method that pinpoints the root causes of problems and solves them. It can be briefly described as a method focusing on quality and efficiency to improve the products and processes in which the products are manufactured by following a scientific and systematic approach in line with the needs of the customers [2]. The Six Sigma method aims to achieve optimum performance in a process with product or service outputs [3]. It is a method that reduces defects in both service and production processes by utilizing data. The main

*Corresponding author: hkaracizmeli@harran.edu.tr
Received:30.05.2022, Accepted:20.09.2022

objective of using this method in the organization is to minimize variability and to improve processes through data-based strategies [4].

The Six Sigma method is composed of five steps: Define, Measure, Analyze, Improve and Control. The initial letters of these steps form the acronym DMAIC, which is used as the name of the method. Pande et al. shared a roadmap for the implementation of this method. They explained how it increases not only the efficiency of companies but also customer satisfaction, while reducing costs [5]. The DMAIC method is implemented as follows. In the Define phase, an initial project description form is created. Considered highly important by Pyzdek, (as cited in Kumar et al.) this form specifies the nature of the problem, the launch and completion dates, team members, along with the scope and objectives of the project [6]. Then the actual work is undertaken. In the Measure phase, the potential root causes are identified using techniques like brainstorming or fishbone. The data about these root causes are collected and analyzed. As Tjahjono et al. note, the data can be analyzed using a number of tools, including pareto graphics and regression analysis [7]. In the Improve stage, some essential improvements are made based on the results of the analysis. Finally, in the Control phase, the project ends with the measures taken to ensure the sustainability of the improvements.

As one would expect, Six Sigma is not a magic wand. The method could be beneficial if adopted across the organization. Caulcutt explained how large companies that used the Six Sigma method, such as Motorola, General Electric and Black & Decker, improved their business processes. He explained how to apply the Six Sigma method and stated that the most critical key to achieving success is to make the method a corporate culture [8].

Six Sigma has proven itself by spreading since the day it was introduced as a process improvement tool. For example, in their study in the chemical industry, Deshpande et al. showed that the Six Sigma method significantly reduced the defects, increased customer satisfaction, and positively affected the market share and employee performance [9]. Kabir et al. increased the productivity and production quality of a company, manufacturing fans through Six Sigma [10].

Most of the earlier studies conducted using the Six Sigma method addressed manufacturing functions. However, the method is used not only in manufacturing, but also in the service departments of businesses, as well as in enterprises that provide direct service. Chakrabarty and Tan examined Six Sigma studies conducted in the service sector. They identified critical success factors and quality parameters, along with key performance indicators that need to be tracked. According to these researchers, “time, cost, employee behavior, accurate information and timely information” are considered as critical quality parameters in this sector [11].

Blakeslee elaborates on how the Six Sigma method proved useful in boosting quality and competitiveness in baggage handling, in which the Sigma Level was 3. He shared the main principles and the steps to be taken [12]. Wyper and Harrison used the Six Sigma method to employ the right person in the right place, at the right time and with the right wage, which are the basic principles of human resources processes. First, they listed the customers of the process and prepared a process map. By using various Six Sigma tools, such as cause and effect diagram and pareto analysis, they managed to reduce personnel costs by 34%. In addition, there was an increase in customer satisfaction [13]. Sánchez-Rebull et al. obtained successful results by using the Six Sigma method in managerial and financial processes in a large German company producing canned food [14]. Mitreva and Kirovski improved the business processes of the microbiology unit in a public hospital serving in the Republic of North Macedonia by using the Six Sigma technique [15].

There are also studies in which the Six Sigma method was integrated with lean manufacturing techniques. Furterer and Elshennawy used Six Sigma and lean manufacturing tools together to improve the services provided in local government processes. As a result, they accelerated the financial transaction processes [16]. Mahmoud et al. developed product features in line with customer needs by the Lean Six Sigma method in a cement production facility [17]. Marrucci et al. integrated Lean Six Sigma and environmental management. They conducted a study to reduce the carbon footprint of a supermarket caused by food and packaging waste [18]. Lavin and Metter preferred the Lean Six Sigma method to improve the quality of health care services in an orthopedics hospital in the USA [19].

Gijo and Rao shared the problems encountered during Six Sigma studies and made suggestions based on their experience, rather than focusing on the success achieved. For example, commonly cited problems included but not limited to the work’s being either too narrow or too wide in scope, the lack of enough resources, issues of

coordination, being too hasty, mistakes made in choosing the project leader [20].

There is a paucity of research on the use of Six Sigma in the retail sector, a component of the service industry. A possible reason for this could be the prior development of the manufacturing sector compared with the service sector. There might be other reasons as well, such as the frequent use of advanced statistical tools with extensive data and the use of complex experimental designs in studies that use this technique. Therefore, researchers might have thought that the method was not appropriate for the service sector. Madhani noted that Lean Six Sigma applications in the retail sector are different from those in the manufacturing and other service sectors. According to Madhani, this difference could be attributed to the unique characteristics of the retail sector, such as the higher employee turnover rate, higher number of branches, customer relations and so forth [21]. In another study, Madhani proposed an efficiency-effectiveness framework to be used the Lean Six Sigma method in the retail industry. This framework aimed to reduce the costs and increase customer satisfaction [22]. However, except for Marrucci et al., no researchers have studied Six Sigma or Lean Six Sigma in supermarkets. This is also supported by Sreedharan and Raju because they reviewed 82 articles on Lean Six Sigma in the service sector, but none of them focused on supermarkets [23]. Similarly, Prakash et al. reviewed 63 articles on the use of Six Sigma in the service sector, but there was not a single study carried out on supermarkets [24].

The Six Sigma method is thought to be very difficult and burdensome for enterprises that do not use it. Given that they do not have enough resources, small and medium-sized enterprises (SMEs) may prefer not to use the method. The Six Sigma method is like a large toolbox. The important thing is to decide which tool to use where. In this study, the Six Sigma method is proposed for process improvement through practical tools without depleting the available resources. This study aimed to improve the inventory levels of a large supermarket in Sanliurfa through the Six Sigma method. Aiming to keep the inventory levels at the optimum level, it also aimed to strengthen the financial position of the company. In this business, excess inventory led to an increase in the products which needed returning. The products with a lower inventory turnover rate occupied a certain place in the warehouse, so they imposed an additional burden on the company. By applying the steps of the Six Sigma method, the present study investigated the causes of the inventory, and it also aimed to increase the financial efficiency of the company by reducing the inventory levels. In short, the widely known DMAIC steps were used at a supermarket to suggest a practical application.

The method followed is detailed in the second part of the study. The results and the improvement actions taken are addressed in the third part, and the results are presented in the fourth.

2. Material and Method

In this study, the phases of Six Sigma were followed. First, the problem was defined in collaboration with the process owner, and the scope of the study was specified. Company management wanted to keep the inventory levels at an effective level to increase profitability and ensure sustainable growth. Therefore, purchasing processes and inventory turnover rates of products were monitored. One of the problems that has arisen recently is the increase in the financial value of inventory due to products with lower inventory turnover.

During the define stage, a project team was established with employees from all departments affected by the problem. The definition of the problem, the purpose of the study, its contribution to the business and its scope were discussed by the team consisting of employees in the inventory management, accounting department, store management and purchasing department. Then, the potential root causes were determined by brainstorming with the team. The root causes were evaluated on a 10-point Likert scale (1 point: Insignificant, 10 points: Very significant) and were ranked according to their level of importance.

Data were collected during the measure phase of the study. The first 10 products with the highest inventory level in terms of their financial value in the last six months were examined. Moreover, the first 10 products with the highest inventory level in terms of quantity in the last six months were investigated. Therefore, the inventory data of the first half of 2019 were obtained thanks to the software used by the supermarket. In this business, no previous research studies had been carried out on products with lower rates of inventory turnover and excess inventory. Therefore, the present study addressed products with lower rates of inventory turnover.

In the analyze phase, the data obtained during the measure phase and the inventories in terms of their

financial value and quantities were analyzed as two different groups. Finally, process defects that led to higher inventory levels were identified and associated with the root causes, and the most common reasons for the problem were revealed. Then, actions were planned to create inventories effectively during the improve phase. Finally, in the control phase, a monitoring system for inventory levels was suggested to clarify the benefits of improvement actions and to ensure their sustainability.

3. Results and Discussion

3.1. Inventory Levels

The supermarket where the study was conducted was a large business that had been actively operating since 2018. The inventory levels in the supermarket in 2018 and in the first half of 2019 were examined. As seen in Figure 1, they increased by approximately 41% in the first half of 2019. This indicates that the problem required an urgent solution.

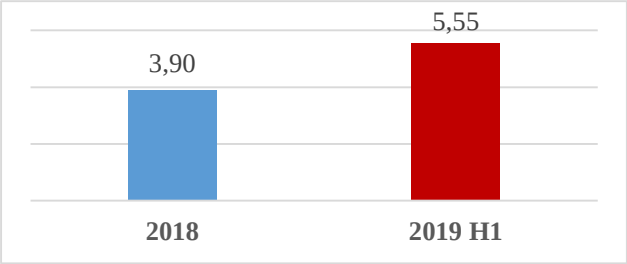

Figure 1. Inventory Levels (Million TL)

3.2. Brainstorming

The potential root causes were identified in the brainstorming session held with the study team to investigate the causes of excessive inventory levels, and they were ranked from highest to lowest in accordance with the total score of importance level (Table 1). It was considered that there was not a particularly effective inventory tracking. Due to the organization of the purchasing team, repeated purchases were often made. The brainstorming session also revealed that there was difficulty in demand forecasting. Based on the potential causes, some detailed research was carried out.

3.3. Quantity-based Inventory Levels

First of all, the products that constituted the highest inventory level in terms of quantity were identified. In Figure 2, products with an inventory level above five thousand are shown. It is seen that Products 1 and 2 have a higher inventory level than the others. A detailed examination revealed that the inventory turnover rate of the first product was high, while the inventory turnover rate of the second product was relatively low.

In addition, the products with the highest inventory level were also examined. It was seen that the top-ranking products in the graph showing value-based inventory levels in Figure 3 were almost the same products as those in Figure 2.

Table 1. Potential root causes of the problem

No	Root causes	Score
1	Failure to follow inventory turnover rates of products	30
2	More than one person making purchases in the same product group	28
3	Products' coming in many different brands	24
4	Offering appealing prices in the purchase of extra products	17
5	Uncertain customer demand	14
6	Some suppliers' having extended lead times	13

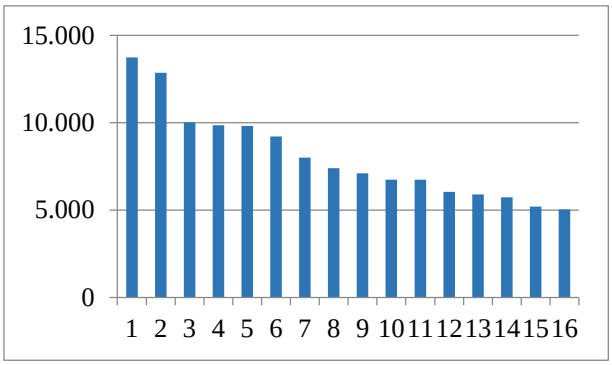

Figure 2. Products with the Highest Inventories Based on Their Quantity

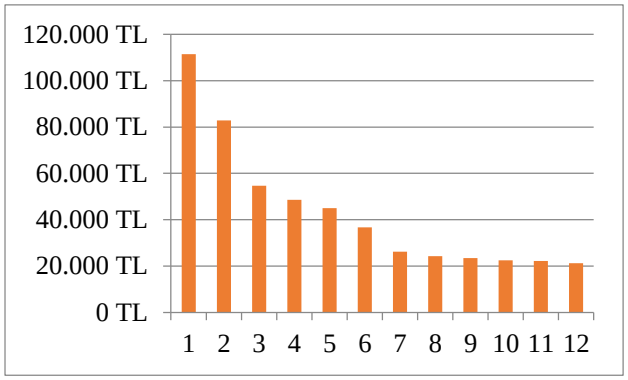

Figure 3. The Inventory Levels of the Products Based on Their Financial Value

3.4. Why is there a surplus of inventory?

Inventory data were examined and analyzed retrospectively in this study. Figure 4 shows the reasons for the inventory of products with a higher financial value and a lower inventory turnover rate. An analysis of the reasons in this group revealed that the major reasons were seeking reasonable prices in big purchases and not being able to forecast the demand. These reasons accounted for 74% of the inventory in terms of financial value in this group. On the other hand, there were also inventories prepared for preliminary purposes due to new products, price volatility and the volatility of seasonal demands. Customers demanded different product sizes, so the same product was more popular in some package sizes than in others. In fact, this was a special case which was related to the reason why the demand forecast was not accurate.

In the next phase of the study, the causes of excess inventory were associated with potential root causes identified during the brainstorming session. The results are presented in Table 2. All the potential root causes appear to be effective. However, the main problem was in the purchasing organization. In line with this, the functions of inventory tracking and demand forecasting were not efficient enough.

Another noteworthy point is that the fifth item, “Customer Demand Uncertainty”, which was a potential root cause, was found to be a key cause of excess inventory, although it was of relatively minor importance in the brainstorming session. Therefore, it is important to take actions that could shape customer demand and make it predictable.

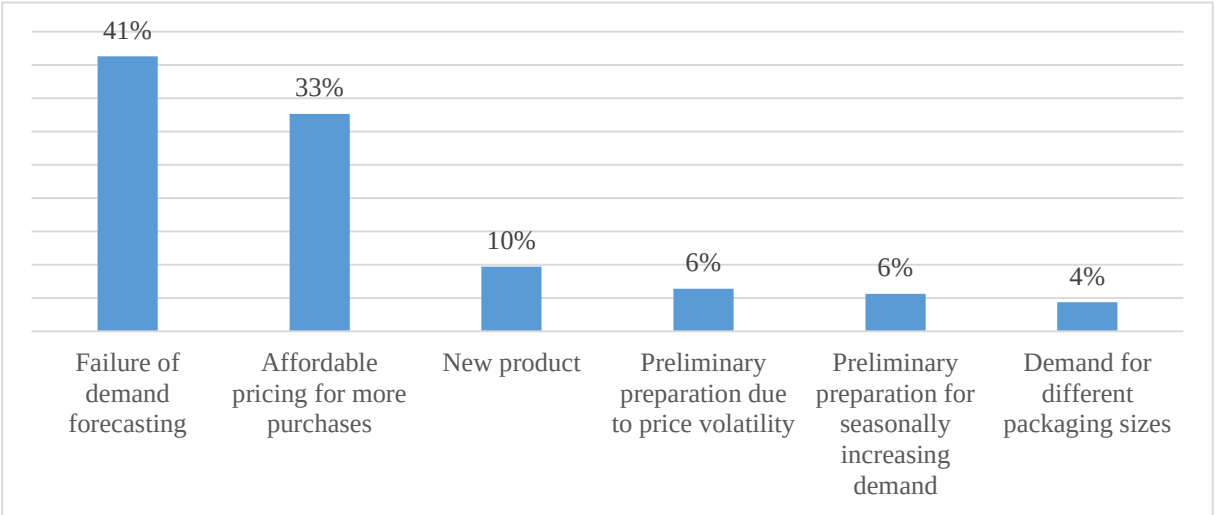

Figure 4. The Causes of Excess Inventory

Table 2. Causes of excess inventory and root causes

Causes of Excess Inventory	**Number of Root Causes**					
	1	**2**	**3**	**4**	**5**	**6**
Failure of demand forecasting	X	X	X		X	
Affordable pricing for more purchases	X			X		X
New product			X		X	
Preliminary preparation due to price volatility				X	X	
Preliminary preparation for seasonally increasing demand			X	X	X	
Demand for different product sizes			X		X	

3.5. Improvement Actions

As a result of the analyses, some actions were planned to improve the process. Being the main problem, the purchasing organization was first examined. In line with the expertise of the purchasing staff and the total workload in the product groups, a scheme was prepared based on product groups. A preparation of a standard work instruction for regular inventory tracking, as well as a system in which inventory turnover rates to be followed based on a product/product group, were suggested.

Demand forecasting is not easy, particularly for supermarkets where the product portfolio is rather diverse. However, professional demand forecasting can be carried out using appropriate software. It is possible to reduce forecast deviations through both long-term and short-term data analysis. It is necessary to pay attention to many parameters, such as volatility arising from seasonal demands, different demands for different brands or different packaging sizes, and the performance of competitors.

It is possible to direct customer demands and make them even more predictable. Thanks to regular monitoring of inventory and demands, it is possible to take a number of actions such as making product combinations, highlighting, making departmental arrangements, discounting, and avoiding products/product groups that are not in demand. When the products with longer delivery periods were examined, it was seen that the problem arose, especially due to the suppliers outside the city.

After taking the necessary actions, we noticed that the sales performance of some of the products increased rapidly. An example of these products is shown in Figure 5. Various strategies were used for this product, including but not limited to discount, departmental arrangement, highlighting and printing brochures.

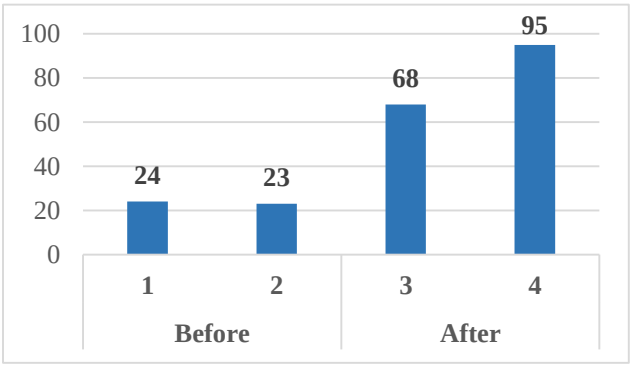

Figure 5. Monthly Sales of Product A (Qty)

4. Conclusion and Suggestions

This study revealed that process improvement can be achieved through the Six Sigma method without depleting the available resources. The Six Sigma method does not only use advanced statistical tools but also uses processes that can be improved with practical tools whenever necessary. The problems mentioned in this study can be solved using software investments in many supermarkets. However, what is

offered in the present study may not appeal to the needs of some businesses, especially those of SMEs that may desire to use process improvement techniques without making much investment.

The results indicated that most of the existing inventory was caused by inaccurate demand forecasts and excess purchases made by the supermarket due to affordable prices offered by wholesalers. When a relationship was established between the potential root causes that emerged while brainstorming with the team and causes of inventory, it was understood that there was a deficiency in the inventory tracking system and demand forecasting processes. The main reason for this was found to be the purchasing organization.

In this study, the purchasing function was reorganized. Necessary standards and work instructions were established. Several suggestions were made regarding demand forecasting. In order to make customer demands more predictable, sales and marketing techniques, such as product combination, highlighting, department arrangement, and discounting, were utilized. Consignment agreements were recommended for products with longer lead times.

The realization of improvement actions helped achieve improvements in the inventory levels. A monitoring plan was prepared to ensure the continuity of the improvements. Based on this plan, outlined in Table 3, the purchasing unit was required to report regularly to the board of directors. Further research could investigate demand forecasting models.

Contributions of the authors

The contributions of each author to the article is equal.

Conflict of Interest Statement

There is no conflict of interest between the authors.

Statement of Research and Publication Ethics

The study is complied with research and publication ethics.

Table 3. Monitoring plan

Items to be monitored	Monitoring frequency
Inventory Levels (Based on Product Groups)	7 days
Inventory Levels (Product-based)	7 days
Inventory Turnover Rates (Product-based)	7 days
Inventory Levels of Product Groups (Brand-based)	15 days

References

[1] O. Akın, The implementation of Six Sigma systems with integrated activity-based cost system in marble sector, Suleyman Demirel University, Social Sciences, Institute of Business Administration Doctoral Thesis, Isparta/Turkey, 2010.
[2] E. Işığıçok, Altı Sigma Kara Kuşaklar İçin Hipotez Testleri Yol Haritası, Marmara Kitapevi Yayınları, Bursa/Turkey, 2011.
[3] P.M. Wilson, Six Sigma – Understanding the concept, implications and challenges, Advanced System Consultants, New York, 1999.
[4] T. Pyzdek, Six Sigma handbook: A complete guide for greenbelts, blackbelts and managers at all levels, McGraw Hill, New York, 2001.
[5] P. S. Pande, R. P. Neuman and R. R. Cavanagh, The Six Sigma way: How GE, Motorola, and other top companies are honing their performance, McGraw-Hill, New York, 2000.

[6] M. Kumar, J. Antony and B. R. Cho, "Project selection and its impact on the successful deployment of Six Sigma", Business Process Management Journal, vol.15 no.5, pp.669-686, 2009.
[7] B. Tjahjono, P. Ball, V. I. Vitanov, C. Scorzafave, J. Nogueira, J. Calleja, M. Minguet, L. Narasimha, A. Rivas, A. Srivastava, S. Srivastava and A. Yadav, "Six Sigma: a literature review", International Journal of Lean Six Sigma, vol.1 no.3, pp.216-233, 2010.
[8] R. Caulcutt, "Why is Six Sigma so successful?", Journal of Applied Statistics, vol.28 no.3-4, pp.301-306, 2001.
[9] P. B. Deshpande, S. L. Makker and M. Goldstein, "Boost competitiveness via Six Sigma", Chemical Engineering Progress, vol.11, pp.65-70, 1999.
[10] M. E. Kabir, S. M. M. I. Boby and M. Lutfi, "Productivity improvement by using Six-Sigma", International Journal of Engineering and Technology, vol.3 no.12, pp.1056-1084, 2013.
[11] A. Chakrabarty and K. C. Tan, "The current state of Six Sigma application in services", Managing Service Quality: An International Journal, vol.17 no.2, pp.194-208, 2007.
[12] J. A. Blakeslee, "Implementing the Six Sigma Solution", Quality Progress, vol.32 no.7, pp.77-85, 1999.
[13] B. Wyper and A. Harrison, "Deployment of Six Sigma methodology in Human Resource function: A case study", Total Quality Management & Business Excellence, vol.11 no.4-5, pp.720-727, 2000.
[14] M. V. Sánchez-Rebull, R. Ferrer-Rullan, A. B. Hernández-Lara and A. Niñerola, "Six Sigma for improving cash flow deficit: a case study in the food can manufacturing industry", International Journal of Lean Six Sigma, vol.11 no.6, pp. 1105-1126, 2020.
[15] E. Mitreva and F. Kirovski, "Application of the methodology of Six Sigma in public health institution", SAR Journal, vol. 4 no. 3, pp.107-113, 2021.
[16] S. Furterer and A. K. Elshennawy, "Implementing of TQM and Lean Sigma tools in local goverment: A framework and a case study", Total Quality Management & Business Excellence, vol.16 no.10, pp.1179-1191, 2005.
[17] A. S. Mahmoud, A. M. Hossian, W. K. Ahmed, M. Aly and M. Khalil, "Lean Six Sigma implementation in cement grinding process – "ABC" plant case study", International Journal of Innovative Research in Technology & Science, vol.6 no.2, pp.1-3, 2018.
[18] L. Marrucci, M. Marchi and T. Daddi, "Improving the carbon footprint of food and packaging waste management in a supermarket of the Italian retail sector", Waste Management, vol. 105, pp.594-603, 2020.
[19] P. Lavin and M. J. Vetter, "Using Lean Six Sigma to increase the effectiveness of an evidence-based quality improvement program", Journal of Nursing Care Quality, vol.37 no.1, pp.81-86, 2022.
[20] E. V. Gijo and T. S. Rao, "Six Sigma implementation - Hurdles and more hurdles", Total Quality Management & Business Excellence, vol.16 no.10, pp.721-725, 2005.
[21] P. M. Madhani, "Performance Optimisation of Retail Industry: Lean Six Sigma Approach", ASBM Journal of Management, vol.13 no.1, pp.74-91, 2020.
[22] P. M. Madhani, "Lean Six Sigma Deployment in Retail Industry: Enhancing Competitive Advantages", The IUP Journal of Business Strategy, vol.17 no.3, pp.25-45, 2020.
[23] V. R. Sreedharan and R. Raju, "A systematic literature review of Lean Six Sigma in different industries", International Journal of Lean Six Sigma, vol.7 no.4, pp.430-466, 2016.
[24] S. Prakash, S. Kumar, G. Soni, R. V. Mahto and N. Pandey, "A decade of the international journal of lean six sigma: bibliometric overview", International Journal of Lean Six Sigma, vol.13 no.2, pp.295-341, 2022.

Bitlis Eren Üniversitesi Fen Bilimleri Dergisi
BİTLİS EREN UNIVERSITY JOURNAL OF SCIENCE
ISSN: 2147-3129/e-ISSN: 2147-3188
VOLUME: 11 NO: 3 PAGE: 836-845 YEAR: 2022
DOI: 10.17798/bitlisfen.1123197

Structural Equation Modeling Approach to Determine the Effect of Attitude towards Statistics on Statistical Self-efficacy Belief

Duygu TOPCU[1], Hayriye Esra AKYÜZ[1*]

[1]*Bitlis Eren University, Faculty of Science and Arts, Department of Statistics, Bitlis, Turkey (ORCID:0000-0002-1373-2732) (ORCID: 0000-0002-1784-5910)*

Keywords: Attitude towards statistics, Bitlis Eren University, Construct validity, Statistical self-efficacy belief, Structural equation modeling, Path analysis.

Abstract
In this study, it is aimed to examine the relationship between students' statistical self-efficacy beliefs and their attitudes towards statistics and to propose a structural equation model by identifying the factors affecting them. IBM SPSS and AMOS package program were used in the data analysis. Data were collected from 330 university students who took statistics and biostatistics lessons to form the sample of the study. As a result of the analysis, it was concluded that the self-efficacy beliefs and attitudes towards to statistics lesson of students were at a moderate level. A positive and significant correlation was obtained between statistical self-efficacy belief and attitude. It was determined that statistical attitude explains 33% of the statistical self-efficacy belief. We propose to use modified multi-factor first-order and multi-factor first-order models for statistical self-efficacy belief and attitude levels, respectively. This result was supported with the values of goodness of fit indices.

1. Introduction

It is known that the attitudes that students who take statistics lesson develop towards statistics and their self-efficacy belief affect their success.

Statistical information and methods are used for making an assessment and taking decisions in any matter. The reason why statistics course is taught in schools is because it is a tool used in different fields, to enable individuals to benefit from this subject in daily life and to look at events more critically [1], [2]. According to Bandura [3], self-efficacy is the beliefs and perceptions that a person creates about his personal skills specific to the situation that concerns a specific job, task, activity or field. Self-efficacy belief affects individuals' emotions, thoughts, forms of motivation, learning methods and using those and their behaviours of asking for help in situations that require support in academic sense [4], [5]. In addition, it has been shown that the effective use of learning methods by individuals affects their success.

Attitude is an orientation which is assigned to the person and which constitutes the person's emotions, thoughts and behaviours related to a psychological object decisively [6]. Aydın and Sevimli [7] stated that self-efficacy is an important factor for developing positive attitude towards statistics education and meeting cognitive competencies.

In many study in the literature, statistical methods such as explanatory (EFA) and confirmatory (CFA) factor analysis, path analysis and structural equation modeling (SEM) are used when examining the relationships between variables [8]-[13].

There are many studies in the literature that investigate self-efficacy and attitude levels. These studies vary according to the subject area.

Aydın and Sevimli [14] aimed to study the validity and reliability of the statistical self-efficacy belief scale developed by Finney and Schraw [15] in Turkish language and culture. Yaşar [16] and Koparan [17] developed a 20-item attitude scale

*Corresponding author: heakyuz@beu.edu.tr
Received: 30.05.2022, Accepted: 23.09.2022

towards statistics, which was determined to be valid and reliable. In order to evaluate the reflections of self-efficacy and attitude levels in teaching practice, a great deal of attention was given to the studies carried out with teachers and pre-service teachers. Altunçekiç et al. [18] discussed the proficiency levels and problem-solving skills of pre-service teachers in science teaching. Çakıroğlu and Işıksal [19] investigated the variables that have an effect on pre-service teachers' self-efficacy beliefs and attitudes towards mathematics. While gender and grade level did not have a statistically significant effect on attitude, it was found that there was a significant difference on self-efficacy perceptions. Uysal and Kösemen [20] examined the general self-efficacy beliefs of pre-service teachers in terms of some demographic variables. Aydın et al. [21] investigated the relationship between pre-service teachers' self-efficacy perceptions and their levels of academic delay of gratification. Gündüz [22] examined statistical literacy and attitudes towards statistics of pre-service teachers. According to the results, it was determined that the students had a positive attitude towards statistics and their statistical literacy levels were generally at a moderate level. Aydın and Sevimli [7] aimed to examine pre-service teachers' self-efficacy beliefs towards statistics and their attitudes towards statistics and the relationships between them. It has been determined that pre-service teachers' self-efficacy beliefs towards statistics course are high and their attitudes are moderate.

On the other hand, students' self-efficacy and attitudes towards statistics lesson is an important concept for statistics learning. In studies conducted with undergraduate students, Bandalos et al. [23] did not find any relationship between self-efficacy and statistical success; Finney and Schraw [15] found an improvement of two standard deviations between pre- and final self-efficacy in the introductory statistics lesson. Girginer et al. [24] examined the relationship between the attitudes of students and their personal characteristics. It was determined that the individual characteristics of the students were effective in their attitudes towards the statistics lesson. Eskici [25] and Salihova and Memmedov [26] used the statistical attitude scale to reveal the attitudes of the students. Emmioğlu et al. [27] investigated the attitudes of students studying in engineering fields towards statistics. Alkan [28] aimed to examine how different applications in the statistics lesson affect the change in students' attitudes towards statistics and whether this effect is statistically significant.

It is extremely important to determine self-efficacy beliefs and attitudes towards statistics, especially in terms of disciplines such as statistics and mathematics where failure anxiety is high. Statistics lessons are taught at the undergraduate level in universities in Turkey. Thus, students' learning and success in the statistics lesson during their graduate education will be very beneficial for scientific studies of students.

In this study, it is aimed that factors that affect university students' self-efficacy beliefs and their attitudes towards statistics are identified, the relations among those factors are determined and a suitable path model is created by presenting the correlations between observed and unobserved variables.

2. Material and Method

In this study, the sample consists of 330 students who take Statistics and Biostatistics lessons at Bitlis Eren University in 2019-2020 academic year. As standardized values which are average score of statistical self-efficacy belief (SEB) and attitude towards statistics (SA) were outside the range of -2.5 and +2.5, 26 questionnaires were excluded from the data set. As the number of students in the population is known, sample size was obtained with the formulation suggested by Sümbüloğlu and Sümbüloğlu [29].

This study was conducted by taking 08/05/2019 dated and 2019/05-XI numbered permission from Bitlis Eren University Ethics Committee. Demographic informations of the students, SEB [14] and SA [17] scales were used in the questionnaire form as the data collection tool in the study. SEB and SA scales were prepared with 14-item 6-point likert scale and 20-item 5-point likert scale, respectively.

The data was analysed via IBM SPSS and AMOS softwares. Firstly, descriptive statistics (number, percentage, average, standard deviation, etc.) were obtained. It was examined with Kolmogorov-Smirnov and Shapiro-Wilk goodness of fit tests whether the data complies with normal distribution. Independent sample t-test/Mann Whitney-U test and One-way Analysis of Variance (ANOVA)/Kruskal Wallis H test were used to determine whether scores of variable obtained from two or more independent samples differ from each other.

In addition, LSD and Bonferroni post-hoc tests were preferred to determine which groups are the source of difference. Before applying the SEM, firstly, outlier and item analysis were conducted to prepare the dataset for analysis. Later, as a statistical method order, EFA, Reliability Analysis and CFA were used to test construct validity of scales. Furthermore; suitable model was tested with path

analysis using SEM. In this study, p-values lower than 0.05 were considered as significant.

2.1. Factor Analysis

Factor analysis is a statistical method that allows to explain a structure that is tried to be explained with a large number of variables (dimensions) that are related to each other, with a smaller number of unrelated new factors (variables). These new factors revealed as a result of the factor analysis are orthogonal to each other, the correlation coefficients between the factors are zero and they are the linear components of the main factors [30]. There are mainly two types of factor analysis that are EFA and CFA.

EFA is used to determine the structure of the items in a scale and to determine under which dimension they are collected [30]. EFA explains the correlation between observable and unobservable variables. Basically, it makes the data easier and more understandable. Furthermore, it explains the covariance and correlations between the observable variables correlatively by the help of fewer number of latent variables.

CFA is a method created with the purpose of presenting the latent structure of a measurement tool. This analysis is developed with the purpose of testing hypotheses formed on factor analysis. Rather than determining with which factors variables have high level correlation as in EFA; CFA determines on which level the variable clusters that affect a certain number of previously designed factors are represented by means of determined factors [31]. While factor analysis allows development of many measurement tools, CFA allows testing whether these models are verified or not for the data set in the study. The purpose of CFA is to test whether the data fit a measurement model. Tested models are known as single factor model, the first level multifactor model, the second level multifactor model and the unrelated model. The model, which is formed by clustering all variables under one dimension, is called the first level single factor dimension. The model, which is formed by clustering more than one variable under independent dimensions, is a first-level multi-factor model. A second-level multi-factor model is formed by collecting the variables under more than one unrelated dimension and then collecting these dimensions under another dimension. An unrelated model is formed by clustering the variables under unrelated dimensions [32].

CFA tests and verifies the hypotheses established via the relationships between the variables. For this, it is necessary to examine the relations between the factors and between the variables and the factors according to the previously established hypotheses.

2.2. Structural Equation Model

SEM is a statistical method, which is based on the definition of observable and unobservable variables in a causal and correlational model based on a certain theory, and brings a hypothesis-testing approach to the multivariate analysis of the relevant structural theory. It associates unobservable variables such as attitude, emotion, intelligence, and satisfaction with observable independent variables [32]. The aim of SEM is to test whether a model with a theoretical basis is compatible with the data obtained. If the fit indices as a result of the tested model show that there is a fit between the model and data, the hypotheses formed structurally are accepted. Otherwise, the hypotheses are rejected.

It contains both observed and latent variables in its structure together. For that reason, it is a modelling method in which CFA and path analysis are used together as a structure. This model explains measurement errors in the research clearly. Variables which cannot be observed directly, but are the main researched variables by the researcher are called latent variables. Since latent variables cannot be measured, researchers measure the latent variable with observed variables that they think to be representing the latent variable [33]. This method is known to be better than other multivariate statistical techniques [34].

SEM consists of two parts. The first part which is the measurement model expresses the correlation of observed variables and latent variables. It is also named as CFA model. Latent variables in the model are calculated by observed variables. The second part of SEM is the structural model. Structural model connects unobservable variables by implementing simultaneous equation systems among them. Structural model is a general model and it expresses the correlation between latent and observed variables [35].

This approach allows the modelling of a phenomenon by considering both the unobserved ‘latent’ constructs and the observed indicators that describe the phenomenon [36]. The measurement equations for endogenous and exogenous variables are given as in Eq. 1 and Eq. 2, respectively.

$$y = \Lambda_y \eta + \varepsilon \tag{1}$$

$$x = \Lambda_y \xi + \delta \tag{2}$$

Structural model is notated mathematically as in Eq. 3 [37]:

$$\eta = \beta\eta + \Gamma\xi + \zeta \quad (3)$$

where
x: Observed exogenous variable,
y: Observed endogenous variable,
η: Latent endogenous variable,
ξ: Latent exogenous variable,
λ: Structural coefficient,
Ɛ: Measurement error in the observed endogenous variable,
δ: Measurement error in the observed exogenous variable,
ζ: Error term related with latent endogenous variable,
β: Structural effect of an endogenous variable to another endogenous variable,
γ: Structural effect from an exogenous variable to an endogenous variable.

SEM and CFA are similar methods. The aim of SEM is to test the established structure and model. Various models are compared in SEM and it is tried to form the most suitable model for the data set. In CFA, it is tried to verify a previously determined model. CFA is a measurement model and tests how the analyzed structure of the factor adjusts to the data. In addition, CFA includes measurement error in the model and estimates such errors. Restrictions in EFA are eliminated with CFA and it allows that various restrictions that can explain the model in the best way are included in the model [35]. Contrary to traditional methods, SEM takes into account all measurement errors in error calculations and obtains much clearer results than other methods [38].

2.3. Path Analysis

Path analysis is a model in which correlation coefficients and regression analysis are used together for modelling more complex correlations among observed variables based on cause-effect relation [39]. The purpose of this analysis is to predict the importance of the hypothetical causal correlations between the variables and to make policy implications [40]. The model in path analysis presents the correlation of exogenous variables with another variable in the model and the degree of effect of such correlation.

A path analysis has two components: path coefficients and a path diagram. Path coefficients represent the mathematical part of the analysis. There are figures to express the effect of variables on another variable. These expressions are called path diagrams [40].

Path analysis has some features which make is superior to multiple regression. The number of dependent variables is only one in multiple regression. However, it is possible to determine a number of dependent variables simultaneously in SEM. In regression models, dependent and independent variables are expressed in a single way with these names. However, a variable can be identified as both dependent and independent variable simultaneously in SEM.

3. Results

Distribution of students according to their demographic characteristics is given in Table 1. According to this; it was determined that 70.7% of the students are female, 29.3% are male; average age is 21.16±1.99; 59.9% are having associate degree and 40.1% are having bachelor's degree education. It was seen that the majority of the students were in the health department and were in the first year (Table 1).

Table 1. Some demographic characteristics

		N	%
Gender	Male	89	29.3
	Female	215	70.7
Age ($\bar{x}$ ± *sd)*		(21.16±1.99)	
Education	Associate Degree	182	59.9
	Bachelor's Degree	122	40.1
Department	Health	222	73.0
	Social	46	15.1
	Other	36	11.8
Class	1	120	39.5
	2	98	32.2
	3	38	12.5
	4	48	15.8

Normal distribution of the data depends on the fact that skewness and kurtosis values are between ±3. According to result of goodness of fit test and skewness/kurtosis values, it was found that SEB and SA levels have normal distribution (p>0.05, Table 2).

Table 2. Kolmogorov-Smirnov goodness of fit test, skewness and kurtosis values

Scale	*p*-value	Skewness	Kurtosis
SEB	0.094	0.671	-0.699
SA	0.137	-0.978	-1.534

The descriptive statistics of the answers given by the students to the SEB and SA scales are given in Table 3-4, respectively.

In Table 3, the means of items vary between 3.3303 and 3.7061. The results show that the two items with the highest perceived self-efficacy are EB5 and EB4.These items are to interpret the results of the statistical method in terms of the research problem

and to choose the right statistical method to answer a research question.

Table 3. Some descriptive statistics for SEB

	Mean	SD*	SE**
EB1	3.3303	1.49263	0.08217
EB2	3.5061	1.43606	0.07905
EB3	3.6030	1.47006	0.08092
EB4	3.6333	1.41274	0.07777
EB5	3.7061	1.39527	0.07681
EB6	3.3879	1.45484	0.08009
EB7	3.5455	1.44169	0.07936
EB8	3.3364	1.53150	0.08431
EB9	3.4121	1.54561	0.08508
EB10	3.5061	1.47984	0.08146
EB11	3.4424	1.45386	0.08003
EB12	3.3758	1.45176	0.07992
EB13	3.6273	1.46401	0.08059
EB14	3.4939	1.53825	0.08468

* standard deviation, ** standard error

Table 4. Some descriptive statistics for SA

	Mean	SD*	SE**
A1	3.1818	1.48661	0.08184
A2	3.3212	1.29759	0.07143
A3	3.3667	1.26999	0.06991
A4	2.9485	1.16447	0.06410
A5	2.9303	1.28043	0.07049
A6	2.4121	1.32769	0.07309
A7	2.5061	1.38872	0.07645
A8	2.6000	1.35180	0.07441
A9	3.3333	1.23934	0.06822
A10	2.5667	1.24631	0.06861
A11	3.2515	1.22800	0.06760
A12	3.3030	1.15606	0.06364
A13	3.0970	1.24126	0.06833
A14	3.3545	1.26144	0.06944
A15	3.4121	1.27156	0.07000
A16	2.9424	1.39463	0.07677
A17	2.9303	1.28043	0.07049
A18	3.3364	1.24951	0.06878
A19	3.1939	1.21988	0.06715
A20	3.2182	1.31428	0.07235

* standard deviation, ** standard error

The two items with the lowest self-efficacy are EB1 and EB8. They are to determine the scale of measurement for a variable and to distinguish between Type I and Type II errors while testing the hypothesis. The average of each item in the scale is above 3 out of 6 points. We can say that self-efficacy of students is at medium level (Table 3).

In Table 4, the item with the highest attitude (A3) states that many problems can be easily solved using statistics. On the other hand, the lowest item (A6) say that understanding statistics does not benefit people. The means of items vary between 2.4121 and 3.3667. We can say that attitudes towards statistics of students are generally at a moderate level except A6 and A7.

Table 5. The test results for SEB and SA levels

Scale	Min	Max	Mean	SD*	SE**
SEB	14	84	48.9061	14.0708	0.7745
SA	19	95	58.2636	12.1056	0.7194

* standard deviation, ** standard error

Since the SEB scale consists of 14 items and is prepared in a 6-point likert type, the highest possible score is 84 and the lowest score is 14. On the other hand, SA scale consists of 20 items and is prepared in a 5-point likert type, the highest possible score is 100 and the lowest score is 20. In Table 5, we see that the ranges for SEB and SA scales are 70 (84-14) and 76 (95-19), respectively. Also, the mean of these scales are 48.9061 and 58.2636. Thus, average self-efficacy and attitude scores for all items are 2.9131 (58.2636/20) and 3.4932 (48.9061/14).

Table 6. Exploratory factor analysis results of statistical self- efficacy belief scale

	Factor			
	SEB1	SEB2	SEB3	Item-total correlation
EB12	0.756			0.520
EB11	0.740			0.623
EB13	0.705			0.625
EB14	0.693			0.534
EB10	0.671			0.618
EB9	0.484			0.558
EB1		0.844		0.468
EB2		0.822		0.557
EB3		0.669		0.598
EB4		0.563		0.541
EB6			0.828	0.475
EB7			0.721	0.576
EB5			0.684	0.596
Reliability	0.826	0.787	0.746	0.880
Explained variance	24.500%	19.760%	16.298%	60.557%
Eigenvalue (Λ)	5.355	1.413	1.104	
KMO =0.883, $\chi 2(78)$ =1510.818, Bartlett's test of spherycity (p) = 0.000				

In Table 6, it was determined that KMO value is 0.883 and the Chi-square value is on acceptable level ($\chi 2(78)$ =1510.818; $p<0.01$, Bartlett's test of spherycity (p) = 0.000). SEB scale is grouped under three theoretical dimensions. These dimensions are named as EB1, EB2 and EB3. Items with low factor load could not be found in the dimensions and item 8 which causes cross loading was removed from the analysis. These three factors explain 60.557% of total variance. First factor EB1 explains 24.500%, second factor EB2 explains 19.760%, third factor EB3 explains 16.298% of total variance. Principal components analysis and varimax, which is one of the orthogonal rotation methods, are used as factorizing method for revealing factor pattern. As a result of EFA, it was determined that factor load values are

above 0.40 (0.484-0.844) and factor loads are on acceptable level (Table 6).

When reliability analysis results for scale and subdimensions are examined; reliability coefficient was found as 0.880 for overall SEB scale, 0.826 for first dimension, 0.787 for second dimension, 0.746 for third dimension. In that case, it can be said that the scale has high degree of reliability (Table 6).

Table 7. Multi-factor first-order CFA model fit indices for statistical self-efficacy belief scale

Modification	RMSEA	CFI	IFI	GFI	CMIN/df
Before	0.086	0.904	0.905	0.906	3.260
	RMSEA	CFI	IFI	GFI	CMIN/df
After	0.077	0.927	0.928	0.924	2.777

(RMSEA: Root Mean Square Error of Approximation, CFI: Comparative Fit Index, IFI: Incremental Fit Index, GFI:Goodness of Fit Index, CMIN/df: chi-square fit statistics/ degree of freedom)

According to CFA, it was seen that structural model result of SEB was statistically significant for p=0.000. It was proven that 13 items and three subdimensions that constitute the scale are correlated with scale structure (Table 7). Modifications were made on the model to obtain goodness of fit results more suitable [41]. New covariances were created between error terms with high covariance (e1-e4; e7-e8). According to multi-factor first-order CFA results, after modification, it was seen that these fit indices were on acceptable level (Table 7).

Table 8. Results of CFA for statistical self-efficacy belief scale

Factor	Factor load	Standard error	t-value (critical ratio)	*p*-value
SEB1				
EB9	0.640			
EB10	0.712	0.106	10.050	0.000
EB11	0.737	0.106	10.299	0.000
EB12	0.653	0.115	8.347	0.000
EB13	0.698	0.103	9.904	0.000
EB14	0.613	0.108	8.955	0.000
SEB2				
EB1	0.602			
B2	0.696	0.104	10.686	0.000
EB3	0.741	0.140	8.728	0.000
EB4	0.632	0.123	8.050	0.000
SEB3				
EB5	0.729			
EB6	0.648	0.097	9.588	0.000
EB7	0.727	0.099	10.440	0.000

In Table 8, it is seen that factor loads are between 0.602 and 0.741 and are statistically significant (p<0.05).

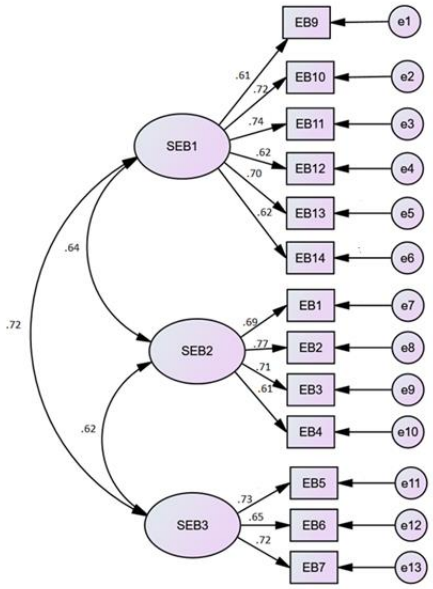

Figure 1. Multi-factor first-order CFA model for statistical self-efficacy belief.

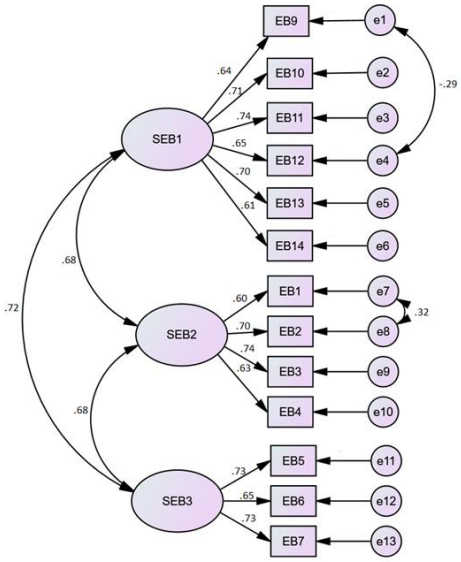

Figure 2. Modified multi-factor first-order CFA model for statistical self-efficacy belief.

It was determined that average scores of SEB and its subdimensions do not statistically significant according to gender, education status and class of students (p>0.05, Table 9).

In Table 10, it was determined that KMO value is 0.857 and Chi-square value is on acceptable level ($\chi 2(66) = 1078.876$; p<0.01). The factors were named as A1, A2 and A3. These factors explain 58.387% of total variance. A1, A2, A3 explains 19.754%, 19.760% and 19.013% of total variance, respectively.

Table 9. Independent t-test and one-way ANOVA results for statistical self-efficacy belief scale

	SEB1	SEB2	SEB3	SEB
Gender				
Male*	3.44±0.93	3.63±1.15	3.70±1.14	3.56±0.87
Female*	3.52±1.10	3.50±1.06	3.51±1.11	3.51±0.92
t-value	-0.651	1.006	1.328	0.425
p-value	0.516	0.315	0.185	0.671
Education				
Associate Degree*	3.49±1.06	3.47±1.09	3.54±1.16	3.50±0.91
Bachelor's Degree*	3.51±1.05	3.64±1.09	3.61±1.06	3.57±0.90
t-value	-0.130	-1.287	-0.596	-0.718
p-value	0.897	0.199	0.552	0.474
Class				
1*	3.42±1.04	3.40±1.03	3.44±1.10	3.42±0.83
2*	3.58±1.10	3.68±1.15	3.77±1.18	3.65±0.96
3*	3.35±1.19	3.59±1.21	3.39±1.09	3.43±1.05
4*	3.63±0.85	3.55±0.99	3.63±1.02	3.60±0.81
F-value	0.929	1.172	1.976	1.488
p-value	0.427	0.321	0.118	0.218

* : Each value is expressed as mean±standard deviation.

Table 10. Exploratory factor analysis of statistical attitude scale

	Factor			
	SA1	SA2	SA3	Item-total corelation
A15	0.718			0.528
A14	0.718			0.560
A16	0.666			0.334
A12	0.636			0.467
A13	0.564			0.526
A19		0.825		0.516
A18		0.742		0.589
A17		0.687		0.395
A20		0.685		0.399
A2			0.837	0.535
A1			0.783	0.507
A3			0.755	0.576
Reliability	0.734	0.756	0.788	0.833
Explained variance	19.754%	19.620%	19.013%	58.387 %
Eigenvalue (Λ)	4.327	1.488	1.191	

KMO =0.857; $\chi 2(66) = 1078.876$; Bartlett's test of spherycity (*p*) = 0.000

It was determined that factor loads are between 0.564-0.837. Items 5-10 which have total item correlation below 0.30 were excluded from the analysis. Reliability coefficient was found as 0.833 for overall SA scale, 0.734 for first dimension, 0.756 for second dimension and 0.788 for third dimension. According to these results, it was determined that the scale has high degree of reliability (Table 10).

Table 11. Multi-factor first-order CFA model fit indices for statistical attitude scale.

RMSEA	CFI	IFI	GFI	CMIN/df
0.029	0.987	0.987	0.966	1.257

The goodness of fit indices of the SA were obtained as 0.029 for RMSEA, 0.966 for GFI, 0.987 for CFI, 1.257 for $\chi 2$ /df and this values were on acceptable level and statistically significant with p=0.000 (Table 11).

Multi-factor first-order CFA model for SA is given in Figure 3.

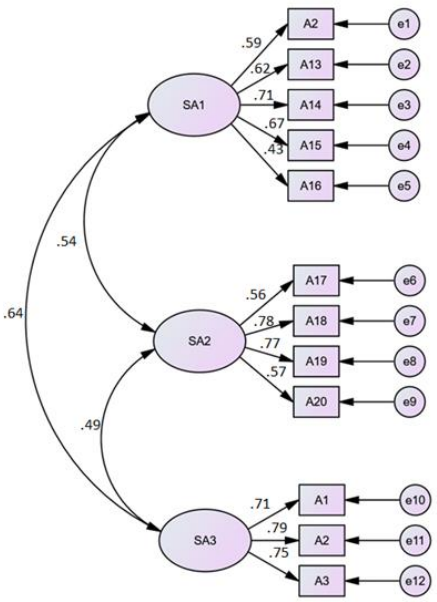

Figure 3. Multi-factor first-order CFA model for statistical attitude.

Table 12. Results of CFA for statistical attitude scale

Factor	Factor load	Standard error	t-value (critical ratio)	*p*-value
SA1				
A12	0.591			
A13	0.619	0.142	7.997	0.000
A14	0.711	0.152	8.689	0.000
A15	0.668	0.151	8.391	0.000
A16	0.425	0.148	6.021	0.000
SA2				
A17	0.558			
A18	0.776	0.152	8.722	0.000
A19	0.773	0.147	8.713	0.000
A20	0.568	0.142	7.356	0.000
SA3				
A1	0.713			
A2	0.788	0.086	11.173	0.000
A3	0.746	0.081	10.875	0.000

As shown in Table 12, it was determined that factor loads are between 0.425 and 0.788 and are statistically significant (p<0.05).

In Table 13, there is no statistically significant difference between average score of SA and its subdimensions according to gender (p>0.05).

Table 13. Independent t-test and one-way ANOVA results for statistical attitude scale

	SA1	SA2	SA3	SA
Gender				
Male*	3.30±0.93	3.20±1.02	3.24±1.21	3.25±0.78
Female*	3.26±0.82	3.22±0.89	3.41±1.05	3.28±0.72
t-test statistics	0.354	-0.160	-1.227	-0.353
p-value	0.723	0.873	0.221	0.724
Education				
Associate Degree*	3.22±0.87	3.12±0.97	3.21±1.10	3.18±0.75
Bachelor's Degree*	3.35±0.81	3.35±0.83	3.57±1.07	3.41±0.70
t-test statistics	-1.307	-2.229	-2.813	-2.584
p-value	0.192	0.027	0.005	0.010
Class				
1*	3.23±0.85	3.01±0.86	3.21±1.14	3.15±0.66
2*	3.31±0.89	3.30±1.01	3.35±1.06	3.32±0.83
3*	3.39±0.81	3.41±1.00	3.96±0.92	3.54±0.70
4*	3.19±0.78	3.40±0.75	3.27±1.10	3.28±0.71
F	0.567	3.407	4.745	2.843
p-value	0.637	0.018	0.003	0.038
LSD	-	1<2; 1<3; 1<4	1<3; 2<3; 4<3	1<3

* : Each value is expressed as mean±standard deviation.

It was determined that SA2 and SA3 subdimension average scores were statistically significant according to education status and class ($p<0.05$). Thus, average score of SA that has bachelor's degree education is higher than the student that has associate degree education. In addition, average score of 3rd class student is higher than other students. According to LSD post-hoc test results; it was seen that SA2 average score of the 1st class student is lower than 2nd, 3rd, 4th class students. SA3 average score of the 3rd class student is higher than 1st, 2nd, 4th class student (Table 13).

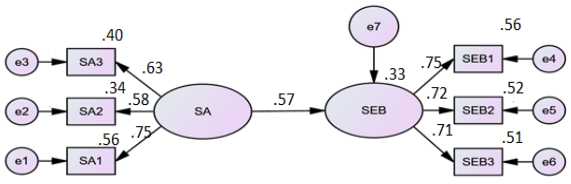

Figure 4. Path diagram.

To prove whether hypothesis test result is verified or not, path diagram was obtained (Figure 4). Correlation coefficients in the path analysis are a measurement of the linear correlations between variables. Research hypothesis is determined as "H_1: statistical attitude affects statistical self-efficacy belief positively". While SA is independent variable, SEB is determined as dependent variable. β is standardized value and hypothesis results are given in Table 14.

Table 14. Result of hypothesis test

Standardized β	*p*-value	accept/reject
0.572	0.000	accept

Hypothesis H_1: statistical attitude → statistical self-efficay belief

According to path analysis results; it is determined that SEB will increase as the coefficient value of SA increases (Table 14). Path coefficients between SA and sub-factors were obtained as 0.75 for SA1, 0.58 for SA2 and 0.63 for SA3. In addition, between SEB and sub-factors were determined as 0.75 for SEB1, 0.72 for SEB2 and 0.71 for SEB3. It was seen that these values are statistically significant ($p<0.05$). As a result of the analysis, standardized β coefficient that affects SEB of SA was determined as 0.572 ($p<0.05$). As a result of path analysis, it was seen that the 33% of the change in SEB is explained with SA.

4. Conclusion and Suggestions

In this study, SEB and SA were grouped under three theoretical dimensions and it was seen that structural models was statistically significant ($p<0.05$). SEB level was found not to be significant ($p>0.05$) in terms of gender, education status and class. However, it was seen that SA level was found not to be significant ($p>0.05$) in terms of gender but found to be significant ($p<0.05$) in terms of education status and class. Modified multi-factor first-order and multi-factor first-order models are proposed for SEB and SA, respectively. As a result of the path analysis, a positive and significant correlation was obtained between SEB and SA.

As a conclusion; it was concluded that students' having positive attitude towards statistics would affect their self-efficacy beliefs positively. University students' self-efficacy beliefs towards the statistics course and their attitudes can also explain the individual's perception of teaching practice along with his/her success in this course. Learning and being successful in statistics during their graduate education will guide them in scientific studies. It will also play an important role in their orientation towards advanced research. This study will be a guide for the factors that the lecturers who teach the statistics lesson should consider in their teaching. Thus, determining self-efficacy belief and attitude levels of students in statistics lesson and taking them into account in the regulation of educational activities will positively affect student achievement. In future studies, different models could be tested by determining a mediator variable between these two scales.

Contributions of the authors

The authors confirm that the contribution is equally for this paper.

Conflict of Interest Statement

There is no conflict of interest between the authors.

Statement of Research and Publication Ethics

The study is complied with research and publication ethics

References

[1] J. M. Shaughnessy and M. Pfannkuch, "How faithful is old faithful? statistical thinking: a story of variation and prediction," *Math. Teach.*, vol. 95, no.4, pp. 252–259, 2004.

[2] K. Makar and A. Rubin, "A framework for thinking about informal statistical inference," *Stat. Educ. Res. J.*, vol. 8, no. 1, pp. 82–105, 2022.

[3] A. Bandura, "Self-efficacy: toward a unifying theory of behavioral change," *Psychol. Rev.*, vol. 84, no. 2, pp. 191–215, 1977.

[4] B. Akkoyunlu, F. Orhan and A. Umay, "A study on developıng teacher self-efficacy scale for computer teachers," *Hacettepe Univ. J. Educ.*, vol. 29, no. 29, pp. 1-8, 2005.

[5] Z. Gan, G. Hu, W. Wang, H. Nang, and Z. An, "Feedback behaviour and preference in university academic English courses: associations with English language self-efficacy," *Assess. Eval. High. Educ.*, vol. 46, no. 5, pp. 740–755, 2021.

[6] M. B. Smith, Attitude Change International Encyclopedia of the Social Sciences. Crowell Collier and Mac Millan, 1968.

[7] E. Aydın and N. E. Sevimli, "An investigation of preservice mathematics teachers' self-efficacy beliefs and attitudes toward statistics," *Istanbul Sabahattin Zaim Univ. J. Fac. Educ*., vol. 1, no. 1, pp. 159–174, 2019.

[8] Z. Çam, K. Z. Deniz, A. Kurnaz, and L. Marten, "School burnout: Testing a structural equation model based on percieved social support, perfectionism and stress variables," *Educ. Sci*., vol. 39, no. 173, pp. 312–327, 2019.

[9] J. Ballantine, X. Guo, and P. Larres, "Psychometric evaluation of the Student Authorship Questionnaire: a confirmatory factor analysis approach," *Stud. High. Educ*., vol. 40, no. 4, pp. 596–609, 2015.

[10] M. Boyacı and M. B. Özhan, "The role of hope and family relations of school burnout among secondary school students: A structural equation modeling," *Educ. Sci*., vol. 43, no. 195, pp. 137-150, 2018.

[11] S. A. Kıray, İ. Çelik, and M. H. Çolakoğlu, "TPACK self-efficacy perceptions of science teachers: A structural equation modeling study," *Educ. Sci.*, vol. 43, no. 195, pp. 253-268, 2018.

[12] A. Ç. Kılınç, M. Polatcan, T. Atmaca, and M. Koşar, "Teacher self-efficacy and individual academic optimism as predictors of teacher professional learning: A structural equation modeling," *Educ. Sci.*, vol. 46, no. 205, pp. 373-394, 2020.

[13] M. Aydogmus, "Investigation of the effect of social entrepreneurship on professional attitude and self-efficacy perception: a research on prospective teachers," *Stud. High. Educ.*, vol. 46, no. 7, pp. 1462–1476, 2021.

[14] E. Aydın and N.E. Sevimli, "The adaptation of the "statistics self- efficacy scale to the Turkish," *J. Educ. Humanit*., vol. 8, no.16, pp. 44–57, 2017.

[15] S. J. Finney and G. Schraw, "Self-efficacy beliefs in college statistics courses," *Contemp. Educ. Psychol.*, vol. 28, no. 2, pp. 161–186, 2003.

[16] M. Yaşar, "İstatistiğe Yönelik Tutum Ölçeği: Geçerlilik ve Güvenirlik Çalışması," *Pamukkale Univ. J. Educ*., vol. 02, no. 36, pp. 59–59, 2014.

[17] T. Koparan, "Development of an attitude scale towards statistics: a study on reliability and validity," *Karaelmas J. Educ. Sci.*, vol. 3, pp. 76–86, 2015.

[18] A.Altunçekiç, S. Yaman and Ö. Koray, "The research on prospective teachers' selfefficacy belief level and problem solving skills," *Kastamonu Educ. J.*, vol. 13, no.1, pp. 93-102, 2005.

[19] E. Çakıroğlu and M. Işıksal, "Preservice elementary teachers' attitudes and self-efficacy beliefs toward mathematics," *Educ. Sci.*, vol. 34, no.151, pp. 132–139, 2009.
[20] İ. Uysal and S. Kösemen, "Analysis of the preservice teachers' general self-esteem beliefs," *J. Res. Educ. Teach.*, vol. 2, no. 2, pp. 217–226, 2013.
[21] R. Aydın, Y. E. Ömür and T. Argon, "Pre-service teachers' perception of self-efficacy and academic delay of gratification," *J. Educ. Sci.*, vol. 40, pp. 1–12, 2014.
[22] N. Gündüz, "An investigation of the relationship between statistical literacy of primary mathematics teachers and their attitudes towards statistics," MsC diss., Kocaeli University, Kocaeli. 2014.
[23] D. L. Bandalos, K. Yates, and T. Thorndike-Christ, "Effects of math self-concept, perceived self-efficacy, and attributions for failure and success on test anxiety," *J. Educ. Psychol*., vol. 87, no. 4, pp. 611–623, 1995.
[24] N. Girginer, A. G. Z. Kaygısız and A. G. A. Yalama, "Doğrusal olmayan kanonik korelasyon analizi ile istatistiğe yönelik tutumlarda üniversite öğrencileri arasındaki bireysel farklılıkların incelenmesi," *Istanbul Univ. Economet. Stat.*, vol. 6, pp. 29–40, 2007, (In Turkish).
[25] M. Eskici, "The effectiveness of statistic class averages unit teaching program," *Trakya J. Educ.*, vol. 3, no. 2, pp. 44–52, 2013.
[26] S. Salihova and V. Memmedova, "Students attitudes toward statistics lesson: validity and reliability study," *Academic Sight Int. Refer. Online J.*, vol. 59, pp. 116–127, 2017.
[27] E. Emmioglu Sarikaya, A. Ok, Y. Capa Aydin, and C. Schau, "Turkish version of the Survey of Attitudes toward Statistics: Factorial structure invariance by gender," *Int. J. High. Educ*., vol. 7, no. 2, p. 121, 2018.
[28] R. Alkan, "Reflections of different practices in introductory statistics courses on the changes in students' attitudes towards statistics," MsC diss., Tokat Gaziosmanpaşa University, Tokat, 2019.
[29] K. Sümbüloğlu and V. Sümbüloğlu, "Sağlık Bilimlerinde Araştırma Yöntemleri," Hatipoğlu Yayınevi, Ankara, 2013, (In Turkish).
[30] M. Norris and L. Lecavalier, "Evaluating the use of exploratory factor analysis in developmental disability psychological research," *J. Autism Dev. Disord.*, vol. 40, no. 1, pp. 8–20, 2010.
[31] Ö. Çokluk, G. Şekercioğlu, Ş. Büyüköztürk, "Sosyal Bilimler İçin Çok Değişkenli İstatistik SPSS ve LISREL Uygulamaları," Pegem Akademi Yayıncılık, Ankara, 2012.
[32] B. M. Byrne, Structural equation modeling with AMOS: Basic concepts, applications, and programming, third edition, 3rd ed. London, England: Routledge, 2016.
[33] H. Ayyıldız and E. Cengiz, "Pazarlama modellerinin testinde kullanılabilecek yapısal eşitlik modeli (YEM) üzerine kavramsal bir inceleme," *Süleyman Demirel Üniversitesi İktisadi ve İdari Bilimler Fakültesi Dergisi*, vol. 11, no. 2, pp. 67-80, 2006.
[34] S. Saraçlı and A. Erdoğmuş, "Determining the effects of information security knowledge on information security awareness via structural equation modelings," *Hacet. J. Math. Stat.*, vol. 48, no. 4, 2018.
[35] G. G. Şimşek and F. Noyan, "Structural equation modeling with ordinal variables: a large sample case study," *Qual. Quant*., vol. 46, no. 5, pp. 1571–1581, 2012.
[36] V. Yilmaz and E. Ari, "The effects of service quality, image, and customer satisfaction on customer complaints and loyalty in high-speed rail service in Turkey: a proposal of the structural equation model," *Transp. Sci*., vol. 13, no. 1, pp. 67–90, 2017.
[37] K. A. Bollen, Structural Equations with Latent Variables: Bollen/structural equations with latent variables, 1st ed. Nashville, TN: John Wiley & Sons, 2014.
[38] M. E. Civelek, "Essentials of Structural Equation Modeling," Zea E-Books, 2018.
[39] C. Lleras, "Path analysis," Encyclopedis of Social Measurement, vol. 3, pp. 25-30, 2005.
[40] Ö. İ. Güneri, A. Göktaş, and U. Kayalı, "Path analysis and determining the distribution of indirect effects via simulation," *J. Appl. Stat.*, vol. 44, no. 7, pp. 1181–1210, 2017.
[41] K. Schermelleh-Engel, H. Moosbrugger and H. Muller, "Evaluating the fit of structural equation models: tests of significance and descriptive goodness-of-fit measures," *Meth. Psychol. Res. Online*, vol. 8, no. 2, pp. 23–74, 2003.

Bitlis Eren Üniversitesi Fen Bilimleri Dergisi
BİTLİS EREN UNIVERSITY JOURNAL OF SCIENCE
ISSN: 2147-3129/e-ISSN: 2147-3188
VOLUME: 11 NO: 3 PAGE: 846-856 YEAR: 2022
DOI: 10.17798/bitlisfen.1126615

The Mechanical and Thermal Behavior of Electrostatic Powder Coating Waste Reinforced Epoxy Composites

Akar DOĞAN[1,2*], Yılmaz KISMET[2]

[1]*Munzur University, Rare Earth Elements Application and Research Centre, Tunceli, Turkey*
[2]*Munzur University, Engineering Faculty, Department of Mechanical Engineering, Tunceli, Turkey*
(ORCID: 0000-0002-6788-1629) (ORCID: 0000-0003-3145-6214)

Keywords: Waste utilization, Epoxy, Composite, TGA, Mechanical Properties.

Abstract

The present study investigates the mechanical and thermal behavior of polyurethane electrostatic powder coating waste reinforced epoxy composites. Different percentages of electrostatic powder coating waste (3, 6, and 9 wt. %) reinforced epoxy composites were manufactured. The mixture of polyurethane powder coating waste and epoxy was mixed with a magnetic stirrer to ensure that the polyurethane powder coating waste was dispersed well in the epoxy, and then the mixture was placed under vacuum and air bubbles were removed. Tensile and three-point tests were performed to determine the changes in the mechanical properties of the materials, and thermogravimetric analysis was conducted to determine the thermal properties. In addition, images were taken with scanning electron microscopy for morphological features. The study revealed that the three-point flexural strength was increased by up to 8% and 15%, respectively, in the samples with 3 wt% and 6 wt% powder coating waste additives. The material's tensile strength decreased by up to 27% with powder coating waste reinforcement. However, the opposite trend was observed in the modulus of elasticity. Additionally, no significant difference was observed in the thermal properties of the materials. Also, from scanning electron microscopy analysis, it was observed that the inclusion of powder coating waste changed the damage mechanism of the material.

1. Introduction

In recent years, composite materials compared to traditional materials such as steel and aluminum have received considerable attention. Polymer matrix composites have replaced most traditional metals in numerous applications, mainly due to their advantages such as lightness, high stiffness, and high strength. Epoxy resins are thermoset polymer materials commonly used in polymer matrix composites. Epoxy resins have been around for nearly half a century. They are the most preferred high-performance thermosetting resins due to their properties such as low curing shrinkage, no volatile matter during curing, high strength, high durability, high adhesion capability, corrosion, and chemical resistance [1,2]. Many reinforcement materials, such as glass fiber and carbon fiber, are frequently used in epoxy polymer matrix composites. In addition, many researchers have carried out studies on natural fibers due to sustainability and cost concerns [3,4].

Recently, with the rapid growth of the industrial sector, many by-products have been produced and waste material has emerged, which has become a major problem [5,6]. For this reason, many researchers have turned their attention to the use of waste materials as reinforcement materials in polymer matrices. Disposal of processing waste is a difficult and costly task for industries. Due to strong environmental safety regulations and awareness, researchers are increasingly seeking new ideas for using industrial wastes such as fly ash, carbon black, metal, and powder coatings to manufacture polymer composites and other industrial applications [7,8].

*Corresponding author: akardogan@munzur.edu.tr
Received: 06.06.2022, Accepted: 23.09.2022

Babu et al. [8] collected waste wear debris during the processing of metallic materials, used it as reinforcement in epoxy material, and characterized it using EDS analysis. The physical, tribological, and viscoelastic behaviors of the prepared composites were evaluated using various tests, and the results were compared with pure epoxy. Ray and Gnanamoorthy [9] investigated the wear behavior of fly ash-filled vinyl ester matrix composites and pure resin. Wear behavior was investigated in weight loss, linear wear, and friction coefficient, and wear mechanisms under abrasive conditions were reported. Panchal et al. [10] investigated the effect of different environmental conditions on the erosion rate of eggshell reinforced epoxy composite. In another study, Ribeiro et al. [11] investigated the mechanical properties of polyester polymer reinforced with glass fiber reinforced plastic wastes obtained from shredding and grinding processes at different rates. Soharu et al. [12] examined the use of concrete waste debris for the manufacturing of fly ash bricks as a sustainable material.

Today, electrostatic powder paints are widely used. As the name suggests, the electrostatic powder coating technique is based on coating electrically conductive materials with powder coating [13,14]. These powder paints, produced by the extrusion method, are sprayed onto the material to be coated electrostatically with a spray gun. Due to the electrostatic attraction force between the material and the powder paint particles, the powder paint particles cling to the surface of the material. With this technique, even materials with very complex geometries can be easily coated to form a film of the desired thickness. However, the disadvantage of this method, which provides a great advantage, is that losses occur during coating. Kismet [13] stated that while a loss of approximately 30-35% occurs in each application in small and medium-sized coating companies, around 5% of waste occurs in mass production coating applications. These waste materials are disposed of by burning. However, researchers, after hydrolyzing this waste element, used it as a reinforcement element in thermoplastic materials such as PP [15], LLDPE [16], PA6 and POM [13], Acetal copolymers [17], and LDPE [18], and examined them thermally, mechanically, and morphologically.

Despite the relatively large amount of research on the use of recycled waste in polymer-based composite materials, no studies have focused on using electrostatic powder coating waste as additives in thermoset polymer materials. Therefore, this study explored a potential waste management solution for thermosetting polymer-based composite materials using powder coating waste as reinforcement or filler. For this reason, composite materials were produced using electrostatic powder coating wastes in different weight ratios in epoxy resin, which is in the thermoset polymer family, as reinforcement material. Pure, 3%, 6%, and 9% powder coating waste reinforced epoxy materials were produced and compared to the tensile test, three-point bending test, thermogravimetric analysis (TGA) results, and scanning electron microscope (SEM) images of the materials.

2. Material and Method

2.1. Material Production

This study used polyurethane (P-Pur) powder coating wastes as reinforcement material. These powder coating wastes were first hydrolyzed using water and alcohol, and thus, the brittle wastes took on a more ductile and elastic structure. Water and trace amounts of alcohol to be used for hydrolysis were mixed for approximately 30 minutes in a magnetic stirrer at room temperature. Powder coating wastes were added to this prepared mixture liquid in a one-to-one ratio. For hydrolysis, the waste materials were kept in the mixing liquid for 60 minutes at approximately 100 °C. The alcohol in the mixing liquid allows all surfaces of the powder coating wastes to be completely hydrolyzed with water. The powder coating wastes, whose structure was changed due to the hydrolysis process, were left to dry at room temperature for 24h and then ground into a powder [14]. The scanning electron microscope (SEM) image of the polyurethane powder coating waste (Pur-PCW) is given in Figure 1.

A two-component epoxy material system consisting of F-1564 FIBERMAK epoxy and hardener was used as the matrix material. The manufacturer recommends the ratio of epoxy and hardener as 3/1. The ratio of polyurethane powder coating waste used as reinforcement was chosen as 3%, 6%, and 9% by weight. As a result of the tests performed, a higher waste ratio was not used because the mechanical properties of the samples reinforced with 9% by weight of polyurethane powder coating wastes were observed to decrease significantly. First of all, the required amount of epoxy-hardener and polyurethane powder coating wastes were taken into a container and mixed with a magnetic stirrer at 30 °C and 100 rpm for 60 minutes to obtain the desired mixture. In the next step, the mixture was kept under a vacuum for 20 minutes to remove the air bubbles in

the mixture. After the vacuum process, the mixture was poured into molds produced for tensile and bending specimens. Then, the materials poured into the molds were cured at room temperature for 48 hours and cured in an oven at 80 °C for 4 hours. This process has been applied to all materials, and the production steps are shown in Figure 2.

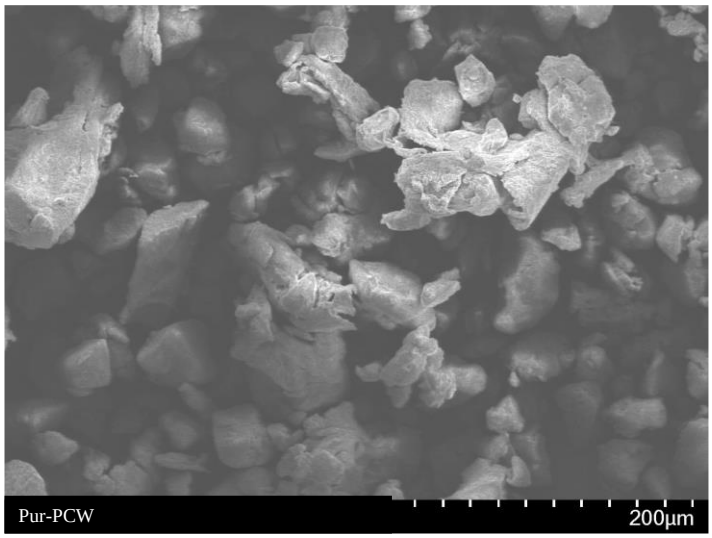

Figure 1. SEM image of polyurethane powder coating waste

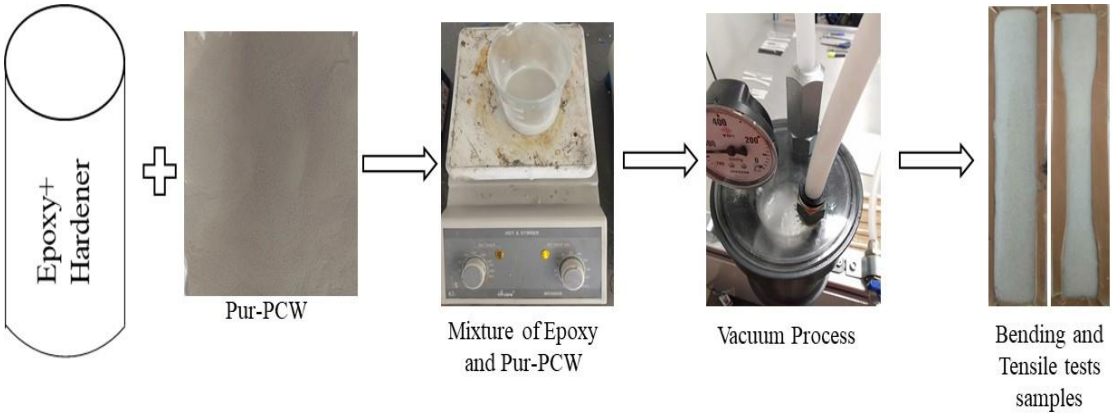

Figure 2. Production of Pur-PCW reinforced Epoxy composite

2.2. Tensile Test

For the tensile test specimens, molds were prepared in a three-dimensional printer following the ASTM D-638 [19] test standard and then covered with adhesive Teflon tape. The dimensions of tensile test specimens are given in Figure 3. Tensile tests were carried out in a Shimadzu brand AG-IC model universal tensile testing device with a load capacity of 100 kN in the mechanical engineering laboratory of Munzur University. The tensile test speed was chosen as 2 mm/min. Figure 4 shows the image taken during the tensile test. The tensile tests were repeated at least 4 times for each material type, and the tensile strength, elasticity modulus, and maximum elongation values of the materials were obtained.

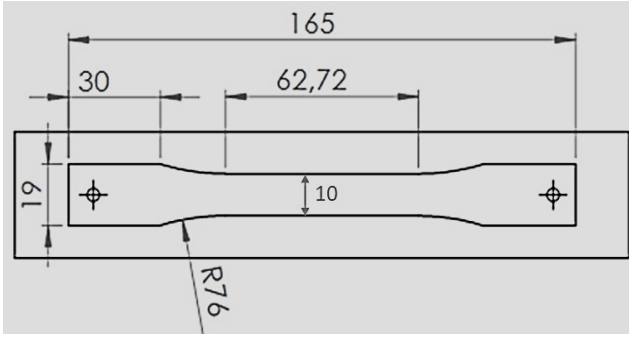

Figure 3. Dimensions of Tensile test samples (Dimension in mm)

Figure 4. Tensile test sample and apparatus

2.3. Three-Point Bending Test

For three-point bending tests, molds with 80 mm in length, 10 mm in width, and 4 mm in depth were prepared, and test specimens were prepared. In addition, three-point bending tests were performed with a Shimadzu brand AG-IC model universal tensile testing device with a load capacity of 100 kN in the mechanical engineering laboratory of Munzur University, as in the tensile tests. Figure 5 shows the three-point bending test specimen and test apparatus. The distance between the supports is 64 mm, and the support diameters are 10 mm. Three-point bending tests were performed at a speed of 1 mm/min and were repeated at least 3 times for each material group. Thanks to this test, the material's bending strength and deflection values were obtained and are given in the result section.

2.4. Thermogravimetric analysis TGA / DTA

TGA/DTA analyses of the samples were carried out using a Shimadzu brand "DTG 60" model device to determine the thermal behavior of the hydrolyzed polyurethane powder coating waste reinforced epoxy materials. Results are reported for the pure sample and reinforced by weight filler with 3%, 6%, and 9%. The changes in the mass of the materials were investigated depending on the temperature change. The samples were heated from room temperature to 600 ^{o}C with a temperature gradient of 10 ^{o}C/min, and the measurements were made under air atmosphere. The mass losses that occur with the increase in temperature are shown with graphics.

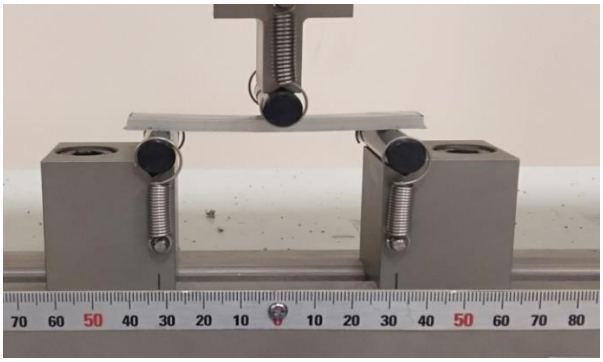

Figure 5. Three-point bending test sample and apparatus

3. Results

3.1. Tensile Test Results

The stress-strain curves obtained during the tensile test are given in Figure 6. As stated above, the tensile test for each material was repeated at least 4 times. The curves given here are those closest to the average of the curves obtained during the tensile test. As can be seen in the figure, the percentage elongation of the materials decreased sharply with the increase of the reinforcement material. Likewise, a decrease in the stress values occurred with the increase in reinforcement material. The linear region, in other words, the Hooke region, gives the material's modulus of elasticity. Here, between 0 and 20 MPa can be considered the elastic region. Looking at the curves, the slope of the curves has increased with the increase of the reinforcement material. Thus, the elastic modulus of the materials has increased with the reinforcement material. Also, the mean values and standard deviations are shown in Table 1. In addition, images of damaged samples obtained at the end of the tensile test are given in Figure 7.

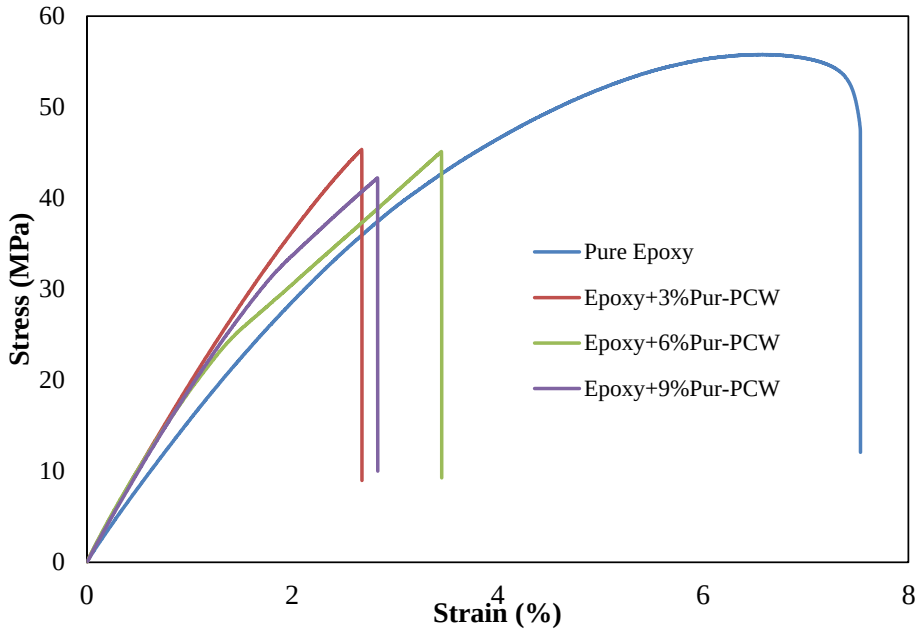

Figure 6. Stress-Strain curves of samples under tensile tests

Figure 7. Images of samples subjected to tensile test

Table 1. Mechanical properties obtained as a result of the tensile test

	Tensile Strength (MPa)	Standard Deviation	Maximum Strain (%)	Standard Deviation	Elastic Modulus (MPa)	Standard Deviation
Pure Epoxy	56.10	0.95	7.56	0.06	1520	15
Epoxy + 3% Pur-PCW	42.86	1.15	2.72	0.09	1812	27
Epoxy + 6% Pur-PCW	44.96	1.54	3.29	0.32	1773	30
Epoxy + 9% Pur-PCW	40.66	1.85	2.74	0.44	1696	46

As seen in Table 1, the tensile strength of pure epoxy material was 56.10 MPa, while the tensile strength of 3%, 6%, and 9% Pur-PCW reinforced epoxy materials was 42.86, 44.96, and 40.66 MPa, respectively. Compared to the pure epoxy material, the tensile strength of the 3% Pur-PCW reinforced material decreased by approximately 23%. Also, the decrease in tensile strength of 6% and 9% Pur-PCW reinforced materials was determined as 20% and 27% compared to pure epoxy material. Similar to the tensile strength, the maximum strain values decreased with the increase of reinforcement material. The maximum strain rates of pure, 3%, 6%, and 9% Pur-PCW reinforced epoxy material were measured at 7.56, 2.72, 3.29, and 2.74, respectively. However, the elasticity modulus of samples increased with the increase of reinforcement material. While the modulus of elasticity of pure epoxy was 1520 MPa, the modulus of elasticity of 3%, 6%, and 9% Pur-PCW reinforced materials were obtained as 1812, 1773, and 1696 MPa, respectively. Dao et al. [20] investigated the mechanical properties of the cerium oxide reinforced epoxy material and obtained similar results. As the porous structure increases due to air gaps and interfacial adhesion defects in particle reinforced composite materials, ductility and strength decrease. For highly porous materials, the tensile stress is below the yield strength. Also, the strain value decreases [21]. Another reason for this decrease is the weak interface adhesion strength between the additives and the matrix material [22].

In Figure 8, SEM images of the damaged surfaces formed after the tensile test are given. As can be seen from the figure, the pores and voids increased with reinforcement material, especially in the 9% Pur-PCW reinforced material. Rana et al. [23] stated that the interface is the weakest phase in composite materials. With the increase of reinforcement, the interface area increased, which caused a decrease in the tensile strength [24]. Poor interfacial bonding creates partially separated micro-voids, which inhibits tension propagation between the reinforcement material and the matrix [25]. As the reinforcement material increases, the degree of this obstacle increases, increasing the material's stiffness [7,8]. The increase in the modulus of elasticity can be explained by the above case.

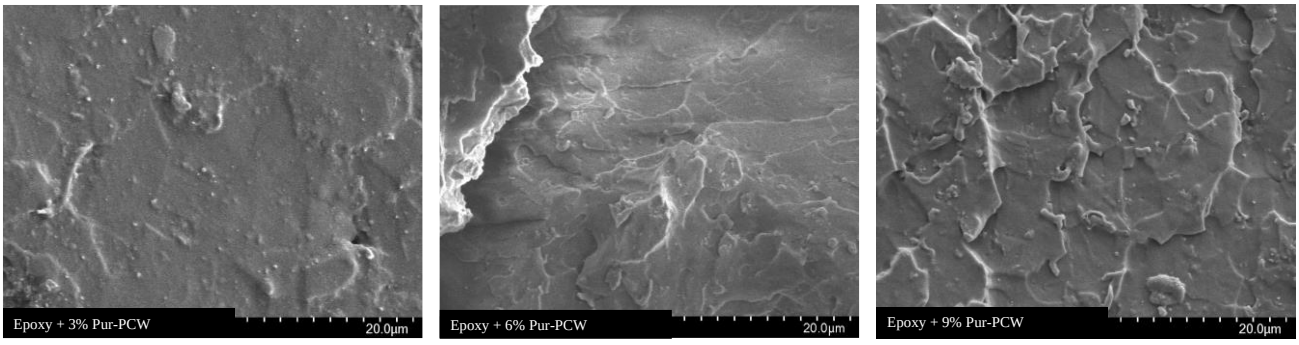

Figure 8. SEM images of the damaged surfaces obtained after the tensile test

3.2. Three-Point Bending Test Results

The stress-strain curves obtained by the three-point bending test of the materials are given in Figure 9. As seen in the figure, the maximum stress value of the 3% Pur-PCW reinforced epoxy material increased slightly. The increase in maximum stress is visible when the reinforcement material is increased to 6%. However, the maximum stress value of 9% Pur-PCW reinforced epoxy material is lower than that of pure epoxy material. Therefore, epoxy materials reinforced with a higher rate of reinforcement material were not produced. Despite the increase in the maximum stress, the deflection values of all Pur-PCW reinforced samples decreased compared to pure epoxy. While the deflection value of pure epoxy material is approximately 19 mm, this value is 13, 14.5, and 9 mm for 3%, 6%, and 9% reinforced epoxy materials, respectively. Figure 10 shows the variation of the average values of three-point flexural strengths with the reinforcement material. The flexural strength of pure epoxy is 101 MPa, while it is 109 MPa for 3% reinforced material and 116 MPa for 6% reinforced material. The flexural strength of 3% and 6% Pur-PCW reinforced samples has increased by 8% and 15% compared to pure epoxy, respectively. However, the flexural strength of 9% Pur-PCW reinforced epoxy samples was measured at 91 MPa, decreased by approximately 10% compared to pure epoxy material. When the standard deviation values were examined, it was observed that this value increased with the increase of the reinforcement material.

Similar results were seen in the mechanical properties of powder coating waste reinforced polyolefin materials investigated by Kısmet [15]. Increasing the reinforcement material increases the interfacial adhesion zone between the matrix-reinforcing material. Thus, possible interfacial adhesion defects increase, and the homogeneous distribution of the reinforcement material in the matrix material decreases. In addition, images of damaged samples obtained at the end of the three-point bending tests are given in Figure 11.

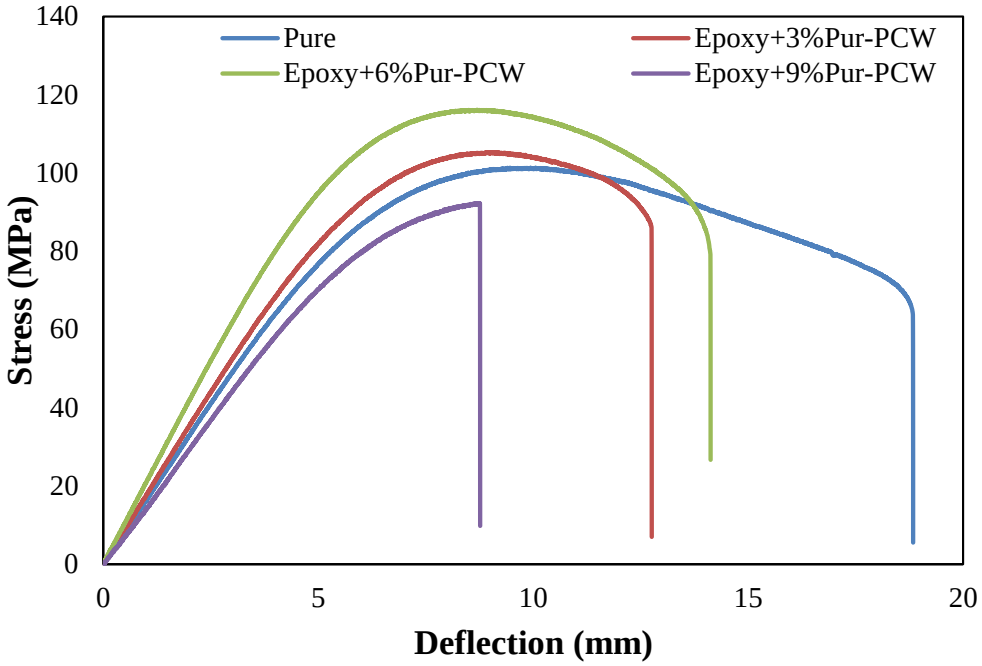

Figure 9. Stress-deflection curves of Three-Point bending tests

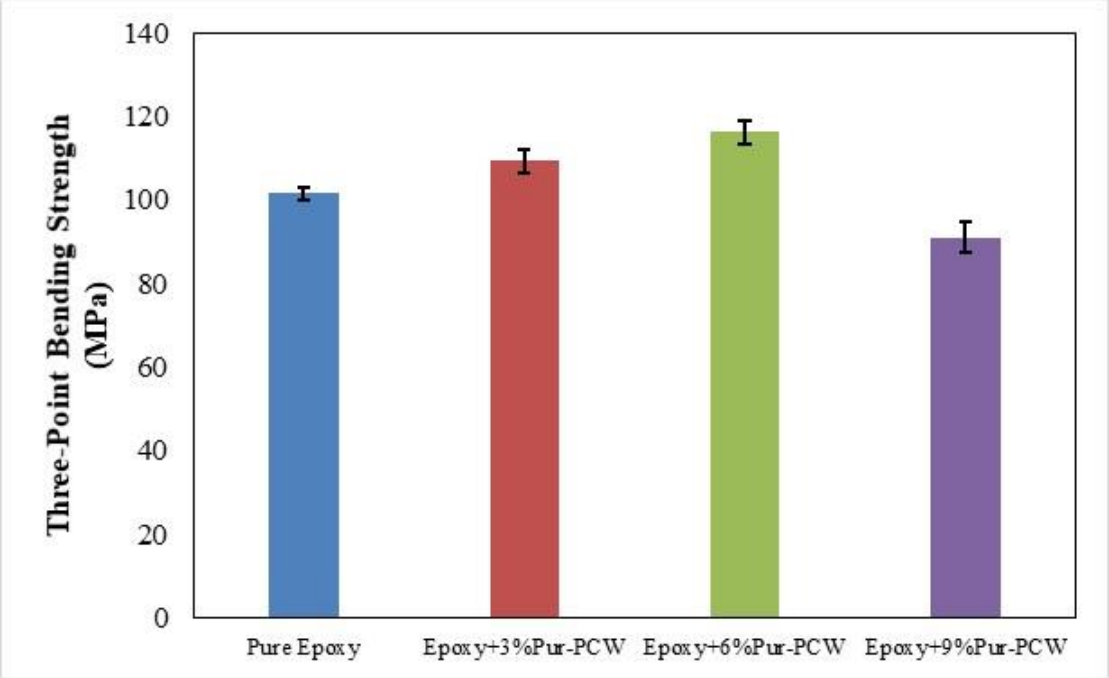

Figure 10. Variation of Bending Strength with reinforcement material

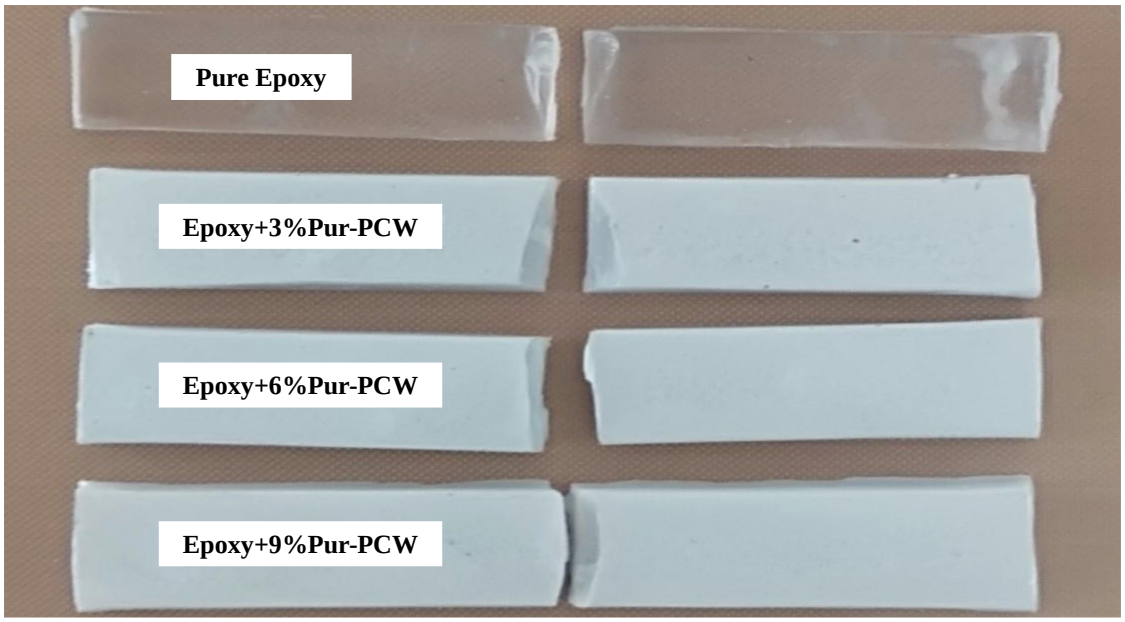

Figure 11. Images of samples subjected to Three-Point bending test

3.3. Thermogravimetric analysis TGA / DTA

One of the most important methods for investigating the thermal stability of materials is thermo-gravimetric analysis (TGA). In this analysis, the variation of the mass-loss with temperature increase is used to determine the materials' thermal stability. Pure epoxy and hydrolyzed powder coating waste reinforced epoxy materials at different weight ratios were subjected to TG analysis, and the graphs obtained are shown in Figure 12. In this TG analysis, the exothermic direction is upwards. From graphs, for pure epoxy and reinforced epoxy materials, thermal degradation does not occur before 270 ºC. The weight loss (1-1.5%) before this temperature is due to the evaporation of moisture from the surface [26-27]. When TGA curves are examined, it is seen that thermal degradation occurs in three steps. A mass loss of about 8% occurred in all materials when the temperature was increased from 270 ºC to 350 ºC. At this step, it can be concluded that weak bonds in the polymer are affected, and there is a low heat output. The second step ends at 460 ºC with a mass loss of 58%, and the third step ends at 600 ºC with a mass loss of 27%. In the first stage, the decomposition rate of the epoxy cross linking network of the resin chain is much higher than carbon-carbon bond breaking. An increase in activation energies and decomposition entropies has been observed in the second stage since the decay rate will be much higher in the second stage. A similar trend in the first phase was also observed in the final phase [28]. As shown in the DTA curves, heat energy passed from the materials to the environment at 360 ºC, forming an exothermic peak. When thermoset materials cure, that is, when they harden, they release heat energy due to reactions. Above this temperature, it is seen that a rapid deterioration occurs in the material by absorbing heat energy from the environment up to 460 ºC. Considering the degradation rate of the materials, it is seen that there is no significant difference, and the deterioration trend is the same.

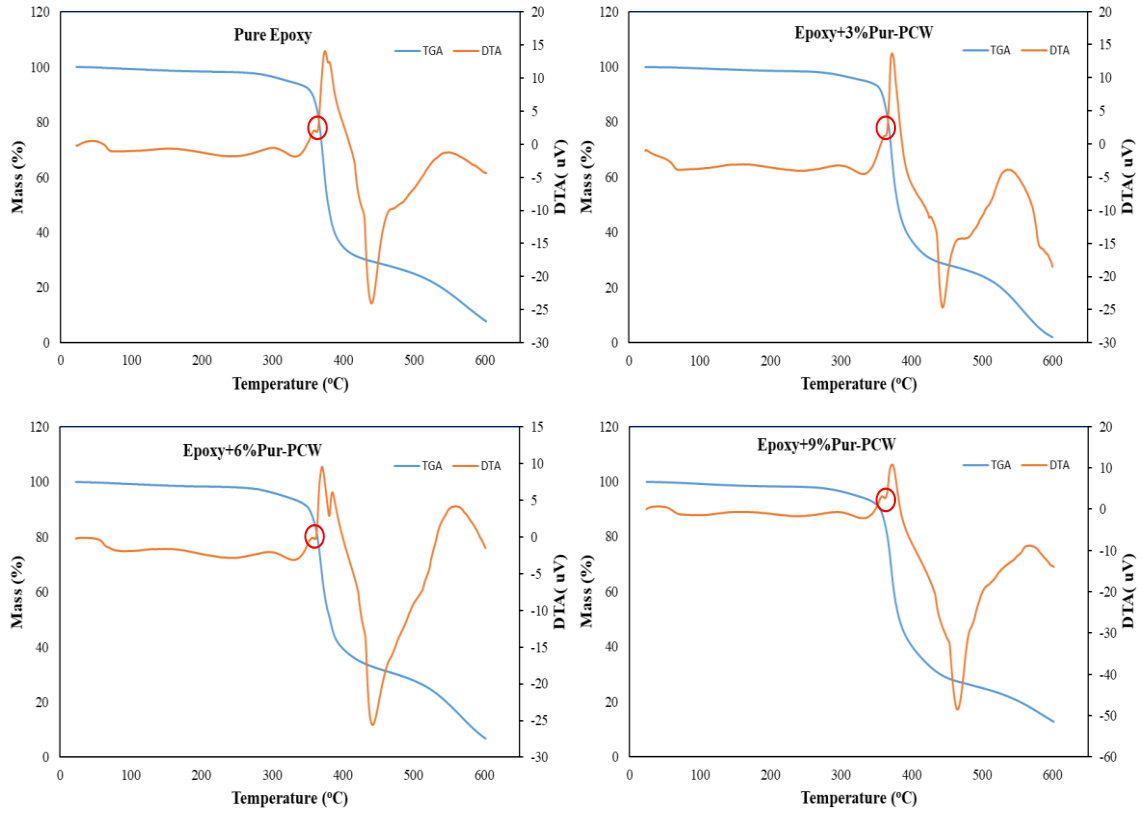

Figure 12. TGA (Blue) and DTA (Yellow) curves of materials

.

4. Conclusion

In this study, various experiments were carried out to determine the mechanical and thermal behavior of electrostatic powder coating waste reinforced epoxy material. The epoxy materials that were reinforced with three different rates of powder coating waste were produced. Tensile test, three-point bending test, and thermogravimetry analysis were performed. Based on the results obtained, the following conclusions can be drawn:

- A decrease was observed in the tensile strength and elongation values of epoxy materials reinforced with electrostatic powder coating waste compared to pure epoxy material. However, there was an increase in the modulus of elasticity.
- Compared to pure epoxy material, it was observed that there was a significant improvement in the three-point bending strength of epoxy materials reinforced with 3% and 6% electrostatic powder coating waste. However, a significant decrease in strength value occurred when the reinforcement material was increased to 9%.
- In the results of TGA and DTA analyses performed on pure and electrostatic powder coating waste reinforced thermoplastic materials, it can be said that the reinforcement element does not have any negative effect on thermal stability in these thermoset composites.

The findings of this study showed a suitable technological option for the disposal of powder coating waste by using thermoset polymer materials. Thus, it will allow the temporary recycling of powder coating wastes and their use in the production of epoxy-based products. However, the mechanical properties of this composite material can be improved by applying various improvements to increase the interfacial adhesion to the electrostatic powder coating waste.

Contributions of the Authors

All authors contributed equally.

Conflict of Interest Statement

There is no conflict of interest between the authors.

Statement of Research and Publication Ethics

The study is complied with research and publication ethics

References

[1] A.H. Karle, M.R Nukulwar, V.B. Tungikar, "Evaluation of mechanical and thermal properties of epoxy composites reinforced with CaSiO3 particulate fillers*," Materials Today: Proceedings*, vol. 46, pp. 325-330, 2021.

[2] A. Dogan, "Single and repeated low-velocity impact response of E-glass fiber-reinforced epoxy and polypropylene composites for different impactor shapes," *Journal of Thermoplastic Composite Materials*, vol. 35, no. 3, pp. 320-336, 2022.

[3] Y. Kısmet, A. Dogan, "Characterization of the mechanical and thermal properties of rape short natural-fiber reinforced thermoplastic composites*," Iranian Polymer Journal*, vol. 31, no. 2, pp. 143-151, 2022.

[4] O. Faruk, A.K. Bledzki, H.P. Fink, M. Sain, "Biocomposites reinforced with natural fibers: 2000–2010," *Progress in Polymer Science*, vol. 37, no. 11, pp. 1552-1596, 2012.

[5] A. Erdoğan, M.S. Gök, V. Koc, A.Günen, "Friction and wear behavior of epoxy composite filled with industrial wastes," *Journal of Cleaner Production*, vol. 237, 117588, 2019.

[6] S. Singh, S. Ramakrishna, M.K. Gupta, "Towards zero waste manufacturing: A multidisciplinary review," *Journal of Cleaner Production, vol.* 168, pp. 1230-1243, 2017.

[7] T. Väisänen, A. Haapala, R. Lappalainen, L. Tomppo, "Utilization of agricultural and forest industry waste and residues in natural fiber-polymer composites: A review," *Waste Management*, vol. 54, pp. 62-73, 2016.

[8] N.B. Karthik Babu, T. Ramesh, S. Muthukumaran, "Physical, tribological and viscoelastic behavior of machining wear debris powder reinforced epoxy composites," *Journal of Cleaner Production*, vol. 272, 122786, 2020.

[9] D. Ray, R. Gnanamoorthy, "Friction and wear behavior of vinylester resin matrix composites filled with fly ash particles," *Journal of Reinforced Plastics and Composites*, vol. 26, no. 1, pp. 5-13, 2007.

[10] M. Panchal, G. Raghavendra, M.O. Prakash, S. Ojha, "Effects of environmental conditions on erosion wear of eggshell particulate epoxy composites," *Silicon*, vol. 10, no. 2, pp. 627-634, 2018.

[11] M.C.S. Ribeiro, A. Fiúza, A.C.M. Castro, F.G. Silva, M.L. Dinis, J.P. Meixedo, M.R. Alvim, "Mix design process of polyester polymer mortars modified with recycled GFRP waste materials," *Composite Structure*, vol. 105, pp. 300-310, 2013.

[12] A.Soharu, B.P. Naven, A. Sil, "Fly ash bricks development using concrete waste debris and self-healing bacteria," *J Mater Cycles Waste Manag*, vol. 24, no. 3, pp. 1037-1046, 2022.

[13] Y. Kısmet, "Investigation of the changes in melt flow indexes (MFI) and densities of polyamide 6 (PA6) and polyoxymethylene (POM) related with hydrolyzed powder coating waste amount," *Pamukkale University Journal of Engineering Sciences*, vol. 22, no. 4, pp. 241-245, 2016.

[14] Y. Kismet, "Entwicklung eines Verfahrens für die Verwertung von Pulverlackrecyclaten," Ph.D. dissertation, Universitätsverlag der TU Berlin, Berlin, Germany, 2012.

[15] Y. Kismet, "Change of mechanical properties of powder recyclate reinforced polyolefin based on gamma radiation," *Polymers*, vol. 9, no. 9, 384, 2017.

[16] Y. Kismet, M.H. Wagner, "Enhancing the potential of employing thermosetting powder recyclates as filler in LLDPE by structural modifications," *Journal of Polymer Engineering*, vol. 37, no. 3, pp. 287-296, 2017.

[17] Y. Kismet, M.H. Wagner, "Mechanical, thermal, and morphological properties of powder coating waste reinforced acetal copolymer," *Polymer Testing*, vol. 82, 106322, 2020.

[18] Y. Kismet, A. Dogan, M.H. Wagner, "Thermoset powder coating wastes as filler in LDPE–Characterization of mechanical, thermal and morphological properties," *Polymer Testing*, vol. 93, 106897, 2021.

[19] Standard Test Method for Tensile Properties of Plastics, ASTM D-638, 2014.

[20] N.N. Dao, M. Dai Luu, Q.K. Nguyen, B.S. Kim, "UV absorption by cerium oxide nanoparticles/epoxy composite thin films," *Advances in Natural Sciences: Nanoscience and Nanotechnology*, vol. 2, no. 4, 045013, 2011.

[21] D. Bourell, J.P. Kruth, M. Leu, G. Levy, D. Rosen, A.M. Beese, A. Clare, "Materials for additive manufacturing," *CIRP annals*, vol. 66, no 2, pp. 659-681, 2017.

[22] X. Zhang, G. Liao, Q. Jin, X. Feng, X. Jian, "On dry sliding friction and wear behavior of PPESK filled with PTFE and graphite," *Tribology International*, vol. 41, no. 3, pp. 195-201, 2008.

[23] S. Rana, M. Hasan, M.R.K. Sheikh, A.N. Faruqui, "Effects of aluminum and silicon carbide on morphological and mechanical properties of epoxy hybrid composites," *Polymers and Polymer Composites*, vol. 30, 09673911211068918, 2022.
[24] S. Afsara, M. Hasan, "Effect of peacock feather and rose stem fibre hybridisation on mechanical properties of polystyrene composites," *Advances in Materials and Processing Technologies*, pp.1-14, 2020.
[25] H.S. Yang, H.J. Kim, H.J. Park, B.J. Lee, T.S. Hwang, "Water absorption behavior and mechanical properties of lignocellulosic filler–polyolefin bio-composites," *Composite Structures*, vol. 72, no. 4, pp. 429-437, 2006.
[26] Y.Q. Li, S.Y. Fu, Y.W. Mai, "Preparation and characterization of transparent ZnO/epoxy nanocomposites with high-UV shielding efficiency," *Polymer*, vol. 47, no. 6, pp. 2127-2132, 2006.
[27] M.K. Lila, G.K. Saini, M. Kannan, I. Singh, "Effect of fiber type on thermal and mechanical behavior of epoxy based composites," *Fibers and Polymers*, vol. 18, no. 4, pp. 806-810, 2017.
[28] S.A. Al-Bayaty, N.J. Jubier, R.A. Al-Uqaily, "Study of Thermal Decomposition Behavior and Kinetics of Epoxy/Polystyrene Composites by using TGA and DSC," *Journal of Xian University of Architecture & Technology*, vol. 12, no. 3, pp. 1331-1341, 2020.

Bitlis Eren Üniversitesi Fen Bilimleri Dergisi
BİTLİS EREN UNIVERSITY JOURNAL OF SCIENCE
ISSN: 2147-3129/e-ISSN: 2147-3188
VOLUME: 11 NO: 3 PAGE: 857-860 YEAR: 2022
DOI: 10.17798/bitlisfen.1128254

An Effective Numerical Technique for Boundary Value Problems Arising from an Adiabatic Tubular Chemical Reactor Theory

Soner AYDINLIK[1*]

[1]*Dogus University, Faculty of Engineering, Department of Software Engineering*
(ORCID: 0000-0003-0321-4920)

Keywords: Fibonacci collocation method, Chemical reactor, Accuracy.

Abstract
Mathematical models for an adiabatic tubular chemical reactor which forms an irreversible exothermic reaction are investigated by an efficient numerical technique, Fibonacci Collocation method. The reaction's steady-state temperature is calculated for several values of three parameters, namely, Peclet and Damkohler numbers and the dimensionless adiabatic temperature increment. When the generated outcomes are compared with the other numerical approaches, it has been sighted that the presented method produces reliable results for this type of problems.

1. Introduction

It is presented a model for an irreversible exothermic reaction produced by an adiabatic tubular chemical reactor [1]. This model can be turned into a BVP of second order [2], as shown below,

$$\begin{cases} y''(x)-\lambda y'(x)+\lambda\mu\left(\beta-y(x)\right)e^{y(x)}=0 \\ y'(0)-\lambda y(0)=0, \quad y'(1)=0, \end{cases} \tag{1}$$

where y is the reaction's steady-state temperature, λ is Peclet number, μ is the Damkohler number and β is the adiabatic temperature increase with no dimensions. The existence of the numerical solutions to (1) for a specific range has been demonstrated by the authors [2]-[3]. In recent years, this equation has been dealt with many numerical methods [4]-[11].

In this study, the problem (1) is solved by Fibonacci collocation method [12]-[15]. Numerical illustrations are carried out to validate the accuracy of the proposed numerical scheme. The reaction's steady-state temperature is calculated for several values of λ, μ and β. The obtained numerical outcomes are compared with the well-known numerical approaches and it has been shown that the results reflect the adequacy of the method and give high accuracy.

The outline of the paper is as follows: In Section 2, Fibonacci collocation method is presented. Section 3 is devoted to the applications of the method for the Adiabatic Tubular Chemical Reactor problem. The conclusions are given in Section 4.

2. Fibonacci Collocation Method

The approach to a function can be suggested with the help of Fibonacci polynomials [16]-[17] as,

$$y(x)\cong y_N(x)=\sum_{n=1}^{N+1} c_n\, F_n(x) \tag{2}$$

where N indicates the approximation polynomial's order. Fibonacci polynomials are identified as

$$F_n(x)=\sum_{k=0}^{n} F(n,k)x^k \tag{3}$$

here, $F(n,k)=\begin{pmatrix} n+k-1 \\ 2 \\ k \end{pmatrix}$. The recurrence relationship is,

*Corresponding author: saydinlik@dogus.edu.tr
Received: 09.06.2022, Accepted: 22.09.2022

$$\begin{aligned} &F_1 = 1, \\ &F_2 = x, \\ &\vdots \\ &F_n(x) = x\,F_{n-1}(x) + F_{n-2}(x) \quad n \geq 3. \end{aligned} \tag{4}$$

(2) can be expressed as a matrix form,

$$y_N(x) = \mathbf{F.C} \tag{5}$$

where $\mathbf{F}(x) = \begin{bmatrix} F_1(x) & F_2(x) & \cdots & F_{N+1}(x) \end{bmatrix}$ and $\mathbf{C} = \begin{bmatrix} c_1 & c_2 & \cdots & c_{N+1} \end{bmatrix}$. Also, Fibonacci polynomials can also be written as a matrix form,

$$\mathbf{F} = \mathbf{PM} \tag{6}$$

and,

$$\mathbf{M} = \begin{pmatrix} 1 & 0 & 1 & 0 & 1 & 0 & 1 & \cdots \\ 0 & 1 & 0 & 2 & 0 & 3 & 0 & \cdots \\ 0 & 0 & 1 & 0 & 3 & 0 & 6 & \cdots \\ 0 & 0 & 0 & 1 & 0 & 4 & 0 & \cdots \\ 0 & 0 & 0 & 0 & 1 & 0 & 5 & \cdots \\ 0 & 0 & 0 & 0 & 0 & 1 & 0 & \cdots \\ 0 & 0 & 0 & 0 & 0 & 0 & 1 & \cdots \\ \vdots & \vdots & \vdots & \vdots & \vdots & \vdots & \vdots & \ddots \end{pmatrix}, \tag{7}$$

$\mathbf{P}(x) = \begin{bmatrix} 1 & x & \cdots & x^N \end{bmatrix}$.

With the help of (5) and (6), the derivatives of $y_N(x)$ can be given as,

$$y_N^{(k)}(x) = \mathbf{P}^{(k)}(x)\mathbf{MC} = \mathbf{P}(x)\mathbf{B}^k\mathbf{MC} \tag{8}$$

Here, $\mathbf{B}^0$ is identity matrix of size $(N+1)$ and

$$\mathbf{B} = \begin{pmatrix} 0 & 1 & 0 & 0 & 0 & 0 & \cdots & 0 \\ 0 & 0 & 2 & 0 & 0 & 0 & \cdots & 0 \\ 0 & 0 & 0 & 3 & 0 & 0 & \cdots & 0 \\ 0 & 0 & 0 & 0 & 4 & 0 & \cdots & 0 \\ 0 & 0 & 0 & 0 & 0 & 5 & \cdots & 0 \\ 0 & 0 & 0 & 0 & 0 & 0 & \cdots & 0 \\ \vdots & \vdots & \vdots & \vdots & \vdots & \vdots & \ddots & N \\ 0 & 0 & 0 & 0 & 0 & 0 & \cdots & 0 \end{pmatrix}. \tag{9}$$

When the collocation points are taken as $x_j = \frac{j}{N}$, $j = 0,1,...,N$, the value of $y_N^{(k)}(x_j)$ can be defined as,

$$y_N^{(k)}(x_j) = \mathbf{P}^{(k)}(x_j)\mathbf{MC} = \mathbf{P}(x_j)\mathbf{B}^k\mathbf{MC} \tag{10}$$

By using (10) in the problem (1), given BVP is transformed into $(N+1)$ algebraic equations. Any suitable root finding method can be used to find $(N+1)$ unknowns of the approximation polynomials.

3. Applications of the Fibonacci Collocation Method for the Adiabatic Tubular Chemical Reactor Problem

The Fibonacci collocation method is applied to the Adiabatic Tubular Chemical Reactor problem in this section. To indicate the accuracy and applicability of the present method, the maximum absolute residual errors are calculated, which is defined by,

$$ME_N = \max_{0 \leq x \leq 1} \left| \begin{matrix} y_N''(x) - \lambda y_N'(x) \\ +\lambda\mu\left(\beta - y_N(x)\right)e^{y_N(x)} \end{matrix} \right| \tag{11}$$

The numerical results of the method ($N = 12$) for different values of β, λ and μ are given in Figure 1 and the comparisons of the numerical results of the presented method (for $N = 13$) with Taylor Wavelet Method (TWM), B-Spline Wavelet, Adomian Method (ADM), Shooting Method, the contraction mapping principle (CMP), Sinc-Galerkin Method, Chebyshev Finite Difference Method (CFDM) for $\lambda = 10, \beta = 3, \mu = 0.02$ are given in Table 1. Besides, absolute residual errors in logarithm base 10 ($\log_{10}|err|$) are given in Figure 2 for the different values of N.

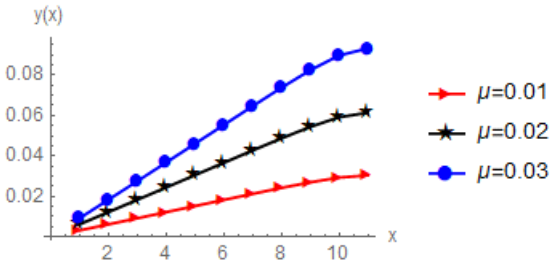

a) $\beta = 3, \lambda = 10$

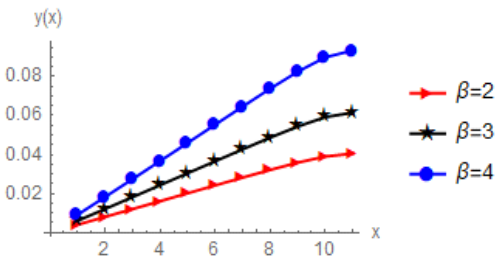

b) $\lambda = 10, \mu = 0.02$

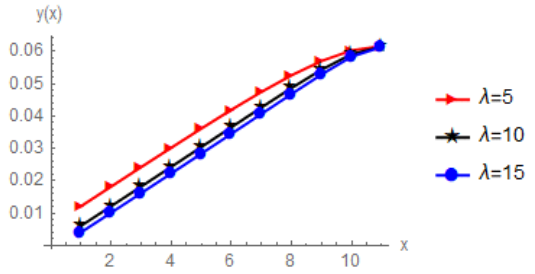

c) $\beta = 3,\ \mu = 0.02$

Figure 1. The numerical outcomes of the present method ($N = 12$) for a) $\beta = 3, \lambda = 10$ and different values of μ, b) $\lambda = 10,\ \mu = 0.02$ and different values of β and c) $\beta = 3,\ \mu = 0.02$ and different values of λ.

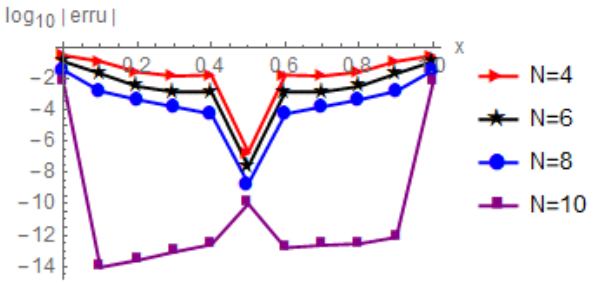

Figure 2. The absolute errors in the logarithm base 10 ($\log_{10}|err|$) different numbers of polynomial degrees (N).

Table 1. The comparison of the numerical outcomes for $\lambda = 10,\ \beta = 3,\ \mu = 0.02$.

x	TWM	B-Spline Wavelet	ADM	Shooting	CFDM	Sinc-Galerkin $N = 20$	Present Method $N = 13$
0	0.006048	0.006045	0.006048	0.006048	0.006048	0.006048	0.006048
0.2	0.018192	0.018194	0.018192	0.018192	0.018192	0.018192	0.018192
0.4	0.030424	0.030424	0.030424	0.030424	0.030424	0.030424	0.030424
0.6	0.042669	0.042675	0.042669	0.042669	0.042669	0.042669	0.042669
0.8	0.054332	0.054332	0.054371	0.054371	0.054371	0.054371	0.054371
1	0.061458	0.062030	0.061458	0.061458	0.061458	0.061458	0.061458

4. Conclusion and Suggestions

The boundary value problem arising from an adiabatic tubular chemical Reactor Theory is solved by an effective and robust technique, Fibonacci collocation method. From numerical results, it can be observed that the this problem is influenced by λ, μ and β. The numerical results reveal that the presented technique achieves high accuracy. Moreover, the presented numerical scheme is capable of solving this type of models.

Statement of Research and Publication Ethics

The study is complied with research and publication ethics

References

[1] R. F. Heinemann and A. B. Poore, “The effect of activation energy on tubular reactor multiplicity,” Chemical Engineering Science, vol. 37, no. 1, pp. 128–131, 1982.

[2] A. B. Poore, “A tubular chemical reactor model, in A Collection of Nonlinear Model Problems “ Contributed to the Proceedings of the AMS-SIAM pp. 28–31, 1989.

[3] R. F. Heinemann and A. B. Poore, “Multiplicity, stability, and oscillatory dynamics of the tubular reactor,” Chemical Engineering Science, vol. 36, no. 8, pp. 1411–1419, 1981.

[4] E. Abdolmaleki and H. Saberi Najafi, “An efficient algorithmic method to solve Hammerstein integral equations and application to a functional differential equation,” Advances in Mechanical Engineering, vol. 9, no. 6, pp. 1-8, 2017.

[5] A. Saadatmandi, M. Razzaghi, and M. Dehghan, “Sinc-galerkin solution for nonlinear two-point boundary value problems with applications to chemical reactor theory,” Mathematical and Computer Modelling, vol. 42, no. 11-12, pp. 1237–1244, 2005.

[6] N. M. Madbouly, D. F. McGhee, and G. F. Roach, “Adomian's method for Hammerstein integral equations arising from chemical reactor theory,” Applied Mathematics and Computation, vol. 117, no. 2-3, pp. 241–249, 2001.

[7] A. Saadatmandi and M. R. Azizi, "Chebyshev finite difference method for a two-point boundary value problems with applications to chemical reactor theory," Iranian Journal of Mathematical Chemistry, vol. 3, pp. 1-7, 2012.
[8] M. Zarebnia and R. Parvaz, "B-spline collocation method for numerical solution of the nonlinear two-point boundary value problems with applications to chemical reactor theory," International Journal of Mathematical Engineering and Science, vol. 3, pp. 6-10, 2014.
[9] J. Rashidinia and M. Nabati, "Sinc-galerkin and sinc-collocation methods in the solution of nonlinear two-point boundary value problems," Computational and Applied Mathematics, vol. 32, no. 2, pp. 315–330, 2013.
[10] H. Q. Kafri, S. A. Khuri, and A. Sayfy, "A fixed-point iteration approach for solving a BVP arising in chemical reactor theory," Chemical Engineering Communications, vol. 204, no. 2, pp. 198–204, 2016.
[11] M. R. Ali and D. Baleanu, "New wavelet method for solving boundary value problems arising from an adiabatic tubular chemical reactor theory," International Journal of Biomathematics, vol. 13, no. 07, p. 2050059, 2020.
[12] A. Kurt, S. Yalçınbaş, and M. Sezer, "Fibonacci collocation method for solving linear differential - difference equations," *Mathematical and Computational Applications*, vol. 18, no. 3, pp. 448–458, 2013.
[13] A. Kurt, S. Yalcinbas, M. Sezer, Fibonacci collocation method for solving high-order linear Fredholm integro-differentialdifference equations, Int. J. Math. Math. Sci. 2013 (2013).
[14] F. Mirzaee and S. F. Hoseini, "Solving systems of linear Fredholm Integro-differential equations with Fibonacci polynomials," *Ain Shams Engineering Journal*, vol. 5, no. 1, pp. 271–283, 2014.
[15] M. Cakmak and S. Alkan, "A numerical method for solving a class of systems of nonlinear pantograph differential equations," *Alexandria Engineering Journal*, vol. 61, no. 4, pp. 2651–2661, 2022.
[16] S. Falcón and Á. Plaza, "The K-fibonacci sequence and the pascal 2-triangle," *Chaos, Solitons & Fractals*, vol. 33, no. 1, pp. 38–49, 2007.
[17] S. Falcón and Á. Plaza, "On K-fibonacci sequences and polynomials and their derivatives," *Chaos, Solitons & Fractals*, vol. 39, no. 3, pp. 1005–1019, 2009.

Bitlis Eren Üniversitesi Fen Bilimleri Dergisi
BİTLİS EREN UNIVERSITY JOURNAL OF SCIENCE
ISSN: 2147-3129/e-ISSN: 2147-3188
VOLUME: 11 NO: 3 PAGE: 861-879 YEAR: 2022
DOI: 10.17798/bitlisfen.1130044

A Comparison of Ensemble and Base Learner Algorithms for the Prediction of Machining Induced Residual Stresses in the Turning of Aerospace Materials

Selim BUYRUKOĞLU[1], Sinan KESRİKLIOĞLU[2*]

[1]*Department of Computer Engineering, Cankiri Karatekin University, Cankiri, Turkey*
[2]*Department of Mechanical Engineering, Abdullah Gul University, Kayseri, Turkey*
(ORCID: 0000-0001-7844-3168) (ORCID: 0000-0002-2914-808X)

Keywords: Residual Stress, Machining, Inconel, Titanium, AdaBoost, Neural Network.

Abstract

The estimation of residual stresses is essential to prevent the catastrophic failures of the components used in the aerospace industry. The objective of this work is to predict the machining induced residual stresses with bagging, boosting, and single-based machine learning models based on the design and cutting parameters used in the turning of Inconel 718 and Ti6Al4V alloys. Experimentally measured residual stress data of these two materials was compiled from the literature, including the surface material of the cutting tools, cooling conditions, rake angles, as well as the cutting speed, feed, and width of cut to show the robustness of the models. These variables were also grouped into different combinations to clearly show the contribution and necessity of each element. Various predictive models in machine learning (AdaBoost, Random Forest, Artificial Neural Network, K-Neighbors Regressor, Linear Regressor) were then applied to estimate the residual stresses on the machined surfaces for the classified groups using the generated data. It was found that the AdaBoost algorithm was able to predict the machining induced residual stresses with a mean absolute error of 18.1 MPa for the IN718 alloy and 31.3 MPa for Ti6Al4V by taking into account all the variables, while the artificial neural network provides the lowest mean absolute errors for the Ti6Al4V alloy. On the other hand, the linear regression model gives poor agreement with the experimental data. All the analyses showed that AdaBoost (boosting) ensemble learning and artificial neural network models can be used for the prediction of the machining induced residual stresses with the small datasets of the IN718 and Ti6Al4V materials.

1. Introduction

Titanium and nickel-based super alloys are widely used in aerospace applications due to their high specific strength, wear, corrosion, and oxidation resistance. Residual stresses are generated in machining due to the inhomogeneous plastic deformation and chip formation processes, and the interactions between the tool and freshly machined surface. The low thermal conductivity of these workpiece materials increases the temperature at the cutting edge of the tool and changes the shape and strength of the parts due to the thermally induced tensile residual stresses. Moreover, the high strength of these super alloys reduces the machinability and increases the cutting and thrust forces during machining, which results in an increase in the level of the comprehensive residual stresses. Since aerospace components are exposed to excessive loads and temperatures due to their critical roles and operations, the thermomechanical residual stresses on the machined surface significantly influence the fatigue life and lead to catastrophic failures of airframes and engine parts. Residual stress is thus one of the most important parameters in evaluating the quality of the machined parts, and eliminating or minimizing the

*Corresponding author: sinan.kesriklioglu@agu.edu.tr
Received: 13.06.2022, Accepted: 01.09.2022

detrimental effects of it with the optimum cutting condition and tool setup is critical to ensure the surface integrity of the aeronautical components [1].

Due to the high usage of these alloys, extensive research and techniques have been conducted to improve the machining characteristics and part quality. The effect of cutting parameters (cutting speed, feed, and width/depth of cut) on the residual stresses was investigated in the machining of Inconel 718 and Ti6Al4V alloys. Holmberg et al. [2] performed cutting experiments and particle finite element simulations to investigate the effect of cutting parameters on the machining induced residual stresses in the orthogonal turning of Ti6Al4V. It was found that the surface residual stresses were tensile in the cutting direction and directly proportional to the feed while high compressive residual stresses were observed at the lowest cutting speed for the cutting conditions tested in the study. The tendency regarding the feed was also similar when cutting Inconel 718 [3], but the mode of residual stress did not change with the cutting speed. The residual stresses induced in the turning of Inconel 718 were also experimentally measured to optimize the cutting parameters for minimum residual stresses through a general algorithm function [4]. Another optimization process was carried out in the turning of Inconel 718 with a coated cutting tool [5]. The cutting tests were designed with the Grey Taguchi method and an ANOVA analysis was performed to investigate the contribution of cutting parameters to the surface residual stresses. It was found that the feed had a significant effect on the residual stress while maximizing the material removal rate, and it was followed by the depth of cut and cutting speed. The contribution of the feed was also similar to the machining of Ti6Al4V [6]. However, increasing the depth of cut result in deeper residual stresses [7].

The influence of the cooling condition, cutting tool material, and rake angle on the magnitude of the surface residual stresses has also been reported in many research papers. It was found that these parameters significantly affect the magnitude and modes (tensile and compressive) of the surface residual stresses induced during the machining operations. Ayed et al. [8] employed cryogenic cooling at various flow rates and pressures in the machining of Ti6Al4V and compared its effectiveness in reducing the surface residual stresses under conventional cooling and dry cutting. Cutting tests showed that cryogenic cooling at the highest flow rate and pressure produced the greatest compressive residual stresses although it reduces the thermal loads in the machining of Ti6Al4V. The impact of flood cooling on the residual stresses induced during the machining of Inconel 718 was also investigated with a coated carbide tool [9]. It was found that the magnitude of tensile residual stresses with the highest cutting speed was similar for dry and flood cooling. The effect of rake angle on the surface residual stresses was studied on the Ti6Al4V thin walls manufactured by selective laser melting. Turning experiments were conducted with zero and positive rake angles besides the various tool nose radius and cutting parameters [10]. It was found that the rake angle and tool nose radiuses influenced the magnitude of the compressive surface residual stresses in both cutting and feed directions. Three-dimensional finite element simulations were also performed to investigate the effect of tool coating on the residual stresses induced during the turning of Ti6Al4V and the results were validated by the experiments [11]. It was concluded that TiAlN coated tools increased the tensile residual stresses on the machined surfaces when compared to the uncoated tungsten carbide tools, although the cutting edge radius of the coated tool was larger than the uncoated tools. However, the residual stresses were more compressive with multilayered cutting tools in a different study [12]. The surface residual stresses also became more tensile with the coated cutting tools in the machining of Inconel 718 [13]. This could be due to the greater heat input into the workpiece materials since the coating provides a thermal barrier to the cutting tool. Simeone et al. [14] studied the influence of cooling on the surface residual stresses in the turning of Inconel 718. The experiments showed that the surface residual stresses were slightly lower under dry conditions with severe cutting conditions.

X-Ray diffraction is used to experimentally measure the surface residual stresses induced during the machining operations [15]. However, this method is expensive and time-consuming, and cannot be used for all combinations of the cutting parameters and tool setup. Therefore, it has been mostly used in the validation of analytical and numerical models. Analytical approaches are also used to calculate the machining induced residual stresses in a variety of materials. An analytical model was developed to predict the residual stresses in the orthogonal turning of AISI 4340 steel [16]. Two different algorithms were used because the hybrid algorithm provided a closer agreement with the experimental measurements than the S-J algorithm at low feed rates. A thermo-mechanical model incorporating the properties of workpiece material and cutting conditions was proposed to estimate the surface residual stresses in orthogonal machining [17]. The predicted and experimental results showed that this model can closely capture the trends of the residual

stress for AISI 316L and 4340 steel alloys. An analytical elasto-plastic model was also employed to obtain the residual stress profiles in the surface and subsurface layers of machined parts [18]. The magnitude and trend of residual stresses were able to be predicted within a short time. However, despite these strengths of analytical models, simplifying assumptions make them difficult to apply for all types of alloys due to the different strain hardening tendencies and toughness during the deformation of the workpiece materials (i.e., turning).

Advances in computer technology have increased the use of numerical models in simulating the machining process. Finite element models were combined with constitutive material models to predict the temperature and stress distribution on the workpiece and cutting tool during and/or after the machining process when all the thermal and mechanical loads are removed. A commercially available three-dimensional finite element model was used with a Lagrangian implicit code to predict the machining induced residual stresses in the turning of Inconel 718 and AISI 316L steel [19]. Finite element simulations showed that regardless of the tool material, the mode of the machining residual stresses was tensile at surface, but it gradually became compressive beneath the machined the surface for Inconel 718. Sahu and Andhare [20] used a similar finite element approach to simulate the turning operation of Ti6Al4V at various cutting conditions. ANOVA analysis was performed to optimize the cutting parameters since the model was able to predict the residual stresses with a mean absolute error of 11%. An implicit two-dimensional plane-strain finite element model [21] was developed to estimate the residual stresses in the turning of Inconel 718 turbine disks, and the proposed model was validated with the experimental measurements and analytical models published in the literature. The predicted values of the finite element model match better with the analytical model by assuming the rigid-plastic constitutive law. Although the numerical simulations provide close agreement with the experimental data in depth profiles when applying the appropriate material models, the magnitude of the residual stresses on the machined surfaces significantly deviates due to the relatively coarse mesh size, which is required to reduce the computation time.

With the impact of artificial intelligence in engineering applications, machine learning-based approaches have become more narrowly applied to predict the surface residual stresses in the literature. In a study, the effect of the machining parameters on the machining induced residual stresses was investigated by employing Artificial Neural Network (ANN) and Genetic Algorithm (GA) [4]. ANN was also used in different research to predict the value of surface residual stresses in the face turning operation [22]. Moreover, the ANN approach was used in the assessment of axial and hoop subsurface residual stresses in the hard turning of 52100 bearing steel [23], and the predicted results under various cutting speeds and feeds were validated with numerical and experimental data. Since only cutting speed, feed rate, and depth of cut were used as input parameters to predict the residual stress with these algorithms for the machining of Inconel 718, this research does not provide insights into the prediction accuracy when using different experimental setups (i.e., machining with coated inserts under flood cooling). The Gaussian Process Regression was also implemented to estimate the surface residual stresses in end milling [24]. A random forest was initially employed to determine the optimum feature set. Then, Gaussian Process Regression, Support Vector Regressor, ANN, and AdaBoost algorithms were employed to predict surface residual stress in end milling. The best prediction performance was obtained through the Gaussian Process Regression. Since all the residual stresses are measured using the same conditions for X-Ray diffraction, the performance of the models was not evaluated for the existence of the uncertainties in the X-Ray measurements. ANN and fuzzy neural network models were compared to highlight the prediction performance of the models for the residual stresses in the welding operation. The fuzzy neural network model provided slightly better performance in the prediction process with the root mean square error (RMSE) of 0.12, R-squared (R2) of 0.91, and mean absolute percentage error (MAPE) of 22.94 compared to the ANN [25]. The ANN technique has also been adapted to predict and optimize the surface residual stresses induced by the laser shock peening process on a Ti6Al4V alloy [26]. The ANN predictions were in good agreement with the experimental results.

Even if all the aforementioned studies were accomplished to obtain promising results, to the best of the authors' knowledge, bagging and boosting ensemble machine learning models have never been used for the prediction of surface residual stresses in the turning operation. Thus, the objective of this work is to predict the residual stresses with the machine learning models in the turning of Inconel 718 and Ti6Al4V alloys. The machining induced residual stress data were extracted from the experimental studies in the literature since performing the cutting experiments on these aerospace materials, and measuring the residual stresses by X-Ray diffraction are expensive., This type of data collection process

also enables us to implement the machine learning models for all the combinations of cutting and design parameters, and a relatively small number of the datasets (i.e., machining induced residual stress). Since most of the researchers concluded that single-based models may perform better than ensemble learning algorithms including bagging and boosting for the regression and classification cases [27], [28], popular single-based models (k- Nearest Neighbors, Naive Bayes, Support Vector Machine, Linear Regression, and Artificial Neural Network) were selected in addition to the ensemble learning algorithms based on the efficiency of the regression problems in different fields. Then, the effectiveness of these models was evaluated based on the R2 value. This statistical metric was also used to determine the optimal bagging and boosting algorithms, including Random Forest and AdaBoost. This paper is also motivated by the comparisons of the bagging (Random Forest) and boosting (AdaBoost) algorithms in terms of prediction accuracy. Additionally, single-based models (Linear Regression, K-Nearest Neighbor, and ANN) were employed to compare the single-based models with the bagging and boosting ensemble machine learning models.

2. Methodology

A brief description of the turning operation is given in this section. The machining terminology used in the datasets and data collection process is explained. The machine learning models to predict the machining induced surface residual stresses in turning of Inconel 718 and Ti6Al4V alloys are also presented. In addition, the metrics are expressed to evaluate the accuracy of the models in estimating the experimentally measured residual stresses.

2.1. Turning Operation

Turning is a material removal process carried out on a CNC or engine lathe to obtain perfect inner and outer cylindrical and/or conical surfaces as well as external and internal threads. In this process, the workpiece rotates at high speeds, and stationary cutting tools, which are made of a much harder material than the workpiece, plastically deform the material to the desired dimensions and shapes. Figure 1 illustrates the schematic representation of the turning operation. A coating is generally required to reduce the friction between the cutting tool and workpiece and increase the wear, oxidation, fatigue, and thermal shock resistance that extend the tool life significantly. High material removal rates are also desired in machining operations to increase process productivity. Cutting speed, feed, and depth/width of cut determine the volume of the material that is being cut. Cutting speed is defined as the rotational or surface speed of the workpiece and is usually expressed in revolution per minute or meter per minute, respectively. Feed is defined as the distance that the cutting tools travel for each revolution of the workpiece, while the depth/width of cut is the distance measured from the surface of the workpiece material to the tool tip, and expressed in millimeters. Since these variables are directly proportional to the material removal rate, increasing them produces higher efficiency in the machining process. However, excessive increases in the speed, feed, and depth of cut accelerate the tool wear due to high cutting forces and temperatures and result in poor surface finishes. Therefore, optimization of the cutting parameters is required with respect to the surface integrity of the workpiece and machining costs in order to efficiently achieve the turning operation of aerospace materials.

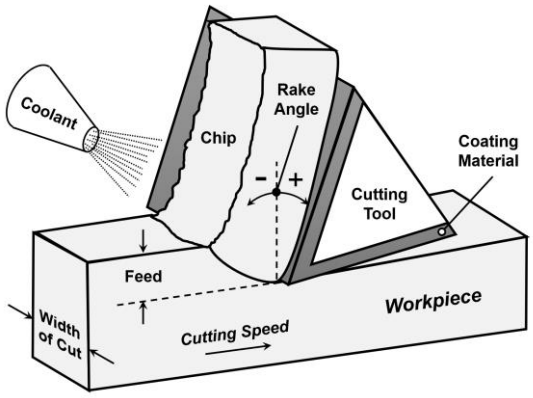

Figure 1. Schematic illustration of turning process

The rake angle is another tool setup parameter that describes the angle of the cutting tool face relative to the workpiece surface, as shown in Figure 1, and it significantly influences the residual stresses in turning since it changes the formation of chip and shear flow. It should be noted that the rake angle is classified as positive, negative, and zero in the data sets of this paper because an adequate sample size could not be found in the literature to numerically show its contribution to the surface residual stresses. Although dry cutting can be the most sustainable option in the machining operation, active cooling is also implemented to reduce the temperature, oxidation, and tool wear in the turning of nickel and titanium alloys. A synthetic water-based metal working fluid (MWF) is commonly used to flood the machining zone for cooling and lubricating the cutting tool while the minimum quantity lubrication (MQL) technique and cryogenic machining (CRYO)

with liquid nitrogen can be considered as alternatives to satisfy the environmental concerns.

2.2. Data Collection

Due to the high cost of the experiments for all possible combinations, the effects of tool material, rake angle, cooling condition, cutting speed, feed, and width of cut on the machining induced surface residual stresses were obtained from the literature and tabulated in Appendix 1 and 2 for the Inconel 718 and Ti6Al4V alloys, respectively. Two different commonly used and commercial aerospace materials were selected to show the robustness of the machine models described in the subsequent section and that the methodology can be extended to other types of materials and machining setups. Only experimentally measured residual stresses by the X-Ray Diffraction technique were compiled from the literature to validate the machine learning models with high confidence.

The datasets used in this study include six independent variables based on the machining setup and cutting parameters. Some of them may play a key role in the prediction of machining induced surface residual stress. Thus, five different groups were created from the entire datasets and then the performances of the machine learning models were compared to reveal the importance of the variables on the prediction of surface residual stress based on the existing data. Table 1 lists all the groups created to clearly show the contribution of the variables to the machining induced residual stresses for aerospace materials.

Table 1. Created groups from the entire residual stress datasets

Group #	Group Name
1	All variables
2	Only cutting parameters (cutting speed, feed and width of cut)
3	Cutting parameters and tool material
4	Cutting parameters and coolant
5	Cutting parameters, tool material and coolant (rake angle is excluded)

2.3. Modelling

Various machine learning models were applied to determine the correct model for the prediction of the surface residual stresses in the turning of aerospace materials. The Decision Tree, k- Nearest Neighbors, Random Forest, AdaBoost, Naive Bayes, Support Vector Machine, Linear Regression, and Artificial Neural Network were first tested and five of the machine learning models were selected based on the r-squared values (R2). AdaBoost, Artificial Neural Network, Random Forest, k-Nearest Neighbors, and Linear Regression were found the best models for the datasets of the Inconel 718 and Ti6Al4V alloys given in Appendix 1 and 2. Each dataset was then separated into training (80%) and test (20%) sets, and 10-fold cross-validation was used in the training set. Finally, models were evaluated based on the test set. In other words, nested cross-validation was used in the training and evaluation process of the machine learning models [29]. Figure 2 shows the flow diagram of the residual stress prediction system used in this study.

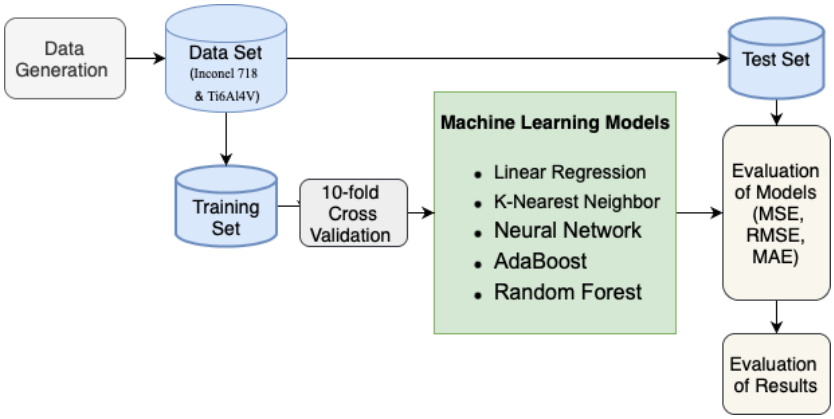

Figure 2. Flow diagram of residual stresses prediction system

AdaBoost

AdaBoost is a type of boosting ensemble algorithm, which was initially proposed by Freund and Schapire [30]. The core principle of it is to combine weak learners for the generation of a strong algorithm. In the working process of the AdaBoost algorithm, a simple learning algorithm is called at each iteration, and then a weight coefficient is assigned to this learning algorithm. The assigned weight coefficient is inversely proportional to the simple learning algorithm's error. In the end, this model provides a solution based on the weighted voting. Even though the AdaBoost algorithm was proposed to solve the classification problems, Drucker adapted it to solve regression problems [31]. The modified version of the algorithms is known as AdaBoost.R2 in the literature. In this study, 100 estimators (decision stumps) were used in the employed AdaBoost.R2 algorithm.

Linear Regression

Simple and multiple linear regressions are mostly used for regression problems in the literature. Single linear regression mostly provides convincing results when the output is predicted using a single predictor. On the other hand, multiple linear regression generally allows for obtaining more effective results if the output is obtained using more than one predictor [32]. A random relationship among variables is created based on the present data to obtain statistical relations. In this study, machining induced residual stresses in the turning of aerospace materials were predicted with more than one predictor, and multiple linear regression can, thus, be employed.

Artificial Neural Network

Artificial neural networks (ANN) are widely used as predictive modeling in different disciplines. The structure of the ANN consists of three layers including the input, hidden, and output layers. Many researchers specified that ANN models are employed with a single hidden layer, giving convincing results and shortening the prediction process. The hidden layer neuron variations were used to determine the optimal number of neurons for a hidden layer [33]. Additionally, a hidden layer with 12 neurons was used in the creation of an ANN structure [34]. It can be inferred from these studies; researchers tend to obtain convincing statistical scores using a variety of neurons in a single hidden layer. Therefore, a single hidden layer was used in the proposed ANN model. In order to determine the optimum number of neurons in the hidden layer, various values were used in the creation process of the ANN model. It is also stated that the number of neurons used in the hidden layer should not be more than twice numbers of neurons in the input layer [35], [36]. Therefore, 3, 6, 9, and 12 neurons were used in the hidden layer, and the ANN model was achieved to provide the best performance through the 6 neurons. Additionally, the maximum number of iterations was set to 300 as a result of trying different values such as 50, 150, 300, and 500. ReLu was used as an activation function while Adam optimization was used as the training algorithm in the employed ANN model. The proposed ANN is, thus, created with the following parameters: a single hidden layer with 6 neurons, number of iterations is 300, activation function was ReLu, and the solver is Adam optimization. Also, the ANN structure is determined for both datasets due to the similar sample sizes. Dataset 1(Datasets of Inconel 718) consists of 97 samples. Dataset 2 (Datasets of Ti6Al4V) consists of 91 samples. Figure 3 presents the structure of the proposed ANN model used in this study.

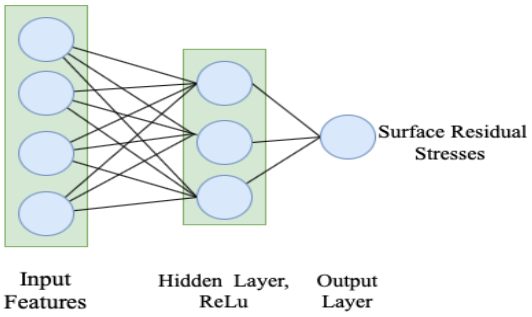

Figure 3. Structure of the employed ANN model

K-Nearest Neighbor (kNN)

The kNN algorithm aims to keep similar things close to each other. Different metrics can be used in order to find close similar things in the creation of a kNN model (i.e. Euclidean, Manhattan, Chebyshev, etc). The K-Neighbors Regressor algorithm was also applied to predict surface residual stress in the turning of Inconel 718 and Ti6Al4V. In the regression problems, the mean of the numerical target of the k nearest neighbors is calculated, and the K-Neighbors Regressor uses the same distance measured as the kNN classification [37]. In this study, the Euclidean criterion was used while calculating the distance values between samples, and the number of neighbors was set to 5, as the default value for the number of neighbors in sklearn is 5.

Random Forest

The Random Forest is a type of ensemble (bagging) algorithm which is an extension of the decision tree. If a model consists of more than one decision tree, it is considered a random forest. In the Random Forest model, the Bootstrap sampling method is used to extract multiple samples from the original samples. Then, decision trees are combined for the prediction. An average estimate is taken from the decision trees used in the random forest to obtain the prediction result [38]. In this study, the number of trees was set to 100, and subsets were not spilt when they were less than 5.

Evaluation Metrics

Mean Squared Error (MSE), Root Mean Square Error (RMSE), Mean Absolute Error (MAE) and R-Squared (R2) are effective evaluation metrics in terms of interpretation of the prediction models [39]. These metrics are calculated as

$$MSE = \frac{1}{n}\sum_{i=1}^{n}\left(P_i - \hat{P}_i\right)^2 \quad (1)$$

$$RMSE = \sqrt{\frac{1}{n}\sum_{i=1}^{n}\left(P_i - \hat{P}_i\right)^2} \quad (2)$$

$$MAE = \frac{1}{n}\sum_{i=1}^{n}\left|P_i - \hat{P}_i\right| \quad (3)$$

$$R^2 = 1 - \frac{RSS}{TSS} \quad (4)$$

where P_i is the actual value, $\hat{P}_i$ is the predicted value from the model, n is the number of observations, RSS is sum of squares of residuals and TSS is total sum of squares.

3. Results and Discussion

This section presents the experimentally measured residual stresses by X-Ray Diffraction in the turning of Inconel 718 and Ti6Al4V alloys and predicted results by the machine learning models described in the previous section. It should be noted that the experimentally measured residual stresses were combined from a variety of research papers focusing on the experimental studies as highlighted in the previous section. However, the experimental measurements by X-Ray Diffraction still include uncertainties [40] and they could be considered an outlier due to the high margin of error in the measurement. Thus, the Mean Absolute Error (MAE) values of the models were mainly used in this paper to evaluate the employed models' efficiency since the Mean Squared Error and Root Mean Squared Error are more sensitive to outliers than the MAE, and R2 is less robust to outliers than the MAE [41]. Moreover, ensemble and some of the single-based algorithms are flexible algorithms (neural network, AdaBoost, Random Forest, etc.) compared to the statistical models (Linear Regression, etc.). In this sense, flexible algorithms usually provide convincing results even if the dataset contains outliers [42].

3.1. The Comparison of Experimental and Predicted Machining Induced Residual Stresses for Inconel 718

The effect of machining variables on the performance of machine learning models for the prediction accuracy of residual stresses in the turning of Inconel 718is presented in Table 2 based on the test scores. The employed AdaBoost algorithm provides the best performance in all data groups with respect to all the metrics used in this study when compared to the other machine learning algorithms. In contrast to the AdaBoost algorithm, Linear Regression has the worst MSE, RMSE and R2 values in the prediction of machining induced residual stresses for Inconel 718. The lowest MAE value (14.9) was obtained with the AdaBoost algorithm when the rake angle is excluded (Group 5). Moreover, the AdaBoost algorithm achieved to obtain an MAE value of 18.1 when all variables are used in the predicted models. In this sense, the efficiency of the Rake Angle can be considered the lowest among the other variables. On the other hand, the AdaBoost algorithm gives the worst MAE value (50.7) when only the cutting parameters (Group 2) are taken into the account in the predictions. When Groups 3 and 4 are used in the prediction process, the performance of the AdaBoost algorithm is higher than the ones with Group 2. However, this algorithm has provided slightly better performance when Group 4 is used in the prediction process as compared to the algorithm performance when Group 3 is used. It means that the cooling can be considered a more effective variable than the tool material type for the machining induced residual stresses of the Inconel 718. Moreover, the best MSE, RMSE, and MAE values in the AdaBoost and ANN models are obtained with Group 5 in which the rake angle data are excluded in the dataset of the prediction process[42].

Table 2. .The effect of the variable existence on the prediction accuracy of residual stresses in the turning of Inconel 718

Group 1 (All variables)				
Model	**MSE**	**RMSE**	**MAE**	**R^2**
AdaBoost	2778	52.7	18.1	0.980
Linear Regression	44334	210.6	152.5	0.677
Neural Network	2995	54.7	29.3	0.978
K-Nearest Neighbor	42843	207.0	140.4	0.688
Random Forest	28490	168.8	128.1	0.792
Group 2 (Only Cutting Parameters)				
Model	**MSE**	**RMSE**	**MAE**	**R^2**
AdaBoost	14133	118.9	50.7	0.897
Linear Regression	73374	270.9	201.3	0.465
Neural Network	26099	161.6	113.3	0.810
K-Nearest Neighbor	51370	226.7	158.5	0.626
Random Forest	31011	176.1	136.1	0.774
Group 3 (Cutting Parameters and Tool Material)				
Model	**MSE**	**RMSE**	**MAE**	**R^2**
AdaBoost	7892	88.8	32.3	0.940
Linear Regression	70788	266.1	201.8	0.480
Neural Network	11050	105.1	61.5	0.920
K-Nearest Neighbor	41450	203.6	136.7	0.700
Random Forest	29801	172.6	130.3	0.780
Group 4 (Cutting Parameters and Coolant)				
Model	**MSE**	**RMSE**	**MAE**	**R^2**
AdaBoost	6754	82.2	32.1	0.950
Linear Regression	73310	270.8	202.9	0.470
Neural Network	12174	110.3	66.6	0.910
K-Nearest Neighbor	54681	233.8	151.5	0.600
Random Forest	30494	174.6	134.9	0.780
Group 5 (Cutting Parameters, Tool Material and Coolant)				
Model	**MSE**	**RMSE**	**MAE**	**R^2**
AdaBoost	1668	40.8	14.9	0.960
Linear Regression	65877	256.7	198.7	0.520
Neural Network	2207	47.0	21.8	0.950
K-Nearest Neighbor	41956	204.8	140.2	0.690
Random Forest	28511	168.9	128.7	0.790

As can be seen from Table 2 and Figure 4, the boosting ensemble learning model (AdaBoost) has a better performance when compared to the bagging ensemble learning model (Random Forest) and single-based models (Artificial Neural Network (ANN), Linear Regression, K-Nearest Neighbor) in the prediction of the surface residual stresses in turning of Inconel 718 alloy. The AdaBoost and ANN can almost exactly estimate 82% of the experimental results. The maximum errors of the AdaBoost and ANN models are 22% and 52% in the test data when all variables are used in the models. On the other hand, ANN has the second-best performance for these five data, and this model achieved the best MAE value (21.8) using Group 5 (Table 2). Generally, the ANN single-based model can be considered better than the bagging (random forest) ensemble learning model in the prediction of surface residual stresses for Inconel 718.

As explained in the section on the data collection process, the datasets were collected from various experimental studies. Thus, in Figures 4-7, the horizontal axis numbers refer to the numbers of each study, and each grid shows the residual stresses from one paper. For instance, the data number between 1 and 10 refers to data obtained from a study while the data number between 30 and 62 refers to data obtained from a different study in Figures 4 and 5. The range of the data for each study is also available in Appendix 1 and 2.

As shown in Figure 4 and 5, the highest difference between the experimental and predicted data points was observed with the Linear Regression. This could be because of the relationship between the mean of the variables (independent and dependent) since the mean is not a complete description of a variable and it is a limitation of this model [43]. On the other hand, although the k-Nearest Neighbor shows better performance than the Linear Regression, the deviations between the experimental and predicted residual stresses are not in an acceptable range for turning of Inconel 718 alloy since it is used in the aerospace industry to manufacture vital parts.

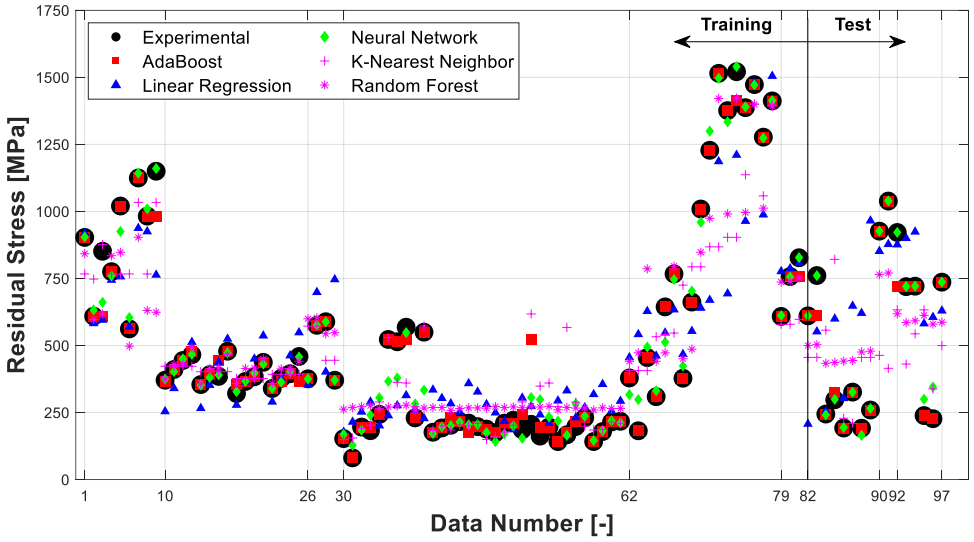

Figure 4. Experimental and predicted residual stresses in the turning of Inconel 718 with all variables

As shown in Figure 5, although the machine learning models are trained precisely, the agreement between the experimental and predicted residual stresses is poor in all the models when only the cutting parameters are used. This means that the information about the machining setup is required to obtain a reasonable residual stress prediction in the turning of Inconel 718. It also confirms that the machine learning algorithms used with only the various cutting parameters [4], [22], [24] do not completely provide the magnitude of the machining induced residual stresses. However, the AdaBoost could still capture 38% of the experimental results with a maximum error of 1% within the test data while the maximum error can be as large as approximately 200% in the AdaBoost and ANN machine learning models.

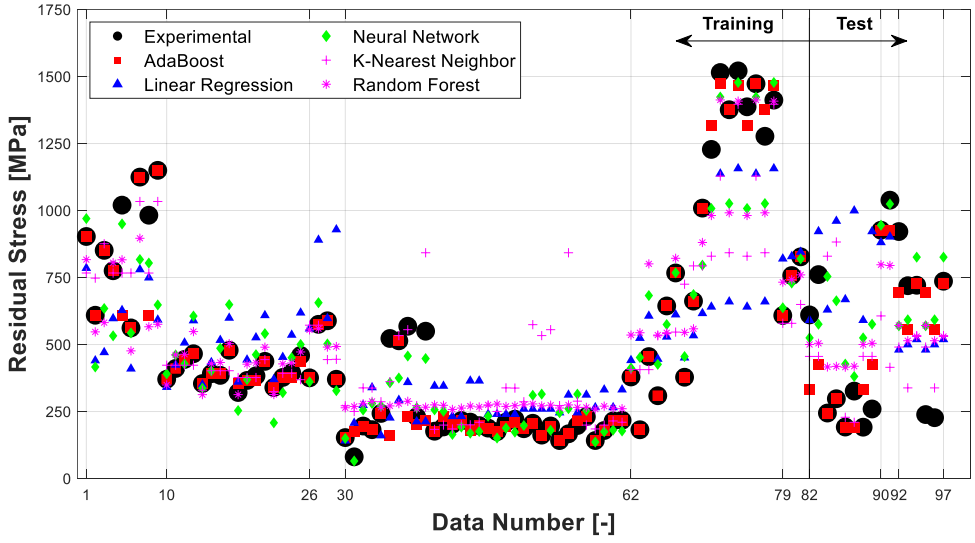

Figure 5. Experimental and predicted residual stresses in turning of Inconel 718 with only cutting parameters

3.2. The Comparison of Experimental and Predicted Machining Induced Residual Stresses for Ti6Al4V

Table 3 shows the effect of the variable contribution on the prediction accuracy of residual stresses in the turning of Ti6Al4V based on the test scores. As it can be seen from Table 3, the Artificial Neural Network (ANN) algorithm has the best performance for all the groups created in this study with respect to the MAE value. This algorithm has achieved providing the same and best MAE values (22.4) using Groups 1 and 5. On the other hand, although the AdaBoost algorithm seems to be the second-best model for the prediction of surface residual stress in the turning of Ti6aI4V, the difference between ANN and AdaBoost is only 0.2 when Group 2 is used in the analysis. In general, the ANN single-based model has better performance compared to the boosting and bagging learning algorithms for the prediction of surface residual stress in the turning of Ti6Al4V. Neural Network has the best MSE, RMSE, and R2 values compared to the other models, as shown in Table 3. The best values of MSE, RMSE, and R2 were obtained using Groups 1 and 5. In contrast to the Neural Network, Linear Regression provided the worst MSE, RMSE, and R2 values among the models presented in Table 3 due to the limitations of the linear regression mentioned in the previous section.

As can be seen from Figure 6 and 7, the AdaBoost and Neural Network algorithms show excellent prediction performance in the range from 86 to 91. However, these two algorithms provide the worst performance in the data numbered between 21 and 33 compared to the other experimental studies as shown in Figure 6. It can be seen in Appendix 2, that the effects of tool material and cooling conditions on the machining induced residual stresses were investigated in the work numbered between 21 and 33 [12]. Since the tool material and cooling type do not significantly influence the prediction accuracy of the machine learning models for the Ti6Al4V alloy (Table 3), these variables can be considered neutral elements in the prediction of machining induced residual stresses.

Table 3. The effect of the variable existence on the prediction accuracy of residual stresses in the turning of Ti6Al4V

Group 1 (All variables)				
Model	**MSE**	**RMSE**	**MAE**	**R^2**
AdaBoost	4364	66.1	31.3	0.960
Linear Regression	68535	261.8	183.6	0.365
Neural Network	1419	37.7	22.4	0.987
K-Nearest Neighbor	53008	230.2	152.8	0.509
Random Forest	40261	200.7	140.8	0.627
Group 2 (Only Cutting Parameters)				
Model	**MSE**	**RMSE**	**MAE**	**R^2**
AdaBoost	15104	122.9	55.9	0.860
Linear Regression	95676	309.3	243.6	0.114
Neural Network	9368	96.8	55.7	0.913
K-Nearest Neighbor	59377	243.7	171.6	0.450
Random Forest	43529	208.6	147.0	0.597
Group 3 (Cutting Parameters and Tool Material)				
Model	**MSE**	**RMSE**	**MAE**	**R^2**
AdaBoost	3967	63.0	33.0	0.963
Linear Regression	74155	272.3	200.0	0.313
Neural Network	2234	47.3	28.7	0.979
K-Nearest Neighbor	52275	228.6	151.7	0.516
Random Forest	41113	202.8	142.9	0.619
Group 4 (Cutting Parameters and Coolant)				
Model	**MSE**	**RMSE**	**MAE**	**R^2**
AdaBoost	4364	66.1	34.7	0.960
Linear Regression	81128	284.8	204.0	0.249
Neural Network	1578	39.7	24.7	0.985
K-Nearest Neighbor	54302	233.0	153.2	0.497
Random Forest	41500	203.7	143.8	0.616
Group 5 (Cutting Parameters, Tool Material and Coolant)				
Model	**MSE**	**RMSE**	**MAE**	**R^2**
AdaBoost	4364	66.1	31.3	0.960
Linear Regression	68535	261.8	183.6	0.365
Neural Network	1419	37.7	22.4	0.987
K-Nearest Neighbor	53008	230.2	152.8	0.509
Random Forest	40521	201.3	140.2	0.625

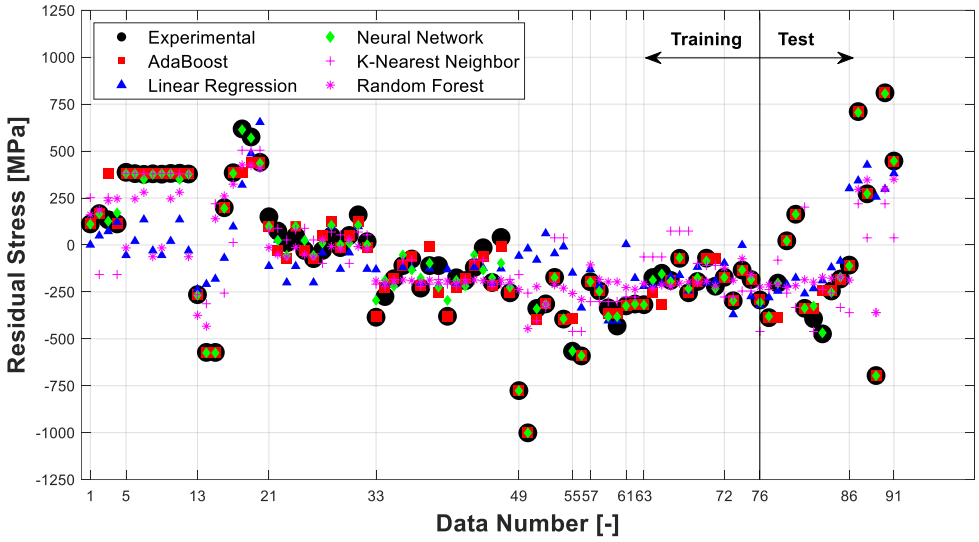

Figure 6. Experimental and predicted residual stresses in the turning of Ti6Al4V with all variables

As shown in Figure 7, each algorithm provided the same results for the samples numbered from 21 – 33 and 57 - 61. When the values of the cutting parameters (cutting speed, feed, width of cut) of these studies are checked in Appendix 2, they have the same values for each sample. Thus, the samples numbered between 21 and 33, 57 and 61 can be considered outliers in the dataset of Group 2. On the other hand, Linear Regression and Random Forest algorithms give similar results for the samples numbered between 33 and 49 while the experimental results and predicted values with the other employed algorithms are different (Figure 7). In this case, they may not be appropriate algorithms for the samples numbered between 33 and 49 because all the variables were changed through the experiments and only the cutting parameters were used in the prediction of machine learning as shown in Figure 7.

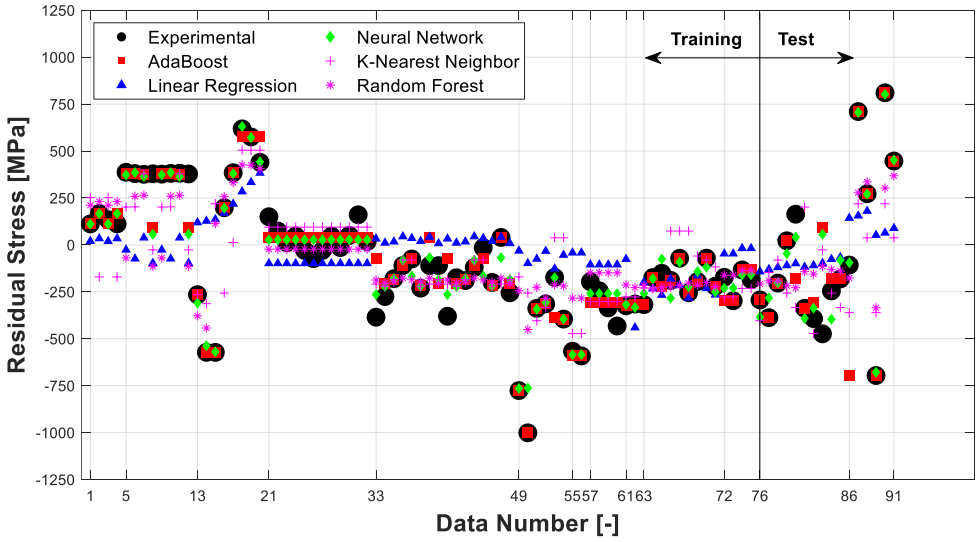

Figure 7. Experimental and predicted residual stresses in the turning of Ti6Al4V with only cutting parameters

Within the groups created from the datasets of Inconel 718 and Ti6Al4V materials, k-Nearest Neighbor and Random Forest algorithms gave similar errors. The maximum deviation between these two models was obtained in Group 2 with an MAE of approximately 25. However, the MAE of these models was still three to seven times greater than the one with the AdaBoost and Neural Network algorithms.

The performance of the employed five machine learning algorithms (Linear Regression, AdaBoost, Neural Network, Random Forest, k-Nearest Neighbor) was varied in the estimation of the residual stresses in the turning of Inconel 718 and Ti6Al4V. As highlighted before, while AdaBoost provided the best statistical scores for the Inconel 718 workpiece, the prediction accuracy was higher with Neural Network for Ti6Al4V. However, both of these algorithms still achieved to provide convincing statistical scores for two different datasets which shows the robustness of these algorithms in this study.

It is known that the use of datasets having a large sample size is a preferred situation when employing Machine Learning algorithms. However, data collection is not an easy task in the turning of difficult-to-cut materials (i.e., Nickel and Titanium alloys) due to the high cost of materials, experiments, and measurements. Although the residual stress predictions with the proposed machine learning models are remarkably in good agreement with the experimental data, the limitation of this research is that it has a relatively small sample size of the datasets for both workpiece materials. Several algorithms employed in this work (i.e., Linear Regression) were, thus, failed in the estimation of the surface residual stresses since the literature has a limited number of studies regarding the experimental investigation of machining induced residual stresses for these aerospace materials. Moreover, in most of the experimental studies used in this paper, all variable combinations were not tested, or an experimental design was not applied. Therefore, the machine learning models estimate the same residual stresses when the variables are grouped (Figure 5 and 7).

As presented in the introduction, ANN was also applied for the prediction of the residual stresses in the welding operation [25]. A hybrid ANN approach was also created for the prediction of the value of surface residual stresses in the face turning operation [22]. Even if the studies presented above fulfilled the aim of their own studies, they have some drawbacks. The first drawback is that there is no case study that was carried out to determine the optimal architecture of the created ANN in the studies presented above. In this sense, a more effective ANN architecture could be created which may improve the its performance in the prediction of the value of surface residual stresses in machining operations. Different iteration numbers of the ANN approaches were not also tested to obtain more reliable results in the prediction of machining induced residual stresses. In the proposed models described in the previous sections, a case study was carried out to determine the optimal structure for each learning algorithm. The second drawback of the existing research papers is that only one dataset has been used to evaluate the performance of the machine learning models. Unlike the presented work, the robustness of these studies has not been tested in the prediction of residual stresses.

4. Conclusions

This paper provides the experimental residual stresses measured by X-Ray Diffraction for various cutting and machine setup parameters used in the turning of aerospace materials. AdaBoost, Linear regression, Neural Network (ANN), K-nearest Neighbor, and Radom Forest machine learning models were used to predict the machining induced surface residual stresses for Inconel 718 and Ti6Al4V alloys. The performances of the models were then tested by calculating the Means Squared Error (MSE), Rooth Mean Square Error (RMSE), and Mean Absolute Error (MAE) as well as the R-squared. The datasets of these two workpieces were also grouped to clearly show the contribution of variables to the machining induced residual stresses. It was found that the AdaBoost gives the best agreement within the models used in this study for all Groups, and including the cooling and tool material type data into the machine learning models significantly increases the prediction accuracy of the models for the Inconel 718. On the other hand, Artificial Neural Network was the best fit in the prediction of surface residual stresses for all the group combinations of Ti6Al4V alloy. However, the MAE of the ANN was almost the same as the AdaBoost model when only cutting parameters were used in the analysis, and including one variable regarding the experimental setup reduced the MAE by approximately 50%. Therefore, the machine setup parameters are needed to accurately predict the machining induced residual stresses with Machine Learning models for Inconel 718 and Ti6Al4V materials. All the analyses showed that the AdaBoost and ANN algorithms can be used to estimate the residual stresses with an acceptable error range despite the small size of the datasets, and prevent the

cost of machining trials, experimental measurements and finite element software. Since the machine learning models with the optimum parameters determined in this study worked properly for both aerospace materials, the presented models can be extended to other types of workpieces. As a future work, the sample size of the datasets can also be increased using linear programming or heuristic models to employ the stacked ensemble models and deep learning algorithms in the prediction of surface residual stresses.

Acknowledgment

The authors gratefully acknowledge partial support of the Faculties of Engineering at Cankiri Karatekin University and Abdullah Gul University.

Contributions of the authors

Both authors developed the concept, designed the manuscript and created the original draft. Sinan Kesriklioglu collected and processed the datasets. Selim Buyrukoglu employed the machine learning models, and analyzed the data. Both authors discussed the results and approved the final version of the manuscript.

Conflict of Interest Statement

There is no conflict of interest between the authors.

Statement of Research and Publication Ethics

The authors declare that this study complies with Research and Publication Ethics.

References

[1] D. Ulutan and T. Ozel, "Machining induced surface integrity in titanium and nickel alloys: Areview", *International Journal of Machine Tools and MAnufacture.* 2011, doi: 10.1016/j.ijmachtools.2010.11.003.

[2] J. Holmberg, J. M. Rodríguez Prieto, J. Berglund, A. Sveboda, and P. Jonsén, "Experimental and PFEM-simulations of residual stresses from turning tests of a cylindrical Ti-6Al-4V shaft," 2018, doi: 10.1016/j.procir.2018.05.087.

[3] Y. Hua and Z. Liu, "Experimental investigation of principal residual stress and fatigue performance for turned nickel-based superalloy Inconel 718," *Materials (Basel).*, 2018, doi: 10.3390/ma11060879.

[4] F. Jafarian, H. Amirabadi, and J. Sadri, "Experimental measurement and optimization of tensile residual stress in turning process of Inconel718 superalloy," *Meas. J. Int. Meas. Confed.*, 2015, doi: 10.1016/j.measurement.2014.11.021.

[5] G. Kartheek, K. Srinivas, and C. Devaraj, "Optimization of Residual Stresses in Hard Turning of Super Alloy Inconel 718," 2018, doi: 10.1016/j.matpr.2017.12.029.

[6] K. Satyanarayana, A. V. Gopal, and N. Ravi, "Studies on surface integrity and its optimisation in turning Ti-6Al-4V," *Int. J. Precis. Technol.*, 2015, doi: 10.1504/ijptech.2015.073837.

[7] D. M. Madyira, R. F. Laubscher, N. Janse Van Rensburg, and P. F. J. Henning, "High speed machining induced residual stresses in Grade 5 titanium alloy," *Proc. Inst. Mech. Eng. Part L J. Mater. Des. Appl.*, 2013, doi: 10.1177/1464420712462319.

[8] Y. Ayed, G. Germain, A. P. Melsio, P. Kowalewski, and D. Locufier, "Impact of supply conditions of liquid nitrogen on tool wear and surface integrity when machining the Ti-6Al-4V titanium alloy," *Int. J. Adv. Manuf. Technol.*, 2017, doi: 10.1007/s00170-017-0604-7.

[9] A. Devillez, G. Le Coz, S. Dominiak, and D. Dudzinski, "Dry machining of Inconel 718, workpiece surface integrity," *J. Mater. Process. Technol.*, 2011, doi: 10.1016/j.jmatprotec.2011.04.011.

[10] G. Le Coz, R. Piquard, A. D'Acunto, D. Bouscaud, M. Fischer, and P. Laheurte, "Precision turning analysis of Ti-6Al-4V skin produced by selective laser melting using a design of experiment approach," *Int. J. Adv. Manuf. Technol.*, 2020, doi: 10.1007/s00170-020-05807-8.

[11] T. Özel and D. Ulutan, "Prediction of machining induced residual stresses in turning of titanium and nickel based alloys with experiments and finite element simulations," *CIRP Ann. - Manuf. Technol.*, 2012, doi: 10.1016/j.cirp.2012.03.100.

[12] A. Paranjpe and A, "RESIDUAL STRESSES IN MACHINED TITANIUM (Ti-6Al-4V) ALLOYS," *Statew. Agric. L. Use Baseline 2015*, 2015.

[13] A. R. C. Sharman, J. I. Hughes, and K. Ridgway, "An analysis of the residual stresses generated in Inconel 718™ when turning," *J. Mater. Process. Technol.*, 2006, doi: 10.1016/j.jmatprotec.2005.12.007.
[14] A. Simeone, T. Segreto, and R. Teti, "Residual stress condition monitoring via sensor fusion in turning of Inconel 718," 2013, doi: 10.1016/j.procir.2013.09.013.
[15] K. Jacobus, R. E. DeVor, and S. G. Kapoor, "Machining-induced residual stress: Experimentation and modeling," *J. Manuf. Sci. Eng. Trans. ASME*, 2000, doi: 10.1115/1.538906.
[16] S. Agrawal and S. S. Joshi, "Analytical modelling of residual stresses in orthogonal machining of AISI4340 steel," *J. Manuf. Process.*, 2013, doi: 10.1016/j.jmapro.2012.11.004.
[17] J. S. Y. Liang and J. C. Su, "Residual stress modeling in orthogonal machining," *CIRP Ann. - Manuf. Technol.*, 2007, doi: 10.1016/j.cirp.2007.05.018.
[18] D. Ulutan, B. Erdem Alaca, and I. Lazoglu, "Analytical modelling of residual stresses in machining," *J. Mater. Process. Technol.*, 2007, doi: 10.1016/j.jmatprotec.2006.09.032.
[19] J. C. Outeiro, J. C. Pina, R. M'Saoubi, F. Pusavec, and I. S. Jawahir, "Analysis of residual stresses induced by dry turning of difficult-to-machine materials," *CIRP Ann. - Manuf. Technol.*, 2008, doi: 10.1016/j.cirp.2008.03.076.
[20] N. K. Sahu and A. B. Andhare, "Prediction of residual stress using RSM during turning of Ti–6Al–4V with the 3D FEM assist and experiments," *SN Appl. Sci.*, 2019, doi: 10.1007/s42452-019-0809-5.
[21] M. Salio, T. Berruti, and G. De Poli, "Prediction of residual stress distribution after turning in turbine disks," *Int. J. Mech. Sci.*, 2006, doi: 10.1016/j.ijmecsci.2006.03.009.
[22] X. Ji, A. H. Shih, M. Rajora, Y. M. Shao, and S. Y. Liang, "A hybrid neural network for prediction of surface residual stress in MQL face turning," 2014, doi: 10.4028/www.scientific.net/AMM.633-634.574.
[23] D. Umbrello, G. Ambrogio, L. Filice, and R. Shivpuri, "An ANN approach for predicting subsurface residual stresses and the desired cutting conditions during hard turning," *J. Mater. Process. Technol.*, 2007, doi: 10.1016/j.jmatprotec.2007.01.016.
[24] M. Cheng *et al.*, "Prediction of surface residual stress in end milling with Gaussian process regression," *Meas. J. Int. Meas. Confed.*, 2021, doi: 10.1016/j.measurement.2021.109333.
[25] J. Mathew, J. Griffin, M. Alamaniotis, S. Kanarachos, and M. E. Fitzpatrick, "Prediction of welding residual stresses using machine learning: Comparison between neural networks and neuro-fuzzy systems," *Appl. Soft Comput. J.*, 2018, doi: 10.1016/j.asoc.2018.05.017.
[26] M. Ayeb, M. Frija, and R. Fathallah, "Prediction of residual stress profile and optimization of surface conditions induced by laser shock peening process using artificial neural networks," *Int. J. Adv. Manuf. Technol.*, 2019, doi: 10.1007/s00170-018-2883-z.
[27] O. Sagi and L. Rokach, "Ensemble learning: A survey," *Wiley Interdisciplinary Reviews: Data Mining and Knowledge Discovery*. 2018, doi: 10.1002/widm.1249.
[28] M. A. Ganaie, M. Hu, A. K. Malik, M. Tanveer, and P. N. Suganthan, "Ensemble deep learning: A review," Apr. 2021, doi: 10.48550/arxiv.2104.02395.
[29] I. Tsamardinos, E. Greasidou, and G. Borboudakis, "Bootstrapping the out-of-sample predictions for efficient and accurate cross-validation," *Mach. Learn.*, 2018, doi: 10.1007/s10994-018-5714-4.
[30] Y. Freund and R. E. Schapire, "Experiments with a New Boosting Algorithm," 1996, Accessed: Sep. 16, 2021. [Online]. Available: http://www.research.att.com/orgs/ssr/people/fyoav,schapireg/.
[31] H. Drucker, "Improving regressors using boosting techniques," *14th Int. Conf. Mach. Learn.*, 1997.
[32] M. Tranmer, J. Murphy, M. Elliot, and M. Pampaka, "Multiple Linear Regression (2 nd Edition)," 2020, Accessed: Sep. 16, 2021. [Online]. Available: https://hummedia.manchester.ac.uk/institutes/cmist/a.
[33] I. Riadi, A. Wirawan, and S. -, "Network Packet Classification using Neural Network based on Training Function and Hidden Layer Neuron Number Variation," *Int. J. Adv. Comput. Sci. Appl.*, 2017, doi: 10.14569/ijacsa.2017.080631.
[34] H. Balaga, N. Gupta, and D. N. Vishwakarma, "GA trained parallel hidden layered ANN based differential protection of three phase power transformer," *Int. J. Electr. Power Energy Syst.*, 2015, doi: 10.1016/j.ijepes.2014.11.028.
[35] G. E. Hinton, S. Osindero, and Y. W. Teh, "A fast learning algorithm for deep belief nets," *Neural Comput.*, 2006, doi: 10.1162/neco.2006.18.7.1527.

[36] S. Karsoliya, "Approximating Number of Hidden layer neurons in Multiple Hidden Layer BPNN Architecture," *Int. J. Eng. Trends Technol.*, 2012.
[37] S. Ray, "A Quick Review of Machine Learning Algorithms," 2019, doi: 10.1109/COMITCon.2019.8862451.
[38] Y. Liu, Y. Wang, and J. Zhang, "New machine learning algorithm: Random forest," 2012, doi: 10.1007/978-3-642-34062-8_32.
[39] D. Chicco, M. J. Warrens, and G. Jurman, "The coefficient of determination R-squared is more informative than SMAPE, MAE, MAPE, MSE and RMSE in regression analysis evaluation," *PeerJ Comput. Sci.*, 2021, doi: 10.7717/PEERJ-CS.623.
[40] X. Fu *et al.*, "Accuracy of X-ray diffraction measurement of residual stresses in shot peened titanium alloy samples," *Nondestruct. Test. Eval.*, 2019, doi: 10.1080/10589759.2019.1573239.
[41] M. R. Abonazel and O. M. Saber, "A comparative study of robust estimators for poisson regression model with outliers," *J. Stat. Appl. Probab.*, 2020, doi: 10.18576/jsap/090208.
[42] M. Kontaki, A. Gounaris, A. N. Papadopoulos, K. Tsichlas, and Y. Manolopoulos, "Efficient and flexible algorithms for monitoring distance-based outliers over data streams," *Inf. Syst.*, 2016, doi: 10.1016/j.is.2015.07.006.
[43] I. Oleaga, C. Pardo, J. J. Zulaika, and A. Bustillo, "A machine-learning based solution for chatter prediction in heavy-duty milling machines," *Meas. J. Int. Meas. Confed.*, 2018, doi: 10.1016/j.measurement.2018.06.028.
[44] A. Kortabarria, A. Madariaga, E. Fernandez, J.a. Esnaola, and P. J. Arrazola, "A comparative study of residual stress profiles on inconel 718 induced by dry face turning," 2011, doi: 10.1016/j.proeng.2011.11.105.
[45] A. B. Sadat, M. Y. Reddy, and B. P. Wang, "Plastic deformation analysis in machining of Inconel-718 nickel-base superalloy using both experimental and numerical methods," *Int. J. Mech. Sci.*, 1991, doi: 10.1016/0020-7403(91)90005-N.
[46] V. Veeranaath, R. K. Das, S. K. Rai, S. Singh, and P. Sharma, "Experimental Study and Optimization of Residual Stresses in Machining of Ti6Al4V Using Titanium and Multi-layered Inserts," 2020, doi: 10.1088/1757-899X/912/3/032028.
[47] J. D. P. Velásquez, A. Tidu, B. Bolle, P. Chevrier, and J. J. Fundenberger, "Sub-surface and surface analysis of high speed machined Ti-6Al-4V alloy," *Mater. Sci. Eng. A*, 2010, doi: 10.1016/j.msea.2009.12.018.
[48] S. Isakson, M. I. Sadik, A. Malakizadi, and P. Krajnik, "Effect of cryogenic cooling and tool wear on surface integrity of turned Ti-6Al-4V," 2018, doi: 10.1016/j.procir.2018.05.061.
[49] Z. Pan, S. Y. Liang, H. Garmestani, D. Shih, and E. Hoar, "Residual stress prediction based on MTS model during machining of Ti-6Al-4V," *Proc. Inst. Mech. Eng. Part C J. Mech. Eng. Sci.*, 2019, doi: 10.1177/0954406218805122.
[50] S. Joshi, A. Tewari, and S. S. Joshi, "Microstructural characterization of chip segmentation under different machining environments in orthogonal machining of Ti6Al4V," *J. Eng. Mater. Technol. Trans. ASME*, 2015, doi: 10.1115/1.4028841.

Appendix 1. Datasets of Inconel 718

Data #	Tool Material	Rake Angle	Coolant Type	Cutting Speed [m/min]	Feed (mm/rev)	Width of Cut [mm]	Surface Residual Stresses [MPa]	Reference
1	Coated	0	MWF	35	0.200	0.4	903	
2	Coated	0	MWF	44	0.100	0.3	609	
3	Coated	0	MWF	53	0.100	0.4	851	
4	Coated	0	MWF	35	0.150	0.3	775	
5	Coated	0	MWF	44	0.150	0.4	1020	[5]
6	Coated	0	MWF	35	0.100	0.2	562	
7	Coated	0	MWF	53	0.200	0.3	1125	
8	Coated	0	MWF	44	0.200	0.2	983	
9	Coated	0	MWF	53	0.150	0.2	1150	
10	Coated	Positive	DRY	50	0.075	0.2	371	
11	Coated	Positive	DRY	50	0.100	0.2	411	
12	Coated	Positive	DRY	50	0.125	0.2	444	
13	Coated	Positive	DRY	50	0.150	0.2	466	
14	Coated	Positive	DRY	60	0.075	0.2	354	
15	Coated	Positive	DRY	60	0.100	0.2	391	
16	Coated	Positive	DRY	60	0.125	0.2	385	
17	Coated	Positive	DRY	60	0.150	0.2	479	
18	Coated	Positive	DRY	70	0.075	0.2	321	[3]
19	Coated	Positive	DRY	70	0.100	0.2	366	
20	Coated	Positive	DRY	70	0.125	0.2	383	
21	Coated	Positive	DRY	70	0.150	0.2	437	
22	Coated	Positive	DRY	80	0.075	0.2	340	
23	Coated	Positive	DRY	80	0.100	0.2	377	
24	Coated	Positive	DRY	80	0.125	0.2	395	
25	Coated	Positive	DRY	80	0.150	0.2	459	
26	NA	0	DRY	30	0.150	0.15	376	
27	NA	0	DRY	30	0.250	0.15	575	[44]
28	NA	0	DRY	70	0.150	0.15	589	
29	NA	0	DRY	70	0.250	0.15	370	
30	Uncoated	Positive	MWF	60	0.015	0.15	153	
31	Uncoated	Positive	MWF	60	0.025	0.3	81	
32	Uncoated	Positive	MWF	60	0.035	0.45	196	
33	Uncoated	Positive	MWF	60	0.045	0.6	182	
34	Uncoated	Positive	MWF	80	0.015	0.15	243	
35	Uncoated	Positive	MWF	80	0.025	0.3	523	
36	Uncoated	Positive	MWF	80	0.035	0.45	514	
37	Uncoated	Positive	MWF	80	0.045	0.6	568	
38	Uncoated	Positive	MWF	100	0.025	0.15	230	
39	Uncoated	Positive	MWF	100	0.015	0.3	550	
40	Uncoated	Positive	MWF	100	0.045	0.45	177	
41	Uncoated	Positive	MWF	100	0.035	0.6	193	
42	Uncoated	Positive	MWF	120	0.025	0.15	203	
43	Uncoated	Positive	MWF	120	0.015	0.3	216	
44	Uncoated	Positive	MWF	120	0.045	0.45	211	
45	Uncoated	Positive	MWF	120	0.035	0.6	197	
46	Uncoated	Positive	MWF	60	0.045	0.15	188	[4]
47	Uncoated	Positive	MWF	60	0.035	0.3	175	
48	Uncoated	Positive	MWF	60	0.025	0.45	210	
49	Uncoated	Positive	MWF	60	0.015	0.6	221	
50	Uncoated	Positive	MWF	80	0.045	0.15	186	
51	Uncoated	Positive	MWF	80	0.035	0.3	206	
52	Uncoated	Positive	MWF	80	0.025	0.45	162	
53	Uncoated	Positive	MWF	80	0.015	0.6	196	
54	Uncoated	Positive	MWF	100	0.035	0.15	142	
55	Uncoated	Positive	MWF	100	0.045	0.3	167	
56	Uncoated	Positive	MWF	100	0.015	0.45	198	
57	Uncoated	Positive	MWF	100	0.025	0.6	231	
58	Uncoated	Positive	MWF	120	0.035	0.15	142	
59	Uncoated	Positive	MWF	120	0.045	0.3	179	
60	Uncoated	Positive	MWF	120	0.015	0.45	215	
61	Uncoated	Positive	MWF	120	0.025	0.6	217	

62	Uncoated	Positive	MWF	45	0.100	0.3	379	
63	Uncoated	Positive	MWF	45	0.125	0.3	182	
64	Uncoated	Positive	MWF	45	0.150	0.3	455	
65	Uncoated	Positive	MWF	50	0.100	0.3	309	
66	Uncoated	Positive	MWF	50	0.125	0.3	644	
67	Uncoated	Positive	MWF	50	0.150	0.3	767	
68	Uncoated	Positive	MWF	55	0.100	0.3	378	
69	Uncoated	Positive	MWF	55	0.125	0.3	662	
70	Uncoated	Positive	MWF	55	0.150	0.3	1009	[14]
71	Uncoated	Positive	MWF	80	0.150	0.3	1228	
72	Uncoated	Positive	MWF	80	0.300	0.3	1515	
73	Uncoated	Positive	MWF	100	0.150	0.3	1376	
74	Uncoated	Positive	MWF	100	0.300	0.3	1521	
75	Uncoated	Positive	DRY	80	0.150	0.3	1387	
76	Uncoated	Positive	DRY	80	0.300	0.3	1473	
77	Uncoated	Positive	DRY	100	0.150	0.3	1277	
78	Uncoated	Positive	DRY	100	0.300	0.3	1412	
79	Ceramic	Positive	MWF	12	0.028	3.24	608	
80	Ceramic	Positive	MWF	21	0.028	3.24	757	[45]
81	Ceramic	Positive	MWF	38	0.028	3.24	827	
82	Coated	Positive	MWF	40	0.150	0.25	611	
83	Coated	Positive	MWF	40	0.250	0.25	761	
84	Coated	Positive	MWF	80	0.150	0.25	244	
85	Coated	Positive	MWF	80	0.250	0.25	298	[13]
86	Coated	Positive	MWF	120	0.150	0.25	192	
87	Coated	Positive	MWF	120	0.250	0.25	326	
88	Uncoated	Positive	MWF	40	0.150	0.25	192	
89	Uncoated	Positive	MWF	40	0.250	0.25	259	
90	Ceramic	Positive	MWF	75	0.028	3.24	926	[45]
91	Ceramic	Positive	MWF	97	0.028	3.24	1039	
92	Coated	0	DRY	40	0.100	0.5	922	
93	Coated	0	DRY	60	0.100	0.5	720	
94	Coated	0	DRY	80	0.100	0.5	721	[9]
95	Coated	0	MWF	40	0.100	0.5	239	
96	Coated	0	MWF	60	0.100	0.5	227	
97	Coated	0	MWF	80	0.100	0.5	736	

Appendix 2. Datasets of Ti6Al4V

Data #	Tool Material	Rake Angle	Coolant Type	Cutting Speed [m/min]	Feed [mm/rev]	Width of Cut [mm]	Surface Residual Stress [MPa]	Reference
1	Uncoated	0	DRY	55	0.100	2	112	[11]
2	Uncoated	0	DRY	90	0.100	2	167	
3	Coated	0	DRY	55	0.100	2	134	
4	Coated	0	DRY	90	0.100	2	112	
5	Coated	0	DRY	50	0.100	1	387	[46]
6	Coated	0	DRY	50	0.200	2	380	
7	Coated	0	DRY	100	0.100	2	376	
8	Coated	0	DRY	100	0.200	1	379	
9	Coated	0	DRY	50	0.100	1	377	
10	Coated	0	DRY	50	0.200	2	381	
11	Coated	0	DRY	100	0.100	2	382	
12	Coated	0	DRY	100	0.200	1	378	
13	Ceramic	0	DRY	20	0.120	5	-265	[47]
14	Ceramic	0	DRY	40	0.120	5	-572	
15	Ceramic	0	DRY	60	0.120	5	-572	
16	Ceramic	0	DRY	140	0.120	5	198	
17	Ceramic	0	DRY	260	0.120	5	385	
18	Ceramic	0	DRY	420	0.120	5	618	
19	Ceramic	0	DRY	540	0.120	5	575	
20	Ceramic	0	DRY	660	0.120	5	440	
21	Uncoated	Negative	DRY	75	0.200	1.2	150	[12]
22	Uncoated	Negative	MQL	75	0.200	1.2	74	
23	Uncoated	Negative	MWF	75	0.200	1.2	11	
24	Uncoated	Negative	DRY	75	0.200	1.2	48	
25	Uncoated	Negative	MQL	75	0.200	1.2	-29	
26	Uncoated	Negative	MWF	75	0.200	1.2	-73	
27	Coated	Negative	DRY	75	0.200	1.2	-29	
28	Coated	Negative	MQL	75	0.200	1.2	47	
29	Coated	Negative	MWF	75	0.200	1.2	-14	
30	Coated	Negative	DRY	75	0.200	1.2	51	
31	Coated	Negative	MQL	75	0.200	1.2	161	
32	Coated	Negative	MWF	75	0.200	1.2	18	
33	Uncoated	0	DRY	100	0.012	0.06	-385	[10]
34	Uncoated	Positive	DRY	40	0.012	0.12	-275	
35	Uncoated	Positive	DRY	40	0.002	0.06	-180	
36	Uncoated	0	DRY	100	0.002	0.12	-110	
37	Uncoated	Positive	DRY	100	0.012	0.12	-75	
38	Uncoated	0	DRY	40	0.002	0.12	-230	
39	Uncoated	Positive	DRY	100	0.002	0.06	-110	
40	Uncoated	0	DRY	40	0.012	0.06	-110	
41	Uncoated	0	DRY	100	0.012	0.06	-380	
42	Uncoated	Positive	DRY	40	0.012	0.12	-175	
43	Uncoated	Positive	DRY	40	0.002	0.06	-190	
44	Uncoated	Positive	DRY	100	0.002	0.12	-120	
45	Uncoated	Positive	DRY	100	0.012	0.12	-15	
46	Uncoated	0	DRY	40	0.002	0.12	-200	
47	Uncoated	Positive	DRY	100	0.002	0.06	40	
48	Uncoated	0	DRY	40	0.012	0.06	-255	
49	Coated	Positive	DRY	90	0.100	0.50	-776	[20]
50	Coated	Positive	DRY	151	0.200	0.50	-1001	
51	Coated	Positive	DRY	70	0.150	0.75	-338	
52	Coated	Positive	DRY	171	0.150	0.75	-314	
53	Coated	Positive	DRY	121	0.230	0.75	-173	
54	Coated	Positive	DRY	121	0.150	0.75	-395	
55	Uncoated	NA	MWF	70	0.150	1.5	-566	[48]
56	Uncoated	NA	CRYO	70	0.150	1.5	-591	
57	Uncoated	Positive	DRY	80	0.200	1	-196	[8]
58	Uncoated	Positive	MWF	80	0.200	1	-245	
59	Uncoated	Positive	CRYO	80	0.200	1	-335	
60	Uncoated	Positive	CRYO	80	0.200	1	-432	
61	NA	0	NA	26	0.100	0.1	-325	[49]
62	NA	0	NA	26	0.500	0.1	-315	

63	Coated	Negative	DRY	45	0.250	0.25	-318	
64	Coated	Negative	DRY	45	0.300	0.5	-174	
65	Coated	Negative	DRY	45	0.350	0.75	-151	
66	Coated	Negative	DRY	60	0.250	0.5	-189	
67	Coated	Negative	DRY	60	0.300	0.75	-71	[6]
68	Coated	Negative	DRY	60	0.350	0.25	-255	
69	Coated	Negative	DRY	75	0.250	0.75	-195	
70	Coated	Negative	DRY	75	0.300	0.25	-71	
71	Coated	Negative	DRY	75	0.350	0.5	-220	
72	Coated	Positive	DRY	23	0.110	1	-172	
73	Coated	Positive	CRYO	23	0.110	1	-298	[50]
74	Coated	Positive	DRY	92	0.110	1	-134	
75	Coated	Positive	CRYO	92	0.110	1	-184	
76	Uncoated	Positive	MWF	70	0.200	0.25	-293	
77	Uncoated	Positive	MWF	100	0.200	0.25	-387	
78	Uncoated	Positive	MWF	125	0.200	0.25	-203	
79	Uncoated	Positive	MWF	150	0.200	0.25	22	
80	Uncoated	Positive	MWF	175	0.200	0.25	164	[7]
81	Uncoated	Positive	MWF	50	0.200	1	-338	
82	Uncoated	Positive	MWF	70	0.200	1	-393	
83	Uncoated	Positive	MWF	100	0.200	1	-474	
84	Uncoated	Positive	MWF	150	0.200	1	-245	
85	Uncoated	Positive	MWF	175	0.200	1	-181	
86	Coated	Negative	DRY	30	0.050	4	-107	
87	Coated	Negative	DRY	60	0.050	4	710	
88	Coated	Negative	DRY	120	0.050	4	272	[2]
89	Coated	Negative	DRY	30	0.150	4	-696	
90	Coated	Negative	DRY	60	0.150	4	810	
91	Coated	Negative	DRY	120	0.150	4	447	

Bitlis Eren Üniversitesi Fen Bilimleri Dergisi
BİTLİS EREN UNIVERSITY JOURNAL OF SCIENCE
ISSN: 2147-3129/e-ISSN: 2147-3188
VOLUME: 11 NO: 3 PAGE: 880-892 YEAR: 2022
DOI: 10.17798/bitlisfen.1135356

Prioritization of Districts in terms of Disaster Preparedness Planning: A Case Study for the Expected Istanbul Earthquake

Ahmet AKTAŞ[1*]

[1]*University of Turkish Aeronautical Association, Department of Industrial Engineering, Ankara (ORCID: 0000-0002-4394-121X)*

Keywords: Disaster management, MCDM, SWARA, WASPAS, Earthquake preparedness planning.

Abstract
Preparedness is the second among the four phases of disaster management after mitigation. In big cities with crowded populations like İstanbul, development of a single holistic disaster preparedness plan would be too complex. At this point, the prioritization of districts is needed because of the existence of a limited amount of available resources (time, staff, money, etc.) plan development stage. This decision can be affected by several factors, so this decision can be defined as a multiple criteria decision-making problem. The main aim in this paper is to develop an analytic approach to obtain the priority rank of districts of the city for disaster preparedness plan development. To do so, a hybrid multiple criteria decision-making model based on SWARA (Stepwise Weight Assessment Ratio Analysis) and WASPAS (Weight Aggregated Sum Product Assessment) is proposed. A case study on earthquake preparedness planning in districts of İstanbul is presented to demonstrate the applicability of the proposed model. Obtained results of the model would be helpful for policy making in volunteer organizations, municipality, and government level.

1. Introduction

Dangerous events that disrupt operations in an area or community are defined as disasters [1]. Disasters can be classified into natural (floods, earthquakes, etc.), technological (cyber-attacks, nuclear attacks, etc.), environmental (air pollution, etc.), and daily hazards (accidents, etc.) classes [2]. Disasters may have economic, material, environmental and social effects and dealing with these effects is in the field of disaster management [3]. It consists a process with four phases as it shown in Figure 1, as follows [4]:

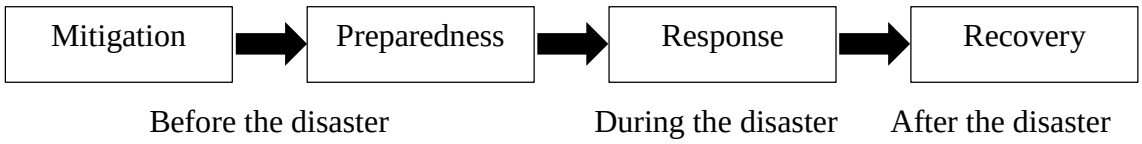

Figure 1. Phases of disaster management

Mitigation means the preventive activities before the disaster like regulation on building standards, education of the community about mitigation strategies and barrier construction. When a disaster is likely to happen, preparedness activities are performed. Preparedness activities consist of preparatory activities such as placing disaster supplies kits, preparing shelters and backup facilities, and planning rescue operations. When the disaster occurs, the response phase is put into action. Search and rescue operations, evacuation of people, and firefighting are some activities related to this phase.

*Corresponding author: aaktas@thk.edu.tr
Received: 24.06.2022, Accepted: 16.08.2022

Finally, the recovery phase corresponds to the repair and reconstruction operations after the disaster to return to normal life in the area.

Istanbul is one of the major cities in Turkey, with a population of more than 15 million people and most of the economic activities in the country occur in this city. According to several research including Parsons et al. [5], an earthquake greater than 7.0 magnitude is expected with a significant probability in Istanbul in the near future. Since the earthquake is likely to happen, preparedness plans for the disaster must be made. However, preparedness plans require an important amount of resources to be allocated and there are 39 districts in İstanbul. So, prioritization of the districts for preparedness planning is needed.

Preparedness planning for a disaster contains various strategic decision problems that require consideration of a number of criteria simultaneously. This kind of problems may have a complex structure and obtaining a solution to them may be difficult because of the conflicts between alternative values on different criteria. Multiple criteria decision making (MCDM) approaches are useful for modelling and solution of decision problems with a finite number of alternatives and criteria [6]. Therefore, MCDM approaches could help in the determination of strategic decisions related to disaster management concept.

Strategic decisions within the context of disaster management have commonly taken interest of researchers. Some of the recent studies can be summarized as follows:

Mitigation scenarios from the cascading effects of a disaster, which can occur by reactivation of a volcano in Italy were analyzed by using a knowledge-based decision support system [7]. ELECTRE-TRI method was used within the system as the decision-making method. Tella and Balogun [8] observed that flood susceptibility model performances vary according to the disaster area, and they focused on developing a spatial flood susceptibility model to mitigate the effects of floods in Ibadan, Nigeria. Obtained results from the integrated model based on FAHP and GIS, they demonstrated that the model provides more accurate results. A spatial decision-making model based on GIS, AHP and TOPSIS was proposed as a tool to be used in the mitigation processes of disasters [9]. The proposed model was presented with a case study on the development of an earthquake risk map in Yalova, Turkey.

Ghavami [10] indicated that the identification of strategic roads in case of a disaster is an important aspect of preparedness plans and modeled the identification process as a spatial decision-making problem. A case study in Mazandaran, Iran, was analyzed using the integrated model he proposed based on GIS and AHP and 220 road sections are classified into very high, high, low and very low strategic classes. Rezaei-Malek et al. [11] proposed a prioritization model to determine the disaster-prone areas in Tehran. By using the Fuzzy PROMETHEE-II-based approach in the study, 22 sub-divisions of the study were analyzed.

The earthquake occurrence risk in İstanbul was considered by Yılmaz and Kabak [12] within the perspective of a need for humanitarian logistic centers. To provide efficient humanitarian relief service in case of a disaster, possible locations for humanitarian logistic centers in the city were evaluated by an Interval Type-2 Fuzzy Set-based AHP – TOPSIS model. Another study on the expected İstanbul earthquake focused on the debris demolition and transfer planning [13]. Numerical analysis of a number of scenarios by using a stochastic MILP model seems as an indicator of the importance of utilization of analytical models for preparedness planning. Barutcu and Ic [14] focused on the need of a field hospital in case of a possible earthquake in Ankara and they handled the site selection decision for the field hospital. A multi-criteria analysis based on the VIKOR method to evaluate three main parks in the city center, which were considered as alternative locations, was conducted by taking eight criteria into account.

As it can be understood from the aforementioned literature findings, different problems related to disaster management decisions have been analyzed by researchers by using various MCDM techniques. However, no studies have taken the prioritization of the districts of a big city for preparedness planning for an expected earthquake so far. Therefore, the main aim of this study is to develop an analytical approach to this strategic decision. To do so, a hybrid MCDM model based on SWARA [15] (Stepwise Weight Assessment Ratio Analysis) and WASPAS [16] (Weight Aggregated Sum Product Assessment) techniques was proposed. Districts of Istanbul, which is a big city with a great expectation of an earthquake occurrence, were prioritized in terms of preparedness planning for the expected great Istanbul Earthquake by using the proposed approach. The main contributions of the study can be listed as follows:

- A multi-criteria analysis model based on SWARA and WASPAS was proposed to determine preparedness planning decisions for an expected earthquake.

- A case study of district prioritization for preparedness planning in a big city is presented.
- 39 districts of Istanbul were evaluated by considering five criteria.

The remainder of the study is organized as follows: 2nd section presents the proposed decision model with basic definitions related to the methodology and decision elements of the model. In the 3rd section, obtained results of the study are given with discussion. The study was concluded in the 4th part by presentation of managerial implications and suggestions for further studies.

2. Proposed Model

In this study, a multi-criteria ranking model based on the SWARA and WASPAS methods was proposed. Within the proposed model, SWARA was used to obtain the importance degree of criteria and WASPAS was used to rank alternatives. This part contains an explanation of the SWARA and WASPAS methods along with a flowchart of the proposed model.

2.1. SWARA

SWARA is a multi-criteria decision-making method, which was introduced by Kersuliene et al. in 2010 [15], makes it possible for decision-makers to state their feelings without using fixed scales or measures. SWARA provides a rational decision according to the aggregated opinions of decision-makers by weighting of decision elements. There are several publications consisting of the SWARA method on decision problems in a wide application area, such as the third part logistics service provider evaluation [17] and country evaluation [18]. Steps of the method are as follows:

Step 1. Ranking of criteria and determination of relative importance scores (s_j):

Each decision-maker ranks all the criteria (x_j) based on the importance degree they define. No importance degree is given to the most important criterion and the remaining criteria were compared with the $(j+1)^{th}$ criterion by assigning an relative importance score denoted by s_j ($0 \leq s_j \leq 1$).

Step 2. Determination of coefficient values (c_j):

Relative importance scores obtained from the decision makers' assessment are used in Eq. (1) to obtain coefficient values. The coefficient value of the most important criterion is equal to "1".

$$c_j = \begin{cases} 1 & ,j = 1 \\ s_j + 1 & ,j > 1 \end{cases} \quad (1)$$

Step 3. Calculation of revised weights (v_j):

Eq. (2) is used to obtain the revised weight value of the decision elements. By this way, importance values of criteria are formed in a descending order of importance rank.

$$v_j = \begin{cases} 1 & ,j = 1 \\ \frac{v_{j-1}}{c_j} & ,j > 1 \end{cases} \quad (2)$$

Step 4. Calculation of relative weights for each decision-maker (w_j):

Relative weight values of the decision elements are calculated using vector normalization of the revised weight values. The mathematical expression of the calculation is given by Eq. (3).

$$w_j = \frac{v_j}{\Sigma_{j=1}^{n} v_j} \quad (3)$$

Step 5. Calculation of final weights (W_j):
The arithmetic mean of the relative weight values for each decision-maker is used to obtain the final weights of the decision elements. In other words, the sum of individual weight values is divided by the number of decision-makers to obtain final weight values.

2.2. WASPAS

WASPAS was introduced into the literature in 2012 by Zavadskas et al. [16] as an integrated form of the Weighted Sum and Weighted Product models. The decision-making procedure in this method follows six steps, including the formation and normalization of the decision matrix, calculation of weighted sum and weighted product values and aggregation of the results of these two models. WASPAS have taken a significant attention of researchers and have been applied in several decision problems like digital library evaluation [19] and green supplier selection [20]. The decision-making process with WASPAS consists of the following steps:

Step 1. Formation of the decision matrix (D):

Decision alternatives are evaluated in this step with respect to each criterion. Either the real numerical values of alternative scores or linguistic or scaled values can be used in the decision matrix. For a decision problem with *n* criteria and *m* alternatives, decision matrix (*D*) can be shown as follows, where d_{ij} denotes the score of alternative *i* with respect to criterion *j*.

$$D = \begin{bmatrix} d_{11} & \cdots & d_{1n} \\ \vdots & \ddots & \vdots \\ d_{m1} & \cdots & d_{mn} \end{bmatrix}$$

Step 2. Determination of a normalized decision matrix (*N*):

In order to mitigate the effects of unit and range differences between alternative scores within the decision-making process, normalization procedures are commonly applied in MCDM methods. In the same sense, a normalization step is applied in WASPAS, too. Eq. (4) and Eq. (5) are applied to obtain normalized values for benefit type and cost type criteria, respectively. In these equations, n_{ij} denotes the normalized value of alternative *i* with respect to criterion *j*.

$$n_{ij} = \frac{d_{ij}}{\max_i d_{ij}} \tag{4}$$

$$n_{ij} = \frac{\min_i d_{ij}}{d_{ij}} \tag{5}$$

A normalized decision matrix is formed using normalized values in the following form:

$$N = \begin{bmatrix} n_{11} & \cdots & n_{1n} \\ \vdots & \ddots & \vdots \\ n_{m1} & \cdots & n_{mn} \end{bmatrix}$$

Step 3. Calculation of weighted sum values for alternatives ($Q_i^{(1)}$):

Alternative scores from the weighted sum model are calculated using the summation the multiplication values of the alternative scores with respect to each criterion and corresponding criterion weight. The mathematical formulation of weighted sum calculation is given by Eq. (6) as follows, where W_j denotes the weight of criterion *j*.

$$Q_i^{(1)} = \sum_{j=1}^{n} W_j n_{ij} \tag{6}$$

Step 4. Calculation of weighted product values for alternatives ($Q_i^{(2)}$):

Alternative scores from the weighted product model are calculated by the multiplication the ${W_j}^{th}$ power of alternative scores with respect to each criterion. The mathematical formulation of weighted product calculation is given by Eq. (7) as follows.

$$Q_i^{(2)} = \prod_{j=1}^{n} {n_{ij}}^{W_j} \tag{7}$$

Step 5. Aggregation of weighted sum and weighted product values for alternatives (Q_i):

In order to ease decision making, results obtained from the weighted sum and weighted product models are aggregated. The resulting value is calculated using Eq. (8), where the effect of weighted sum and weighted product models are assumed to be equal.

$$\begin{aligned} Q_i &= 0.5 * Q_i^{(1)} + 0.5 * Q_i^{(2)} \\ &= 0.5 * \sum_{j=1}^{n} W_j n_{ij} + 0.5 * \prod_{j=1}^{n} {n_{ij}}^{W_j} \end{aligned} \tag{8}$$

The assumption of equal effect of weighted sum and product on the final decision can be generalized using an effect coefficient of λ ($0 \leq \lambda \leq 1$) for the weighted sum model as it is given in Eq. (9) as follows:

$$\begin{aligned} Q_i &= \lambda * Q_i^{(1)} + (1-\lambda) * Q_i^{(2)} \\ &= \lambda * \sum_{j=1}^{n} W_j n_{ij} + (1-\lambda) * \prod_{j=1}^{n} {n_{ij}}^{W_j} \end{aligned} \tag{9}$$

The final decision converges to the results of the weighted sum model by the increasing values of λ and converges to the results of the weighted product model by the decreasing values.

2.3. Steps of the Proposed Model

Since the proposed model consists of the steps of two MCDM models, the decision-making process by using the integrated model is explained in this part. The process starts with the problem definition phase, which contains the definition of the problem goal, criteria and alternatives and decision-making group. The second phase of the process is the calculations made by SWARA, which are as the weight calculations from the individual assessments of each decision-maker and determination of final weights by aggregation. The last phase of the proposed approach is the evaluation of alternatives by WASPAS method. Criteria weights obtained in the second phase are used in the WASPAS phase to obtain weighted sum and weighted product

values. A flowchart for the proposed model is given in Figure 2 as follows:

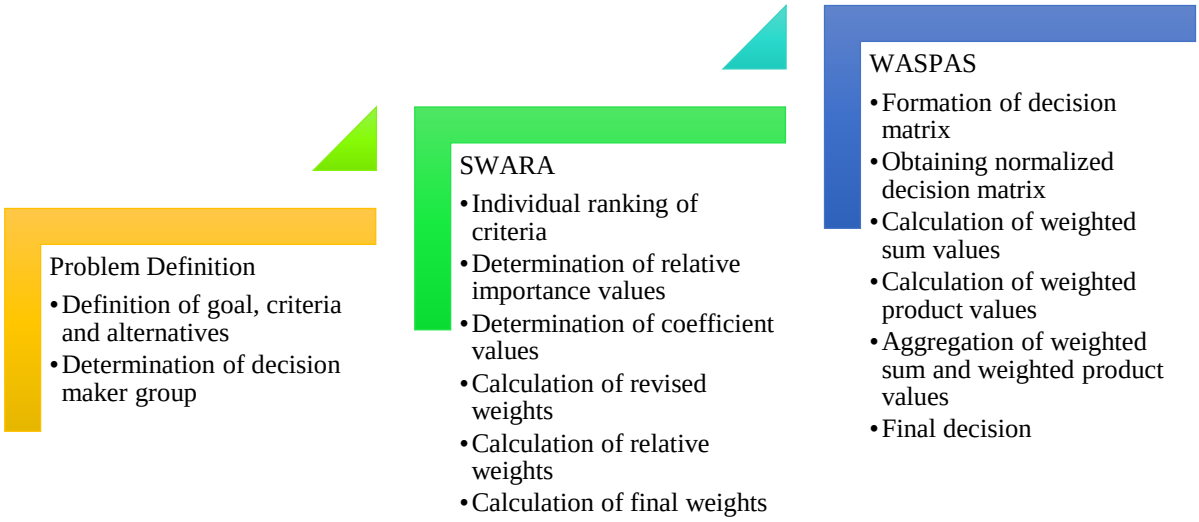

Figure 2. Flowchart of the proposed model

3. Case Study

The losses caused by the Marmara Earthquake in 1999 increased the awareness of the precautions to be taken in İstanbul. Furthermore, strike risk of a major earthquake with a magnitude greater than 7.5 in İstanbul is very high in the next decades. Therefore, preparedness planning for İstanbul is an urgent issue. However, İstanbul is a big city with 39 districts (Figure 3) and allocation of scarce resources on disaster management to all districts at the same time is not possible. For this reason, the prioritization of districts must be made using some analytical models.

Figure 3. Map of the city with its districts [21]

In this part of the study, a case study of districts' prioritization for earthquake preparedness planning in İstanbul is presented. To do so, definitions of decision goal and criteria were firstly given with the problem data for each district. Then, importance degree of each criterion was determined by an expert

group of five people. The expert group consisted of two experts from the Earthquake and Soil Investigation Directorate of the Metropolitan Municipality of İstanbul, two experts from a state university's Civil Engineering Department and an expert in sociological studies. Their opinions were collected to determine the importance of criteria and finally, data provided by the Metropolitan Municipality was used to determine the rank of districts for earthquake preparedness planning.

3.1. Problem Definition

İstanbul is a big and beautiful city with a population greater than 15 million and it contains important financial institutions, production facilities and historical buildings. Due to its population, contributions to the country's economy and world heritage, this city needs to be protected against disasters. So the decision goal in this study is the determination of the rank of districts of İstanbul.

A set of meetings were established by the expert group to determine the factors that could be effective in the ranking decision. The criteria chosen by the expert group are listed as follows:

- Population (x_1): Population is an important aspect for preparedness planning. The number of people who will be affected by the possible earthquake in districts is considered an important factor.
- Disaster assembly points (x_2): In case of an earthquake, people should directly go to the nearest disaster assembly point. Since some districts may have high population density in İstanbul, this criterion is measured by the area per capita in disaster assembly points (m^2).
- Building damage (x_3): Strength of a considerable number of existing buildings in İstanbul have the risk of being damaged by the expected earthquake and building damage may worsen the effect of the earthquake on people. Therefore, building damage is an important factor in earthquake preparedness planning. In this study, this criterion is defined by the proportion of buildings expected to be heavily or very heavily damaged in a 7.5 magnitude earthquake.
- Expected number of deaths (x_4): The most important cause of damage related to disasters is the death of people in the disaster region and during preparedness planning, minimization of the expected number of deaths should be considered as an important factor.
- Expected number of heavy injuries (x_5): Similar to the C_4 criterion, heavily injuries suffered by people because of a disaster is an important factor. The less number of heavily injuries occur, the more efficient care services after the disaster can be.

Since the aim of the study is to rank districts of İstanbul, alternatives are these 39 districts. The hierarchical structure of the problem is represented in Figure 4 as follows:

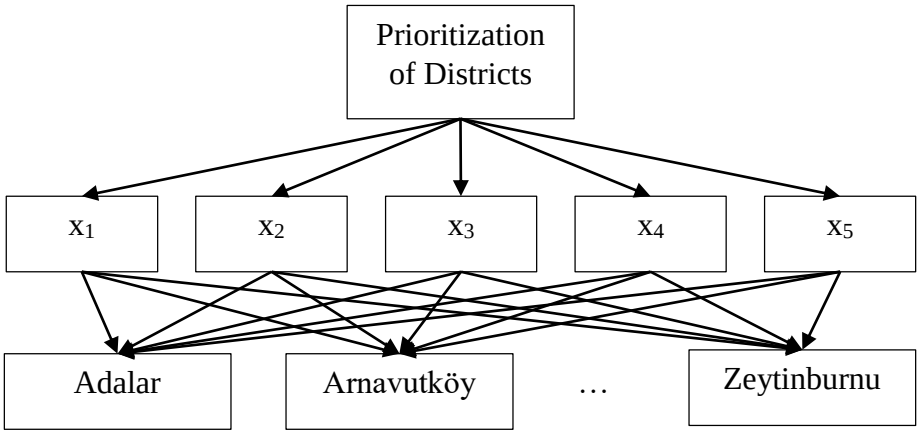

Figure 4. Hierarchical structure of the problem

3.2. Determination of Criteria Weights

As it mentioned earlier, an expert group of five people evaluated decision criteria and their assessments were used to calculate criterion weights using the SWARA method. Steps for weight calculation are given in this part.

Step 1. Ranking of the criteria and determination of relative importance scores:

Ranking of criteria and relative importance scores were collected from each member of the expert group separately and are given in Table 1 as follows:

Table 1. Criteria rankings and relative importance scores given by experts

E1		E2		E3		E4		E5	
Rank	s_j	Rank	s_j	Rank	s_j	Rank	s_j	Rank	s_j
x_1		x_4		x_3		x_1		x_1	
x_3	0.700	x_5	0.450	x_4	0.900	x_4	0.600	x_3	0.800
x_5	0.400	x_1	0.600	x_5	0.600	x_3	0.400	x_4	0.600
x_2	0.200	x_3	0.300	x_1	0.500	x_5	0.500	x_5	0.500
x_4	0.800	x_2	0.100	x_2	0.300	x_2	0.200	x_2	0.700

Step 2. Determination of coefficient values:

By using the data in Table 1 and Eq. (1), coefficient values for criteria evaluations made by experts were determined. The coefficient values of the criteria are given in Table 2 as follows:

Table 2. Coefficient values of the criteria

E1			E2			E3			E4			E5		
Rank	s_j	c_j	Rank	s_j	c_j	Rank	s_j	c_j	Rank	s_j	c_j	Rank	s_j	c_j
x_1	0.000	1.000	x_4	0.000	1.000	x_3	0.000	1.000	x_1	0.000	1.000	x_1	0.000	1.000
x_3	0.700	1.700	x_5	0.450	1.450	x_4	0.900	1.900	x_4	0.600	1.600	x_3	0.800	1.800
x_5	0.400	1.400	x_1	0.600	1.600	x_5	0.600	1.600	x_3	0.400	1.400	x_4	0.600	1.600
x_2	0.200	1.200	x_3	0.300	1.300	x_1	0.500	1.500	x_5	0.500	1.500	x_5	0.500	1.500
x_4	0.800	1.800	x_2	0.100	1.100	x_2	0.300	1.300	x_2	0.200	1.200	x_2	0.700	1.700

Step 3. Calculation of revised weights (v_j):

c_j values in Table 2 and Eq. (2) was used to calculate revised weights of criteria. The revised weight values are given in Table 3 as follows:

Table 3. Coefficient values of the criteria

E1			E2			E3			E4			E5		
Rank	c_j	v_j	Rank	c_j	v_j	Rank	c_j	v_j	Rank	c_j	v_j	Rank	c_j	v_j
x_1	1.000	1.000	x_4	1.000	1.000	x_3	1.000	1.000	x_1	1.000	1.000	x_1	1.000	1.000
x_3	1.700	0.588	x_5	1.450	0.690	x_4	1.900	0.526	x_4	1.600	0.625	x_3	1.800	0.556
x_5	1.400	0.420	x_1	1.600	0.431	x_5	1.600	0.329	x_3	1.400	0.446	x_4	1.600	0.347
x_2	1.200	0.350	x_3	1.300	0.332	x_1	1.500	0.219	x_5	1.500	0.298	x_5	1.500	0.231
x_4	1.800	0.195	x_2	1.100	0.301	x_2	1.300	0.169	x_2	1.200	0.248	x_2	1.700	0.136

Step 4. Calculation of relative weights for each decision-maker (w_j):

Relative weight values of decision elements were calculated using Eq. (3) and the resulting values are given in Table 4 as follows:

Table 4. Relative weights of criteria

E1			E2			E3			E4			E5		
Rank	v_j	w_j	Rank	v_j	w_j	Rank	v_j	w_j	Rank	v_j	w_j	Rank	v_j	w_j
x_1	1.000	0.392	x_4	1.000	0.363	x_3	1.000	0.446	x_1	1.000	0.382	x_1	1.000	0.440
x_3	0.588	0.230	x_5	0.690	0.250	x_4	0.526	0.235	x_4	0.625	0.239	x_3	0.556	0.245
x_5	0.420	0.165	x_1	0.431	0.157	x_5	0.329	0.147	x_3	0.446	0.171	x_4	0.347	0.153
x_2	0.350	0.137	x_3	0.332	0.120	x_1	0.219	0.098	x_5	0.298	0.114	x_5	0.231	0.102
x_4	0.195	0.076	x_2	0.301	0.109	x_2	0.169	0.075	x_2	0.248	0.095	x_2	0.136	0.060

Step 5. Calculation of final weights (W_j):

Final weights of criteria were calculated using arithmetic mean of relative weight values of the corresponding criteria and are given in Table 5 as follows:

Table 5. Final weights of criteria

Criteria	W_j
x_1	0.265
x_2	0.099
x_3	0.252
x_4	0.222
x_5	0.162

As it is seen from Table 5, the most important criterion is determined as the population. This means that population must be considered primarily for disaster preparedness planning ranking of districts based on the aggregated opinions of the expert group. Building damage and expected number of deaths follow the population criterion, respectively. The disaster assembly points criterion is seen as the least important aspect of district ranking.

The calculated values in this phase will be used in the Weighted Sum and Weighted Product models as weighting factors.

3.3. Ranking of Districts

The WASPAS method was used in this study to determine the rank of districts. The steps applied to obtain district ranking are given in this part as follows:

Step 1. Formation of the decision matrix:

Score values for each district in terms of each criterion were collected from different data sources. For example, population data of districts were obtained from the population statistics shared by the Turkish Statistics Institute [22], districts' scores in terms of disaster assembly points criterion were gathered from an article on a news website [23] and data on building damage, expected number of deaths and heavy injuries were collected from some reports about the possible losses of the expected earthquake in each district published by the Istanbul Metropolitan Municipality [24]. The decision matrix for the case study is given in Table 6.

Table 6. Decision matrix

Districts	x_1	x_2	x_3	x_4	x_5	Districts	x_1	x_2	x_3	x_4	x_5
Adalar	16372	3.45	0.2363	76	61	Gaziosmanpaşa	493096	0.55	0.0544	140	83
Arnavutköy	312023	1.96	0.0409	0	0	Güngören	283083	0.67	0.1198	754	415
Ataşehir	427217	1.86	0.0583	89	47	Kadıköy	485233	0.78	0.0724	190	93
Avcılar	457981	0.42	0.0915	465	239	Kağıthane	454550	0.94	0.0466	84	44
Bağcılar	744351	0.53	0.1007	1179	652	Kartal	480738	0.38	0.0647	176	87
Bahçelievler	605300	0.18	0.1296	1633	879	Küçükçekmece	805930	0.51	0.1448	1515	925
Bakırköy	228759	0.93	0.2216	1046	581	Maltepe	525566	0.65	0.0743	234	130
Başakşehir	503243	1.96	0.0696	71	45	Pendik	741895	0.68	0.0645	195	101
Bayrampaşa	274884	1.73	0.1353	520	340	Sancaktepe	474668	1.22	0.0512	48	24

Table 6. Decision matrix (cont.)

Beşiktaş	178938	4.45	0.0552	26	14	Sarıyer	349968	1.35	0.0472	33	21
Beykoz	248595	0.60	0.0521	25	16	Şile	41627	3.33	0.0387	0	0
Beylikdüzü	398122	4.05	0.1477	527	276	Silivri	209014	2.29	0.1010	58	27
Beyoğlu	233322	1.63	0.1084	217	150	Şişli	284294	0.98	0.0490	55	27
Büyükçekmece	269160	1.57	0.1148	288	154	Sultanbeyli	349485	0.90	0.0585	73	38
Çatalca	76131	2.02	0.0599	4	2	Sultangazi	543380	3.13	0.0340	57	27
Çekmeköy	288585	0.95	0.0285	1	0	Tuzla	284443	1.27	0.1182	268	169
Esenler	447116	0.86	0.0909	638	352	Ümraniye	726758	0.44	0.0428	42	17
Esenyurt	977489	0.86	0.0936	1003	543	Üsküdar	525395	1.03	0.0470	95	42
Eyüpsultan	417360	2.11	0.0866	168	110	Zeytinburnu	293839	0.76	0.1315	668	374
Fatih	382990	0.83	0.1783	1484	985						

Step 2. Determination of the normalized decision matrix:

As mentioned in section 2.3., normalization of the decision matrix was made using Eq. (4) and Eq. (5). In this case study, x_2 is a benefit type criterion and the other criteria (x_1, x_3, x_4, and x_5) are cost type criteria. Therefore, Eq. (4) was used to calculate normalized values for criterion x_2 and Eq. (5) was used to obtain normalized values of other criteria. A normalized decision matrix is given in Table 7.

Table 7. Normalized decision matrix

Districts	x_1	x_2	x_3	x_4	x_5	Districts	x_1	x_2	x_3	x_4	x_5
Adalar	0.017	0.052	1.000	0.047	0.062	Gaziosmanpaşa	0.504	0.327	0.230	0.086	0.084
Arnavutköy	0.319	0.092	0.173	0.000	0.000	Güngören	0.290	0.269	0.507	0.462	0.421
Ataşehir	0.437	0.097	0.247	0.055	0.048	Kadıköy	0.496	0.231	0.307	0.116	0.094
Avcılar	0.469	0.429	0.387	0.285	0.243	Kağıthane	0.465	0.191	0.197	0.051	0.045
Bağcılar	0.761	0.340	0.426	0.722	0.662	Kartal	0.492	0.474	0.274	0.108	0.088
Bahçelievler	0.619	1.000	0.548	1.000	0.892	Küçükçekmece	0.824	0.353	0.613	0.928	0.939
Bakırköy	0.234	0.194	0.938	0.641	0.590	Maltepe	0.538	0.277	0.315	0.143	0.132
Başakşehir	0.515	0.092	0.295	0.043	0.046	Pendik	0.759	0.265	0.273	0.119	0.103
Bayrampaşa	0.281	0.104	0.573	0.318	0.345	Sancaktepe	0.486	0.148	0.217	0.029	0.024
Beşiktaş	0.183	0.040	0.234	0.016	0.014	Sarıyer	0.358	0.133	0.200	0.020	0.021
Beykoz	0.254	0.300	0.221	0.015	0.016	Şile	0.043	0.054	0.164	0.000	0.000
Beylikdüzü	0.407	0.044	0.625	0.323	0.280	Silivri	0.214	0.079	0.427	0.036	0.027
Beyoğlu	0.239	0.110	0.459	0.133	0.152	Şişli	0.291	0.184	0.207	0.034	0.027
Büyükçekmece	0.275	0.115	0.486	0.176	0.156	Sultanbeyli	0.358	0.200	0.248	0.045	0.039
Çatalca	0.078	0.089	0.254	0.002	0.002	Sultangazi	0.556	0.058	0.144	0.035	0.027
Çekmeköy	0.295	0.189	0.121	0.001	0.000	Tuzla	0.291	0.142	0.500	0.164	0.172
Esenler	0.457	0.209	0.385	0.391	0.357	Ümraniye	0.743	0.409	0.181	0.026	0.017
Esenyurt	1.000	0.209	0.396	0.614	0.551	Üsküdar	0.537	0.175	0.199	0.058	0.043
Eyüpsultan	0.427	0.085	0.367	0.103	0.112	Zeytinburnu	0.301	0.237	0.557	0.409	0.380
Fatih	0.392	0.217	0.755	0.909	1.000						

Step 3. Calculation of weighted sum values for districts:

By using Eq. (6) with normalized values presented in Table 7 and criteria weights given in Table 5, weighted sum values for each district were determined. Weighted sum values are presented in Table 8.

Table 8. Weighted sum values of districts

Districts	Weighted Sum	Districts	Weighted Sum	Districts	Weighted Sum
Adalar	0.282	Büyükçekmece	0.271	Maltepe	0.302
Arnavutköy	0.137	Çatalca	0.094	Pendik	0.339
Ataşehir	0.207	Çekmeköy	0.128	Sancaktepe	0.208
Avcılar	0.367	Esenler	0.383	Sarıyer	0.166
Bağcılar	0.610	Esenyurt	0.611	Şile	0.058
Bahçelievler	0.768	Eyüpsultan	0.255	Silivri	0.185
Bakırköy	0.555	Fatih	0.679	Şişli	0.159
Başakşehir	0.237	Gaziosmanpaşa	0.257	Sultanbeyli	0.193
Bayrampaşa	0.356	Güngören	0.402	Sultangazi	0.201
Beşiktaş	0.117	Kadıköy	0.273	Tuzla	0.281
Beykoz	0.159	Kağıthane	0.211	Ümraniye	0.292
Beylikdüzü	0.387	Kartal	0.285	Üsküdar	0.230
Beyoğlu	0.244	Küçükçekmece	0.766	Zeytinburnu	0.396

According to the results of the weighted sum model, Bahçelievler is ranked as first. It is followed by Küçükçekmece and Fatih, respectively. The population in Kağıthane is a bit higher than that in Bahçelievler, but the expected number of deaths in Bahçelievler is extremely high. Also, the population of Fatih is less than many districts, but the building damage criterion score of this district requires the district to be considered primarily. Şile has the last priority, which has almost the least risky values for damage from the earthquake.

Step 4. Calculation of weighted product values for districts:

Eq. (7) was used to obtain the weighted product values for districts. The results of the weighted product model are given in Table 9.

Table 9. Weighted product values of districts

Districts	Weighted Product	Districts	Weighted Product	Districts	Weighted Product
Adalar	0.082	Büyükçekmece	0.241	Maltepe	0.261
Arnavutköy	0.000	Çatalca	0.027	Pendik	0.254
Ataşehir	0.143	Çekmeköy	0.000	Sancaktepe	0.116
Avcılar	0.356	Esenler	0.376	Sarıyer	0.094
Bağcılar	0.587	Esenyurt	0.552	Şile	0.000
Bahçelievler	0.743	Eyüpsultan	0.206	Silivri	0.111
Bakırköy	0.473	Fatih	0.611	Şişli	0.108
Başakşehir	0.147	Gaziosmanpaşa	0.200	Sultanbeyli	0.135
Bayrampaşa	0.324	Güngören	0.390	Sultangazi	0.105
Beşiktaş	0.064	Kadıköy	0.226	Tuzla	0.251
Beykoz	0.086	Kağıthane	0.144	Ümraniye	0.127
Beylikdüzü	0.326	Kartal	0.229	Üsküdar	0.152
Beyoğlu	0.213	Küçükçekmece	0.737	Zeytinburnu	0.381

According to the results of the weighted product model, Bahçelievler is ranked as first, again. However, there were some small changes in the ranking of the districts. For example, Arnavutköy's priority value was decreased, since it has the least risky value in terms of expected number of deaths criterion. The utilization of a single model may lead decision-makers not take some points into account correctly. Therefore, an aggregated result of these two models may provide better results.

Step 5. Aggregation of weighted sum and weighted product values for districts:

Eq. (8) was used to determine the aggregated values of districts obtained from the weighted sum and weighted product models. Both of the weighted sum and weighted product models were considered to affect decision-making process equally, so λ value is assumed to be 0.5 and the resulting values are presented in Table 10.

Table 10. Aggregated values of districts

Districts	Aggregated value	Districts	Aggregated value	Districts	Aggregated value
Adalar	0.182	Büyükçekmece	0.256	Maltepe	0.282
Arnavutköy	0.069	Çatalca	0.061	Pendik	0.296
Ataşehir	0.175	Çekmeköy	0.064	Sancaktepe	0.162
Avcılar	0.362	Esenler	0.380	Sarıyer	0.130
Bağcılar	0.598	Esenyurt	0.582	Şile	0.029
Bahçelievler	0.755	Eyüpsultan	0.230	Silivri	0.148
Bakırköy	0.514	Fatih	0.645	Şişli	0.134
Başakşehir	0.192	Gaziosmanpaşa	0.229	Sultanbeyli	0.164
Bayrampaşa	0.340	Güngören	0.396	Sultangazi	0.153
Beşiktaş	0.091	Kadıköy	0.249	Tuzla	0.266
Beykoz	0.122	Kağıthane	0.177	Ümraniye	0.209
Beylikdüzü	0.356	Kartal	0.257	Üsküdar	0.191
Beyoğlu	0.228	Küçükçekmece	0.751	Zeytinburnu	0.389

It can be concluded from the aggregated values of districts that disaster preparedness planning in İstanbul must start from Bahçelievler district. The crowded population of the district and expected number of deaths and building damages in the district makes it be considered primarily in this context. Küçükçekmece, Fatih, Bağcılar, and Esenyurt follow the district, respectively.

4. Conclusion and Suggestions

Disaster management is of critical importance for policymaker in countries. There are four phases in this context, which can be listed as mitigation, preparedness, response and recovery. If it is too late to mitigate the disaster, detailed plans should be prepared for emergency response when the disaster occurs. Otherwise, the recovery process after the disaster could be harder for the community.

Istanbul is a major city in Turkey and it is expected that earthquakes at a magnitude greater than 7.0 will occur in the forthcoming decades. The crowded population and economic activities in the city show that it is impossible to mitigate the effects of the expected earthquake. For this reason, preparedness planning is crucial for policy makers in this city. However, scarce resources to be allocated for the preparation of these plans require a prioritization study among the districts in the city. In this study, ranking of Istanbul's districts was determined using a hybrid decision-making model based on SWARA and WASPAS.

The location of each district causes different levels of risk, and the possible damage in case of the earthquake is various. So, proposed multi-criteria analysis model provides an analytic basis for the ranking of districts. According to results obtained from the case study taking five criteria into account, Bahçelievler seems to have a priority for a preparedness planning for the expected earthquake and Şile seems to be the district, which will be affected less by the earthquake.

Many complex decisions related to disaster management requires consideration of several criteria simultaneously. Therefore, multi-criteria analysis of disaster management decision problems could be focused on by researchers in further studies for any type of disasters. The main limitation of this study is

the limited number of criteria considered. In further studies, ranking results obtained by inserting other criteria that could affect the ranking of districts into analysis can be examined. Also, a comparison of ranking results of other weighting and ranking methods could also be presented.

Policy making for disaster preparedness is a key issue for governments and municipalities, because they have limited planning resources and they must successfully respond to the disaster. The results of the study could provide a scientific basis for preparedness planning to the expected İstanbul earthquake and may lead other researchers to use such analyses for other types of disasters.

Statement of Research and Publication Ethics

The study is complied with research and publication ethics.

References

[1] R. S. Oktari, K. Munadi, R. Idroes, and H. Sofyan, "Knowledge management practices in disaster management: Systematic review," *International Journal of Disaster Risk Reduction*, vol. 51, 101881, 2020.

[2] N. R. Mosteanu, A. Faccia, and L. Cavaliere, "Disaster Management Digitalization and Financial Resources: key factors to keep the organization ongoing", Proceedings of the 4-th International Conference on Cloud and Big Data Computing, pp. 118-122, 2020.

[3] R. Oloruntoba, R. Sridharan, and G. Davison, "A proposed framework of key activities and processes in the preparedness and recovery phases of disaster management," *Disasters*, vol. 42, pp. 541-570, 2018.

[4] W. Sun, P. Bocchini, and B. D. Davison, "Applications of artificial intelligence for disaster management," *Natural Hazards*, vol. 103, pp. 2631-2689, 2020.

[5] T. Parsons, S. Toda, R. S. Stein, A. Barka, and J. H. Dieterich, "Heightened Odds of Large Earthquakes Near Istanbul: An Interaction-Based Probability Calculation," *Science*, vol. 288, pp. 661-665, 2000.

[6] B. Ecer, "Hesitant Fuzzy Linguistic Decision Approach for Stroller Selection," *BEU Journal of Science*, vol. 10, pp. 1464-1473, 2021.

[7] B. Caroleo, E. Palumbo, M. Osella, A. Lotito, G. Rizzo, E. Ferro, A. Attanasio, S. Chiusano, G. Zuccaro, M. Leone, and D. D. Gregorio, "A Knowledge-Based Multi-Criteria Decision Support System Encompassing Cascading Effects for Disaster Management," *International Journal of Information Technology & Decision Making*, vol. 17, pp. 1469-1498, 2018.

[8] A. Tella, and A. L. Balogun, "Ensemble fuzzy MCDM for spatial assessment of flood susceptibility in Ibadan, Nigeria," *Natural Hazards*, vol. 104, pp. 2277-2306, 2020.

[9] K. B. Y. Kumlu, and Ş. Tüdeş, "Determination of earthquake-risky areas in Yalova City Center (Marmara region, Turkey) using GIS-based multicriteria decision-making techniques (analytical hierarchy process and technique for order preference by similarity to ideal solution)," *Natural Hazards*, vol. 96, pp. 999-1018, 2019.

[10] S. M. Ghavami, "Multi-criteria spatial decision support system for identifying strategic roads in disaster situations," *International Journal of Critical Infrastructure Protection*, vol. 24, pp. 23-36, 2019.

[11] M. Rezaei-Malek, S. A. Torabi, and R. Tavakkoli-Moghaddam, "Prioritizing disaster-prone areas for large-scale earthquakes' preparedness: Methodology and application," *Socio-Economic Planning Sciences*, vol. 67, pp. 9-25, 2019.

[12] H. Yılmaz, and Ö. Kabak, "Prioritizing distribution centers in humanitarian logistics using type-2 fuzzy MCDM approach," *Journal of Enterprise Information Management*, vol. 33, pp. 1199-1232, 2020.

[13] N. Aydin, "Designing reverse logistics network of end-of-life-buildings as preparedness to disasters under uncertainty," *Journal of Cleaner Production*, vol. 256, 120341, 2020.

[14] I. Barutcu, and Y. T. Ic, "Selecting the field hospital location for earthquakes: an application for Ankara Province in Turkey," *International Journal of Emergency Services*, vol. 11, pp. 168-187, 2022.

[15] V. Keršuliene, E. K. Zavadskas, and Z. Turskis, "Selection of rational dispute resolution method by applying new step-wise weight assessment ratio analysis (Swara)," *Journal of Business Economics and Management*, vol. 11, pp. 243-258, 2010.

[16] E. K. Zavadskas, Z. Turskis, J. Antucheviciene, and A. Zakarevicius, "Optimization of weighted aggregated sum product assessment", *Electronics and Electric Engineering*, vol. 122, pp. 3-6, 2012.

[17] T. Arsu, and E. Ayçin, E., "Evaluation of Third-Party Reverse Logistics Service Provider Selection Criteria with Fuzzy SWARA Method", *Journal of Yasar University*, vol. 16, pp. 1282-1300, 2021.
[18] B. Ecer, "Kararsız Bulanık Dilsel Terimler Temelli SWARA Yöntemi ile Ülke Değerlendirme Kriterlerinin Ağırlıklandırılması," in *Bulanık Çok Kriterli Karar Verme Yöntemleri - Ms Excel ® ve Software Çözümlü Uygulamalar*, Ankara: Nobel Akademik Yayıncılık, 2021, pp. 217-229.
[19] M. Yörükoğlu, and S. Aydin, "Digital Library Evaluation by SWARA-WASPAS Method," *International Journal of Industrial and Manufacturing Engineering*, vol. 14, pp. 444-447, 2020.
[20] B. Ecer, "WASPAS Yöntemi ile Yeşil Tedarikçi Seçimi," in *Çok Kriterli Karar Verme Yöntemleri: MS Excel ® Çözümlü Uygulamalar*, Ankara: Nobel Akademik Yayıncılık, 2020, pp. 209-220.
[21] Vikipedi, "İstanbul haritası," [Online]. Available: https://tr.wikipedia.org/wiki/%C4%B0stanbul#/media/Dosya:Istanbul_location_districts.svg. [Accessed: June 01, 2022].
[22] Turkish Statistics Institute, "Veri portalı," [Online]. Available: https://data.tuik.gov.tr/Bulten/DownloadIstatistikselTablo?p=PbEEZq9dLdCxTZT6EO2cURnZ2bTR3p1DGrFrQF7MNMh8XEYmRZkBRR5OTinJpNxD. [Accessed: June 01, 2022].]
[23] T24, "İstanbul'da hangi ilçede, kaç tane toplanma alanı var?," October, 03, 2019 [Online]. Available: https://t24.com.tr/haber/istanbul-hangi-ilcede-kac-tane-toplanma-alani-var,842165. [Accessed: June 01, 2022].
[24] İstanbul Metropolitan Municipality Earthquake and Soil Investigation Directorate, "Güncel çalışmalarımız," [Online]. Available: https://depremzemin.ibb.istanbul/guncelcalismalarimiz/#olasi-deprem-kayip-tahmnler-le-ktapiklari. [Accessed: June 01, 2022].

Bitlis Eren Üniversitesi Fen Bilimleri Dergisi
BİTLİS EREN UNIVERSITY JOURNAL OF SCIENCE
ISSN: 2147-3129/e-ISSN: 2147-3188
VOLUME: 11 NO: 3 PAGE: 893-901 YEAR: 2022
DOI: 10.17798/bitlisfen.1137179

On Saturated Numerical Semigroups with Multiplicity p Prime Numbers

Ahmet ÇELİK[1*]

[1]*Adıyaman University, Vocational School of Technical Sciences, Depatrtment of Computer Technologies, Adıyaman, TÜRKİYE*
(ORCID: 0000-0001-5980-0625)

Keywords: Saturated numerical semigroups, Isole gaps, Perfect, Pseudo-Frobenius number.

Abstract
In this paper, we will give some results for saturated numerical semigroups with multiplicity p prime number and conductor η where $p<10$.

1. Introduction

Let $\mathbb{Z}=\{...,-1,0,1,...\}$ integers set and $\Omega=\{a\in\mathbb{Z}: a\geq 0\}$ be non-negative integers set. and integers set, respectively. $\Delta\subseteq\Omega$ is called a numerical semigroup if $0\in\Delta$, $a_1+a_2\in\Delta$, for all $a_1,a_2\in\Delta$ and $\#(\Omega\backslash\Delta)$ is finite ($\#(Y)$ is cardinality the set of Y).

Let Δ be a numerical semigroup. The largest element of the set of $\mathbb{Z}\backslash\Delta$ is called the Frobenius number of Δ, and it is denoted by $\nu(\Delta)$. The smallest nonzero element of Δ is called the multiplicity of Δ and is denoted by $\mu(\Delta)$. Also, the number $\pi(\Delta)=\#(\{0,1,2,...,\nu(\Delta)\}\cap\Delta)$ is called determine number of Δ. For the numerical semigroup,

$$\Delta=<u_1,u_2,...,u_k>=\{\lambda_0=0,\lambda_1,\lambda_2,...,\lambda_{n-1},\lambda_n=\nu(\Delta)+1,\rightarrow...\},$$

where $\lambda_j<\lambda_{j+1}$ for $j=1,2,...,n=\pi(\Delta)$. Also, the arrow means $\lambda\in\Delta$, for all $\lambda\geq\nu(\Delta)+1$. In this case, the number $\eta=\nu(\Delta)+1$ is called conductor of Δ [1], [5].

Let $\Delta=<u_1,u_2,...,u_k>$ be a numerical semigroup. Then the cardinality of elements $u_1,u_2,...,u_k$, that is, k is called embedding dimension of Δ, and is denoted by $e(\Delta)$. It is known that $e(\Delta)\leq\mu(\Delta)$. So, the numerical semigroup $\Delta=<u_1,u_2,...,u_k>$ is called Maksimal Embedding Dimension (MED) if $\mu(\Delta)=e(\Delta)$. The numerical semigroup Δ is Arf if $\lambda_1+\lambda_2-\lambda_3\in\Delta$ for all $\lambda_1,\lambda_2,\lambda_3\in\Delta$ such that $\lambda_1\geq\lambda_2\geq\lambda_3$. If Δ is an Arf numerical semigroup then Δ is MED. But, its converse is not true. For example, The numerical semigroup $\Delta=<3,7,11>=\{0,3,6,7,9,10,\rightarrow...\}$ is MED but not is Arf, since $7+7-6=8\notin\Delta$ [2], [3], [4], [6]. Δ is called saturated numerical semigroup if $p+r_\Delta(x)\in\Delta$, for all $p,x\in\Delta-\{0\}$, where $r_\Delta(x)=\gcd\{\lambda\in\Delta:\lambda\leq x\}$. It known that a saturated numerical semigroup is Arf. But, an Arf numerical semigroup can not a saturated. For example, $\Delta=<5,8,11,12,14>$ is Arf but it is not saturated [7], [10].

Let Δ be a numerical semigroup and $0\neq\lambda\in\Delta$. The set $Ap(\Delta,\lambda)=\{y\in\Delta: y-\lambda\notin\Delta\}$ is Apery set of Δ according to λ. The element g is a gap of Δ if $g\in\Omega$ but $g\notin\Delta$, we denote the set of gaps of Δ, by $\rho(\Delta)$, i.e. $\rho(\Delta)=\{g\in\Omega: g\notin\Delta\}$. The element $g\in\rho(\Delta)$ is a pseudo-Frobenius number if $g+\lambda\in\Delta$, for all $\lambda\in\Delta$, $\lambda\neq 0$. And the set of all

*Corresponding author: acelik@adiyaman.edu.tr
Received: 28.06.2022, Accepted: 07.09.2022

pseudo-Frobenius number of Δ, we denote by $PF(\Delta)$. Also, the set $SG(\Delta)=\{g\in PF(\Delta): 2g\in\Delta\}$ is called the set of special gaps of Δ [6].

For a numerical semigroup Δ, $t\in\rho(\Delta)$ is called isole gap if $t-1,t+1\in\Delta$. The set of isole gaps of Δ is denoted by $I(\Delta)$, that is, $I(\Delta)=\{t\in\rho(\Delta): t-1,t+1\in\Delta\}$. Also, the numerical semigroup Δ is called perfect if $I(\Delta)=\phi$ (for details see [8], [9]).

In this study, we will give some results about the set of Pseudo-Frobenius and the set of isole gaps of Δ. Also, we will examine whether Δ will be perfect such that Δ is saturated numerical semigroup with multiplicity p prime number and conductor η where $p<10$ and $\eta\not\equiv 1(p)$.

2. Main Results

Theorem 2.1. ([6]) If $\Delta=<a_1,a_2,...,a_n>$ is a MED numerical semigroup then $Ap(\Delta,a_1)=\{0,a_2,a_3,...,a_n\}$.

Proposition 2.2. ([5]). Let $\Delta=<a_1,a_2,...,a_n>$ be a numerical semigroup. Then we have $PF(\Delta)=\{x-\lambda: x\in Ap(\Delta,\lambda),\ x>\nu(\Delta)\}$.

Theorem 2.3. ([7]) Let Δ be a numerical semigroup with $\mu(\Delta)=2$ and conductor η. Then, the Δ saturated numerical semigroup is $\Delta=<2,2\eta+1>$, for $\eta\equiv 0(\mathrm{mod}\,2)$.

Theorem 2.4. ([7]) Let Δ be a numerical semigroup with $\mu(\Delta)=3$ and conductor η. Then, Δ is saturated if Δ is one of following numerical semigroups:

(1) $\Delta=<3,\eta+1,\eta+2>$ for $\eta\equiv 0(3)$.
(2) $\Delta=<3,\eta,\eta+2>$ for $\eta\equiv 2(3)$.

Theorem 2.5. ([7]) Let Δ be a numerical semigroup with $\mu(\Delta)=5$ and conductor η. Then, Δ is saturated if Δ is one of following numerical semigroups:

1) $\Delta=<5,\eta+1,\eta+2,\eta+3,\eta+4>$ for $\eta\equiv 0(5)$

2) $\Delta=<5,\eta,\eta+1,\eta+2,\eta+4>$ for $\eta\equiv 2(5)$

3) $\Delta=<5,\eta,\eta+1,\eta+3,\eta+4>$ for $\eta\equiv 3(5)$

4) $\Delta=<5,\eta,\eta+2,\eta+3,\eta+4>$ for $\eta\equiv 4(5)$.

Theorem 2.6. ([7]) Let Δ be a numerical semigroup with $\mu(\Delta)=7$ and conductor η. Then, Δ is saturated if Δ is one of following numerical semigroups:

1) $\Delta=\langle 7,\eta+1,\eta+2,\eta+3,\eta+4,\eta+5,\eta+6\rangle$ for $\eta\equiv 0(7)$

2) $\Delta=\langle 7,\eta,\eta+1,\eta+2,\eta+3,\eta+4,\eta+6\rangle$ for $\eta\equiv 2(7)$

3) $\Delta=\langle 7,\eta,\eta+1,\eta+2,\eta+3,\eta+5,\eta+6\rangle$ for $\eta\equiv 3(7)$

4) $\Delta=\langle 7,\eta,\eta+1,\eta+2,\eta+4,\eta+5,\eta+6\rangle$ for $\eta\equiv 4(7)$

5) $\Delta=\langle 7,\eta,\eta+1,\eta+3,\eta+4,\eta+5,\eta+6\rangle$ for $\eta\equiv 5(7)$

6) $\Delta=\langle 7,\eta,\eta+2,\eta+3,\eta+4,\eta+5,\eta+6\rangle$ for $\eta\equiv 6(7)$.

Theorem 2.7. Let $\Delta =< 2, 2\eta +1 >$ be a saturated numerical semigroup for $\eta \equiv 0(2)$. Then, we have, $PF(\Delta) = \{2\eta -1\}$.

Proof. Let $\Delta =< 2, 2\eta +1 >$ be a saturated numerical semigroup with $\mu(\Delta) = 2$ and conductor $\eta \equiv 0(2)$. Then we wite that, $\Delta =< 2, 2\eta +1 >= \{0, 2, 4, 6, ..., 2\eta -2, 2\eta, \rightarrow ...\}$, and the set of gaps of Δ is $\rho(\Delta) = \{1, 3, 5, ..., 2\eta -1\}$. Thus, we find that the set of Pseudo-Frobenius elements of Δ is

$$PF(\Delta) = \{x-2 : x \in Ap(\Delta, 2),\ x > \nu(\Delta) = 2\eta -1\} = \{2\eta -1\}$$

since

$$Ap(\Delta, 2) = \{x \in \Delta : x-2 \notin \Delta\} = \{0, 2\eta +1\}.$$

Theorem 2.8. Let Δ be a saturated numerical semigroup with prime multiplicity $\mu(\Delta) = p$ and conductor η, where $2 < p < 10$ and $\eta \equiv j(p)$.

i) If $j = 0$ then $PF(\Delta) = \{\eta -1, \eta -2, \eta -3, ..., \eta -(p-1)\}$.
ii) If $j \neq 0$ then $PF(\Delta) = \{\eta -k : k = 1, 2, ..., j-1, j+1, ..., p\}$.

Proof. Let Δ be a saturated numerical semigroup with prime multiplicity $\mu(\Delta) = p$ and conductor η, where $p < 10$ and $\eta \equiv j(p)$.

i) If $j = 0$ then we write the saturated numerical semigroup Δ as following: for $p = 3, 5, 7$ respectively:
   (a) $\Delta =< 3, \eta +1, \eta +2 >$,
   (b) $\Delta =< 5, \eta +1, \eta +2, \eta +3, \eta +4 >$,
   (c) $\Delta = \langle 7, \eta +1, \eta +2, \eta +3, \eta +4, \eta +5, \eta +6 \rangle$.

Now, we can explain the above cases as follows:

(a) Let Δ be a saturated numerical semigroup is $\Delta =< 3, \eta +1, \eta +2 >$. Then we have
$$\Delta =< 3, \eta +1, \eta +2 >= \{0, 3, 6, ..., \eta -6, \eta -3, \eta, \rightarrow ...\}.$$
In this case, we have that,
$$\rho(\Delta) = \{1, 2, 4, 5, 7, 8, ..., \eta -7, \eta -5, \eta -4, \eta -2, \eta -1\}$$
and $Ap(\Delta, 3) = \{0, \eta +1, \eta +2\}$. So, we find that
$$PF(\Delta) = \{x-3 : x \in Ap(\Delta, 3),\ x > \nu(\Delta) = \eta -1\} = \{\eta -1, \eta -2\}.$$

(b) Let Δ be a saturated numerical semigroup is $\Delta =< 5, \eta +1, \eta +2, \eta +3, \eta +4 >$. Then we write
$$\Delta =< 5, \eta +1, \eta +2, \eta +3, \eta +4 >= \{0, 5, 10, ..., \eta -5, \eta \rightarrow ...\}$$
and
$$\rho(\Delta) = \{1, 2, 3, 4, 6, 7, 8, 9, 11, ..., \eta -4, \eta -3, \eta -2, \eta -1\}.$$
Thus, we obtain
$$PF(\Delta) = \{x-5 : x \in Ap(\Delta, 5),\ x > \nu(\Delta) = \eta -1\} = \{\eta -1, \eta -2, \eta -3, \eta -4\}$$
since $Ap(\Delta, 5) = \{x \in \Delta : x-5 \notin \Delta\} = \{0, \eta +1, \eta +2, \eta +3, \eta +4\}$.

(c) Let Δ be a saturated numerical semigroup $\Delta = \langle 7, \eta +1, \eta +2, \eta +3, \eta +4, \eta +5, \eta +6 \rangle$. We have
$$\Delta =< 7, \eta +1, \eta +2, \eta +3, \eta +4, \eta +5, \eta +6 >= \{0, 7, 14, ..., \eta -14, \eta -7, \eta, \rightarrow ...\}$$
and
$$\rho(\Delta) = \{1, 2, 3, 4, 5, 6, 8, 9, 10, 11, 12, 13, 15, ..., \eta -8, \eta -6, \eta -2, \eta -1\}.$$
We find that

$$PF(\Delta)=\{x-7:\ x\in Ap(\Delta,7),\ x>\nu(\Delta)=\eta-1\}=\{\eta-1,\eta-2,\eta-3,\eta-4,\eta-5,\eta-6\}$$

since $Ap(\Delta,7)=\ \ x\in\Delta:\ x-7\notin\Delta\ \ =\{0,\eta+1,\eta+2,\eta+3,\eta+4,\eta+5,\eta+6\}$.

Considering the above explanations, we obtain

$$PF(\Delta)=\{\eta-1,\eta-2,\eta-3,...,\eta-(p-1)\}$$

for $2<p<10$ and $\eta\equiv 0(p)$.

ii) If $j\neq 0$ then we write the saturated numerical semigroup Δ as following:

(a) For $p=3$;

The saturated numerical semigroup is $\Delta=<3,\eta,\eta+2>$ for $\eta\equiv 2(3)$. Then, we write

$$\Delta=<3,\eta,\eta+2>=\{0,3,6,9,...,\eta-5,\eta-2,\eta,\rightarrow...\},$$

$$\rho(\Delta)=\{1,2,4,5,7,8,...,\eta-6,\eta-4,\eta-3,\eta-1\}$$

and

$$Ap(\Delta,3)=\{0,\eta,\eta+2\}.$$

Thus, we find that $PF(\Delta)=\{x-3:\ x\in Ap(\Delta,3),\ x>\nu(\Delta)=\eta-1\}=\{\eta-1,\eta-3\}$.

(b) For $p=5$;

(1) If the saturated numerical semigroup is $\Delta=<5,\eta,\eta+1,\eta+2,\eta+4>$ for $\eta\equiv 2(5)$, then we have

$\Delta=<5,\eta,\eta+1,\eta+2,\eta+4>=\{0,5,10,...,\eta-7,\eta-2,\eta,\rightarrow...\}$,

$\rho(\Delta)=\{1,2,3,...,\eta-6,\eta-5,...,\eta-3,\eta-1\}$ and $Ap(\Delta,5)=\{0,\eta,\eta+1,\eta+2,\eta+4\}$. So, we find that , $PF(\Delta)=\{x-5:\ x\in Ap(\Delta,5),\ x>\nu(\Delta)=\eta-1\}=\{\eta-1,\eta-3,\eta-4,\eta-5\}$.

(2) If the saturated numerical semigroup is $\Delta=<5,\eta,\eta+1,\eta+3,\eta+4>$ for $\eta\equiv 3(5)$, then we write

$$\Delta=<5,\eta,\eta+1,\eta+3,\eta+4>=\{0,5,10,...,\eta-8,\eta-3,\eta,\rightarrow...\}$$

$$\rho(\Delta)=\{1,2,3,...,\eta-7,\eta-6,\eta-5,\eta-4,\eta-2,\eta-1\}$$

and

$$Ap(\Delta,5)=\{0,\eta,\eta+1,\eta+3,\eta+4\}\ .$$

Thus, we obtain that

$$PF(\Delta)=\{x-5:\ x\in Ap(\Delta,5),\ x>\nu(\Delta)=\eta-1\}=\{\eta-1,\eta-2,\eta-4,\eta-5\}.$$

(3) If the saturated numerical semigroup is $\Delta=<5,\eta,\eta+2,\eta+3,\eta+4>$ for $\eta\equiv 4(5)$, then we find that

$$\Delta=<5,\eta,\eta+2,\eta+3,\eta+4>=\{0,5,10,...,\eta-9,\eta-4,\eta,\rightarrow...\}$$

$$\rho(\Delta)=\{1,2,3,...,\eta-8,\eta-7,\eta-6,\eta-5,\eta-3,\eta-2,\eta-1\}$$

and

$$Ap(\Delta,5)=\{0,\eta,\eta+2,\eta+3,\eta+4\}.$$

Thus, we write that

$$PF(\Delta)=\{x-5:\ x\in Ap(\Delta,5),\ x>\nu(\Delta)=\eta-1\}=\{\eta-1,\eta-2,\eta-3,\eta-5\}.$$

(c) For $p=7$;

(1) If the saturated numerical semigroup is $\Delta=\langle 7,\eta,\eta+1,\eta+2,\eta+3,\eta+4,\eta+6\rangle$ for $\eta\equiv 2(7)$, then we have

$$\Delta=<7,\eta,\eta+1,\eta+2,\eta+3,\eta+4,\eta+6>=\{0,7,14,21,...,\eta-9,\eta-2,\eta,\rightarrow...\}$$

and

$$\rho(\Delta)=\{1,2,3,...,6,8,...,13,15,...,\eta-8,\eta-7,...,\eta-3,\eta-1\}.$$

Thus, we find that

$$PF(\Delta)=\{x-7: x\in Ap(\Delta,7),\ x>F(\Delta)=\eta-1\}=\{\eta-7,\eta-6,\eta-5,\eta-4,\eta-3,\eta-1\}$$ since $Ap(\Delta,7)=\{0,\eta,\eta+1,\eta+2,\eta+3,\eta+4,\eta+6\}$.

Making same operations, we find followings:

(2) If the saturated numerical semigroup is $\Delta=\langle 7,\eta,\eta+1,\eta+2,\eta+3,\eta+5,\eta+6\rangle$ for $\eta\equiv 3(7)$, then we have $PF(\Delta)=\{\eta-7,\eta-6,\eta-5,\eta-4,\eta-2,\eta-1\}$.

(3) If the saturated numerical semigroup is $\Delta=\langle 7,\eta,\eta+1,\eta+2,\eta+4,\eta+5,\eta+6\rangle$ for $\eta\equiv 4(7)$, then we have $PF(\Delta)=\{\eta-7,\eta-6,\eta-5,\eta-3,\eta-2,\eta-1\}$.

(4) If the saturated numerical semigroup is $\Delta=\langle 7,\eta,\eta+1,\eta+3,\eta+4,\eta+5,\eta+6\rangle$ for $\eta\equiv 5(7)$, then we have $PF(\Delta)=\{\eta-7,\eta-6,\eta-4,\eta-3,\eta-2,\eta-1\}$.

(5) If the saturated numerical semigroup is $\Delta=\langle 7,\eta,\eta+2,\eta+3,\eta+4,\eta+5,\eta+6\rangle$ for $\eta\equiv 6(7)$, then we have $PF(\Delta)=\{\eta-7,\eta-5,\eta-4,\eta-3,\eta-2,\eta-1\}$.

Finally, we obtain following results for a saturated numerical semigroup Δ ,with $\mu(\Delta)=p$ is prime number and conductor η, where $2<p<10$ and $\eta\equiv j(p)$:

i) If $j=0$ then $PF(\Delta)=\{\eta-1,\eta-2,\eta-3,...,\eta-(p-1)\}$.
ii) If $j\neq 0$ then $PF(\Delta)=\{\eta-k: k=1,2,...,j-1,j+1,...,p\}$.

Theorem 2.9. The saturated numerical semigroup Δ given by Theorem 2.3. is not perfect,

Proof. Let Δ be a saturated numerical semigroup which given by Theorem 2.3. Then, $\Delta=<2,2\eta+1>$, with $\mu(\Delta)=2$ and conductor $\eta\equiv 0(\mathrm{mod}\,2)$. In this case, we write $\Delta=<2,2\eta+1>=\{0,2,4,6,..,2\eta,\rightarrow...\}$ and $\rho(\Delta)=\{1,3,5,...,2\eta-1\}$. In this case, we obtain the set of isole gaps of Δ is $I(\Delta)=\{y\in\rho(\Delta): y-1,y+1\in\Delta\}=\{\rho(\Delta)\}\neq\phi$, that is, Δ is not perfect.

Theorem 2.10. Let Δ be a saturated numerical semigroup with $\mu(\Delta)=p$ is prime number and conductor η, where $2<p<10$ and $\eta\equiv j(p)$.

(i) If $j=2$ then $I(\Delta)=\{\nu(\Delta)\}$
(ii) If $j\neq 2$ then $I(\Delta)=\phi$.

Proof. Let Δ be a saturated numerical semigroup with prime multiplicity $\mu(\Delta)=p$ and conductor η, where $2<p<10$ and $\eta\equiv j(p)$.

(i) If $j=2$ then we have the following saturated numerical semigroups:

(1) For $p=3$;

The saturated numerical semigroup is $\Delta=<3,\eta,\eta+2>$ for $\eta\equiv 2(3)$ and we write $\Delta=<3,\eta,\eta+2>=\{0,3,6,9,...,\eta-5,\eta-2,\eta,\rightarrow...\}$. Therefore, we obtain the set of isole gaps of Δ is $I(\Delta)=\{y\in\rho(\Delta): y-1,y+1\in\Delta\}=\{\eta-1\}=\{\nu(\Delta)\}$ since

$$\rho(\Delta)=\{1,2,4,5,7,8,...,\eta-6,\eta-4,\eta-3,\eta-1\}.$$

(2) For $p=5$;

The saturated numerical semigroup is $\Delta =< 5, \eta, \eta+1, \eta+2, \eta+4 >$ for $\eta \equiv 2(5)$, then we have

$$\Delta =< 5, \eta, \eta+1, \eta+2, \eta+4 >= \{0, 5, 10, ..., \eta-7, \eta-2, \eta, \rightarrow ...\}$$

and

$$\rho(\Delta) = \{1, 2, 3, 4, 6..., \eta-6, ..., \eta-3, \eta-1\}.$$

Thus, we obtain that

$$I(\Delta) = \{y \in \rho(\Delta): y-1, y+1 \in \Delta\} = \{\eta-1\} = \{\nu(\Delta)\}.$$

(3) For $p = 7$;

The saturated numerical semigroup is $\Delta = \langle 7, \eta, \eta+1, \eta+2, \eta+3, \eta+4, \eta+6 \rangle$ for $\eta \equiv 2(7)$, then we have

$$\Delta =< 7, \eta, \eta+1, \eta+2, \eta+3, \eta+4, \eta+6 >= \{0, 7, 14, 16, ..., \eta-9, \eta-2, \eta, \rightarrow ...\}$$

and

$$\rho(\Delta) = \{1, 2, 3, 4, 5, 6, 8, ..., \eta-8, \eta-7, ..., \eta-3, \eta-1\}.$$

So, we find that

$$I(\Delta) = \{y \in \rho(\Delta): y-1, y+1 \in \Delta\} = \{\eta-1\} = \{\nu(\Delta)\}.$$

(ii) If $j \neq 2$ then we have the following saturated numerical semigroups:

(1) If $j = 0$ then we write the saturated numerical semigroup Δ as following:

for $p = 3, 5, 7$ respectively:

(a) $\Delta =< 3, \eta+1, \eta+2 >$,

(b) $\Delta =< 5, \eta+1, \eta+2, \eta+3, \eta+4 >$,

(c) $\Delta = \langle 7, \eta+1, \eta+2, \eta+3, \eta+4, \eta+5, \eta+6 \rangle$.

Now, we can explain the above cases as follows:

(a) Let Δ be a saturated numerical semigroup is $\Delta =< 3, \eta+1, \eta+2 >$. Then we have we obtain the set of isole gaps of Δ is $I(\Delta) = \{y \in \rho(\Delta): y-1, y+1 \in \Delta\} = \phi$ since

$$\Delta =< 3, \eta+1, \eta+2 >= \{0, 3, 6, ..., \eta-6, \eta-3, \eta, \rightarrow ...\}$$

and

$$\rho(\Delta) = \{1, 2, 4, 5, 7, 8, ..., \eta-7, \eta-5, \eta-4, \eta-2, \eta-1\}.$$

(b) The saturated numerical semigroup is $\Delta =< 5, \eta+1, \eta+2, \eta+3, \eta+4 >$. Then we write

$$\Delta =< 5, \eta+1, \eta+2, \eta+3, \eta+4 >= \{0, 5, 10, ..., \eta-5, \eta, \rightarrow ...\}$$

and

$$\rho(\Delta) = \{1, 2, 3, 4, 6, 7, 8, 9, ..., \eta-4, \eta-3, \eta-2, \eta-1\}.$$

So, we find that $I(\Delta) = \{y \in \rho(\Delta): y-1, y+1 \in \Delta\} = \phi$.

(c) Let Δ be a saturated numerical semigroup is

$\Delta = \langle 7, \eta+1, \eta+2, \eta+3, \eta+4, \eta+5, \eta+6 \rangle$.

In this case, we obtain that $I(\Delta) = \phi$ since $\Delta = \{0, 7, 14, ..., \eta-14, \eta-7, \eta, \rightarrow ...\}$ and

$\rho(\Delta) = \{1, 2, 3, 4, 5, 6, 8, 9, 10, 11, 12, 13, ..., \eta-8, \eta-6, \eta-2, \eta-1\}$.

(2) If $j = 3$ then we write the saturated numerical semigroup Δ as following:

for $p = 5, 7$ respectively:

(a) $\Delta =< 5, \eta, \eta+1, \eta+3, \eta+4 >$,

(b) $\Delta = \langle 7, \eta, \eta+1, \eta+2, \eta+3, \eta+5, \eta+6 \rangle$.

Now, we can explain the above cases as follows:

(a) If the saturated numerical semigroup is $\Delta =< 5, \eta, \eta+1, \eta+3, \eta+4 >$ for $\eta \equiv 3(5)$ then we write $\Delta =< 5, \eta, \eta+1, \eta+3, \eta+4 >= \{0, 5, 10, ..., \eta-8, \eta-3, \eta, \rightarrow ...\}$
$\rho(\Delta) = \{1, 2, 3, ..., \eta-7, \eta-6, \eta-5, \eta-4, \eta-2, \eta-1\}$. Thus, we obtain

$$I(\Delta) = \{y \in \rho(\Delta): y-1, y+1 \in \Delta\} = \phi.$$

(b) If the saturated numerical semigroup is $\Delta = \langle 7, \eta, \eta+1, \eta+2, \eta+3, \eta+5, \eta+6 \rangle$ for $\eta \equiv 3(7)$, then we have $I(\Delta) = \{y \in \rho(\Delta): y-1, y+1 \in \Delta\} = \phi$ since
$\Delta = \langle 7, \eta, \eta+1, \eta+2, \eta+3, \eta+5, \eta+6 \rangle = \{0, 7, 14, 21, ..., \eta-10, \eta-3, \eta, \rightarrow ...\}$ and

$$\rho(\Delta) = \{1, 2, 3, 4, 5, 6, 8, ..., \eta-5, \eta-4, \eta-2, \eta-1\}.$$

(3) If $j = 4$ then we write the saturated numerical semigroup Δ as following:
for $p = 5, 7$ respectively:

(a) $\Delta =< 5, \eta, \eta+2, \eta+3, \eta+4 >$,

(b) $\Delta = \langle 7, \eta, \eta+1, \eta+2, \eta+4, \eta+5, \eta+6 \rangle$.

Now, we can explain the above cases as follows:

(a) If the saturated numerical semigroup is $\Delta =< 5, \eta, \eta+2, \eta+3, \eta+4 >$ for $\eta \equiv 4(5)$ then we write $\Delta =< 5, \eta, \eta+2, \eta+3, \eta+4 >= \{0, 5, 10, ..., \eta-9, \eta-4, \eta, \rightarrow ...\}$,
$\rho(\Delta) = \{1, 2, 3, 4, 6, ..., \eta-8, \eta-7, \eta-6, \eta-5, \eta-3, \eta-2, \eta-1\}$. Thus, we obtain

$$I(\Delta) = \{y \in \rho(\Delta): y-1, y+1 \in \Delta\} = \phi.$$

(b) If the saturated numerical semigroup is $\Delta = \langle 7, \eta, \eta+1, \eta+2, \eta+4, \eta+5, \eta+6 \rangle$ for $\eta \equiv 4(7)$, then we have $I(\Delta) = \{y \in \rho(\Delta): y-1, y+1 \in \Delta\} = \phi$ since

$$\Delta = \langle 7, \eta, \eta+1, \eta+2, \eta+4, \eta+5, \eta+6 \rangle = \{0, 7, 14, 21, ..., \eta-11, \eta-4, \eta, \rightarrow ...\}$$

and

$$\rho(\Delta) = \{1, 2, 3, 4, 5, 6, 8, ..., \eta-10, ..., \eta-5, \eta-3, \eta-2, \eta-1\}.$$

(4) If $j = 5$ then we write the saturated numerical semigroup
$\Delta = \langle 7, \eta, \eta+1, \eta+3, \eta+4, \eta+5, \eta+6 \rangle = \{0, 7, 14, 21, ..., \eta-12, \eta-5, \eta, \rightarrow ...\}$ .In this case, we obtain that $I(\Delta) = \{y \in \rho(\Delta): y-1, y+1 \in \Delta\} = \phi$ since

$$\rho(\Delta) = \{1, 2, 3, 4, 5, 6, 8, ..., \eta-11, ..., \eta-6, \eta-4, \eta-3, \eta-2, \eta-1\}.$$

(5) If $j = 6$ then we write the saturated numerical semigroup
$\Delta = \langle 7, \eta, \eta+2, \eta+3, \eta+4, \eta+5, \eta+6 \rangle = \{0, 7, 14, 21, ..., \eta-13, \eta-6, \eta, \rightarrow ...\}$. Thus, we find that $I(\Delta) = \{y \in \rho(\Delta): y-1, y+1 \in \Delta\} = \phi$ since

$$\rho(\Delta) = \{1, 2, 3, 4, 5, 6, 8, ..., \eta-14, ..., \eta-5, \eta-4, \eta-3, \eta-2, \eta-1\}.$$

Corollary 2.11. Let Δ be a saturated numerical semigroup with prime multiplicity $\mu(\Delta) = p$ and conductor η, where $2 < p < 10$ and $\eta \equiv j(p)$.

(i) If $j = 2$ then Δ not perfect

(ii) If $j \neq 2$ then Δ is perfect.

Proof. It is clear.

Corollary 2.12 Let Δ be a saturated numerical semigroup with prime multiplicity $\mu(\Delta) = p$ and conductor η, where $p < 10$ and $\eta \equiv j(p)$. Then, we have $PF(\Delta) = SG(\Delta)$.

Proof Let Δ be a saturated numerical semigroup with prime multiplicity $\mu(\Delta)=p$ and conductor η, where $p<10$ and $\eta \equiv j(p)$. Then, it is clear that $SG(\Delta)\subseteq PF(\Delta)$.

(1) For $p=2$;

If $\eta \equiv 0(2)$ then $\Delta =<2,2\eta+1>=\{0,2,4,6,...,2\eta-2,2\eta,\rightarrow ...\}$ and we write $PF(\Delta)=\ 2\eta-1$ from Theorem 2.7.

If $x\in PF(\Delta)\Rightarrow x=2\eta-1\Rightarrow 2x=4\eta-2=(3\eta)+(\eta-2)\in\Delta\Rightarrow x\in SG(\Delta)$.

(2) For $p=3$;

(a) If $\eta\equiv 0(3)$ then $\Delta =<3,\eta+1,\eta+2>=\{0,3,6,9,..,\eta-6,\eta-3,\eta,\rightarrow ...\}$ and we write $PF(\Delta)=\{\eta-1,\eta-2\}$ from Theorem 2.8/(i). Let $x\in PF(\Delta)$.

If $x=\eta-1\Rightarrow 2x=2\eta-2=(\eta-3)+(\eta+1)\in\Delta\Rightarrow x\in SG(\Delta)$

or

if $x=\eta-2\Rightarrow 2x=2\eta-4=(\eta-6)+(\eta+2)\in\Delta\Rightarrow x\in SG(\Delta)$.

(b) If $\eta\equiv 2(3)$ then $\Delta =<3,\eta,\eta+2>=\{0,3,6,9,...,\eta-8,\eta-5,\eta-2,\eta,\rightarrow ...\}$ and we write $PF(\Delta)=\{\eta-1,\eta-3\}$ from Theorem 2.8/(ii). Let $x\in PF(\Delta)$

if $x=\eta-1\Rightarrow 2x=2\eta-2=(\eta-2)+(\eta)\in\Delta\Rightarrow x\in SG(\Delta)$

or

if $x=\eta-3\Rightarrow 2x=2\eta-6=(\eta-8)+(\eta+2)\in\Delta\Rightarrow x\in SG(\Delta)$.

If we make same operations for $p=5$ and $p=7$, we obtain $PF(\Delta)\subseteq SG(\Delta)$. Thus, the proof is completed.

Example 2.13. We put $p=3$ and $\eta=9$, in Theorem 2.4/(1) Then, we write $\Delta =<3,10,11>=\{0,3,6,9,\rightarrow ...\}$ MED and saturated numerical semigroup since $\mu(\Delta)=e(\Delta)=3$. Here, $f(\Delta)=8, n(\Delta)=3, \rho(\Delta)=\{1,2,4,5,7,8\}$ and $Ap(\Delta,3)=\{0,10,11\}$. In this case, we find that

$$PF(\Delta)=\{x-3:\ x\in Ap(\Delta,3),\ x>F(\Delta)=8\}=\{10-3,11-3\}=\{9,8\}$$

and

$$I(\Delta)=\{y\in H(\Delta):\ y-1, y+1\in\Delta\}=\phi .$$

That is, $\Delta =<3,10,11>=\{0,3,6,9,\rightarrow ...\}$ numerical semigroup is perfect. Also,

$$SG(\Delta)=\{x\in PF(\Delta):\ 2x\in\Delta\}=\{8,9\}=PF(\Delta).$$

Example 2.14. We put $p=5$ and $\eta=12$, in Theorem 2.5/(2) Then, we write $\Delta =<5,12,13,14,16>=\{0,5,10,12,\rightarrow ...\}$ saturated numerical semigroup. Here, $\mu(\Delta)=5$, $f(\Delta)=11$, $n(S)=3$, $\rho(\Delta)=\{1,2,3,4,6,7,8,9,11,\rightarrow ...\}$ and $Ap(\Delta,5)=\{0,12,13,14,16\}$.

Thus, we obtain

$$PF(\Delta)=\{x-5:\ x\in Ap(\Delta,5),\ x>F(\Delta)=11\}=\{7,8,9,11\}$$

and

$$I(\Delta)=\{y\in H(\Delta):\ y-1, y+1\in\Delta\}=\{11\}.$$

Therefore, the numerical semigroup Δ is not perfect and, we find that

$$SG(\Delta) = \{ x \in PF(\Delta) : 2x \in \Delta \} = \{7,8,9,11\} = PF(\Delta)$$

Statement of Research and Publication Ethics
The study is complied with research and publication ethics

References

[1] R. Froberg, C. Gotlieb and R. Haggkvist, "On numerical semigroups," *Semigroup Forum*, vol. 35, pp.63-68, 1987.
[2] S. İlhan and H.İ. Karakaş, "Arf numerical semigroups," *Turkish J. Math.*, vol.41, pp.1448-1457, 2017.
[3] J.C.Rosales, P.A.García-Sánchez, J.I.García-García and M.B.Branco, "Numerical semigroups with maximal embedding dimension," *Int. J. Commut. Rings*, vol. 2, pp.47–53, 2003.
[4] J. C. Rosales, P.A.García-Sánchez, J.I.García-García, M.B.Branco, "Arf numerical semigroups," *J. Algebra*, vol. 276, pp. 3–12, 2004.
[5] J.C.Rosales and P.A.Garcia-Sanchez, Numerical semigroups, New York: Springer 181, 2009.
[6] A. Assi and P.A.Garcia-Sanchez, Numerical semigroups and applications, https://hal.archives-ouvertes.fr/hal-01085760, pp 47, 2014.
[7] A.Çelik, Some results on saturated numerical semigroups, Doctoral thesis, Dicle University, 2018.
[8] M. A. Moreno Frias and J.C.Rosales, "Perfect numerical semigroups," *Turkish J. Math*., vol. 43,pp. 1742 – 1754, 2019.
[9] J. S. Harold, "On isolated gaps in numerical semigroups," *Turkish J. Math.*, vol.46, pp.123-129, 2022.
[10] S. İlhan, "On a family of telescopic numerical semigroups," *Acta Univ. Apulensis Math. Inform*, vol. 67, pp.13-18, 2021

Bitlis Eren Üniversitesi Fen Bilimleri Dergisi
BİTLİS EREN UNIVERSITY JOURNAL OF SCIENCE
ISSN: 2147-3129/e-ISSN: 2147-3188
VOLUME: 11 NO: 3 PAGE: 902-910 YEAR: 2022
DOI: 10.17798/bitlisfen.1139679

Residual Stress Measurement of a Single-step Sintered Planar Anode Supported SC-SOFC Using Fluorescence Spectroscopy

Yunus SAYAN[1,2*], Jung-Sik KİM[2], Houzheng WU[2]

[1] *Bitlis Eren University, Faculty of Engineering and Architecture, Department of Mechanical Engineering, Bitlis, Türkiye*
[2]*Loughborough University, School of Aeronautical, Automotive, Chemical and Material Engineering Loughborough, United Kingdom*
(ORCID: 0000-0002-0871-6842) (ORCID: 0000-0002-3696-7251) (ORCID: 0000-0002-7628-3890)

Keywords: Residual Stress, Fluorescence Spectroscopy, Sintering, Solid Oxide Fuel Cell.

Abstract
The fluorescence spectroscopy technique was used to measure the residual stress between the cathode and electrolyte of an anode supported planar single-chamber solid oxide fuel cell. The cell was made of (NiO-CGO): (CGO): (LSCF-CGO), as anode:electrolyte:cathode and the test was carried out after sintering at room temperature. The measured stress between these layers arises from the sintering stress caused by differential shrinkage from layers during sintering and the thermal expansion co-efficient mismatch between the layers during cooling. Therefore, the residual stress in the cathode and electrolyte layer of the cell due to co-efficient of thermal expansion mismatch during cooling was calculated analytically so as to find sintering stress. According to findings a maximum compressive residual stress of -1084 MPa occurred at the place contiguous to electrolyte layer. The estimated residual stresses in the cell's cathode and electrolyte layer owing to CTE mismatch for the duration of cooling was calculated as -324 MPa and 15.96 MPa, respectfully. Furthermore, total mean residual compressive stress between cathode and electrolyte was obtained from fluorescence spectroscopy as -703.795. Thus, the main contribution of this residual stress is the stress growth during sintering (-395.755 MPa) due to different shrinkage behavior of adjacent layers.

1. **Introduction**

The composites of multi-layered ceramic may undergo substantial magnitude of residual stress during cooling from sintering temperature. Residual stress particularly occurs when they are comprised of considerably thick layers made of different laminations or materials. In addition, different co-efficient of thermal expansion (CTE) between layers and elastic constants among neighboring layers and between the component phases are the main cause of the residual stress [1], [2]. Furthermore, the resistance of a cell to residual stress-induced cracking or deformation is significantly affected by the layered structure's geometry on layer thickness. The general stress area may be quite complex and thus difficult to predict by theoretical calculations. In order to avoid cracking and delamination, a precise control of both distribution and magnitude of residual stress is needed. To assess the residual stress in the components of multi-layered ceramic, a development of reliable experimental method is substantially desired. X-ray diffraction, neutron diffraction and piezo-spectroscopic analysis of photo-stimulated fluorescence are some techniques existed to evaluate the residual stress in ceramic materials [1], [3].

In the present study, residual stress between electrolyte and cathode of an anode supported planar single chamber solid oxide fuel cell (SC-SOFC) was measured by the fluorescence spectroscopy technique. This technique can be applied to the materials which must have the luminescent ability. Luminescent material contains $Al_2O_3:Cr^{3+}$, $BaSO_4$, end so on.; for more information about luminescence

*Corresponding author: ysayan@beu.edu.tr
Received: 02.07.2022, Accepted: 23.09.2022

materials can be found in references [4], [5]. In addition, in order to stimulate luminescence, an energy source is required. There are an extensive range of energy sources that can be used, as, UV emission of a gas discharge, cathode rays, X rays, etc., and their variation offers an appropriate classification for luminescence phenomena [4], [5].

It is common knowledge that vast majority of ceramics are optically transparent, aside from pore scattering and grain boundary, because of their large band gabs. Nevertheless, when the existence of trace impurities in polycrystalline ceramics, mostly transition-metal ions and rare-earth ions, are suitably excited, they can generate intense fluorescence. These specific lines usually originate from electronic transition of dopant ions and, moreover, they are excessively sensitive to the local ionic surroundings in the host crystal. Therefore, distortion which alters the interionic distances can bring about change in the characteristic lines. Furthermore, the present degeneracy of the energy states is eliminated by that distortion which reduces the crystal's symmetry, and consequently leads to splitting and shifting of the lines in the spectra. The link amongst the change in energy of the electronic state and strain (equally stress) is defined as the piezo spectroscopic effect [6], [7].

Al_2O_3:Cr^{3+} polycrystalline ceramics powders are chosen to be utilized between the electrolyte (CGO) and cathode (LSCF-CGO) of the cell because they both do not possess luminescent ability. Al_2O_3 corundum are preferably selected by reason of the fact that (1) its sintering temperature is above 1400˚C as per CGO [8]; (2) it has decent chemical and thermal stability, and moderately good strength [9]; (3) it can increase the electrolyte (CGO) ionic conductivity [10], [11]; (4)) it is inactive toward electrolyte material at 1200˚ [11], [12]. However, utilizing alumina powder between these layers to measure the stress may have adverse or beneficial effect on the cell sinterability in addition to cathode electrical and catalytic properties. These effects are not examined and ignored in this study.

The residual stress for alumina-based ceramics can be investigated by Chromium ions (Cr^{+3}) fluorescence spectroscopy method. This technique utilizes the shift in fluorescence bands. These bands are related to Cr which is persistent impurities in Al_2O_3 (alumina) [6], [7], [13], [14]. The oxygen ions' octahedral arrangement surrounding the chromium ions in alumina results in a crystal field and this brings about two closely-separated R1 and R2 bands that fluoresce at a wavelength of nearly 694 nm [14], [15]. Different composition of chromium, temperature change and stress application all distort octahedral and associated crystal field and leads to alterations in the energies of the R1 and R2 fluorescence peaks. This technique basically explained by Huang et al. as a laser being focused on the surface of the sample by using an optical microprobe. The laser interacts with chromium ions in alumina and results in luminescence. Once the materials subject to a stress the luminescence frequency peaks in the spectrum varies accordingly. This fact aids one to acquire the measurement of the mean stress distribution in materials [13]. When the materials undergo tensile stress, fluorescence spectra changes towards higher wavenumber, and vice versa when they undergo compressive stress [16]. Following base equation (Equation 1) gives the connection between stress, σ, and energy change, Δv, (in wavenumbers, cm^{-1}), in the Al_2O_3 corundum form [3], [6], [7], [14], [15], [17], [18]:

$$\Delta v=\Pi_{11}\sigma_{11}+\Pi_{22}\sigma_{22}+\Pi_{33}\sigma_{33} \quad (1)$$

Where the corundum crystallographic axes (a, m, c) are represented with the tensor axes (1, 2, and 3). The uppercase of Pi (Π) defines the piezo-spectroscopy coefficient. In addition, the threefold rotational symmetry around the corundum c axis should essentially give rise to the m and an axes to be equivalence. For that reason, it is assumed here that conventional notation of Π_{11}, Π_{22}, Π_{33} can be utilized as $\Pi_{11} = \Pi_{22} = \Pi_a$ and $\Pi_{33} = \Pi_b$. Furthermore, these two piezo-spectroscopy coefficients (Π_a and Π_b) are not the same for the fluorescence lines of R1 and R2. Consequently, under the hydrostatic conditions, ($\sigma_{11}= \sigma_{22} = \sigma_{33} = \sigma$), the above base equation (Equation 1) can be rearranged as follows [14], [15]:

$$\Delta v=(2\Pi_a+\Pi_b)\,\sigma \quad (2)$$

Though the Π_a and Π_b, for R1 and R2 fluorescence lines, respectively, are different [6], [14], [19], the pressure sensitivity of them ($2\Pi_a + \Pi_b$) is approximately the same [20]–[22]. To calculate residual stress between the cathode and electrolyte of the cell, R1 line shifts will here be of interest. The piezo-spectroscopic coefficient for R1 line can be calculated from the definition given in the following parenthesis (2/3 of ($2\Pi_a + \Pi_b$)) for polycrystalline A_2O_3 and as a result, it can be found as $(7.59 \times 2) / 3 = 5.06$ cm^{-1} GPa^{-1} [3], [6].

Furthermore, residual stress in the sintered cell is caused by (1) stress growth during sintering owing to different shrinkage rate of layers and (2) thermal expansion misfit of layers while cooling from 1200˚C to 20˚C. When the sintered cell's residual stress at 20˚C (assumed to be room

temperature) because of different thermal expansion mismatch during cooling is calculated, afterwards the residual stress developed during sintering can be predicted from residual stress measurement at room temperature applying fluorescence spectroscopy technique. Equation 3 can be easily utilized so as to obtain residual stress contribution due to CTE misfit for two different layers. However, the sintered cell consists of three different layers, cathode, electrolyte and anode. Nevertheless, the equation 3 can still be utilized for the cell in this study if one accept electrolyte and anode as one sheet because the anode and electrolyte possess close shrinkage properties [23] and CTE (see Table 1). Besides, the anode itself is composed of 40% of electrolyte (CGO) material before sintering and the electrolyte thickness is relatively small comparing to anode for the anode supported planar SC-SOFC. Therefore, the anode/electrolyte layers can be presumed to be one composite layer containing NiO-CGO materials with certain porosity.

$$\sigma_1 = \frac{(\alpha_2 - \alpha_1)\Delta T}{\frac{1}{\hat{E}_1} + \frac{t_1}{t_2}\frac{1}{\hat{E}_2}} \quad \text{and} \quad \sigma_2 = \frac{(\alpha_1 - \alpha_2)\Delta T}{\frac{1}{\hat{E}_2} + \frac{t_2}{t_1}\frac{1}{\hat{E}_1}} \quad [24] \quad (3)$$

$$\hat{E} = \frac{E}{1-v} \quad [24] \quad (4)$$

$$v = \frac{E}{2G} - 1 \quad [25] \quad (5)$$

Where E is the young`s modulus, v the Poisson ratio, σ the residual stress in layers, α the coefficient of thermal expansion, G the shear modulus, ΔT the change in temperature, and t the layer thickness. Subscripts 1 represents the cathode layer and subscript 2 represents the single composite new layer.

In the present study, the total residual stress after sintering between electrolyte and cathode of an anode supported planar single chamber solid oxide fuel cell (SC-SOFC) caused by sintering stress due to differential shrinkage from layers during sintering and thermal expansion co-efficient mismatch between layers during cooling was measured utilizing fluorescence spectroscopy at room temperature (20ºC). In addition, equation 2, 4 and 5 were used to calculate analytically the residual stress in cathode layer of the cell owing to CTE misfit during cooling at 20ºC. By subtracting the calculated residual stress from total residual stress, the sintering residual stress contribution was estimated.

2. Experimental

2.1. Row Materials

The cell was comprised of (NiO-CGO): (CGO): (LSCF-CGO), as anode:electrolyte:cathode materials (A:E:C). Green layers were made via tape-casting process and composed of 60 wt% NiO–40 wt% $Ce_{0.8}Gd_{0.2}O_{2-\delta}$ as anode (NiO-CGO), $Ce_{0.8}Gd_{0.2}O_{2-\delta}$ as electrolyte (CGO) and 50 wt% $La_{0.6}Sr_{0.4}Co_{0.2}Fe_{0.8}O_{3-\delta}$ –50 wt%CGO (20% Gd) as cathode (LSCF-CGO). These layers were purchased from Maryland tape-casting Ltd, USA [26]. In order to obtain the designed thicknesses of the electrolyte and electrodes for the anode-supported planar SC-SOFC, these green layers were stacked and subsequently hot-pressed. Details of the chemicals made the green tapes are given by the supplier, and can be found in reference [23]. In addition, the particle size of the cathode green band was chosen to be 1 µm, as opposed to 0.3 µm for the electrolyte and anode green tapes, so as to retard the sintering of the cathode.

2.2. Cell Preparation

Individual layers of green tape, around a thickness of 20 µm per layer, were stacked sequentially on top each other in accordance with the required thickness of cathode, electrolyte and anode. Alumina fine particles (CTM-DAR. 99.99% purity and possession a mean particle size of 200 nm) were sprinkled carefully for a reasonably homogeneous distribution between electrolyte and cathode during stacking step as presented in Figure 1 so as to make a cell for fluorescence spectroscopy measurement. Thereafter, these stacked layers were hot-pressed at 60 ˚C and 2 MPa with a dwelling time of 5 minutes using Carvel Heated Bench Top Hot Press (model: 3853CE-8, USA) with the purpose of allowing individual layers combined together to form a complete cell. The hot pressed cell then sintered at a temperature of 1200 ˚C for 1 hour. A heating and cooling rate profile during sintering were determined as following: 1˚C min^{-1} heating rate from 20 ˚C to 500 ˚C, a heating rate of 2 ˚C min^{-1} from 500 ˚C to 900 ˚C, 1 ˚C min^{-1} heating rate from 900 ˚C to 1200 ˚C; and 3 ˚C min^{-1} cooling rate from 1200 ˚C to 20 ˚C. As a result, an anode supported SC–SOFC was obtained and possesses the width (W) and length (L) of 40 mm × 40 mm (W × L). Moreover, the anode, electrolyte and cathode of the cell has a thickness of 800:20:40 µm, respectively.

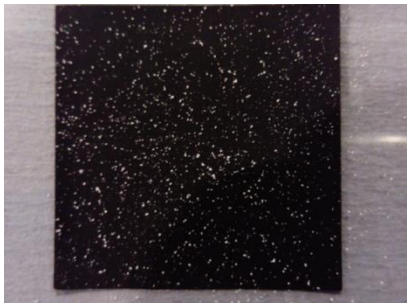

Figure 1. Distribution of sprinkled alumina powder on the surface of stacked cathode layers before stacking electrolyte layers.

2.3. Porosity Measurement

The technique applied to assess the mean porosity of the cathode, electrolyte and anode of the cell can be explained as follows: Back scatter SEM images of cross-sectional areas of the cell layers (anode, cathode and electrolyte), having a Mag 2.00 KX, 10 µm scale and 8.5 mm WD, were taken separately. Thereafter, the obtained SEM images were sent to the ImageJ program and were set to 8-bit image quality in order for threshold analysis. Each images' threshold was adjusted carefully. The percentage of the black regions on the SEM images, corresponding to the percentage of the porous region, were read on the ImageJ program and noted (Table 2).

2.4. The Estimation of the New Values of Young`s Modulus, CTE, and Poisson Ratio

The cell which has the three-layered structure (the cathode, electrolyte and anode) were assumed to be a two-layered structure so as to utilize equation 3. It was supposed that and electrolyte (CGO) and anode (NiO-CGO) as one composite layer because the composite anode comprises of 60% of NiO and 40% of electrolyte (CGO) material before sintering. Furthermore, their shrinkage and CTE properties are close to each other (see Table 1). In addition, the electrolyte thickness is relatively thin compared to the anode for the anode supported planar SC-SOFC. Thereby, anode/electrolyte layers can be assumed to be one layer containing NiO-CGO materials with certain porosity and are defined as a single composite layer. Moreover, the cathode also consists of different composition, 50%LSCF-50%CGO, before sintering, however, the co-efficient of thermal expansion and the shrinkage rate [23] of the CGO electrolyte and cathode are quite different (see Table 1). Therefore, the sintered anode supported planar SC-SOFC can be assumed to has two layers which are designated as a composite cathode layer and a single composite new layer. Additionally, the cell's cathode layer possesses certain porosities after sintering. Thus, the pore percentage and each material composition should be taken into consideration to obtain true value of Poisson ratio, Young`s modulus and thermal expansion coefficient of these materials. The inclusion principle can be easily used in order for finding these values.

Table 1. Estimated properties of some materials from literature with around 99% relative density.

	Material properties		
	CTE (K^{-1})	E (GPa)	v
NiO	13.3 x 10^{-6} [27]	220 [28]	0.31 (calculated from equation 5)
CGO	12.96 x 10^{-6} [24]	200 [24]	0.33 [24]
LSCF	16.12 x 10^{-6} [29]	157 (152 at 95.4 density) [30]	0.3 [30]

Estimated properties of some materials (NiO, CGO and LSCF) with around 99% relative densities used in this study are summarized in Table 1. This information was obtained from literature. The single composite new layer, however, contains CGO, NiO and certain porosities. The sum of the CGO volume in the composite anode and electrolyte gives the CGO volume in the single composite new layer. Likewise, the pores of the electrolyte and composite anode were summed to calculate the single composite new layer's porosity. Considering the NiO, CGO and total porosity of the single composite new layer (see Table 2), the new values of CTE, Poisson ratio, and Young`s modulus of this layer were calculated using the information provided in Table 1 and Table 2 by easily utilizing inclusion principles. Furthermore, the composite cathode is composed of CGO, LSCF and porosity. Therefore, its new properties were calculated based on its composition in the same way as single composite new layer (see Table 2) (each layer's mass ratio in the green tape was presumed to be equal with the volume ratio). In addition, the thickness of cathode and single composite new layer after sintering were calculated according to approximately 18% shrinkage of each layer from SEM results.

Table 2. New material properties calculated based on their composition and porosity ratio using simple inclusion principle

	LSCF %	CGO %	NiO %	Porosity	CTE (K^{-1}) x 10^{-6}	E (GPa)	Ê (GPa)	v	t (μm)
Cathode	37.39	37.39	0	25.22	10.87	133.48	174.6	0.235	32.8
Single composite new layer	0	29	41	30	9.21	148.2	190.7	0.223	672.4

2.5. Fluorescence Spectroscopy for Determination of Residual Stress

Residual stress of Al_2O_3 inclusions between electrolyte and cathode of the cell was measured using Fluorescence spectroscopy. Figure 2 displays an illustrative alumina inclusion sitting in between electrolyte and cathode layers of planar SC-SOFC. Furthermore, mapping on alumina for the measurement points of the fluorescence spectra and its initial point are also shown in the same figure. A step size of 1 μm for a 40 × 9 points on x and y direction, respectively, (mapping of 39 μm × 8 μm) was determined to take measurements. In order to obtain non-distorted and reasonable fluorescence spectra from the points on alumina particles, a representative 9 points on y direction for each 24 points along x direction, out of 40 × 9 points, were chosen for the measurement of the stress, as displayed in Figure 2. Measurements of the fluorescence spectrum were taken on the locations where proper alumina was found for simplicity.

A true confocal Raman microscope (The LabRAM HR High Resolution Raman/PL Microscope system, Horiba, Japan) was utilized to obtain fluorescence spectra from alumina located between electrolyte and cathode layer of the sintered anode supported planar SC-SOFC. Fluorescence spectra were also taken from unstressed alumina which are positioned on the top of the glass plate during measurement for reference spectrum. Each fluorescence spectra were taken over 14268 cm^{-1}–14539 cm^{-1} spectrum with a 633 nm red line of a 17 mW He-Ne laser. In addition, a 50X objective lens in cooperation with a confocal setup which comprised two 50 μm pinhole apertures at 90˚ to one another providing an approximate 1 μm beam diameter on the specimen surface were used to take measurements. Furthermore, the grating of the scanning spectrometry was set to 1800 cm^{-1}.

An interest area for each measurement was selected by using the optical microscope concentrated on the top surface plane of the cell cross-section area where alumina situated and on the top of the unstressed reference alumina powders located on the top of the glass plate by changing of the sample stage height. All experiments (together with calibration) were done in a controlled atmosphere at 22 $\pm$ 2˚C. A step size of 1 μm for a 10 μm × 1 μm for unstressed alumina powders positioned on the glass sheet and a 39 μm × 8 μm mapping for alumina between layers were set to take measurements. In addition, acquiring time was adjusted to 10 seconds for each point. Thereafter, curve-fitting algorithms included in the Origin 2015 software were used to analyze the obtained data. The mean reference spectrum was calculated by averaging the 10 measured strain-free alumina powder spectrum. Moreover, in order to obtain energy change (Δv), the mean R1 fluorescence peak of unstressed alumina was subtracted from R1 fluorescence peak of stressed alumina located between electrolyte and cathode of the cell. Finally, dividing energy change by 5.06 cm^{-1} GPa^{-1} as defined above paragraphs, the total stress at each point was obtained.

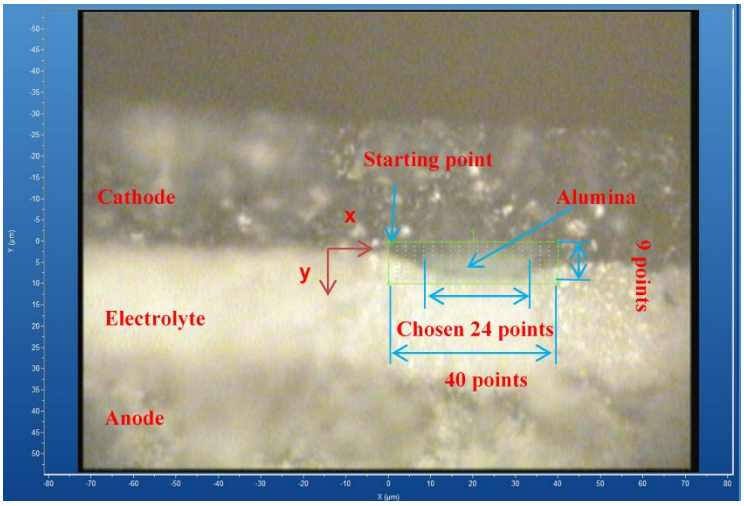

Figure 2. A representative illustration of an alumina particle sitting in between cathode and electrolyte layers of a SC-SOFC and mapping positions on alumina for fluorescence spectrum measurement.

3. Results and Discussion

One of the fluorescence spectra obtained from the cell and the one from reference alumina are shown in Figure 3. The shift ($\Delta\nu$) of peaks, R1 and R2, can be clearly seen on the figure. According to Figure 3 the shift is in the direction of lower wavenumber (from 14404 cm^{-1} to 14398.9 cm^{-1}); demonstrating a compressive stress. All measurements taken from the cell have shift towards lower wavenumber according to acquired results. This shows that all particles of alumina are under compressive stress therein the placed position in the cell after sintering.

The map of the residual stress in a particle positioned between electrolyte and cathode of the anode supported planar SC-SOFC at room temperature are shown in Figure 4. The measured residual stress between the cathode and single composite new layer after sintering originates from different shrinkage behavior of layers during sintering and CTE mismatch of these layers during cooling. Alumina powder existing between layers of the cell may affect the cell sinterability compared to the similar cell sintered without alumina powder. Thus, the residual stress in the actual cell sintered without alumina powders may not be the same with that of the cell sintered with alumina powder. Nevertheless, this effect was neglected as a first approach for the good of quantifying the residual stress in the cell by using fluorescence spectroscopy. Although the actual cell might have different residual stress in comparison to the similar cell that alumina powders were located between layers, using fluorescence spectrum for the cell residual stress measurement can aid one to assess the stress distribution in the cell and therefore gain better knowledge of entire sintering process.

In accordance with Figure 4, a maximum compressive residual stress of -1084 MPa occurred at the place near electrolyte layer. The electrolyte higher densification by comparison cathode (according to the SEM images of past puplication, cathode possess higher porosity than electrolyte) could be the explanation for the residual stress location of the cell, which were detected in the previous study [23]. The higher densification of electrolye maight cause more pressure on alumina section in the electrolyte during sintering. In addition, the main observed point for the cell is the absence of symmetrical residual stress distribution along the x direction from the alumina particles, having an area of relatively higher stress near the x = 0–10 region. This might be explained as the location of the measured alumina particles has not the same equidistant to the edges of the cell. Thus, bending effect owing to the different shrinkage of layers has asymmetrical impacts to the alumina powders. For example, if the powder of the measured alumina is closer to one of the cell edge, the effect of compressive stress will be greater at the alumina edge which is facing the edge of cell far away from it. Furthermore, for each point in the x-direction, the average residual stress throughout the y-direction was also calculated (see Table 3).

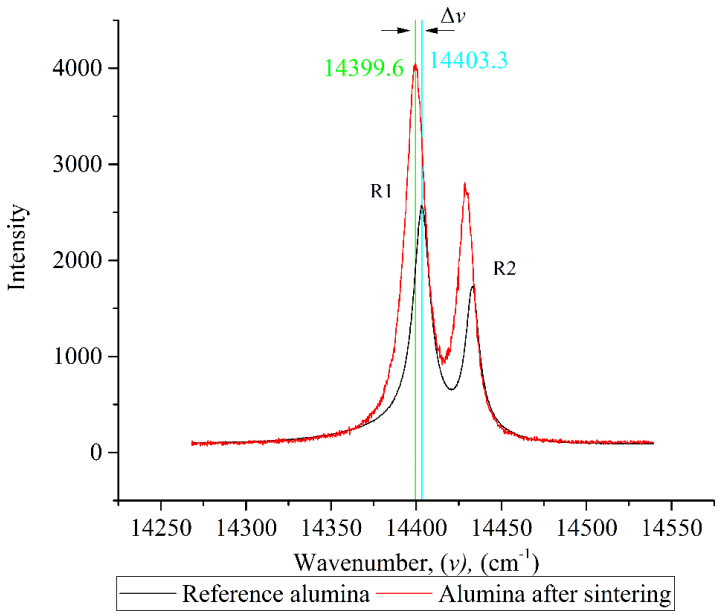

Figure 3. Representative fluorescence spectrum from a cell with a thickness ratio: 40:1:2, A:E:C and the shift (Δv) from reference spectrum after sintering.

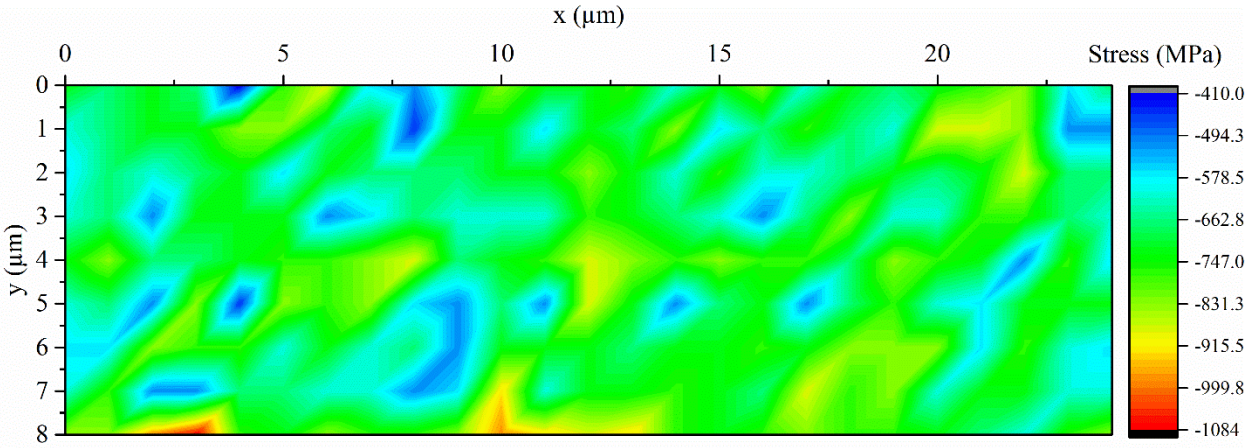

Figure 4. Residual stress results of cell from Fluorescence spectroscopy.

Table 3. Mean stress measurement along y direction on alumina sintered with SC-SOFC

Mean stress measurement along y direction on alumina sintered with SC-SOFC (MPa)									
	X direction	0	1	2	3	4	5	6	7
Cell		-651.182	-703.883	-675.337	-739.017	-675.337	-721.45	-721.45	-686.316
	X direction continue	8	9	10	11	12	13	14	15
Cell		-633.615	-640.203	-769.759	-686.316	-796.11	-752.192	-695.1	-706.079
	X direction continue	16	17	18	19	20	21	22	23
Cell		-701.687	-708.275	-732.429	-736.821	-714.863	-712.667	-739.017	-655.574
	X direction continue	24							
Cell		-640.203							

The total average residual stress on the alumina particles located between the cell's electrolyte and cathode was measured to be -703.795 MPa at room temperature utilizing fluorescence spectroscopy. The overall average residual stress includes sintering stress during sintering and co-efficient of thermal expansion mismatch stress during cooling. The estimated residual stresses in the cell's cathode layer because of CTE mismatch during cooling was calculated as -324 MPa. Likewise, the estimated residual stresses in the single composite new layer was found to be 15.96 MPa from calculation. These results show that the dominant factor of the total mean residual stress is the stress developed during sintering (-395.755 MPa) owing to different shrinkage behavior of layers as the stress due to CTE misfit is low compared to residual stress arisen during sintering.

4. Conclusions

The fluorescence spectroscopy technique was applied to measure the total residual stress between electrolyte and cathode of a cell after sintering at room temperature. The residual stress in the cathode and electrolyte layer of the cell because of CTE misfit during cooling was also obtained from the analytical equations. According to results a high total residual stress of -703.795 MPa measured between the electrolyte and cathode of the cell after sintering. The stress developed during sintering (sintering stress=-395.755 MPa) due to different shrinkage behavior of adjacent layers is the main contribution of this residual stress compared to stress developed during cooling because of CTE mismatch.

Acknowledgment

The work was supported by the Turkish Ministry of Higher Education and the EPSRC's the India-UK Collaborative Research Initiative in Fuel Cells project on "Modelling Accelerated Ageing and Degradation of Solid Oxide Fuel Cells" (EP/I037059/1), and also the EPSRC's UK-Korea Collaborative Research Activity in Fuel Cells project on "Novel diagnostic tools and techniques for monitoring and control of SOFC stacks" (EP/M02346X/1).

Conflict of Interest Statement

There is no conflict of interest between the authors.

Contributions of the authors

All contributions to this study belong to the authors.

Statement of Research and Publication Ethics

The study is complied with research and publication ethics

References

[1] G. De Portu, L. Micele, Y. Sekiguchi, and G. Pezzotti, "Measurement of residual stress distributions in Al_2O_3 / 3Y-TZP multilayered composites by fluorescence and raman microprobe piezo-spectroscopy," Acta Mater., vol. 53, no. 5, pp. 1511–1520, 2005.

[2] P. Z. Cai, D. J. Green, and G. L. Messing, "Constrained densification of alumina/zirconia hybrid laminates, II: viscoelastic stress computation," J. Am. Ceram. Soc., vol. 48, no. 8, pp. 1940–1948, 1997.

[3] H. Z. Wu, S. G. Roberts, and B. Derby, "Residual stress distributions around indentations and scratches in polycrystalline Al_2O_3 and Al_2O_3 / SiC nanocomposites measured using fluorescence probes," Acta Mater., vol. 56, no. 1, pp. 140–149, 2008.

[4] B. C. Feldmann, T. Jüstel, C. R. Ronda, and P. J. Schmidt, "Inorganic luminescent materials : 100 years of research and application," Adv. Funct. Mater., vol. 13, no. 7, pp. 511–516, 2003.

[5] A. Edgar, "Luminescent," in Springer Handbook of electronic and photonic materials, 2nd Editio., S. Kasap and P. Capper, Eds. Springer, 2017, pp. 997–1012.

[6] J. He and D. R. Clarke, "Determination of the Piezospectroscopy coefficients for chromium-doped sapphire," J. Am. Ceram. Soc., vol. 78, no. 5, pp. 1347–1353, 1995.

[7] L. Grabner, "Spectroscopic technique for the measurement of residual stress in sintered Al_2O_3," J. Appl. Physic, vol. 580, no. 1978, pp. 1–5, 1996.

[8] D. Di Marco et al., "Dielectric properties of pure alumina from 8 GHz to 73 GHz," J. Eur. Ceram. Soc., vol. 36, no. 14, pp. 3355–3361, 2016.

[9] P. Auerkari, "Mechanical and physical properties of engineering alumina ceramics," Espoo, 1996.

[10] H. N. Kim, H. J. Park, and G. M. Choi, "The effect of alumina addition on the electrical conductivity of

Gd-doped ceria," J. Electroceramics, vol. 17, no. 2–4, pp. 793–7982, 2006.
[11] R. Chockalingam, S. Chockalingam, and V. R. W. Amarakoon, "The electrical properties of microwave sintered gadolinia doped ceria – alumina nano-composite electrolyte," J. Power Sources, vol. 196, no. 4, pp. 1808–1817, 2011.
[12] J. Lee, K. Choi, B. Ryu, B. Shin, and I. Kim, "Effects of alumina additions on sintering behavior of gadolinia-doped ceria," Ceram. Int., vol. 30, no. 5, pp. 807–812, 2004.
[13] S. Huang, J. G. P. Binner, B. Vaidhyanathan, and R. I. Todd, "Quantitative analysis of the residual stress and dislocation density distributions around indentations in alumina and zirconia toughened alumina (ZTA) ceramics," J. Eur. Ceram. Soc., vol. 34, no. 3, pp. 753–763, 2014.
[14] G. A. Myers, C. A. Michaels, and R. F. Cook, "Quantitative mapping of stress heterogeneity in polycrystalline alumina using hyperspectral fl uorescence microscopy," Acta Mater., vol. 106, pp. 272–282, 2016.
[15] C. A. Michaels and R. F. Cook, "Determination of residual stress distributions in polycrystalline alumina using fl uorescence microscopy," Mater. Des., vol. 107, pp. 478–490, 2016.
[16] M. Materials, S. Centre, and G. Street, "Fragmentation in alumina fibre reinforced epoxy model composites monitored using fluorescence spectroscopy," J. Mater. Sci., vol. 31, no. 13, pp. 3349–3359, 1996.
[17] Q. Ma and D. R. Clarke, "Stress measurement in single-crystal and polycrystalline ceramics using their optical fluorescence," J. Am. Ceram. Soc., vol. 76, no. 6, pp. 1433–1440, 1993.
[18] R. . Todd, A. R. Boccaccini, R. Sinclair, R. B. Yallee, and R. J. Young, "Thermal residual stresses and their toughening effect in Al_2O_3 platelet reinforced glass," Acta Mater., vol. 47, no. 11, pp. 3233–3240, 1999.
[19] E. Feher and M. D. Sturge, "Effect of stress on the trigonal splittings of d3 ions in sapphire (a-Al_2O_3)," Phys. Rev., vol. 172, no. 2, pp. 243–249, 1968.
[20] J. He, I. . Beyerlein, and D. . Clarke, "Load transfer from broken fibers in continuous fiber Al_2O_3-Al composites and dependence on local volume fraction," J. Mech. Phys. Solids, vol. 47, pp. 465–502, 1999.
[21] R. G. Munro, G. J. Piermarini, and S. Block, "Model line shape analysis for the ruby R lines used for pressure measurement," J. Appl. Physic, vol. 57, no. 2, pp. 165–169, 1985.
[22] D. D. Ragan, D. R. Clarke, and D. Schiferl, "Silicone fluid as a high-pressure medium in diamond anvil cells," Am. Inst. Physic, vol. 2, no. 1996, pp. 494–496, 67AD.
[23] Y. Sayan, V. Venkatesan, E. Guk, H. Wu, and J. S. Kim, "Single-step fabrication of an anode supported planar single-chamber solid oxide fuel cell," Int. J. Appl. Ceram. Technol., no. April, pp. 1–13, 2018.
[24] A. Atkinson and A. Selçuk, "Residual stress and fracture of laminated ceramic membranes," Acta Mater., vol. 47, no. 3, pp. 867–874, 1999.
[25] A. Selçuk and A. Atkinson, "Elastic properties of ceramic oxides used in solid oxide fuel cells (SOFC)," J. Eur. Ceram. Soc., vol. 17, no. 12, pp. 1523–1532, 1997.
[26] "Maryland Tape Casting." [Online]. Available: http://www.marylandtapecasting.com/.
[27] S. C. Singhal and K. Kendall, High temperature solid oxide fuel cells:fundementals, design and applications. Oxford: Elsevier Advanced Technology, 2003.
[28] S. Bandopadhyay, "Evaluation of elastic properties of reduced NiO-8YSZ anode- supported bi-layer SOFC structures at elevated temperatures in ambient air and reducing environments," J. Mater. Sci. Lett., no. July, pp. 778–785, 2009.
[29] K. Raju, S. Kim, J. H. Yu, S. H. Kim, Y. H. Seong, and I. S. Han, "Rietveld refinement and estimation of residual stress in GDC-LSCF oxygen transport membrane ceramic composites," Ceram. Int., vol. 44, no. February, pp. 10293–10298, 2018.
[30] Y. Chou, J. W. Stevenson, T. R. Armstrong, and L. R. Pederson, "Mechanical properties of LSCF mixed-conducting perovskites made by the combustion synthesis technique," J. Am. Ceram. Soc., vol. 83, pp. 1457–1464, 2000.

Bitlis Eren Üniversitesi Fen Bilimleri Dergisi
BİTLİS EREN UNIVERSITY JOURNAL OF SCIENCE
ISSN: 2147-3129/e-ISSN: 2147-3188
VOLUME: 11 NO: 3 PAGE: 911-921 YEAR: 2022
DOI: 10.17798/bitlisfen.1140727

Measurement of Indoor Seasonal and Regional Radon (222Rn) Gas Activity in Çanakkale (Turkey)

Aydın BÜYÜKSARAÇ[1*], Muhammed Fatih KULUÖZTÜRK[2]

[1]*Çanakkale Onsekiz Mart University Çan Vocational School TR-17400 Çanakkale-TURKEY*
[2]*Bitlis Eren University, Department of Electrical-Electronics Engineering, TR-13000, Bitlis-TURKEY*
(ORCID: 0000-0002-4279-4158) (ORCID: 0000-0001-8581-2179)

Keywords: Indoor Radon exhalation, Radiation, Annual effective dose equivalent, Excess lifetime cancer risk.

Abstract

Radon gas, which undergoes radioactive decay, can cause damage to the lung tissue and lung cancer over time in indoor environments where it is inhaled. Radon gas radioactivity concentrations were measured using CR-39 passive solid state nuclear track detectors (SSNTD) in the basement and ground floor simultaneously in summer and winter periods in 17 dwellings in Çanakkale Center and Kepez regions (Turkey). Accordingly, an average of 163.67 $Bq.m^{-3}$ in basements in summer, 63.26 $Bq.m^{-3}$ in ground floors in summer, 148.73 $Bq.m^{-3}$ in basements in winter, and 77.57 $Bq.m^{-3}$ in ground floors in winter. In addition, annual effective dose equivalent (AEDE) values and excess lifetime cancer risk (ELCR) parameters were calculated using radon activity concentrations. Accordingly, the basement and mean AEDE values in the summer period were found to be 4.52 $\mu Sv.y^{-1}$ and 1.59 $\mu Sv.y^{-1}$, respectively. In winter, it was found as 3.75 $\mu Sv.y^{-1}$ and 1.95 $\mu Sv.y^{-1}$.

1. Introduction

There is natural radioactivity of earth's crust or cosmic origin, and artificial radioactivity resulting from nuclear tests and accidents. Regionally, radioactivity can be found in different concentrations. Since ionizing radiation negatively affects human health in proportion to the amount of exposure, it is important to determine the radiation level in living areas and to take possible precautions.

There are four basic decay chains in nature and the most dominant source of naturally occurring ionizing radiation is radon gas (^{222}Rn). Radon, the only gas intermediate product of the ^{238}U natural decay chain found in soils and rocks, is a chemically stable, colorless and odorless gas. Radon gas taken into the body through respiration turns into ^{210}Pb, a relatively long-lived and toxic radioisotope, by emitting ionizing radiations with a rapid decay mechanism. Because of these properties, radon gas is the second most important cause of lung cancer after smoking [1]. In 2018, it is estimated that there were close to 2 million new cancer cases and 1.7 million deaths in the world. In Turkey, an average of 23,000 men and 4,500 women are diagnosed with lung cancer annually. Studies show that there is a link between indoor radon gas exposure and lung cancer, although radon gas levels are relatively low in residential buildings [2]. Radon gas is found in relatively low concentrations (~15 Bqm^{-3}) due to atmospheric changes outside the buildings [3]. The reason for the direct or indirect concentration of radon gas indoor is the ^{226}Ra isotope in the soil [4]. Radon gas in the ambient can create high concentrations due to cracks and gaps in buildings, water used at home or building materials [5]-[8]. Indoor radon concentration varies depending on the type of soil in which the houses are located, the rocks around or under the building, the construction materials, the water source coming to the house, the temperature and pressure differences, the use of natural gas or other fossil fuels, and the living habits of the people.

Determination of radon levels indoor where people spend a long time is very important for human health. For this reason, indoor radon gas levels are investigated in different environments. Many studies have been reported with active or passive methods in different countries for the detection of radon gas in

*Corresponding author: absarac@comu.edu.tr
Received: 05.07.2022, Accepted: 05.08.2022

dwellings (Table 1). When the results obtained are compared with the previous studies in the world and in Turkey, it is revealed that there are quite compatible results, especially with randomly selected samples from the world. In fact, it shows very close values with Sweden, which is generally accepted as high radon concentration. Considering the climatic conditions, it can be accepted that the low ventilation in the winter season in countries such as Sweden, Germany, Pennsylvania (USA), and Tehran (Iran) increases the value. In addition, the low or variable values in countries such as Kuwait and Colombia can be attributed to climatic conditions and more ventilation due to the hot climate. In addition to this, examples of different countries should also be discussed in detail in terms of different living cultures, habits, and differences in house types.

When it is considered for Turkey, this time, assuming that there are similar living habits and considering the climatic conditions as the determinant, cities such as Içel and Kahramanmaraş are located in the region with Mediterranean climate characteristics, and the summer period lasts for a long time. On the other hand, cities such as Edirne, Istanbul, Bitlis, Kırıkkale, Sivas, Adapazarı, Bayburt are settlements where the cold period is longer or equal to the warm period. However, there are no significant differences between these cities. Very high values were encountered in an old settlement in Ahlat (Bitlis), and therefore the average values were considerably higher. Most of the examples given from both Turkey and the world include the radon concentration values in the bedroom or living room. In the study conducted in Çanakkale within the scope of this study, values were obtained from both normal living areas and basement floors where life partially continues. The fact that the values especially in the basement floors are high is one of the most important differences. However, although measurements were taken in the basement floors in Edirne, for example, values as high as those in Çanakkale could not be reached.

Since nuclear trace detectors are cheap and easy to use, there are many studies using CR-39 nuclear trace detectors among these studies. In addition to these advantages, it also has disadvantages such as not being able to receive instantaneous data due to being a passive detector, not knowing the existence of possible background traces at the beginning and changing the count result according to the user while counting the traces. However, manufacturers have minimized this margin of error with products such as etching baths and robotic assisted automatic counting systems.

In this study, it was aimed to determine the radon gas levels in the basement and ground floors of the same buildings in different ground conditions, in winter and summer periods, in Çanakkale center and Kepez regions, using CR-39 passive nuclear trace detectors.

2. Material and Method

In the frame of this study, CR-39 passive SSNTD (Solid State Nuclear Tracking Detectors) were used to determine regional and seasonal changes in radon gas concentration in 17 dwellings in Çanakkale.

2.1. Sampling Area

The dwellings where the detector will be placed were selected from Çanakkale center and Kepez regions depending on the soil content structure (Figure 1). In seasonal total, 34 detectors were placed in selected dwellings. Two detectors are installed in each house, one in the basement and the other on the ground floor. The rooms where the detectors were placed were mostly chosen as the bedroom or living room where the households spent more time.

The color separation seen on the map represents different ground conditions. Çanakkale is a coastal city and mainly consists of marine alluvium. Sand and silt are predominantly found in the alluvium. 12 detectors are placed in the built dwellings on the alluvium (Al). 5 detectors are located within the structures on the Alçıtepe (Aç) formation, which has sandstone, marl and mudstone characteristics. As can be seen from this information, the effect of Çanakkale soils, which are mostly dominated by granular soil units, on radon concentration was observed in this study. Granular units, due to their high permeability, allow radon gas to be easily discharged from underground to the surface. In this case, it is expected that there will be more radon gas emission to the indoor environment.

Table 1. Some indoor radon studies in literature.

Location	^{222}Rn Activity (Bq.m^{-3})	Specifications	Reference
Germany	70 mean	44,629 dwellings For 40 years period SSNTD	[9]
USA, Pennsylvania	181, 178, 161, 143 autumn, winter, spring, summer respectively mean values	1,808,294 dwellings For 40 years period, seasonal SSNTD	[3]
Columbia, Menizales	50 max. 85 geometric mean	202 houses; Related to location area, floor level, wall and floor material and number of people living in the house, SSNTD	[10]
Kuwait	7±1 – 404±21 at school 13±1 - 595±30 at basement of residential dwellings	150 sites at school classrooms and basement of residential dwellings	[11]
İran, Tehran	31 – 460.2 average 104	30 dwellings	[12]
Sweden	151 mean	60,809 houses, for 5 years period SSNTD	[13]
Turkey, İçel	Winter 13-59 range, 44 mean Summer 22-159 range, 23 mean	100 houses, bedrooms and living rooms, Seasonal, SSNTD	[14]
Turkey, Edirne	49.2	88 houses at basement, SSNTD	[15]
Turkey, Çanakkale (Ezine)	9-300 range, 67.9 mean	58 dwellings, summer season, SSNTD	[16]
Turkey, Bayburt	17-125 range, 56 mean	44 houses, SSNTD	[17]
Turkey, Sivas	Winter mean 89 Summer mean 98	98 houses, seasonal SSNTD	[18]
Turkey, Adapazarı	59.9 at houses, 57.1 at schools 61.7 mean	31 schools and 50 dwellings SSNTD	[19]
Turkey, Kırıkkale	Winter 17-484 range, 86.94 mean Summer 14-288 range, 63.27 mean	150 houses, seasonal SSNTD	[20]
Turkey, Bitlis (Ahlat)	10-2031 range 259.86 mean	50 houses related to construction material SSNTD	[21]
Turkey, İstanbul	17.4 ground floor, 8.5 first floor	16 dwellings in a university campus, Related to floor level, Active AlphaGuard detector	[22]
Turkey, Kahramanmaraş	Winter 8.52-53.12 range, 67.30 mean Summer 4.74-22.79 range, 52.25 mean	12 dwellings in a university campus, seasonal Active Rad7 detector	[23]
Turkey, Çanakkale	Basement winter 148.73 summer 163.67 Ground floor winter 77.57 summer 63.26	17 buildings, basement and ground floors, seasonal SSNTD	Present Study

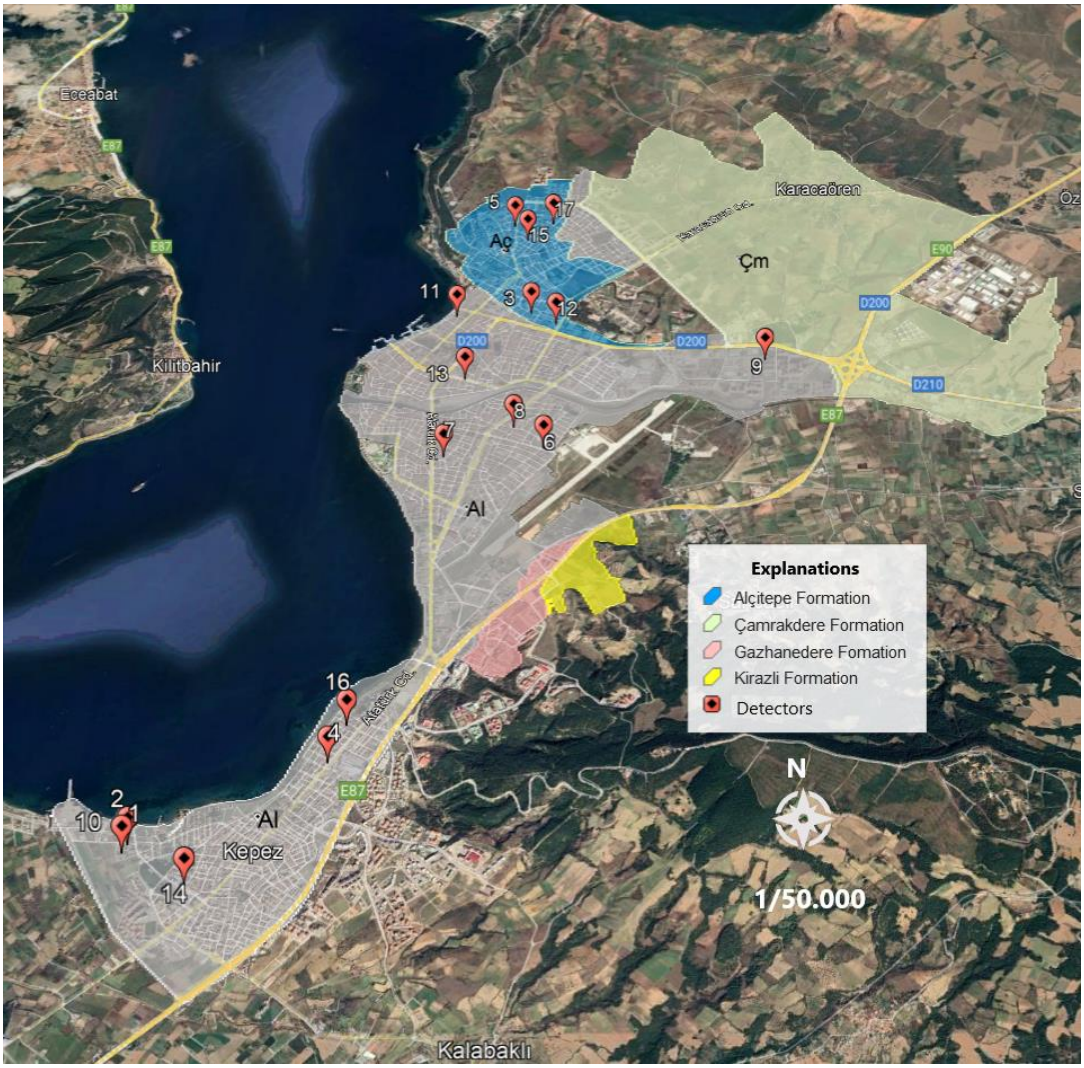

Figure 1. Distribution of CR-39 detectors in the study area. Al: Alluvium, Aç: Alçıtepe formation (mudstone, marl, siltstone, sandstone, calcarenite and locally thin conglomerate unit), Çm: Çamrakdere formation (mudstone-claystone, siltstone, sandstone, conglomerate and calcareous unit)

2.2. Measurements of Procedures

Detectors were placed in the selected dwellings for approximately 100-125 days between the months of June-September and October-January, since the detectors used had to be kept in the environment for a minimum of 80 days due to the calibration determined by the manufacturer. At the end of this period, the detectors collected were brought to the laboratory and the chemical etching process was started. 10mm×10mm and 1mm thick detectors, whose IDs are engraved as dot-code on them and placed in the diffusion chamber (which has 10 µm airgaps for effective diffusion of radon atoms (in the range of 10^{-4} µm) [24], are placed on 12 slides.

After chemical etching (6M NaOH, 9 hours, 90°C), counts were made with a (×40) zoom optical microscope and RadoSYS automatic counting system with a 3-megapixel camera. The trace densities were determined by counting the traces in the images taken from nine different surfaces on each detector for five times (Figure 2). Counts were made using the software RadoMeter RSV8 TA/8 v4.52 available for the Linux operating system. Then, with the help of the equation including the calibration coefficient, exposure time and trace densities given by the detector manufacturer, the radon gas activity concentrations were obtained in Bqm^{-3} (Eq. 1) [24].

$$C_{Rn}(Bq.m^{-3}) = 1000 \times TD \times CF/t \qquad (1)$$

Where C_{Rn} is the radon gas activity value, TD is the trace density obtained from the count, CF is the calibration coefficient of the CR-39 detectors (41.44 h.kBq.[m^3(track.mm^{-2})]$^{-1}$) and t is the exposure time in the dwellings [21].

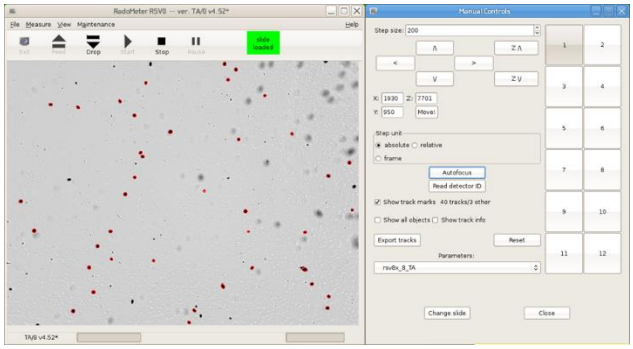

Figure 2. Determination of trace densities by counting the traces 5 times in the images taken from 9 different surfaces on each detector.

2.3. Calculation of Radiological Effects

In order to determine the possible harmful effects of radon gas, parameters such as the amount of exposure and cancer risk are calculated by using the radon activity concentration values. The following expression is used when calculating the Annual Effective Dose Equivalent (AEDE).

$$AEDE(\mu Sv.y^{-1}) = C_{Rn} \times EF \times T \times DCF \qquad (2)$$

Where CRn is radon activity concentration value (Bq.m^{-3}), EF is Equilibrium Factor of radon and its products for buildings (0.4) [25], T is exposure time to indoor radon gas (7000 h.y^{-1}) and DCF is dose conversion factor (9×10-6 mSv (Bq.h.m^{-3})$^{-1}$) [25].

Using the annual effective radon dose exposed, the Excess Lifetime Cancer Risk (ELCR) value originating from radon gas is calculated with the help of the equation below.

$$ELCR = AEDE \times ALT \times RF \qquad (3)$$

Where ALT is average lifetime (70 years), and RF is fatal risk factor per Sv (0.05) [26]. The ELCR value reveals a relative relationship to the probability of developing cancer disease in relation to AEDE [27],[28].

3. Results and Discussion

When the indoor radon gas concentration measurement results covering Çanakkale center and Kepez Town are evaluated, two different average values emerge. The seasonal average activity value in the basement floors was 163.67 Bq.m^{-3} (Table 2) in summer and 148.73 Bq.m^{-3}, (Table 3) in winter. However, abnormal values emerged at 2 points (dwelling ID numbers: 11 and 15) within these values in basement floor measurements (Figure 3). Radon gas activity observed in basements is higher than in other floors, since radon gas first enters the basements in the buildings and reaches the upper floors after creating a certain concentration there. In addition, the fact that ventilation possibilities or periods are weak compared to other floors also contributes to this difference.

If these values are not taken into account, the summer average is 81.03 Bq.m^{-3} and the winter average is 83.61 Bq.m^{-3}, as expected. On the other hand, there are 5 dwellings (dwelling ID numbers: 8, 10, 11, 13, 15) exceeding 100 Bq.m^{-3} in the basement floors during the summer period. There are 4 dwellings (dwelling ID numbers: 10, 11, 13, 15) exceeding 100 Bq.m^{-3} in the basement floors during the winter period. On the ground floors, there are 1 dwelling in the summer period and 3 dwellings in the winter period, with a value of more than 100 Bq.m^{-3} (dwelling ID numbers: 6 and 8, 10, respectively).

The seasonal average activity value on the ground floors was found to be 63.63 Bq.m^{-3} in summer and 77.57 Bq.m^{-3} in winter (Figure 4). Radon gas concentration measurements were made simultaneously in the ground and basement floors. Despite this, the average activity values of the basement floors were found to be higher than those of the ground floors both in the summer and winter periods. When evaluated specifically for the dwelling, the activity value measured in the winter period is higher than that measured in the summer period in 52.94% of the basement floors. In 70.59% of the dwellings on the ground floor, the activity value measured in the winter period was found to be higher than in the summer period.

Table 2. Radon activity concentrations in summer season.

Summer Season								
	Basement				Ground Floor			
Dwelling ID	Rn Activity ($Bq.m^{-3}$)	Error	AEDE ($\mu Sv.y^{-1}$)	ELCR (%)	Rn Activity ($Bq.m^{-3}$)	Error	AEDE ($\mu Sv.y^{-1}$)	ELCR (%)
1	43.58	1.58	1.10	0.004	82.99	1.85	2.09	0.007
2	56.03	1.63	1.41	0.005	76.52	1.11	1.93	0.007
3	44.74	1.51	1.13	0.004	27.63	3.44	0.70	0.002
4	76.49	0.38	1.93	0.007	48.62	1.07	1.23	0.004
5	80.99	2.98	2.04	0.007	58.22	2.37	1.47	0.005
6	20.32	1.02	0.51	0.002	156.62	4.08	3.95	0.014
7	55.19	1.28	1.39	0.005	59.05	1.64	1.49	0.005
8	118.55	0.19	2.99	0.010	76.00	0.43	1.92	0.007
9	81.11	0.38	2.04	0.007	43.00	3.49	1.08	0.004
10	292.12	0.30	7.36	0.026	84.49	0.86	2.13	0.007
11	760.57	0.57	19.17	0.067	41.66	2.61	1.05	0.004
12	52.28	0.36	1.32	0.005	53.72	0.64	1.35	0.005
13	131.10	0.14	3.30	0.012	50.68	1.12	1.28	0.004
14	87.60	1.20	2.21	0.008	76.83	1.60	1.94	0.007
15	806.34	0.58	20.32	0.071	55.15	1.57	1.39	0.005
16	36.61	2.50	0.92	0.003	38.68	0.45	0.97	0.003
17	38.72	3.48	0.98	0.003	45.52	0.76	1.15	0.004
Min.	20.32		0.51	0.002	27.63		0.70	0.002
Max.	806.34		20.32	0.071	156.52		3.95	0.014
Mean	163.67		4.12	0.014	63.26		1.59	0.006
TAEK	400				400			

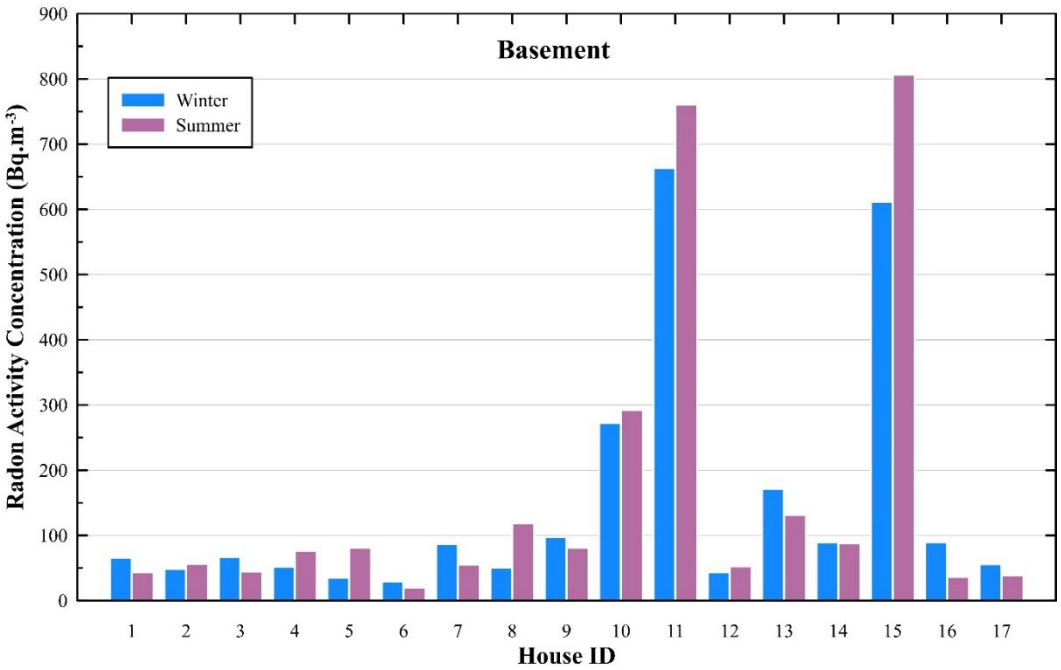

Figure 3. Seasonal radon measurements in basement.

Table 3. Radon activity concentrations related to winter season

Winter Season								
Basement					**Ground Floor**			
Dwelling ID	Rn Activity ($Bq.m^{-3}$)	Error	AEDE ($\mu Sv.y^{-1}$)	ELCR (%)	Rn Activity ($Bq.m^{-3}$)	Error	AEDE ($\mu Sv.y^{-1}$)	ELCR (%)
1	65.68	1.92	1.66	0.006	83.28	1.26	2.10	0.007
2	48.66	2.09	1.23	0.004	81.17	0.98	2.05	0.007
3	66.69	2.51	1.68	0.006	23.06	2.10	0.58	0.002
4	52.03	1.46	1.31	0.005	70.78	1.44	1.78	0.006
5	35.09	12.35	0.88	0.003	36.33	1.33	0.92	0.003
6	29.13	1.13	0.73	0.003	46.34	1.34	1.17	0.004
7	86.49	1.20	2.18	0.008	39.36	2.11	0.99	0.003
8	50.55	2.32	1.27	0.004	143.61	1.64	3.62	0.013
9	97.39	3.16	2.45	0.009	53.75	2.79	1.35	0.005
10	272.27	0.32	6.86	0.024	207.66	0.73	5.23	0.018
11	662.93	0.41	16.71	0.058	62.94	0.91	1.59	0.006
12	43.65	2.45	1.10	0.004	45.12	0.77	1.14	0.004
13	171.52	3.31	4.32	0.015	84.47	2.96	2.13	0.007
14	89.53	1.83	2.26	0.008	95.72	0.81	2.41	0.008
15	611.36	0.55	15.41	0.054	98.95	4.29	2.49	0.009
16	89.68	1.02	2.26	0.008	94.82	1.27	2.39	0.008
17	55.78	2.41	1.41	0.005	51.36	1.71	1.29	0.005
Min.	29.13		0.73	0.003	23.06		0.58	0.002
Max.	662.93		16.71	0.058	207.66		5.23	0.018
Mean	148.73		3.75	0.013	77.57		1.95	0.007
TAEK	400		1.00		400		1.00	

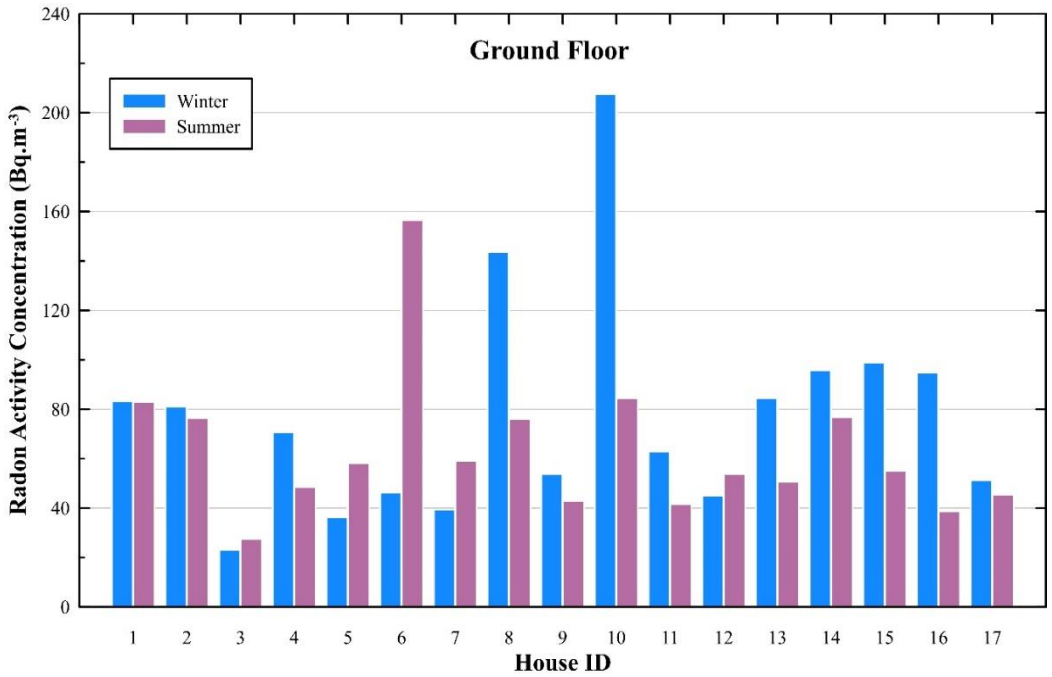

Figure 4. Seasonal radon measurements in ground floors.

It has been determined that 58.82% of the basement floors of the same dwellings are higher than the values measured on the ground floor during the summer period. In the winter period, this value was determined as 47.06%. The seasonal comparison of basements and ground floors is given in Figure 5 for summer and Figure 6 for winter seasons.

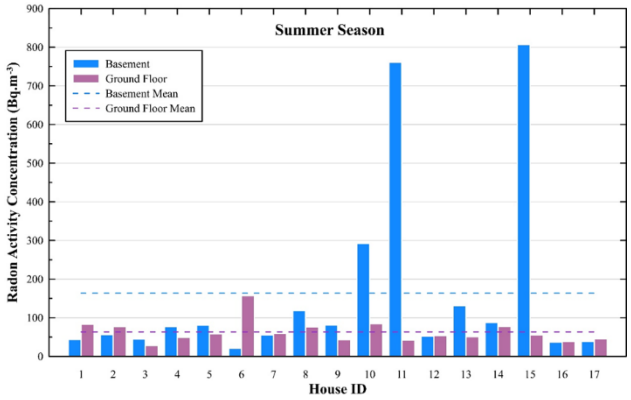

Figure 5. Comparison of basements and ground floors for the summer season.

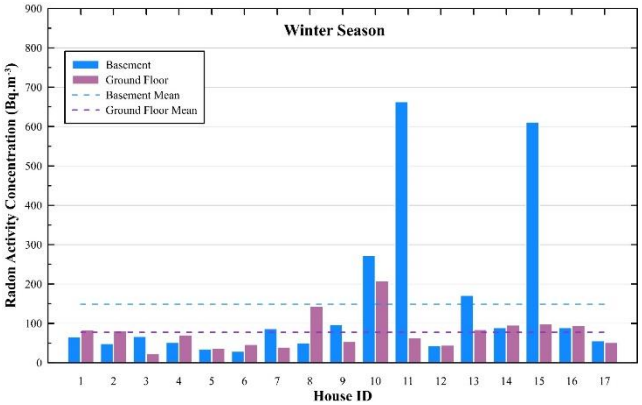

Figure 6. Comparison of basements and ground floors for the winter season.

The mean annual effective dose equivalent (AEDE) and excess lifetime cancer risk (ELCR) were calculated and are given in Table 2 for the summer period and Table 3 for the winter period. The mean annual effective dose equivalent and the excess lifetime cancer risk were determined by calculating the summer and winter averages of radon activity. AEDE was between 0.51-20.32 $\mu Sv.y^{-1}$ in basements for the summer period, with a mean value of 4.12 $\mu Sv.y^{-1}$. The ground floors ranged from 0.70-3.95 $\mu Sv.y^{-1}$ and the mean value was 1.59 $\mu Sv.y^{-1}$. For the winter period, basements ranged from 0.73-16.71 $\mu Sv.year^{-1}$ and the mean value was 3.75 $\mu Sv.y^{-1}$. The ground floors ranged from 0.58-5.23 $\mu Sv.y^{-1}$ and the mean value was 1.95 $\mu Sv.y^{-1}$. Although these average values remain within the range of the action level (3–10 $\mu Sv.y^{-1}$) recommended by the ICRP [29] in basements, they are mainly caused by abnormal values. In addition, it remained below the action level (3–10 $\mu Sv.y^{-1}$) recommended by the ICRP [29] for ground floors. The lifetime cancer risk (ELCR) value represents the percentage of cancer risk, or the probability of having cancer in every 100,000 people. The ELCR was on average in basements and ground floors 14×10^{-3} and 6×10^{-3} percent for the summer period respectively. Similarly, it was on average in basements and ground floors 13×10^{-3} and 7×10^{-3} percent for the winter period respectively. Most of the selected buildings have the characteristics of the lower floor and upper floor of the same residence, which are defined as duplexes. For this reason, life in these residences continues in the form of basement and ground floor at the same time.

(a)

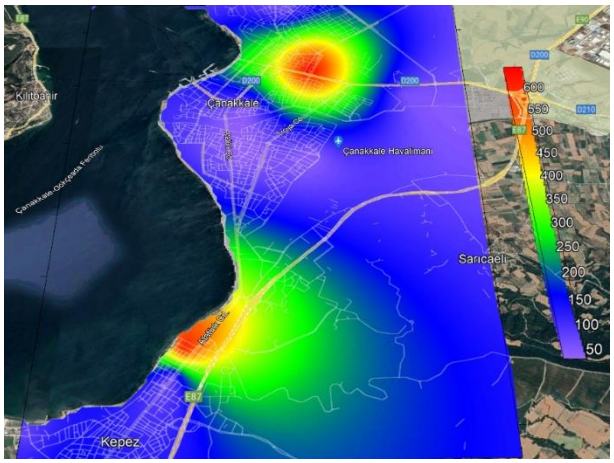

(b)

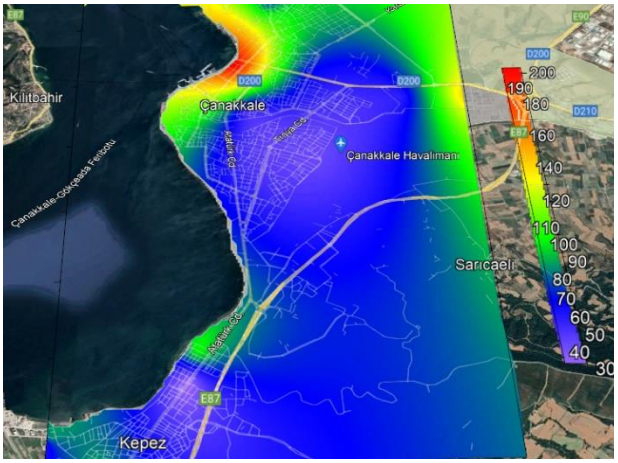

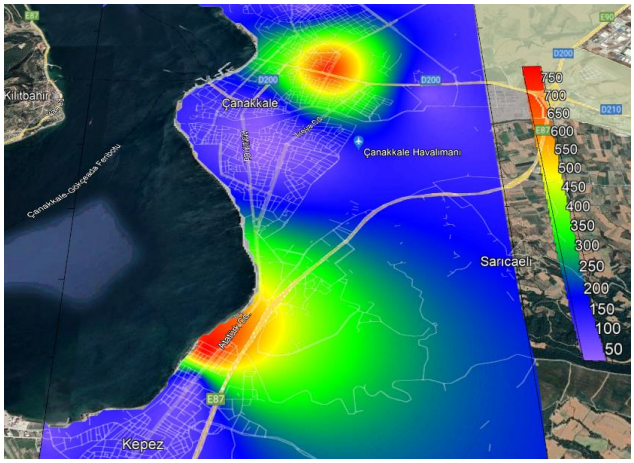

(c)

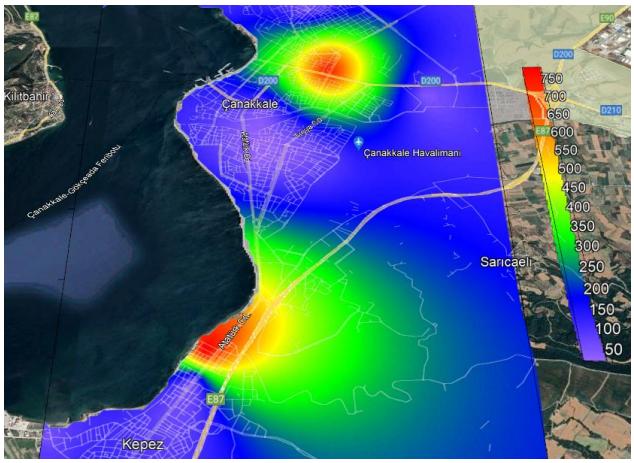

(d)

Figure 7. (**a**) Basement floor distribution in the winter period, (**b**) Ground floor distribution in the winter period, (**c**) Basement floor distribution in the summer period, (**d**) Ground floor distribution in the summer period.

4. Conclusion

In this study, radon gas levels, covering 17 buildings in Central settlement and Kepez region of Çanakkale in Northwest of Turkey, were measured simultaneously in both the basements and the ground floors. When the obtained activity concentration results were evaluated in general, a general average result of 113.31 Bq.m^{-3} was obtained. The general radon concentration value obtained because of the studies carried out in 5500 houses in Turkey, regardless of season or floor, was determined as 82.66 Bq.m^{-3} [30]. In a study conducted in Ezine, Çanakkale [16], measurements were made in 58 houses and an average value of 67.90 Bq.m^{-3} was obtained. When the results obtained in this study are evaluated from this point of view, activity concentration values above the average values obtained both in Çanakkale and throughout Turkey were obtained. The reason for these high average activity values is the high values obtained in both seasons in the two basement floors 11 and 15. When the general average is calculated by excluding the values of these two houses, a value of 75.53 Bq.m^{-3} is obtained. Observations were made comparing seasonal, spatial, domestic behavior conditions and soil conditions. Accordingly, no dramatic difference was observed in the radon gas levels in the basements or ground floors. Since there is less ventilation in the basement floors, there are increased values in radon gas levels compared to the floors above the basement. The values in 2 basements with no ventilation were measured much higher than the accepted value (between 600-800 Bq.m^{-3}). Radon gas levels observed in dwellings with an older construction year, especially in old residential areas of the city, are higher. On the other hand, although there is no significant difference in value depending on soil conditions, the radon gas values observed in the rock environment are higher than those in alluvial conditions. In some ground floors with insufficient ventilation, the value exceeded 100 Bq. The mean annual effective dose equivalent (AEDE) and excess lifetime cancer risk (ELCR) is at a level that does not require any action in the absence of abnormal values. However, in basements with abnormal values, conditions have arisen that require taking precautions. All these results reveal that ventilation conditions are the main reason affecting indoor natural radon gas values unless there is a very specific source. Even if the ventilation conditions are respected, the presence of 4-5 times more radon gas in the indoor breathing air should be considered as a risk of life in the indoor ambient. Annual effective dose equivalent (AEDE) showed high values in rarely visited areas where Rn concentrations accumulate due to improper ventilation. The average radon concentration measured in the basements of the houses was significant for the annual effective dose for the residents. Although the soil conditions do not show a significant change for the study area, radon gas leaks from the cracks and shows a higher concentration, especially in the areas where rocks are dominant. On the other hand, since it is easily exposed on sandy soils, its concentration in indoor environments also decreases.

Acknowledgment

This work was supported by Çanakkale Onsekiz Mart University, the Scientific Research Coordination Unit, Project number: FHD-2021-3649.

Contributions of the authors

All contributions to this study belong to the authors.

Conflict of Interest Statement

There is no conflict of interest between the authors.

Statement of Research and Publication Ethics

The study is complied with research and publication ethics

References

[1] WHO (World Health Organisation), *World Cancer Report*. WHO Press, 2014.

[2] NRC, *Health Effects of Exposure to Radon. BEIR VI Report*. National Academy Press, Washington, DC.), 1999.

[3] K. R. Kellenbenz and K. M. Shakya, "Spatial and temporal variations in indoor radon concentrations in Pennsylvania, USA from 1988 to 2018". *Journal of Environmental Radioactivity*, vol. 233, pp. 106594, 2021.

[4] M. Baskaran, "Radon: a tracer for geological, geophysical and geochemical studies. In: Radon: A Tracer for Geological, Geophysical and Geochemical Studies". *Springer International Publishing*, 2016.

[5] H. Kayakökü, Ş. Karatepe, M. Doğru, "Measurements of radioactivity and dose assessments in some building materials in Bitlis, Turkey". *Applied Radiation and Isotopes*. vol. 115, pp. 172-179, 2016.

[6] O. Baykara, Ş. Karatepe, M. Doğru, "Assessments of natural radioactivity and radiological hazards in construction materials used in Elazig, Turkey". *Radiation Measurements*. vol. 46, pp. 153-158, 2011.

[7] M. Rafique and M. H. Rathore, "Determination of radon exhalation from granite, dolerite and marbles decorative stones of the Azad Kashmir area, Pakistan". *Internatioanl Journal of Environmental Science and Technology*, vol. 10, pp. 1083–1090, 2013.

[8] E. Işık, A. Büyüksaraç, E. Avşar, M. F. Kuluöztürk, M. Günay, "Characteristics and properties of Bitlis ignimbrites and their environmental implications". *Materiales de Construccion*. vol. 70, pp. 338, 2020.

[9] E. Petermann and P. Bossew, "Mapping indoor radon hazard in Germany: The geogenic component". *Science of the Total Environment*. vol. 780, pp. 146601, 2021.

[10] A. Giraldo-Osorio, A. Ruano-Ravina, M. Pérez-Ríos, L. Varela-Lema, J. M. Barros-Dios and N.E. Arias-Ortiz, "Residential Radon in Manizales, Colombia: Results of a Pilot Study". *Int J Environ Res Public Health*. vol. 18, no. 3, pp. 1228, 2021.

[11] L. Al-Awadi and A. R. Khan, "Indoor radon levels in schools and residential dwellings in Kuwait". *International Journal of Environmental Science and Technology*, vol. 16, pp. 2627–2636, 2019.

[12] M. Shahbazi Sehrani, S. Boudaqpoor, M. Mirmohammadi, "Measurement of indoor radon gas concentration and assessment of health risk in Tehran". *Iran International Journal of Environmental Science and Technology*, vol. 16, pp. 2619–2626, 2019.

[13] B. Olsthoorn, T. Rönnqvist, C. Lau, S. Rajasekaran, T. Persson, M. Mansson, A.V. Balatsky, "Indoor radon exposure and its correlation with the radiometric map of uranium in Sweden". *Science of the Total Environment*. vol. 811, pp. 151406, 2022.

[14] H. Kumbur, O. Zeren, M. Köksal, B. Özçınar, "Investigation of Radon Levels in Houses in İçel". *Ecology Environment Journal*, vol. 25, no. 7, pp. 25-31, 1997.

[15] A. Bozkurt and E. Kam, "Indoor Radon Measurement in The City of Edirne, Turkey". *AIP Conference Proceedings*, vol. 899, pp. 395, 2007.

[16] Y. Örgün, N. Altınsoy, S. Y. Şahin, B. Ataksor, N. Çelebi, "A study of indoor radon levels in rural dwellings of Ezine (Çanakkale, Turkey) using solid-state nuclear track detectors". *Radiation Protection Dosimetry*, vol. 131, no. 3, pp. 379–384, 2008.

[17] B. Küçükömeroğlu, A. Kurnaz, N. Damla, U. Çevik, N. Çelebi, B. Ataksor, H. Taşkın, "Environmental radioactivity assessment for Bayburt, Turkey". *Journal of Radiological Protection*, vol. 29, no 3, pp. 417-428, 2009.

[18] M. Mıhçı, A. Büyüksaraç, A. Aydemir, N. Çelebi, "Indoor and outdoor Radon concentration measurements in Sivas, Turkey, in comparison with geological setting". *Journal of Environmental Radioactivity,* vol. 101, pp. 952-957, 2010.

[19] E. Kapdan and N. Altınsoy, "A comparative study of indoor radon concentrations between dwellings and schools". *Radiation Physics and Chemistry*. vol. 81, pp.383-386, 2012.

[20] N. Bingöldağ and P. Otansev, "Determination of natural radiation levels and lifetime cancer risk in Kırıkkale, Turkey". *Radiochimica Acta,* vol. 106, no. 5, pp. 401-411, 2018.

[21] M. F. Kuluöztürk, A. Büyüksaraç, F. Özbey, S. Yalçın and M. Doğru, "Determination of indoor radon gas levels in some buildings constructed with Ahlat stone in Ahlat/Bitlis". *International Journal of Environmental Science and Technology*. vol. 16, pp. 5033–5038, 2019.

[22] O. Günay, S. Aközcan, F. Kulalı, "Measurement of indoor radon concentration and annual effective dose estimation for a university campus in Istanbul". *Arabian Journal of Geosciences*. 12, 171, 2019.

[23] E. Küçükönder, "Kahramanmaraş İlinde Bina İçi Mevsimsel Radon Gazı Aktivitesi Ölçümü". *BEU Journal of Science*, vol. 10, no. 3, pp. 891-901, 2021.

[24] RadoSYS, *RadoSYS User Manual,* Hungary, 2011.

[25] United Nations Scientific Committee on the Effects of Atomic Radiation (UNSCEAR), "Sources, effects and risks of ionization radiation. Report to The General Assembly, with Scientific Annexes B: Exposures from Natural Radiation Sources". United Nations, New York, 2000.

[26] International Commission on Radiological Protection (ICRP), "Quantities and Units in Radiation Protection Dosimetry". *ICPR Report 51*, 1993.

[27] M. Çelik Karakaya, M. Doğru, N. Karakaya, H. Çingilli Vural, F. Kuluöztürk and S. Şahin Bal, "Radioactivity concentrations and dose assessments of therapeutic peloids from some Turkish spas". *Clay Minerals*. vol. 50, pp. 221-232, 2015.

[28] G. Ponciano-Rodriguez, M. I. Gaso, M. A. Armienta, C. Trueta, I. Morales, R. Alfaro and N. Segovia, "Indoor radon exposure and excess of lung cancer mortality: the case of Mexico-an ecological study". *Environmental Geochemical Health*. vol. 43, pp. 221-234, 2021.

[29] International Commission on Radiological Protection (ICRP), "Protection against Rn-222 at home and at work International Commission on Radiological Protection Publication 65". *Ann. Pergamon Press, Oxford*, vol. 23, no. 2, 1993.

[30] S. Y. Baş and S. A. Selçuk, "An Assessment on Measures for Reducing the Effects of Radon Gas in Buildings". *SETSCI Conference Proceedings*, vol. 4, no. 3, pp. 207-212, 2019.

Bitlis Eren Üniversitesi Fen Bilimleri Dergisi
BİTLİS EREN UNIVERSITY JOURNAL OF SCIENCE
ISSN: 2147-3129/e-ISSN: 2147-3188
VOLUME: 11 NO: 3 PAGE: 922-930 YEAR: 2022
DOI: 10.17798/bitlisfen.1141741

Generation and Transmission of Action Potential in Nerve Cells and Neuron Populations Based on the Realistic Hodgkin-Huxley Neuron Model

Ramazan TEKİN[1*]

[1]*Department of Computer Engineering, Batman University, Batman, Turkey*
(ORCID: 0000-0003-4325-6922)

Keywords: Action Potential, Post-synaptic Potentials, Nerve Cell, Hodgkin-Huxley model.

Abstract

There are several types of nerve cells in the central nervous system. Thanks to the synaptic connections, these cells form large and complicated networks. However, these cells have a stereotypical electrical activity called action potential (AP) or spike. In this work, the mechanisms of formation of this typical electrical signal and the methods of transferring from one cell to another were investigated using Hodgkin-Huxley neuron model. It has been seen that the formation of AP is based on the principle of "all or nothing law" and ion channel dynamics are critical in the typical form of AP. It has been shown that signal transduction between nerve cells is transmitted by post-synaptic potential and that these signals may be cell depolarizing or polarizing. Finally, it has been discussed that these electrical activities are quantities that can be measured by various methods at the micro and macro level.

1. Introduction

The brain and spinal cord that make up the central nervous system (CNS) have special cells called nerve cells or neurons, which are considered the smallest unit of the brain. The CNS consists of approximately 10^{12} nerve cells with complex synaptic connections with each other and almost 50 times as many cells called glia[1]. Glia cells' main task is meeting the energy requirement of the CNS and maintaining its stable structure [2].

Figure 1 shows Golgi-Cox staining of various types of cells in an adult mouse brain. Golgi-Cox staining images of cerebral cortex neurons and glial cells are shown in Figures 1A and Figure 1B. Hippocampal granule cells are seen in Figure 1C, Purkinje cell in Figure 1D, and dendritic spines in Figure 1E (scale bars are 500 µm in A, 50 µm in D, and 5 µm in E). As can be seen in Figure 1, it is seen that even neurons in a small cross-section have a rather complex structure. When the whole brain is considered, it is clearly understood how complex and enormous the brain is, with billions of neuron bodies and fiber connections in the form of a dense network.

In this study, comprehensive information about the general structure of nerve cells, electrical activity and how electrical activity occurs in neuron populations is presented. In order to demonstrate the generation and transmission of electrical signals between neurons, simulations involving single and multiple nerve cells were performed. In these simulations, pyramidal and interneuron neurons based on the realistic Hodgkin-Huxley neuron model are used. Thus, it was revealed how neurons transfer electrical signals to each other through synaptic connections. Although neurons have a very complex structure, it has been shown that the form of the electrical signal they create has a stereotyped structure in line with experimental studies. In addition, it has been revealed that this electrical signal is formed based on the all-or-nothing principle.

*Corresponding author: ramazan.tekin@batman.edu.tr
Received: 06.07.2022, Accepted: 05.09.2022

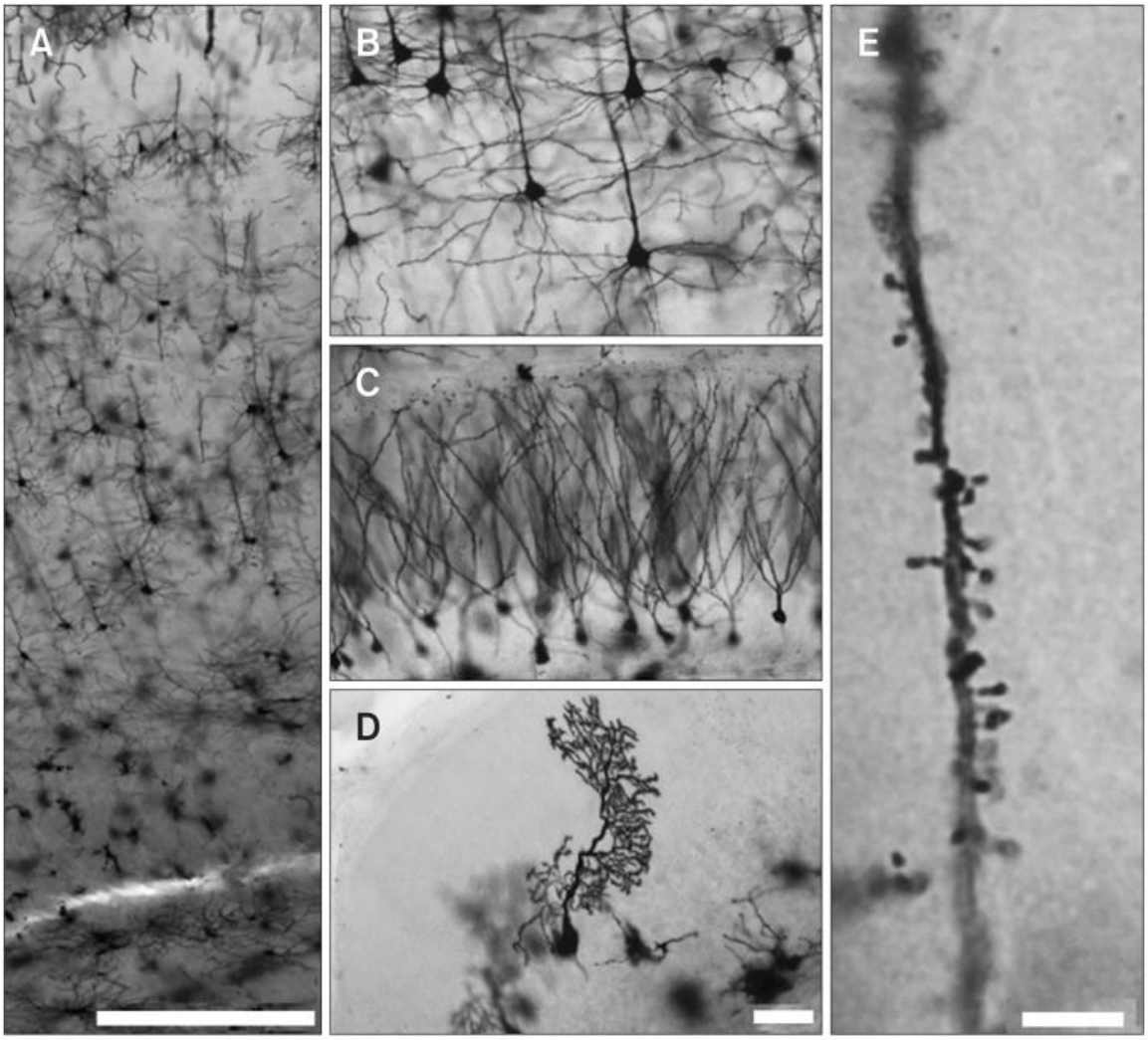

Figure 1. Golgi-Cox stained image of adult mouse brain (Retrieved from [5], based on open access policy)

2. Nerve Cell

There are quite many different types of nerve cells with different characteristics in the human brain, these cells are very similar in structure, as seen in Figure 2. However, it is stated that most of the brain functions in humans and other living things are related to the anatomical connections formed by these cells [3]. In the vertebrate cortex, each neuron usually has more than approximately 10^4 synaptic connections from neighboring neurons via the soma and its dendrites.

Neurons communicate with each other thanks to these large and complex network structures [2]. The synapses at these connections are usually in the form of chemical synaptic connections that replace the membrane potential of the neighboring neuron (post-synaptic neuron) with neurotransmitters. Cells such as muscle and cardiac cells have electrical synapses that communicate through the gap junction. The connection distance between cell bodies can be one (1) meter, as in a single axon in the human spinal cord, 1or a few millimeters, as in the brain. Axon thickness is in the range of about 1 μm to 500 μm, and thicker axons can transmit the signal faster [1]. Some axons are covered with a myelin sheath, an oil-like insulating material made up of regular spaces called nodes of Ranvier, which allows the signal to jump from one node to the next [3].

A typical nerve cell and neuron have a cell body called soma, dendrites that provide synaptic connections, an axon that transmits the signal formed in the cell body, and finally synaptic terminals that transmit this signal to other cells [2,3]. The soma is the largest component of a neuron. The main functions of the soma are to synthesize proteins, produce the necessary energy for the cell, and manage other vital functions of the cell. Another of the most important tasks of the soma is to transfer the signal/information it receives with the help of dendritic inputs to other cells via its synaptic terminals [5].

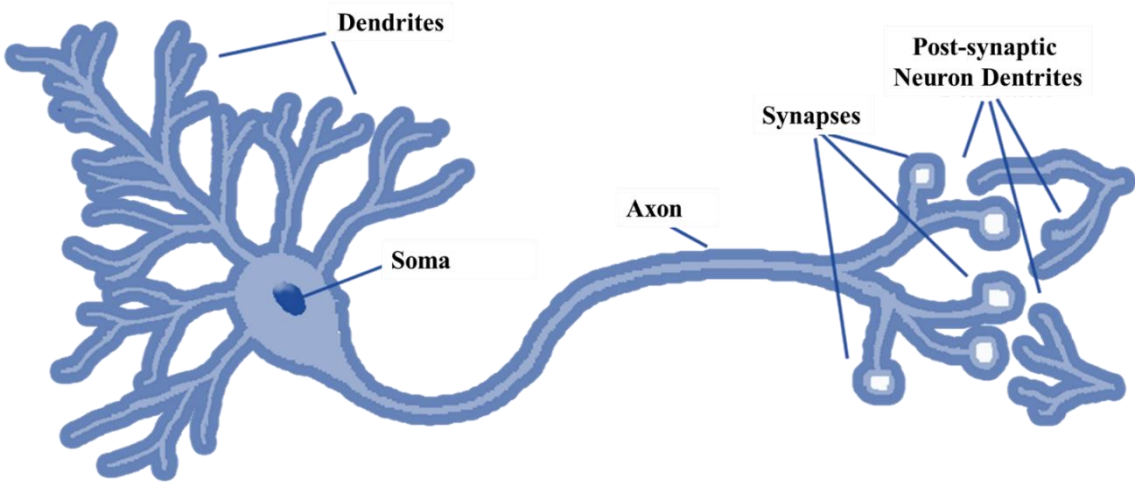

Figure 2. Schematic structure of an example nerve cell (motor neuron)

In addition, the cell body has a selectively permeable cell membrane called the membrane, which determines the basic characteristic of the electrical signal formed in the nerve cells. The selectively permeable porous structure of the cell membrane controls the transition of ionic molecules into or out of the cell. Dendritic and axonal projections of neurons, which are not found in other cells, enable the cell to communicate with other cells[1].

Although neurons make synaptic connections mostly by chemical and electrical mechanisms, they can also have ephatic synaptic connections[6]. They provide the transmission of the signal formed in the cell body as a result of synaptic connections, dendritic and/or axonal inputs to other neurons. Here, the source neuron that generates the signal is called the pre-synaptic cell, and the target neuron to which the signal is transmitted is called the post-synaptic cell[2]. Communication between pre-synaptic and post-synaptic cells takes place through structures called synaptic gap[3]. As shown in Figure 2, dendrites are structures that have many protrusions in a tree-like structure and that transfer a large number (thousands) of pre-synaptic inputs to the cell body thanks to this projection.

Although the main task of the dendrites is to transmit the signal transmitted from the pre-synaptic cell to the cell body, sometimes the incoming signal can be partially processed (gathered) in the dendrites and then transmitted to the soma[7]. But the main specialized cell unit for this process is the soma. The signal generated in the soma is carried to the synaptic terminals via the axon, which is longer than 1 m in humans[8]. Axons receive the action potential, which is a fast and transient electrical signal with an amplitude of about 100 mV and a period of 1 ms − 2 ms, from the cell body, and transfer it to the target cell via synaptic connections at a speed of about $0.5\ \mathrm{m/s}$ to $120\ \mathrm{m/s}$[1]. Thus, electrical signals produced in the soma can reach other associated neurons in the brain, or to the muscles through the innervation of effector muscles and glands via the motor cortex[5,9]. This electrical signal starts at the axon hillock and can be transmitted along the axon with almost no change[3]. Axons are divided into two types: whitish thick axons covered with myelin and thin axons without myelin[10]. Myelinated axons have several advantages such as faster conduction and less energy requirement[11]. There are many synaptic terminals called telodendria, which connect with the post-synaptic cell at the endpoints of axons[7].

3. Modeling and Simulation

In this study, simulations involving a single pyramidal nerve cell seen in Figure-3(A) were carried out to examine the nascency and form of AP. In addition, excitatory pyramidal (PY) cells and inhibitory interneurons (IN) were used in the cortical network (Figure-3(B)) designed to examine the transmission of electrical signals between neurons. The study was based on a single-compartment Hodgkin-Huxley neuron model with high biological reality for both PY and IN cell types. These mathematical models are generally expressed as follows[12–15]:

$$C\frac{dV}{dt} = I_{Na} + I_K + I_L + I \quad (1)$$

$$I_{Na} = G_{Na}m^3h(E_{Na} - V) \quad (2)$$

$$I_K = G_K n^4(E_K - V) \quad (3)$$

$$I_L = G_L(E_L - V) \quad (4)$$

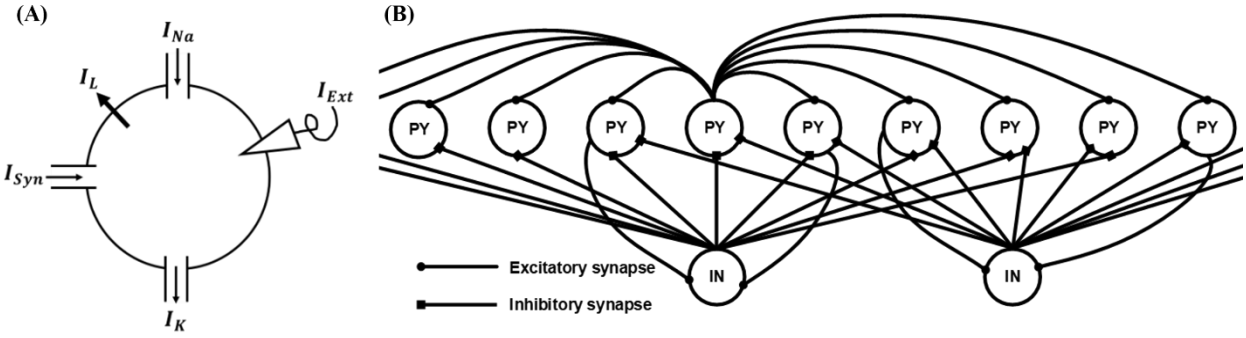

Figure 3. Schematic structure of single-cell and multi-cell applications

The voltage dependent channel currents given here are ionic currents, where I_{Na}, I_K and I_L represent sodium (Na^+), potassium (K^+) and leakage current, respectively. In addition, in the equations here, I denotes the sum of synaptic currents (I_{syn}) and/or external DC excitation current (I_{ext}), V denotes membrane voltage and $C = 1\mu F$ denotes cell membrane capacitance corresponding to unit area. The ionic current parameters $G_{Na} = 51.6$ mS, $G_K = 10$ mS, $G_L = 0.0452$ mS are the maximum values of sodium, potassium and leakage conductivities, respectively. E_{Na}, E_K, E_L are sodium, potassium, and leakage current reversal nernst potential values, respectively. On the other hand, m, h, and n gate dynamics are time-varying activation variables dependent on voltage-dependent ratio constants α_m, β_m, α_h, β_h, $\alpha_n$and β_n variables [13, 14].

In neuronal networks, the electrical potential generated by the pre-synaptic cell on the post-synaptic cell can be excitatory or inhibitory. In equation 1, which expresses the single-compartment cell model, the synaptic conductances caused by these potentials are represented by I_{syn} in the external current I and are generally expressed as follows[13–15].

$$I_{syn} = g_e(t)(V - E_e) + g_i(t)(V - E_i) \quad (5)$$

$$\tau_e \frac{dg_e}{dt} = -g_e \text{and} \tau_i \frac{dg_i}{dt} = -g_i \quad (6)$$

where V is the membrane voltage, time-dependent $g_e(t)$ and $g_i(t)$ are the excitatory and inhibitory synaptic conductivities, respectively. And $E_e = 0$ mV and $E_i = -75$ mV represent excitatory and inhibitory synaptic reversal potentials, respectively. Finally, $\tau_e = 2.7\,ms$ and $\tau_i = 10.5\,ms$ excitatory and inhibitory synaptic time constants, respectively [14].

In order to the cortical network model to be compatible with the anatomical and morphological bases, the study by Bazhenov et al. [16] was taken as reference and models were performed using 100 PY and 25 IN cells while maintaining the ratio of 4:1. Schematic representations of single-cell and multi-cell (cortical network) simulations are presented in Figure 3. As seen in Figure 3 (A), an external DC current (I_{ext}) was applied to examine the nascency and form of the AP. In order to examine the post-synaptic potentials, the cortical network whose schematic structure is presented in Figure 3(B) was created.

There are excitatory and inhibitory projections in the cortical network. Excitatory projections can be between PY cells (PY-PY) and from PY cells to IN cells (PY-IN), whereas Inhibitory projections can only be from IN cells to PY cells (IN-PY). Connection spreads are ±5%, ±1%, and ±5% for PY-PY, PY-IN, and IN-PY, respectively [16].

4. Action Potential

Nerve and muscle cells, which are excitable cells, have sodium (Na^+) and potassium (K^+) ion channels in their membranes. Thanks to the change in the internal and external (Na^+) and (K^+) concentrations of the ion channels, the electrical potentials on the membrane change. This electrical change is transmitted in waves along the cell axon and transferred to other cells, as in dominoes, via synaptic connections. As seen in Figure 4A, the resting membrane potential of a post-synaptic neuron that receives multiple pre-synaptic impulses (spike pulses) in a sufficiently strong external stimulus or in a short time window rises from a negative value (approximately -70 ∓ 10 mV) to a positive value (approximately $+40 \mp 10$ mV). Then it becomes negatively charged again by balancing the intracellular and extracellular ion concentration[2, 10, 17, 18].

The output of the membrane voltage is expressed as depolarization (discharge) and its decrease again as repolarization (charge) (Figure 4A). This charge and discharge event takes place due to the displacement of ionic substances, mainly Na^+, K^+,

Ca^{++} and Cl^{-}, along the cell membrane from the outside to the inside and from the inside to the outside, and the concentration difference between the intracellular and the extracellular. In this displacement process, ion pumps using adenosine triphosphate (ATP) energy also play an active role[18]. This electrical signal, in the form of a pulse with an amplitude of about 100 mV, formed in this way is called Action Potential (AP) or spike[2]. These electrical signals are of great importance for the cell, and they have a critical importance in the communication of nerve cells with each other, and thus in the realization of many body functions. Although AP is caused by many different environmental factors, it has a very stereotypical structure in the entire nervous system. For this reason, a signal carrying visual information and a signal carrying information about smell are similar to each other [3].

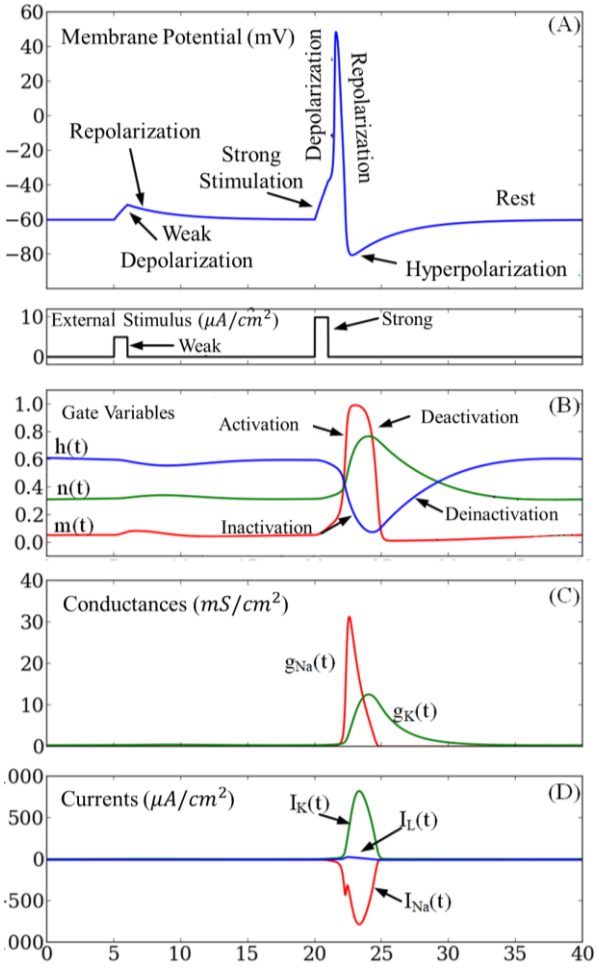

Figure 4. Action Potential and ionic channel dynamics according to the Hodgkin-Huxley model

Figure 4 shows the variations of a simulated AP and other ionic dynamics using mathematical models derived from a series of studies by Hodgkin and Huxley. The graphics in the figures are fully compatible with the work of Hodgkin and Huxley and were obtained as a result of our simulation-based on these models.

As seen in Figure 4A, with a sufficiently large excitation, the membrane voltage depolarizes by exceeding the critical voltage value. In the depolarization phase, the activation variables m and n increase, while the inactivation variable h decreases (Figure 4B). Since the Na^+ activation gate time constant $\tau_m(V)$ is faster than the others, the variable m is also faster than the others. The rapidly activated Na^+ channels depolarize the membrane voltage (V), increasing it up to the E_{Na} level. After the membrane voltage has reached its peak, the slower gate variables (n and h) come into play; the inactivation variable $h \to 0$ causes the Na^+ current to be passive, and the activation variable $n \to 1$ causes the outward K^+ current to be activated slowly. As seen in Figure 4C, the variation of sodium conductivity rises and falls rapidly, while potassium conductivity has a slower activity. This situation is related to the rate of change of the time constants seen in Figure 5. Then, the membrane voltage is repolarized towards the V_{rest} level with the effect of K^+ current and leakage current. The curves of the changes in channel currents are given in Figure 4D.

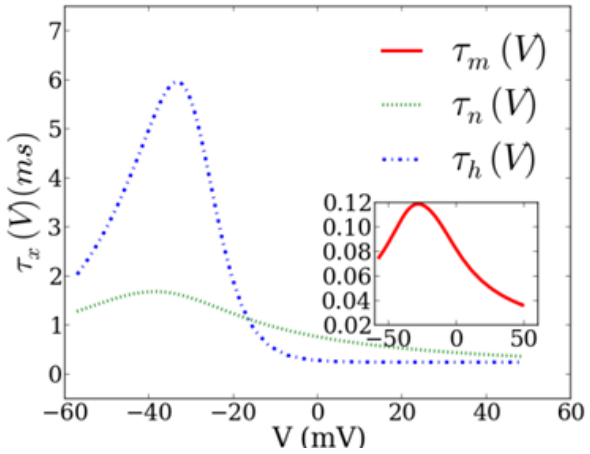

Figure 5. Time constants of activation and inactivation gates according to the Hodgkin-Huxley model

When the membrane voltage is $V \approx V_{rest}$, as seen in Figure 5, since voltage dependent $\tau_n(V) \cong 1.1\text{ms}$ and $\tau_h(V) \cong 2\text{ms}$ have relatively larger values than $\tau_m(V) \cong 0.08ms$, the improvement/correction variables n and h are slower. Accordingly, even when the membrane voltage is at about rest level ($V \cong V_{rest}$) in the continuation of the AP, the K^+current continues to be active and causes the membrane voltage to become hyperpolarized by pulling it below the rest level. At the end of the AP activity, the

membrane voltage of the hyperpolarized cell is brought back to the resting potential by the Na^+sodium-potassium ion pump. When the Na^+ current is inactivated (h is low), it cannot be used for a new regenerative function and a second AP cannot be triggered, this period is called the absolute refractory period. On the contrary, the period in which the current is de-inactivated, in which the system can generate a new AP with a sufficient (greater than normal) excitation is called the relative refractory period[19].

5. Electrical Activity in Neuron Populations

In general, it can be said that the potential difference and AP formation across the membrane is due to the concentration difference of K^+, Na^+ cations and Cl^- and large organic anions (Figure 7). However, the electrical activity that emerges as a result of these ionic channel activities in a post-synaptic nerve cell is shaped by some factors. These factors are the APs that emerge by exceeding the threshold value in pre-synaptic cells, and the sub-threshold potentials (PSP, post-synaptic potentials) created by these APs in the post-synaptic cell. In vivo synaptic conductances can be excitatory or inhibitory. If synaptic activity produces an excitatory potential in the postsynaptic cell, it is called excitatory post-synaptic potential (EPSP), and if it generates an inhibitory potential, it is called inhibitory post-synaptic potential (IPSP)[14].

As stated in Chapter 4, AP formation generally begins with rapidly increasing Na^+ ion permeability, and as a result of the influx of Na^+ ions into the cell due to the concentration difference, the intracellular potential rises rapidly. After a certain voltage value, the Na^+ ion permeability decreases. On the contrary, the permeability of K^+ ions increases and these ions flow from inside the cell to the outside, causing the inside of the cell to become negative again compared to the external environment. Thus, AP, which is a stereotypical signal lasting 1-2 ms, or in other words, a spike is formed. It processes the formation of this electrical signal according to the "all or nothing" law[10]. As seen in Figure 6A, this was demonstrated by Weidmann [20] applying square-shaped stimuli to Sheep Purkinje cells. On the other hand, Figure 6B shows the simulation results using the Hodgkin-Huxley neuron model. Both experimental and model results show us that AP occurs according to the all-or-nothing law.

PSPs are also associated with events occurring at the post-synaptic membrane. When the AP reaches the synapse, it changes the permeability of the next post-synaptic membrane by releasing some chemicals called mediators or transmitters, and as a result, ions cross the membrane and create a potential across the membrane. As can be seen in Figure 7 inner graph, if this potential depolarizes the membrane voltage, an EPSP will occur, increasing the probability of spike firing. If the membrane voltage is polarized, as can be seen in Figure 7 inner graph, IPSP will occur on the contrary. The form of PSPs is not stereotyped like APs and depends on the rate of neurotransmitters released. A typical PSP has an amplitude of 5mV to 10mV and a period of 10ms to 50ms. Therefore, multiple PSPs must occur in succession at appropriate times for supra-threshold stimulation required to generate AP in the post-synaptic cell soma. In other words, phase coherence between post-synaptic and pre-synaptic cells is vital for the formation of AP in the cell. Therefore, efficient signal transmission between nerve cells is possible only if there is phase synchronization [21].

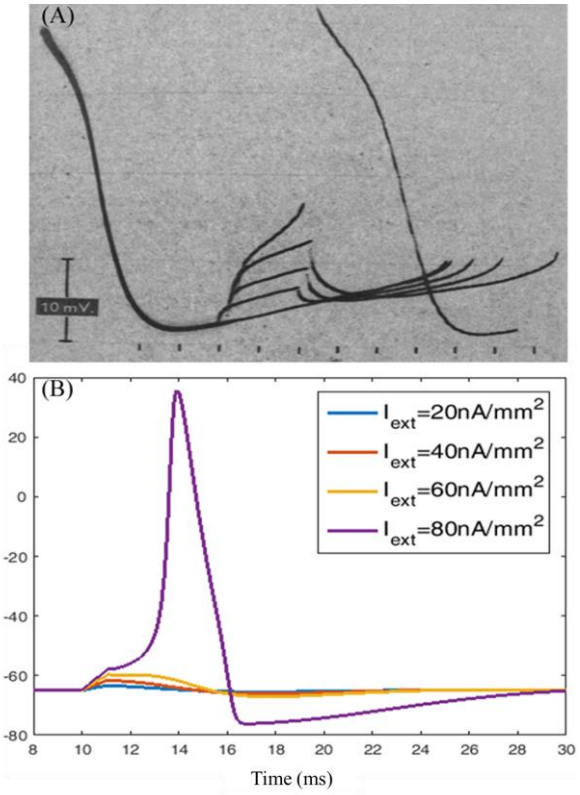

Figure 6. The all-or-none law. (A) Sheep Purkinje cell AP forms [20], (B) AP forms according to the Hodgkin-Huxley neuron model

Due to the various types of ionic channels, many ionic currents occur across the nerve cell membrane towards the inside and/or outside of the cell. In this case, due to ionic currents, massively magnetized parallel directional dipoles (double poles) appear. The synchronization of the electrical activity created by these oppositely charged dipoles allows the

electric field formed in the cell membrane to be monitored at a macroscopic level [22].

The most known method of measuring brain electrical activity is Electroencephalography (EEG), which is recorded from the scalp [22, 23]. Richard Caton (1842-1926) is considered the first scientist to investigate brain potentials. He studied cat and rabbit brains and measured electrical current activities with a galvanometer. Later, Napoleon Cybulski (1854-1919) graphically demonstrated the electroencephalogram by adding a photographic addition to the galvanometer, and was the first to observe epileptic EEG activity with electrical stimulation in a dog [24]. The first electroencephalogram recording from the human skull was made in 1929 by Hans Berger [25]. In 1935, electroencephalography emerged in today's clinical field and the modern era of EEG recording (Grass Model I) began. However, since the spatial resolution of EEG is low, more advanced techniques are used today. Some of these are electrocorticography (ECoG) which can be measured from the surface of the cortex, micro-EEG (or LFP) which can be measured from deep brain tissue, or techniques with a very high spatial resolution that can be directly measured intracellularly[26].

The formation of synchronized electrical activities in the CNS is made possible by various distant and/or near projections. For example, vertical pyramidal cells [27] arranged in the form of columns in the neocortex are synchronized by thalamocortical projections from the thalamus[28]. In addition, it is stated that astrocytic signaling has critical importance in maintaining synchronization and modulates sleep states and sleep/wake transitions [29]. These synchronized electrical signals, which can be observed macroscopically, can be measured by electroencephalography (EEG) from the skull surface or by electrocorticography (ECOG) method directly from the cortical surface inside the skull. An important point to know here is that the contribution of APs to these electrical signals is almost nonexistent and that these signals are composed of post-synaptic potential sums formed in a synchronized manner [30]. While the contribution of synchronized neurons in the measurement region to the electrical signals in question is directly related to the number of these neurons, the contribution of nonsynchronous neurons is proportional to the square root of their number [22].

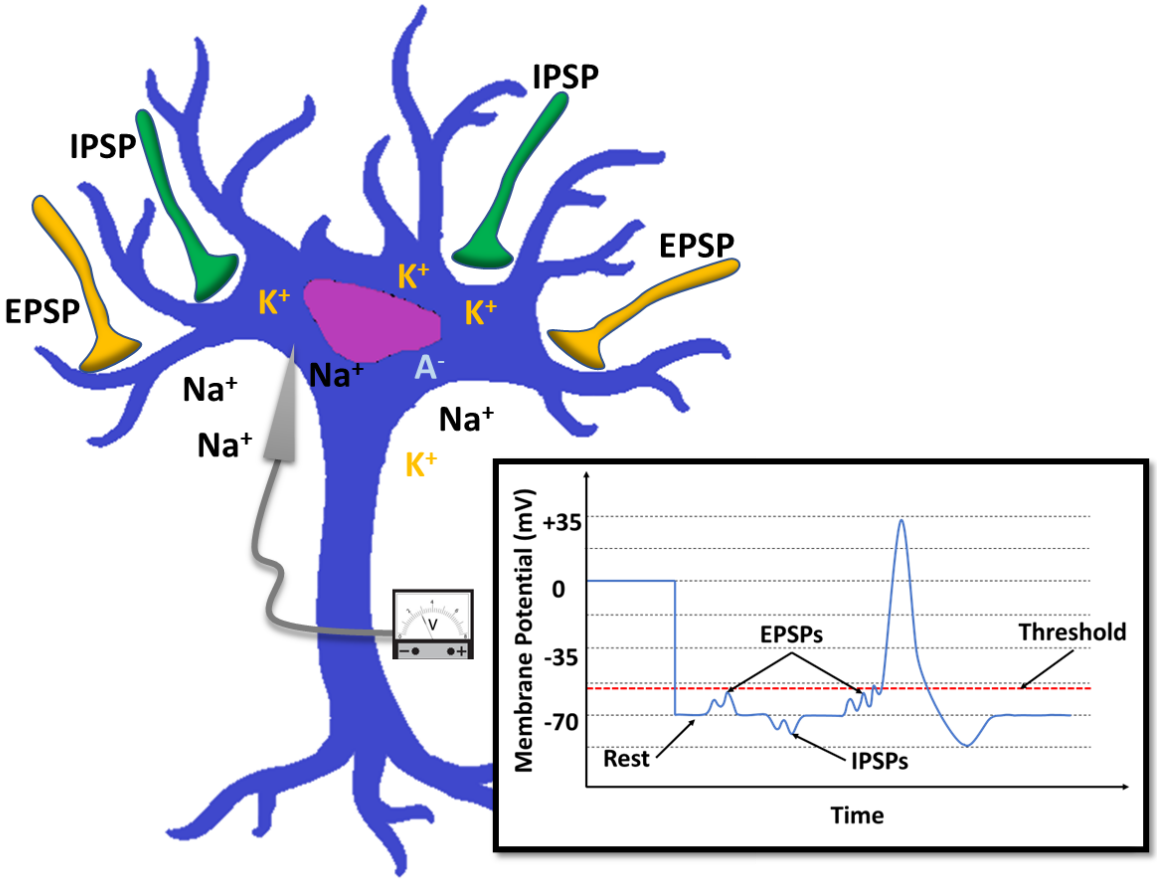

Figure 7. Electrical charge difference between inside and outside of the cell and PSP inputs

Accordingly, in the case of measuring with the electroencephalography method, it is assumed that there are approximately 10^8 neurons in the area where the electrode is placed. Accordingly, let's assume that the proportion of cells with synchronized activity is 10% of the total number of cells (i.e. 10^7 cells). In this case, from the expression $10^7/\sqrt{10^8} = 1000$, it can be said that the contribution of synchronized cells to the measured electrical signal is 1000 times more than nonsynchronous cells.

6. Discussion and Conclusion

In this study, the general structure of the nerve cell, its electrical activity, and how electrical activity occurs in neuron populations are focused on. The simulations results showed that although nerve cells have a very complex structure, AP has a stereotyped form in nerve cells and is formed according to the "all or nothing" principle. This principle is of critical importance and demonstrates that realistic neuronal models can also be applied to digital circuits An example of hardware designs made for this purpose is the I&F-based Memristive Integrate-and-Fire (MIF) model[31]. Furthermore, considering the computational cost, various reduced HH-based models such as FitzHugh–Nagumo, Hindmarsh–Rose, Morris–Lecar, I&F, or Izhikevich can be used for this purpose[32].

It has been observed that ion channel gate dynamics have a critical role on the form of AP. It has been observed that neurons conduct/transmit this electrical signal to each other through synaptic connections, and depending on the type of synaptic connection, this signal can create an effect that depolarizes (EPSP) or polarizes (IPSP) membrane voltage in the post-synaptic cell. Finally, how the electrical activities of large populations of neurons are measured at micro or macro scales, and the methods used for this purpose are discussed.

According to this study, neurons show that they process information with the AP signal, which is a stereotyped signal formed according to the "all or nothing" principle. Accordingly, it seems possible to develop integrated circuits in which neurons can be imitated. Thus, digital neuronal networks can be created with these electronic neurons. As a result, digital systems can be designed that mimic the cognitive functions of the brain.

Statement of Research and Publication Ethics

The study is complied with research and publication ethics.

References

[1] J. D. Enderle and J. D. Bronzino, *Introduction to biomedical engineering*. New York: Academic press, 2012.

[2] W. Gerstner and W. M. Kistler, *Spiking neuron models: Single neurons, populations, plasticity*. Cambridge: Cambridge Univ. Press, 2002.

[3] E. R. Kandel, J. H. Schwartz, T. M. Jessell, S. A. Siegelbaum, and A. J. Hudspeth, *Principles of neural science*, 4th Ed. New York: McGraw-hill, 2000.

[4] S. Zaqout and A. M. Kaindl, "Golgi-cox staining step by step," *Front Neuroanat*, vol. 10, no. 38, 2016.

[5] D. L. Schacter, D. T. Gilbert, and D. M. Wegner, *Psychology*. New York: Worth Publishers, 2011.

[6] M. Shafiei, S. Jafari, F. Parastesh, M. Ozer, T. Kapitaniak, and M. Perc, "Time delayed chemical synapses and synchronization in multilayer neuronal networks with ephaptic inter-layer coupling," *Communications in Nonlinear Science and Numerical Simulation*, vol. 84, p. 105175, 2020.

[7] H. C. Tuckwell, *Introduction to theoretical neurobiology: linear cable theory and dendritic structure*, vol. 1. Cambridge University Press, 1988.

[8] J. N. Sleigh, A. M. Rossor, A. D. Fellows, A. P. Tosolini, and G. Schiavo, "Axonal transport and neurological disease," *Nature Reviews Neurology*, vol. 15, no. 12, pp. 691–703, 2019.

[9] L. C. Zayia and P. Tadi, *Neuroanatomy, motor neuron*. In *StatPearls [Internet]*. Treasure Island, FL, USA: StatPearls Publishing, 2021.

[10] J. E. Hall, *Guyton and Hall textbook of medical physiology e-Book*. Amsterdam: Elsevier Health Sciences, 2015.

[11] F. Rattay and T. Tanzer, "A simple model considering spiking probability during extracellular axon stimulation," *PLoS One*, vol. 17, no. 4, p. e0264735, 2022.

[12] A. L. Hodgkin and A. F. Huxley, "A quantitative description of membrane current and its application to conduction and excitation in nerve," *Journal of physiology*, vol. 117, no. 4, p. 500, 1952.

[13] R. Brette et al., "Simulation of networks of spiking neurons: A review of tools and strategies," *Journal of Computational Neuroscience*, vol. 23, no. 3, pp. 349–398, Dec. 2007.
[14] A. Destexhe, M. Rudolph, J. M. Fellous, and T. J. Sejnowski, "Fluctuating synaptic conductances recreate in vivo-like activity in neocortical neurons," *Neuroscience*, vol. 107, no. 1, pp. 13–24, 2001.
[15] L. Muller, R. Brette, and B. Gutkin, "Spike-timing dependent plasticity and feed-forward input oscillations produce precise and invariant spike phase-locking," *Frontiers in Computational Neuroscience*, vol. 5:45, Nov. 2011.
[16] M. Bazhenov, I. Timofeev, M. Steriade, and T. J. Sejnowski, "Model of thalamocortical slow-wave sleep oscillations and transitions to activated States," *Journal of neuroscience*, vol. 22, no. 19, pp. 8691–8704, 2002.
[17] B. Hille, *Ion channels of excitable membranes*, 3rd ed. Sunderland, MA: Sinauer Associates Inc., 2001.
[18] E. M. Izhikevich, "Polychronization: computation with spikes," *Neural computation*, vol. 18, no. 2, pp. 245–282, 2006.
[19] E. M. Izhikevich, *Dynamical systems in neuroscience: geometry of excitability and bursting*. Cambridge: MIT press, 2007.
[20] S. Weidmann, "Effect of current flow on the membrane potential of cardiac muscle," *Journal of physiology*, vol. 115, no. 2, pp. 227–236, 1951.
[21] A. V. Andreev, V. A. Maksimenko, A. N. Pisarchik, and A. E. Hramov, "Synchronization of interacted spiking neuronal networks with inhibitory coupling," *Chaos Solitons Fractals*, vol. 146, p. 110812, 2021.
[22] P. L. Nunez and R. Srinivasan, *Electric fields of the brain: the neurophysics of EEG*, New York: Oxford Univ. Press, 2006.
[23] E. Niedermeyer and F. H. L. da Silva, *Electroencephalography: Basic Principles, Clinical Applications, and Related Fields*, 5th Ed. Baltimore: Williams Wilkins, 2005.
[24] M. A. B. Brazier, *A history of the electrical activity of the brain: The first half-century*, London: Pitman Medical Publishing, 1961.
[25] H. Berger, "On the electroencephalogram of man.," *Electroencephalogr. Clin. Neurophysiol.*, vol. 28, no. Suppl, pp. 37–74, 1969.
[26] G. Buzsáki and X.-J. Wang, "Mechanisms of Gamma Oscillations," *Annu. Rev. Neurosci*, vol. 35, no. 1, pp. 203–225, 2012, doi: 10.1146/annurev-neuro-062111-150444.
[27] V. B. Mountcastle, "The columnar organization of the neocortex," *Brain*, vol. 120, no. 4, pp. 701–722, 1997.
[28] F. H. L. da Silva, "The generation of electric and magnetic signals of the brain by local networks," in *Comprehensive human physiology*, Greger Rainer and Windhorst Uwe, Eds. Berlin, Heidelberg: Springer, 1996, pp. 509–531.
[29] J. F. Oliveira and A. Araque, "Astrocyte regulation of neural circuit activity and network states," *Glia*, 2022.
[30] C. Bédard, H. Kröger, and A. Destexhe, "Modeling extracellular field potentials and the frequency-filtering properties of extracellular space.," *Biophysical Journal*, vol. 86, no. 3, pp. 1829–1842, 2004.
[31] S. M. Kang et al., "How to build a memristive integrate-and-fire model for spiking neuronal signal generation," *EEE Trans. Circuits Syst. I, Reg. Papers*, vol. 68, no. 12, pp. 4837–4850, 2021.
[32] E. M. Izhikevich, "Which model to use for cortical spiking neurons?" *IEEE Trans. Neural. Netw.*, vol. 15, no. 5, pp. 1063–1070, 2004.

Bitlis Eren Üniversitesi Fen Bilimleri Dergisi
BİTLİS EREN UNIVERSITY JOURNAL OF SCIENCE
ISSN: 2147-3129/e-ISSN: 2147-3188
VOLUME: 11 NO: 3 PAGE: 931-942 YEAR: 2022
DOI: 10.17798/bitlisfen.1161170

Investigation of Antiviral Potential of Food Carotenoids and Apocarotenoids against RNA-dependent RNA Polymerase of Hepatitis C Virus

Özkan FİDAN[1*]

[1]*Depertmant of Bioengineering, Faculty of Life and Natural Sciences, Abdullah Gül University, Kayseri, Türkiye, 38080*
(ORCID: 0000-0001-5312-4742)

Keywords: Carotenoids, Apocarotenoids, Hepatitis C Virus, RNA-dependent RNA polymerase inhibitors, Virtual Screening

Abstract
Hepatitis C disease have been a global health threat and affects a significant portion of world population. Hepatitis C have also been a silent health threat for Turkiye, where there are around half million people infected with Hepatitis C Virus (HCV). Disease burden and mortality are expected to increase gradually in the next 20 years in Turkiye. Unavailability of enough data on the currently-available drugs in routine clinical practice, their side effects and interactions with other drugs, and their efficacies on the less common genotypes indicates the necessity of alternative treatment options. Natural products from herbal and medicinal plants can indeed provide an alternative as being drug-like dietary supplements. In particular, the carotenoids and apocarotenoids are underexplored in their antiviral potential, including anti-HCV activities. Therefore, we focused on the virtual screening of various carotenoids and apocarotenoids against the RNA-dependent RNA polymerase (RdRp) of HCV. Molecular docking experiments showed strong binding affinities of the ligands to both palm and thumb domains of RdRp of HCV. In fact, some of them such as neoxanthin, crocin, canthaxanthin and cryptoflavin bound quite strongly to both domains compared to native ligands and current antiviral drugs. MD simulation for neoxanthin-RdRp complex confirmed the stability of the ligand within the binding cavity of RdRp throughout 100 ns simulation. This clearly indicated the potential of carotenoids, specifically neoxanthin, as RdRp inhibitor in treating HCV. Thus, this study not only discovered anti-HCV drug candidates with the properties of easy-to-access and low cost, but also paved the way for the development of carotenoid or apocarotenoid based dietary supplement candidates for the prevention and treatment of HCV.

1. Introduction

Hepatitis C is a blood borne disease and affects around 3% of the world population. The cause of hepatitis C, Hepatitis C virus (HCV), has been a global threat for the public health. According to World Health Organization (WHO), around 3-4 million new cases of HCV infection has been annually reported, indicating an ongoing global public health issue [1], [2]. Additionally, HCV is one of the main causes of advanced liver diseases such as hepatocellular carcinoma, cirrhosis, and liver failure [2], [3]. The transmission of HCV is mostly due to direct percutaneous exposure to blood and becomes different based on the classifications of the countries. The infection rates in low and high endemic countries differ at around 20%. In developed regions of the world, the intravenous drug abuse is the most common way of transmission for HCV, while invasive procedures or unsterile medical procedures and instruments are the most widely-seen reasons for the transmission of HCV in poor regions [1], [4], [5].

*Corresponding author: ozkan.fidan@agu.edu.tr
Received: 12.08.2022, Accepted: 23.09.2022

In addition, people who inject drugs, men who have sex with men, and prisoners were reported as high-risk populations [6]. Furthermore, there currently exist seven genotypes and numerous subtypes of the virus, which complicates targeting of treatment [7]. Globally, HCV genotypes 1 is the most common hepatitis C infection occupying of 44% of all cases, while genotypes 3 and 4 causes 25% and 15% of all hepatitis C cases, respectively [6].

Based on the data and information provided in the Turkiye Viral Hepatitis Prevention and Control Programme (2018-2023), in Turkiye, approximately 250,000-550,000 in the population over the age of 18 are infected with HCV and the vast majority of them is not aware that they are infected with HCV [8], [9]. In another study conducted in 2014, the number of HCV infected people in Turkiye was estimated to be around 514,000. However, according to the same study; 81,300 (16%) people was HCV-infected, the annual number of newly diagnosed patients was 5,500 (1.1%), and the annual number of patients receiving treatment was estimated to be 4,200 (0.8%). Based on the data from the Ministry of Health in Turkiye, anti-HCV positivity was 3.8% in hemodialysis patients, 1.7% in peritoneal dialysis patients, 1.96% in kidney transplant patients, and 7.6% in liver transplant patients. HCV was also reported to be the second most common cause of liver transplantation in Turkiye. It was also pointed out that if HCV is not treated and does not become under control, the disease burden and mortality are expected to increase gradually in the next 20 years [9]–[11].

The treatment of hepatitis C has been historically prolonged and leads to multiple several severe side effects [12]. In 1990s, pegylated interferon and ribavirin (PEG/RBV) combination therapy was the only treatment option. However, this antiviral agent did not have high efficacy in the eradication of HCV and led to common side effects [13]. Genotype 1 was particularly more resistant to interferon and this led to the lower success rate of the combination therapy for genotype 1 compared to other genotypes [14]. In 2011, first direct acting antiviral agents (DAA), boceprevir and telaprevir, were approved to treat the genotype 1 together with the combination therapy. DDA led to an increase in the rates of sustained viral response, yet greater toxicity, high cost, and less safety in patients with advanced diseases were observed for these drugs [15]. Since 2011, various antiviral drugs such as DNA and RNA polymerase inhibitors, RNA protease inhibitors, and RNA serine protease inhibitors have been approved for hepatitis C. These recent drugs had shorter therapies, less toxicity and did exclude the PEG/RBV therapy from the treatment process of hepatitis C patients [14], [15]. Nevertheless, the majority of the current scientific evidence for these drugs depends on expert opinion, case-control series, cohort studies. It was also reported that some of phase 2 and 3 clinical trials for these antiviral agents were conducted with a reduced number of patients and select groups. Unavailability of adequate amount of data on the use of these drugs in routine clinical practice, their side effects and interactions with other drugs, and their efficacies on the less common genotypes set forth the necessity of alternative treatment options/drugs [15]. The new candidates should be easy-to-access, effective for all genotypes, and low cost. Particularly, natural products from medicinal and herbal plants might provide an alternative option for HCV as being drug-like dietary supplements.

Carotenoids and their cleaved derivatives, apocarotenoids, are widely seen in nature with more 1200 identified members [16], [17]. They were isolated mainly from plant and algal species, yet some non-phototrophic fungi, bacteria and archaea also produce carotenoids and apocarotenoids [18], [19]. These colorful natural products help to protect photosynthetic organisms from the photo-oxidative damages. On the other hand, in non-photosynthetic organisms, they protect the cells from oxidative damages with their strong antioxidant properties [20]. Furthermore, carotenoids and apocarotenoids have various applications such as food colorants, food supplements and nutraceuticals for cosmetics industry, and pharmaceuticals. Particularly, their health-promoting properties render them as alternative option for the treatment and prevention of various diseases such as cardiovascular diseases, COVID-19, cervical and prostate cancers [21]–[23].
Even though the health benefits and biological activities of carotenoids and apocarotenoids have been explicitly reported in literature, their antiviral potential was underexplored. Particularly, their antiviral potential against HCV, for which there is a need for low cost, and easy-to-access drug and/or dietary supplement candidates, was not extensively studied. In literature, there are two studies in which bacterioruberin and pigment extract including carotenoids were tested for their antiviral potentials [24], [25]. The study with bacterioruberin was aimed to conduct *in vitro* antiviral tests for this carotenoid against RNA-dependent RNA polymerase (RdRp) of HCV and revealed that bacterioruberin is indeed a promising RdRp inhibitor [24]. Additionally, in literature, some of carotenoids including astaxanthin, lycopene and β-carotene were reported to have preventive and supportive of treatment in viral diseases, yet no direct antiviral potentials of these

natural compounds were studied [26]–[29]. Therefore, in this study, we evaluated the antiviral potentials of some of the food carotenoids and apocarotenoids against RdRp of HCV using molecular docking and molecular dynamics (MD) simulation. Our findings indicated that these food natural products often had low binding energy scores. In particular, neoxanthin had the strongest affinity to RdRp of HCV, showing the potential inhibitory effect against the receptor. The molecular docking results was further confirmed by MD simulation, during which neoxanthin was stable in the RdRp of HCV. Our results not only uncovered the potential of food carotenoids and apocarotenoids as antiviral agents, but also provide an initial data for the development of dietary supplementary candidates for the treatment and prevention of hepatitis C disease.

2. Material and Method

2.1. Ligand library and preparation

The ligand library was designed to be consist of carotenoids and apocarotenoids. In addition, the original substrates for the receptor protein structures as well as known antiviral agents were added to the library. Upon the creation of the ligand library, their 3D structures were downloaded from PubChem database in sdf format. For the compounds without 3D structures, their 2D structure files were downloaded and converted to 3D structures using Open Babel GUI software. Subsequently, the conversion of all the sdf files with 3D structures to pdb files were also conducted in Open Babel GUI software. In the last step of ligand preparation, AutoDock Tools software was used, in which aromatic carbon and rotatable bonds were detected, torsion number was automatically set, non-polar hydrogens and Gasteiger charges were added to all ligands. They all were saved as pdbqt files [30].

2.2. Receptor Preparation

The receptor protein was the Hepatitis C virus RNA-dependent RNA polymerase NS5B. Two different crystal structure files (PDB IDs: 2GIR and 2GIQ) were available for this protein with non-nucleoside polymerase inhibitors (NNI-2 and NNI-3). NNI-2 binds to the palm binding domain, while NNI-3 binds to the thumb 1 site of RdRp of HCV [31]. In this study, it was aimed to investigate the potential non-nucleoside inhibitors with strong binding affinities towards both domains. Both receptors were prepared using AutoDock Tools software, with which water molecules were deleted from the PDB files of the receptor proteins, and polar hydrogen atoms and Kollmans charges were added to them. Then, both were saved as pdbqt files to proceed molecular docking experiments [30].

2.3. Molecular docking experiments

In order for conducting a virtual screening for the molecules in the ligand library against RdRp of HCV, the grid boxes were determined for both target domains of RdRp of HCV. This was done using the positions of the NNI ligands interacting with the specific target domains in the receptor. The grid box coordinates for 2GIR was at x = −33.10, y = -12.39, and z = 34.80 with sizes of 33.54, 38.52, and 28.90 Å. For 2GIQ, it was at x = 14.14, y = -8.40, and z = -13.10 with sizes of 47.24, 41.07, and 34.82 Å. After determining the grid boxes, the prepared flexible ligands were docked against the fixed rigid receptor protein using AutoDock Vina in the Windows command line window upon the preparation of config files with necessary information (receptor, grid box coordinates, number of modes: 10, energy range: 8 and exhaustiveness: 16) [32]. Pymol was used for the visualization purposes.

2.4. Molecular dynamics simulation

Molecular docking experiments resulted in the indication of strong binding affinity of neoxanthin towards both target sites of RdRp of HCV. Although similar strong binding affinities were shortlisted for some other ligands, neoxanthin with the lowest binding energy score was selected for further validation of its stable binding to the receptor protein using MD simulation. The NPT ensemble MD simulation was performed using the 2GIQ-neoxanthin complex with the parameters at 300 K temperature for a duration of 100 ns. Since the drugs perform their actions in human body under constant temperature and pressure conditions. Therefore, NPT ensemble condition was enabled during the simulation process and kept the temperature and pressure constant while allowing the system volume to change during the simulation. Desmond module of Schrödinger was used to perform MD simulation under energy-minimized complex system and isosmotic environment was created to neutralize the existing charges by the addition of 0.15 M NaCl [30], [33].

3. Results and Discussion

3.1. Design of the ligand library

The ligand library was designed to include carotenoids and apocarotenoids, mostly found in the herbal and medicinal plants. The list of the all ligand molecules used in this study was tabulated in Table 1. Various food-derived carotenoids as well as some of the glycosylated derivatives were included in the library. For instance, β-carotene is very common in many foods such as dark orange and green fruits, and vegetables, such as mango, apricot, cantaloupe, carrots, red peppers, pumpkin, sweet potatoes, broccoli, and leafy greens. β-cryptoxanthin are commonly found in tropical fruits, such as mango, papaya and tangerine. Leafy greens, corn, and green vegetables such as broccoli, brussel sprouts, green beans, peas, and zucchini are the major sources for lutein. Tomato has lycopene as the dominant carotenoid, which can also be found in other fruits such as watermelon, pink grapefruit, and Japanese persimmons. Zeaxanthin is available in egg yolks, corn, corn meal, and leafy greens. Neoxanthin is found as a major carotenoid in all green leaves and other photosynthetic tissues and in many algae, and in some flowers [34]–[38]. On the other hand, glycosylated carotenoids such as zeaxanthin diglucoside, bacterioruberin diglucoside, and astaxanthin diglucoside are found in algae and bacteria including thermophilic, endophytic and psychrotrophic bacteria [17], [39]–[41]. The glycosylated derivatives were added to the ligand library to evaluate the effect of glycosyl group on the antiviral potential of carotenoids. The library also has some commonly known apocarotenoids from herbal plants such as saffron [42]–[44]. The carotenoid database, including the apocarotenoids, was also used in designing the ligand library as a helpful database [16]. We also added the native NNI molecules from the crystal structures of the RdRp of HCV and these pre-confirmed compounds allowed to compare our results with the known RdRp inhibitors [31]. Finally, some of the currently-used antiviral drug molecules such as favipiravir, remdesivir, sofusbavir, paxlovid and molnupiravir were also added for the comparison of the results with the current-used antiviral agents.

3.2. Molecular docking

To validate the molecular docking protocol, we firstly conducted molecular docking with the native ligands found in the crystal structure of RdRp of HCV. NNI-2 and NNI-3 were reported to bind palm and thumb

Table 1. List of compounds in the ligand library and their binding energy scores against Thumb 1 and Palm domains of RdRp of HCV. Binding energies are in kcal/mol.

Compounds	Thumb Domain	Palm Domain		Compounds	Thumb Domain	Palm Domain
Alpha-carotene	-9.0	-8.9		Zeaxanthin Diglucoside	-8.8	-9.3
Cucurbitaxanthin A	-8.7	-9.4		Astaxanthin Diglucoside	-9.1	-9.7
Cucurbitaxanthin B	-8.7	-9.0		Bacteroruberin Diglucoside	-8.7	-9.0
Beta-carotene	-9.3	-9.1		Bixin	-6.9	-7.2
Phytoene	-6.2	-7.6		Safranal	-5.5	-5.6
Luteoxathin	-9.2	-9.9		Picocrocin	-6.9	-8.0
Cryptoflavin	-9.8	10.3		Crocetin aldehyde	-6.9	-6.7
Canthaxanthin	-9.3	-9.2		Crocetin	-7.3	-7.3
Capsanthin	-8.9	-9.3		Crocin	-8.2	-9.7
Capsarubin	-8.3	-9.5		3-hydroxycyclocitral	-5.6	-5.5
Lycopene	-8.5	-8.1		Crocusatin H	-6.3	-6.4
Violaxanthin	-8.6	-9.1		Apo-12'-capsorbibal	-7.2	-8.1
Beta-cryptoxanthin	-8.9	-9.2		Apo-12'-zeaxanthinal	-7.8	-7.7
Fucoxanthin	-9.1	-9.4		Apo-12'-violaxanthal	-8.0	-8.0
Lutein	-9.1	-9.5		Native ligand (NN2)	-8.9	-8.9
Neoxanthin	-9.0	-10.4		Native ligand (NN3)	-8.2	-8.3
Phytofluene	-7.5	-6.9		Favipiravir	-5.2	-5.9
Latoxanthin	-9.0	-9.4		Molnupiravir	-6.9	-8.0
Zeaxanthin	-9.2	-9.2		Paxlovid	-7.9	-8.2
Astaxanthin	-9.2	-9.7		Remdesivir	-7.6	-8.2
Bacterioruberin	-9.1	-7.7		Sofusbavir	-7.9	-8.5

domains of RdRp of HCV, respectively [31]. The binding energy score of NNI-2 to the palm domain is -8.9 kcal/mole, while the one of NNI-3 to thumb domain is -8.3 kcal/mole. This indicated their strong binding affinities towards the corresponding domains of RdRp of HCV and validated the molecular docking protocols. Then, all the carotenoids and apocarotenoids, as well as some of the approved antiviral drugs were docked against both domains of RdRp. The binding energy scores of each ligand were tabulated in Table 1. Our docking experiments revealed that in general carotenoids and long-chain apocarotenoids bound strongly to both palm and thumb domains of the receptor protein. In specific, various carotenoids such as cryptoflavin, neoxanthin, astaxanthin, capsarubin, luteoxanthin had very low binding energies towards palm domain, whereas canthaxanthin, cryptoflavin, β-carotene, neoxanthin had strong affinities to the thumb domain of RdRp of HCV. Another important finding is that the glycosylated carotenoids did not change the binding affinities, except bacterioruberin diglucoside had an improved the binding affinity from -7.7 to -9.7 kcal/mole towards only palm domain. For the other glycosylated carotenoids, there is no significant change in the binding energy scores.

In addition, a glycosylated apocarotenoids, crocin, had lower binding energies to both domains of receptor protein compared to its non-glycosylated derivative, crocetin. This indicated that glycosylated carotenoids and apocarotenoids might provide better biological activities. Similar phenomena were recently reported for glycosylated flavonoids against the main protease of SARS-CoV-2 in an *in silico* study [45]. The glycosylated natural products were known to have a better solubility and pharmacological properties [46]. On the other hand, for the smaller apocarotenoids such as safranal, crocusatin H and 3-hydroxycyclocitral, the binding affinities to both domains were weak. Similar results were obtained for favipiravir as a quite small antiviral agent. The other currently-used antiviral agents has low binding energy scores for both domains of RdRp of HCV with an average score of around -8 kcal/mole (Table 1). Obviously, many carotenoids had indeed stronger binding affinities towards both palm and thumb domains as compared to these approved antiviral drugs, indicating the high antiviral potential of carotenoids and apocarotenoids.

3.3. Molecular dynamics simulation

Since the binding energy score of neoxanthin was the lowest among all (Table 1), the MD simulation was performed for the ligand-receptor complex with neoxanthin in order to confirm its stability within palm domain of RdRp of HCV. MD simulation was executed for 100 ns using the Schrodinger Desmond program. The Root Mean Square Deviation (RMSD) was measured to observe the average change in the backbone of receptor protein as well as structural shifts. As shown in Figure 1, RMSD profile for the receptor protein revealed that the protein was stable throughout the simulation with around 1.5-1.75 Å RMSD value, which was perfectly acceptable. Similarly, RMSD value for neoxanthin ligand was also within the acceptable range (2.4-3.2 Å), although there was a fluctuation for around 50 ns. However, it was stabilized at around 3.2 Å at the end of MD simulation. Despite this short fluctuation, ligand was adjusted to be stable within the binding pocket of the palm domain. RMSD trajectories indicated stable behaviors for both ligand and receptor molecules

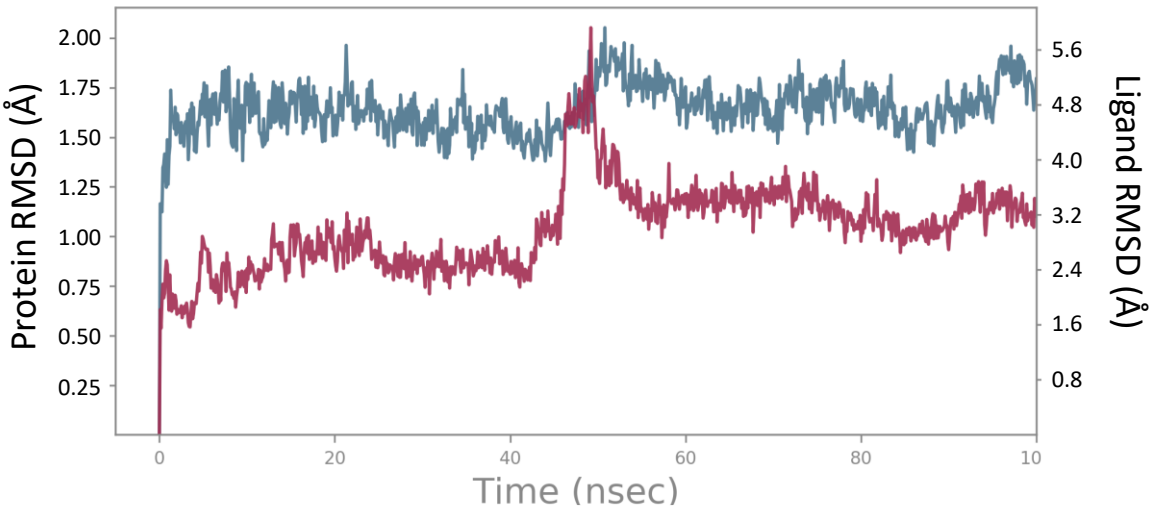

Figure 1. RMSD profiles of the backbone of RNA-dependent RNA polymerase of Hepatitis C virus (blue) and neoxanthin (pink) throughout 100 ns MD simulation.

within the complex with very little fluctuations (Figure 1).

Root Mean Square Fluctuation (RMSF) profile was also measured to characterize local changes in the protein chain and ligand atom positions. Figure 2 showed RMSF profiles for both protein and ligand. RMSF value observed for the majority of the residues of receptor protein was stable within the range of 0.6-2 Å. But there are some residues, particularly terminal residues were fluctuated up to around 3 Å (Figure 2A). We evaluated the RMSF values for the residues located in the binding pocket and found that they were not among the fluctuated residues. This confirmed the acceptable fluctuations within the receptor protein active site. RMSF value of neoxanthin showed that the majority of its atoms was stable within the range of 1-2 Å, except atoms numbered as 7, 8, 9, 41 and 44 had small fluctuations. All of these atoms are located in the ring with epoxy functional group (Figure 2B).

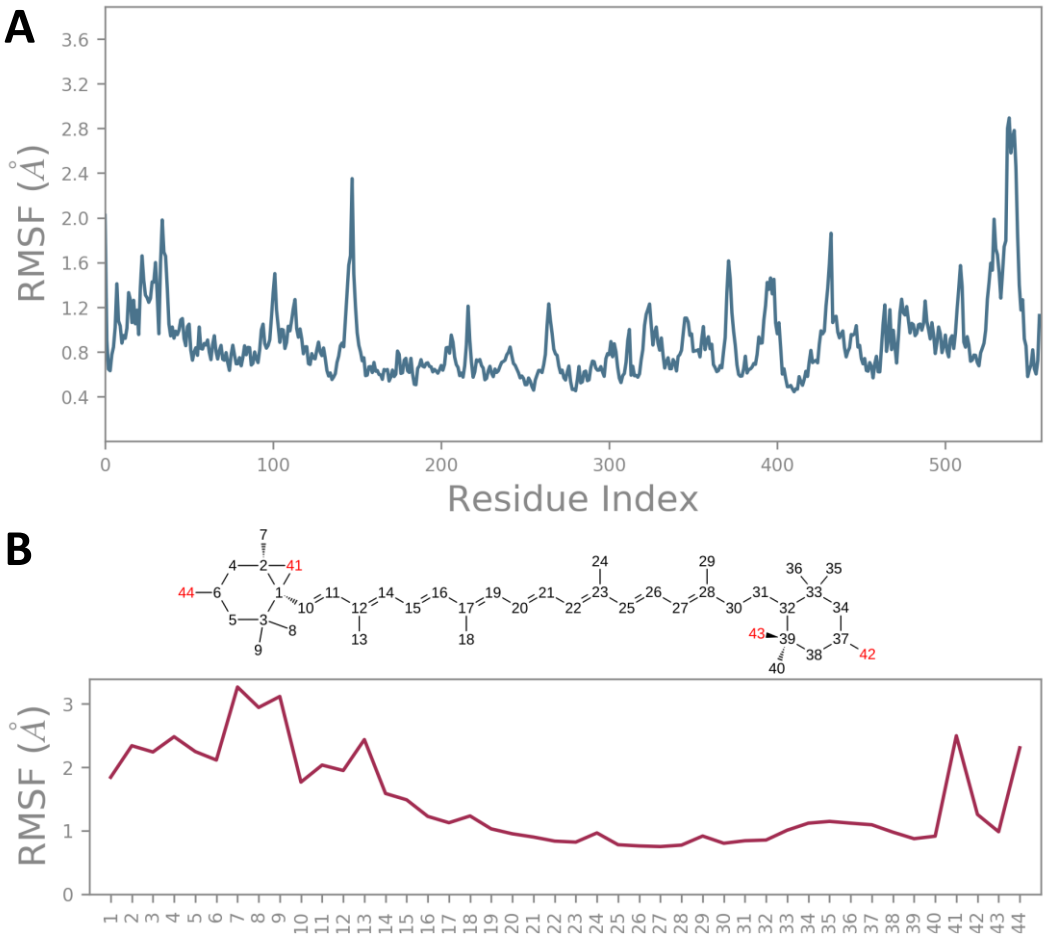

Figure 2. RMSF profiles of RNA-dependent RNA polymerase of Hepatitis C virus (A) and neoxanthin throughout 100 ns MD simulation and its structure (B).

Protein secondary structure elements (SSE) analysis revealed that receptor protein had α-helices (37.844%) and β-sheets (9.33%)) with a total SSE of 46.77%, which were conserved during MD simulation. The stability of the receptor-ligand complex during MD simulation was due to the various interactions such as hydrogen bonds, hydrophobic and ionic interactions, and water bridges. These interactions demonstrated in Figure 3. Neoxanthin had hydrophobic interactions with the following amino acid residues of RdRp of HCV: ALA15, ALA16, PHE193, TYR195, CYS366, TRP397, PRO404, VAL405, MET414, TYR415, ILE447 and TYR448, while the hydroxyl group of neoxanthin created water bridges with some of the residues of receptor protein (Figure 3). The intensities of all the interactions were measured throughout the simulation period and demonstrated as interaction fractions in Figure 4. Some of these interacting residues such as MET414, ILE447, TYR448, ASN316 and PHE193 were listed among the key residues interacting with native NNI-2 molecule. Particularly, the mutant RdRp of HCV with MET414LEU replacement was reported to lead to increased resistance to NNI molecules [31].

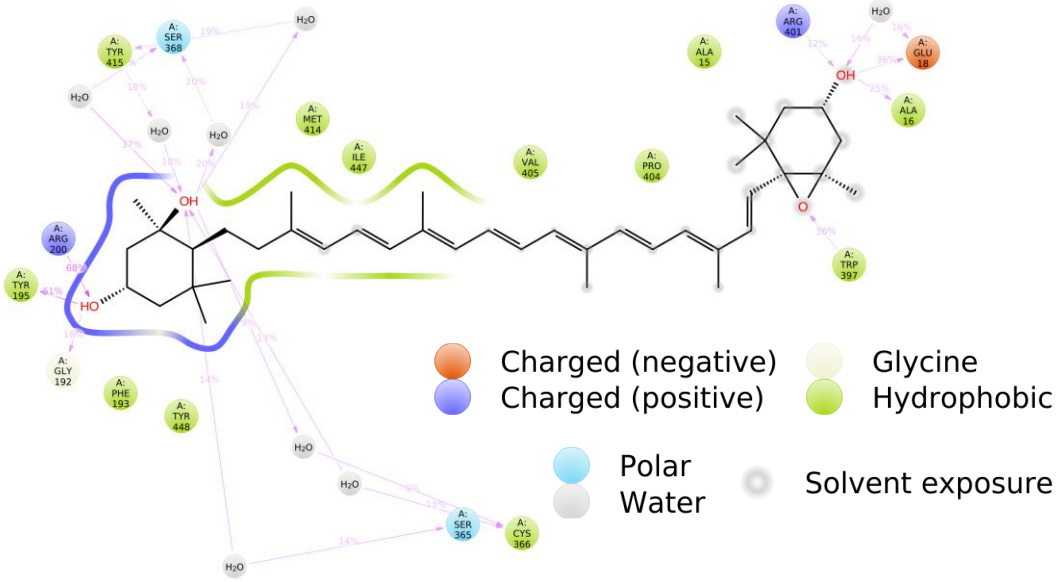

Figure 3. The protein–ligand contacts observed after MD simulation for RNA-dependent RNA polymerase of Hepatitis C virus complexed with neoxanthin.

3.4. Antiviral potential of hit molecules

A wide variety of health benefits and biological activities have been reported for carotenoids and apocarotenoids, yet their antiviral activities have not been extensively investigated. In addition, in literature, some of carotenoids and apocarotenoids such astaxanthin, lycopene, β-carotene and crocin were reported and suggested to have preventive and supportive of treatment in viral diseases [27], [28], [47]–[50]. Nevertheless, it is due to the antioxidant and anti-inflammatory properties of these molecules. In other words, their antiviral properties were not directly examined. In specific, their antiviral potential against HCV, for which there is a need for low cost, and easy-to-access drug and/or dietary supplement candidates, was not extensively studied. Thus, they attracted the attentions of researcher as a new research area exploring their antiviral capacity. In particular, COVID-19 pandemic speeded up this new research field to discover and develop new antiviral agents and/or dietary supplements for the treatment and prophylaxis of COVID-19. For example, in a recent paper, fucoxanthin and siphonaxanthin were tested against SARS-CoV-2 using *in silico* as well as *in vitro* techniques. Siphonaxanthin from *Codium fragile* exhibited a strong antiviral activity (IC50: 87.4 μM) against SARS-CoV-2. With its low acute toxicity and promising pharmacokinetic properties, siphonaxatnhin were suggested to be used in the treatment and prevention of COVID-19 through the inhibition of ACE2 binding site of spike protein of SARS-CoV-2 [51]. In another study, carotenoid-including microalgae extracts showed antiviral activity against Herpes Simplex Virus Type 1. Ethanol extract of *Haematococcus pluvialis* showed the inhibition of virus infection by around 85% [25]. Furthermore, the antiviral potential of bacterioruberin was investigated in an *in vitro* study against RdRp of HCV. This study revealed that bacterioruberin is a promising RdRp inhibitor for the treatment of Hepatitis C disease [24]. We observed the same results in this study for bacterioruberin, which showed quite strong binding affinities to both domains of RdRp, indicating its potential as RdRp inhibitor in the treatment of Hepatitis C disease.

Neoxanthin as one of the hit molecules is known to have photoprotective role as an antioxidant compound [52], [53]. However, to our knowledge, there is no study, even *in silico* studies, showing its antiviral potential. Another important hit molecule in this study is cryptoflavin. In a study, it was listed among the carotenoids of marine-origin extracts, which showed antibacterial activities against isolated from human specimens such as *Escherichia coli*, *Klebsiella pneumonia*, and *Staphylococcus aureus* [54]. However, no antiviral potential of this carotenoid was reported in literature. Furthermore, astaxanthin and canthaxanthin also had low binding energies and were reported to be used as an anti-aging agent and supplement in the treatment of Alzheimer's and Parkinson's disease, high cholesterol, strokes and cancer, respectively [55]. They were also tested

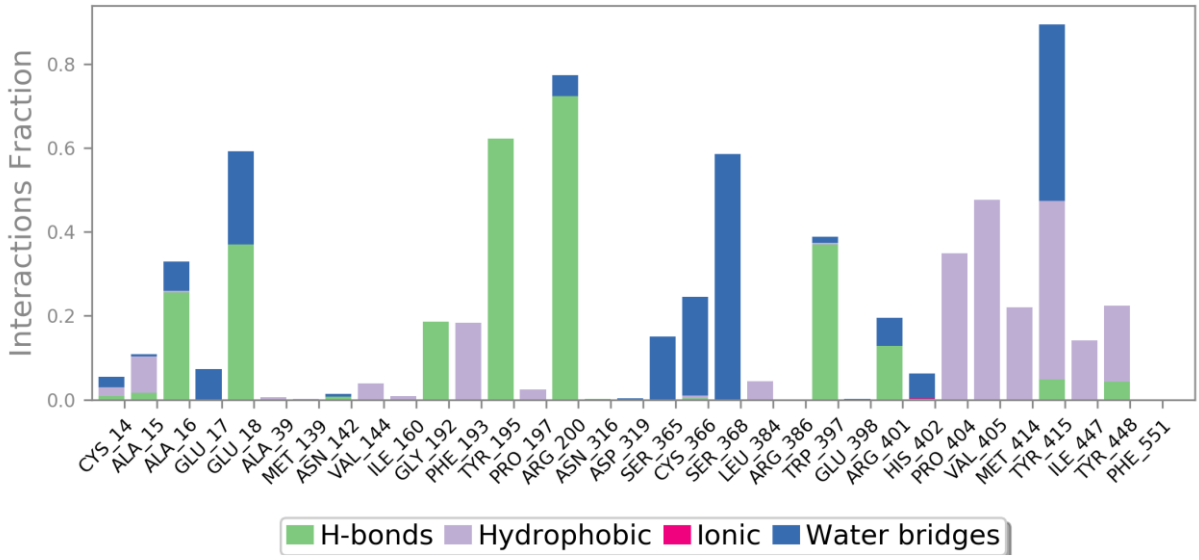

Figure 4. Interaction fractions for the protein–ligand complex observed during MD simulation for RNA-dependent RNA polymerase of Hepatitis C virus complexed with neoxanthin.

papain-like protease of SARS-CoV-2 and had the lowest binding energies (canthaxanthin, –9.4 kcal/mole and astaxanthin, –9.3 kcal/mole) [56]. In our study, such low binding energy scores were also found for these two important carotenoids as non-nucleoside RdRp inhibitors. The most promising apocarotenoids in this study was crocin, which is the primary pigment for the color of saffron herb. It was suggested to be considered as prophylactic agent during COVID-19 pandemic and some *in silico* studies exhibited its antiviral potential against SARS-CoV-2 [23], [50], [57]. For instance, crocin had strong binding affinities towards various drug targets of SARS-CoV-2, showing its multiple mechanisms of action, which is important for its effectiveness in the treatment of various mutants of SARS-CoV-2 [23]. This study pointed out the antiviral potential of crocin against HCV.

Considering the health benefits and various biological activities of carotenoids and apocarotenoids, as well as their potential for being dietary supplements, most of the molecules in this study, particularly the ones with low binding energies, can be used in the treatment and prevention of various viral diseases, including Hepatitis C, as antiviral agents and/or dietary supplements. In fact, further *in vitro* and *in vivo* studies are required to confirm the initial findings presented in this study.

4. Conclusion

Molecular docking screening of selected carotenoids and apocarotenoids revealed that the majority of them had relatively strong binding affinities to both palm and thumb domains of RdRp of HCV. In fact, some of them such as neoxanthin, crocin, canthaxanthin and cryptoflavin bound quite strongly to both domains. MD simulation for neoxanthin-RdRp complex confirmed that it was stable within the binding cavity of RdRp throughout 100 ns simulation process, indicating the inhibitory effect of neoxanthin on the drug target protein of HCV. Additionally, since carotenoids and apocarotenoids have been originally found in various plants and fruits, they can be considered as potential dietary supplement candidates. Thus, this study not only discovered antiviral drug candidates in treating Hepatitis C disease, but also opened the door for the development of carotenoid or apocarotenoid based dietary supplement candidates for the prevention and treatment of HCV. The availability of current literature with *in vitro* studies on bacterioruberin as anti-HCV candidate supported our findings that the compounds in this study with low binding energies can indeed become RdRp inhibitors for HCV. However, further studies are still essential to confirm the findings of our *in silico* study for the translation of this idea into clinic.

Acknowledgement

This study was partially supported by the Scientific and Technological Research Council of Turkiye with the project number 221Z280.

Statement of Research and Publication Ethics

This study complies with research and publication ethics.

References

[1] V. A. Morozov and S. Lagaye, "Hepatitis C virus: Morphogenesis, infection and therapy," *World J Hepatol*, vol. 10, pp. 186–212, 2018. https://doi.org/10.4254/WJH.V10.I2.186

[2] E. Tang and L. Angeles, "Hepatitis C virus. A review.," *West J Med*, vol. 155, pp. 164–168, 1991.

[3] M. P. Manns, M. Buti, J-M. Pwalotsky, H. Razavi, N. Terrault, and Z. Younossi, "Hepatitis C virus infection," *Nat Rev Dis Prim*, vol. 3, pp. 1–19, 2017. https://doi.org/10.1038/nrdp.2017.6

[4] A. J. Millman, N. P. Nelson, and C. Vellozzi, "Hepatitis C: Review of the Epidemiology, Clinical Care, and Continued Challenges in the Direct Acting Antiviral Era," *Curr Epidemiol reports*, vol. 4, pp. 174–185, 2017. https://doi.org/10.1007/S40471-017-0108-X

[5] A. M. Hauri, G. L. Armstrong, and Y. J. F. Hutin, "The global burden of disease attributable to contaminated injections given in health care settings," *Int J STD AIDS*, vol. 15, pp. 7–16, 2004. https://doi.org/10.1258/095646204322637182

[6] C. W. Spearman, G. M. Dusheiko, M. Hellard, and M. Sonderup, "Hepatitis C," *Lancet*, vol. 394, pp. 1451–1466, 2019. https://doi.org/10.1016/S0140-6736(19)32320-7

[7] A. A. Rabaan, S. H. Al-Ahmed, A. M. Bazzi, W. A. Alfouzan, S. A, Alsuliman, F. A. Aldrazi, and S. Haque, "Overview of hepatitis C infection, molecular biology, and new treatment," *J Infect Public Health*, vol. 13, pp. 773–783, 2020. https://doi.org/10.1016/J.JIPH.2019.11.015

[8] N. Tozun, O. Ozdogan, Y. Cakaloglu, R. Idilman, Z. Karasu, U. Akarca, S. Kaymakoglu, and O. Ergonul, "Seroprevalence of hepatitis B and C virus infections and risk factors in Turkey: a fieldwork TURHEP study," *Clin Microbiol Infect*, vol. 21, pp. 1020–1026, 2015. https://doi.org/10.1016/J.CMI.2015.06.028

[9] "Türkiye Viral Hepatit Önleme ve Kontrol Programi", Accessed: Aug. 01, 2022. [Online]. Available: https://hsgm.saglik.gov.tr/tr/bulasicihastaliklar-haberler/turkiye-viral-hepatit-onleme-ve-kontrol-programi.html

[10] H. Razavi *et al.*, "The present and future disease burden of hepatitis C virus (HCV) infection with today's treatment paradigm," *J Viral Hepat*, vol. 21, pp. 34–59, 2014. https://doi.org/10.1111/JVH.12248

[11] E. Gower, C. Estes, S. Blach, K. Razavi-Shearer, and H. Razavi, "Global epidemiology and genotype distribution of the hepatitis C virus infection," *J Hepatol*, vol. 61, pp. S45–S57, 2014. https://doi.org/10.1016/J.JHEP.2014.07.027

[12] B. Henry, "Drug pricing and challenges to hepatitis c treatment access," *J Heal Biomed law*, vol. 14, pp. 265–283, 2018.

[13] J. H. Hoofnagle and L. B. Seeff, "Peginterferon and Ribavirin for Chronic Hepatitis C," *N Engl J Med*, vol. 355, pp. 2444–2451, 2006. https://doi.org/10.1056/NEJMCT061675

[14] M. Zając, I. Muszalska, A. Sobczak, A. Dadej, S. Tomczak, and A. Jelińska, "Hepatitis C – New drugs and treatment prospects," *Eur J Med Chem*, vol. 165, pp. 225–249, 2019. https://doi.org/10.1016/J.EJMECH.2019.01.025

[15] R. González-Grande, M. Jiménez-Pérez, C. G. Arjona, and J. M. Torres, "New approaches in the treatment of hepatitis C," *World J Gastroenterol*, vol. 22, pp. 1421–1432, 2016. https://doi.org/10.3748/WJG.V22.I4.1421

[16] J. Yabuzaki, "Carotenoids Database: structures, chemical fingerprints and distribution among organisms," *Database*, vol. 2017, pp. 1–11, 2017 https://doi.org/10.1093/DATABASE/BAX004

[17] O. Fidan and J. Zhan, "Discovery and engineering of an endophytic *Pseudomonas* strain from *Taxus chinensis* for efficient production of zeaxanthin diglucoside," *J Biol Eng*, vol. 13, pp. 1–18, 2019. https://doi.org/10.1186/S13036-019-0196-X

[18] J. Dzib-Cauich, R. Us-Camas, and R. Rivera-Madrid, "Natural Sources of Apocarotenoids and Their Applications," in *Biol Chem Appl Apocarotenoids*, S. Ramamoorthy, R. R. Madrid, C, G. P. Doss, Eds. Boca Raton: CRC Press, pp. 11–39, 2020. https://doi.org/10.1201/9780429344206-2

[19] C. Zhang, "Biosynthesis of Carotenoids and Apocarotenoids by Microorganisms and Their Industrial Potential," in *Prog Carotenoid Res*, L. Q. Zepka, E. Jacob-Lopes and V. V. De Rosso, Eds. London: IntechOpen, pp. 85–105, 2018. https://doi.org/10.5772/INTECHOPEN.79061

[20] R. W. Tuveson, R. A. Larson, and J. Kagan, "Role of cloned carotenoid genes expressed in Escherichia coli in protecting against inactivation by near-UV light and specific phototoxic molecules," *J Bacteriol*,

vol. 170, pp. 4675–4680, 1988. https://doi.org/10.1128/jb.170.10.4675-4680.1988

[21] A. J. Simkin, "Carotenoids and Apocarotenoids in Planta: Their Role in Plant Development, Contribution to the Flavour and Aroma of Fruits and Flowers, and Their Nutraceutical Benefits," *Plants (Basel)*, vol. 10, pp. 2321, 2021. https://doi.org/10.3390/PLANTS10112321

[22] Y. Sharoni *et al.*, "Carotenoids and apocarotenoids in cellular signaling related to cancer: A review," *Mol Nutr Food Res*, vol. 56, pp. 259–269, 2012. https://doi.org/10.1002/MNFR.201100311

[23] S. Mujwar, L. Sun, and O. Fidan, "*In silico* evaluation of food-derived carotenoids against SARS-CoV-2 drug targets: Crocin is a promising dietary supplement candidate for COVID-19," *J Food Biochem*, vol. 2022 May 11, pp. e14219, 2022. https://doi.org/10.1111/JFBC.14219

[24] G. E. Hegazy, M. M. Abu-Serie, G. M. Agu-Elela, H. Ghozlan, S. A. Sabry, N. A. Soliman, and Y. R. Abdel-Fattah, "*In vitro* dual (anticancer and antiviral) activity of the carotenoids produced by haloalkaliphilic archaeon *Natrialba* sp. M6," *Sci Rep*, vol. 10, pp. 5986, 2020. https://doi.org/10.1038/s41598-020-62663-y

[25] S. Santoyo, L. Jaime, M. Plaza, M. Herrero, I.Rodriguez-Meizoso, E. Ibañez, and G. Reglero, "Antiviral compounds obtained from microalgae commonly used as carotenoid sources," *J Appl Phycol*, vol. 24, pp. 731–741, 2011. https://doi.org/10.1007/s10811-011-9692-1

[26] S. Fakhri, Z. Nouri, S. Z. Moradi, and M. H. Farzaei, "Astaxanthin, COVID-19 and immune response: Focus on oxidative stress, apoptosis and autophagy," *Phyther Res*, vol. 34, pp. 2790–2792, 2020. https://doi.org/10.1002/PTR.6797

[27] D. J. Kaio, P. H. Rondo, J. M. Souza, A. V Firmino, L. A. Luzia, and A. A. Segurado, "Vitamin A and beta-carotene concentrations in adults with HIV/AIDS on highly active antiretroviral therapy," *J Nutr Sci Vitaminol*, vol. 59, pp. 496–502, 2013. https://doi.org/10.3177/jnsv.59.496

[28] S. Seren, M. Mutchnick, D. Hutchinson, O. Harmanci, Y. Bayraktar, S. Mutchnick, K. Sahin, and O. Kucuk, "Potential role of lycopene in the treatment of hepatitis C and prevention of hepatocellular carcinoma," *Nutr Cancer*, vol. 60, pp. 729–735, 2008. https://doi.org/10.1080/01635580802419772

[29] J. Talukdar, B. Bhadra, T. Dattaroy, V. Nagle, and S. Dasgupta, "Potential of natural astaxanthin in alleviating the risk of cytokine storm in COVID-19," *Biomed Pharmacother*, vol. 132, pp. 110886, 2020. https://doi.org/10.1016/j.biopha.2020.110886

[30] O. Fidan, S. Mujwar, and M. Kciuk, "Discovery of adapalene and dihydrotachysterol as antiviral agents for the Omicron variant of SARS-CoV-2 through computational drug repurposing," *Mol Divers*, vol. 1, pp. 1–13, 2022. https://doi.org/10.1007/S11030-022-10440-6

[31] S. Le Pogam, H. Kang, S. F. Harris, V. Leveque, A. M. Giannetti, S. Ali, W.-R. Jiang, S. Rajyaguru, G. Tavares, C. Oshiro, T. Hendricks, K, Klumpp, J. Symons, M. F. Browner, N. Cammack, I. Nájera, "Selection and Characterization of Replicon Variants Dually Resistant to Thumb- and Palm-Binding Nonnucleoside Polymerase Inhibitors of the Hepatitis C Virus," *J Virol*, vol. 80, pp. 6146–6154, 2006. https://doi.org/10.1128/JVI.02628-05

[32] O. Trott and A. J. Olson, "AutoDock Vina: improving the speed and accuracy of docking with a new scoring function, efficient optimization, and multithreading," *J Comput Chem*, vol. 31, pp. 455–461, 2010. https://doi.org/10.1002/jcc.21334

[33] S. Mujwar and R. K. Harwansh, "*In silico* bioprospecting of taraxerol as a main protease inhibitor of SARS-CoV-2 to develop therapy against COVID-19," *Struct Chem*, vol. 1, pp. 1–12, 2022. https://doi.org/10.1007/S11224-022-01943-X

[34] M. E. O'Neill, Y. Carroll, B. Corridan, B. Olmedilla, F. Granado, I. Blanco, H. Van den Berg, I. Hininger, A. M. Rousell, M. Chopra, S. Southon, and D. I. Thurnham, "A European carotenoid database to assess carotenoid intakes and its use in a five-country comparative study," *Br J Nutr*, vol. 85, pp. 499–507, 2001. https://doi.org/10.1079/BJN2000284

[35] D. B. Rodriguez-Amaya, "Latin American food sources of carotenoids," *Arch Latinoam Nutr*, vol. 49, , pp. 74S-84S, 1999.

[36] J. M. Holden, A. L. Eldridge, G. R. Beecher, I. M. Buzzard, A. S. Bhagwat, C. S. Davis, L. W. Douglass, E. S. Gebhardt, D. Haytowitz, and S. Schakel, "Carotenoid Content of U.S. Foods: An Update of the Database," *J Food Compos Anal*, vol. 12, pp. 169–196, 1999. https://doi.org/10.1006/JFCA.1999.0827

[37] B. Setiawan, A. Sulaeman, D. W. Giraud, and J. A. Driskell, "Carotenoid Content of Selected Indonesian Fruits," *J Food Compos Anal*, vol. 14, pp. 169–176, 2001. https://doi.org/10.1006/JFCA.2000.0969

[38] A. J. Meléndez-Martínez, G. Britton, I. M. Vicario, and F. J. Heredia, "Does the carotenoid neoxanthin occur in orange juice?," *Food Chem*, vol. 107, pp. 49–54, 2008. https://doi.org/10.1016/J.FOODCHEM.2007.07.022

[39] T. Řezanka, L. Nedbalová, I. Kolouchová, and K. Sigler, "LC–MS/APCI identification of glucoside esters and diesters of astaxanthin from the snow alga *Chlamydomonas nivalis* including their optical stereoisomers," *Phytochemistry*, vol. 88, pp. 34–42, 2013. https://doi.org/10.1016/J.PHYTOCHEM.2013.01.003

[40] B. Tian and Y. Hua, "Carotenoid biosynthesis in extremophilic *Deinococcus–Thermus* bacteria," *Trends Microbiol*, vol. 18, pp. 512–520, 2010. https://doi.org/10.1016/J.TIM.2010.07.007

[41] N. J. C. Fong, M. L. Burgess, K. D. Barrow, and D. R. Glenn, "Carotenoid accumulation in the psychrotrophic bacterium *Arthrobacter agilis* in response to thermal and salt stress," *Appl Microbiol Biotechnol*, vol. 56, pp. 750–756, 2001. https://doi.org/10.1007/S002530100739

[42] M. H. Walter, D. S. Floss, and D. Strack, "Apocarotenoids: Hormones, mycorrhizal metabolites and aroma volatiles," *Planta*, vol. 232, pp. 1–17, 2010. https://doi.org/10.1007/S00425-010-1156-3

[43] E. H. Harrison and L. Quadro, "Apocarotenoids: Emerging Roles in Mammals," *Annu Rev Nutr*, vol. 38, pp. 153–172, 2018. https://doi.org/10.1146/ANNUREV-NUTR-082117-051841

[44] S. M. C, A. Treesa Mathew, S. Rekha, P. G. R, and C. Author, "Apocarotenoids: A Brief Review," *Int J Res Rev*, vol. 7, pp. 252–256, 2020.

[45] S. A. Cherrak, H. Merzouk, and N. Mokhtari-Soulimane, "Potential bioactive glycosylated flavonoids as SARS-CoV-2 main protease inhibitors: A molecular docking and simulation studies," *PLoS One*, vol. 15, pp. e0240653, 2020. https://doi.org/10.1371/JOURNAL.PONE.0240653

[46] S. I. Elshahawi, K. A. Shaaban, M. K. Kharel, and J. S. Thorson, "A comprehensive review of glycosylated bacterial natural products," *Chem Soc Rev*, vol. 44, pp. 7591–7697, 2015. https://doi.org/10.1039/C4CS00426D

[47] S. Fakhri, Z. Nouri, S. Z. Moradi, and M. H. Farzaei, "Astaxanthin, COVID-19 and immune response: Focus on oxidative stress, apoptosis and autophagy," *Phytother Res*, vol. 34, pp. 2790–2792, 2020. https://doi.org/10.1002/ptr.6797

[48] S. Fakhri, F. Abbaszadeh, L. Dargahi, and M. Jorjani, "Astaxanthin: A mechanistic review on its biological activities and health benefits," *Pharmacol Res*, vol. 136, pp. 1–20, 2018. https://doi.org/10.1016/J.PHRS.2018.08.012

[49] J. Talukdar, B. Bhadra, T. Dattaroy, V. Nagle, and S. Dasgupta, "Potential of natural astaxanthin in alleviating the risk of cytokine storm in COVID-19," *Biomed Pharmacother*, vol. 132, pp. 110886, 2020. https://doi.org/10.1016/J.BIOPHA.2020.110886

[50] A. A. Mentis, M. Dalamaga, C. Lu, and M. G. Polissiou, "Saffron for 'toning down' COVID-19-related cytokine storm: Hype or hope? A mini-review of current evidence," *Metab Open*, vol. 11, pp. 100111, 2021. https://doi.org/10.1016/j.metop.2021.100111

[51] S. K. Yim, I. Kim, B. Warren, J. Kim, K. Jung, and B. Ku, "Antiviral Activity of Two Marine Carotenoids against SARS-CoV-2 Virus Entry *In Silico* and *In Vitro*," *Int J Mol Sci*, vol. 22, pp. 6481, 2021. https://doi.org/10.3390/ijms22126481

[52] A. P. Rumengan, E. S. Mandiangan, W. A. Tanod, D. S. J. Paransa, C. P. Paruntu, and D. M. H. Mantiri, "Identification of pigment profiles and antioxidant activity of Rhizophora mucronata mangrove leaves origin Lembeh, North Sulawesi, Indonesia," *Biodiversitas J Biol Divers*, vol. 22, pp. 2805–2816, 2021. https://doi.org/10.13057/BIODIV/D220730

[53] C. Giossi, P. Cartaxana, and S. Cruz, "Photoprotective Role of Neoxanthin in Plants and Algae," *Molecules*, vol. 25, pp. 4617, 2020. https://doi.org/10.3390/MOLECULES25204617

[54] H. Ibrahim, M. Shaaban, A. A. M. Hanafi, and K. M. Abdulsalam, "Inhibition of bacteria isolated from human specimens by selected marine-origin extracts," *Egypt J Exp Biol (Bot)*, vol. 16, pp. 91–103, 2020. https://doi.org/10.5455/egyjebb.20200509032540

[55] S. U. Kadam and P. Prabhasankar, "Marine foods as functional ingredients in bakery and pasta products," *Food Res Int*, vol. 43, pp. 1975–1980, 2010. https://doi.org/110.1016/J.FOODRES.2010.06.007

[56] T. M. Karpiński, M. Kwaśniewski, M. Ożarowski, and R. Alam, "*In silico* studies of selected xanthophylls as potential candidates against SARS-CoV-2 targeting main protease (Mpro) and papain-like protease (PLpro)," *Herba Pol*, vol. 67, pp. 1–8, 2021. https://doi.org/10.2478/hepo-2021-0009

[57] S. Soleymani, R. Zabihollahi, S. Shahbazi, and A. Bolhassani, "Antiviral Effects of Saffron and its Major Ingredients," *Curr Drug Deliv*, vol. 15, pp. 698–704, 2018. https://doi.org/10.2174/1567201814666171129210654